

STRUCTURAL PERFORMANCE OF CONCRETE-FILLED COLD-FORMED STAINLESS STEEL MEMBERS

By

LI Lianghao

李良浩

B.Eng. (Hons)

The University of Hong Kong

A thesis submitted in partial fulfilment of the requirements for
the Degree of Doctor of Philosophy
at The University of Hong Kong

July 2017



Abstract of thesis entitled

STRUCTURAL PERFORMANCE OF CONCRETE-FILLED COLD-FORMED STAINLESS STEEL MEMBERS

Submitted by

LI Lianghao

For the Degree of Doctor of Philosophy at The University of Hong Kong
in July 2017

The structural performance of concrete-filled cold-formed stainless steel members has been investigated in this study. The current design rules for concrete-filled steel tubular members are applicable to carbon steel only and these design rules may not be appropriate for stainless steel. The structural performance of concrete-filled cold-formed stainless steel members was investigated using stub column, beam and beam-column tests. Cold-formed ferritic stainless steel square and rectangular hollow sections of grade EN 1.4003 and cold-formed austenitic stainless steel circular hollow sections of grade EN 1.4301 were used to fabricate the composite members. Concrete of nominal cylinder compressive strengths 40, 80 and 120 MPa were filled into the stainless steel tubes.

The experimental investigation included material tests, stub column, beam and beam-column tests. The test program consists of one square hollow section, four rectangular hollow sections and four circular hollow sections. Tensile coupons were extracted from each hollow section and tested to determine the corresponding material properties. In addition, the material properties of cold-formed ferritic stainless steel at elevated temperatures ranged from 22 – 1000 °C were also obtained by coupon tests. Flexural behaviour of cold-formed ferritic stainless steel square and rectangular hollow sections under four-point bending



was also investigated, and new slenderness limits for section classification are proposed. A total of 22 stub column tests were carried out on concrete-filled cold-formed ferritic stainless steel square and rectangular hollow sections, and another 18 stub column tests were also conducted on concrete-filled cold-formed austenitic stainless steel circular hollow sections. The test program for beams included 23 concrete-filled cold-formed ferritic stainless steel square and rectangular members and 18 concrete-filled cold-formed austenitic stainless steel circular members. The beam-column tests were conducted on concrete-filled cold-formed ferritic stainless steel square and rectangular sections and a total of 48 specimens were bent about minor axis to determine the structural behaviour under combined axial load and bending conditions.

Accurate finite element models were developed and verified against the experimental results. The finite element models were used to perform extensive parametric studies in order to provide complementary data to facilitate the development of design rules. The extensive parametric studies included 165 stub columns, 171 beams and 239 beam-columns, for concrete-filled cold-formed ferritic stainless steel square and rectangular hollow sections as well as 168 stub columns and 165 beams for concrete-filled cold-formed austenitic stainless steel circular hollow sections.

The experimental and numerical results as well as available data from the literature were used to assess the applicability of current design specifications, including the American specification, European code and Australian standard designated for concrete-filled carbon steel tubular members, to concrete-filled stainless steel tubular members. Improved design rules are proposed in this study. In addition, the material properties of ferritic stainless steel at elevated temperatures and the slenderness limits on classification of ferritic stainless steel hollow sections specified in the European code were also examined. The current design rules and proposed design rules were evaluated by reliability analysis.

(484 words)



DECLARATION

I declare that this thesis represents my own work, except where due acknowledgement is made, and that it has not been previously included in a thesis, dissertation or report submitted to this University or to any other institution for a degree, diploma or other qualification.

Signed _____

LI Lianghao



ACKNOWLEDGEMENTS

Foremost, the author would like to express my sincere gratitude to my supervisor Prof. Ben Young for the guidance throughout my PhD study and research. Special thanks are due for the patience, motivation, insightful advice and immense knowledge received from Prof. Ben Young over the past four years of study.

The author would like to acknowledge the financial support from The University of Hong Kong through the HKU Foundation Postgraduate Fellowship during the period of study. In addition, the seed funding programme for basic research provided by The University of Hong Kong is gratefully acknowledged.

Many thanks to my friends and colleagues at The University of Hong Kong, in particular Dr. HUANG Yuner, Dr. CAI Yancheng, Dr. ZHANG Jiahui, Dr. SU Meini, Dr. WANG Liping, Dr. ZHAO Ou, Dr. MA Jialin, Mr. LI Haiting and Mr. CHEN Mantai, for their kind suggestions and valuable discussions upon the research work.

The experimental work was conducted at the Structure Laboratory in the Department of Civil Engineering, The University of Hong Kong. The author would like to thank all the technicians who contributed to the work. The author is grateful to STALA Tube Finland for supplying the stainless steel test specimens.

Last but not least, the author would like to express heartfelt thankfulness to the author's parents and sister for their continuous support and unconditional love.



TABLE OF CONTENTS

DECLARATION	iii
ACKNOWLEDGEMENTS	iv
TABLE OF CONTENTS.....	v
LIST OF FIGURES	xv
LIST OF TABLES.....	xx
LIST OF NOTATIONS	xviii

CHAPTER 1 INTRODUCTION 1

1.1 BACKGROUND	1
1.2 OBJECTIVES.....	2
1.3 OUTLINE OF THE THESIS	4

CHAPTER 2 LITERATURE REVIEW 7

2.1 GENERAL	7
2.2 AXIALLY-LOADED CFST COLUMNS	7
2.2.1 Confinement effect	7
2.2.2 Local buckling of steel tube.....	9
2.2.3 Influence of concrete strength.....	10
2.2.4 Influence of yield strength of steel	12
2.3 BEHAVIOUR OF CFST BEAM-COLUMNS	13
2.4 CONFINED CONCRETE MODELS	17
2.5 CONCLUDING REMARKS	21

CHAPTER 3 MATERIAL PROPERTIES OF STAINLESS

STEEL 23

3.1 INTRODUCTION	23
3.2 MATERIAL PROPERTIES AT ROOM TEMPERATURE	24



3.2.1	Cold-formed ferritic stainless steel	24
3.2.1.1	<i>Flat coupon tests</i>	25
3.2.1.2	<i>Corner coupon tests</i>	26
3.2.2	Cold-formed austenitic stainless steel.....	27
3.3	MATERIAL PROPERTIES OF COLD-FORMED FERRITIC STAINLESS STEEL AT ELEVATED TEMPERATURES	28
3.3.1	Test devices.....	28
3.3.2	Test specimens	29
3.3.3	Test procedure.....	30
3.3.3.1	<i>Steady state tests</i>	30
3.3.3.2	<i>Transient state tests</i>	31
3.3.4	Test results	31
3.3.4.1	<i>General</i>	31
3.3.4.2	<i>Elastic modulus</i>	33
3.3.4.3	<i>Yield strength</i>	34
3.3.4.4	<i>Ultimate strength</i>	34
3.3.4.5	<i>Ductility</i>	35
3.3.4.6	<i>Thermal expansion in transient state test</i>	35
3.3.4.7	<i>Vickers hardness test for tested specimens</i>	36
3.3.5	Design proposal for material properties.....	37
3.3.5.1	<i>Predictive equations for material properties at elevated temperatures</i>	37
3.3.5.2	<i>Reliability analysis</i>	38
3.3.5.2.1	<i>ASCE approach</i>	38
3.3.5.2.2	<i>Eurocode approach</i>	39
3.3.5.3	<i>Comparisons of experimental and predicted strengths</i>	40
3.4	CONCLUDING REMARKS	43

CHAPTER 4 CLASSIFICATION AND FLEXURAL BEHAVIOUR OF COLD-FORMED FERRITIC STAINLESS STEEL SHS & RHS 66

4.1	INTRODUCTION	66
-----	--------------------	----



4.2	EXPERIMENTAL INVESTIGATION.....	67
4.2.1	Test specimens	67
4.2.2	Test setup and operation	68
4.2.3	Test results	69
4.3	FINITE ELEMENT MODEL AND VERIFICATION	70
4.3.1	Finite element model	70
4.3.2	Boundary and loading conditions	71
4.3.3	Material model.....	72
4.3.4	Verification of finite element model.....	73
4.3.5	Parametric study	73
4.4	RELIABILITY ANALYSIS	74
4.5	ASSESSMENT OF EXISTING SLENDERNESS LIMITS.....	76
4.5.1	General.....	76
4.5.2	Slenderness limits for Class 3 cross-sections	76
4.5.3	Slenderness limits for Class 2 cross-sections	78
4.5.4	Slenderness limits for Class 1 cross-sections	78
4.6	COMPARISON OF MOMENT CAPACITIES.....	79
4.6.1	General.....	79
4.6.2	American Specification and Australian/New Zealand Standard	80
4.6.3	European Code.....	83
4.6.4	Direct strength method.....	84
4.6.5	Continuous strength method	87
4.7	CONCLUDING REMARKS	87

CHAPTER 5 STUB COLUMN BEHAVIOUR OF CONCRETE-FILLED COLD-FORMED FERRITIC STAINLESS STEEL SHS & RHS .. 103

5.1	INTRODUCTION	103
5.2	EXPERIMENTAL INVESTIGATION.....	104
5.2.1	Test specimens	104
5.2.2	Geometric imperfection measurements	106
5.2.3	Stub column tests	107



5.3	EXPERIMENTAL RESULTS AND DISCUSSION	108
5.3.1	Axial load-strain curves	108
5.3.2	Typical failure modes	109
5.3.3	Effect of local buckling.....	110
5.3.4	Effect of concrete strength.....	111
5.3.5	Ductility index	111
5.4	FINITE ELEMENT MODEL AND VERIFICATION	112
5.4.1	General.....	112
5.4.2	Boundary and loading conditions	112
5.4.3	Material modelling of cold-formed ferritic stainless steel tubes	113
5.4.4	Material modelling of concrete.....	113
5.4.5	Modelling of concrete-stainless steel tube interface.....	115
5.4.6	Verification of finite element model.....	116
5.5	PARAMETRIC STUDY	116
5.6	RELIABILITY ANALYSIS	117
5.7	COMPARISON BETWEEN TEST AND CODE PREDICTED STRENGTHS	118
5.7.1	General.....	118
5.7.2	AISC 360	118
5.7.3	ACI 318.....	120
5.7.4	Eurocode 4	121
5.7.5	AS 5100.6	122
5.8	CONCLUDING REMARKS	122

CHAPTER 6 STUB COLUMN BEHAVIOUR OF CONCRETE-FILLED COLD-FORMED AUSTENITIC STAINLESS STEEL CHS 137

6.1	INTRODUCTION	137
6.2	EXPERIMENTAL INVESTIGATION.....	138
6.2.1	General.....	138
6.2.2	Instrumentation and test setup	139
6.3	EXPERIMENTAL RESULTS AND DISCUSSION	140



6.3.1	Axial load behaviour of stub columns	140
6.3.2	Test results	141
6.3.3	Effect of infill concrete	142
6.4	NUMERICAL MODELLING.....	143
6.4.1	General.....	143
6.4.2	Material properties.....	143
6.4.2.1	<i>Stainless steel</i>	143
6.4.2.2	<i>Confined concrete model</i>	144
6.4.3	Boundary conditions and element types	146
6.4.4	Modelling of concrete-stainless steel tube interface.....	147
6.4.5	Verification of finite element model.....	148
6.5	PARAMETRIC STUDY	148
6.6	RELIABILITY ANALYSIS	149
6.7	COMPARISON BETWEEN TEST AND CODE PREDICTED STRENGTHS	150
6.7.1	General.....	150
6.7.2	AISC 360	150
6.7.3	ACI 318.....	152
6.7.4	Eurocode 4	153
6.7.5	AS 5100.6	154
6.8	CONCLUDING REMARKS	155

CHAPTER 7 FLEXURAL BEHAVIOUR OF CONCRETE- FILLED COLD-FORMED FERRITIC STAINLESS STEEL SHS & RHS..... 168

7.1	INTRODUCTION	168
7.2	EXPERIMENTAL INVESTIGATION.....	170
7.3	TEST RESULTS AND DISCUSSION	171
7.3.1	Moment-curvature curves	171
7.3.2	Relative horizontal movement of concrete to stainless steel tube ...	173
7.3.3	Flexural stiffness	174
7.4	FINITE ELEMENT MODEL AND VERIFICATION	175



7.4.1	Element and mesh.....	175
7.4.2	Material modelling of cold-formed ferritic stainless steel tubes	175
7.4.3	Material modelling of confined concrete.....	176
7.4.4	Boundary and loading conditions	177
7.4.5	Interaction of contact surface between concrete infill and stainless steel tube	178
7.4.6	Verification of the finite element model.....	178
7.5	PARAMETRIC STUDY	179
7.6	RELIABILITY ANALYSIS	179
7.7	COMPARISON BETWEEN TEST AND CODE PREDICTED STRENGTHS	180
6.7.1	General.....	180
6.7.2	AISC 360	181
6.7.3	ACI 318.....	183
6.7.4	Eurocode 4.....	184
6.7.5	AS 5100.6	185
6.7.6	Method proposed by Han (2004) and modification of Han's method	185
7.8	CONCLUDING REMARKS	186

CHAPTER 8 FLEXURAL BEHAVIOUR OF CONCRETE- FILLED COLD-FORMED AUSTENITIC STAINLESS STEEL CHS..... 200

8.1	INTRODUCTION	200
8.2	EXPERIMENTAL INVESTIGATION.....	201
8.2.1	General.....	201
8.2.2	Specimens	202
8.2.3	Four-point bending tests	202
8.3	TEST RESULTS AND DISCUSSION	203
8.3.1	Moment-curvature curves.....	203
8.3.2	Flexural stiffness.....	204
8.4	FINITE ELEMENT MODEL VERIFICATION.....	205



8.4.1	Finite element model	205
8.4.2	Verification of finite element model.....	208
8.5	PARAMETRIC STUDY	208
8.6	RELIABILITY ANALYSIS	209
8.7	COMPARISON BETWEEN TEST AND CODE PREDICTED STRENGTHS	210
8.7.1	General.....	210
8.7.2	AISC 360	211
8.7.3	ACI 318.....	212
8.7.4	Eurocode 4.....	213
8.7.5	AS 5100.6	213
8.7.6	Method proposed by Han (2004) and modification of Han's method	214
8.8	CONCLUDING REMARKS	215

CHAPTER 9 BEAM-COLUMN BEHAVIOUR OF CONCRETE-FILLED COLD-FORMED FERRITIC STAINLESS STEEL SHS & RHS .. 228

9.1	INTRODUCTION	228
9.2	EXPERIMENTAL INVESTIGATION.....	229
9.2.1	General.....	229
9.2.2	Material testing	230
9.2.3	Test specimens	230
9.2.4	Imperfection measurements.....	232
9.2.5	Beam-column tests.....	232
9.2.6	Determination of loading eccentricities	234
9.3	EXPERIMENTAL RESULTS	235
9.3.1	Failure mode and ultimate loads.....	235
9.3.2	Load-deformation behaviour	235
9.3.3	Confinement factor	236
9.3.4	Strength index	237
9.3.5	Ductility index	237



9.4	FINITE ELEMENT MODEL VERIFICATION.....	238
9.4.1	Development of finite element model	238
9.4.2	Element types.....	238
9.4.3	Material modelling.....	239
9.4.4	Boundary conditions	240
9.4.5	Interaction of contact surface between concrete infill and stainless steel tube	240
9.4.6	Global imperfections and loading conditions	241
9.4.7	Validation of finite element model	242
9.5	PARAMETRIC STUDY	243
9.6	RELIABILITY ANALYSIS	245
9.6.1	AISC approach.....	245
9.6.2	Eurocode approach	247
9.7	COMPARISON BETWEEN TEST AND CODE PREDICTED STRENGTHS	248
9.7.1	General.....	248
9.7.2	AISC 360	249
9.7.3	Eurocode 4.....	252
9.7.4	Proposed equations by Lai et al. (2015)	255
9.7.5	Proposed equations by Choi et al. (2006).....	257
9.7.6	Modified design method	258
9.8	CONCLUDING REMARKS	259

CHAPTER 10 CONCLUSIONS..... 292

10.1	EXPERIMENTAL STUDY	292
10.2	NUMERICAL STUDY	293
10.3	DESIGN RECOMMENDATIONS.....	294
10.4	FUTURE RESEARCH.....	297

REFERENCES 298



APPENDIX A STRESS-STRAIN CURVES OF COLD-FORMED STAINLESS STEEL BY TENSILE COUPON TESTS	315
APPENDIX B COLD-FORMED FERRITIC STAINLESS STEEL HOLLOW SECTIONS BEAM TESTS	323
APPENDIX C CONCRETE-FILLED COLD-FORMED FERRITIC STAINLESS STEEL STUB COLUMNS.....	334
APPENDIX D CONCRETE-FILLED COLD-FORMED AUSTENITIC STAINLESS STEEL STUB COLUMNS.....	346
APPENDIX E CONCRETE-FILLED COLD-FORMED FERRITIC STAINLESS STEEL FLEXURAL MEMBERS	354
APPENDIX F CONCRETE-FILLED COLD-FORMED AUSTENITIC STAINLESS STEEL FLEXURAL MEMBERS	367



APPENDIX G CONCRETE-FILLED COLD-FORMED FERRITIC STAINLESS STEEL BEAM COLUMN.....	375
PUBLICATIONS.....	400



LIST OF FIGURES

Figure 3.1:	Locations of tensile flat and corner coupons in the cross-sections.....	54
Figure 3.2:	Static stress-strain curves obtained from tensile coupon tests in flat portions	54
Figure 3.3:	Static stress-strain curves obtained from tensile coupon tests in corner portions	55
Figure 3.4:	Locations of tensile curved coupons in the circular cross-sections.....	55
Figure 3.5:	Static stress-strain curves obtained from tensile coupon tests in curved portions	56
Figure 3.6:	Test set-up.....	57
Figure 3.7:	Locations of coupons and welds in RHS $100 \times 40 \times 2$ and $80 \times 60 \times 4$	58
Figure 3.8:	Dimensions of coupon specimen	59
Figure 3.9:	Definition of symbols	59
Figure 3.10:	Stress-strain curves of section $80 \times 60 \times 4$ at different temperatures obtained from coupon tests by transient state method	60
Figure 3.11:	Stress-strain curves of section $100 \times 40 \times 2$ at different temperatures obtained from coupon tests by transient state method	60
Figure 3.12:	Comparison of elastic modulus reduction factors.....	61
Figure 3.13:	Comparison of yield strength reduction factors.....	61
Figure 3.14:	Comparison of ultimate strength reduction factors.....	62
Figure 3.15:	Stress-strain curves of section $80 \times 60 \times 4$ obtained from steady state tests	62
Figure 3.16:	Stress-strain curves of section $100 \times 40 \times 2$ obtained from steady state tests.....	63



Figure 3.17:	Failed ferritic stainless steel coupon specimens of section 80×60×4 at various temperatures obtained from steady state tests	63
Figure 3.18:	Failed ferritic stainless steel coupon specimens of section 100×40×2 at various temperatures obtained from steady state tests	64
Figure 3.19:	Thermal expansion of ferritic stainless steel grade EN 1.4003 at elevated temperatures.....	64
Figure 3.20:	Vickers Hardness test results of tested specimens by steady state test.....	65
Figure 4.1:	Four-point bending test setup	95
Figure 4.2:	Moment-curvature curves of tested specimens.....	96
Figure 4.3:	Locations of κ_{pl} , $\hat{\kappa}_{pl}$ and definition of rotation capacity on moment-curvature curve of specimen 120×80×3	97
Figure 4.4:	Corner material property extended beyond the corner region of the cross-sections.....	97
Figure 4.5:	Class 3 limit of element subject to compression.....	98
Figure 4.6:	Class 3 limit of element subject to bending	98
Figure 4.7:	Class 2 limit of element subject to compression.....	99
Figure 4.8:	Class 2 limit of element subject to bending	99
Figure 4.9:	Class 1 limit of element subject to bending	100
Figure 4.10:	Class 1 limit of element subject to compression.....	100
Figure 4.11:	Comparison of experimental and numerical results with nominal strengths by ASCE and AS/NZS	101
Figure 4.12:	Comparison of experimental and numerical results with nominal strengths by EC3	101
Figure 4.13:	Comparison of experimental and numerical results with nominal strengths by modified EC3	102
Figure 4.14:	Comparison of experimental and numerical results with nominal strengths by DSM	102
Figure 5.1:	Measured local plate imperfection profiles for Section 100×40×2.....	128



Figure 5.2:	Schematic test arrangement for stub column tests: (a) arrangement for strain gauges; (b) arrangement for LVDTs ...	129
Figure 5.3:	Axial load-strain response for series 60×40×4 stub columns ..	130
Figure 5.4:	Axial load-strain response for series 60×60×3 stub columns ..	131
Figure 5.5:	Axial load-strain response for series 80×60×4 stub columns ..	131
Figure 5.6:	Axial load-strain response for series 100×40×2 stub columns	132
Figure 5.7:	Axial load-strain response for series 120×80×3 stub columns	132
Figure 5.8:	Failure modes of stub columns	133
Figure 5.9:	Vertical tangent method for specimen 100×40×2C40.....	134
Figure 5.10:	Extension of corner material properties to flat portions	135
Figure 5.11:	Typical stress-strain curve for confined concrete	135
Figure 5.12:	Comparison of experimental and AISC predicted strengths ...	135
Figure 5.13:	Comparison of experimental and EC4 predicted strengths	136
Figure 6.1:	Locations of strain gauge in the cross-section	160
Figure 6.2:	Test arrangement for stub column tests	161
Figure 6.3:	Axial load-strain curves	162
Figure 6.4:	Definition of ultimate strengths corresponding to different strain levels	164
Figure 6.5:	Normalized ultimate axial loads	164
Figure 6.6:	Discontinuity of existing confined concrete model and proposal of new model.....	165
Figure 6.7:	Mesh of finite element model	165
Figure 6.8:	Comparison of experimental and numerical strengths with AISC 360 (2010) predicted strengths	166
Figure 6.9:	Comparison of experimental and numerical strengths with AS 5100.6 (2004) predicted strengths	166
Figure 6.10:	Comparison of experimental and numerical strengths with modified AS 5100 predicted strengths.....	167
Figure 7.1:	Schematic setup of four-point bending test	195
Figure 7.2:	Moment-curvature curves of section 60×40×4.....	195
Figure 7.3:	Moment-curvature curves of section 60×60×3.....	196
Figure 7.4:	Moment-curvature curves of section 100×40×2.....	196
Figure 7.5:	Moment-curvature curves of section 120×80×3.....	197



Figure 7.6:	Relative movement-moment-curvature curve of specimen 80×120×3C80	197
Figure 7.7:	Comparison of experimental and AISC predicted strength	198
Figure 7.8:	γ_m and ζ relationship for the modified Han's method	199
Figure 8.1:	Test arrangement for four-point bending tests.....	221
Figure 8.2:	Stiffening at support.....	222
Figure 8.3:	Moment-curvature curves of Section 60.5×2.8	222
Figure 8.4:	Moment-curvature curves of Section 76.3×3.0	223
Figure 8.5:	Moment-curvature curves of Section 114.3×3.0	223
Figure 8.6:	Moment-curvature curves of Section 165.2×3.0	224
Figure 8.7:	Stress blocks used to calculate the flexural strength of circular CFT beam	225
Figure 8.8:	Comparison of experimental and numerical strengths with AISC 360 (2010) predicted strengths	226
Figure 8.9:	Comparison of experimental and numerical strengths with EC4 (2004) predicted strengths	226
Figure 8.10:	Comparison of experimental and numerical strengths with Han's (2004) predicted strengths	227
Figure 8.11:	Comparison of experimental and numerical strengths with Modified Han method predicted strengths.....	227
Figure 9.1:	Locations of tensile corner and flat coupons in the cross- sections.....	274
Figure 9.2:	Sign convention and location of global geometric imperfection measurements	274
Figure 9.3:	Schematic arrangement for beam-column tests for series 40×60×4, 60×60×3 and 40×100×2	275
Figure 9.4:	Schematic arrangement for beam-column tests for series 80×120×3.....	276
Figure 9.5:	Arrangement of strain gauges for beam-column tests	277
Figure 9.6:	Flexural buckling of series 40×60×4C80	277
Figure 9.7:	Axial load versus moment curves for combined loading tests	278
Figure 9.8:	Load-deflection behaviour of series 80×120×3C40	282
Figure 9.9:	Effect of the relative strength ratio on the shape of the P-M interaction curve	283



Figure 9.10:	Extension of corner material properties to flat portions	284
Figure 9.11:	Experimental and numerical load-lateral deflection at mid-height curves for typical combined loading specimens	285
Figure 9.12:	Definition of N_u and $N_{u,prep}$ on the beam-column interaction curve.....	286
Figure 9.13:	Different form of interaction curve for CFT beam-columns ...	286
Figure 9.14:	Comparison with AISC Method-1 predicted strengths.....	287
Figure 9.15:	Comparison with AISC Method-2 predicted strengths.....	288
Figure 9.16:	Comparison with EC4 predicted strengths	289
Figure 9.17:	Example of determination of design resistance from EC4 for specimen 60×60×3C40e8	290
Figure 9.18:	The predictions from EC4 versus different e/D ratio	291
Figure 9.19:	Comparison with modified predicted member strengths	291



LIST OF TABLES

Table 2.1	Parameters for the CFST concrete stress-strain model in compression.....	22
Table 3.1	Mill certificate data for virgin coil material (from Stalatube)....	45
Table 3.2	Tensile flat coupon test results of cold-formed ferritic stainless steel	45
Table 3.3	Tensile corner coupon test results of cold-formed ferritic stainless steel.....	45
Table 3.4	Tensile coupon test results of cold-formed austenitic stainless steel	45
Table 3.5	Material properties obtained from steady state tests at ambient temperature.....	46
Table 3.6	Material properties obtained from transient state tests at ambient temperature.....	46
Table 3.7	Elastic modulus and reduction factors at elevated temperatures obtained from steady state tests.....	47
Table 3.8	Elastic modulus and reduction factors at elevated temperatures obtained from transient state tests.....	48
Table 3.9	Reduction factors of yield strength of section 80×60×4 obtained from steady state tests	48
Table 3.10	Reduction factors of yield strength of section 100×40×2 obtained from steady state tests	49
Table 3.11	Strength reduction factors obtained from transient state tests ...	50
Table 3.12	Reduction factors of ultimate strength obtained from steady state tests.....	51
Table 3.13	Ductility of ferritic stainless steel obtained from steady state tests	51
Table 3.14	Ductility of ferritic stainless steel obtained from steady state tests	52
Table 3.15	Ductility of ferritic stainless steel obtained from steady state tests	52

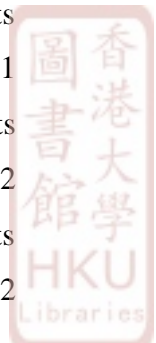


Table 3.16	Ductility of ferritic stainless steel obtained from steady state tests	52
Table 3.17	Reliability analysis for different design rules by ASCE approach	53
Table 3.18	Reliability analysis for different design rules by Eurocode approach	53
Table 4.1	Measure dimensions of the beam specimens	89
Table 4.2	Comparison of test strengths with finite element analysis results	90
Table 4.3	Parametric study results	91
Table 4.4	Comparison of the experimental and numerical results with the nominal moment capacities.....	93
Table 4.5	Comparison of the experimental and numerical results with the nominal moment capacities.....	94
Table 5.1	Measure dimensions of the stub column specimens	124
Table 5.2	Measure local buckling strengths of the stub column specimens	124
Table 5.3	Results for ultimate load, ultimate strain, ductility index, FEA results and ratio of N_{Exp} / N_{FEA}	125
Table 5.4	Parametric study results	126
Table 5.5	Comparison of test and FEA strengths with design strengths for all specimens	127
Table 5.6	Limits in current design rules for rectangular CFST columns .	127
Table 6.1	Measured specimen dimensions.....	156
Table 6.2	Experimental test results	157
Table 6.3	Parametric study results	158
Table 6.4	Comparison of test and FEA strengths with design strengths for all specimens	159
Table 7.1	Measured dimensions of the stub column specimens	188
Table 7.2	Experimental results	189
Table 7.3	Flexural stiffness results.....	190
Table 7.4	Parametric study results	191

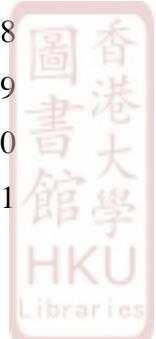


Table 7.5	Comparison of test and FEA strengths with design strengths for all specimens	193
Table 7.6	Slenderness limits for rectangular CFST members.....	193
Table 7.7	Comparison of the tests and numerical results with the design moment capacities.....	194
Table 8.1	Measured dimensions of the stub column specimens	217
Table 8.2	Experimental results and comparisons.....	218
Table 8.3	Parametric study results	219
Table 8.4	Comparison of test and FEA strengths with design strengths..	220
Table 9.1	Specimen dimensions and measured eccentricities of series RHS 40×60×4	260
Table 9.2	Specimen dimensions and measured eccentricities of series RHS 60×60×3	261
Table 9.3	Specimen dimensions and measured eccentricities of series RHS 40×100×2	262
Table 9.4	Specimen dimensions and measured eccentricities of series RHS 80×120×3	263
Table 9.5	Measured global geometric imperfections at mid-length.....	264
Table 9.6	Experimental results	265
Table 9.7	Comparison of the test failure loads with FE failure loads for varying imperfection amplitudes.....	266
Table 9.8	Parametric study results for specimens tested against cross section strength.....	268
Table 9.9	Parametric study results for specimens tested against member strength.....	270
Table 9.10	Reliability analysis for different design rules by AISC approach	272
Table 9.11	Reliability analysis for different design rules by Eurocode approach	272
Table 9.12	Slenderness limits in AISC 360 (2010).....	273



LIST OF NOTATIONS

All symbols are defined where they first appear in the text. In most cases only one meaning has been assigned to each symbol, but where this is not the case, the interpretation will be provided in the text. The symbols are listed as follows:

a	Coefficient used in the proposed predictive equation
A_c	Cross-sectional area of concrete
A_s	Cross-sectional area of steel section
B	Overall width of cross-section
b	Flat width of the flange
COV	Coefficient of variation
C_p	Correction factor
C_y	Compression strain factor in American Specification and Australian/New Zealand Standard
c	Coefficient used in the proposed predictive equation
D	Overall depth of cross-section
DI	Ductility index
d	Flat portion of the web
d_{\max}	The maximum diameter of the coarse aggregate
d_w	Depth of the compressed portion of the web
e	Initial loading eccentricity
e_0	Nominal loading eccentricity
E_c	Initial elastic modulus of concrete
E_o	Initial elastic modulus
E_T	Initial elastic modulus at temperature $T^\circ\text{C}$
EI	Flexural rigidity of the cross-section about the plane of bending



EI_{ACI}	Unfactored predicted flexural stiffness by the American concrete institute
EI_{AISC}	Unfactored predicted flexural stiffness by the American Institute of Steel Construction
EI_{AS5100}	Unfactored predicted flexural stiffness by the Australian Code
EI_{EC4}	Unfactored predicted flexural stiffness by the European Code
f_{bo} / f_c'	Ratio of the compressive strength to uniaxial compressive strength
f_c'	Cylinder compressive strength of concrete
f_{cu}	Cubic compressive strength of concrete
f_{cr}	Critical elastic buckling stress for steel tube
F_m	Mean value of fabrication factor
f_r	Residual stress of concrete
f_y	Yield strength at ambient temperature
$f_{y,T}$	Yield strength at temperature $T^\circ\text{C}$
f_u	Ultimate strength at ambient temperature
$f_{u,T}$	Ultimate strength at temperature $T^\circ\text{C}$
$f_{0.01}$	Strength at 0.01% strain at ambient temperature
$f_{0.5}$	Strength at 0.5% strain at ambient temperature
$f_{0.5,T}$	Strength at 0.5% strain at temperature $T^\circ\text{C}$
$f_{1.0}$	Strength at 1.0% strain at ambient temperature
$f_{1.0,T}$	Strength at 1.0% strain at temperature $T^\circ\text{C}$
$f_{1.5}$	Strength at 1.5% strain at ambient temperature
$f_{1.5,T}$	Strength at 1.5% strain at temperature $T^\circ\text{C}$
$f_{2.0}$	Strength at 2.0% strain at ambient temperature
$f_{2.0,T}$	Strength at 2.0% strain at temperature $T^\circ\text{C}$
G_F	Fracture energy
I_c	Moment of inertia of concrete section
I_s	Moment of inertia of steel section



K	Plate buckling coefficient
K_c	Ratio of the second stress invariant on the tensile meridian to that on the compressive meridian
$k_{d,n}$	Design (ultimate limit state) fractile factor
k_E	Reduction factor of elastic modulus at elevated temperatures
$k_{E,Chen\&Young}$	Reduction factor of elastic modulus at elevated temperatures predicted by Chen and Young (2006)
$k_{E,EC3}$	Reduction factor of elastic modulus at elevated temperatures predicted by EC3 (2005b)
$k_{E,Proposed}$	Reduction factor of elastic modulus at elevated temperatures predicted by proposed equation
$k_{E,Test}$	Reduction factor of elastic modulus at elevated temperatures obtained from test results
k_u	Reduction factor of ultimate strength at elevated temperatures
$k_{u,Chen\&Young}$	Reduction factor of ultimate strength at elevated temperatures predicted by Chen and Young (2006)
$k_{u,EC3}$	Reduction factor of ultimate strength at elevated temperatures predicted by EC3 (2005b)
$k_{u,Proposed}$	Reduction factor of ultimate strength at elevated temperatures predicted by proposed equation
k_y	Reduction factor of yield strength at elevated temperatures
$k_{y,Chen\&Young}$	Reduction factor of yield strength at elevated temperatures predicted by Chen and Young (2006)
$k_{y,EC3}$	Reduction factor of yield strength at elevated temperatures predicted by EC3 (2005b)
$k_{y,Proposed}$	Reduction factor of yield strength at elevated temperatures predicted by proposed equation
L	Length of specimen
L_e	Effective length of specimen
m	Coefficient used in the proposed predictive equation



M_{ACI}	Unfactored design moment capacity predicted by the American concrete institute
M_{AISC}	Unfactored design moment capacity predicted by the American Institute of Steel Construction
M_{AS5100}	Unfactored design moment capacity predicted by the Australian Code
M_{crl}	Critical elastic local buckling moment
M_{DSM}	Nominal moment capacity (Unfactored design moment capacity) predicted by the direct strength method
$M_{DSM,H\&Y}$	Nominal moment capacity (Unfactored design moment capacity) predicted by the modified direct strength method by Huang and Young
M_d	Moment capacities predicted by design rules
M_{EC3}	Nominal moment capacity (Unfactored design moment capacity) predicted by the European code
M_{Exp}	Experimental ultimate moment (test moment capacity)
$M_{EC3}^{\#}$	Nominal moment capacity (Unfactored design moment capacity) predicted by the modified European code
M_{FEA}	Ultimate moment predicted by finite element analysis
$M_{G\&T}$	Nominal moment capacity (Unfactored design moment capacity) predicted by the modified European code by Gardner and Theofanous
M_{Han}	Ultimate moment predicted by Han (2006)
$M_{Han}^{\#}$	Ultimate moment predicted by modified Han's method
M_{Hollow}	Experimental ultimate moment of hollow sections
$M_{inelastic}$	Nominal moment capacity (Unfactored design moment capacity) predicted by the approach by inelastic reserve capacity in American Specification and Australian/New Zealand Standard
$M_{inelastic}^{*}$	Nominal moment capacity (Unfactored design moment capacity) predicted by the approach by inelastic reserve capacity for



	specimens with the ratio of the depth of the compressed portion of the web to its thickness exceeded the slenderness ratio
M_m	Mean value of material factor
M_{nd}	Nominal flexural strength for distortional buckling in direct strength method
M_{ne}	Nominal flexural strength for lateral-torsional buckling in direct strength method
M_{nl}	Nominal flexural strength for local buckling in direct strength method
M_{pl}	Plastic bending moment
M_u	Experimental and numerical ultimate moments
$M_{u,end}$	Ultimate end moment
$M_{u,mid}$	Ultimate moment at mid-height
M_y	Yield moment or elastic moment
$M_{yielding}$	Nominal moment capacity (Unfactored design moment capacity) predicted by the approach by initiation of yielding in American Specification and Australian/New Zealand Standard
n	Ramberg-Osgood parameter
N_0	Summation of ultimate load-carrying capacity of concrete and steel tube
N_{ACI}	Unfactored design axial compressive capacity predicted by the American concrete institute
N_{AISC}	Unfactored design axial compressive capacity predicted by the American Institute of Steel Construction
N_{AISC-1}	Unfactored axial strength predicted by AISC design Method-1
N_{AISC-2}	Unfactored axial strength predicted by AISC design Method-2
N_{AS5100}	Unfactored design axial compressive capacity predicted by the Australian Code
N_{Choi}	Unfactored axial strength predicted by Choi et al. (2006)



N_{EC4}	Unfactored design axial compressive capacity predicted by the European Code
N_{Exp}	Experimental ultimate axial compressive strength
N_{FEA}	Numerical ultimate axial compressive strength
N_{Lai}	Unfactored axial strength predicted by Lai et al. (2015)
N_{LB}	Axial compressive load when local buckling occurs
N_u	Experimental and numerical ultimate axial compressive strength
N_{u-m}	Experimental or numerical design member strength
N_{u-s}	Experimental or numerical design cross-section strength
P_0	Nominal squash load
P_m	Mean value of tested-to-predicted factor
R	Rotation capacity
r	Radius of the curved beam specimen between the LVDTs located at the two loading points
r_i	Inner radius
r_o	Outer radius
S_e	Effective section modulus
S_f	Gross section modulus
T	Temperature in °C
t	Thickness
V_F	Coefficient of variation of fabrication factor
V_p	Coefficient of variation of tested-to-predicted load ratio
V_m	Coefficient of variation of material factor
V_r	Combined COV incorporating both model and basic variable uncertainties
V_δ	COV of the tests relative to the resistance model
W_{el}	Elastic modulus of cross-section
W_{pl}	Plastic modulus of cross-section
β_0	Reliability index



β_1	Reliability index
γ_{M2}	Partial resistance factor
δ_0	Global imperfection amplitude
δ_y	Lateral deflection at mid-height
$\sigma_{0.01}$	0.01% tensile proof stress
$\sigma_{0.2}$	0.2% tensile proof stress
ε	Material factor in European Code
ε_{c0}	The strain at which the stress achieves first peak of the confined concrete model
ε_{Exp}	Axial strain corresponding to ultimate strength
ε_f	Tensile strain at fracture based on gauge length of 25 mm
ε_u	Tensile strain at ultimate strength based on gauge length of 25 mm
ε_{pl}	Logarithmic plastic strain
$\varepsilon_{85\%}$	Axial strain corresponding to 85% of the ultimate strength on the unloading branch
η	Shape factor
κ	Curvature
κ_{Exp}	Curvature corresponding to the experimental ultimate moment
κ_{FEA}	Curvature corresponding to the ultimate moment predicted by finite element analysis
κ_{pl}	Curvature corresponding to the plastic moment (M_{pl}) on the ascending branch of moment-curvature curve
κ_{pl}^{\wedge}	Curvature corresponding to the plastic moment (M_{pl}) on the descending branch of moment-curvature curve
λ	Plate slenderness parameter in American Institute of Steel Construction
λ_p	Compactness limit in American Institute of Steel Construction
λ_r	Noncompactness limit in American Institute of Steel Construction
λ_{limit}	Slenderness limit in American Institute of Steel Construction



ν_c	Poisson's ratio of concrete
ν_s	Poisson's ratio of steel
ρ	Value in calculating effective area in American Specification, Australian/New Zealand Standard and European Code
$\sigma_{0.01}$	0.01% tensile proof stress
$\sigma_{0.2}$	0.2% tensile proof stress
σ_{true}	True stress
σ_u	Tensile strength
τ_{crit}	Critical stress for the friction model
ϕ_0	Resistance factor
ϕ_i	Resistance factor
Δ	Axial displacement of the specimen
Δ_u	Axial displacement at the ultimate load
$\Delta_{85\%}$	Axial displacement when the load drops to 85% of the ultimate load on the descending branch



CHAPTER 1

INTRODUCTION

1.1 Background

The concrete-filled steel tubular structures offer numerous structural benefits, including high strength, favorable ductility and large energy absorption capacities. Compared with reinforced concrete structures or steel structures, the infilled concrete prevents the inward local buckling of the steel tube, while the steel tube provides confinement to the infill concrete. Moreover, the steel tube can serve as the formwork for placing concrete, which can reduce the construction cost. Experimental investigations on the axial strength of concrete-filled steel tube (CFST) columns have been performed on a variety of cross-sectional shapes such as circular (Gardner and Jacobson, 1967; O’Shea and Bridge, 2000; Lai and Varma, 2015), rectangular and square (Schneider, 1998; Lai et al., 2014), elliptical (McCaan et al., 2015) and tube-in-tube double skin sections (Tao et al., 2004). Meanwhile the stress-strain behaviour of confined concrete was examined by Mander et al. (1988a; 1988b). The use of high strength concrete offers optimal use of material if the combination of concrete and steel is properly designed (Giakoumelis and Lam, 2004; Ellobody et al., 2006). The research topics on CFST also cover fire resistance (Kodur, 1999; Han et al., 2003b) and stainless steel CFST members (Young and Ellobody, 2006; Ellobody and Young, 2006; Lam and Gardner, 2008; Uy et al., 2011). A comprehensive overview of developments and applications of CFST members can be found in Han et al. (2014).



Stainless steel has been increasingly used as structural and architectural component due to their aesthetic appearance, superior corrosion resistance, excellent ductility and better fire resistance compared with traditional carbon steel. Over the past 30 years, stainless steel has been used in construction applications (Baddoo, 2008). However, most of the previous investigations and applications of stainless steel were mainly focused on hollow sections, and very few researches on concrete-filled stainless steel sections were found. Concrete infilling into stainless steel tube maintains the aesthetic and durable appearance. The excellent ductility of stainless steel when used as the outer steel tube in the concrete-filled steel tubular members can further enhance the energy absorption capacities and fire resistances. However, the current design specifications and standards such as American specification AISC 360 (2016), American code ACI 318 (2014), EC4 (2004) and AS 5100.6 (2004) were designated for concrete-filled carbon steel tubular members only but not for concrete-filled stainless steel members. Thus, it is necessary to conduct a comprehensive study on the structural performance of concrete-filled stainless steel tubular members and assess the applicability of current design specifications and standards to the design of concrete-filled stainless steel tubular members as well as propose design rules for these members.

1.2 Objectives

The objective of this thesis is to study the structural performance of concrete-filled cold-formed stainless steel members, in order to assess the applicability of current design specifications and standards to concrete-filled stainless steel tubular members, and propose new design recommendations.

Firstly, a comprehensive experimental investigation of concrete-filled cold-formed stainless steel members including stub column, beam and



beam-column tests was conducted. The specimens consisted of different cross-sectional shapes. The square and rectangular hollow sections were made of cold-formed ferritic stainless steel grade EN 1.4003, while the circular hollow sections were fabricated with cold-formed austenitic stainless steel grade EN 1.4301. Prior to member tests, tensile coupon tests were carried out to obtain the stress-strain relationship and the key parameters such as 0.2% proof stress, ultimate strength and strain at fracture of the stainless steel materials. Concrete of nominal cylinder compressive strengths of 40, 80 and 120 MPa were produced and filled into the stainless steel tubes. In addition, the slenderness limits on classification of ferritic stainless steel hollow sections specified in EC3 (2015) were also assessed by conducting flexural tests on cold-formed ferritic stainless steel members.

Secondly, finite element models were developed for the stub columns, beams and beam-columns to provide complementary data to facilitate a more reliable design. The finite element models were verified against all the experimental data conducted in this study and the verified models were used to conduct an extensive parametric study. Various design parameters such as sectional geometries, member lengths and initial loading eccentricities were investigated.

Finally, the experimental and numerical results as well as the data from the literature were used to assess the appropriateness of the current design specifications and standards designated for concrete-filled carbon steel tubular members but not for concrete-filled stainless steel members. New design recommendations were proposed in this study.

1.3 Outline of the Thesis

A total of ten chapters will be presented in this thesis. A brief introduction to the background of concrete-filled steel tubular member is reviewed in this chapter. The research objectives of the research study and the outline of this thesis are also presented.

Chapter 2 provides a detail review of previous studies on concrete-filled steel tubular members. The review focused on the key parameters affecting the behaviour of concrete-filled steel tubular members. The previous investigations on stub columns, beams and beam-columns of concrete-filled steel tubular members were covered in this chapter.

Chapter 3 presents a series of beam tests on cold-formed ferritic stainless steel hollow sections. The experimental and numerical results together with the available data were used to assess the slenderness limits on classification of ferritic stainless steel hollow sections specified in EC3 (2015). The design rules on flexural resistance of cold-formed ferritic stainless steel hollow sections were also examined.

Chapter 4 presents the experimental investigations on the material properties of cold-formed ferritic stainless steel grade EN 1.4003 and austenitic stainless steel grade EN 1.4301 at room temperatures. The material properties of cold-formed ferritic stainless steel grade EN 1.4003 under elevated temperatures were also examined by tensile coupon tests.

Chapters 5 and 6 examine the stub column behaviour of concrete-filled stainless steel tubular sections. The tested sections included square and rectangular sections,



which were made of cold-formed ferritic stainless steel. The circular sections were fabricated using cold-formed austenitic stainless steel. The specimens were filled with concrete with nominal cylinder compressive strengths of 40, 80 and 120 MPa. The experimental and numerical results together with data from literature were used to compare with the current design specifications American specification AISC 360 (2016), American code ACI 318 (2014), EC4 (2004) and AS 5100.6 (2004).

Chapters 7 and 8 present the flexural behaviour of concrete-filled stainless steel tubular members subjected to bending. The tested beam specimens were coming from the same batch of stainless steel sections as those investigated in chapters 4 and 5. The experimental and numerical results were compared with the current design specifications American specification AISC 360 (2016), American code ACI 318 (2014), EC4 (2004) and AS 5100.6 (2004). The proposed design equations by Han (2004) were also assessed and modifications to Han's equations were also proposed.

Chapter 9 provides the beam-column behaviour of concrete-filled ferritic stainless steel members. The tested specimens included square and rectangular sections and bent against minor axis for those rectangular sections. The specimens were filled with concrete with nominal cylinder compressive strengths of 40 and 80 MPa. A finite element model was developed by verifying the test results. The verified model was used to simulate the beam-column behavior and obtained further data in the parametric study covering a wide range of section sizes and slenderness ratios. The experimental data, together with the numerical results were used to assess the applicability of the current beam-column design provision provided in



AISC 360 (2016), ACI 318 (2014) and EC4 (2004). The design proposals by other researchers were also evaluated.

Chapter 10 is the summary of the whole thesis. The conclusions and findings of this research project were presented.



CHAPTER 2

LITERATURE REVIEW

2.1 General

Concrete-filled steel tubes (CFST) are members in which the hollow steel tubes filled with concrete inside the tubes. CFSTs are designed to maximize the efficiency in using the two materials by means of synergy of their interaction, i.e., the concrete can be used to delay the local buckling of slender steel sections, and the steel sections can be used to confine the concrete core thus increasing the compressive resistance in the ultimate and post-ultimate stages. Research on the experimental and numerical investigations on concrete-filled steel tubes are reviewed in the chapter, including both the stub column, beam and beam-column tests. The confined concrete models proposed by different researchers are also reviewed.

2.2 Axially-Loaded CFST Columns

2.2.1 Confinement effect

Furlong (1967) conducted a series of tests on short and long concrete-filled circular and square steel columns. The effects of width-to-thickness ratio and the strength ratio of concrete to steel on the axial strength were thoroughly investigated. The study of ultimate loads revealed that the steel and concrete resist load somewhat independent of one another and confinement effect was not obvious.



Gardner and Jacobson (1967) carried out an experimental investigation on axially-loaded CFST circular short columns. Carbon steel of yield strength from 363 to 650 MPa and normal strength concrete of cylinder strengths ranged from 25.0 to 43.3 MPa were used in the experimental study. It was found that dilation had significant effect on the behaviour of CFST for which the dilation of concrete was smaller than that of steel at the initial stage. The expansion of concrete after cracking triggered confinement from the steel tube due to rapid dilation of concrete than steel tube. The strength and ductility was enhanced due to the confinement effect.

Tomii et al. (1977) collected a total of 270 stub column results for CFST columns of square, circular and octagonal sections to examine the factors such as cross-sectional shape of the steel tubes and properties of concrete on the strength and ductility of the CFST columns. Confinement was found on circular and octagonal sections but the square sections provided little confinement due to plate bending rather than hoop stresses.

Schneider (1998) experimentally studied the effect of the steel tube shape and wall thickness on the ultimate strength of composite columns. A total of 14 specimens were tested and analytical models were further adopted to investigate the adequacy of design specifications. It was reported that the confinement was not observed for most specimens until the axial load reached approximately 92% of the yield strength of columns. Besides, the square and rectangular sections did not offer significant confinement to the infill concrete beyond the yield load of the CFST columns.

Johansson (2002) examined the influence of concrete strength and the steel tube thickness on confinement provided by the steel tube to the concrete core. Fifteen

columns were tested under concentric loading condition for the circular CFST short columns. The loading response at the post-yield stage was classified into three different categories: strain softening, perfectly plastic and strain hardening. It was found that the post-yield behaviour was greatly affected by the confinement level, which was related to the efficiency of the steel tube in confining the concrete core from forming cracks in the concrete.

2.2.2 Local buckling of steel tube

The behaviour and ultimate load carrying capacity were greatly influenced by local buckling of the steel tubes. Ge and Usami (1992) studied the strength of concrete-filled thin-walled steel box columns with and without stiffeners under cyclic compressive loads. It was observed that local plate buckling was successfully delayed by the infill concrete compared with empty sections and the increase in deformation became faster after local buckling of the steel plate occurred in CFST columns.

Wright (1995) derived the limiting breadth-to-thickness (b/t) ratio for the elastic buckling of plates in contact with concrete using the energy method. It was shown that considerable improvements in strength and ductility of CFST columns compared with the hollow sections. The limiting b/t ratio can be greatly relaxed from the hollow sections.

Uy and Bradford (1996) showed that the plate buckling coefficient K accounting for local buckling mode was equal to 10.3 for two clamped unloaded sides condition of steel plates in composite steel-concrete members, which is greatly enhanced compared with the value of 4.0 in the case of hollow steel tube condition.



Liang and Uy (2000) studied the post-local buckling behaviour of steel plates in concrete-filled welded thin-walled box columns theoretically. They proposed a set of effective width formulae in the calculation of ultimate strength for short thin-walled concrete-filled box columns in compression.

Bradford et al. (2002) proposed a closed form solution for the local buckling stress of a thin-walled circular tube with concrete infill using the Ritz-based method. It was shown that the elastic buckling stress is of $\sqrt{3}$ times the unfilled steel counterpart.

2.2.3 Influence of concrete strength

Concrete strength is one of the most important parameters that affect the behaviour and load-carrying capacity of CFST members. O'Shea and Bridge (1998) conducted tests on circular thin-walled CFST filled with medium and high strength concrete. Concrete of two nominal strengths 50 and 80 MPa were used to fill the circular specimens. Both the ultimate strength and ductility were improved for the specimens filled with medium strength concrete under concentric loading condition. However, only those specimens filled with high strength concrete and thicker outer tubes revealed confinement effects.

Elremaily and Azizinamini (2002) tested CFST columns with concrete cylinder compressive strength ranged between 34 and 103 MPa. The CFST columns exhibited very high level of energy dissipation and ductility. It was found that the specimens with high strength concrete developed bulges rapidly and a sudden change in the rate of axial shortening was observed. The formation of bulge was more gradual for the specimens with normal strength concrete.

Giakoumelis and Lam (2004) experimentally examined the behaviour of circular CFST with various concrete strengths under axial load on a total of 15 specimens with nominal concrete cube strength of 30, 60 and 100 MPa. The specimens with high strength concrete achieved their peak load at small end shortening while those with normal strength concrete gained the ultimate load with large displacement. The bond between the steel and concrete became more critical as the concrete strength increased, and the reduction on axial capacity of columns due to bonding was negligible for normal concrete strength specimens. However, the largest variation on ultimate strength between non-greased and greased specimens with high strength concrete was 17%.

Ellobody et al. (2006) conducted a study over a wide range of concrete cube strengths ranging from 30 to 110 MPa. An accurate finite element model was developed to carry out the analysis. The results obtained from parametric study were compared with the column design rules specified in the American Specifications (ACI 318, 1999; AISC, 1999) and Australian Standards (1994) and conservative predictions were found. However, the predictions by Eurocode 4 (1994) were generally unconservative.

Liew and Xiong (2012) conducted a series of tests on ultra-high strength concrete-filled composite columns with the cylinder compressive strength up to 200 MPa. The ultra-high strength concrete-filled steel tubular columns can achieve ultra-high compressive capacities, but brittle behaviour was observed at the post-peak load stage especially for those slender sections. A minimum steel contribution ratio of 0.30 or a minimum of 1% volume of steel fibers should be satisfied in order to ensure sufficient ductility of the ultra-high strength concrete-filled composite columns.

2.2.4 Influence of yield strength of steel

The yield strength of the steel has significant influence on the behaviour of CFST columns. Generally, it was found that higher confining stress can be provided by the steel tube with larger yield stress (Schneider, 1998; O’Shea and Bridge, 2000). Han et al. (2005) studied the behaviour of concrete-filled stub columns with steel yield strength ranged from 282 to 404 MPa and filled with self-consolidating concrete. It was clear that the ductility of the CFST columns decreased with the use of high strength steel. However, the use of high strength steel can enlarge the confinement factor, which can directly affect the post-yield behaviour of CFST columns. A simplified model was developed for the determination of section capacity and the axial load versus axial deformation relationships of the CFST stub columns. The comparison showed that the EC4 (1994) overestimated the ultimate load-carrying capacities of 2.7% for square sections and 0.6% for circular sections.

Uy (2001) tested the concrete-filled high strength steel box stub columns. The yield strength of steel was around 784 MPa from tensile coupon tests and 755 MPa from stub column tests, and the concrete cylinder compressive strength was about 30 MPa. It was found that the EC 4 (1994) underestimated the ultimate strength of short concrete-filled high strength steel box columns.

Mursi and Uy (2004) experimentally studied the thin-walled steel short columns fabricated using high strength steel and filled with normal strength concrete. The high strength steel with yield strength of 761 MPa was used to fabricate the specimens. It was found that the EC4 (1994) was not applicable to the design of short and slender CFST columns with high strength steel tubes due to its vulnerable nature to local buckling. A modified analysis approach was proposed which is more suitable for design applications.



Sakino et al. (2004) carried out an extensive experimental study on CFST columns with the cold-formed steel yield strength varied from 262 to 835 MPa, covering mild steel to high yield steel. They pointed out that the confining stress by the steel tube to the concrete core can be established as a linear function of the tube yield strength from the 114 centrally-loaded stub column test results.

2.3 Behaviour of CFST Beam-Columns

Varma et al. (2002, 2004) examined the behaviour of high strength square concrete-filled steel tube beam-columns. The parameters of width-to-thickness ratio (32 to 48), yield stress of steel tube (266 to 630 MPa), concrete strength (110 MPa) and axial load level (10 to 40% of the sectional axial load carrying capacity) on the behaviour of CFST beam-columns were studied. The axial and flexural stiffness, moment capacity and ductility was determined from the axial force-moment-curvature responses of the CFST beam-columns and methods to predict the aforementioned factors were proposed.

Han et al. (2003a) conducted a total of 30 concrete-filled thin-walled square and rectangular steel beam-column tests. Variables such as depth-to-width ratio of steel tube, concrete strength and axial load level were examined. A mechanic model was developed and good agreement with the test results was shown.

Inai et al. (2004) conducted a total of 65 CFST beam-column tests on 33 circular and 32 square specimens. The main test parameters were steel strengths (400, 590 and 780 MPa), diameter- (width-) to-thickness ratios of steel tube and concrete strengths (40 and 90 MPa). It was concluded that the use of high-strength concrete reduced the ductility of the CFST beam-columns, but this could be improved by adapting smaller diameter- (width-) to-thickness ratios or using high yield strength

steel tubes. Only the circular CFST columns with D/t ratio smaller than 75 showed confinement effect, and those with D/t larger than 75 and square columns did not reveal obvious confinement benefits from steel tubes. The local buckling of steel tube affected the moment capacities of square CFST columns with large b/t ratio, and due consideration should be accounted for when estimating the strength.

The current available guidance such as AISC specification AISC 360 (2016) and European code EC 4 (2004) provide design equations for CFT beam-columns specified for carbon steel specimens. Other researchers also pursued rational design equations to CFT beam-columns. Choi et al. (2006) proposed a set of equations for the design of square concrete filled tube beam-columns based on the AISC axial load-moment interaction curve. Furthermore, Choi et al. (2008) proposed a simplified axial load-moment interaction curve especially for the square steel tube filled with high-strength concrete. Lai et al. (2015) focused on the behaviour of non-compact and slender CFT members classified according to AISC specification AISC 360 (2010) and a set of equations were proposed to those members under combined loading conditions.

One of the important points in the axial load-moment interaction curve is the pure moment capacity, which is an indicator of the moment resistance of the CFST beam-column members. The behaviour of concrete-filled carbon steel tubes under bending condition have been investigated by several researchers. Lu and Kennedy (1994) conducted a series bending tests on square and rectangular CFST members. The test results indicated that the ultimate moment resistance of concrete-filled steel tube was enhanced by approximately 10 to 30 % over that of pure steel tube, depending on the ratio of area between steel and concrete. The flexural stiffness of the CFST was also increased. The relative slip between the steel tube and concrete

core was not detrimental. It was concluded that the shear-span-to-depth ratio of 1-5 had no or little influence on the bending resistances of respective members.

Zhao and Grzebieta (1999) carried out a series of study on compact, non-compact and slender SHS sections subjected to bending. It was found that the concrete infill can significantly increase the ductility. The increase in ultimate moment capacity depends mainly on the filled material strength.

Elchalakani et al. (2001) conducted twelve circular CFST beam tests on specimens with diameters varying from 34 to 110 mm and wall thicknesses between 1 to 3 mm. The slender sections exhibited significant strain-hardening effect. It was shown that the EC4 (1992) can accurately predict the moment capacities.

Gho and Liu (2004) investigated the flexural behavior of concrete-filled steel rectangular sections filled with high strength materials. Concrete with compressive cylinder strength $f_c' = 56.3 \sim 90.9$ MPa, and the yield strength of steel higher than 400 MPa was used to fabricate the specimens. Good ductility was observed for all specimens and local buckling was noted on the compressive face of the specimens. The comparison with the previous research test data showed that EC4 (1994), ACI (2002) and AISC (1999) conservatively predicted the flexural strengths by 9%, 12% and 15%, respectively.

Han (2004) and Han et al. (2006) carried out a series of experimental study on circular and square CFST member under bending. A set of calculation formulae on moment versus curvature curves and the flexural stiffness of concrete-filled steel tubular beams were proposed, and a mechanic model for predicting the moment capacities was developed by Han (2004). The mechanics model achieved

good agreement in predicting the bending moment resistance of CFST beams (Han, 2004; Han et al., 2006).

Chitawadagi and Narasimhan (2009) focused on the strength deformation behaviour of circular concrete-filled steel tubes subjected to pure bending and a total of ninety-nine specimens were tested. The effects of different parameters such as steel tube thickness, the cross-sectional area of concrete and strength of infill concrete on the moment capacity and curvature of CFST beam members were examined. The measured flexural strengths were compared with the values predicted by EC4 (1999) and AISC (1999) code provisions. An interaction model was developed for predicting moment and curvature of the CFST flexural members.

Lu et al. (2009) developed a finite element model to study the flexural performance of circular concrete-filled thin-walled steel tubular beams. The model was verified against a set of test data and good agreement was achieved. The stress and strain distributions across the composite section in the whole loading procedure was investigated. The composite action between the steel and concrete was analyzed and a strut-tie model was proposed for the load transfer mechanism of the circular CFST flexural members.

Wang et al. (2014) developed a numerical model and investigated the flexural behaviour of rectangular CFST members analytically. A finite element model verified against 70 test results was used to investigate the residual failure patterns of the core concrete, the typical residual deformations of outer steel tube and the stress and strain distributions across the composite section in the whole loading procedure. It was shown that the interaction of steel and concrete in the composite



beam offer stress redistribution between steel and concrete and this made the composite beams with high flexural capacity and ductility.

2.4 Confined Concrete Models

There are several well-known confined concrete models used by different researchers to describe the material properties of concrete core in order to duplicate the load-deformation history of CFST members. Some typical constitutive models are reviewed herein.

Sakino et al. (2004) presented a confined concrete model for both rectangular and square hollow sections. The effective stress-strain curve is expressed as:

$$Y = \frac{VX + (W - 1)X^2}{1 + (V - 2)X + WX^2} \quad (2.1)$$

in which $X = \varepsilon_c / \varepsilon_{co}$, $Y = \sigma_c / \sigma_{co}$, $V = E_c \varepsilon_c / \sigma_{co}$, $W = 1.50 - 0.017 f_c + 2.39 \sqrt{\sigma_h}$, where $E_c = 6900 + 3320 \sqrt{f_c}$ in MPa, $\varepsilon_{co} = 0.94 \times f_c^{0.25} \times 10^{-3}$, and $f_c = f_c' \times 1.67 D^{-0.112}$. The parameters required to complete the whole stress-strain curve are listed in Table 2.1. The f_c is the concrete compressive strength accounting for the scale effect, ε_{co} is the strain at f_c , σ_{co} is the confined concrete strength, ε_{co} is the strain at σ_{co} , and σ_h is the hoop stress in the steel tube.

Another commonly adopted confined concrete model comprises three different parts. The first part starts from the origin and linear up to the proportional limit, which is assumed to be $0.5 f_{cc}$, and the elastic modulus follows the formula provided in ACI (1999) as $E_{cc} = 4700 \sqrt{f_{cc}}$ MPa, where f_{cc} is the maximum



strength of the confined concrete and the corresponding strain ε_{cc} have been proposed by Mander et al. (1988a) as shown in Eqs (2.2) and (2.3).

$$f_{cc} = f_c' + k_1 f_l \quad (2.2)$$

$$\varepsilon_{cc} = \varepsilon_c (1 + k_2 \frac{f_l}{f_c'}) \quad (2.3)$$

where ε_c is the strain at the unconfined compressive cylinder strength of concrete f_c' and it is taken as 0.003 in accordance with ACI (1999). The parameters k_1 and k_2 are constant values and taken as 4.1 and 20.5 as recommended by Richart et al. (1928). Regarding the parameter f_l , Hu et al. (2003) proposed the following formulae based on the D/t ratio of the steel tube and the yield strength f_y of steel.

$$f_l / f_y = \begin{cases} 0.043646 - 0.000832(D/t) & \text{for } 21.7 \leq D/t \leq 47 \\ 0.006241 - 0.0000357(D/t) & \text{for } 47 < D/t \leq 150 \end{cases} \quad (2.4)$$

The second part defines the nonlinear portion starting from the proportional limit $0.5f_{cc}$ to the maximum confined concrete strength f_{cc} and the stress-strain relationship was given by Saenz (1964) as shown in Eq. (2.5).

$$f = \frac{E_{cc}\varepsilon}{1 + (R + R_E - 2)\left(\frac{\varepsilon}{\varepsilon_{cc}}\right) - (2R - 1)\left(\frac{\varepsilon}{\varepsilon_{cc}}\right)^2 + R\left(\frac{\varepsilon}{\varepsilon_{cc}}\right)^3} \quad (2.5)$$

$$\text{where } R_E = \frac{E_{cc}\varepsilon_{cc}}{f_{cc}}, \quad R = \frac{R_E(R_\sigma - 1)}{(R_\varepsilon - 1)^2} - \frac{1}{R_\varepsilon}, \quad R_\sigma = R_\varepsilon = 4.$$

The third part of the confined concrete stress-strain curve starts from the maximum confined concrete strength f_{cc} and ends at $f_u = rk_3f_{cc}$ with the



corresponding $\varepsilon_u = 11\varepsilon_{cc}$. The parameter k_3 is defined in Eq. (2.6) by Hu et al. (2003).

$$k_3 = \begin{cases} 1 & \text{for } 21.7 \leq D/t \leq 40 \\ 0.0000339(D/t)^2 - 0.0100085(D/t) + 1.3491 & \text{for } 40 \leq D/t \leq 150 \end{cases} \quad (2.6)$$

The parameter r can be taken as 1.0 for concrete with cube strength of 30 MPa and 0.5 for concrete with cube strength of 100 MPa and linear interpolation for the strengths in between as recommend by Ellobody and Young (2006).

Han et al. (2007) proposed a new stress-strain relationship for CFST circular and square section. The proposed model was related to the confinement factor ξ , which is determined from $\xi = A_s f_y / A_c f_{ck}$, where A_s and A_c are the cross-sectional areas of the steel and concrete; f_y is the yield strength of steel, f_{ck} equals to $0.67 f_{cu}$ for normal strength concrete and f_{cu} is the cube strength of concrete. The stress-strain model is shown as following:

$$y = \begin{cases} 2x - x^2 & (x \leq 1) \\ \frac{x}{\beta_0(x-1)^\eta + x} & (x > 1) \end{cases} \quad (2.7)$$

where $x = \varepsilon / \varepsilon_0$, $y = \sigma / \sigma_0$; $\sigma_0 = f_c'$ (MPa); $\varepsilon_0 = \varepsilon_c + 800\xi^{0.2} \times 10^{-6}$; $\varepsilon_c = (1300 + 12.5 f_c') \times 10^{-6}$;

$$\eta = \begin{cases} 2 & \text{(circular section)} \\ 1.6 + 1.5x & \text{(square section)} \end{cases}$$

$$\beta_0 = \begin{cases} (2.36 \times 10^{-5})^{[0.25+(\xi-0.5)^7]} (f_c')^{0.5} \times 0.5 \geq 0.12 & \text{(circular section)} \\ \frac{(f_c')^{0.1}}{1.2\sqrt{1+\xi}} & \text{(square section)} \end{cases}$$



Tao et al. (2013) proposed a stress-strain curve for confined concrete based on previous work by Samani and Attard (2012) and Binici (2005). The proposed model is suitable for both the circular and rectangular sections. The ascending portion OA is expressed by the following equation:

$$\frac{\sigma}{f_c'} = \frac{A \cdot X + B \cdot X^2}{1 + (A - 2)X + (B + 1)X^2} \quad 0 < \varepsilon \leq \varepsilon_{c0} \quad (2.8)$$

where $X = \varepsilon / \varepsilon_{c0}$; $A = \frac{E_c \varepsilon_{c0}}{f_c'}$; $B = \frac{(A - 1)^2}{0.55} - 1$. The strain at peak stress under uniaxial compression ε_{c0} is calculated from Eq. (2.9).

$$\varepsilon_{c0} = 0.00076 + \sqrt{(0.626 f_c' - 4.33) \times 10^{-7}} \quad (2.9)$$

and the strain ε_{cc} is determined in accordance with Samani and Attard (2012):

$$\frac{\varepsilon_{cc}}{\varepsilon_{c0}} = e^k, \quad k = (2.9224 - 0.00367 f_c') \left(\frac{f_B}{f_c'} \right)^{0.3124+0.002 f_c'} \quad (2.10)$$

The confining stress (f_B) provided to the concrete by the steel tube is determined as follow:

$$f_B = \begin{cases} \frac{(1 + 0.027 f_y) e^{-0.02 \frac{D}{t}}}{1 + 1.6 e^{-10} (f_c')^{4.8}} & \text{(circular section)} \\ \frac{0.25(1 + 0.027 f_y) e^{-0.02 \sqrt{B^2 + D^2} / t}}{1 + 1.6 e^{-10} (f_c')^{4.8}} & \text{(rectangular section)} \end{cases} \quad (2.11)$$

The descending branch is defined by an exponential function:



$$\sigma = f_r + (f_c' - f_r) \exp \left[- \left(\frac{\varepsilon - \varepsilon_{cc}}{\alpha} \right)^\beta \right] \quad \varepsilon_{cc} \leq \varepsilon \quad (2.12)$$

where f_r is the residual stress of the horizontal portion and determined as follows:

$$f_r = \begin{cases} 0.7(1 - e^{-1.38\xi_c})f_c' \leq 0.25f_c' & \text{(circular section)} \\ 0.1f_c' & \text{(rectangular section)} \end{cases} \quad (2.13)$$

and the parameter α is determined as,

$$\alpha = \begin{cases} 0.04 - \frac{0.036}{1 + e^{6.08\xi_c - 3.49}} & \text{(circular section)} \\ 0.005 + 0.0075\xi_c & \text{(rectangular section)} \end{cases} \quad (2.14)$$

This model provided good agreements with experimental results.

2.5 Concluding Remarks

This chapter has firstly reviewed the previous investigations on axially-loaded CFST columns and the CFST beam-columns. Furthermore, the current investigations on the confined concrete models are also summarized. It is shown that the investigation on concrete-filled cold-formed stainless steel is very limited. Therefore, the structural performance of concrete-filled cold-formed stainless steel members is investigated in this study.



Parameters	Circular columns	Square columns
σ_h / σ_y	$\frac{4.1}{23} \times \left(\frac{2t \times 0.19}{D - 2t} \right)$	$\frac{2t^2(b-t)}{b^3}$
σ_{cco} / f_c	$1 + \frac{4.1}{f_c} \times \left(\frac{2t \times 0.19\sigma_y}{D - 2t} \right)$	1.0
$\varepsilon_{cco} / \varepsilon_{co}$	$1.0 + 4.7 \times \left(\frac{\sigma_{cco}}{f_c} - 1 \right)$ for $\frac{\sigma_{cco}}{f_c} \leq 1.5$ $3.4 + 20 \times \left(\frac{\sigma_{cco}}{f_c} - 1 \right)$ for $\frac{\sigma_{cco}}{f_c} > 1.5$	

Table 2.1. Parameters for the CFST concrete stress-strain model in compression.

CHAPTER 3

MATERIAL PROPERTIES OF STAINLESS STEEL

3.1 Introduction

The material properties of cold-formed stainless steel were investigated by means of tensile coupon tests to determine the yield stress (0.2% proof stress), elastic modulus and other key properties. Tensile flat and corner coupons were extracted from cold-formed ferritic stainless steel rectangular and square hollow sections. Tensile curved coupons were machined from cold-formed austenitic stainless steel circular hollow sections. In addition, the material properties of cold-formed ferritic stainless steel under elevated temperatures were also examined in this study.

Section 3.2 presents the investigation on material properties of cold-formed ferritic stainless steel square and rectangular hollow sections as well as cold-formed austenitic stainless steel circular hollow sections at room temperature. The elastic modulus, yield strength (0.2% proof stress) and ultimate tensile strength were determined in order to facilitate calculation of nominal strength of structural members reported in the following chapters.

Section 3.3 presents the material properties of cold-formed ferritic stainless steel at elevated temperatures obtained from steady state and transient state tests. In the steady state tests, the specimens were heated to a specified temperature and then



tensile stress was applied until failure of the specimen. While prescribed tensile stress was applied prior to heating of specimen until failure in the transient state condition. Generally speaking, steady state test method is comparatively easier to perform and able to generate the stress-strain curve directly compared to transient state test method. However, transient state test method is more realistic to actual fire condition. In this study, the nominal temperatures employed in the steady state tests ranged from 22 (ambient temperature) to 900°C, while the stress levels used in the transient state tests were ranged from 0 to 450 MPa. The test results obtained in this study and available data (Manninen and Säynäjäkangas, 2012) were compared with design values given in EC3 (2005b) and the unified equation proposed by Chen and Young (2006). It is shown that the existing design rules could not accurately predict the ferritic stainless steel material properties at elevated temperatures. Modification to the current design rules for ferritic stainless steel at elevated temperatures is proposed.

3.2 Material Properties at Room Temperature

3.2.1 Cold-formed ferritic stainless steel

Tensile coupon tests were conducted to determine the material properties of cold-formed ferritic stainless steel sections 60×40×4, 60×60×3, 80×60×4, 100×40×2 and 120×80×3, of ferritic grade EN 1.4003. The material properties of the coil material are summarized in Table 3.1. Tensile coupons taken from both the flat and corner regions of the ferritic stainless steel specimens were tested. The static 0.2% proof stress ($\sigma_{0.2}$), static ultimate tensile strength (σ_u), elongation at fracture (ε_f), initial elastic modulus (E_o) and the Ramberg-Osgood parameter (n) using the Ramberg-Osgood expression $n = \ln(0.01/0.2)/\ln(\sigma_{0.01}/\sigma_{0.2})$ were determined and shown in Tables 3.2 and 3.3 for the flat and corner coupon tests.



Necking effect was observed for all tests near the mid-length of coupon specimens after reaching ultimate strength. The static 0.2% proof stress ($\sigma_{0.2}$) is treated as yield stress (f_y) of this stainless steel material.

3.2.1.1 Flat coupon tests

Flat coupon specimens were prepared in accordance with the requirements specified in EN ISO 6892-1 (2016) and ASTM E8 (2011) using a 6 mm wide coupon and a gauge length of 25.0 mm. The locations of the flat coupon specimens in the cross-sections are shown in Fig. 3.1. MTS testing machine was used to conduct the coupon tests. The coupon specimens were tested under displacement control method. Tensile load was applied to the specimens at a constant rate of 0.05 mm/min from commencement of the test to proportional limit in order to obtain sufficient data to determine the initial elastic modulus (E_o), as recommended by Huang and Young (2014c). Loading rate was changed to 0.8 mm/min after the proportional limit to ultimate strength and further followed by a higher loading rate of 2 mm/min to fracture. The coupon tests were paused by 100 seconds near the 0.2% proof stress and ultimate strength to obtain the static load by allowing relaxation of plastic stress.

The measured material properties of flat coupon tests are summarized in Table 3.2. The static stress-strain curves for the five sections are shown in Fig. 3.2. The static and test flat coupon stress-strain curves for the five sections are shown in Appendix A1. The static 0.2% proof stress ($\sigma_{0.2}$) ranged from 381 to 479 MPa and the ultimate tensile strength (σ_u) ranged from 443 to 492 MPa. The Ramberg-Osgood parameter (n) ranged from 6 to 8 for cold-formed ferritic stainless steel material. The elongation at fracture (ε_f) for the 25.0 mm gauge length ranged from 9.9%



to 29.7%. The abnormal brittle flat coupon behaviour of section 60×40×4 was attributed to the relative small section with slightly large thickness compared with other sections. The cold-forming process had significant influence on the flat portion of the section, which could lead to the brittle behaviour. Repeated tests were conducted in order to confirm the reliability of the results and similar outcomes were obtained.

3.2.1.2 Corner coupon tests

Strength enhancement is introduced to the cold-formed stainless steel specimens during the cold-forming process. The corner regions of the specimen are subjected to higher degree of cold-forming compared with the flat portions. Hence, it is necessary to conduct corner coupon tests. As shown in Fig. 3.1, corner coupon specimens were taken near the welds of the sections and prepared with 4 mm width and 25 mm gauge length. Two holes of 7 mm diameter were drilled at a distance of 20 mm from both ends of the specimens. The coupon specimen was loaded between two pins through the two drilled holes. The coupon specimens were tested under displacement control method and tensile load was applied to the specimens at a constant rate of 0.05 mm/min from commencement of the test to proportional limit. After that the loading rate was changed to 0.8 mm/min until fracture of the specimens. Similar to the flat coupons, the corner coupon tests were paused by 100 seconds near the 0.2% proof stress and ultimate strength to obtain the static stress-strain relationship of the ferritic stainless steel. The corner coupon tests were conducted using the same MTS machine as the flat coupons.

The measured material properties obtained from corner coupon tests are summarized in Table 3.3. The static stress-strain curves for the five sections are



shown in Fig. 3.3. The static and test corner coupon stress-strain curves for the five sections are shown in Appendix A2. The static 0.2% proof stress ($\sigma_{0.2}$) ranged from 533 to 593 MPa and the ultimate tensile strength (σ_u) ranged from 577 to 640 MPa. The Ramberg-Osgood parameter (n) ranged from 4 to 6 for cold-formed ferritic stainless steel material. The elongation at fracture (ε_f) for the 25.0 mm gauge length ranged from 11.5% to 13.1%. Significant enhancement at the corner region due to the cold-forming process was observed.

3.2.2 Cold-formed austenitic stainless steel

The material properties of the four cold-formed austenitic stainless steel circular hollow sections were determined by tensile coupon tests. The four sections, including CHS 60.5×2.8, 76.0×3.0, 114.3×3.0 and 165.2×3.0, were made of austenitic stainless steel grade EN 1.4301, commonly known as type 304 austenitic stainless steel. A curved coupon was machined from the 90 degrees from the welding seam for each section, as shown in Fig. 3.4. The dimension of the curved tensile coupon was designed as recommended by Huang and Young (2014c). Two stain gauges were affixed on the two sides of the coupon specimens and a 25 mm extensometer was used to record the elongation of the gauge length. Tensile load was applied to the specimens at a constant rate of 0.05 mm/min from the commencement of test to proportional limit of the material in order to obtain sufficient data to determine the elastic modulus, as recommended by Huang and Young (2014c). The loading rate was changed to 0.8 mm/min after proportional limit until fracture of the specimens. The tests were paused by 100 seconds near the yield and ultimate strengths in order to obtain the static load by allowing plastic stress relaxation. The elastic modulus (E_o), 0.01% proof stress ($\sigma_{0.01}$) and 0.2% proof stress ($\sigma_{0.2}$) used to determine the Ramberg-Osgood parameter,



ultimate tensile strength (σ_u), strain at ultimate tensile strength (ε_u) and the elongation at fracture (ε_f) over a gauge length of 25 mm were measured. The Ramberg-Osgood parameter (n) calculated from the Ramberg-Osgood expression $n = \ln(0.01/0.2) / \ln(\sigma_{0.01} / \sigma_{0.2})$ is also summarized in Table 3.4.

The austenitic stainless steel behaved in a very ductile manner. The test specimens elongated by 59 to 71% of the 25.0 mm gauge length at fracture, as shown in Table 3.4 and Fig. 3.5. The static and test curved coupon stress-strain curves for the five sections are shown in Appendix A3. The static 0.2% proof stress ($\sigma_{0.2}$) ranged from 258 to 296 MPa and the ultimate tensile strength (σ_u) ranged from 678 to 709 MPa. The Ramberg-Osgood parameter (n) ranged from 4 to 9 for cold-formed ferritic stainless steel material. The cold-formed austenitic stainless steel exhibited significant strain-hardening effect with the ratio of ultimate tensile strength (σ_u) to the 0.2% proof stress ($\sigma_{0.2}$) ranged from 2.31 to 2.74.

3.3 Material Properties of Cold-formed Ferritic Stainless Steel at Elevated Temperatures

3.3.1 Test devices

MTS 810 Universal Testing Machine was used to conduct the tensile coupon tests. The test set-up is shown in Fig. 3.6. MTS model 653.04 high temperature furnace, which contains three independent-controlled heating elements with a maximum temperature of 1400 °C were used to control the temperature to desirable level with accuracy of ± 1 °C. The air temperature inside the furnace was measured by three internal thermal couples. Two external thermal couples were attached to the surface of the coupon specimen to measure the actual temperature of the specimen. MTS 632.54 F-11 high temperature axial extensometer was used to capture the



displacement of the test specimens. The gauge length of the extensometer was 25 mm and the range limit was ± 2.5 mm. Generally, the ductility of stainless steel under high temperature is better than that at low temperature, and the strain may exceed the range limit of the extensometer. The extensometer was reset when it approaches approximately 80% of the range limit during testing in order to avoid any damage to the extensometer.

3.3.2 Test specimens

The test specimens were extracted from cold-formed ferritic stainless steel rectangular hollow sections (RHS) with nominal dimension ($D \times B \times t$) $80 \times 60 \times 4$ and $100 \times 40 \times 2$, where D , B and t are the depth, breath and thickness in millimeter of the cross-section. The coupons were taken from the faces at 90 degrees from the weld in the longitudinal direction of the stainless steel sections, as shown in Fig. 3.7. The test specimens were prepared in accordance with the ASTM E21 (2009) for tensile testing of metals at elevated temperatures, as shown in Fig. 3.8. A total of 56 tests (31 steady state tests and 25 transient state tests) was conducted in this study. The actual dimensions of the cross sectional areas if the specimens within the gauge length were measured by micrometer and the measured dimensions were used to determine the cross-sectional area of each coupon.

The specimens were labelled in such a way that the test method, nominal dimensions of cross-section from which the coupon specimens were extracted and the nominal temperature under which the test was conducted can be identified. For example, in the label “S100×40×2T400R”, the first letter indicates the test method, where “S” represents steady state test and “T” represents transient state test. The coupon specimen was extracted from cross-section of nominal dimensions



$100 \times 40 \times 2$ ($D \times B \times t$) and was tested under the nominal temperature of 400 °C. If the specimen was a repeated test, the letter “R” is added in the suffix of the label.

3.3.3 Test procedure

3.3.3.1 Steady state tests

The coupon specimen was heated up to a specified temperature then loaded until failure under the maintained temperature in the steady state test. The nominal temperatures selected in this study were 22 (ambient temperature), 100, 200, 300, 400, 450, 500, 550, 600, 700, 750, 800 and 900 °C for coupons extracted from each hollow section. The thermal expansion of specimen was allowed by only gripping the upper end of the specimen while the lower end was free to expand. The specified temperature on the coupon specimen was measured by the external thermal couples. After the temperature measured by the external thermal couples reached the pre-selected temperature and stable for 8 min, the lower end is gripped. Displacement control was used in applying the tensile load. The loading rate of 0.2 mm/min was used and strain rate obtained from the extensometer was approximately 0.006/min, which is within the range 0.005 ± 0.002 /min as specified in ASTM Standard E21 (2009). It is noteworthy that the ferritic stainless steel generally suffers from ductile failure and obvious necking can be observed from the tested specimens. All the specimens were tensioned until failure except for the 800 and 900 °C and the whole stress-strain curve including the ductility can be obtained. A total of 31 coupon specimens were tested by the steady state test method.



3.3.3.2 Transient state tests

The specimen was subjected to a maintained specified level of stress and then the temperature was increased until it failed in the transient state test. The nominal stress levels employed in the tests were 0, 50, 100, 150, 200, 250, 300, 350, 400, 420 and 450 MPa. Load control was adopted in the test program since it can maintain the stress level during the whole test process. The air temperature within the furnace was increased at a constant rate of 15 °C/min and this heating rate is appropriate since the use of stainless steel in exposed unprotected structural application is commonplace (Gardner et al., 2010). The stress level of 0 MPa was intended to obtain the thermal expansion of the specimen by allowing the lower end of the specimen free to expand while keeping the temperature increased from 22 to 1000°C at a constant rate. Test results of transient state tests were converted to stress-strain curve of the specimens at different temperature. Thermal strain, evaluated from the 0 MPa transient state test, was subtracted from the total measured strain. A total of 25 coupon specimens were conducted under the transient state test method.

3.3.4 Test results

3.3.4.1 General

The material properties of ferritic stainless steel grade EN 1.4003 of tensile flat coupons extracted from both sections RHS 80×60×4 and 100×40×2 at ambient temperature are presented in Table 3.5. The elastic modulus (E_o), various strengths including yield strength (f_y), which is the 0.2% proof stress ($f_{0.2}$), 0.5% strength ($f_{0.5}$), 1.0% strength ($f_{1.0}$), 1.5% strength ($f_{1.5}$) and 2.0% strength ($f_{2.0}$) are presented in the table. The table also summaries the ultimate tensile strength (f_u), strain at ultimate strength (ε_u) and strain at fracture (ε_f) of 25.0 mm gauge



length. The Ramberg-Osgood parameter (n), calculated from the expression $n = \ln(0.01/0.2) / \ln(f_{0.01} / f_{0.2})$, is also presented in Table 3.5. For the determination of parameter n , the strengths $f_{0.01}$ and $f_{0.2}$ are the intersection points of the stress-strain curve obtained from the proportional lines off-set by 0.01% and 0.2% strain, respectively. The $f_{0.5}$, $f_{1.0}$, $f_{1.5}$ and $f_{2.0}$ are the stresses corresponding to the intersection points of the stress-strain curve and the non-proportional vertical lines specified at the given strain levels, as shown in Fig. 3.9. The actual stainless steel temperature was obtained from the average value measured by the external thermal couples at the beginning, middle and end of the tests.

The test results obtained from transient state tests were converted into stress-strain curves, as shown in Figs 3.10 and 3.11. The specimens were loaded under 11 different stress levels up to 450 MPa. The stress level was maintained during the test and the duration of each test was generally less than one hour, for which the creep effect was considered negligible (Kankamge and Mahendran, 2011). The material properties obtained from the transient state test results at ambient temperature are presented in Table 3.6. The extensometer was removed before fracture of the coupon specimens since the strain would increase rapidly at the end of the tensile test under load control. Therefore, the ultimate strain (ε_u) and fracture strain (ε_f) cannot be recorded. The ultimate strength (f_u) also cannot be obtained from transient state tests since it may not match the 11 stress levels selected, as shown in Figs 3.10 and 3.11.



3.3.4.2 Elastic modulus

As an important indicator of the stiffness of structural steel at elevated temperatures, the elastic modulus affects the load-bearing capacity of steel structure significantly. The deterioration of elastic modulus at elevated temperature quantitatively reflects the performance of structural steel. The elastic modulus of steel at elevated temperature is determined from the tangent modulus of initial linear portion, of the stress-strain curve at the corresponding temperature. The reduction factor k_E is defined as the ratio of elastic modulus at some elevated temperatures (E_T) to that at ambient temperature (E_o). Reduction factors are recommended in European, American and Australian standards due to its simplicity. The reduction factors obtained from both the steady state tests and transient state tests are presented in Tables 3.7 and 3.8, respectively.

The reduction factors of elastic modulus obtained from this experimental study were compared with current design guidance of EC3 (2005b) and the unified equation proposed by Chen and Young (2006) for stainless steel, as shown in Fig. 3.12. The prediction by EC3 (2005b) generally passes through the average values of the steady state and transient state test values from room temperature to 500°C, which reveals that the EC3 (2005b) prediction was based on the combination of both the two test methods. This is suitable since the reduction factors will be applied to characteristic material strengths. However, the reduction factors obtained from the tests decreased rapidly after 500°C and the prediction by EC3 (2005b) are quite unconservative, which will lead to unsafe design. The unified equation by Chen and Young (2006), which were proposed based on the lower bound of previous research work on elevated temperature properties of stainless steel, provides quite safe predictions at elevated temperatures.



3.3.4.3 Yield strength

The reduction factors of yield strength ($f_{y,T} / f_y$), 0.5% strength ($f_{0.5,T} / f_{0.5}$), 1.0% strength ($f_{1.0,T} / f_{1.0}$), 1.5% strength ($f_{1.5,T} / f_{1.5}$) and 2.0% strength ($f_{2.0,T} / f_{2.0}$) determined by the ratio of the strength at elevated temperatures to that at ambient temperature for steady state tests are presented in Tables 3.9 and 3.10. For transient state tests, Table 3.11 summarises the reduction factors of yield strength ($f_{y,T} / f_y$) and the available 0.5% strength ($f_{0.5,T} / f_{0.5}$). The ultimate strain obtained from the transient state tests was generally less than 1%, as shown in Figs 3.10 and 3.11, hence, the 1.0%, 1.5% and 2.0% strengths could not be obtained. Fig. 3.13 depicts the comparison of the reduction factors of yield strength obtained from both the steady state and transient state tests with EC3 (2005b) and unified equation proposed by Chen and Young (2006). The reduction factors of yield strength for EN 1.4003 generally lie above the recommendations of EC3 up to 400°C. After that the reduction factors from EC3 are unconservative, which mean unsafe for using EN 1.4003 for temperature beyond 400°C. The unified equation proposed by Chen and Young (2006) provided conservative predictions from ambient temperature to around 550°C and became unconservative for higher temperature.

3.3.4.4 Ultimate strength

The reduction factors of ultimate strength were calculated based on the ratio of ultimate strength at a particular temperature ($f_{u,T}$) to that at ambient temperature (f_u) from steady state tests given in Table 3.12. As shown in Fig. 3.14, the reduction factors of ultimate strength predicted by EC3 (2005b) overestimated the performance of ferritic stainless steel at elevated temperatures. The predictions of unified equation proposed by Chen and Young for duplex stainless steel grade EN



1.4462 (2006) agrees well with the test results up to 400°C, but unconservative for temperature higher than 400°C.

3.3.4.5 Ductility

Ductility of steel is defined as the level of deformation that the steel can undergo before failure. The stress-strain curves obtained from the steady state tests at different temperatures were plotted in Figs 3.15 and 3.16. The effect of elevated temperatures on the ductility of ferritic stainless steel was studied by comparing the strains at fracture. It is interesting to note that the ductility generally decreases from ambient temperature to around 450°C and then increases afterwards. The values of the ductility for all the tested specimens are summarized in Table 3.13.

The failed ferritic stainless steel tensile coupon specimens at various temperatures obtained from the steady state tests are shown in Figs 3.17 and 3.18. It can be seen that necking appeared for all the specimens before failure and no brittle failure was observed. It is shown that lacking of ductility would not be a concern for ferritic stainless steel at elevated temperatures.

3.3.4.6 Thermal expansion in transient state test

Thermal expansion is the characteristic of expansion of a stainless steel material caused by heating and is defined as the expansion of unit length of a material when the temperature rises. The test specimen was heated at 15°C/min from 22°C (ambient temperature) to 1000°C by allowing the lower end of the specimen free to expand. Fig. 3.19 shows the measured thermal strain of ferritic stainless steel grade EN 1.4003 at elevated temperatures. The thermal strain was calculated by



change in length (Δl) divided by its original length (l_o). The thermal strain gradually increased up to around 750°C and then decreased until it reaches approximately 850°C. The thermal strain increased again from 850°C onwards. The decrease of thermal stain from around 750°C to 850°C may be attributed to the phase change of material occurred in the stainless steel. Furthermore, the thermal expansion predictions by EC3 (2005b) covers the austenitic stainless steel only. Comparison between the test results and the EC3 (2005b) predictions show that the thermal elongation could not apply to ferritic stainless steel.

3.3.4.7 Vickers hardness test for tested specimens

The hardness of tested specimens by steady state method was measured by ESEWAY Hardness Tester under Vickers hardness test method after the specimens completely cool-down at ambient temperature. The Vickers Hardness number is an expression of hardness obtained by dividing the force applied to a Vickers indenter by the surface area of the permanent indentation made by the indenter (ASTM E384, 2016). The Vickers indenter is a square-based pyramidal-shaped diamond with face angle of 136°. The Vickers hardness number 300 HV30 indicates the obtained hardness value 300 using the load 30 kilograms-force (kgf). The load used in the test was 30 kgf and the specimens were tested under the maintained load for 10 seconds. The hardness test results are shown in Fig. 3.20. The hardness of the tested specimens decreases after 450°C and it lost approximately 25% at 700°C compared to that under ambient temperature. However, the hardness increases dramatically after 750°C and the hardness of the tested specimen for 900°C is 59% higher than that at ambient temperature for section 100×40×2 and 43.4% for section 80×60×4. This can be owing to the phase change in the material took place between 750 and 850°C. The atomic structure



changed from a face centered cubic (FCC) to a body centered cubic (BCC) structure within the steel material (Choi et al., 2014).

3.3.5 Design proposal for material properties

3.3.5.1 Predictive equations for material properties at elevated temperatures

The European code EC3 (2005b) and previous researches (Manninen and Säynäjäkangas, 2012; Gardner et al., 2010) proposed different sets of reduction factors of elastic modulus, yield strength and ultimate strength for ferritic stainless steel grade EN 1.4003. However, the comparisons of the abovementioned reduction factors and the experimental results obtained from this study reveal that the available proposal cannot accurately predict the material properties of ferritic stainless steel grade EN 1.4003 at elevated temperatures. Hence, modifications to the design rules in predicting the reduction factors for ferritic stainless steel are necessary.

A set of predictive equations was proposed having similar format of the proposed predictive equations for cold-formed stainless steel by Chen and Young (2006) and high strength steel by Kankamge and Mahendran (2011). In this study, the predictive equations are developed based on the experimental results of cold-formed ferritic stainless steel and also the results reported by Manninen and Säynäjäkangas (2012) for cold-rolled sheets in annealed condition. The proposed equations for the reduction factors of elastic modulus, yield strength and ultimate strength with different values of the coefficients are shown in Eqs (3.1) – (3.3). The coefficients a , b , c and m for ferritic stainless steel grade EN 1.4003 are shown in Table 3.14. It is shown that the predictions of the reduction factors using



the proposed equations generally agree well with the test results obtained from this study and also the results reported by Manninen and Säynäjäkangas (2012), as shown in Figs 3.12 - 3.14.

$$k_E = \frac{E_T}{E_o} = a - \frac{(T-b)^m}{cT} \quad (3.1)$$

$$k_y = \frac{f_{y,T}}{f_y} = a - \frac{(T-b)^m}{cT} \quad (3.2)$$

$$k_u = \frac{f_{u,T}}{f_u} = a - \frac{(T-b)^m}{cT} \quad (3.3)$$

3.3.5.2 Reliability analysis

3.3.5.2.1 ASCE approach

Reliability analysis was adopted to assess the applicability of the proposed design equations of reduction factors for ferritic stainless steel grade EN 1.4003 at elevated temperatures. The reliability analysis is detailed in Commentary of the ASCE specification SEI/ASCE-8 (ASCE, 2002) and it is widely adopted to appraise the reliability of structure based on experimental data. However, the target reliability index (β_0) and the resistance factor (ϕ_0) are not suggested in the design specification for stainless steel material properties. In order to facilitate reliability analysis, the target reliability index (β_0) of value 2.50 was adopted in this study, and the design rules are considered to be reliable if the reliability index is greater than or equal to 2.50. The load combinations of 1.35 DL + 1.5 LL and 1.2 DL + 1.6 LL were selected for the determination of reliability index of EC3 (2005b) and unified equation proposed by Chen and Young (2006), respectively. The load combination 1.2 DL + 1.6 LL was also adopted for the proposed equations in this study. The live load to dead load ratio of 1/5 was used. Statistical parameters M_m , F_m , V_M and V_F presented in Table 3.15 were adopted in the



calculation of reliability index in Eq. 6.2-2 in the ASCE specification (ASCE, 2002), where M_m is the mean value of material factor, F_m is the mean value of fabrication factor, V_M is the coefficient of variation of material factor and V_F is the coefficient of variation of fabrication factor. The statistic parameters P_m and V_P are the mean value of experimental-to-design load ratios and the corresponding coefficient of variation of test-to-predicted load ratios. The correction factor C_p was also used in the calculation of reliability index in order to compensate the influence due to limited number of data in accordance with Eq. K2.1.1-4 in the North American Specification for cold-formed steel structural members (AISI S100, 2016). In order to facilitate direct comparison, a load combination of 1.2 DL + 1.6 LL was used to calculate the resistance factors (ϕ_l). Table 3.16 summarizes the number of data to achieve the reliability analysis. The results from reliability analysis by the ASCE approach are presented in Table 3.17.

3.3.5.2.2 Eurocode approach

The reliability of the proposed design equations was demonstrated through statistical analysis in accordance with EC0 (2002). Table 3.18 summarizes the key statistical parameters adopted in the Eurocode reliability analysis. These parameters include the design (ultimate limit state) fractile factor $k_{d,n}$, which was determined for the case “ V_x unknown” for n tests and n is the population of the test data under consideration, and b is the average ratio of test to design model resistance based on a least square fit to all data, V_δ is the COV of the tests relative to the resistance model, V_r is the combined COV incorporating both model and basic variable uncertainties, and γ_{M2} is the partial safety factor. The adopted value of γ_{M2} is 1.25 in the current EN 1993-1-4 (2015). The ratio of mean to nominal yield strengths (i.e. the material over-strength) is 1.2 and the COV of



yield strength, ultimate tensile strength and geometrical properties are taken as 0.045, 0.050 and 0.050, as recommended by Afshan et al. (2015). The material over-strength ratio is defined as the ratio of the mean value of the yield strength produced by the manufacturers to the specified value in EN 10088-4 (2009). The results from reliability analysis by European approach are presented in Table 3.18.

3.3.5.3 Comparisons of experimental and predicted strengths

The reduction factors of elastic modulus of the test specimens from this study and the available data (Manninen and Säynäjäkangas, 2012) are compared with the design predictions by EC3 (2005b), the unified equation proposed by Chen and Young (2006) and the proposed predictive equation. As shown in Fig. 3.12 and Table 3.17, where $k_{E,Test}$, $k_{E,EC3}$, $k_{E,Chen\&Young}$ and $k_{E,Proposed}$ are the reduction factors of elastic modulus obtained from the experimental results in this study and available data (Manninen and Säynäjäkangas, 2012), predicted values by EC3 (2005b), predicted values by the unified equation proposed by Chen and Young (2006) and proposed predictive equation, respectively. The EC3 (2005b) is unconservative in predicting the elastic modulus with a mean value of $k_{E,Test} / k_{E,EC3}$ equals to 0.88 and COV of 0.286, which may lead to unconservative design. The resistance factors (ϕ_0 and ϕ_1) of 0.55 are recommended to achieve the reliability indices (β_0 and β_1) of 2.50 and 2.60, respectively. The unified equation proposed by Chen and Young (2006) offers very safe predictions for elastic modulus with a mean value of $k_{E,Test} / k_{E,Chen\&Young}$ equals to 1.53 and COV of 0.842. The resistance factors (ϕ_0 and ϕ_1) of 0.25 are recommended for the reliability indices (β_0 and β_1) of 2.60. It is observed by the reliability analysis that both the two design rules cannot accurately predict the elastic modulus for ferritic stainless steel under elevated temperatures. The reduction factors calculated by the

proposed predictive equation Eq. 3.1 provides most accurate and least scattered predictions with the mean value of $k_{E,Test} / k_{E,Proposed}$ equals to 1.04 and *COV* of 0.174. The corresponding resistance factors (ϕ_0 and ϕ_1) of 0.80 are recommended for the reliability indices (β_0 and β_1) of 2.65. The reliability analyses by the Eurocode approach obtained partial factor γ_{M2} greater than 1.25 for all design method, as shown in Table 3.18. The calculated partial factor γ_{M2} for the proposed predictive equation ($\gamma_{M2}=1.95$) is the smallest one comparing with other design methods. The proposed predictive equation is more reliable than other design methods and it is recommended as a relatively safe design method for the reduction factors of elastic modulus of ferritic stainless steel grade EN 1.4003 at elevated temperatures.

The reduction factors of yield strength of the test specimens and the available data were also compared with the design values by the two design rules and proposed predictive equation Eq. 3.2. As elucidated in Fig. 3.13 and Table 3.17, the $k_{y,Test}$, $k_{y,EC3}$, $k_{y,Chen\&Young}$ and $k_{y,Proposed}$ are the value of reduction factors obtained from test results, predicted values by EC3 (2005b), predicted values by the unified equation proposed by Chen and Young (2006) and predictive values by the proposed equation, respectively. Overall speaking, EC3 (2005b) provides slightly unconservative estimation on the yield strength reduction factors with a mean value of $k_{y,Test} / k_{y,EC3}$ equals to 0.92 and *COV* of 0.169. The resistance factors (ϕ_0 and ϕ_1) of 0.70 and 0.75 are recommended for the reliability indices (β_0 and β_1) of 2.60 and 2.50. The unified equation proposed by Chen and Young (2006) generally provides safe predictions with a mean value of $k_{y,Test} / k_{y,Chen\&Young}$ equals to 1.10 and *COV* of 0.308. To achieve reliability indices (β_0 and β_1) of 2.50, which matches the target reliability index, it is recommended to adopt the resistance factor of 0.70. The predictions on reduction factors by the proposed

predictive equation provides good agreement with the experimental results in this study and available data (Manninen and Säynäkangas, 2012) with a mean value of $k_{y,Test} / k_{y,Proposed}$ equals to 1.01 and *COV* of 0.095. The resistance factors (ϕ_0 and ϕ_1) of 0.90 are recommended for the reliability indices (β_0 and β_1) of 2.50. The calculated value of γ_{M_2} for the proposed predictive equation is found to be 1.25, which equals to the target value, as shown in Table 3.18. However, the calculated value of γ_{M_2} for EC3 (2005b) and the unified equation proposed by Chen and Young (2006) failed to meet the requirement with γ_{M_2} of 1.87 and 3.09, respectively.

Both the EC3 (2005b) and unified equation proposed by Chen and Young (2006) provide unconservative estimation for the ultimate strength reduction factors, as shown in Fig. 3.14 and Table 3.17. It should be noted that the design parameter for duplex stainless steel grade EN 1.4462 by Chen and Young (2006) was chosen to facilitate comparison. The mean values of 0.87 and 0.79 for $k_{u,Test} / k_{u,EC3}$ and $k_{u,Test} / k_{u,Chen\&Young}$ indicate that both the two design rules provide unsafe design. EC3 (2005b) has a *COV* of 0.134, which is less scattered than that of 0.337 by the unified equation (Chen and Young, 2006). The resistance factors (ϕ_0 and ϕ_1) of 0.70 and 0.75 are recommended for the reliability indices (β_0 and β_1) of 2.65 and 2.55 for EC3 (2005b). However, the unified equation has poor performance with recommended resistance factors (ϕ_0 and ϕ_1) of 0.45 to obtain reliability indices (β_0 and β_1) of 2.65, which is largely due to the fact that design parameter for duplex stainless steel was chosen to compare the results of ferritic stainless steel. The reduction factors calculated by the proposed predictive equation Eq. 3.3 provides most accurate and least scattered predictions with the mean value of $k_{u,Test} / k_{u,Proposed}$ equals to 1.01 and *COV* of 0.133. The resistance factors (ϕ_0 and ϕ_1) of 0.90 are recommended for the reliability indices (β_0 and β_1) of 2.50. The



partial factor γ_{M2} calculated by Eurocode approach is found to be 1.39 for the proposed predictive equation, failed to satisfy the codified value of 1.25, but better than the calculated values of γ_{M2} for EC3 (2005b) ($\gamma_{M2} = 1.95$) and unified equation proposed by Chen and Young (2006) ($\gamma_{M2} = 6.16$). The proposed predictive equation may be adopted for reduction factor of ultimate strength of ferritic stainless steel grade EN 1.4003 at elevated temperatures with similar but better reliability level as EC3 (2005b).

3.4 Concluding Remarks

This chapter presents the experimental investigation on the material properties of cold-formed ferritic and austenitic stainless steel. The material properties of cold-formed ferritic stainless steel under elevated temperatures were also depicted. Tensile coupon tests were conducted on both the flat and corner regions of cold-formed ferritic stainless steel rectangular and square sections. Strength enhancement in corner regions were observed for rectangular and square hollow sections. Tensile curved coupon tests were carried out on cold-formed austenitic stainless steel circular sections.

A test program on the material properties of ferritic stainless steel grade EN 1.4003 at elevated temperatures has been presented. The tests were carried out on tensile coupons extracted from cold-formed stainless steel sections $100 \times 40 \times 2$ and $80 \times 60 \times 4$. A total of 31 steady state tests was conducted under different temperatures ranged from 22 to 900°C . Furthermore, a total of 25 transient state tests were conducted under different stress levels. The elastic modulus, yield strength, ultimate strength as well as the thermal expansion obtained from this study and the available data were compared with the design predictions by EC3 (2005b) and the unified equation proposed by Chen and Young (2006). The EC3



(2005b) predicted the elastic modulus quite well from ambient temperature to 450 °C, but unconservatively predicted from 450 °C onwards. The unified equation proposed by Chen and Young (2006) provided safe predictions for elastic modulus. The reduction factors of yield strength are accurately predicted by EC3 (2005b) from ambient temperature to 400 °C, but unconservatively from 400 °C onwards. The unified equation proposed by Chen and Young (2006) provided safe predictions from ambient temperature to 550 °C but unconservative predictions from 550 °C onwards for the yield strength. The reduction factors of ultimate strength predicted by EC3 (2005b) overestimated the performance of ferritic stainless steel at elevated temperatures, whereas the predictions by Chen and Young (2006) agrees well with the test results up to 400 °C, but unconservative for temperature of 400 °C and above. The thermal expansion predictions by EC3 (2005b) covers the austenitic stainless steel only. It is shown that the EC3 (2005b) overestimated the thermal elongation, and hence could not apply to ferritic stainless steel.

A new set of predictive equations was proposed for the reduction factor of elastic modulus, yield strength and ultimate strength based on the test results and the available data (Manninen and Säynäjäkangas, 2012) for ferritic stainless steel. The reliability analysis elucidated that the proposed equations agree well with the test results. It is recommended that the proposed equations on the material properties of ferritic stainless steel grade EN 1.4003 at elevated temperatures can be used.

Section ($D \times B \times t$)	$\sigma_{0.2}$ (MPa)	σ_u (MPa)	ε_f (%)
60×40×4	371	508	27
60×60×3	343	495	35
80×60×4	381	481	29
100×40×2	344	497	43
120×80×3	343	495	35

Table 3.1. Mill certificate data (from Stalatube).

Section ($D \times B \times t$)	E_o (GPa)	$\sigma_{0.01}$ (MPa)	$\sigma_{0.2}$ (MPa)	σ_u (MPa)	ε_u (%)	ε_f (%)	n
60×40×4	206	293	479	492	0.7	9.9	6
60×60×3	210	265	449	463	7.7	23.8	6
80×60×4	210	287	451	464	1.3	22.1	7
100×40×2	200	295	420	452	15.8	28.9	8
120×80×3	200	261	381	443	13.8	29.7	8

Table 3.2. Tensile flat coupon test results of cold-formed ferritic stainless steel.

Section ($D \times B \times t$)	E_o (GPa)	$\sigma_{0.01}$ (MPa)	$\sigma_{0.2}$ (MPa)	σ_u (MPa)	ε_u (%)	ε_f (%)	n
60×40×4	209	322	573	640	1.0	13.1	5
60×60×3	200	308	533	577	1.0	11.9	5
80×60×4	209	296	593	633	1.0	13.0	4
100×40×2	200	334	544	586	0.8	11.7	6
120×80×3	203	329	559	597	0.7	11.5	6

Table 3.3. Tensile corner coupon test results of cold-formed ferritic stainless steel.

Section ($D \times t$)	E_o (GPa)	$\sigma_{0.01}$ (MPa)	$\sigma_{0.2}$ (MPa)	σ_u (MPa)	ε_u (%)	ε_f (%)	n
60.5×2.8	196	187	296	708	53	60	6
76.0×3.0	202	123	258	709	51	59	4
114.3×3.0	195	196	293	678	60	71	7
165.2×3.0	201	191	267	684	64	70	9

Table 3.4. Tensile curved coupon test results of cold-formed austenitic stainless steel.



Specimen	T (°C)	E_o (GPa)	f_y (MPa)	$f_{0.5}$ (MPa)	$f_{1.0}$ (MPa)	$f_{1.5}$ (MPa)	$f_{2.0}$ (MPa)	f_u (MPa)	ε_u (%)	ε_f (%)	n
S100×40×2T22	22.4	195	441	445	450	452	455	484	13.5	26.3	10.1
S80×60×4T22	22.5	208	468	477	490	492	491	492	1.5	22.1	7.0

Table 3.5. Material properties obtained from steady state tests at ambient temperature.

Specimen	T (°C)	E_o (GPa)	f_y (MPa)	$f_{0.5}$ (MPa)	n
S100×40×2T22	22.3	184.2	452.0	457.9	9.9
S80×60×4T22	22.5	207.8	429.8	451.2	5.0

Table 3.6. Material properties obtained from transient state tests at ambient temperature.



Specimen	T (°C)	E_T (GPa)	E_T / E_o	Specimen	T (°C)	E_T (GPa)	E_T / E_o
S100×40×2T22	22.4	194.5	1.000	S80×60×4T22	22.5	208.4	1.000
S100×40×2T100	97.1	165.8	0.853	S80×60×4T100	102.9	210.7	1.011
S100×40×2T200	196.9	171.3	0.881	S80×60×4T200	204.9	209.3	1.004
S100×40×2T200R	199.7	175.1	0.900	S80×60×4T300	302.8	202.8	0.973
S100×40×2T300	297.2	176.9	0.910	S80×60×4T300R	299.6	194.0	0.931
S100×40×2T400	397.0	173.6	0.892	S80×60×4T400	399.6	182.2	0.874
S100×40×2T400R	396.0	179.2	0.921	S80×60×4T400R	397.9	182.2	0.874
S100×40×2T450	440.2	158.5	0.815	S80×60×4T450	447.6	184.8	0.887
S100×40×2T500	493.6	161.4	0.830	S80×60×4T500	497.8	157.9	0.758
S100×40×2T550	537.7	155.5	0.799	S80×60×4T550	544.4	153.0	0.734
S100×40×2T600	592.6	98.5	0.507	S80×60×4T600	590.1	132.5	0.636
S100×40×2T650	-	-	-	S80×60×4T650	653.4	93.3	0.447
S100×40×2T700	700.6	28.6	0.147	S80×60×4T700	696.2	70.2	0.337
S100×40×2T750	745.6	11.1	0.057	S80×60×4T750	746.8	49.7	0.239
S100×40×2T800	803.8	41.9	0.215	S80×60×4T800	789.7	48.2	0.231
S100×40×2T900	905.6	32.8	0.168	S80×60×4T900	887.9	47.0	0.226

Table 3.7. Elastic modulus and reduction factors at elevated temperatures obtained from steady state tests.

T (°C)	100×40×2		80×60×4	
	E_T (GPa)	E_T / E_o	E_T (GPa)	E_T / E_o
22	184.2	1.000	207.8	1.000
50	187.7	1.019	211.1	1.016
100	175.0	0.950	202.6	0.975
150	167.0	0.907	192.8	0.928
200	157.4	0.854	185.0	0.891
250	154.0	0.836	186.4	0.897
300	149.2	0.810	179.9	0.866
350	144.7	0.785	179.7	0.865
400	148.1	0.804	178.8	0.860
450	139.9	0.759	171.1	0.824
500	120.1	0.652	150.2	0.723

Table 3.8. Elastic modulus and reduction factors at elevated temperatures obtained from transient state tests.

Specimen	$f_{y,T} / f_y$	$f_{0.5,T} / f_{0.5}$	$f_{1.0,T} / f_{1.0}$	$f_{1.5,T} / f_{1.5}$	$f_{2.0,T} / f_{2.0}$
S80×60×4T22	1.000	1.000	1.000	1.000	1.000
S80×60×4T100	0.955	0.951	0.933	0.925	0.923
S80×60×4T200	0.910	0.908	0.886	0.880	0.880
S80×60×4T300	0.890	0.882	0.858	0.851	0.848
S80×60×4T300R	0.920	0.906	0.874	0.868	0.864
S80×60×4T400	0.821	0.838	0.810	0.803	0.801
S80×60×4T400R	0.789	0.791	0.788	0.790	0.791
S80×60×4T450	0.765	0.760	0.745	0.739	0.736
S80×60×4T500	0.637	0.636	0.620	0.612	0.608
S80×60×4T550	0.492	0.488	0.472	0.465	0.462
S80×60×4T600	0.355	0.355	0.342	0.336	0.333
S80×60×4T650	0.252	0.250	0.242	0.231	0.230
S80×60×4T700	0.158	0.159	0.154	0.154	0.153
S80×60×4T750	0.104	0.103	0.101	0.100	0.099
S80×60×4T800	0.076	0.081	0.083	0.087	0.088
S80×60×4T900	0.067	0.070	0.072	0.074	0.076

Table 3.9. Reduction factors of yield strength of section 80×60×4 obtained from steady state tests.



Specimen	$f_{y,T} / f_y$	$f_{0.5,T} / f_{0.5}$	$f_{1.0,T} / f_{1.0}$	$f_{1.5,T} / f_{1.5}$	$f_{2.0,T} / f_{2.0}$
S100×40×2T22	1.000	1.000	1.000	1.000	1.000
S100×40×2T100	1.011	1.014	1.014	1.000	0.991
S100×40×2T200	0.888	0.886	0.880	0.881	0.878
S100×40×2T200R	0.883	0.877	0.871	0.869	0.867
S100×40×2T300	1.001	0.996	0.993	0.979	0.966
S100×40×2T400	0.914	0.921	0.949	0.955	0.957
S100×40×2T400R	0.895	0.906	0.938	0.951	0.927
S100×40×2T450	0.824	0.832	0.870	0.882	0.886
S100×40×2T500	0.740	0.750	0.767	0.768	0.766
S100×40×2T550	0.493	0.494	0.489	0.485	0.480
S100×40×2T600	0.330	0.337	0.332	0.326	0.321
S100×40×2T700	0.127	0.128	0.130	0.130	0.130
S100×40×2T750	0.073	0.073	0.086	0.088	0.089
S100×40×2T800	0.106	0.111	0.117	0.120	0.123
S100×40×2T900	0.070	0.072	0.075	0.077	0.078

Table 3.10. Reduction factors of yield strength of section 100×40×2 obtained from steady state tests.

T (°C)	100×40×2				80×60×4			
	f_y (MPa)	$f_{y,T} / f_y$	$f_{0.5}$ (MPa)	$f_{0.5,T} / f_{0.5}$	f_y (MPa)	$f_{y,T} / f_y$	$f_{0.5}$ (MPa)	$f_{0.5,T} / f_{0.5}$
22	452.0	1.000	457.9	1.000	429.9	1.000	207.8	1.000
50	445.5	0.986	-	-	425.9	0.991	211.1	1.016
100	425.4	0.941	434.4	0.949	414.9	0.965	202.6	0.975
150	420.9	0.931	421.3	0.920	404.8	0.942	192.8	0.928
200	413.6	0.915	421.1	0.920	398.3	0.927	185.0	0.891
250	408.7	0.904	417.0	0.911	389.5	0.906	186.4	0.897
300	408.2	0.903	412.4	0.901	387.4	0.901	179.9	0.866
350	408.0	0.903	409.5	0.894	384.0	0.893	179.7	0.865
400	400.7	0.887	403.3	0.881	-	-	-	-
450	369.0	0.816	371.3	0.811	-	-	-	-
500	352.8	0.781	352.8	0.771	-	-	-	-
550	257.5	0.570	258.6	0.565	-	-	-	-
600	181.4	0.401	177.6	0.388	-	-	-	-

Table 3.11. Strength reduction factors obtained from transient state tests.

Specimen	f_u (MPa)	$f_{u,T} / f_u$	Specimen	f_u (MPa)	$f_{u,T} / f_u$
S100×40×2T22	483.9	1.000	S80×60×4T22	492.0	1.000
S100×40×2T100	457.5	0.945	S80×60×4T100	458.3	0.932
S100×40×2T200	427.5	0.883	S80×60×4T200	436.7	0.888
S100×40×2T200R	423.8	0.876	S80×60×4T300	421.3	0.856
S100×40×2T300	447.7	0.925	S80×60×4T300R	433.6	0.881
S100×40×2T400	439.8	0.909	S80×60×4T400	395.0	0.803
S100×40×2T400R	438.7	0.907	S80×60×4T400R	388.8	0.790
S100×40×2T450	410.8	0.849	S80×60×4T450	365.7	0.743
S100×40×2T500	348.9	0.721	S80×60×4T500	305.2	0.620
S100×40×2T550	220.7	0.456	S80×60×4T550	232.9	0.473
S100×40×2T600	150.6	0.311	S80×60×4T600	169.7	0.345
S100×40×2T650	-	-	S80×60×4T650	120.1	0.244
S100×40×2T700	59.5	0.123	S80×60×4T700	77.0	0.157
S100×40×2T750	41.0	0.085	S80×60×4T750	49.8	0.101
S100×40×2T800	65.8	0.136	S80×60×4T800	51.1	0.104
S100×40×2T900	39.8	0.082	S80×60×4T900	44.7	0.091

Table 3.12. Reduction factors of ultimate strength obtained from steady state tests.

Specimen	ε_f (%)	Specimen	ε_f (%)
S100×40×2T22	26.3	S80×60×4T22	22.1
S100×40×2T100	21.8	S80×60×4T100	18.0
S100×40×2T200	23.6	S80×60×4T200	15.5
S100×40×2T200R	21.9	S80×60×4T300	16.1
S100×40×2T300	14.5	S80×60×4T300R	16.0
S100×40×2T400	14.6	S80×60×4T400	13.4
S100×40×2T400R	14.3	S80×60×4T400R	13.3
S100×40×2T450	17.4	S80×60×4T450	19.2
S100×40×2T500	24.2	S80×60×4T500	32.5
S100×40×2T550	37.4	S80×60×4T550	41.9
S100×40×2T600	69.3	S80×60×4T600	36.2
S100×40×2T700	82.1	S80×60×4T700	35.2
S100×40×2T750	63.3	S80×60×4T750	42.1
S100×40×2T800	85.8	S80×60×4T800	> 25.5
S100×40×2T900	> 49.1	S80×60×4T900	106.1

Table 3.13. Ductility of ferritic stainless steel obtained from steady state tests.



	T (°C)	a	b	c	d
k_E	$22 \leq T \leq 550$	1	22	200	1.63
	$550 < T \leq 900$	0.75	550	0.0743	0.64
k_y	$22 \leq T \leq 400$	1	22	78.3	1.41
	$400 < T \leq 700$	0.86	400	9.6	1.49
	$700 < T \leq 900$	0.125	700	0.26	0.48
k_u	$22 \leq T \leq 400$	1	22	41.2	1.31
	$400 < T \leq 700$	0.85	400	8.7	1.47
	$700 < T \leq 900$	0.13	700	0.29	0.4

Table 3.14. Proposed coefficients for ferritic stainless steel grade EN 1.4003.

	$k_E = E_T / E_o$	$k_y = k_{y,T} / f_y$	$k_u = f_{u,T} / f_u$
M_m	1.10	1.10	1.10
F_m	1.00	1.00	1.00
V_M	0.10	0.10	0.05
V_F	0.05	0.05	0.05

Table 3.15. Parameters M_m , F_m , V_M and V_F for reliability analysis by ASCE approach (2002).

	$k_E = E_T / E_o$	$k_y = k_{y,T} / f_y$	$k_u = f_{u,T} / f_u$
100×40×2 (Steady)	15	14	15
80×60×4 (Steady)	16	13	16
100×40×2 (Transient)	11	11	0
80×60×4 (Transient)	11	8	0
Manninen and Säynäjäkangas (2012)	0	10	10
Total number of data	53	62	41

Table 3.16. Number of data used to obtain reduction factors of material properties under elevated temperatures.



	$\frac{k_{E,Test}}{k_{E,EC3}}$	$\frac{k_{E,Test}}{k_{E,Chen\&Young}}$	$\frac{k_{E,Test}}{k_{E,Proposed}}$	$\frac{k_{y,Test}}{k_{y,EC3}}$	$\frac{k_{y,Test}}{k_{y,Chen\&Young}}$	$\frac{k_{y,Test}}{k_{y,Proposed}}$	$\frac{k_{u,Test}}{k_{u,EC3}}$	$\frac{k_{u,Test}}{k_{u,Chen\&Young}}$	$\frac{k_{u,Test}}{k_{u,Proposed}}$
Mean (P_m)	0.88	1.53	1.04	0.92	1.10	1.01	0.87	0.79	1.01
COV (V_p)	0.286	0.842	0.174	0.169	0.308	0.095	0.134	0.337	0.133
Number of data	53	53	53	62	62	62	41	41	41
Resistance factor (ϕ_0)	0.55	0.25	0.80	0.70	0.70	0.90	0.70	0.45	0.90
Reliability index (β_0)	2.50	2.60	2.65	2.60	2.50	2.50	2.65	2.65	2.50
Resistance factor (ϕ_1)	0.55	0.25	0.80	0.75	0.70	0.90	0.75	0.45	0.90
Reliability index (β_1)	2.60	2.60	2.65	2.50	2.50	2.50	2.55	2.65	2.50

Table 3.17. Reliability analysis for different design rules by ASCE approach.

	$\frac{k_{E,Test}}{k_{E,EC3}}$	$\frac{k_{E,Test}}{k_{E,Chen\&Young}}$	$\frac{k_{E,Test}}{k_{E,Proposed}}$	$\frac{k_{y,Test}}{k_{y,EC3}}$	$\frac{k_{y,Test}}{k_{y,Chen\&Young}}$	$\frac{k_{y,Test}}{k_{y,Proposed}}$	$\frac{k_{u,Test}}{k_{u,EC3}}$	$\frac{k_{u,Test}}{k_{u,Chen\&Young}}$	$\frac{k_{u,Test}}{k_{u,Proposed}}$
n	53	53	53	62	62	62	41	41	41
$k_{d,n}$	3.285	3.285	3.285	3.255	3.255	3.255	3.347	3.347	3.347
b	0.929	1.197	1.031	0.994	1.189	1.013	0.911	0.907	0.999
V_δ	0.573	0.568	0.248	0.227	0.439	0.098	0.206	0.558	0.128
V_r	0.579	0.574	0.262	0.242	0.447	0.129	0.223	0.564	0.153
γ_{M2}	6.11	4.67	1.95	1.87	3.09	1.25	1.95	6.16	1.39

Table 3.18. Reliability analysis for different design rules by Eurocode approach.



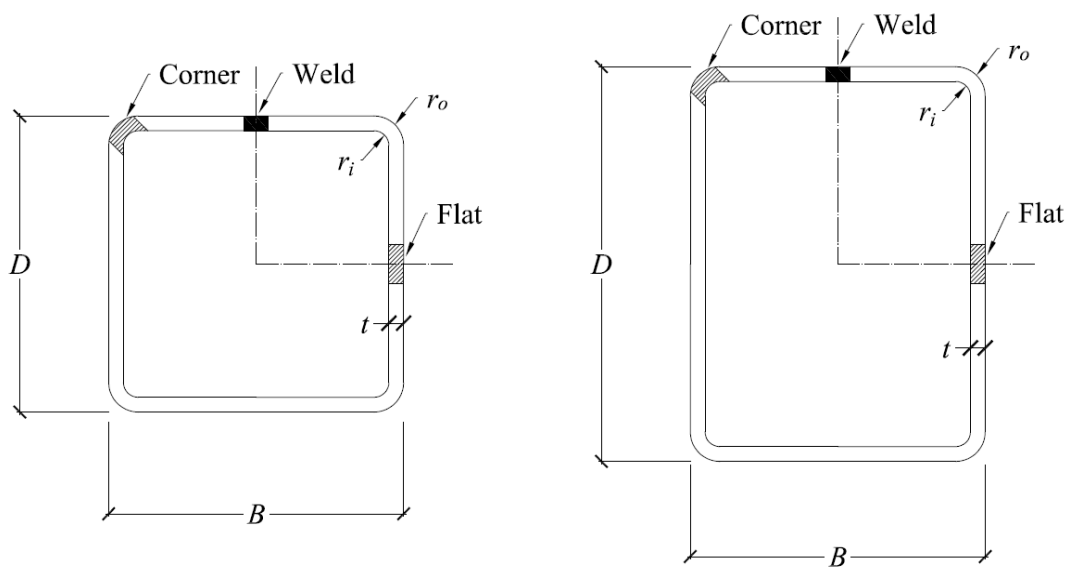


Figure 3.1. Locations of tensile flat and corner coupons in the cross-sections.

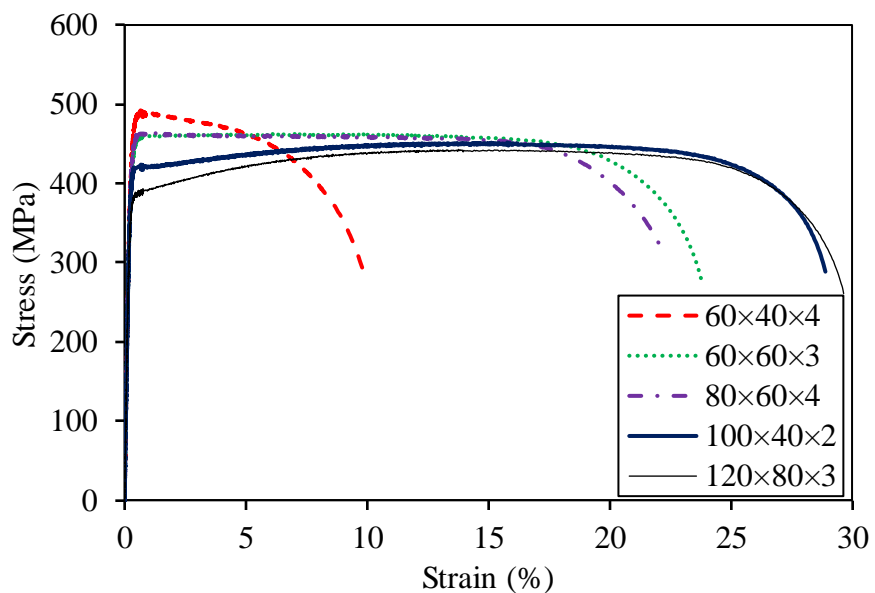


Figure 3.2. Static stress-strain curves obtained from tensile coupon tests in flat portions.

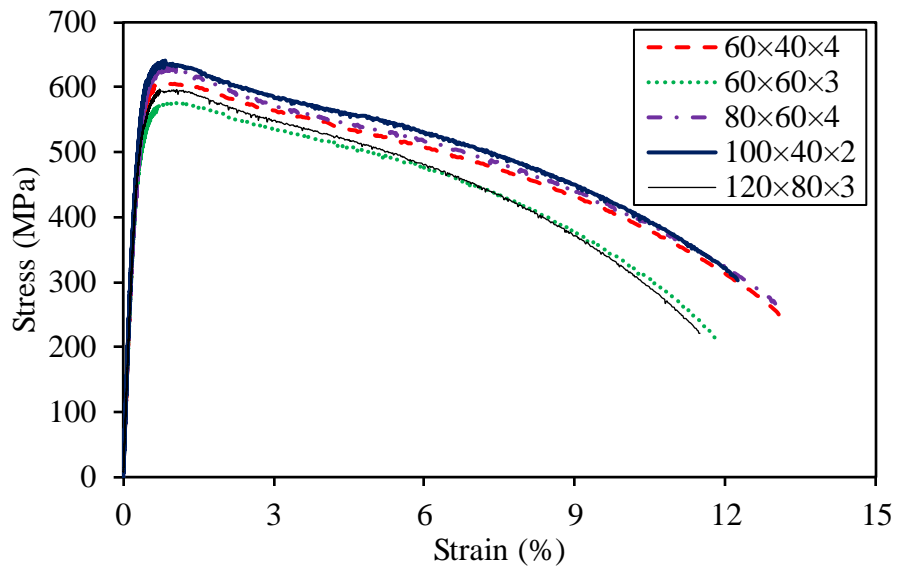


Figure 3.3. Static stress-strain curves obtained from tensile coupon tests in corner portions.

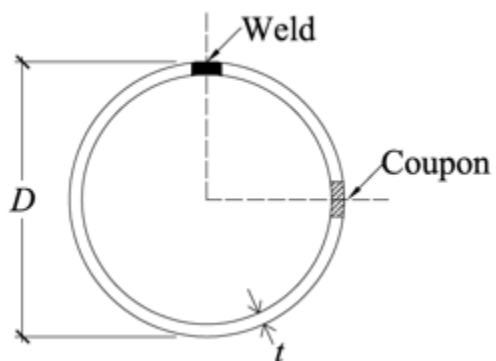


Figure 3.4. Locations of tensile curved coupons in the circular cross-sections.



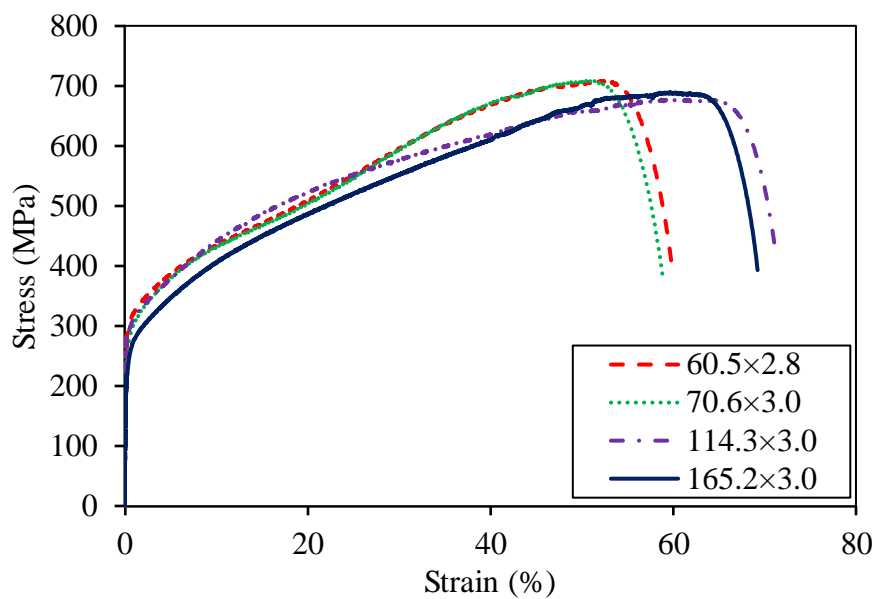


Figure 3.5. Static stress-strain curves obtained from tensile coupon tests in curved portions.

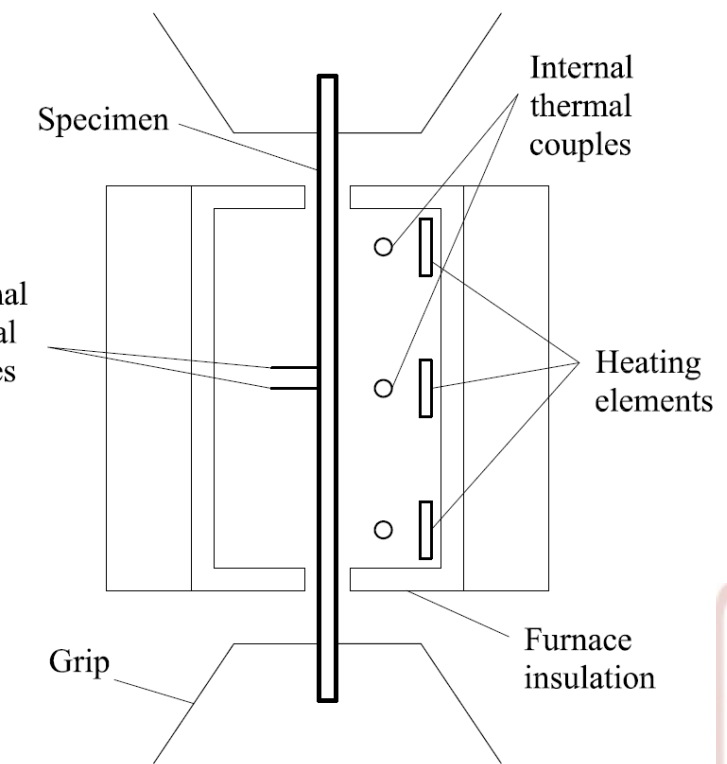
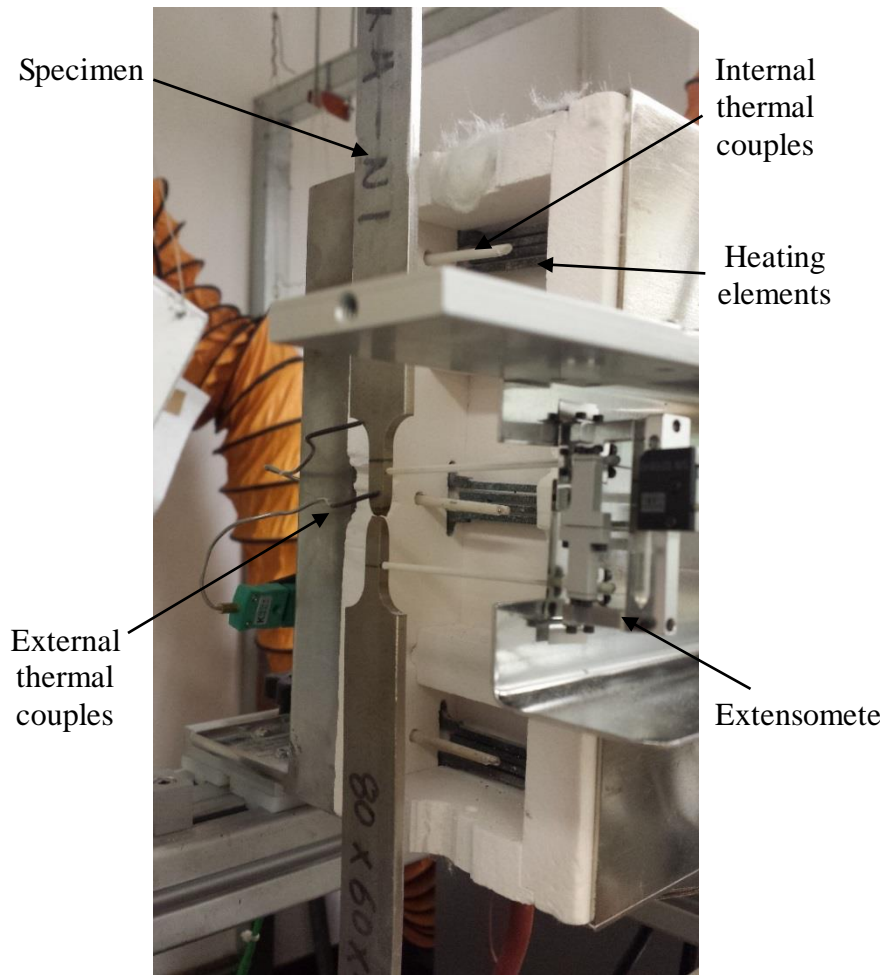


Figure 3.6. Test set-up.

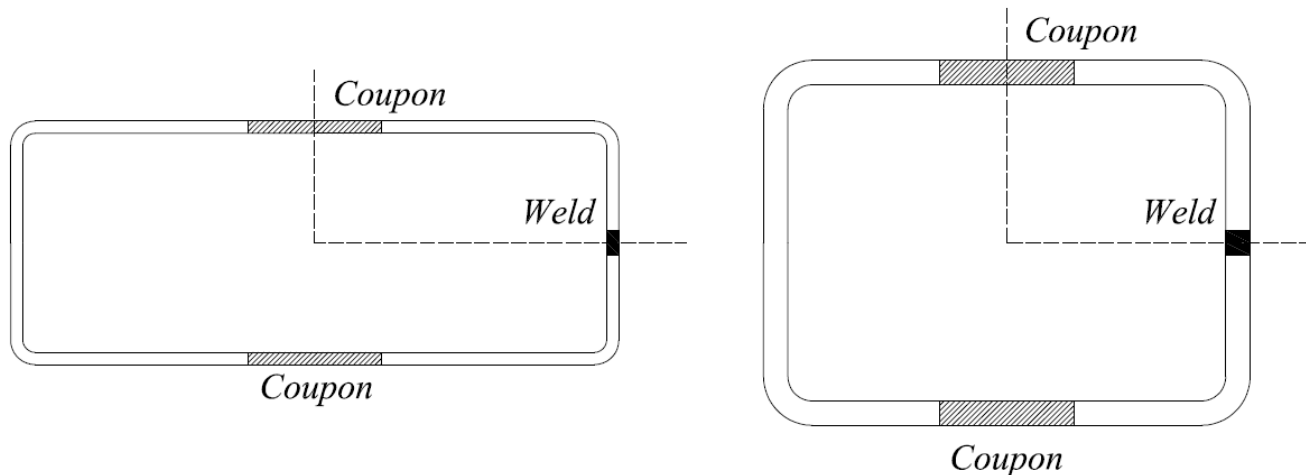
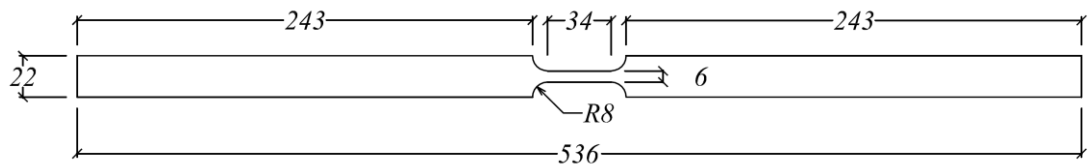


Figure 3.7. Locations of coupons and weld in section RHS 100×40×2 and 80×60×4.



Note: units in mm.

Figure 3.8. Dimensions of coupon specimen.

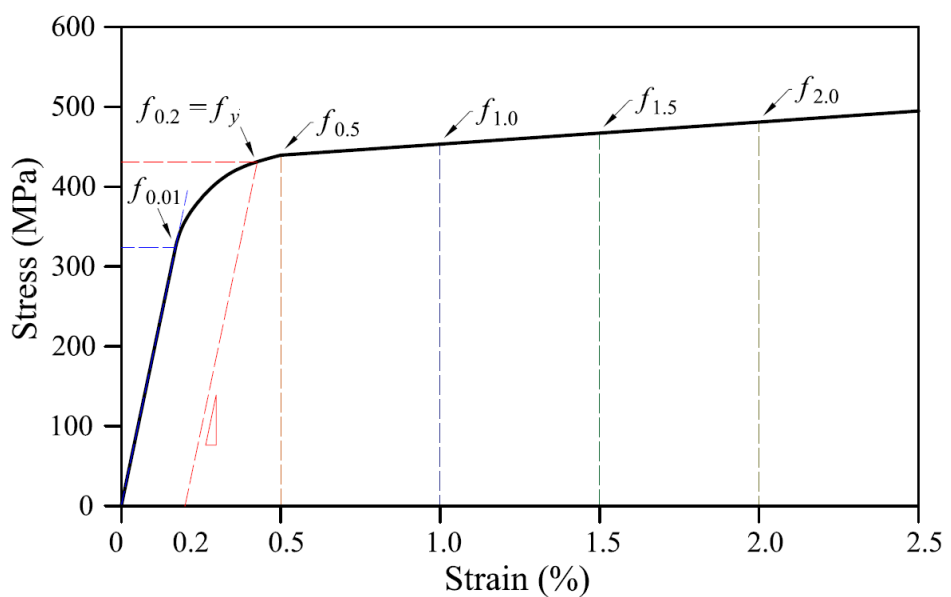


Figure 3.9. Definition of symbols.



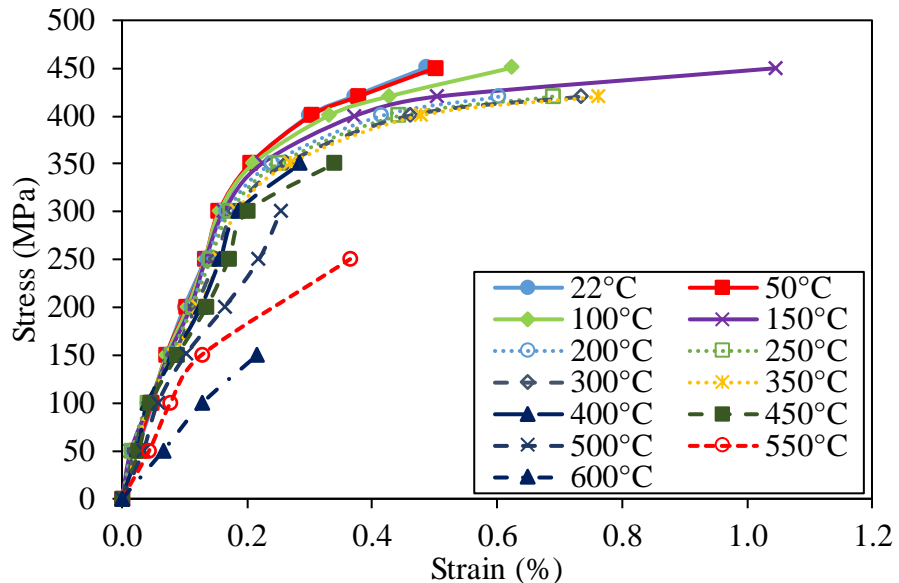


Figure 3.10. Stress-strain curves of section 80×60×4 at different temperatures obtained from coupon tests by transient state method.

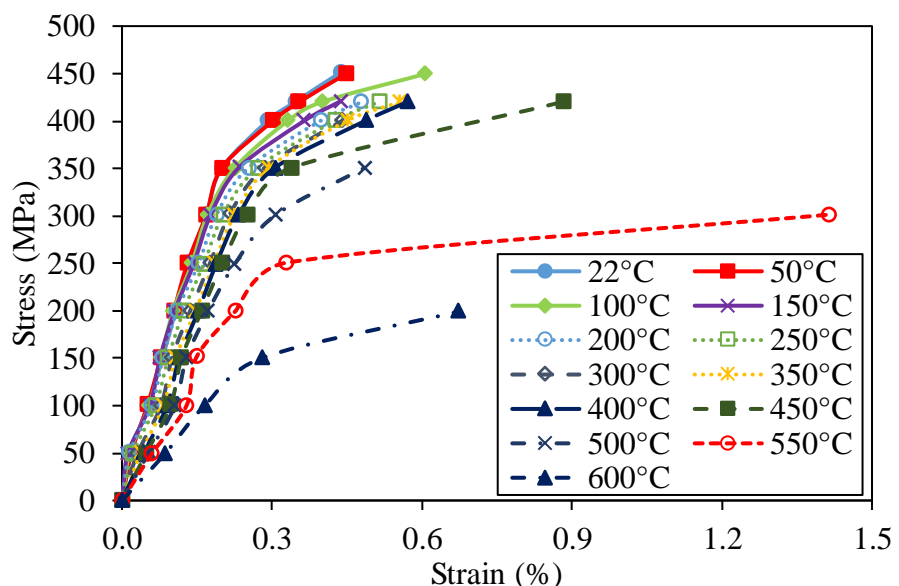


Figure 3.11. Stress-strain curves of section 100×40×2 at different temperatures obtained from coupon tests by transient state method.

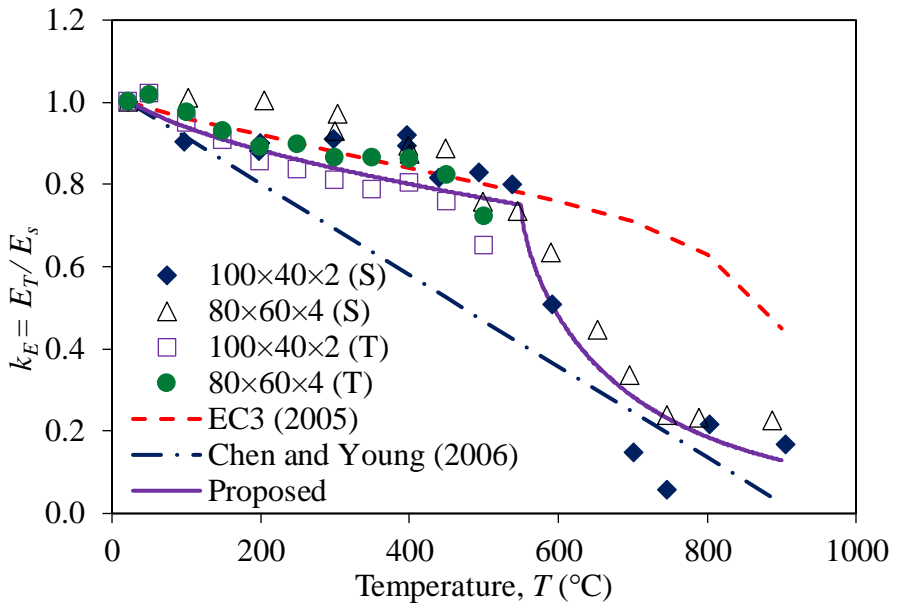


Figure 3.12. Comparison of elastic modulus reduction factors.

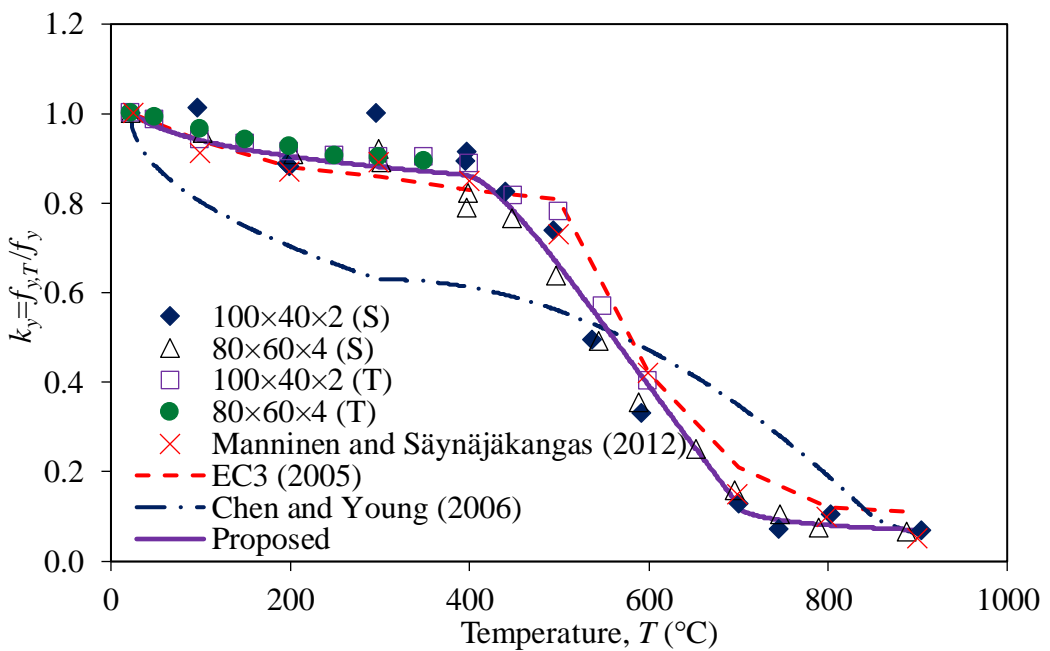


Figure 3.13. Comparison of yield strength reduction factors.

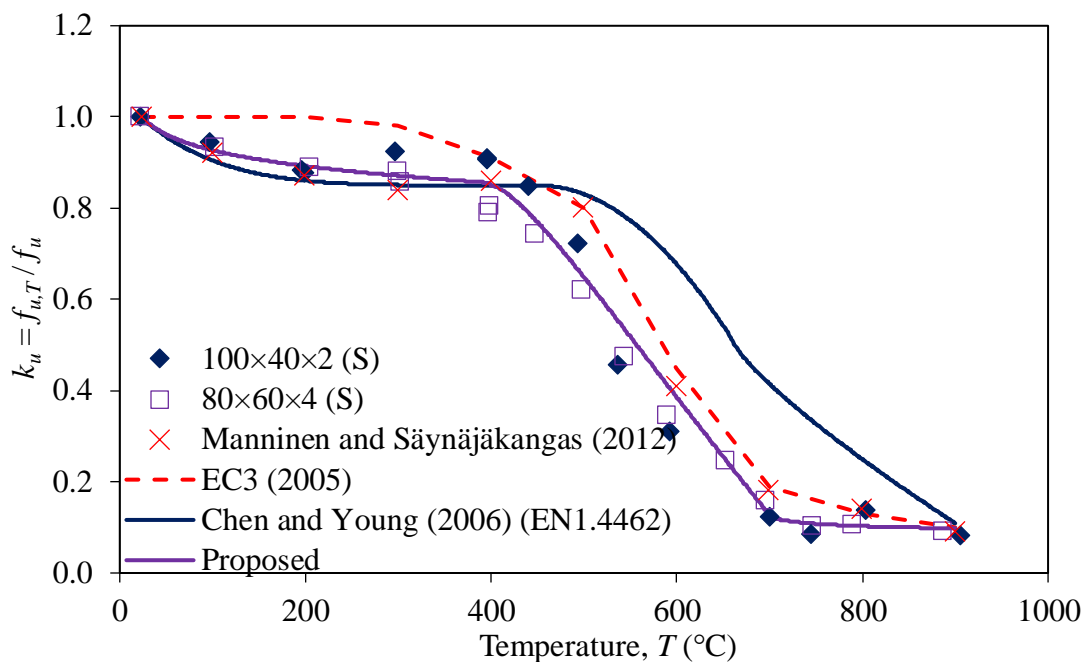


Figure 3.14. Comparison of ultimate strength reduction factors.

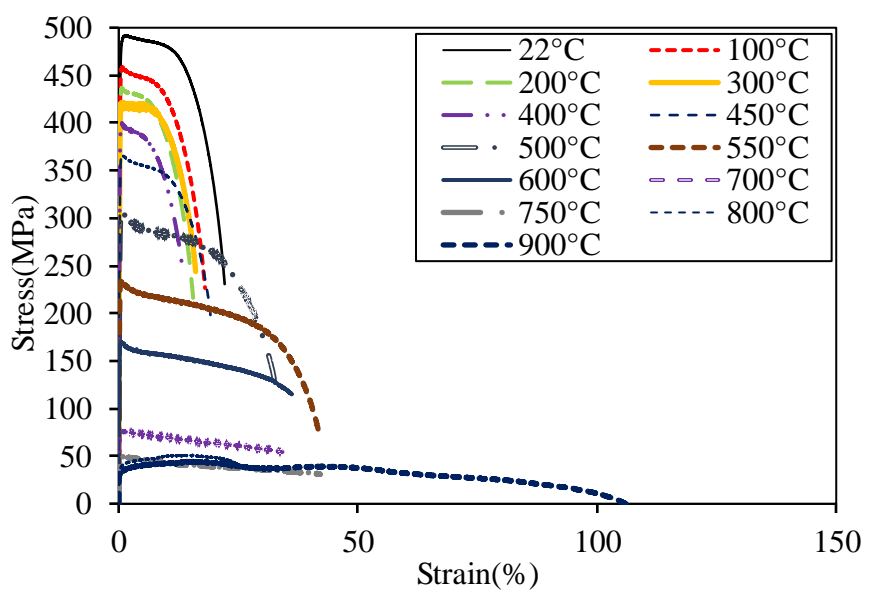


Figure 3.15. Stress-strain curves of section 80x60x4 obtained from steady state tests.



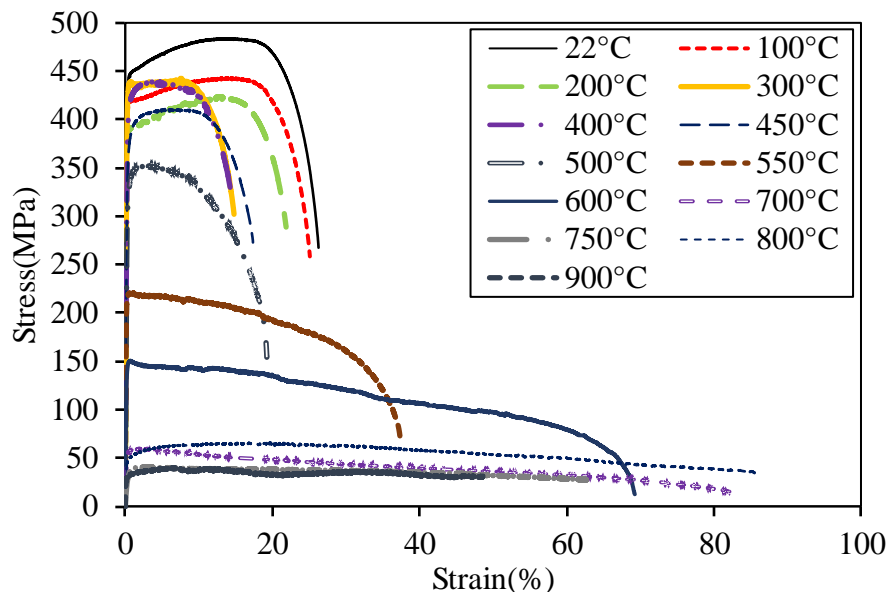


Figure 3.16. Stress-strain curves of section 100×40×2 obtained from steady state tests.

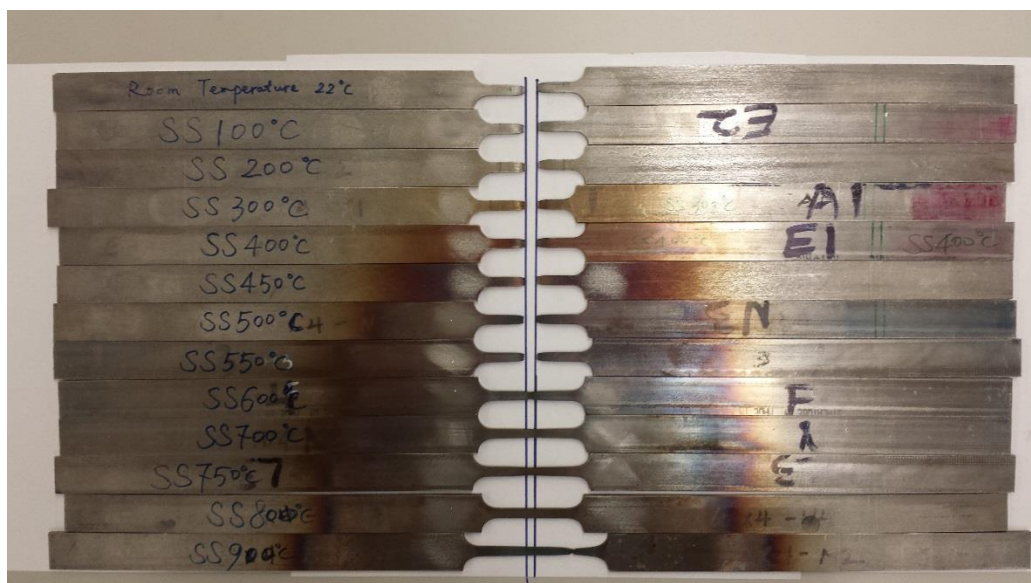


Figure 3.17. Failed ferritic stainless steel coupon specimens of section 80×60×4 at various temperatures obtained from steady state tests.

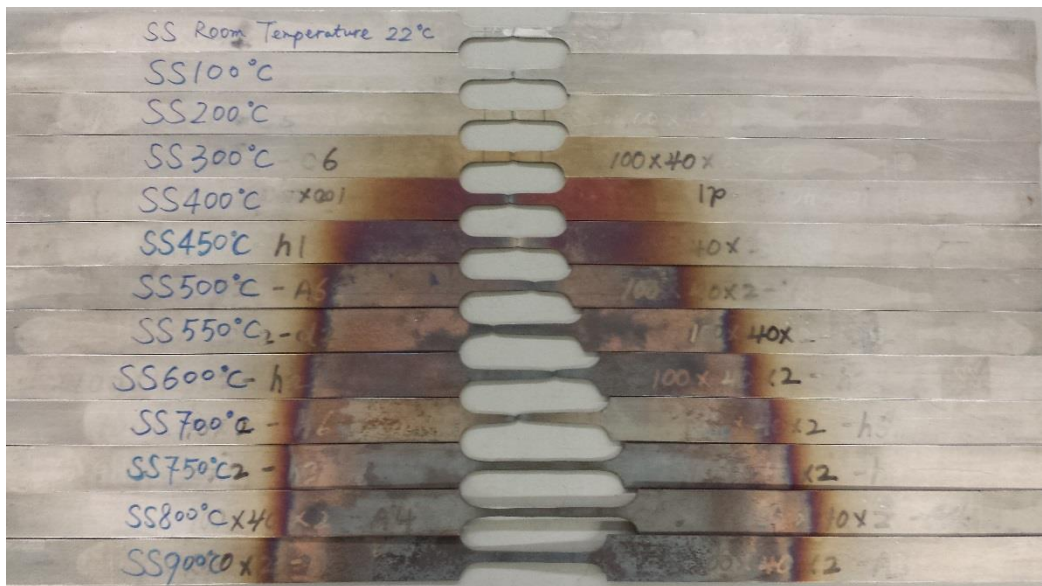


Figure 3.18. Failed ferritic stainless steel coupon specimens of section 100×40×2 at various temperatures obtained from steady state tests.

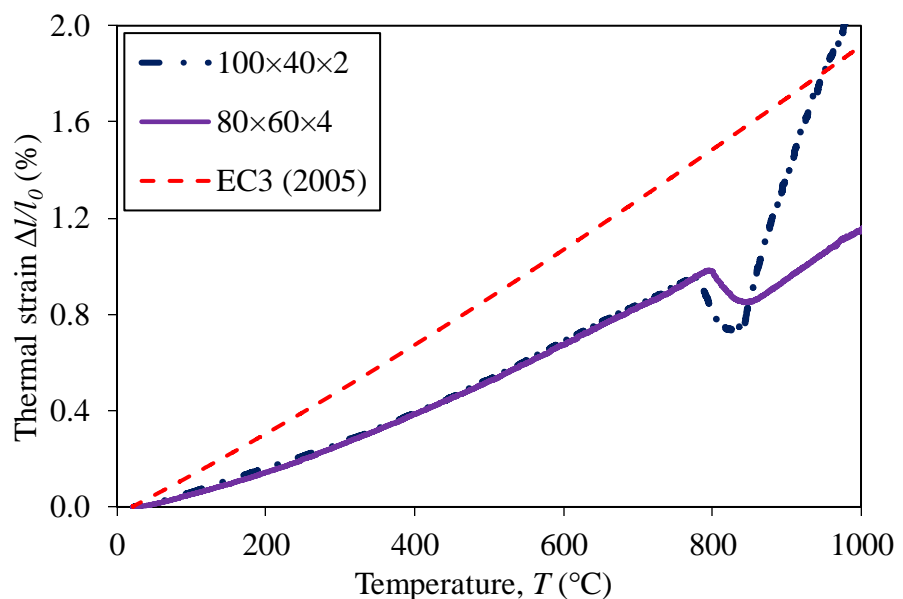


Figure 3.19. Thermal expansion of ferritic stainless steel grade EN 1.4003 at elevated temperatures.



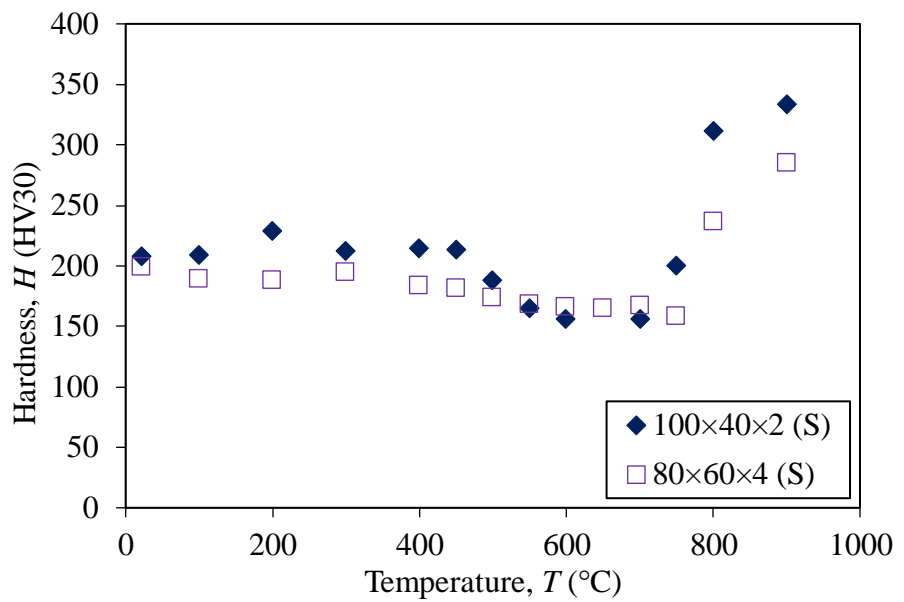


Figure 3.20. Vickers Hardness test results of tested specimens by steady state test.



CHAPTER 4

CLASSIFICATION AND FLEXURAL BEHAVIOUR OF COLD-FORMED FERRITIC STAINLESS STEEL SHS & RHS

4.1 Introduction

This chapter is aimed to study the flexural behaviour of ferritic stainless steel hollow sections. A series of tests on both square and rectangular hollow sections of ferritic stainless steel grade EN 1.4003 subjected to bending was conducted. A finite element model was developed. It is shown that the model can accurately simulate the flexural behaviour of the ferritic stainless steel beams.

The 176 experimental and numerical data obtained from this study as well as data collected from previous investigations (Afshan and Gardner, 2013a; Bock et al., 2015; Zhao et al., 2015; Zhao et al., 2016a) were compared with design predictions calculated from the current specifications EC3 (2015), SEI/ASCE-8 (2002), AS/NZS-4673 (2001), direct strength method (DSM) (AISI-S100, 2016) and continuous strength method (Afshan and Gardner, 2013b) for cold-formed ferritic stainless steel beams. The modified direct strength method by Huang and Young (2014b) for lean duplex stainless steel members was also assessed to study the applicability to ferritic stainless steel members. Reliability study was



conducted to assess the applicability of the current design specifications to ferritic stainless steel beams. Modification to European code (EC3, 2015) for design of cold-formed ferritic stainless steel beams is also presented.

4.2 Experimental Investigation

4.2.1 Test specimens

Four-point bending tests were conducted on ferritic stainless steel square and rectangular sections. A total of ten specimens, including one square hollow section and four rectangular hollow sections, were tested in this study. The rectangular hollow sections were tested about both the major and minor axes. The nominal aspect ratio (D/B) of the specimens varied from 0.4 to 2.5, and the nominal thickness varied from 2.0 to 4.0 mm. The nominal flat-depth-to-thickness (d/t) ratio varied from 6 to 46, where d is the flat portion of overall depth of the sections. The specimens were labelled in a way that the nominal dimensions including the overall depth of web (D), overall width of flange (B), and thickness (t) of the cross-section can be identified. For example, the label 80×60×4R refers to the specimen with nominal cross-sectional dimensions depth (D), width (B), thickness (t) equal to 80, 60 and 4 mm. If the test was a repeated one, a symbol of “R” is added in the label. The specimen labelling also reveals on which axis the specimen was bent. For example, the label 80×60×4 indicates that the specimen was subjected to major axis bending. However, the label 60×80×4 indicates minor axis bending of the same section. The measured specimen dimensions are shown in Table 4.1, where D and B are the outer cross-section depth and width, respectively, t is the plate thickness, r_o and r_i are the external and internal corner radii, respectively, and L is the member length. The elastic section modulus W_{el}



and plastic section modulus W_{pl} for each specimen are also summarized in Table 4.1.

4.2.2 Test setup and operation

A total of ten four-point bending tests were conducted to determine the bending moment capacities and curvatures of the specimens. The schematic view of the four-point bending test arrangement is shown in Fig. 4.1. The beams were simply supported and were simulated by half-round and roller support conditions. Both major and minor axes bending tests were conducted for rectangular hollow sections. The moment span and shear span were carefully designed so that no specimen was failed due to shear failure. The beam specimens were either 1200 mm or 1400 mm in length. For the 1200 mm long specimens, the moment span and shear span were 400 and 330 mm, respectively. For the 1400 mm long specimens, the moment span and shear span were 500 and 380 mm, respectively. Load transferring plates of 90 mm width were placed between the beam specimen and roller/half-rounds to provide uniform distributed loads at the supports and loading points. Stiffening plates of 90 mm width were clamped to the web of the specimens at the supports and loading points in order to prevent any possible web crippling. In addition, wooden blocks were inserted at the locations of supports and loading points to prevent any possible local bearing failure. Three displacement transducers (LVDTs) were placed at the bottom of the two loading points and mid-span of the specimen to record vertical displacements. The readings were used to obtain curvatures of the specimens. A servo-controlled hydraulic testing machine was used to apply compressive force to the specimen by displacement control method at a constant loading rate of 1.0 mm/min. The static load was recorded by pausing the applied load for 100 seconds near ultimate load.



4.2.3 Test results

All the specimens failed within the moment span and no shear failure was observed. Out-of-plane bending was not observed for all the tests. Experimental ultimate moments (M_{Exp}) and the corresponding curvatures (κ_{Exp}) of the tested specimens are summarized in Table 4.2. Experimental ultimate moment (M_{Exp}) was calculated by multiplying half the ultimate static load to the level arm, which is the length of moment span. Curvature was obtained by calculating the radius (r) of the curved beam specimen from the readings of the three LVDTs located at the two loading points and mid-span of each specimen, such that $\kappa = 1/r$. The weight of the half-round, roller and steel plates were included in the calculation of ultimate moment. The static moment-curvature curve for each specimen is plotted in Fig. 4.2(a). Normalized moment-curvature curves were obtained by dividing the experimental moments by plastic moment (M_{pl}) and dividing the experimental curvature by the curvature corresponding to the plastic moment (κ_{pl}), as shown in Fig. 4.2(b).

The theoretical elastic moment capacity (M_y) and plastic moment capacity (M_{pl}) were calculated by multiplying the relevant section moduli derived from the full section with the 0.2% proof stress ($\sigma_{0.2}$) obtained from flat coupon tests at room temperature as reported in Chapter 3 of the thesis. The experimental ultimate moments (M_{Exp}) were compared with the theoretical elastic and plastic moments, and conservative predictions on moment capacity of the tested specimens were found, as shown in Table 4.2. The mean values of M_{Exp} / M_y and M_{Exp} / M_{pl} ratios are 1.35 and 1.12 with the corresponding coefficient of variation (COV) of 0.131 and 0.106, respectively. Due to the occurrence of local buckling before reaching yield strength in the compressive flange, the specimen 40×100×2 has M_{Exp} / M_y and M_{Exp} / M_{pl} ratios of 0.94 and 0.84, respectively.



Rotation capacity (R), as shown in Fig. 4.3, is a commonly used measure of ductility for flexural member. The rotation capacity (R) was evaluated according to Eq. (4.1).

$$R = \frac{\kappa_{pl}^{\hat{}}}{\kappa_{pl}} - 1 \quad (4.1)$$

in which $\kappa_{pl}^{\hat{}}$ is the total curvature of the specimen when the moment-curvature curve falls back below the plastic moment capacity (M_{pl}) as obtained from the test results, and κ_{pl} is the elastic part of the total curvature when M_{pl} is reached on the ascending branch, defined as $\kappa_{pl} = M_{pl} / (E_o I)$, where I is the moment of inertia of full section, and E_o is the initial elastic modulus of the steel section. The theoretical plastic moment capacity (M_{pl}) was calculated by multiplying the plastic section modulus derived from full section with the 0.2% proof stress ($\sigma_{0.2}$) obtained from the flat coupon tests. Full rotation capacities were not recorded due to excessive deformations in some of the beam tests, which resulted in termination of tests. However, ultimate load was reached for all beam tests in this study. For these cases, the maximum recorded curvatures were treated as $\kappa_{pl}^{\hat{}}$ and the corresponding rotation capacities (R) are shown in Table 4.2.

4.3 Finite Element Model and Verification

4.3.1 Finite element model

The finite element package ABAQUS version 6.12 (ABAQUS, 2012) was employed to perform numerical study in order to replicate the experimental results. Upon the verification of the finite element model, parametric study was carried out to extend the available experimental data to sections of wider range of slenderness ratio. The material properties obtained from the flat and corner



coupon tests were incorporated in the finite element model. Measured dimensions of specimens were used to verify the finite element model, and centerline dimensions of the cross-sections were used. Four-node doubly curved shell element with reduced integration (S4R) was used in the model. Mesh size of 10×10 mm was used for the flat portion of specimens while finer mesh element size was used for the corner portion.

4.3.2 Boundary and loading conditions

The finite element model was developed to simulate the experimental results, thus the boundary and loading condition were carefully modelled in order to achieve better agreement. The compressive concentrated load was transferred from the roller and half-rounded bar to the load transferring plates and then to the specimen, as shown in Fig. 4.1. In the finite element model, the interface between the load transferring plates and the specimen was modelled by coupling constraint in all degrees of freedom by kinematic method. The load transferring plate was modelled as a surface set on a face of exact size of the load transferring plate partitioned from the specimen. The partitioned face was then coupled to a reference point and the coupling constraint was applied to the respective supports and loading points. The two loading points that modelled as two reference points were restrained against all degrees of freedom except for the vertical and horizontal displacement as well as rotation about the bending axis. Similarly, the two supports were restrained against all degrees of freedom, while displacement in the vertical direction was restricted. In addition, the horizontal displacement was also restricted at the half-round support in the model. Loading was applied to the loading points by displacement control method, which was identical to the actual tests, with a specified displacement value. The specified displacement value



was chosen to be a relatively large value in order to ensure the beam can reach its ultimate bending moment. Static RIKS step in the ABAQUS library was used to apply the loading and the nonlinear geometric parameter (*NLGEOM) was included to allow large displacement analysis, which is similar to the finite element model in Huang and Young (2014b).

4.3.3 Material model

Tensile coupon tests were conducted on both the flat and corner regions of the specimens. The measured stress-strain relationships were used in the finite element model. The true stress (σ_{true}) and logarithmic plastic strain (ε_{pl}) were converted from the static engineering stress (σ) and strain (ε) obtained from the tensile coupon tests. The cold-forming process introduces significant strength enhancement to the corner region. The strength enhancement was found to extend into the flat region of the section by Theofanous and Gardner (2010). Accordingly, the strength enhancement due to cold-forming effect was included into the finite element model. The strength enhancement of corner region was assumed to extend by two times the thickness of the section beyond the corner region (2010), as shown in Fig. 4.4. The corner material properties, as derived from corner coupon tests, were thus applied to the corner region and also extended to the adjacent flat portion of two times the thickness. Flat coupon material properties were used for the rest of the section. The finite element model with extended corner material region was approximately 5% more accurate than that without extended corner material region.



4.3.4 Verification of finite element model

The ultimate moment capacities predicted by the finite element model (M_{FEA}) were compared with the experimental ultimate moments (M_{Exp}). The mean value of experimental-to-FEA moment capacity (M_{Exp} / M_{FEA}) is 1.01 with COV of 0.047, as shown in Table 4.2. The maximum difference in moment capacity between the experimental and numerical results was found to be 10% for the specimen $60 \times 60 \times 3$. The failure modes obtained from the numerical analyses are in good agreement with the experimental results.

The finite element model was also used to obtain the moment capacity of sections conducted by previous investigations (Afshan and Gardner, 2013a; Bock et al., 2015; Zhao et al., 2015; Zhao et al., 2016a). The numerical results were also compared with the test results reported by Afshan and Gardner (2013a), Bock et al. (2015), Zhao et al. (2015 and 2016a). Good agreement on the moment capacity was achieved between the numerical results and the results from the previous investigations. The experimental-to-FEA moment capacity (M_{Exp} / M_{FEA}) is 1.00 with COV of 0.072. This further proves that the finite element model is able to predict the moment capacity very well.

4.3.5 Parametric study

Upon the validation of the finite element model, an extensive parametric study was conducted based on the verified finite element model. A total of 151 cold-formed ferritic stainless steel hollow flexural members was performed. The material properties adopted in this parametric study were obtained from the flat and corner coupon test results of section $100 \times 40 \times 2$.



The 151 specimens in this parametric study cover both square and rectangular hollow sections. The square hollow sections include five different overall profiles (overall depth \times overall width) ranged from 60 \times 60 to 300 \times 300. The rectangular hollow sections comprise seven different overall profiles ranged from 120 \times 80 to 300 \times 100. In order to cover a wide range of slenderness ratio, the thickness of sections varied from 1 to 12 mm and the flat-depth-to-thickness (d/t) ratio cover the range of 3.8 to 116. The aspect ratio of the overall depth to flange widths (D/B) varied from 0.25 to 4. The moment span and shear span of each specimen were carefully designed so that specimens would not fail by shear. The parametric study results are summarized in Table 4.3.

4.4 Reliability Analysis

Reliability analysis was carried out to assess the appropriateness of the current design specifications on the predictions of moment capacity of cold-formed ferritic stainless steel hollow sections. The reliability analysis is detailed in the Commentary of the ASCE Specifications SEI/ASCE-8 (ASCE, 2002) and the performance of a design rule is assessed by the reliability index (β_0). The limit state format in the ASCE Specification for Load and Resistance Factor Design (LRFD) provides the expressions for deriving the resistance factors. The capacity (ϕR_n) must be greater than the demand (γQ) in the LRFD format through $\phi R_n > \sum \gamma_i Q_i$. The design rule is considered to be safe if the reliability index is larger than the target reliability index (β_0) and the value of 2.50 was selected as the target reliability index in this study. The resistance factor (ϕ_0) of 0.90 was used as specified in SEI/ASCE-8 (2002), AS/NZS-4673 (2001), AISI-S100 (2016) for direct strength method (DSM) and the modified DSM by Huang and Young (2014b). A different value of 0.91 was adopted as the resistance factor in EC3 (2015) and continuous strength method (CSM) (Afshan and Gardner, 2013b).



Different load combinations were adopted in this study in accordance with different specifications. Load combination of 1.2 DL + 1.6 LL was specified in SEI/ASCE-7 (2013) and 1.2 DL + 1.5 LL for AS/NZS-4673 (2001), where DL is dead load and LL is live load. The same combination of 1.2 DL +1.6 LL was used for the direct strength method and the modified DSM by Huang and Young (2014b). The load combination of 1.35 DL + 1.5 LL was used in EC3 (2015) and also adopted for continuous strength method. The live load to dead load ratio of 1/5 was used. Statistical parameters $M_m = 1.10$, $F_m = 1.00$, $V_M = 0.10$ and $V_F = 0.05$ were adopted in the calculation of reliability index in Eq. (6.2-2) in the American Specification SEI/ASCE-8 (2002), where M_m is the mean value of material factor, F_m is the mean value of fabrication factor, V_M is the coefficient of variation of material factor and V_F is the coefficient of variation of fabrication factor. The statistic parameters P_m and V_P are the mean value of experimental-to-design or FEA-to-design load ratios and the corresponding coefficient of variation. The correction factor C_p was also used in the calculation of reliability index in order to compensate the influence due to limited number of data in accordance with Eq. (K2.1.1-4) in the North American Specification for cold-formed steel structural members AISI-S100 (2016). In order to facilitate direct comparison, a constant resistance factor (ϕ_l) of 0.90 and load combination of 1.2 DL +1.6 LL were used to calculate the respective reliability index (β_l) for all the aforementioned design rules. The results of reliability analysis are shown in Table 4.4.

4.5 Assessment of Existing Slenderness Limits

4.5.1 General

The experimental and numerical results are compared with existing slenderness limits for ferritic stainless steel. The determination of slenderness limits for classification follows the provisions of EC3 (2015). The section classification is detailed in EC3 (2015) and all the constituent elements should be classified by comparing their flat-width-to-thickness ratio to codified slenderness limits. The cross-sectional response is assumed to be related to its most slender element. Class 4 cross-sections are classified as slender sections and local buckling will prevent the sections from reaching their nominal yield strength in compression. Effective width concept is introduced to determine the element strength by taking account of the local buckling effect. Class 3 cross-sections can reach their compressive yield strength prior to the onset of local buckling. However, the Class 3 cross-sections cannot attain their plastic moment capacities. Both the Class 1 and Class 2 cross-sections can reach their plastic moment capacities and the Class 1 cross-sections can sustain their plastic moment capacities over large rotations. However, it should be noted that despite the existence of Class 1 cross-sections, plastic global analysis is not permitted for structural stainless steel in EC3 (2015).

4.5.2 Slenderness limits for Class 3 cross-sections

The slenderness limits for Class 3 cross-sections is firstly assessed. The moment capacity (M_u) obtained from the numerical study as well as previous investigations (Afshan and Gardner, 2013a; Bock et al., 2015; Zhao et al., 2015; Zhao et al., 2016) was normalized by the respective elastic moment capacities



(M_y) and plotted against the slenderness parameters (c/te) for both the element subject to compression (flange) and element subject to bending (web), as shown in Figs 4.5 and 4.6, respectively. The slenderness parameter is specified in EC3 (2015), where c is the flat width of the elements, t is the plate thickness and $\varepsilon = \sqrt{235 / \sigma_{0.2} * E_o / 210,000}$. EC3 (2015) specified the Class 3 limit for element subject to compression to be 37.0 based on all relevant published test data on stainless steel summarized by Gardner and Theofanous (2008). In SEI/ASCE-8 (2002) and AS/NZS-4673 (2001), the element subject to compression for SHS and RHS is referring to uniformly compressed stiffened element, and the equivalent slenderness limit can be calculated when the slenderness factor (λ) in Eq. 2.2.1-4 of the SEI/ASCE-8 (2002) and Eq. 2.2.1.2(4) of the AS/NZS-4673 (2001) equals to 0.673 which is fully effective element. Hence, the slenderness limit is equivalent to 38.2. It is found that all the current slenderness limits are too conservative for the cold-formed ferritic stainless steel. The slenderness limit of 42.0 in EC3 (2005) for carbon steel was also used to compare with stainless steel, which is also found to be conservative, as shown in Fig. 4.5. Therefore, it is suggested to relax the existing slenderness limit to the value of 51.0 for Class 3 element subject to compression.

For element subject to bending, EC3 (2015) specified the value of 90.0 as the slenderness limit and it is found that this value generally provides good predictions. The slenderness limit of 124.0 in EC3 (2005a) for carbon steel is not conservative for cold-formed ferritic stainless steel. Hence, the current slenderness limit in EC3 (2015) of 90.0 for Class 3 element subject to bending is suitable.



4.5.3 Slenderness limits for Class 2 cross-sections

The Class 2 slenderness limits specified in EC3 (2015) for stainless steel and EC3 (2005a) for carbon steel are shown in Figs 4.7 and 4.8. The Class 2 sections can attain their plastic moment capacities (M_{pl}) so that the moment capacity (M_u) obtained from the experimental and numerical investigations as well as previous investigations (Afshan and Gardner, 2013a; Bock et al., 2015; Zhao et al., 2015; Zhao et al., 2016) was normalized by respective M_{pl} and plotted against the slenderness parameters ($c/t\epsilon$). It can be seen that the EC3 (2015) slenderness limit of 35.0 is conservative, while the slenderness limit of 38.2 in EC3 (2005a) for carbon steel provides better predictions, as shown in Fig. 4.7. Hence, it is recommended to relax the slenderness limit to 38.2 for element subject to compression. For element subject to bending, the slenderness limit of 76.0 in EC3 (2015) provides good predictions, as shown in Fig. 4.8. The slenderness limit of 83.0 in EC3 (2005a) for carbon steel is not conservative for cold-formed ferritic stainless steel.

4.5.4 Slenderness limits for Class 1 cross-sections

The rotation capacities (R) of all those specimens which can attain their plastic moment capacities are plotted against the slenderness parameter ($c/t\epsilon$) of constituent elements, as shown in Figs 4.9 and 4.10. The rotation capacities were determined by Eq. (4.1). The rotation capacity for Class 1 sections in EC3 (2015) is not specified. Hence, the requirement of $R = 3$ in EC3 (2005a) for carbon steel is adopted in this study. The same requirement on rotation capacity is also used by Gardner and Theofanous (2008), Huang and Young (2014b) for stainless steel flexural members. EC3 (2015) specifies the value of 33.0 and 72.0 for elements subject to compression and bending, respectively. The slenderness limits as



specified in EC3 (2005a) for carbon steel adopt the same value as EC3 (2015) for stainless steel. For element subject to compression, the slenderness limit of 33.0 appears not conservative as shown in Fig. 10, and similar conclusion was also drawn by Bock et al. (2015). Therefore, it is recommended that the slenderness limit of 28.0 should be adopted for Class 1 elements subject to compression. For element subject to bending, the slenderness limit of 72.0 is suitable for cold-formed ferritic stainless steel, as shown in Fig. 4.10.

In summary, it is recommended that the slenderness limits ($b/t\epsilon$) of 28.0, 38.2 and 51.0 be used for Classes 1, 2 and 3 of element subject to compression, respectively, for cold-formed ferritic stainless steel. The existing slenderness limits ($d/t\epsilon$) of 72.0, 76.0 and 90.0 in EC3 (2015) are suitable for Classes 1, 2 and 3 of element subject to bending, respectively.

4.6 Comparison of Moment Capacities

4.6.1 General

The nominal moment strengths (unfactored design strengths) of the test specimens and specimens from parametric study as well as data from previous investigations (Afshan and Gardner, 2013a; Bock et al., 2015; Zhao et al., 2015; Zhao et al., 2016b) were calculated according to SEI/ASCE-8 (2002), AS/NZS-4673 (2001), EC3 (2015), DSM (AISI-S100, 2016), modified DSM by Huang and Young (2014b) and CSM (Afshan and Gardner, 2013b). The material properties from flat coupon test of section 100×40×2 were used in the calculation of nominal moment strength for the specimens in the parametric study. Effective width method for sectional capacity was adopted in the design rules in SEI/ASCE-8 (2002), AS/NZS-4673 (2001) and EC3 (2015). The effective width method involves



iteration process in order to locate the neutral axis under bending moment. The direct strength method and continuous strength method utilizes the gross section to determine the moment capacity rather than the element effectiveness, and iteration is not required.

Discrepancy exists in the calculation using the effective width method among the SEI/ASCE-8 (2002) and AS/NZS-4673 (2001) against EC3 (2015) regarding the flat width to where the reduction factor (ρ) is applied when considering the element in bending. The reduction factor shall be applied to the full flat width of the bending element, which is the unreduced full width of the web, in the design rules of ASCE (2002) and AS/NZS (2001). However, the reduction factor should be applied solely to the compression portion of the web in EC3 (2015). The calculation in SEI/ASCE-8 (2002) and AS/NZS-4673 (2001) may lead to the sum of effective widths b_1 and b_2 calculated from Section 2.2.2 in the SEI/ASCE-8 (2002) and the sum of effective widths b_{e1} and b_{e2} calculated from Section 2.2.2 in the AS/NZS-4673 (2001) larger than the depth of neutral axis. This is avoided by treating the compressive portion of the web as fully effective.

4.6.2 American Specification and Australian/New Zealand Standard

The SEI/ASCE-8 (2002) and AS/NZS-4673 (2001) for the design of cold-formed stainless steel structural members provides two alternative procedures for the calculation of flexural capacity. The two procedures are based on the concept of initiation of yielding and inelastic reserve. Both the two methods are assessed in this study.



The Procedure I design method is based on the concept of initiation of yielding, which assumes linear stress distribution through the cross-section and the maximum stress is the yield stress that reaches the extreme fiber of the cross-section. This procedure is similar to the treatment of Class 3 and Class 4 sections in EC3 (2015). The effective section modulus should be first determined using the effective width method and then multiplied by the yield strength to obtain the moment capacity ($M_{yielding}$). This procedure is expected to provide conservative predictions, especially for the stocky sections, due to the fact that plastic design is not taken into consideration. The mean value of the experimental-to-design or FEA-to-design ratio ($M_u / M_{yielding}$) is 1.27 and the corresponding *COV* equals to 0.136. This procedure is considered to be reliable with the reliability indices (β_0) for SEI/ASCE-8 (2002) and AS/NZS-4673 (2001) equal to 3.13 and 2.93, respectively.

The Procedure II design method involves the concept of inelastic reserve, which allows the spread of plasticity through the cross-section. Elastic-plastic stress distribution is allowed for the stiffened elements, referred as internal elements in EC3 (2015), with the depth of the compressed portion of the web to its thickness within the codified limit. The calculation of moment capacity ($M_{inelastic}$) is based on the equilibrium of assumed stress distribution through the depth of the effective section by means of effective width concept similar to the Procedure I. It should be noted that the Procedure II design method is applicable to sections with the ratio of the depth of the compressed portion of the web to its thickness smaller than codified slenderness limit. In this study, there were 15 out of 176 specimens exceeding this limit. The mean value of experimental-to-design or FEA-to-design ratio ($M_u / M_{inelastic}$) is 1.18 and the corresponding *COV* equals to 0.131, which is less conservative and less scattered than the first procedure. The reliability indices

(β_0) for SEI/ASCE-8 (2002) and AS/NZS-4673 (2001) are 2.90 and 2.69, respectively, which are considered to be reliable.

It should be noted that the predicted strengths determined by the two different procedures are identical for sections with compression strain factor (C_y) equals to 1, as shown in Fig. 4.11. The Procedure II design method provided less conservative predictions for sections with compression strain factor (C_y) larger than 1 due to the introduction of plastic stress. There are 75 specimens with compression strain factor (C_y) larger than 1. The Procedure II design method provides good predictions with $M_u / M_{inelastic}$ equals to 1.11 and COV of 0.061 for these sections, as shown in Table 4.5. The reliability indices (β_0) for SEI/ASCE-8 (2002) and AS/NZS-4673 (2001) are 2.93 and 2.70, respectively, which are larger than the target value of 2.50.

The application of the Procedure II design method to specimens exceeded the codified slenderness limit, of which the ratio of the depth of the compression portion in the web (d_w) to its thickness does not exceed the slenderness ratio (λ_l), is also assessed. A total of 15 ferritic stainless steel hollow section specimens exceeded the abovementioned limit in this study. The results show that the Procedure II provides good predictions to these specimens with $M_u / M_{inelastic}$ equals to 1.04 and COV of 0.072, as shown in Table 4.4. The reliability index (β_0) for SEI/ASCE-8 (2002) is 2.63, which is considered to be reliable. However, it failed to meet the target value of 2.50 for AS/NZS-4673 (2001) with reliability index (β_0) equals to 2.40.



4.6.3 European Code

The moment capacities of cold-formed ferritic stainless steel flexural members were calculated in accordance with EC3 (2015). According to EC3 (2015), the moment capacity should be calculated by Eqs (6.13 to 6.15) as specified in EC3 (2005a), except for the differences on the reduction factor ρ . Classification is required for both the compressive flange as well as the web subject to bending of the section. The overall class is determined by the most slender constituent element in the section. The calculation of moment capacities for Class 1 and Class 2 sections are based on the plastic moment capacities (M_{pl}) for the fully unreduced sections, which provide an upper bound to the nominal moment capacities calculated by this method. Elastic moment capacities (M_y) calculated from the unreduced full sections are treated as the nominal moment capacities for Class 3 sections. As for Class 4 sections, moment capacities were calculated based on the effective width method in order to account for local buckling, which is similar to the Procedure I design method as specified in SEI/ASCE-8 (2002) and AS/NZS-4673 (2001). The comparison of the experimental-to-design or FEA-to-design ratio (M_u / M_{EC3}) is shown in Fig. 4.12. It reveals that the EC3 (2015) predictions are quite conservative with the mean value of M_u / M_{EC3} equals to 1.25 and *COV* of 0.102, as presented in Table 6. The reliability index (β_0) equals to 3.07, which is greater than the target reliability index of 2.50. A total of 108 specimens are classified as Class 4 sections in this study, and the mean value of experimental-to-design or FEA-to-design ratio is 1.32 with a *COV* of 0.068. The rest of the 68 specimens are classified as Classes 1, 2 or 3 sections and the mean value of experimental-to-design or FEA-to-design ratio for these sections is 1.13 with a *COV* of 0.085.



In order to further improve the EC3 (2015) provisions for the design of cold-formed ferritic stainless steel flexural members, the effective width formula for internal element is modified and expressed in Eq. (4.2):

$$\rho = \frac{0.772}{\bar{\lambda}_p} - \frac{0.3}{\bar{\lambda}_p^2} \quad (4.2)$$

The nominal strengths determined using the proposed slenderness limits for classification in Section 4.5 and the effective width formula above are represented as $M_{EC3}^{\#}$ in this study. The comparison of the experimental-to-design or FEA-to-design ratio ($M_u / M_{EC3}^{\#}$) is shown in Fig. 4.13 and Table 4.4. The mean value of experimental-to-design or FEA-to-design ratio ($M_u / M_{EC3}^{\#}$) is 1.11 and the *COV* equals to 0.082. It is shown that the proposed design formula has improved the accuracy compared to the current EC3 (2015). The proposed design formula is considered to be reliable with the reliability index (β_0) of 2.66. A total of 84 specimens are of Class 1, 2 or 3 sections and the mean value of experimental-to-design or FEA-to-design ratio for these specimens equals to 1.11 with *COV* of 0.077. Improved accuracy is also found for Class 4 sections with mean value of $M_u / M_{EC3}^{\#}$ equals to 1.09 and *COV* of 0.083.

4.6.4 Direct strength method

The direct strength method (DSM) is detailed in Chapter F in the North American Specification for the design of cold-formed steel structural members (AISI-S100, 2016). The direct strength method involves elastic stability of gross section. Compared with the effective width method that requires the determination of the effective width for each element, whereas the direct strength method does not require iterative process. The determination of moment capacity requires the calculation of minimum of the nominal flexural strength for lateral-torsional

buckling (M_{ne}), local buckling (M_{nl}) and distortional buckling (M_{nd}). In this study, all specimens were doubly-symmetric sections. The specimens did not fail by lateral-torsional buckling and distortional buckling. For fully braced beams, the maximum of the nominal lateral-torsional buckling strength (M_{ne}) should be taken as the yield moment (M_y), as specified in Clause F3.2.1 of the Commentary on the North American Specification (AISI-S100C, 2016). Therefore, the nominal flexural strength (M_{DSM}) is then calculated by Eq. 4.3:

$$M_{DSM} = \begin{cases} M_y & \text{for } \lambda_l \leq 0.776 \\ \left[1 - 0.15 \left(\frac{M_{crl}}{M_y} \right)^{0.4} \right] \left(\frac{M_{crl}}{M_y} \right)^{0.4} M_y & \text{for } \lambda_l > 0.776 \end{cases} \quad (4.3)$$

where $\lambda_l = \sqrt{M_y / M_{crl}}$. It is noteworthy that the yield moment ($M_y = S_f f_y$) is the moment capacity calculated based on the elastic section modulus (S_f) of fully unreduced section multiplied by the yield strength (f_y), which is the 0.2% proof stress. The critical elastic local buckling moment (M_{crl}) was obtained from CUFSM (Schafer and Ádány, 2006).

The DSM (AISI-S100, 2016) allows design with inelastic reserve strength for sections with λ_l smaller than 0.776, and the inelastic reserve moment capacity for slenderness factor $\lambda_l \leq 0.776$ is determined by Eq. (4.4):

$$M_{DSM} = M_y + \left(1 - \frac{1}{C_{yl}^2} \right) (M_{pl} - M_y) \quad \text{for } \lambda_l \leq 0.776 \quad (4.4)$$

where $C_{yl} = \sqrt{0.776 / \lambda_l} \leq 3$, $M_{pl} = Z_f f_y$. The incorporation of inelastic reserve provides more accurate predictions. The ratio of experimental-to-yield-strength or FEA-to-yield-strength (M_u / M_y) is plotted against the slenderness factor (λ_l) for each specimen, as shown in Fig. 4.14. It should be noted that the average value of shape factor ($\eta = Z_f / S_f$) was 1.24 for all the specimens with $\lambda_l \leq 0.776$. The



mean value of experimental-to-design or FEA-to-design ratio (M_u / M_{DSM}) is 1.18 with COV of 0.066. The direct strength method is considered to be reliable with the reliability index (β_0) of 3.19. It is found that the direct strength method provides conservative predictions for a total of 85 specimens with λ_l smaller or equal to 0.776 with mean value of M_u / M_{DSM} equals to 1.22 and a COV of 0.051. For specimens with λ_l larger than 0.776, slightly better predictions for the 91 specimens with mean value of M_u / M_{DSM} equals to 1.15 and a COV of 0.068.

Huang and Young (2014b) proposed the modified direct strength equations for cold-formed lean duplex stainless steel bending members. The applicability of the modified DSM equations by Huang and Young (2014b) was also assessed for cold-formed ferritic stainless steel bending members. The modified equations are shown herein:

$$M_{DSM,H\&Y} = \begin{cases} 1.1((0.776 - \lambda_l) + 1)M_y & \text{for } \lambda_l \leq 0.776 \\ \left(1 - 0.15\left(\frac{M_{crl}}{1.1M_y}\right)^{0.4}\right)\left(\frac{M_{crl}}{1.1M_y}\right)^{0.4} 1.1M_y & \text{for } \lambda_l > 0.776 \end{cases} \quad (4.5)$$

It should be noted that the slenderness factor λ_l was also modified to be $\lambda_l = \sqrt{1.1M_y / M_{crl}}$. The modified DSM equations proposed by Huang and Young (2014b) provide very good agreement with the experimental and numerical results with the mean value of experimental-to-design or FEA-to-design ratio ($M_u / M_{DSM,H\&Y}$) equals to 1.02 and the COV of 0.096. Moreover, the modified DSM equations proposed by Huang and Young (2014b) is reliable with the reliability index (β_0) of 2.50. There are 82 specimens with λ_l smaller or equal to 0.776, and 94 specimens with λ_l larger than 0.776. The mean values of $M_u / M_{DSM,H\&Y}$ for specimens with $\lambda_l \leq 0.776$ and $\lambda_l > 0.776$ are 0.94 and 1.08 with COV of 0.063 and 0.069, respectively. It is shown that the modified DSM



equations proposed by Huang and Young (2014b) provide the most accurate predictions among the design rules considered in this study.

4.6.5 Continuous strength method

The continuous strength method (CSM) is a strain-based design approach which relates the cross-sectional resistance to the cross-sectional deformation capacity. The continuous strength method generally provides good predictions especially for stocky sections with the allowance for strain hardening. The latest modification on CSM is detailed in Afshan and Gardner (2013b). The continuous strength method is applicable to sections with a slenderness value $\bar{\lambda}_p \leq 0.68$, since there is no significant benefit derived from strain hardening beyond this limit (Afshan and Gardner, 2013b). The section capacities for slender sections ($\bar{\lambda}_p > 0.68$) may be determined using the effective width method or direct strength method (DSM). There are 83 specimens fulfilled the requirement of CSM in this study. The experimental and numerical results were compared with the predictions from CSM (M_{CSM}) and it was found the CSM provides good predictions with the mean value of experimental-to-design or FEA-to-design ratio (M_u / M_{CSM}) equals to 1.11 and the COV of 0.080. The continuous strength method is thus recommended for the predictions of moment capacities of sections with $\bar{\lambda}_p \leq 0.68$ for cold-formed ferritic stainless steel sections.

4.7 Concluding Remarks

Experimental and numerical investigations of cold-formed ferritic stainless beams have been presented in this chapter. A series of tests was conducted on square and rectangular hollow sections under four-point bending condition. Coupon tests were conducted to determine the material properties of the ferritic stainless steel



specimens. A finite element model was developed and verified with cold-formed ferritic stainless steel beams. It is shown that the model accurately simulates the flexural behaviour of the ferritic stainless steel beams in this study. A comprehensive parametric study was performed. The slenderness limit of elements, rotation capacities, curvatures and moment capacities of the cold-formed ferritic stainless steel hollow sections were examined. A total of 161 experimental and numerical results as well as the data obtained from the previous investigations (Afshan and Gardner, 2013a; Bock et al., 2015; Zhao et al., 2015; Zhao et al., 2016) were compared with the design predictions obtained from SEI/ASCE-8 (2002), AS/NZS-4673 (2001), EC3 (2015), direct strength method (AISI-S100, 2016), modified direct strength method by Huang and Young (2014b) and continuous strength method (Afshan and Gardner, 2013b). Reliability analysis was also carried out to assess the reliability of these design rules. It is found that the modified DSM equations proposed by Huang and Young (2014b) provided the most accurate predictions for cold-formed ferritic stainless steel beams. Modification to current European code was proposed and the modified equation provides more accurate and less scattered predictions compared to the current EC3 (2015). It is recommended that the modified direct strength method proposed by Huang and Young (2014b) can be used in the design of cold-formed ferritic stainless steel beams of square and rectangular hollow sections. Furthermore, the slenderness limits specified in EC3 (2015) for stainless steel and EC3 (2005a) for carbon steel were assessed. It is shown that the current slenderness limits in EC3 (2015) for element subject to bending is suitable for ferritic stainless steel, but not for element subject to compression and the limits can be relaxed. Therefore, new slenderness limits are proposed for element subject to compression in cold-formed ferritic stainless steel.

Specimen	<i>D</i> (mm)	<i>B</i> (mm)	<i>t</i> (mm)	<i>r_o</i> (mm)	<i>r_i</i> (mm)	<i>L</i> (mm)	<i>W_{el}</i> (mm ³)	<i>W_{pl}</i> (mm ³)
60×40×4	59.9	40.1	3.84	6.5	3.8	1199.3	10055	12761
40×60×4	40.1	59.9	3.83	6.5	3.8	1199.5	7941	9608
60×60×3	60.2	60.0	2.71	5.8	3.8	1199.5	10845	12848
100×40×2	99.7	40.2	1.94	5.7	4.0	1400.5	12697	16035
40×100×2	40.2	99.7	1.94	5.7	4.0	1401.5	7630	8485
80×60×4	80.3	60.1	3.73	7.6	4.3	1200.0	20943	25606
80×60×4R	80.4	59.9	3.73	7.6	4.3	1199.0	20917	25582
60×80×4	60.0	80.3	3.73	7.6	4.3	1201.0	17796	20933
120×80×3	120.0	79.9	2.81	6.3	4.1	1400.5	36161	43456
80×120×3	79.9	120.0	2.81	6.3	4.1	1401.5	29070	32904

Table 4.1. Measured dimensions of the beam specimens.



Specimen	M_{Exp} (kNm)	κ_{Exp} ($\times 10^{-4}$ mm $^{-1}$)	Failure mode	R	M_{FEA} (kNm)	κ_{FEA} ($\times 10^{-4}$ mm $^{-1}$)	Failure mode	$\frac{M_{Exp}}{M_{FEA}}$	$\frac{\kappa_{Exp}}{\kappa_{FEA}}$	$\frac{M_{Exp}}{M_y}$	$\frac{M_{Exp}}{M_{pl}}$	
60×40×4	7.2	6.41	F	>10.48 ^a	7.4	6.20	F	0.97	1.03	1.49	1.18	
40×60×4	5.0	6.38	F	>7.35 ^a	5.4	7.02	F	0.93	0.91	1.31	1.08	
60×60×3	6.9	4.99	F	7.96	6.3	3.86	F	1.10	1.29	1.42	1.20	
100×40×2	7.3	1.83	F	2.67	7.6	2.48	F	0.97	0.74	1.37	1.08	
40×100×2	3.0	1.44	L+F	0.00	2.9	1.28	L+F	1.03	1.12	0.94	0.84	
80×60×4	13.9	4.99	F	>14.04 ^a	13.6	3.49	F	1.02	1.43	1.47	1.21	
80×60×4R	14.0	4.94	F	>14.03 ^a	13.6	3.49	F	1.03	1.42	1.49	1.22	
60×80×4	10.8	4.20	F	8.24	10.8	3.49	F	1.00	1.20	1.35	1.14	
120×80×3	20.6	1.32	F	2.82	19.6	1.64	F	1.05	0.80	1.50	1.24	
80×120×3	13.0	0.98	F	2.03	12.7	0.84	F	1.02	1.17	1.17	1.04	
								Mean	1.01	1.11	1.35	1.12
								COV	0.047	0.216	0.131	0.106

^a Full rotation capacity was not attained and R based on maximum recorded deformation.

Table 4.2. Comparison of test strengths with finite element analysis results.



Specimen ($D \times B \times t$)	M_{FEA} (kNm)	K_{FEA} ($\times 10^{-4} \text{ mm}^{-1}$)	Specimen ($D \times B \times t$)	M_{FEA} (kNm)	K_{FEA} ($\times 10^{-4} \text{ mm}^{-1}$)
60×60×6	12.7	6.6	300×150×10	380.0	1.2
60×60×4	8.8	5.0	300×150×7	263.0	0.9
60×60×2	4.4	2.6	300×150×6.5	244.0	0.8
60×60×1.5	3.0	1.3	300×150×6	224.5	0.7
60×60×1	1.6	0.9	300×150×5.5	204.4	0.6
120×120×12	100.7	3.0	300×150×4.5	160.9	0.3
120×120×6	52.4	1.9	300×150×4	135.8	0.3
120×120×3	24.2	0.6	300×150×3.5	108.6	0.2
120×120×2.5	18.4	0.5	300×150×3	84.6	0.2
120×120×2	13.2	0.4	150×300×10	217.3	0.8
120×120×1.5	8.8	0.4	150×300×7	133.8	0.4
120×120×1	4.0	0.3	150×300×6.5	128.5	0.4
180×180×8	158.1	1.4	150×300×6	123.0	0.4
180×180×5	92.8	0.5	150×300×5.5	96.1	0.4
180×180×4	68.9	0.4	150×300×4.5	76.0	0.3
180×180×3.5	57.7	0.4	150×300×3.5	50.9	0.3
180×180×3	43.5	0.3	150×300×3	41.1	0.2
180×180×2.5	32.7	0.3	250×100×10	233.1	1.2
180×180×2	22.2	0.2	250×100×8	186.7	1.6
240×240×10	351.7	1.0	250×100×6	141.0	1.4
240×240×5.5	170.2	0.3	250×100×5.5	129.2	1.2
240×240×5	146.9	0.3	250×100×5	117.5	1.0
240×240×4.5	124.4	0.3	250×100×4.5	105.3	0.8
240×240×4	110.1	0.2	250×100×4	92.7	0.6
240×240×3	68.1	0.1	250×100×3.5	78.8	0.4
240×240×2.5	56.7	0.1	250×100×3	63.7	0.3
300×300×12	659.2	0.8	250×100×2.5	52.0	0.3
300×300×8	416.5	0.3	100×250×10	112.2	1.4
300×300×7	297.3	0.4	100×250×8	90.3	1.0
300×300×6.5	304.2	0.2	100×250×6	63.0	0.6
300×300×5.5	235.4	0.2	100×250×5.5	59.2	0.5
300×300×5	208.2	0.3	100×250×5	50.4	0.4
300×300×4	140.8	0.2	100×250×4.5	42.7	0.8
300×300×3.5	118.5	0.2	100×250×4	37.6	0.4
160×120×5	66.1	1.6	100×250×3.5	28.3	0.4
160×120×3.5	44.9	0.7	100×250×3	23.1	0.5
160×120×3	36.3	0.5	300×100×10	319.0	1.2
160×120×2.5	26.6	0.4	300×100×8	251.4	1.2
160×120×2	18.0	0.3	300×100×7	220.3	1.2
160×120×1.5	12.6	0.2	300×100×6.5	204.7	1.3
120×160×5	51.7	1.0	300×100×6	188.9	1.0
120×160×3.5	31.4	0.6	300×100×5.5	172.9	0.8
120×160×3	25.5	0.6	300×100×5	156.3	0.7
120×160×2.5	20.2	0.5	300×100×4.5	138.9	0.5
120×160×2	14.0	0.3	300×100×4	120.9	0.4

Table 4.3. Parametric study results (Cont.).



120×160×1.5	9.0	0.2	300×100×3.5	97.6	0.3
120×80×6	41.1	2.3	100×300×10	128.6	1.0
120×80×4	27.8	2.3	100×300×8	100.4	0.7
120×80×3	20.9	1.7	100×300×7	83.4	0.5
120×80×2.5	17.0	0.9	100×300×6.5	75.0	0.5
120×80×2	14.5	1.2	100×300×6	70.2	0.5
120×80×1.5	8.8	0.5	100×300×5.5	59.1	0.4
120×80×1	4.4	0.3	100×300×5	51.1	0.4
80×120×6	29.8	2.6	100×300×4.5	43.7	0.4
80×120×4	20.2	1.7	100×300×4	37.2	0.3
80×120×3	14.1	0.9	100×300×3.5	30.5	0.3
80×120×2.5	11.6	0.8	280×70×9	219.9	1.2
80×120×2	7.9	0.8	280×70×8	196.8	1.2
80×120×1.5	5.2	0.5	280×70×6.5	163.3	1.4
250×150×10	288.9	1.3	280×70×6	148.5	1.4
250×150×6	171.5	0.9	280×70×5.5	136.0	1.1
250×150×5.5	156.4	0.7	280×70×5	123.4	0.9
250×150×5	141.0	0.6	280×70×4.5	110.0	0.7
250×150×4.5	124.3	0.4	280×70×4	96.2	0.5
250×150×4	105.6	0.3	280×70×3.5	80.6	0.4
250×150×3.5	85.5	0.3	280×70×3	63.4	0.3
250×150×3	64.7	0.2	70×280×9	67.4	1.2
250×150×2.5	47.8	0.2	70×280×8	59.4	1.0
150×250×10	193.7	1.2	70×280×6.5	45.7	0.7
150×250×6	101.6	0.4	70×280×6	41.4	0.6
150×250×5.5	93.3	0.4	70×280×6	41.4	0.6
150×250×5	90.0	0.4	70×280×5	31.6	0.5
150×250×4.5	69.1	0.4	70×280×4.5	27.4	0.5
150×250×4	64.2	0.3	70×280×4	23.4	0.5
150×250×3.5	37.0	0.6	70×280×3.5	19.5	0.4
150×250×3	38.7	0.3			
150×250×2.5	29.2	0.3			

Table 4.3. Parametric study results (Cont.).

	ASCE			AS/NZS			EC3		DSM		CSM
	$\frac{M_u}{M_{yielding}}$	$\frac{M_u}{M_{inelastic}}$	$\frac{M_u}{M_{inelastic}^*}$	$\frac{M_u}{M_{yielding}}$	$\frac{M_u}{M_{inelastic}}$	$\frac{M_u}{M_{inelastic}^*}$	$\frac{M_u}{M_{EC3}}$	$\frac{M_u}{M_{EC3}^\#}$	$\frac{M_u}{M_{DSM}}$	$\frac{M_u}{M_{DSM,H\&Y}}$	$\frac{M_u}{M_{CSM}}$
Number of data	176	161	15*	176	161	15*	176	176	176	176	83
Mean (P_m)	1.27	1.18	1.04	1.27	1.18	1.04	1.25	1.11	1.18	1.02	1.11
COV (V_P)	0.136	0.131	0.072	0.136	0.131	0.072	0.102	0.082	0.066	0.096	0.080
Resistance factor (ϕ_0)	0.90	0.90	0.90	0.90	0.90	0.90	0.91	0.91	0.90	0.90	0.91
Reliability index (β_0)	3.13	2.90	2.63	2.93	2.69	2.40	3.07	2.66	3.19	2.50	2.69
Resistance factor (ϕ_1)	0.90	0.90	0.90	0.90	0.90	0.90	0.90	0.90	0.90	0.90	0.90
Reliability index (β_1)	3.13	2.90	2.63	3.13	2.90	2.63	3.27	2.86	3.19	2.50	2.89

* Specimens that exceeded the limit ($d_w / t > \lambda_1$) of the approach by inelastic reserve capacity in ASCE and AS/NZS

Modified design rules

Table 4.4. Comparison of the experimental and numerical results with the nominal moment capacities.

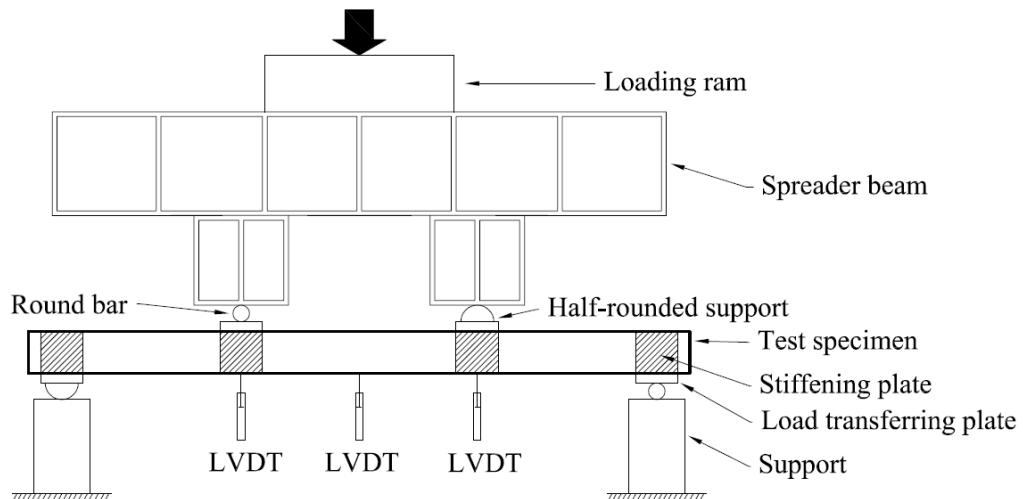


	ASCE	AS/NZS	EC3				DSM			
	$C_y \geq 1$	$C_y \geq 1$	Class 1, 2, 3		Class 4		$\lambda_l \leq 0.776$		$\lambda_l > 0.776$	
	$\frac{M_u}{M_{inelastic}}$	$\frac{M_u}{M_{inelastic}}$	$\frac{M_u}{M_{EC3}}$	$\frac{M_u}{M_{EC3}^{\#}}$	$\frac{M_u}{M_{EC3}}$	$\frac{M_u}{M_{EC3}^{\#}}$	$\frac{M_u}{M_{DSM}}$	$\frac{M_u}{M_{DSM,H\&Y}}$	$\frac{M_u}{M_{DSM}}$	$\frac{M_u}{M_{DSM,H\&Y}}$
Number of data	75	75	68	84	108	92	85	82	91	94
Mean (P_m)	1.11	1.11	1.13	1.11	1.32	1.09	1.22	0.94	1.15	1.08
$COV (V_P)$	0.061	0.061	0.085	0.077	0.068	0.083	0.051	0.063	0.068	0.069
Resistance factor (ϕ_0)	0.90	0.90	0.91	0.91	0.91	0.91	0.90	0.90	0.90	0.90
Reliability index (β_0)	2.93	2.70	2.75	2.76	3.43	2.59	3.35	2.27	3.07	2.81
Resistance factor (ϕ_1)	0.90	0.90	0.90	0.90	0.90	0.90	0.90	0.90	0.90	0.90
Reliability index (β_1)	2.93	2.93	2.95	2.96	3.63	2.78	3.35	2.27	3.07	2.81

Modified design rules

Table 4.5. Comparison of the experimental and numerical results with the nominal moment capacities.



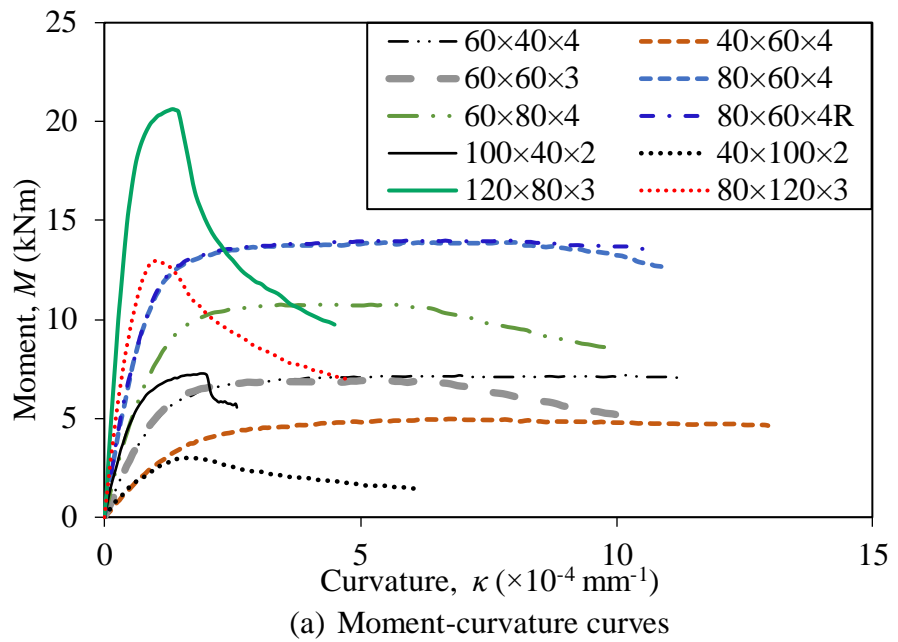


(a) Schematic set up of the bending test

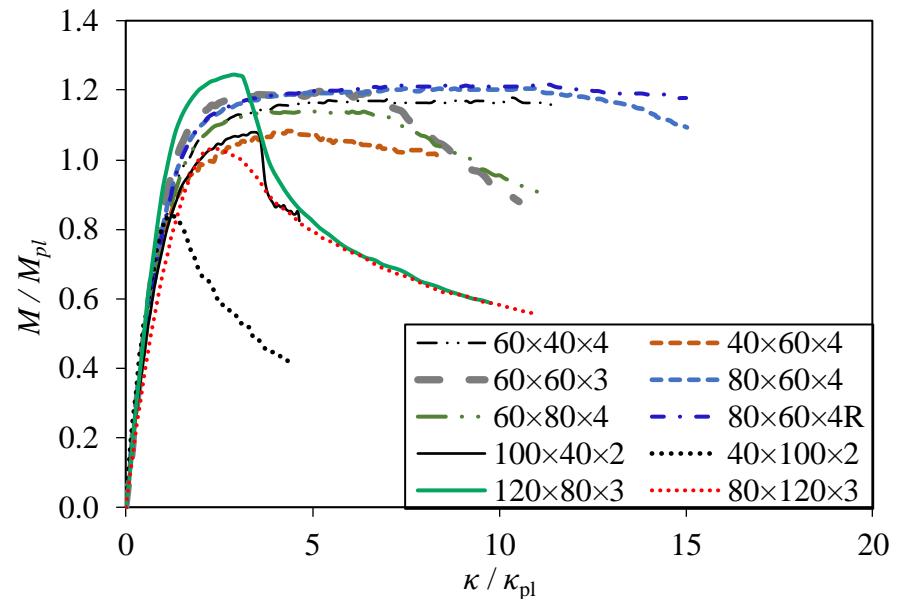


(b) Bending test setup of specimen 60×80×4

Figure 4.1. Four-point bending test setup.



(a) Moment-curvature curves



(b) Normalized moment-curvature curves

Figure 4.2. Moment-curvature curves of tested specimens.



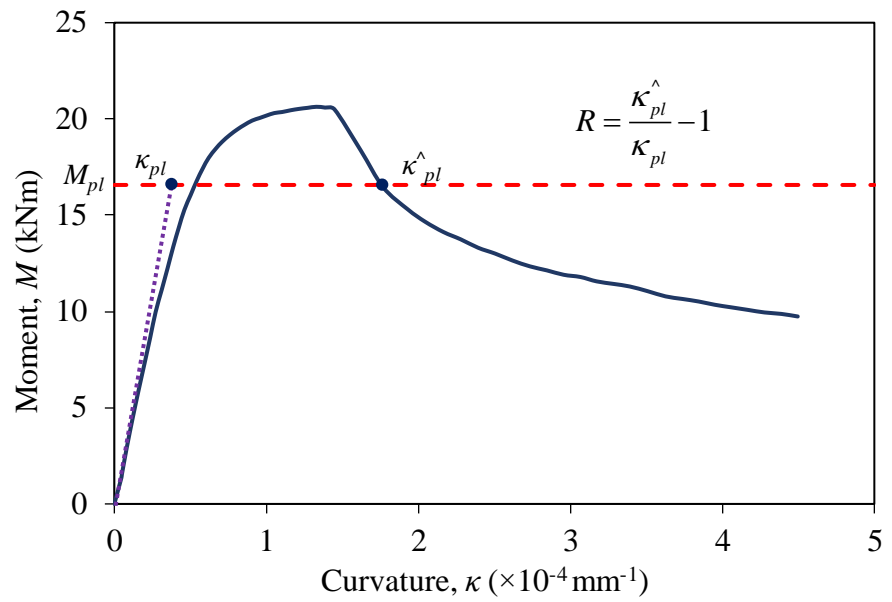


Figure 4.3. Locations of κ_{pl} , κ_{pl}^{\wedge} and definition of rotation capacity on moment-curvature curve of specimen 120×80×3.

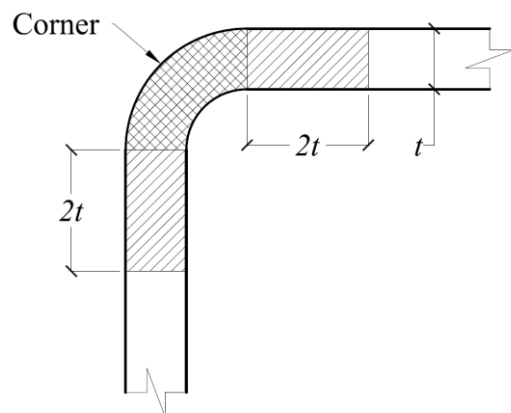
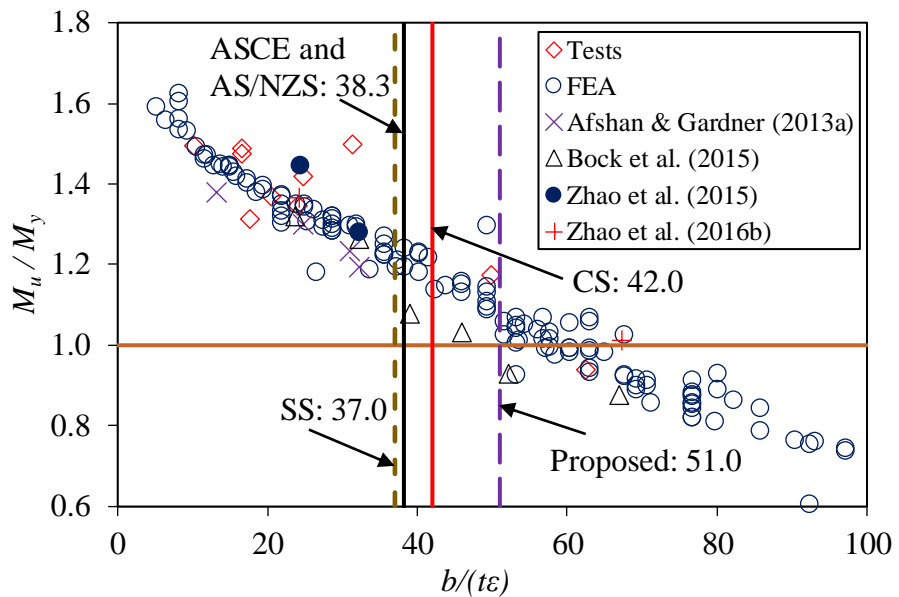


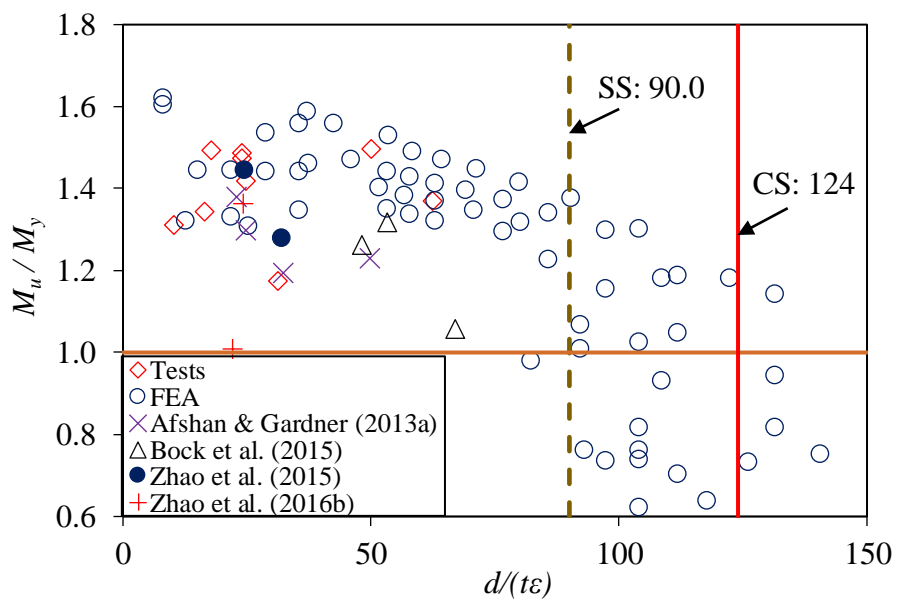
Figure 4.4. Corner material property extended beyond the corner region of the cross-sections.





Note: "SS" Stainless steel limit in EC3 (2015); "CS" Carbon steel limit in EC3 (2005a)

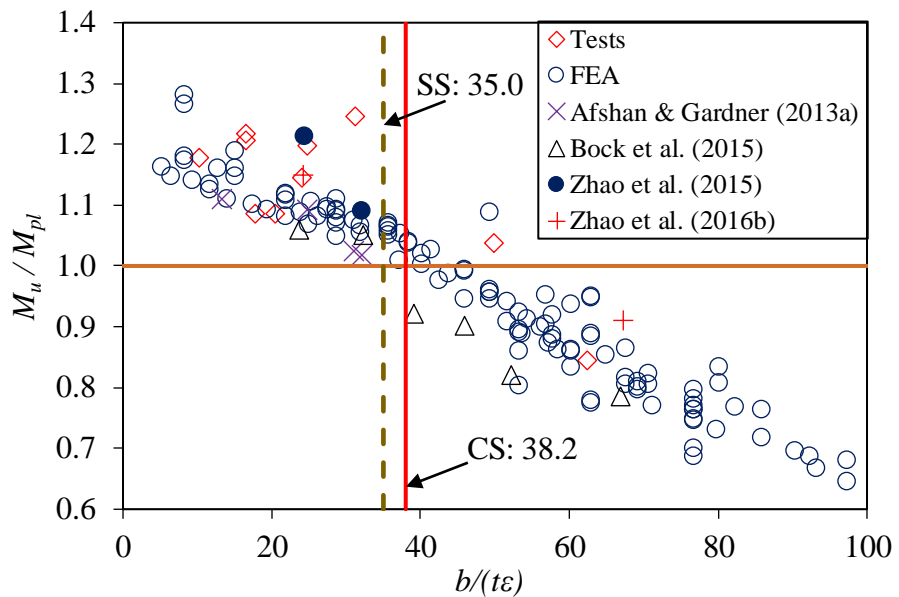
Figure 4.5. Class 3 limit of element subject to compression.



Note: "SS" Stainless steel limit in EC3 (2015); "CS" Carbon steel limit in EC3 (2005a)

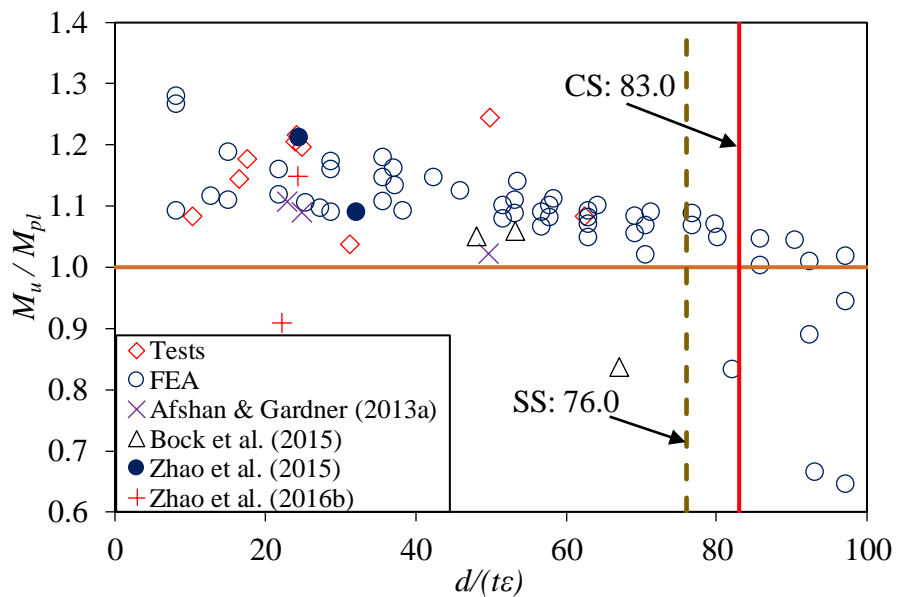
Figure 4.6. Class 3 limit of element subject to bending.





Note: "SS" Stainless steel limit in EC3 (2015); "CS" Carbon steel limit in EC3 (2005a)

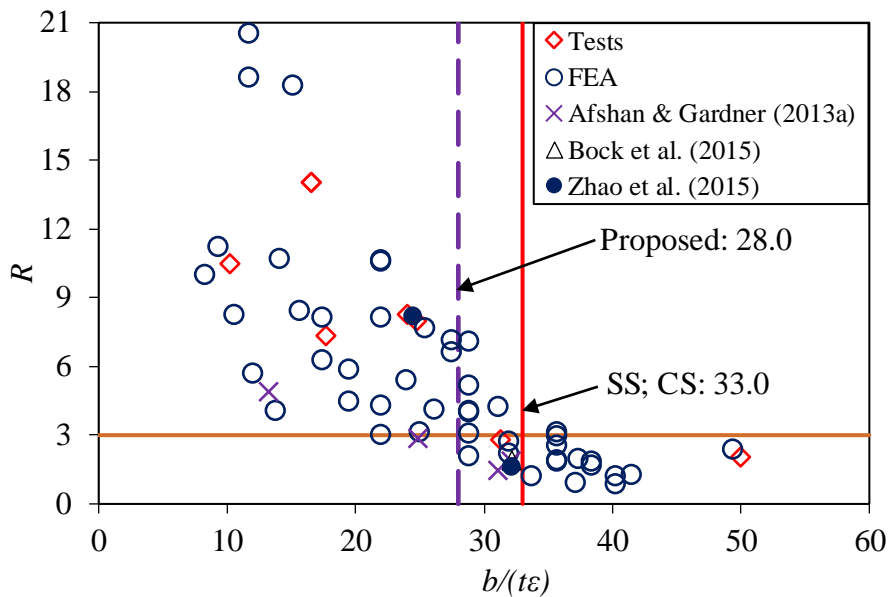
Figure 4.7. Class 2 limit of element subject to compression.



Note: "SS" Stainless steel limit in EC3 (2015); "CS" Carbon steel limit in EC3 (2005a)

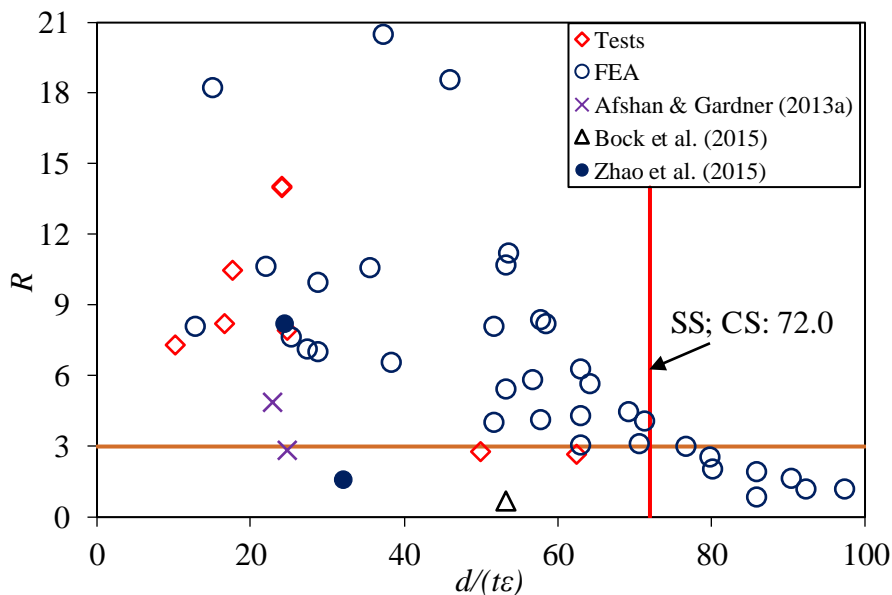
Figure 4.8. Class 2 limit of element subject to bending.





Note: “SS” Stainless steel limit in EC3 (2015); “CS” Carbon steel limit in EC3 (2005a)

Figure 4.9. Class 1 limit of element subject to bending.



Note: “SS” Stainless steel limit in EC3 (2015); “CS” Carbon steel limit in EC3 (2005a)

Figure 4.10. Class 1 limit of element subject to compression.



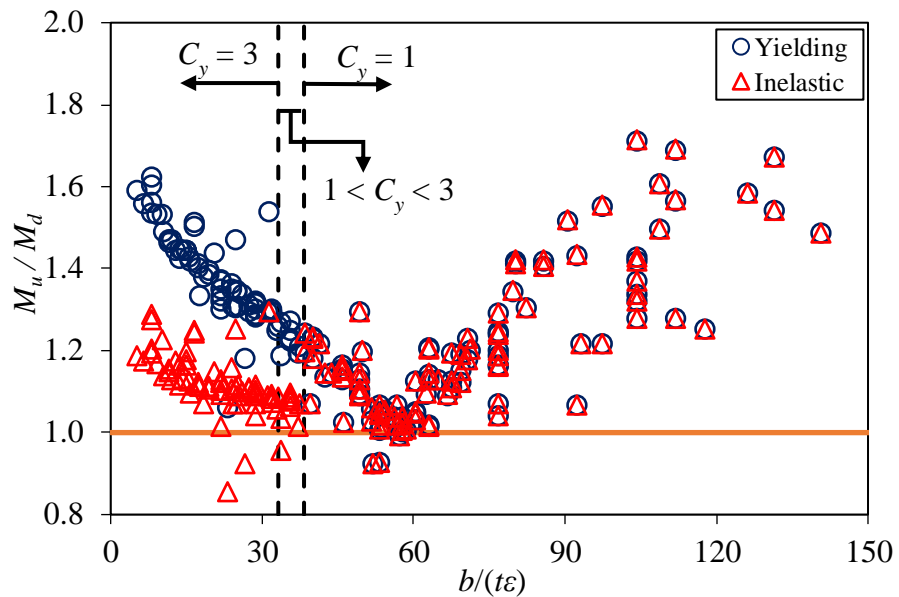


Figure 4.11. Comparison of experimental and numerical results with nominal strengths predicted by ASCE and AS/NZS.

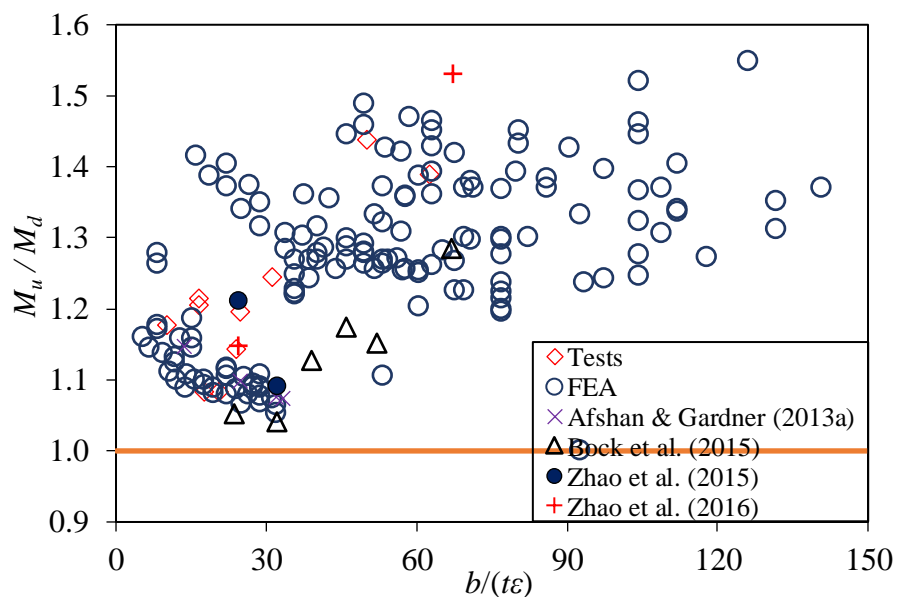


Figure 4.12. Comparison of experimental and numerical results with nominal strengths predicted by EC3.



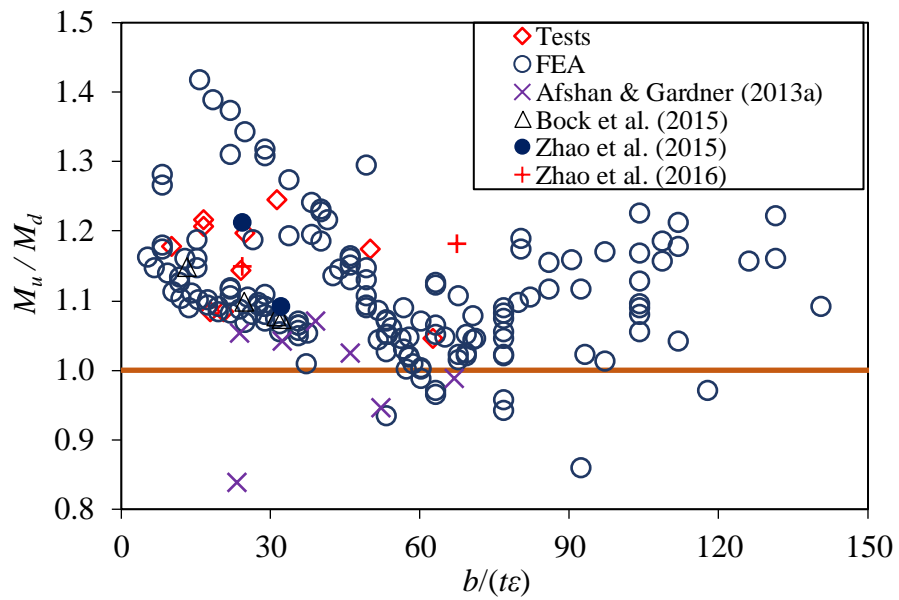


Figure 4.13. Comparison of experimental and numerical results with nominal strengths predicted by modified EC3.

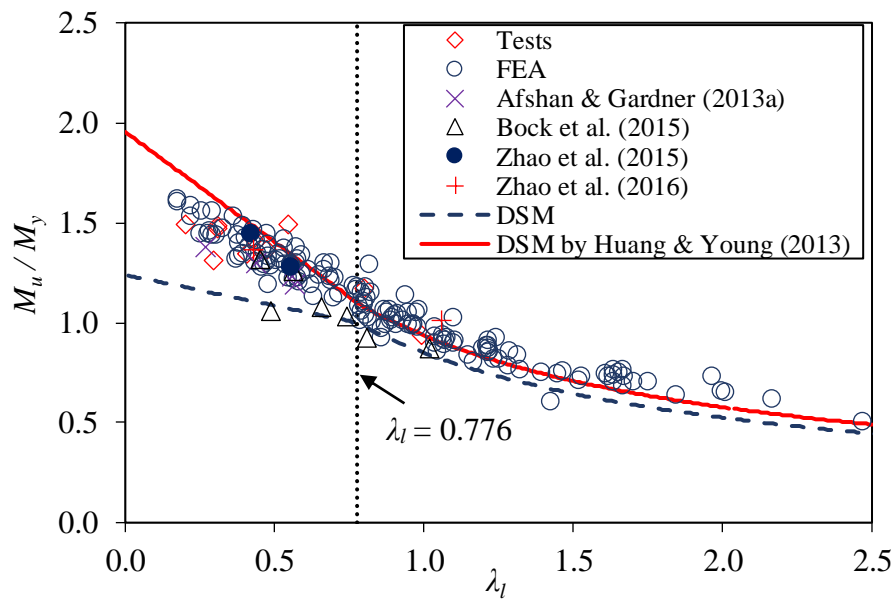


Figure 4.14. Comparison of experimental and numerical results with nominal strengths predicted by DSM.



CHAPTER 5

STUB COLUMN BEHAVIOUR OF CONCRETE-FILLED COLD-FORMED FERRITIC STAINLESS STEEL SHS & RHS

5.1 Introduction

Concrete-filled steel tubular (CFST) structures offer structural advantages such as high strength, favorable ductility and fire resistance over reinforced concrete or pure steel structures. The steel tube acts as formwork and provides confinement to the infill concrete. The concrete infill prevents possible inward buckling of outer steel tube resulting in higher buckling resistance of the composite structure.

Most of the previous studies on CFST structures were based on conventional carbon steel. However, stainless steel offers better corrosion resistance, ductility and aesthetic appearance compared to carbon steel. Up-to-date, research on the structural compressive behaviour of concrete-filled stainless steel tubular (CFSST) sections includes Young and Ellobody (2006), Ellobody and Young (2006), Lam and Gardner (2008) and Uy et al. (2011). CFSST columns exhibit more gradual yielding behaviour and better ductility on the axial load-strain curves compared with concrete-filled carbon steel columns (Uy et al., 2011).



With the advancement in concrete technology, the production of high-strength concrete (HSC) up to 120 MPa (cylinder strength) or even higher strength is easily achievable. Examples on application of HSC include Petronas Tower in Kuala Lumpur, and the International Commerce Center in Hong Kong in which concrete of cylinder strengths 80 and 90 MPa were used, respectively (Liew, 2015). The application of HSC offers higher strength-to-weight ratio than normal strength concrete (NSC). However, the brittleness of HSC can cause possible abrupt failure of the concrete structure and it is the major concern on using HSC.

The main objective of this chapter is to investigate the compressive behaviour of concrete-filled cold-formed ferritic stainless steel columns. A total of 22 stub column tests were conducted on square and rectangular sections fabricated using ferritic stainless steel grade EN 1.4003 and filled with concrete of nominal cylinder compressive strengths 40, 80 and 120 MPa. A finite element model was developed and verified against the experimental results. The verified model was used to carry out an extensive parametric study. The experimental and numerical results were used to assess the applicability of existing design methods designated for cross-sectional compression capacity of conventional concrete-filled carbon steel columns as presented in American specification ANSI/AISC 360 (2016), American code ACI 318 (2014), EC4 (2004) and AS 5100.6 (2004). These codes are referred as “AISC”, “ACI”, “EC4” and “AS5100” in the following sections.

5.2 Experimental Investigation

5.2.1 Test specimens

An experimental program involving 5 hollow and 17 concrete-filled specimens has been carried out. The test specimens consist of one square hollow section



(SHS) and four rectangular hollow sections (RHS). The nominal depth and width of the SHS and RHS ranged from 40 to 120 mm and the nominal plate thickness ranged from 2 to 4 mm. Steel end plates of 25 mm were welded to both ends of each specimen. The filled concrete had the nominal cylinder compressive strengths of 40, 80 and 120 MPa. The specimens were labelled in such a way that the nominal dimensions including the overall depth of the web (D), overall width of the flange (B), plate thickness (t) of the cross-section as well as the nominal infill concrete strength of the specimen can be identified. For example, the label 120×80×3C120 refers to the specimen with nominal cross-sectional dimensions depth (D), width (B), thickness (t) equals to 120, 80 and 3 mm. The symbol “C120” means that the specimen had nominal concrete cylinder compressive strength equals to 120 MPa. If the test was a repeated one, a symbol of “R” will be added after the concrete strength. The measured specimen dimensions are shown in Table 5.1.

The specimens were cut into designed length and then milled flat at both ends. An end plate was welded to one end of the specimen while the other end was left open for concrete casting. To fill up the small gap due to shrinkage and achieve uniform compressive loading to the stainless steel tube and concrete, a thin layer of plaster was applied to the open end of the specimen before welding of the other end plate.

Standard concrete cylinders of size 150×300 mm were cast and tested to determine the compressive strength (f_c') and the elastic modulus (E_c) of concrete. Two cylinders were tested at 28 days after casting and two further cylinder tests were performed for each grade of concrete at the time of each series of stub column tests. All the stub column tests were completed within three days



after the 28 days of casting so that the concrete strength enhancement is minimal. The elastic modulus of concrete was also determined by suitable compressometer according to ASTM C469 (2014). The concrete cylinder compressive strengths for the 40, 80 and 120 MPa concrete were 42.6, 80.9 and 114.6 MPa whilst the corresponding elastic moduli were 27.5, 41.8 and 50.9 GPa, respectively.

5.2.2 Geometric imperfection measurements

Initial local geometric imperfections of specimens were measured for each hollow section. The measurements were performed at the mid-length of the specimens using the linear variable differential transformer (LVDT) with an accuracy of 0.001 mm. The measurement of local imperfection was conducted at 2 mm intervals on each side of the cross-section. It was assumed that the local geometric imperfections were zero (reference point) at the corner and the vertical relative distance of the flat portion to the corner was treated as the geometric imperfection, as suggested by Huang and Young (2012). The convex and concave profiles are indicated by positive and negative values, respectively. Fig. 5.1 plots the measured local plate imperfection profiles along the four sides for section 100×40×2. The maximum measured absolute local imperfections were 0.249, 0.168, 0.265, 0.341 and 0.468 mm for sections 60×40×4, 60×60×3, 80×60×4, 100×40×2 and 120×80×3, respectively. The measured local plate imperfection profiles along the four sides for all sections are shown in Appendix C1 of this thesis.



5.2.3 Stub column tests

A total of 22 stub column tests were performed – one empty tube and three concrete-filled tubes (with nominal concrete cylinder strengths of 40, 80 and 120 MPa) were tested for each of the five sections. Two specimens were repeated in order to assess the reliability of the tests. All the specimens were prepared in compliance with the recommendations in Ziemian (2010) and the length was designed to be three times the longer length of depth (D) or width (B) for each specimen to avoid any overall buckling. Strain gauges were mounted at the four corners of the specimens to measure the longitudinal strains and an additional strain gauge at the center of the flat portion of the more slender web to detect any possible local buckling, as illustrated in Fig. 5.2(a). All the strain gauges were affixed at mid-height of the specimens. Three LVDTs were used to capture the axial shortening of the specimens. A special bearing was located at the top of the specimens and the gaps between the bearing plates and specimens can be eliminated by rotating the special bearing. The special bearing was then fixed-locked under a 3 kN preloading force in order to achieve fixed-end support condition. The schematic test arrangement is shown in Fig. 5.2(b). Similar test setup was also adopted by Ma et al. (2015b). All the tests were conducted at a constant displacement rate of 0.3 mm/min. It is not recommended to pause during the tests for concrete-filled composite members since concrete cracks would occur after elastic stage of the material. The drop of loading under pause comprised plastic relaxation and loss of strength due to cracking of concrete.



5.3 Experimental Results and Discussion

5.3.1 Axial load-strain curves

The measured axial load is plotted against the axial strain for all tested stub columns, as shown from Figs 5.3 – 5.7. Clear advantages such as enhanced strength, ductility and elastic stiffness of composite stainless steel over their bare (hollow) stainless steel counterpart are shown especially for the slender sections. It is shown that little strain hardening response was found for all the axial load-strain curves. This is due to the low ultimate strength (f_u) to yield strength (f_y) ratio of cold-formed ferritic stainless steel grade EN 1.4003.

The axial load-strain curves share common features. All the curves had the initial elastic stage for which the axial load increases proportionally as the axial strain increases. As the initial Poisson's ratio of concrete ($\nu_c = 0.2$) is smaller than that of stainless steel ($\nu_s = 0.3$), no confinement effect will take place at this stage. The elastic stage is followed by a transitional plastic stage (Uy et al., 2011; Lai, 2015). The Poisson's ratio of concrete increases significantly and becomes larger than that of steel due to the forming of internal microcracks (Lai, 2015). Confinement takes place due to the expansion of inner concrete. The transition at this stage is attributed to the nonlinear behaviour of concrete and gradual yielding of steel tube. After that the composite columns attained their ultimate strength, and the ultimate strains were depending on the infilled concrete strength and the effectiveness of confinement. If enough confinement is provided, take specimen 60×40×4C40 and 60×60×3C40 for example, the axial load can be maintained at a nearly constant level after the transitional stage. The axial load would decrease after reaching the ultimate strength if the column was lack of confinement.



5.3.2 Typical failure modes

The typical failure modes for the concrete-filled stub columns were shown in Fig. 5.8 (a). All the CFSST columns failed by local buckling with outward bulges compared with alternate buckling of steel plates in convex and concave surfaces for hollow stub columns. The CFSST columns filled with normal strength concrete (e.g., specimen 100×40×2C40) had obvious outward bulges at the four faces at about the same height. The stainless steel tube was cut at the bulge location to have a better view of the concrete failure, as shown in Fig. 5.8 (b). It is obvious that the core concrete crushed locally and no apparent shear plane was found. For the stub columns with infill concrete strength of 80 MPa and 120 MPa (e.g., 100×40×2C80 & 100×40×2C120), two obvious bulges were observed at opposite faces at different heights of the stub columns and the deformations at the stockier faces were not obvious, especially for specimens filled with 120 MPa concrete (e.g., 100×40×2C120). Inclined concrete cracks was observed when the stainless steel tube was cut at the location of opposite bulges, as shown in Fig. 5.8 (c), and it is believed that the failure was due to the combination of crushing and shear failure, and shear failure became dominant as the concrete strength increased (Lai, 2015). This is further confirmed by the specimen 100×40×2C120 for which a sudden loss of axial load as shown in Fig. 5.6 along with a loud bang sound during the test. Apparent bulges were observed after the sudden loss of axial strength. Inclined concrete cracks was observed but no obvious crushing of concrete was found for the specimen 100×40×2C120, as shown in Fig. 5.8 (d). Depending on the concrete strength as well as the confining stress provided by the stainless steel tube, the failure modes changed from compressive crushing to shear failure in the concrete. The ductility of the CFSST stub columns decrease as the failure of concrete changes from compressive crushing to shear failure.

5.3.3 Effect of local buckling

Local buckling can trigger failure of steel plate and the filled concrete can delay composite member failure by preventing the inward buckling of the stainless steel tube. Uy and Bradford (1996) revealed that the plate minimum buckling coefficient K accounts for local buckling mode was equal to 10.3 for two clamped unloaded sides condition of steel plates in composite steel-concrete members, which is greatly enhanced compared with the value of 4 in hollow steel tube condition. The local buckling was detected by strain gauges in this study and the local buckling load was determined using the vertical tangent method proposed by Venkataramaish and Roorda (1982). Ma et al. (2015b) employed the same method to evaluate the local buckling stress of cold-formed high-strength steel tubular sections. The determination of local buckling load is illustrated in Fig. 5.9. The corresponding axial load of the dashed cross is the local buckling strength of the composite section. Local buckling was only found on the tests for section 100×40×2. The axial strengths when local buckling occur (N_{LB}) are shown in Table 5.2 and the axial strengths are compared with the summation of ultimate load-carrying capacity of concrete and stainless steel tube ($N_0 = f_c' A_c + f_u A_s$). All the materials are fully utilized if the ratio between N_{Exp} and N_0 is larger than unity. The hollow stainless steel tube was failed by local buckling and only 77% of the ultimate strength was obtained due to local buckling as well as effect from geometric imperfection and residual stress. However, the concrete infill can greatly reduce the influence of local buckling with the increased ratio of N_{LB} / N_0 for more than 17%. The ratios of N_{Exp} / N_0 for concrete-filled specimens are greater than unity due to the confinement effect. This further proved that the composite structure can effectively utilize both the concrete and steel materials, and thus reduce the material cost in construction.

5.3.4 Effect of concrete strength

The filled concrete strength adopted in this experimental study covers from normal to high strengths (40, 80 and 120 MPa) and it is not surprising that more ductile behaviour was achieved when normal strength concrete was used, as shown in Figs 5.3 – 5.7. The use of high strength concrete can cause abrupt loss of the axial load-carrying capacity for the slender stainless steel tubes (larger d/t), e.g., specimens 100×40×2C120 and 120×80×3C120. The sudden loss of compressive strength is not desirable and it is recommended to use stocky stainless steel tubes if high strength infill concrete is employed.

5.3.5 Ductility index

The ductility of a column can be quantified by its ductility index (DI), which was adopted by Han (2002) and defined as:

$$DI = \frac{\varepsilon_{85\%}}{\varepsilon_{Exp}} \quad (5.1)$$

where ε_{Exp} is the axial strain corresponding to ultimate strength N_{Exp} , and $\varepsilon_{85\%}$ is the strain corresponding to 85% of the ultimate strength on the unloading branch. Specimens with DI close to 1.0 have the load drops quickly, while those with large value of DI can maintain the load closer to the ultimate load for larger axial shortening. Values of DI for some specimens are not available due to the tests were not continued for the load drop to 85% of the ultimate load. The values of DI are listed in Table 5.3. Overall, it is observed that the ductility reduces as the slenderness (d/t) of the stainless steel tube and the strength of concrete increases.



5.4 Finite Element Model and Verification

5.4.1 General

A finite element model was developed in order to replicate the experimental results. Parametric study was carried out to extend the available experimental data to sections with wider range of slenderness and aspect ratio (D/B) upon the verification of the finite element model. The finite element package ABAQUS version 6.14 (ABAQUS, 2014) was employed to perform the numerical study. The material properties obtained from the flat and corner coupon tests as reported in Chapter 3 were incorporated in the finite element model. Measured dimension of specimens were used in this study and the model was created based on the centerline dimensions of cross-sections. Four-node doubly curved shell element with reduced integration (S4R) which has six degrees of freedom per node was used for modelling stainless steel tubes. The three dimensional 8-node linear brick solid element with reduced integration (C3D8R) is used to model the concrete infilled. The C3D8R element can effectively model the concrete cracking (Lai et al., 2015). Huang and Young (2012) illustrated that the finite element model including residual stress was only 1% more accurate than that without considering residual stress for cold-formed stainless steel hollow stub column members, which revealed that the effect of residual stress is insignificant. Hence, residual stress is not considered in the finite element models of concrete-filled cold-formed stainless steel members in this study.

5.4.2 Boundary and loading conditions

The fixed-end stub columns were compressed between the two bearing plates and the ends of the stub columns were simulated by restraining against all degrees of



freedom, except for the vertical displacement at the loaded end. No translational and rotational degrees of freedom were restrained for the other nodes other than the two ends. The boundary conditions were modelled by two reference points which are coupled with the surfaces of the cross-section at both ends. The reference points were located at 25 mm away from each end of the stub column specimens to account for the rigid end plates. The axial load was applied by a specified axial displacement to the nodes at one end of the stub columns, which is identical to the stub column tests. Static RIKS step in the ABAQUS library was used to apply the loading and the nonlinear geometric parameter (*NLGEOM) was also included to allow large displacement analysis.

5.4.3 Material modelling of cold-formed ferritic stainless steel tubes

The measured stainless steel stress-strain curves from tensile flat and corner coupon tests as reported in Chapter 3 were used in the finite element model. The true stress (σ_{true}) and logarithmic plastic strain (ε_{pl}) were converted from the static engineering stress (σ) and strain (ε) obtained from the tensile coupon tests. In order to account for the strength enhancement on the corner region due to the cold-rolling process, the corner properties were extended beyond the curved corner portions into the flat portions by the length of two times the thickness of the section, as shown in Fig. 5.10. Due account of strength enhancement on corner region was also adopted in Ma et al. (2015b), Gardner and Nethercot (2004) and Ashraf et al. (2006).



5.4.4 Material modelling of concrete

The concrete core expands laterally and was confined by the steel tubes under axial compression. This confinement can greatly enhance the strength and ductility of the concrete depending on the concrete strength and the slenderness of the steel tube as discussed before. The concrete material behaviour was modelled using the modified concrete damaged plasticity material model proposed by Tao et al. (2013). This material model defines a set of material parameters and a strain hardening/softening function based on calibration of a wide range of experimental data. The initial elastic modulus (E_c) was taken as the measured values and the Poisson's ratio (ν_c) was set to be 0.2 as recommended in ACI 318 (2014).

The plasticity model comprises several parameters including dilation angle (ψ), flow potential eccentricity (e), ratio of the compressive strength to uniaxial compressive strength (f_{b0} / f_c'), the ratio of the second stress invariant on the tensile meridian to that on the compressive meridian (K_c) and viscosity parameter to define the nonlinearity of the confined concrete. All the parameters were determined in accordance with Tao et al. (2013).

The typical stress-strain curve adopted from Tao et al. (2013) for confined concrete is shown in Fig. 5.11. The ascending portion OA is expressed by the following equation:

$$\frac{\sigma}{f_c'} = \frac{A \cdot X + B \cdot X^2}{1 + (A - 2)X + (B + 1)X^2} \quad 0 < \varepsilon \leq \varepsilon_{c0} \quad (5.2)$$

$$\text{where } X = \varepsilon / \varepsilon_{c0}; A = \frac{E_c \varepsilon_{c0}}{f_c'}; B = \frac{(A - 1)^2}{0.55} - 1.$$

The descending branch is defined by an exponential function:



$$\sigma = f_r + (f_c' - f_r) \exp \left[- \left(\frac{\varepsilon - \varepsilon_{cc}}{\alpha} \right)^\beta \right] \quad \varepsilon_{cc} \leq \varepsilon \quad (5.3)$$

where f_r is the residual stress of the horizontal portion as shown in Fig. 5.11.

The stub column specimens were subjected to pure compression and the tensile properties of concrete is not sensitive in modelling the compressive response of the columns. The tensile strength was modelled by linear relation up to failure stress $0.1f_c'$ and after which it was characterized by form of fracture energy (G_F) (Tao et al., 2013) defined as:

$$G_F = \left(0.0469d_{\max}^2 - 0.5d_{\max} + 26 \right) \left(\frac{f_c'}{10} \right)^{0.7} \quad (5.4)$$

where d_{\max} is the maximum diameter of the coarse aggregate.

5.4.5 Modelling of concrete-stainless steel tube interface

The contact between the concrete and stainless steel tube was modelled by surface-based contact. “Hard contact” is defined in the normal direction, which allows separation of the contact elements but penetration is prohibited. The contact in tangential direction follows the Coulomb friction model proposed by Han et al. (2007). The friction model allows stress transmission between the stainless steel tube and concrete up to the limit τ_{crit} and after which relative slip starts and the shear stress was kept in the level of τ_{crit} . The penalty friction formulation with coulomb friction coefficient was taken as 0.6 as recommended by Han et al. (2007). No additional bond between the stainless steel tube and concrete infill such as adhesive bonding was included in the model. The shear stress limit was calculated by Eq. (5.5) as specified by Han et al. (2007):



$$\tau_{crit} = 0.75 \left[2.314 - 0.0195 (\max[D, B] / t) \right] > 0 \quad (5.5)$$

5.4.6 Verification of finite element model

The finite element model was validated with all the experimental results in terms of ultimate loads obtained from the finite element analysis N_{FEA} against the test strengths N_{Exp} , as shown in Table 5.3. The mean value of N_{Exp} / N_{FEA} equals to 1.04 with the corresponding coefficient of variation (COV) of 0.029. A maximum difference of 9% is found between the experimental and numerical ultimate axial strength for specimen 120×80×3C80. Good agreement has been achieved in terms of the ultimate axial strength of concrete-filled cold-formed ferritic stainless steel stub columns between the experimental and numerical results.

5.5 Parametric Study

An extensive parametric study was performed on concrete-filled cold-formed ferritic stainless steel stub columns using the verified finite element model. A total of 165 specimens were analyzed in this parametric study and the stress-strain curves obtained from the flat and corner coupon tests of section 120×80×3 as reported in Chapter 3 were used in modelling the material of stainless steel tubes. The parametric study covers both square and rectangular sections. The square sections have six different overall profiles (overall depth × overall width) ranged from 95×95 to 315×315. Six different profiles were also covered for rectangular sections ranged from 200×100 to 400×100. The aspect ratio (D/B) for all the profiles ranged from 1 to 3. The thickness of the sections varies in order to cover a wide range of slenderness ratios from stocky to slender sections. The three different concrete strengths and the corresponding measured elastic modulus (E_c) in the experimental study were used for each thickness of each profile. The length



of each specimen was three times the longer length of overall depth (D) and overall width (B), which is identical to the experimental study. The specimens in the parametric study shares the same labelling system as that of the test specimens, and the ultimate axial strengths obtained from the finite element analysis are listed in Table 5.4.

5.6 Reliability Analysis

Reliability analysis was conducted to assess the reliability of current design methods on predicting the load-carrying capacity of concrete-filled cold-formed ferritic stainless steel stub columns. Reliability analysis is detailed in the specification AISC 360 (2016). A target reliability index of 2.50 is used in this study and the larger the value of β means the more reliable and safer the design method is. The resistance factor (ϕ_0) of 0.90 was used for the axially loaded stub columns. Load combination of 1.2DL+1.6LL was used for specifications AISC 360 (2016) and ACI 318 (2014). The combinations of 1.35DL+1.5LL and 1.2DL+1.5LL were used for EC4 (2004) and Australian standard AS 5100.6 (2004), respectively. The live load to dead load ratio of 1/5 was used. Statistical parameters $M_m = 1.10$, $F_m = 1.00$, $V_M = 0.10$ and $V_F = 0.05$ were adopted in the calculation of the reliability index, where M_m is the mean value of material factor, F_m is the mean value of fabrication factor, V_M is the coefficient of variation of material factor and V_F is the coefficient of variation of fabrication factor. The statistic parameters P_m and V_p are the mean value of experimental-to-design or FEA-to-design load ratios and coefficient of variation of experimental-to-design or FEA-to-design load ratios, respectively. The correction factor C_p was also used in the calculation of reliability index to compensate the influence due to limited number of data sample. The values of the reliability index are shown in Table 5.5 for all design rules.



5.7 Comparison Between Test and Code Predicted Strengths

5.7.1 General

There are several well-known design standards available for design of concrete-filled carbon steel columns, such as American specification AISC 360 (2016), American code ACI 318 (2014), EC4 (2004) and Australian standard AS 5100.6 (2004). However, none of these standards address the design of concrete-filled stainless steel columns. The design strengths obtained from the aforementioned design standards are compared with the experimental and numerical results presented in this chapter to evaluate their applicability. All the partial safety factors have been set to be unity and the material properties have been taken as the measured values for the comparison made in this section. In the calculation of the design predictions, the yield strength (f_y) of the carbon steel was taken as the 0.2% proof stress of the stainless steel material. At the same time, the limitations on applying the design rules, such as limits on concrete strengths and steel tube slenderness (d/t) ratio, are ignored to check the feasibility of the design rules on predicting the sectional load-carrying capacity of CFST columns. The limits on applying the design rules from different design standards are summarized in Table 5.6.

5.7.2 AISC 360

The American specification AISC 360 (2016) classifies rectangular CFSTs into three categories, i.e., compact, noncompact and slender sections depending on the steel tube slenderness (d/t) ratio. The compact sections with slenderness ratio less than or equal to compactness limit ($\lambda_p = 2.26\sqrt{E_s/f_y}$) can develop yield strength



before local buckling of the steel tube and provide adequate confinement of the concrete infill to develop its compressive strength up to $0.85f_c'$. It is noteworthy that the use of CFST with slenderness ratio larger than the compactness limit was not allowed in previous version of AISC 360. The compressive strength of rectangular stub columns with compact tubes is determined by Eq. (5.6).

CFSTs with steel tubes having slenderness ratio greater than compactness limit but less than or equal to noncompactness limit ($\lambda_r = 3.00\sqrt{E_s / f_y}$) are classified as noncompact sections. This noncompactness limit is conservatively developed by elastic local buckling of steel tubes as detailed in Lai et al. (2014). The steel tubes of noncompact sections can reach their yield strength with local buckling but it is believed that the concrete infill will suffer from significant volumetric dilation after the compressive strength exceeds $0.70f_c'$ due to insufficient confinement by the steel tubes (Lai et al., 2014).

Steel tubes with slenderness ratio larger than slenderness limit ($\lambda_{limit} = 5.00\sqrt{E_s / f_y}$) are not permitted to use in CFSTs. Slender CFSTs, which have slenderness ratio greater than noncompact limit, undergo elastic local buckling and cannot reach the material yield strength. The filled concrete will have significant volumetric dilation after compressive strength exceeding $0.70f_c'$ and the dilation will accelerate the failure of the steel tube. The axial compressive strength of the slender rectangular CFST stub columns is determined based on the critical elastic buckling stress f_{cr} for the steel tubes and compressive strength of $0.70f_c'$ for the concrete portion.

The ratio of the experimental or numerical strengths over design strengths obtained using AISC 360 (2016) are plotted against the plate slenderness



parameter $\lambda = (d/t) \cdot \sqrt{f_y/E_s}$, as shown in Fig. 5.12. The design strengths are quite conservative with the mean value of experimental or numerical to design strengths ratio equals to 1.38 and *COV* of 0.131, as presented in Table 5.5. The predictions for slender sections perform worse as the slenderness parameter increases, which reveals that the AISC 360 (2016) underestimates elastic buckling stress of slender section compared with the noncompact sections adopting the same allowable concrete compressive strength. The reliability index (β_0) for AISC is 3.47, which is considered to be very reliable.

$$N_{AISC} = \begin{cases} A_s f_y + 0.85 f_c' A_c & \text{if } b/t \leq 2.26 \sqrt{\frac{E_s}{f_y}} \\ A_s f_y + 0.70 f_c' A_c & \text{if } 2.26 \sqrt{\frac{E_s}{f_y}} < b/t \leq 3.00 \sqrt{\frac{E_s}{f_y}} \\ A_s f_{cr} + 0.70 f_c' A_c & \text{if } 3.00 \sqrt{\frac{E_s}{f_y}} < b/t \end{cases} \quad (5.6)$$

where $f_{cr} = \frac{9E_s}{(d/t)^2}$.

5.7.3 ACI 318

The American Concrete Institute design guidance ACI 318 (2014) allows design of CFST to a narrower range of steel tubes with slenderness ratio (d/t) less than or equal to $\sqrt{3E_s/f_y}$ compared with AISC 360 (2016). The design equation is similar to the compact section design in AISC 360 and no explicit confinement effect is allowed. The compressive design resistance N_{ACI} for rectangular CFST stub columns can be calculated by Eq. (5.7). The ACI predictions are conservative with the mean value of experimental or numerical to design strengths ratio equals to 1.18 and *COV* of 0.065. This method is considered to be reliable with the reliability index (β_0) of 3.18, which is larger than the target value of 2.50.



$$N_{ACI} = 0.85A_c f_c' + A_s f_y \quad (5.7)$$

5.7.4 Eurocode 4

The nominal compressive resistance of concrete-filled carbon steel tubes in EC4 (2004) is based on the plastic resistance of the cross section by a simple summation of the steel and concrete contributions, as given by Eq. (5.8). The reduction factor 0.85 of concrete strength for composite columns in EC4 (2004) takes account for the influence of long time acting loads (not creep and shrinkage). However, it is believed that the peeling off of the concrete in the stainless steel tube is impossible, which leads to a more favorable development of concrete strength, and the reduction factor is removed (CIDECT, 1998). The EC4 (2004) allows using rectangular steel tubes with slenderness ratio (D/t) less than or equal to $52 \cdot (235/f_y)^{0.5}$, where D is the overall depth of the cross section. The EC4 (2004) design strengths agree well with the experimental and numerical results with the mean value of 1.07 and COV of 0.075, and it is reliable with the reliability index (β_0) equals to 2.58. The good performance of the EC4 (2004) predictions can be due to the low f_u/f_y ratio of ferritic stainless steel, which leads to the plastic sectional resistance close to the ultimate section resistance. The ratio of the experimental or numerical over design strengths obtained by EC4 (2004) are plotted against the slenderness factor of $D/t\sqrt{f_y/235}$, as shown in Fig. 5.13. The slenderness limit of value 52 for plastic resistance is conservative and it is proposed to relax the limit to 85.

$$N_{EC4} = A_c f_c' + A_s f_y \quad (5.8)$$



5.7.5 AS 5100.6

The Australian standard AS 5100.6 (2004) assumes that the steel tube yields before the concrete reaches its ultimate stress state (Tao et al., 2008). The sectional capacity under axial compression for rectangular concrete-filled tubes N_{AS5100} is calculated by summing up the contribution of concrete and steel tube, and different capacity factors of 0.6 and 0.9 are applied to concrete and steel respectively, as shown in Eq. (5.9). The AS 5100 underestimated the load-carrying capacity with the mean value of 1.51 and COV of 0.070 due to the applied capacity factors. The reliability index (β_0) for AS 5100 is 3.94, which is considered to be reliable.

$$N_{AS5100} = 0.6A_c f'_c + 0.9A_s f_y \quad (5.9)$$

5.8 Concluding Remarks

Experimental and numerical investigations on concrete-filled cold-formed ferritic stainless steel stub columns have been conducted in this study. A series of experimental study were conducted on square and rectangular sections for a total of 22 specimens. A finite element model was developed to duplicate the experimental results and the finite element model agrees well with the experimental results. An extensive parametric study was carried out using the verified finite element model to obtain complementary data. A total of 182 experimental and numerical results were used to assess the applicability of the existing design rules for cross-sectional compressive capacity of conventional concrete-filled carbon steel columns as presented in American specification AISC 360 (2016), American code ACI 318 (2014), EC4 (2004) and Australian standard AS 5100.6 (2004). It is found that the EC4 (2004) provides the best predictions on the axial compressive strength of concrete-filled cold-formed ferritic stainless



steel stub columns, which can be attributed to the low f_u / f_y ratio of ferritic stainless steel, and thus appropriate for the design of concrete-filled cold-formed ferritic stainless steel stub columns.



Specimen	D (mm)	B (mm)	t (mm)	d / t	r _o (mm)	r _i (mm)	L (mm)	A _s (mm ²)
60×40×4C0	59.9	40.1	3.821	12.3	6.5	3.8	179.2	653.0
60×40×4C40	59.9	40.1	3.816	12.3	6.5	3.8	178.9	652.4
60×40×4C40R	59.8	40.1	3.796	12.3	6.5	3.8	179.5	648.6
60×40×4C80	59.9	40.1	3.792	12.4	6.5	3.8	179.5	648.4
60×40×4C120	59.8	40.1	3.817	12.3	6.5	3.8	179.1	651.9
60×60×3C0	60.3	60.1	2.833	17.2	5.8	3.8	179.8	610.6
60×60×3C40	60.3	60.1	2.827	17.2	5.8	3.8	180.3	609.9
60×60×3C80	60.2	60.1	2.830	17.2	5.8	3.8	179.7	609.8
60×60×3C120	60.3	60.1	2.829	17.2	5.8	3.8	179.2	609.8
80×60×4C0	80.1	59.8	3.735	17.4	7.6	4.3	239.8	941.5
80×60×4C40	80.1	59.9	3.709	17.5	7.6	4.3	239.7	936.1
80×60×4C80	80.3	59.9	3.723	17.5	7.6	4.3	239.9	940.8
80×60×4C120	80.2	59.8	3.717	17.5	7.6	4.3	240.0	938.0
80×60×4C120R	80.2	59.9	3.740	17.4	7.6	4.3	240.1	943.6
100×40×2C0	99.7	40.2	1.948	45.3	5.7	4.0	300.1	508.1
100×40×2C40	99.7	40.2	1.944	45.4	5.7	4.0	299.9	507.3
100×40×2C80	99.7	40.2	1.946	45.4	5.7	4.0	300.0	507.7
100×40×2C120	99.7	40.2	1.949	45.3	5.7	4.0	300.0	508.3
120×80×3C0	120.0	79.9	2.803	38.3	6.3	4.1	360.1	1051.0
120×80×3C40	119.9	79.9	2.803	38.3	6.3	4.1	359.8	1051.1
120×80×3C80	120.0	79.9	2.805	38.3	6.3	4.1	359.9	1051.6
120×80×3C40	120.0	79.9	2.807	38.3	6.3	4.1	359.9	1052.5

Table 5.1. Measured dimensions of stub column specimens.

Specimen	N _{LB} (kN)	$\frac{N_{LB}}{N_0}$	$\frac{N_{Exp}}{N_0}$
100×40×2C0	157.5	0.69	0.77
100×40×2C40	375.3	0.99	1.06
100×40×2C80	485.0	0.95	1.05
100×40×2C120	559.2	0.86	1.04

Note: $N_0 = f_c' A_c + f_u A_s$

Table 5.2. Measured local buckling strengths of stub column specimens.



Specimen	N_{Exp} (kN)	ε_{Exp} (%)	DI	N_{FEA} (kN)	N_{Exp} / N_{FEA}
60×40×4C0	374.1	1.76	1.63	--	--
60×40×4C40	477.5	1.25	--	464.0	1.03
60×40×4C40R	481.0	1.28	--	464.0	1.04
60×40×4C80	531.8	0.78	4.91	527.4	1.01
60×40×4C120	585.1	0.61	3.81	596.2	0.98
60×60×3C0	332.7	1.32	1.47	--	--
60×60×3C40	484.2	1.01	--	457.5	1.06
60×60×3C80	594.7	0.59	2.13	570.9	1.04
60×60×3C120	712.2	0.57	1.66	689.4	1.03
80×60×4C0	532.1	1.30	1.47	--	--
80×60×4C40	712.6	1.10	--	678.0	1.05
80×60×4C80	878.6	0.60	2.00	828.5	1.06
80×60×4C120	999.6	0.45	2.04	993.9	1.01
80×60×4C120R	976.6	0.45	1.73	993.9	0.98
100×40×2C0	185.5	0.33	1.50	--	--
100×40×2C40	398.3	0.58	1.35	376.9	1.06
100×40×2C80	534.6	0.41	1.16	511.6	1.04
100×40×2C120	674.1	0.40	1.08	660.2	1.02
120×80×3C0	445.5	0.35	1.33	--	--
120×80×3C40	870.8	0.55	1.74	834.1	1.04
120×80×3C80	1255.2	0.40	1.17	1152.2	1.09
120×80×3C40	1610.3	0.38	1.05	1487.2	1.08
				Average	1.04
				COV	0.029

Table 5.3. Results for ultimate load, ultimate strain, ductility index (DI), FEA results and ratio of N_{Exp} / N_{FEA} .



Specimen	N_{FEA} (kN)	Specimen	N_{FEA} (kN)	Specimen	N_{FEA} (kN)
300×300×10C40	9368.2	270×270×3C80	6948.0	200×100×2C120	2785.5
300×300×10C80	12333.1	270×270×3C120	9722.3	200×100×1.5C40	1136.3
300×300×10C120	15518.9	95×95×1C40	532.7	200×100×1.5C80	1753.3
300×300×8C40	8272.2	95×95×1C80	855.6	200×100×1.5C120	2636.7
300×300×8C80	11352.9	95×95×1C120	1225.6	250×100×6C40	3008.2
300×300×8C120	14420.7	300×200×10C40	7284.5	250×100×6C80	3781.1
300×300×5C40	6217.2	300×200×10C80	9041.2	250×100×6C120	4615.6
300×300×5C80	9400.5	300×200×10C120	11031.4	250×100×4C40	2135.0
300×300×5C120	12756.6	300×200×5C40	4657.1	250×100×4C80	2992.8
300×300×4C40	5364.2	300×200×5C80	6731.3	250×100×4C120	3842.4
300×300×4C80	8560.5	300×200×5C120	8902.9	250×100×3.5C40	1959.6
300×300×4C120	11983.9	300×200×4.5C40	4413.3	250×100×3.5C80	2830.4
300×300×3C40	4972.2	300×200×4.5C80	6420.7	250×100×3.5C120	3756.2
300×300×3C80	8350.3	300×200×4.5C120	8803.8	250×100×3C40	1787.8
300×300×3C120	11864.9	300×200×3.5C40	3774.3	250×100×3C80	2700.6
300×300×2C40	4462.5	300×200×3.5C80	6012.1	250×100×3C120	3590.1
300×300×2C80	8005.7	300×200×3.5C120	8585.9	250×100×2.5C40	1653.8
300×300×2C120	11206.1	300×200×3C40	3630.9	250×100×2.5C80	2510.1
250×250×10C40	7308.4	300×200×3C80	6287.8	250×100×2.5C120	3439.9
250×250×10C80	9271.1	300×200×3C120	8133.4	250×100×2C40	1508.8
250×250×10C120	11369.9	300×200×2.5C40	3638.7	250×100×2C80	2413.8
250×250×8C40	6302.2	300×200×2.5C80	6362.8	250×100×2C120	3376.7
250×250×8C80	8361.5	300×200×2.5C120	7937.7	350×200×6C40	5695.6
250×250×8C120	10608.1	300×100×9C40	4581.8	350×200×6C80	8085.1
250×250×5C40	4912.7	300×100×9C80	5448.2	350×200×6C120	10910.5
250×250×5C80	7092.6	300×100×9C120	6360.6	350×200×5C40	5109.3
250×250×5C120	9344.0	300×100×7C40	3854.5	350×200×5C80	7541.2
250×250×4C40	4314.6	300×100×7C80	4764.1	350×200×5C120	10230.2
250×250×4C80	6400.6	300×100×7C120	5750.6	350×200×4C40	4540.7
250×250×4C120	8765.3	300×100×5C40	2811.1	350×200×4C80	6989.4
250×250×3C40	3659.4	300×100×5C80	3792.0	350×200×4C120	9803.5
250×250×3C80	5982.8	300×100×5C120	4803.6	350×200×3.5C40	4149.3
250×250×3C120	8485.2	300×100×4C40	2399.6	350×200×3.5C80	7179.4
200×200×10C40	5511.9	300×100×4C80	3411.5	350×200×3.5C120	9622.7
200×200×10C80	6659.4	300×100×4C120	4499.3	350×200×3C40	4169.2
200×200×10C120	7961.9	300×100×3C40	2027.2	350×200×3C80	6756.5
200×200×8C40	4724.4	300×100×3C80	3046.6	350×200×3C120	9253.6
200×200×8C80	5892.1	300×100×3C120	4175.6	350×200×2.5C40	3835.3
200×200×8C120	7344.4	300×100×2C40	1781.4	350×200×2.5C80	6445.1
200×200×4C40	3128.1	300×100×2C80	2867.1	350×200×2.5C120	9258.2
200×200×4C80	4541.2	300×100×2C120	4000.6	400×200×8C40	7691.0
200×200×4C120	6001.6	200×100×6C40	2515.1	400×200×8C80	10325.0
200×200×3C40	2541.6	200×100×6C80	3123.9	400×200×8C120	13105.0
200×200×3C80	4005.7	200×100×6C120	3786.1	400×200×6C40	6216.0

Table 5.4. Parametric study results (Cont.).

200×200×3C120	5546.5	200×100×4C40	1912.5	400×200×6C80	9056.1
200×200×2C40	2208.6	200×100×4C80	2581.8	400×200×6C120	12016.3
200×200×2C80	3712.2	200×100×4C120	3273.6	400×200×5C40	5612.8
200×200×2C120	5269.6	200×100×3C40	1538.1	400×200×5C80	8564.8
200×200×1.5C40	2098.5	200×100×3C80	2230.4	400×200×5C120	11492.5
200×200×1.5C80	2686.3	200×100×3C120	2947.1	400×200×4.5C40	5345.9
200×200×1.5C120	5397.6	200×100×2.5C40	1385.7	400×200×4.5C80	8548.0
315×315×3C40	5584.2	200×100×2.5C80	2088.1	400×200×4.5C120	11089.0
315×315×3C80	9218.5	200×100×2.5C120	2914.7	400×200×3.5C40	4790.2
315×315×3C120	12960.5	200×100×2C40	1240.9	400×200×3.5C80	7672.1
270×270×3C40	4296.2	200×100×2C80	2077.0	400×200×3.5C120	10701.2

Table 5.4. Parametric study results (Cont.).

	$\frac{N_u}{N_{AISC}}$	$\frac{N_u}{N_{ACI}}$	$\frac{N_u}{N_{EC4}}$	$\frac{N_u}{N_{AS5100}}$
Number of data	182	182	182	182
Mean (P_m)	1.38	1.18	1.07	1.51
$COV(V_p)$	0.131	0.065	0.075	0.070
Resistance factor (ϕ_0)	0.90	0.90	0.90	0.90
Reliability index (β_0)	3.47	3.18	2.58	3.94

Table 5.5. Comparison of test and FEA strengths with design strengths for all specimens.

Standards	Range of f_y (MPa)	Range of f_c' (MPa)	Range of slenderness ratio
AISC 360 (2016)	$f_y \leq 525$	$21 \leq f_c' \leq 70$	$d/t \leq 5.00 \sqrt{\frac{E_s}{f_y}}$
ACI 318 (2014)	$f_y \leq 345$	$17 \leq f_c' \leq 65$	$d/t \leq \sqrt{\frac{3E_s}{f_y}}$
EC4 (2004)	$f_y \leq 460$	$20 \leq f_c' \leq 60$	$D/t \leq 52 \cdot \sqrt{\frac{235}{f_y}}$
AS 5100.6 (2004)	$f_y \leq 350$	$25 \leq f_c' \leq 65$	$D/t \leq 40 \cdot \sqrt{\frac{235}{f_y}}$

Note: D is the overall depth of a RHS, d is the flat portion of the overall depth of a RHS

Table 5.6. Limits in current design rules for rectangular CFST columns.



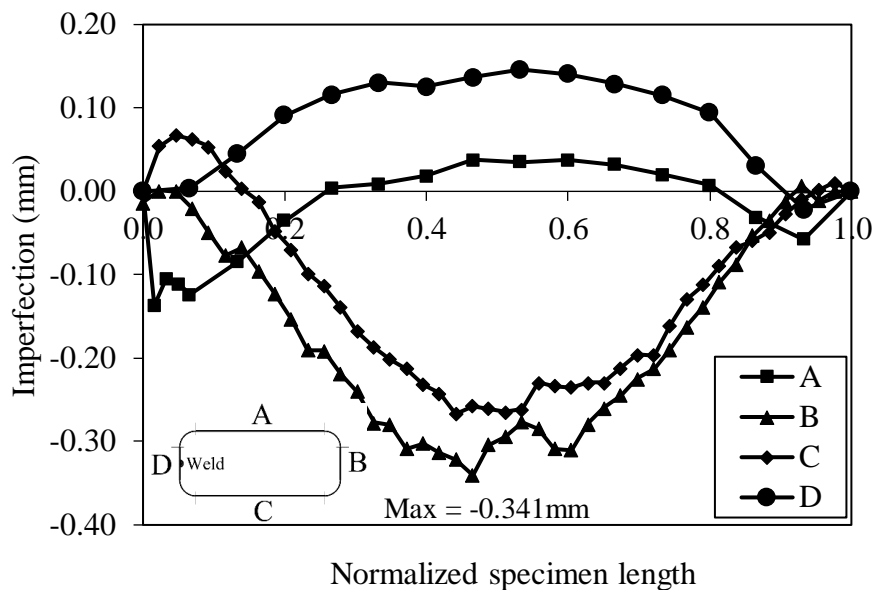


Figure 5.1. Measured local plate imperfection profiles for Section 100×40×2.

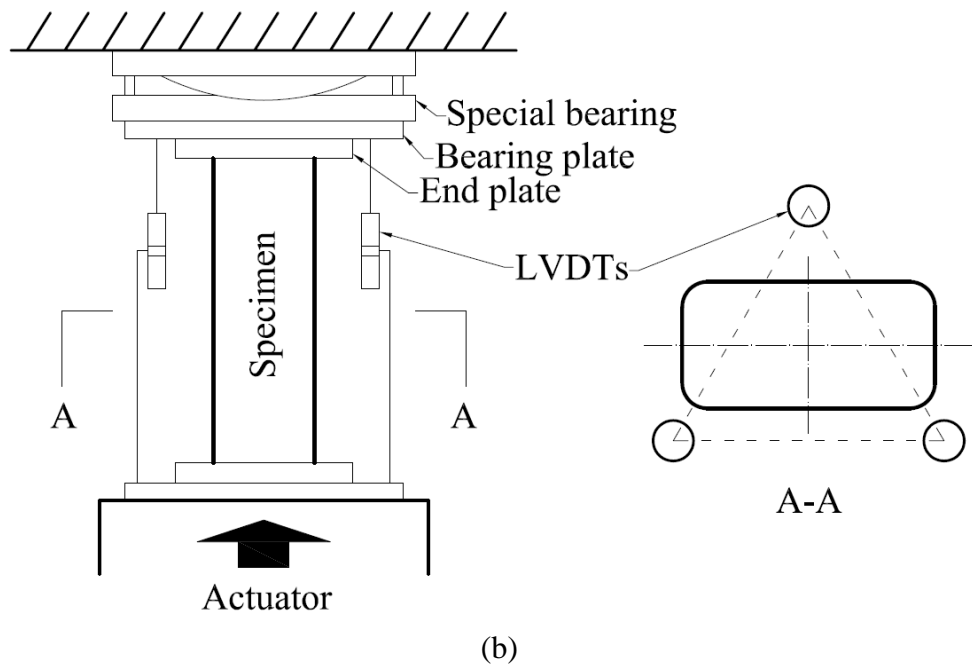
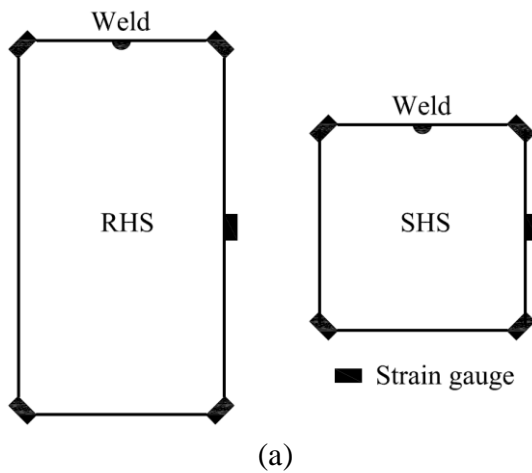


Figure 5.2. Schematic test arrangement for stub column tests: (a) arrangement for strain gauges; (b) arrangement for LVDTs.

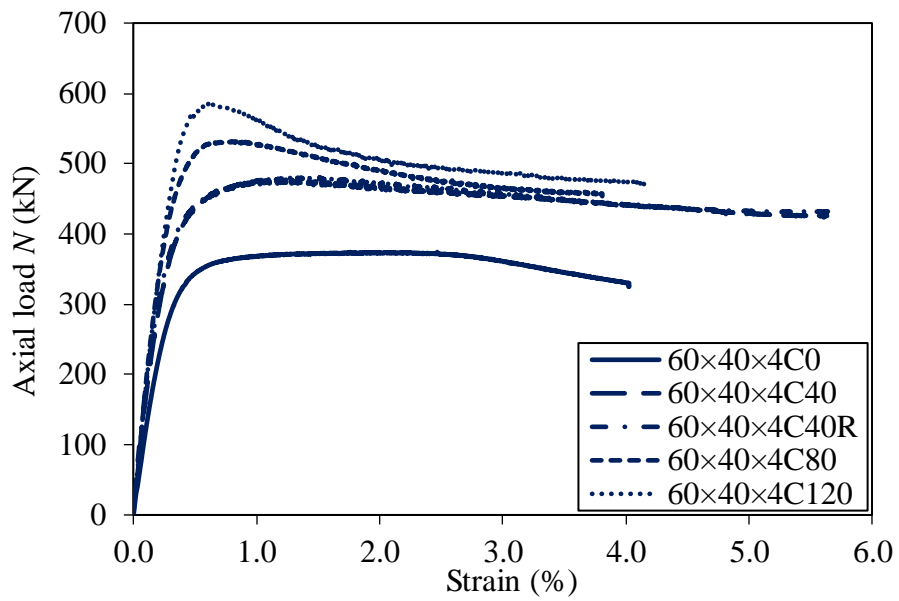


Figure 5.3. Axial load-strain response for series $60 \times 40 \times 4$ stub columns.

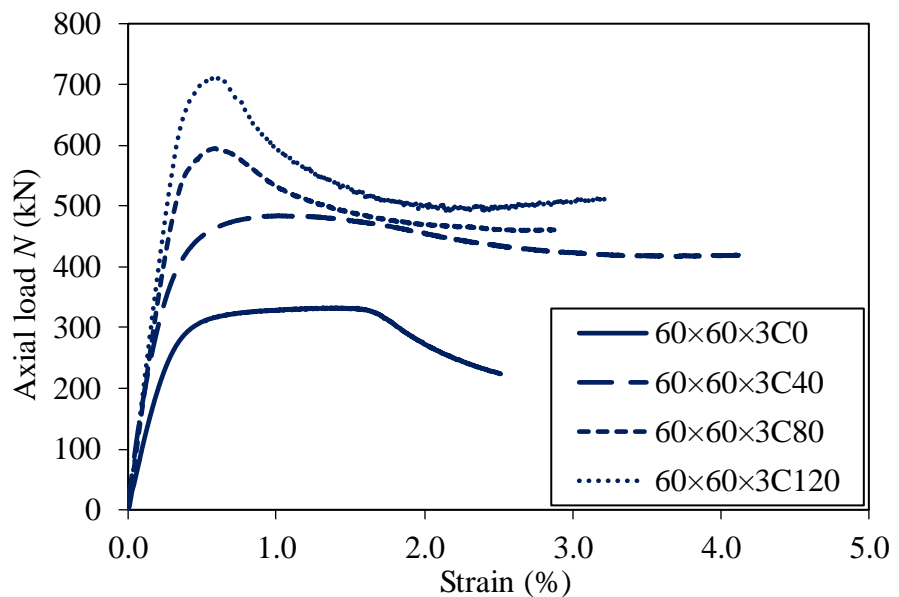


Figure 5.4. Axial load-strain response for series $60 \times 60 \times 3$ stub columns.

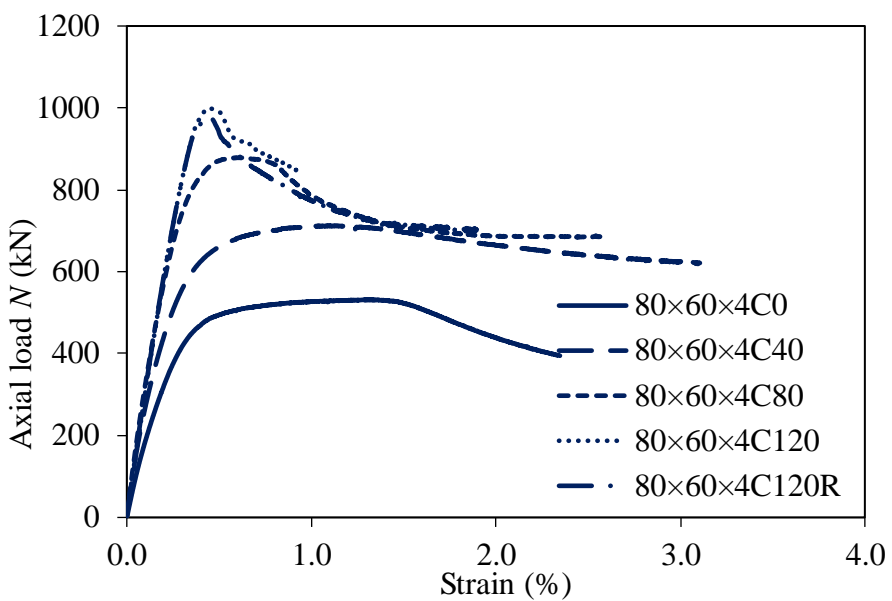


Figure 5.5. Axial load-strain response for series $80 \times 60 \times 4$ stub columns.

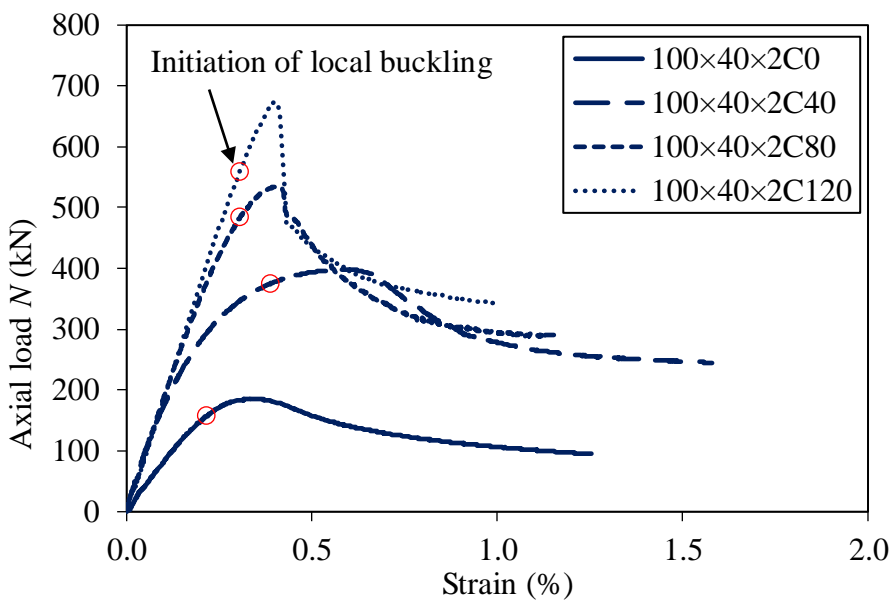


Figure 5.6. Axial load-strain response for series $100 \times 40 \times 2$ stub columns.



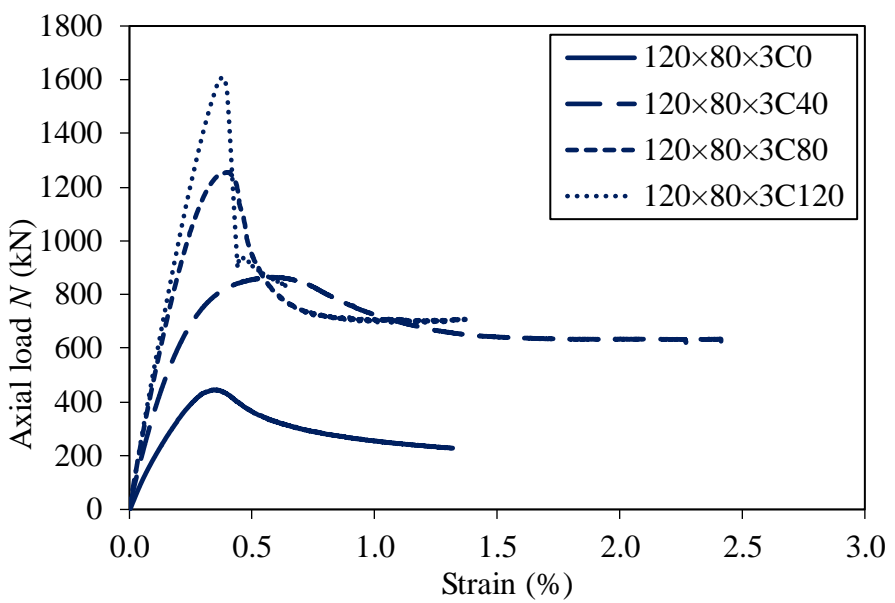
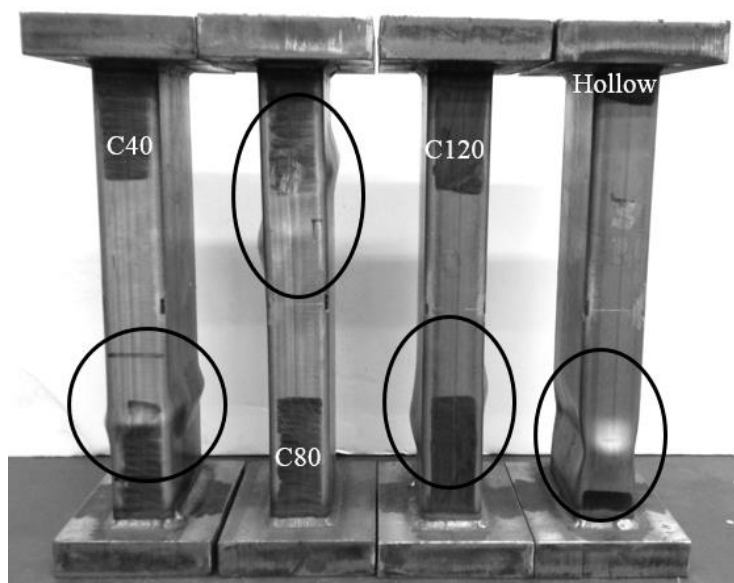
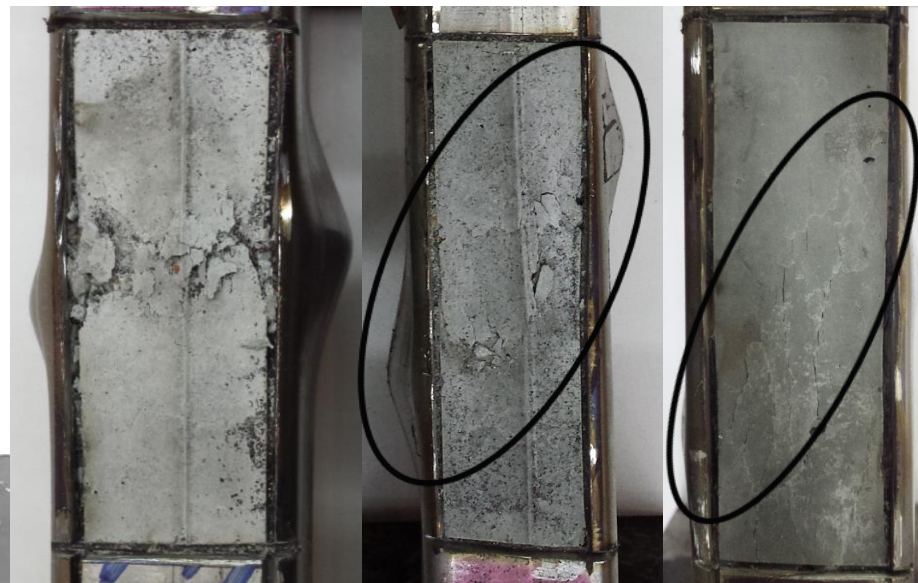


Figure 5.7. Axial load-strain response for series 120×80×3 stub columns.





(a) Series 100×40×2



(b) Specimen 100×40×2C40

(c) 100×40×2C80

(d) 100×40×2C120

Figure 5.8. Failure modes of stub columns.

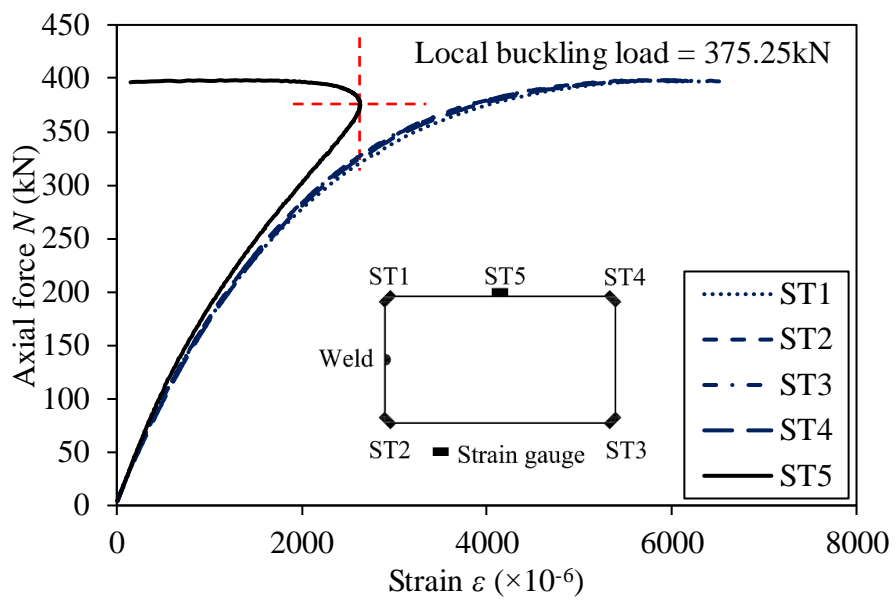


Figure 5.9. Vertical tangent method for specimen 100×40×2C40.

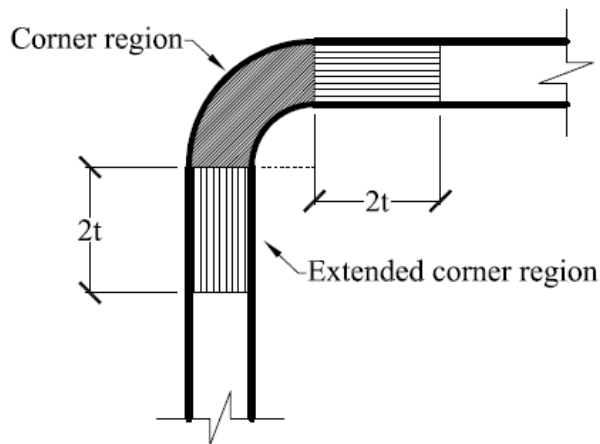


Figure 5.10. Extension of corner material properties to flat portions.



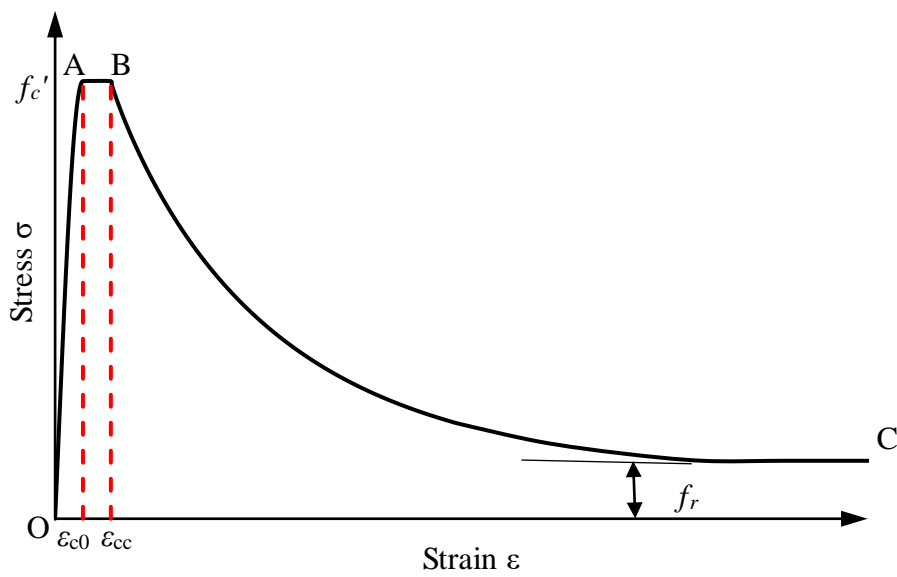


Figure 5.11. Typical stress-strain curve for confined concrete.

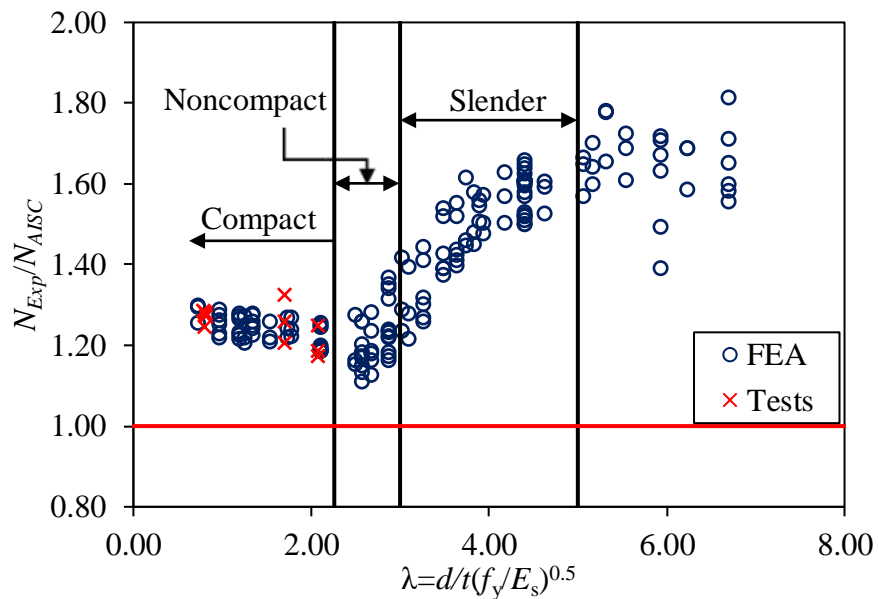


Figure 5.12. Comparison of experimental and AISC predicted strengths.



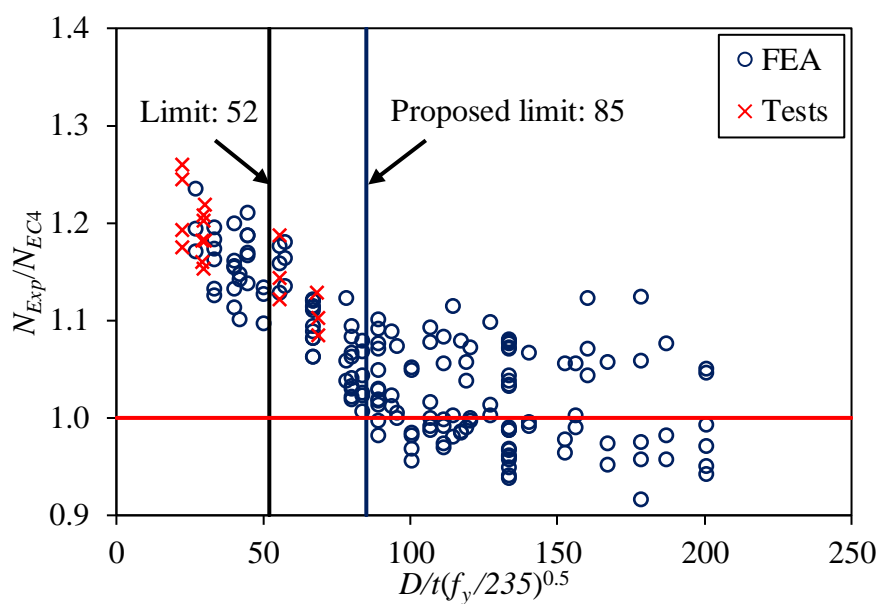


Figure 5.13. Comparison of experimental and EC4 predicted strengths.



CHAPTER 6

STUB COLUMN BEHAVIOUR OF CONCRETE-FILLED COLD-FORMED AUSTENITIC STAINLESS STEEL CHS

6.1 Introduction

This chapter presents an experimental investigation on concrete-filled cold-formed austenitic stainless steel circular sections. A total of 18 specimens were tested comprising 14 concrete-filled specimens and 4 hollow specimens for comparison. A finite element model was developed based on the modified confined concrete model and it is shown that the finite element model can accurately predict the axial compressive capacity of concrete-filled stainless steel circular sections. A comprehensive parametric study was carried out based on the verified finite element model. The parametric study involves a total of 168 specimens covering the diameter-to-thickness ratio (D/t) ranged from 30 to 245. The experimental and numerical results together with the available data from the literature (Lam and Gardner, 2008; Uy et al., 2011) were compared with the existing design methods for composite carbon steel sections including American specification AISC 360 (2016), American code ACI 318 (2014), EC4 (2004) and AS 5100.6 (2004). It was found that the existing design guidance for concrete-filled carbon steel section may be safely applied to concrete-filled stainless steel circular section except for EC4 (2004). Modification to AS 5100 was also carried



out and it is found that the AS 5100 provides the most accurate predictions on concrete-filled circular stainless steel stub columns.

6.2 Experimental Investigation

6.2.1 General

An experimental study was performed to assess the axial compressive response of concrete-filled cold-formed stainless steel circular hollow sections. Austenitic stainless steel grade EN 1.4301, which is commonly known as 304 austenitic stainless steel, was used to fabricate the tube specimens. Tests were performed on four different section sizes – CHS 60.5×2.8, CHS 76.0×3.0, CHS 114.3×3.0 and CHS 165.2×3.0. Concrete of nominal cylinder compressive strengths 40, 80 and 120 MPa were filled into the stainless steel tubes. Tensile coupon tests were conducted to obtain the stress-strain relationship of the stainless steel before commencement of the column tests. The concrete strength was obtained from standard cylinder and cube tests at the time of column tests. A total of 18 specimens were tested comprising 14 concrete-filled specimens and 4 hollow specimens for comparison. The specimens were labelled in such a way that the nominal dimensions including the outer diameter (D), material thickness (t) and the nominal infill concrete cylinder compressive strength can be identified. For example, the label 165.2×3.0C80 indicates the specimen of outer diameter 165.2 mm and thickness equals to 3.0 mm. The symbol “C80” means that the specimen had nominal infill concrete cylinder compressive strength equals to 80 MPa. A symbol “C0” indicates the specimen was a hollow section without any infill concrete. If the test was a repeated one, a symbol “R” would be added after the concrete strength. The measured specimen dimensions are shown in Table 6.1.



Both standard cylinders and cubes were cast and tested to determine the cylinder compressive strength (f_c') and cube compressive strength (f_{cu}) of the concrete. Four cylinders and two cubes were cast for each concrete strength at the same time of stub column casting. All the concrete-filled stub column tests were carried out at 28 days after casting and were completed within two days so that the concrete strength enhancement is minimal. The elastic modulus of concrete (E_c) was also determined by suitable compressometer using concrete cylinder in according to ASTM C469 (2014). The concrete cylinder compressive strengths for the concrete of nominal cylinder strengths 40, 80 and 120 MPa were 36.4, 85.8 and 120.0 MPa, whilst the corresponding cube strengths were 46.0, 93.6 and 125.7 MPa. The elastic modulus determined from concrete cylinders were 23.9, 33.1 and 39.0 GPa for the concrete of nominal cylinder strengths 40, 80 and 120 MPa, as shown in Table 6.1.

6.2.2 Instrumentation and test setup

A total of 18 stub column tests were performed with one hollow and three concrete-filled specimens with three different concrete cylinder compressive strengths for each of the four section sizes. Two concrete-filled specimens were chosen to be repeated in order to check the reliability of the tests. The lengths of the specimens were designed to be three times the out diameter of the tubes to ensure that the specimens were not failed by overall flexural buckling, yet still long enough to contain the same initial residual stress pattern as a much longer member cut from the same stock (Ziemian, 2010). Four strain gauges were affixed at the mid-height of the specimens to monitor the longitudinal strain, as shown in Fig. 6.1. A total of three linear variable differential transducers (LDVTs) were used to capture the axial shortening of the specimens, as shown in Fig. 6.2(a). A



special bearing was located on top of the specimen and the gap between the bearing plate and specimen can be eliminated by rotating the special bearing. To avoid end failure results from load concentration, two end-stiffeners steel rings with height of 10 mm were applied to each end of each specimen. To prevent any voids and achieve uniform application of compressive loading on the stub column specimens, a thin layer of plaster was applied to the two ends of the concrete-filled specimens and hardened under a small pre-loading force. The test set-up is shown in Fig. 6.2(b). Similar test setup was also adopted in (Young and Hartono, 2002; Ma et al., 2015b; Zhao et al., 2016b). An INSTRON 5000 kN hydraulic testing machine was used to conduct all the stub column tests. All the specimens were tested under a constant displacement rate of 0.5 mm/min.

6.3 Experimental Results and Discussion

6.3.1 Axial load behaviour of stub columns

The axial load-strain curves obtained from the concrete-filled circular stub column tests are shown in Fig. 6.3 (a)-(d). The axial strains were measured from both the strain gauges and LVDTs, where the strain gauge measurements were used for the elastic part of the axial load-strain curves and after that the readings from LVDTs were used. The results clearly show the advantage of composite stainless steel columns over their bare stainless steel counterparts. Generally, the stockier stainless steel tubes with normal strength concrete exhibited more ductile behaviour. However, the enhancement in strength due to infill concrete is more significant for those slenderer sections filled with high strength concrete.

It is noteworthy that the axial load-strain curves for specimens 60.5×2.8C40, 60.5×2.8C40R, 76.3×3.0C40 and 114.3×3.0C40 exhibited strong strain-hardening



response with the load kept increasing until the end of tests. All the above-mentioned tests were stopped due to the excessive axial deformation and it is believed that the stainless steel tube can exert high confinement on the normal strength concrete after undergoing significant plastic deformation. If the confinement is not effective enough, no obvious strain-hardening response will be observed and instead a nearly horizontal flat one can be expected, like the specimen 165.2×3.0C40, for which the cross-section slenderness is large. For the rest of specimens, a clear descending portion was shown for each of them. This is due to the premature crushing of the high strength concrete core at the initial stage. The Poisson's ratio for stainless steel (ν_s) was 0.3 larger than that of concrete (ν_c), which was 0.2 as recommended in ACI 318 (2014), at the early stage and the lateral dilation of stainless steel was larger than that of concrete. Thus, the steel tube provides no or even negative confinement to the concrete core (Lai, 2015). The high strength concrete was more brittle than the normal strength concrete and the crushing of high strength concrete caused the drop of axial load due to insufficient confinement provided. It is believed the reason why the load increased again at the later stage is due to the strain hardening effect of stainless steel (Uy et al., 2011).

6.3.2 Test results

The ultimate axial loads (N_{Exp}) and the corresponding axial strain (ε_{Exp}) are summarized in Table 3. In this study, the ultimate axial loads (N_{Exp}) is taken as the value at 2.0% axial strain for those specimens without clear descending portions. This is due to the fact that for those concrete-filled circular stainless steel with clear peak loads in this experimental study and test results reported by Uy et al. (2011), the strain corresponding to peak strength is smaller than 2.0%. In



addition, the steel tube is believed to be yielded at or before 2.0% strain (Lai, 2015) and no significant strain hardening behaviour of stainless steel tube have taken place at 2.0% strain, which is shown in Fig. 6.4, so that a conservative estimation can be provided.

6.3.3 Effect of infill concrete

The strength and modulus are greatly enhanced for the concrete-filled sections compared with the hollow ones, as shown in Fig. 6.3. The concrete strength has obvious effect on the shape of the axial load-strain curve. The stainless steel tubes filled with normal strength concrete behaved in a very ductile manner and the ductility decreases as the strength of concrete increases as expected. The ductility of composite sections filled with nominal concrete cylinder compressive strengths of 80 and 120 MPa were lower than those hollow sections.

To further assess the effects of concrete strengths on the composite sections, the ultimate axial loads (N_{Exp}) are normalized with the nominal squash load (N_o) defined in Eq. (6.1):

$$N_o = f_y A_s + f_c' A_c \quad (6.1)$$

The normalized ultimate axial loads are plotted against the D/t ratio for each specimen including the hollow specimens, as shown in Fig. 6.5, and also summarized in Table 6.2. It is evident that the sections with smaller D/t ratio and lower concrete strength are more effective to exert confinement on concrete, and make better use of both the stainless steel and concrete materials. However, the ratio of N_{Exp} / N_o are larger for hollow specimens compared with concrete-filled specimens. This could be due to the fact that concrete is much more brittle than



the austenitic stainless steel and the crushing of concrete hinder the development of strain hardening response of stainless steel. In the concrete-filled aspect, it is recommended to adopt sections with small D/t ratio and normal strength concrete since this is the best combination for the develop of confinement effect.

6.4 Numerical Modelling

6.4.1 General

In parallel with the experimental study, a numerical study using nonlinear finite element analysis package ABAQUS version 6.14 (ABAQUS, 2014) was performed. The aim of the numerical study was to replicate the ultimate axial loads obtained from the tests. Upon the verification of the finite element model, an extensive parametric study was carried out to generate further data over a wide range of slenderness ratios and a total of 168 numerical data were obtained.

6.4.2 Material properties

6.4.2.1 Stainless Steel

ABAQUS requires the stainless steel material properties to be specified in the format of true stress and logarithm plastic strain. The true stress (σ_{true}) and logarithmic plastic strain (ε_{pl}) were converted from the static engineering stress (σ) and strain (ε) obtained from the tensile coupon tests in the experimental study by Eqs (6.2) and (6.3).

$$\sigma_{true} = \sigma(1 + \varepsilon) \quad (6.2)$$

$$\varepsilon_{pl} = \ln(1 + \varepsilon) - \frac{\sigma_{true}}{E_s} \quad (6.3)$$



6.4.2.2 Confined concrete model

Extensive researches were conducted to investigate the confined concrete behaviour and a commonly adopted confined concrete model comprises three different parts. The first part starts from the origin and linear up to the proportional limit, which is assumed to be $0.5f_{cc}$, and the elastic modulus follows the formula provided in ACI 318 (2014) as $E_{cc} = 4700\sqrt{f_{cc}}$ MPa, where f_{cc} is the maximum strength of the confined concrete and the corresponding strain ε_{cc} have been proposed by Mander et al. (1988a) as Eqs (6.4) and (6.5).

$$f_{cc} = f_c' + k_1 f_l \quad (6.4)$$

$$\varepsilon_{cc} = \varepsilon_c (1 + k_2 \frac{f_l}{f_c'}) \quad (6.5)$$

where ε_c is the strain at the unconfined cylinder compressive strength of concrete f_c' and it is taken as 0.003 in accordance with ACI 318 (2014). The parameters k_1 and k_2 are constant values and taken as 4.1 and 20.5, respectively, as recommended by Richart et al. (1928). Regarding the parameter f_l , Hu et al. (2003) proposed the following formulae based on the D/t ratio of the steel tube and the yield strength f_y of steel.

$$f_l / f_y = \begin{cases} 0.043646 - 0.000832(D/t) & \text{for } 21.7 \leq D/t \leq 47 \\ 0.006241 - 0.0000357(D/t) & \text{for } 47 < D/t \leq 150 \end{cases} \quad (6.6)$$

The second part defines the nonlinear portion starting from the proportional limit $0.5f_{cc}$ to the maximum confined concrete strength f_{cc} and the stress-strain relationship was given by Saenz (1964) as Eq. (6.7).

$$f = \frac{E_{cc}\varepsilon}{1 + (R + R_E - 2)\left(\frac{\varepsilon}{\varepsilon_{cc}}\right) - (2R - 1)\left(\frac{\varepsilon}{\varepsilon_{cc}}\right)^2 + R\left(\frac{\varepsilon}{\varepsilon_{cc}}\right)^3} \quad (6.7)$$

$$\text{where } R_E = \frac{E_{cc}\varepsilon_{cc}}{f_{cc}}, R = \frac{R_E(R_\sigma - 1)}{(R_\varepsilon - 1)^2} - \frac{1}{R_\varepsilon}, R_\sigma = R_\varepsilon = 4.$$

The third part of the confined concrete stress-strain curve starts from the maximum confined concrete strength f_{cc} and ends at $f_u = rk_3 f_{cc}$ with the corresponding $\varepsilon_u = 11\varepsilon_{cc}$. The parameter k_3 is defined in Eq. (6.8) by Hu et al. (2003).

$$k_3 = \begin{cases} 1 & \text{for } 21.7 \leq D/t \leq 40 \\ 0.0000339(D/t)^2 - 0.0100085(D/t) + 1.3491 & \text{for } 40 \leq D/t \leq 150 \end{cases} \quad (6.8)$$

The parameter r can be taken as 1.0 for concrete with cube strength of 30 MPa and 0.5 for concrete with cube strength of 100 MPa and linear interpolation for those strengths in between as recommended by Ellobody and Young (2006).

However, it should be noted that this stress-strain curve for confined concrete is found to be discontinuous at the point of proportional limit $0.5f_{cc}$, as shown in Fig. 6.6. In order to modify this stress-strain curve, a new model is proposed by replacing the second part of the curve with a new equation and keeping the proportional limit and maximum confined concrete strength unchanged. Different mathematical models were tried in this study, such as polynomial function, logarithm function and exponential function. However, the exponential function in Eq. (6.9) was adopted.

$$f = f_{cc}x^b \quad (6.9)$$

where $b = \ln(0.5) / \ln(0.5f_{cc} / E_{cc})$. In addition, the elastic moduli are taken as the measured values in this study and the formula provided in ACI 318 (2014) should be used if test data is not available. The Poisson's ratio (ν_c) was taken as 0.2 as recommended in ACI 318 (2014).



The concrete material behaviour was modelled using the damaged plasticity material model. The key parameters including dilation angle (ψ), flow potential eccentricity (e), ratio of the compressive strength to uniaxial compressive strength (f_{b0} / f_c'), the ratio of the second stress invariant on the tensile meridian to that on the compressive meridian (K_c) and viscosity parameter are taken as the recommended values proposed by Tao et al. (2013). The stub column specimens are subjected to pure compression and the tensile properties of concrete was not sensitive in modelling the compressive response of the columns. The tensile strength was modelled by linear relation up to failure stress $0.1f_c'$ and after which it was characterized by form of fracture energy (G_F) as recommended by Tao et al. (2013).

6.4.3 Boundary conditions and element types

The composite stub columns were compressed under fixed-ended condition and the ends of the stub columns were simulated by restraining against all degrees of freedom, except for the displacement at the loaded end in the direction of the applied load. No translational and rotational degrees of freedom were restrained for the other nodes other than the two ends. The boundary conditions were modelled by two reference points which are coupled with the surfaces of the composite section at both ends. The axial load was applied by a specified axial displacement to the nodes at one end of the stub columns and the specified value was large enough for the specimen to reach ultimate axial load. Static RIKS step in the ABAQUS library was used to apply the loading and the nonlinear geometric parameter (*NLGEOM) was also included to allow large displacement analysis.



The stainless steel tubes of the composite stub columns were modelled using a fine mesh of four-node S4R shell elements. These elements have six degrees of freedom per node and reduced integration in the plan of the element, and they are widely used in modelling either hollow steel section (Huang and Young, 2012; Zhao et al., 2016b) or concrete-filled steel tubes (Lai et al., 2014; Lai and Varma, 2015). The concrete core was meshed with eight-node solid elements with reduced integration (C3D8R), as shown in Fig. 9.6. These elements have three degrees of freedom per node and reduced integration, which is computationally effective in modelling cracking of concrete (Lai and Varma, 2015).

6.4.4 Modelling of concrete-stainless steel tube interface

The contact interaction between the concrete core and stainless steel tube was modelled in both the normal and tangential directions. In the normal direction, hard contact with penalty constraint method was used, which allows separation but prohibits penetration between the concrete and stainless steel tube. The contact in tangential direction follows the Coulomb friction model proposed by Han et al. (2007). The friction model allows stress transmission between the stainless steel tube and concrete up to the limit τ_{crit} . The coulomb friction coefficient between the stainless steel tube (master surface) and the concrete infill (slave surface) was set to be 0.6. No additional bond between the stainless steel tube and concrete infill such as adhesive bonding was included in the model. The shear stress limit was calculated by Eq. (6.10) specified by Han et al. (2007) as following:

$$\tau_{crit} = 2.314 - 0.0195(D/t) > 0 \quad (6.10)$$

6.4.5 Verification of finite element model

The results obtained from the finite element analysis were compared with the experimental results in term of the ultimate axial loads. The ultimate loads obtained from finite element analysis N_{FEA} and the ratio of N_{Exp} / N_{FEA} are shown in Table 6.2. The mean value of N_{Exp} / N_{FEA} equals to 1.05 with the corresponding coefficient of variation (*COV*) of 0.059. A maximum difference of 13% is found between the experimental and numerical ultimate axial loads for specimen 76.3×3.0C80. Good agreement has been achieved for the concrete-filled circular stainless steel stub columns in terms of the ultimate axial loads. The axial load versus axial shortening curves for all the experimental and numerical results are shown in Appendix D for all the specimens.

6.5 Parametric Study

An extensive parametric study was carried out using the validated model aiming to extend the available data over a wider range of cross-sectional slenderness ratios. The adopted austenitic stainless steel stress-strain curve was obtained from the tensile coupon test on material cut from the CHS 60.5×2.8 specimen. A total of 168 specimens were analyzed in this parametric study covering the slenderness ratio (D/t) from 30.0 to 245.0, including compact, noncompact and slender sections. The diameter of the analyzed specimens ranged from 140.0 to 406.0 mm and the material thickness varied from 1.0 to 10.0 mm. The three different concrete strengths and the corresponding elastic modulus (E_c) in the experimental study were used for each thickness of each profile. The length of each specimen was three times the diameter (D), which is identical to the experimental study. The specimens in the parametric study shares the same



labelling system as that of the test specimens and the ultimate axial load obtained from the finite element analysis are shown in Table 6.3.

6.6 Reliability Analysis

Reliability analysis was performed to assess the appropriateness of current design equations for composite carbon steel structure on the predictions of load-carrying capacity of concrete-filled cold-formed stainless steel stub columns. Reliability analysis is detailed in the specification AISC 360 (2016). The target reliability index (β_0) of 2.50 is used as a lower limit in this study and the design rules are reliable if the reliability index is greater than or equal to 2.50. The resistance factor (ϕ_0) of 0.90 was used for the axially-loaded stub columns. The load combination of 1.2DL+1.6LL was used for specifications AISC 360 (2016) and ACI 318 (2014). The combination of 1.35DL+1.5LL was used for EC4 (2004), and 1.2DL+1.5LL was used for both Australian standard AS 5100.6 (2004) and the modified AS 5100 method. The live load to dead load ratio of 1/5 was used. Statistical parameters $M_m = 1.10$, $F_m = 1.00$, $V_m = 0.10$ and $V_F = 0.05$ were adopted in the calculation of the reliability index, where M_m is the mean value of material factor, F_m is the mean value of fabrication factor, V_m is the coefficient of variation of material factor and V_F is the coefficient of variation of fabrication factor. The statistic parameters P_m and V_p are the mean value of tested-to-predicted or FEA-to-predicted load ratios and coefficient of variation of fabrication factor, respectively. The correction factor C_p was also used in the calculation of reliability index in order to compensate the influence due to limited number of data sample. The values of reliability index are also shown in Table 6.4 for all design rules.



6.7 Comparison Between Test and Code Predicted Strengths

6.7.1 General

The current available design specification for composite sections such as American specification AISC 360 (2016), American code ACI 318 (2014), EC4 (2004) and Australian standard AS 5100.6 (2004) are for concrete-filled carbon steel members only, and none of these standards address the design of concrete-filled stainless steel columns. Based on the experimental and numerical studies presented in this chapter, the design codes are compared with the test and parametric study results as well as the available data from literature (Lam and Gardner, 2008; Uy et al., 2011). For all the comparison made in this study, all the material partial safety factors are set to be unity and the material properties are taken as the measured values. In addition, all the code limitations on the concrete strength and steel strength are ignored to check the feasibility of the design codes.

6.7.2 AISC 360

The AISC 360 (2016) classified the concrete-filled circular steel tube members into three different types, i.e., compact, noncompact and slender sections depending on the cross-sectional slenderness ratio (D/t). The compact sections are those sections with slenderness ratio less than or equal to compactness limit ($\lambda_p = 0.15E_s / f_y$). This compactness limit is based on the equation for local buckling limit of concrete-filled circular steel tube by von Karman model proposed by Bradford et al. (2002). By nondimensionalizing the slenderness ratio $\lambda = 125 \geq (D/t)(f_y / 250)$, one obtains, $125(250/f_y)(E_s/200000) = 0.156(E_s/f_y) \geq (D/t)$. The compact sections can reach yielding before local



buckling of stainless steel tube and sufficient confinement on the concrete core can be provided by the stainless steel tube so that the concrete can develop its compressive strength up to $0.95f_c'$ for circular sections. The axial compressive strength of compact composite circular stub column can be calculated conservatively using Eq. (6.11).

$$N_{AISC} = N_p = A_s f_y + 0.95 f_c' A_c \quad (6.11)$$

Composite circular sections with slenderness ratio larger than the compactness limit but less than or equal to noncompactness limit ($\lambda_r = 0.19E_s/f_y$) are classified as noncompact sections. Noncompact sections can reach yield strength of the steel tube with local buckling, but cannot provide enough confinement to the concrete core to reach its full compressive strength (Lai et al., 2015). Only $0.7f_c'$ is allowed in the design equation for the concrete strength because it is believed that the concrete core would undergo significant volumetric dilation after this stress. Thus, the compressive strength of noncompact composite circular stub columns is calculated using Eq. (6.12).

$$N_{AISC} = N_y = A_s f_y + 0.70 f_c' A_c \quad (6.12)$$

Composite circular stub columns with slenderness ratio greater than noncompactness limit λ_r are classified as slender. The slender sections cannot reach its yield strength due to elastic buckling of the stainless steel tube and the available steel strength should be calculated by $f_{cr} = 0.72f_y/(D/t \cdot f_y/E_s)^{0.2}$. The concrete core would undergo significant volumetric dilation of after the compressive strength exceeds $0.70f_c'$. The compressive strength of circular composite sections for slender sections are calculated as Eq. (6.13):

$$N_{AISC} = N_{cr} = A_s f_{cr} + 0.70 f_c' A_c \quad (6.13)$$

The AISC 360 (2016) does not permit the use of steel tube with slenderness ratio greater than $0.31E_s / f_y$ due to lack of experimental data. Those specimens with slenderness ratio exceeding the limit in the parametric study were treated as slender sections and the design strength were calculated according to Eq. (6.13) in this study. The ratio of experimental over design strengths obtained by AISC 360 (2016) N_u / N_{AISC} are plotted against the slenderness parameter $\lambda = D / t \cdot (f_y / E_s)$, as shown in Fig. 6.7. The AISC 360 (2016) are conservative with the mean value of experimental-to-design strength or FEA-to-design strength ratio N_u / N_{AISC} equals to 1.25 and COV of 0.144, as shown in Table 6.4. All the ratios of N_u / N_{AISC} for noncompact and slender sections are larger than unity, which reveals that the AISC 360 (2016) underestimates the confinement effect from stainless steel tube to concrete and elastic buckling stress of slender sections. The reliability index (β_0) of AISC is 3.02, which is considered to be reliable.

6.7.3 ACI 318

The American Concrete Institute design guidance ACI 318 (2014) allows the design and use of concrete-filled circular composite columns with slenderness ratio (D/t) smaller than or equals to $\sqrt{8E_s / f_y}$. The design formulae are identical for both the rectangular and circular sections without explicit confinement effect included. The axial compressive strength is calculated by Eq. (6.14). The ACI predictions are conservative with the mean value of experimental-to-design strengths or FEA-to-design strength ratio N_u / N_{ACI} equals to 1.22 and COV of 0.186 and it is considered to be reliable with the reliability index (β_0) of 2.69, which is larger than the target value of 2.50.

$$P_{ACI} = 0.85A_c f_c + A_s f_y \quad (6.14)$$



6.7.4 Eurocode 4

The EC4 (2004) explicitly incorporate the effect of confinement for circular hollow sections. The load bearing capacity of concrete is increased due to the impeded transverse strain (CIDECT, 1998). Compared with the design strengths for rectangular sections, the concrete contribution is increased while the stainless steel contribution decreases for circular sections, as shown in Eq. (6.15).

$$N_{EC4} = \eta_{ao} A_s f_y + A_c f_c' (1 + \eta_{co} \frac{t}{D} \frac{f_y}{f_c'}) \quad (6.15)$$

where η_{ao} and η_{co} are given by the following expression for stub column members:

$$\eta_{ao} = 0.25(3 + 2\bar{\lambda}) \quad (\text{but } \leq 1.0) \quad (6.16)$$

$$\eta_{co} = 4.9 - 18.5\bar{\lambda} + 17\bar{\lambda}^2 \quad (\text{but } \geq 0) \quad (6.17)$$

where $\bar{\lambda}$ is the relative slenderness and obtained by $\bar{\lambda} = \sqrt{N_{pl,R} / N_{cr}}$. The $N_{pl,R}$ is the plastic resistance to compression and should be calculated by $N_{pl,R} = A_s f_y + A_c f_c'$. The N_{cr} is the elastic buckling load of the member calculated by Euler critical load $N_{cr} = (EI)_{eff} \pi^2 / l^2$ and the $(EI)_{eff}$ is the effective stiffness for the composite column consists of the sum of the stiffness of the components. The effect of confinement is only considered for compact columns up to a relative slenderness of $\bar{\lambda} \leq 0.5$.

The EC4 allows the use of circular steel tubes with slenderness ratio (D/t) smaller than or equal to $90 \cdot (235 / f_y)$. The EC4 design strengths agree well with the experimental and numerical results with the mean value of 0.93 and COV of 0.128. However, the EC4 (2004) is considered not reliable with the reliability index (β_0) equals to 1.89, which is less than the target value of 2.50.



6.7.5 AS 5100.6

The Australian standard AS 5100.6 (2004) assumes that the steel yields before the concrete reaches its ultimate stress state (Tao et al., 2008). The formula used for calculating the axial compressive strength of composite circular sections is virtually the same as those suggested in EC4 (2004), except that different values have been used for the capacity factors, as shown in Eq. (6.18). The capacity factors ϕ and ϕ_c are 0.9 and 0.6 specified for steel and concrete in AS 5100.6 for section capacity, respectively. The AS 5100.6 underestimated the load-carrying capacity with the mean value of 1.45 and *COV* of 0.102 due to the applied capacity factors, as shown in Fig. 6.8. The reliability index (β_0) for AS 5100.6 is 3.61, which is considered to be very reliable.

$$P_{AS5100} = \phi \eta_{ao} A_s f_y + \phi_c A_c f_c' (1 + \eta_{co} \frac{t}{D} \frac{f_y}{f_c}) \quad (6.18)$$

A modification to the AS 5100.6 (2004) was proposed based on Eq. (6.18) and the reduction factor η_{ao} to the steel strength is removed from the equation since the pronounced response to cold-working of stainless steel makes more ductile behaviour of the material. Besides, the capacity factors ϕ and ϕ_c of 0.9 and 0.6 specified in AS 5100.6 are recommended to be modified to 1.0 and 0.85, as shown in Eq. (6.19). The modified AS 5100 design equation performs very well with the mean value of N_u / N_{AS5100} [#] equals to 1.02 and *COV* of 0.101, as shown in Fig. 6.9. The scatter of the modified AS 5100 design equation is mainly due to the different definition of ultimate strength for those stocky specimens filled with normal strength concrete without clear descending proportion in the axial load-strain curves. The reliability index (β_0) for modified AS 5100 is 2.53, which is larger than the target value of 2.50, and considered to be reliable.



$$P_{AS5100}^{\#} = \phi A_s f_y + \phi_c A_c f_c' (1 + \eta_{co} \frac{t}{D} \frac{f_y}{f_c'}) \quad (6.19)$$

6.8 Concluding Remarks

Experimental and numerical studies on concrete-filled circular stainless steel stub columns have been presented in this chapter. The experimental program including a total of 18 stub column tests were carried out in parallel with material testing on stainless steel and concrete. A finite element model was developed to duplicate the experimental results using a modified confined concrete model. The finite element model predicts well with the experimental results and an extensive parametric study was carried out using the verified finite element model. A total of 212 experimental and numerical results as well as available data from literature (Lam and Gardner, 2008; Uy et al., 2011) were compared with the existing design rules for sectional compressive capacity of conventional concrete-filled carbon steel columns as presented in American specification AISC 360 (2016), American code ACI 318 (2014), EC4 (2004) and Australian standard AS 5100.6 (2004). Modification to AS 5100 was also carried out and it is found to provide the most accurate predictions on concrete-filled circular stainless steel stub columns.



Specimen	<i>D</i> (mm)	<i>t</i> (mm)	<i>A_s</i> (mm ²)	<i>A_c</i> (mm ²)	<i>f_{c'}</i> (MPa)	<i>f_{cu}</i> (MPa)	<i>E_c</i> (GPa)
60.5×2.8C0	60.5	2.77	502.4	--	--	--	--
60.5×2.8C40	60.4	2.78	504.1	2362.2	36.4	46.0	23.9
60.5×2.8C40R	60.4	2.76	500.3	2361.4	36.4	46.0	23.9
60.5×2.8C80	60.4	2.75	498.3	2364.8	85.8	93.6	33.1
60.5×2.8C120	60.6	2.77	504.0	2382.4	120.0	125.7	39.0
76.0×3.0C0	76.4	2.94	679.0	--	--	--	--
76.0×3.0C40	76.4	2.95	680.4	3900.6	36.4	46.0	23.9
76.0×3.0C80	76.4	2.95	680.2	3898.8	85.8	93.6	33.1
76.0×3.0C80R	76.3	2.95	679.3	3894.8	85.8	93.6	33.1
76.0×3.0C120	76.3	2.95	679.0	3895.4	120.0	125.7	39.0
114.3×3.0C0	114.4	2.92	1022.8	--	--	--	--
114.3×3.0C40	114.4	2.91	1019.5	9265.6	36.4	46.0	23.9
114.3×3.0C80	114.4	2.95	1031.3	9243.9	85.8	93.6	33.1
114.3×3.0C120	114.5	2.91	1021.2	9266.5	120.0	125.7	39.0
165.2×3.0C0	165.2	2.96	1509.6	--	--	--	--
165.2×3.0C40	165.2	2.98	1520.2	19920.6	36.4	46.0	23.9
165.2×3.0C80	165.4	2.96	1508.3	19968.8	85.8	93.6	33.1
165.2×3.0C120	165.3	2.97	1515.9	19952.8	120.0	125.7	39.0

Table 6.1. Measured specimen dimensions.

Specimens	N_{Exp} (kN)	ε_{Exp}	N_{Exp} / N_o	N_{FEA} (kN)	N_{Exp} / N_{FEA}
60.5×2.8C0	266.4	7.32	1.79	--	--
60.5×2.8C40	358.0	2.00	1.53	327.1	1.09
60.5×2.8C40R	362.8	2.00	1.54	327.1	1.11
60.5×2.8C80	495.5	1.63	1.41	474.4	1.04
60.5×2.8C120	578.5	1.06	1.34	556.4	1.04
76.3×3.0C0	328.6	6.54	1.88	--	--
76.3×3.0C40	489.3	2.00	1.54	505.4	0.97
76.3×3.0C80	682.4	1.09	1.34	612.4	1.11
76.3×3.0C80R	694.4	1.25	1.36	612.4	1.13
76.3×3.0C120	869.2	0.95	1.35	804.2	1.08
114.3×3.0C0	376.8	2.46	1.59	--	--
114.3×3.0C40	864.1	2.00	1.50	939.3	0.92
114.3×3.0C80	1240.2	1.03	1.20	1244.5	1.00
114.3×3.0C120	1766.7	0.69	1.31	1615.0	1.09
165.0×3.0C0	479.9	1.32	1.19	--	--
165.0×3.0C40	1438.3	1.31	1.27	1434.2	1.00
165.0×3.0C80	2312.2	0.75	1.09	2237.2	1.03
165.0×3.0C0	2699.3	0.68	0.97	2518.1	1.07
			Mean	1.05	
			COV	0.059	

Table 6.2. Experimental test results.



Specimen	N_{FEA} (kN)	Specimen	N_{FEA} (kN)	Specimen	N_{FEA} (kN)
140×1C40	755.5	245×3.5C120	5549.8	406×4.5C80	11650.2
140×1C80	1381.5	245×4C40	3045.2	406×4.5C120	14658.3
140×1C120	1650.4	245×4C80	4956.0	406×5C40	7684.4
140×1.5C40	853.5	245×4C120	5574.7	406×5C80	13032.4
140×1.5C80	1483.3	245×5C40	3570.9	406×5C120	14932.7
140×1.5C120	1876.1	245×5C80	4956.0	406×7C40	9022.3
140×2C40	956.3	245×5C120	6540.9	406×7C80	13608.9
140×2C80	1525.7	245×8C40	5509.2	406×7C120	15661.0
140×2C120	1937.0	245×8C80	6976.2	406×10C40	12498.6
140×2.5C40	1053.1	245×8C120	8219.4	406×10C80	15879.4
140×2.5C80	1584.3	324×1.5C40	3855.1	406×10C120	20037.3
140×2.5C120	2028.8	324×1.5C80	5935.0	150×1C40	790.4
140×3C40	1220.4	324×1.5C120	7824.1	150×1C80	1427.4
140×3C80	1677.5	324×2C40	3726.3	150×1C120	1835.3
140×3C120	2043.8	324×2C80	6454.3	155×1C40	826.9
140×3.5C40	1478.7	324×2C120	8295.7	155×1C80	1472.9
140×3.5C80	1902.6	324×2.5C40	4134.7	155×1C120	1901.4
140×3.5C120	2318.8	324×2.5C80	6715.8	160×1C40	885.5
198×1C40	1367.8	324×2.5C120	8547.7	160×1C80	1573.6
198×1C80	2570.1	324×3C40	4491.9	160×1C120	2067.3
198×1C120	3066.3	324×3C80	7125.2	170×1C40	961.2
198×1.5C40	1538.8	324×3C120	9052.5	170×1C80	1649.7
198×1.5C80	2553.3	324×3.5C40	4696.5	170×1C120	2288.9
198×1.5C120	3441.7	324×3.5C80	7380.2	175×1C40	992.2
198×2C40	1685.0	324×3.5C120	9268.8	175×1C80	1851.0
198×2C80	2963.9	324×4C40	4873.9	175×1C120	2594.1
198×2C120	3473.4	324×4C80	8241.1	180×1C40	1061.7
198×2.5C40	1782.9	324×4C120	9373.0	180×1C80	1949.4
198×2.5C80	2963.9	324×5C40	5241.9	180×1C120	2516.2
198×2.5C120	3598.7	324×5C80	8566.3	185×1C40	1129.0
198×3C40	1959.8	324×5C120	9573.1	185×1C80	2037.3
198×3C80	3114.4	324×6C40	5906.6	185×1C120	2628.8
198×3C120	3687.0	324×6C80	8541.4	190×1C40	1186.5
198×4C40	2305.4	324×6C120	8881.0	190×1C80	2195.3
198×4C80	3275.6	324×8C40	7912.4	190×1C120	2842.9
198×4C120	3892.1	324×8C80	10135.1	210×1C40	1393.0
198×5C40	3020.3	324×8C120	12710.9	210×1C80	2589.6
198×5C80	3901.5	324×10C40	9434.9	210×1C120	3588.0
198×5C120	4819.1	324×10C80	12013.3	220×1C40	1486.9
245×1C40	1769.8	324×10C120	14073.2	220×1C80	2782.4
245×1C80	3369.9	406×2C40	5478.6	220×1C120	3646.7
245×1C120	4768.4	406×2C80	9421.2	225×1C40	1525.4
245×1.5C40	2248.2	406×2C120	13006.7	225×1C80	2932.6
245×1.5C80	3630.0	406×2.5C40	6129.8	225×1C120	3779.7
245×1.5C120	4712.6	406×2.5C80	9500.2	230×1C40	1583.1

Table 6.3. Parametric study results (Cont.).



245×2C40	2268.5	406×2.5C120	12964.5	230×1C80	3048.8
245×2C80	3920.5	406×3C40	6346.1	230×1C120	4145.6
245×2C120	5095.0	406×3C80	10411.2	235×1C40	1632.6
245×2.5C40	2582.6	406×3C120	13550.8	235×1C80	3256.8
245×2.5C80	4554.2	406×3.5C40	6891.9	235×1C120	4175.6
245×2.5C120	5199.4	406×3.5C80	12532.3	240×1C40	1697.8
245×3C40	2736.1	406×3.5C120	13949.2	240×1C80	3243.9
245×3C80	4715.6	406×4C40	7210.1	240×1C120	4448.9
245×3C120	5549.8	406×4C80	12772.8	245×1C40	1759.8
245×3.5C40	2843.7	406×4C120	14189.2	245×1C80	3541.3
245×3.5C80	4795.6	406×4.5C40	7497.2	245×1C120	4682.2

Table 6.3. Parametric study results (Cont.).

	$\frac{N_u}{N_{AISC}}$	$\frac{N_u}{N_{ACI}}$	$\frac{N_u}{N_{EC4}}$	$\frac{N_u}{N_{AS5100}}$	$\frac{N_u}{N_{AS5100}^{\#}}$
Number of data	212	212	212	212	212
Mean (P_m)	1.25	1.22	0.93	1.45	1.02
$COV(V_p)$	0.144	0.186	0.128	0.102	0.101
Resistance factor (ϕ_0)	0.90	0.90	0.90	0.90	0.90
Reliability index (β_0)	3.02	2.69	1.89	3.61	2.53

Note: $N_{AS5100}^{\#}$ modified AS5100 method.

Table 6.4. Comparison of test and FEA strengths with design strengths for all specimens.

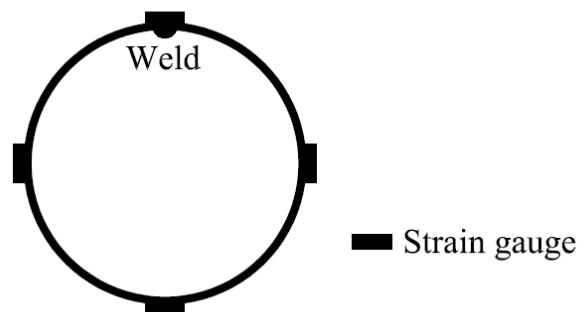
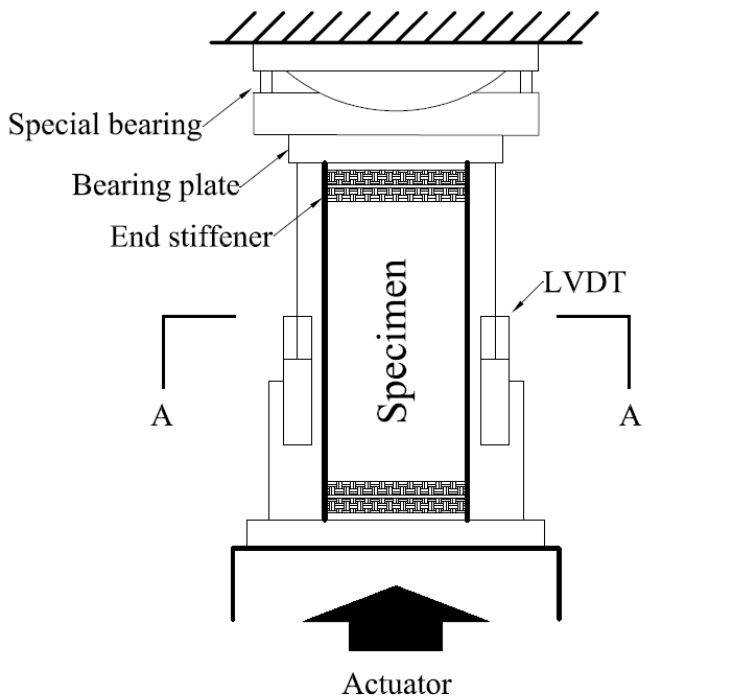
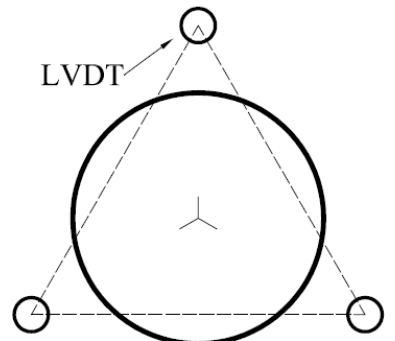


Figure 6.1. Locations of strain gauge in the cross-section.



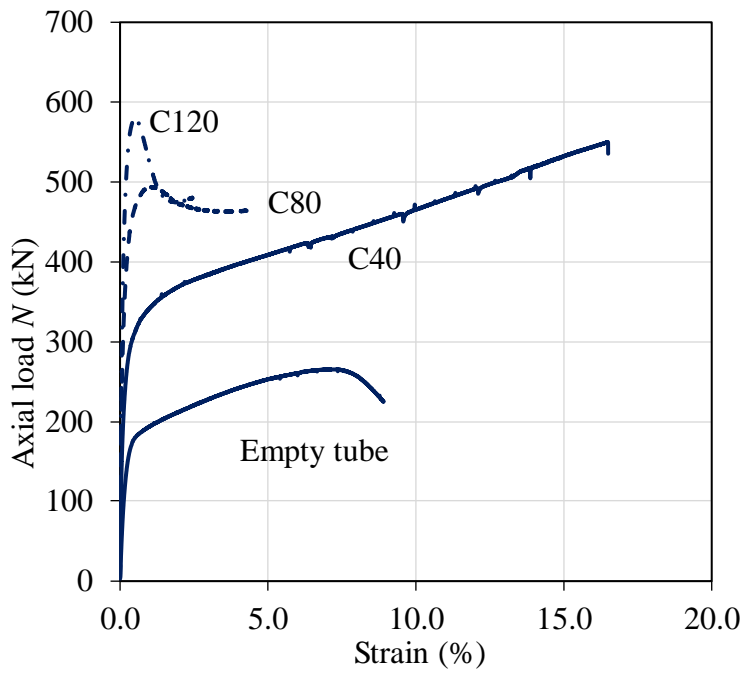


(a) Arrangement for transducers

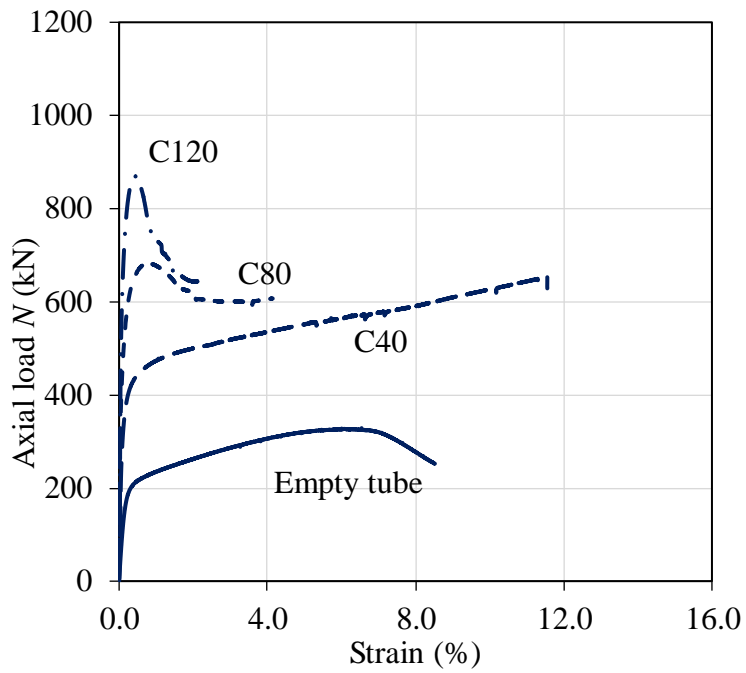


(b) Test set-up

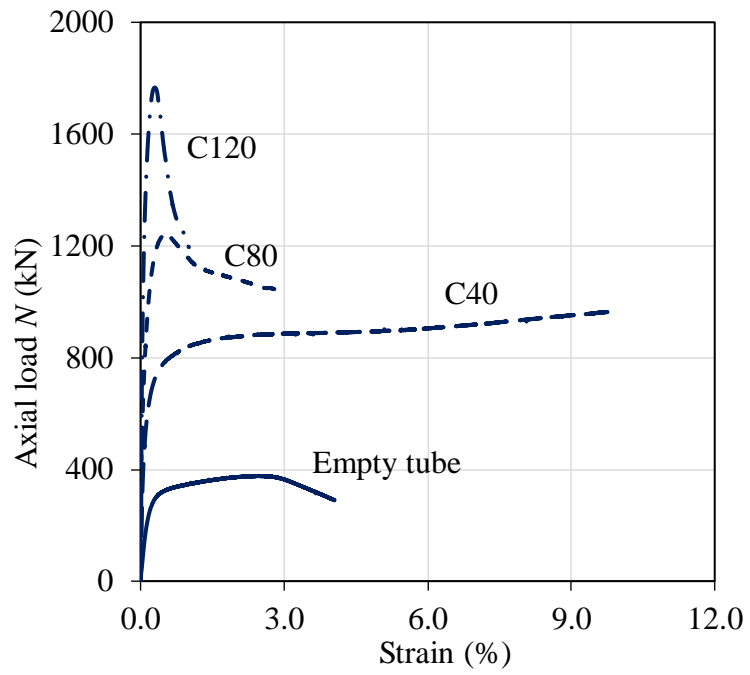
Figure 6.2. Test arrangement for stub column tests.



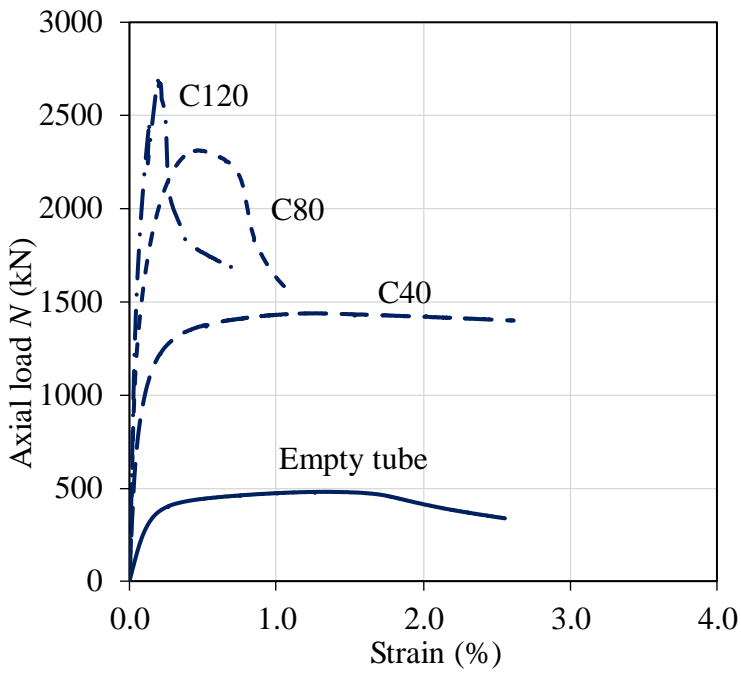
(a) CHS 60.5×2.8 composite stub columns



(b) CHS 76.0×3.0 composite stub columns



(c) CHS 114.3×3.0 composite stub columns



(d) CHS 165.2×3.0 composite stub columns

Figure 6.3. Axial load-strain curves.

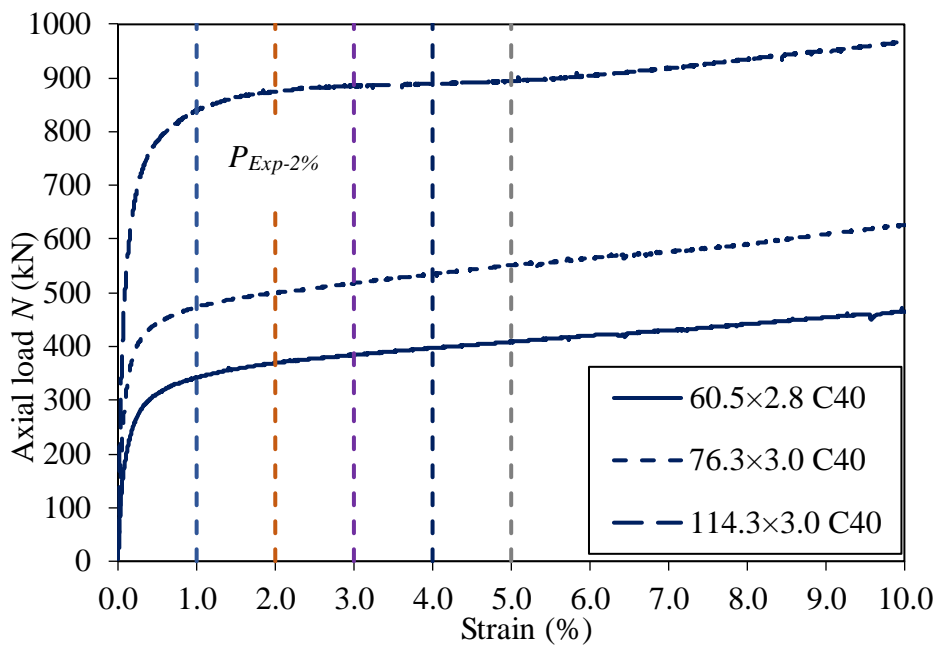


Figure 6.4. Definition of ultimate strengths corresponding to different strain levels.

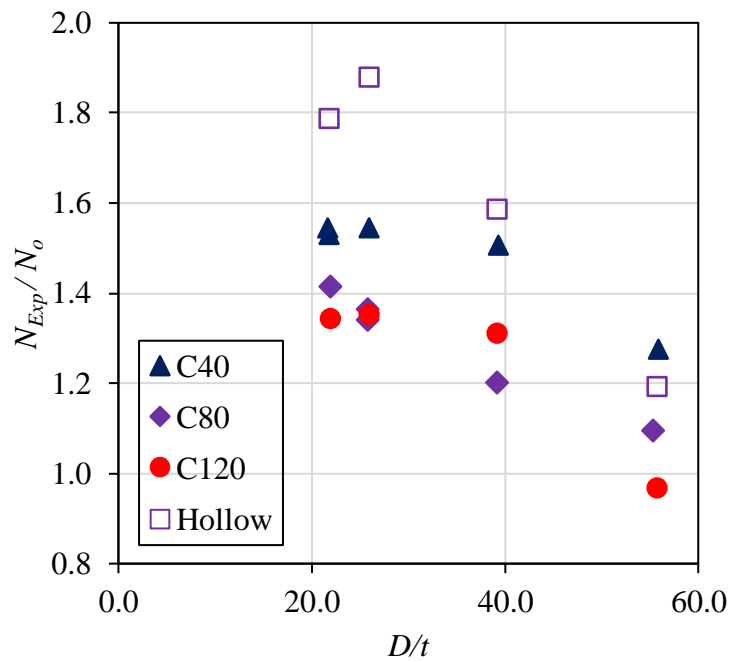


Figure 6.5. Normalized ultimate axial loads.



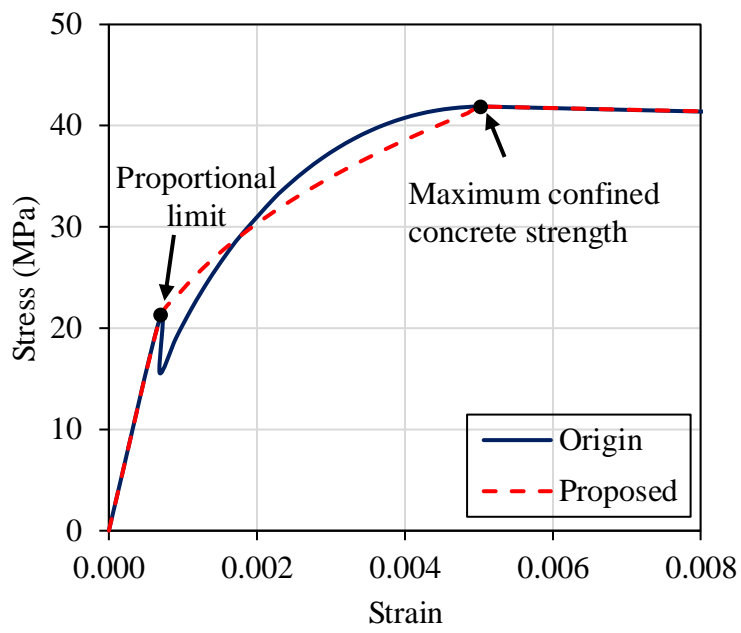


Figure 6.6. Discontinuity of existing confined concrete model and proposal of new model.

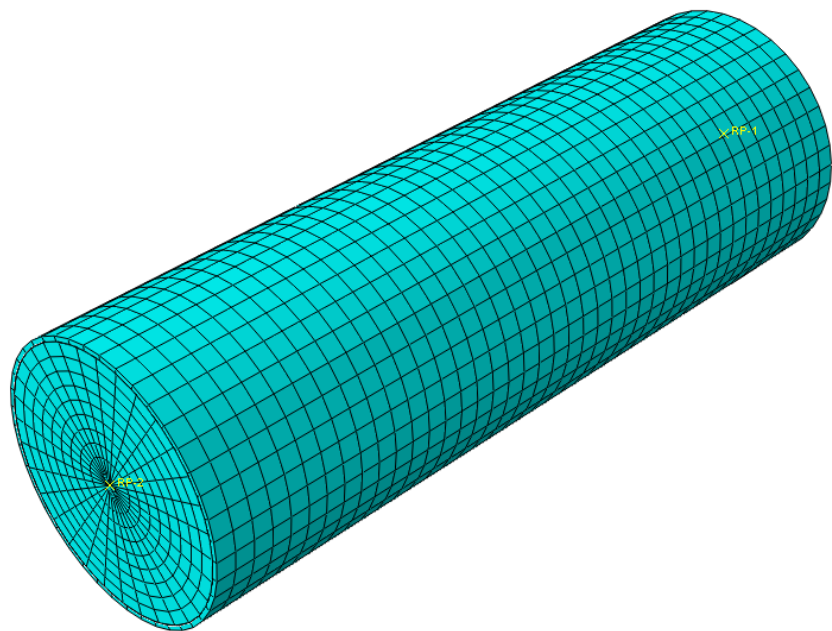


Figure 6.7. Mesh of finite element model.



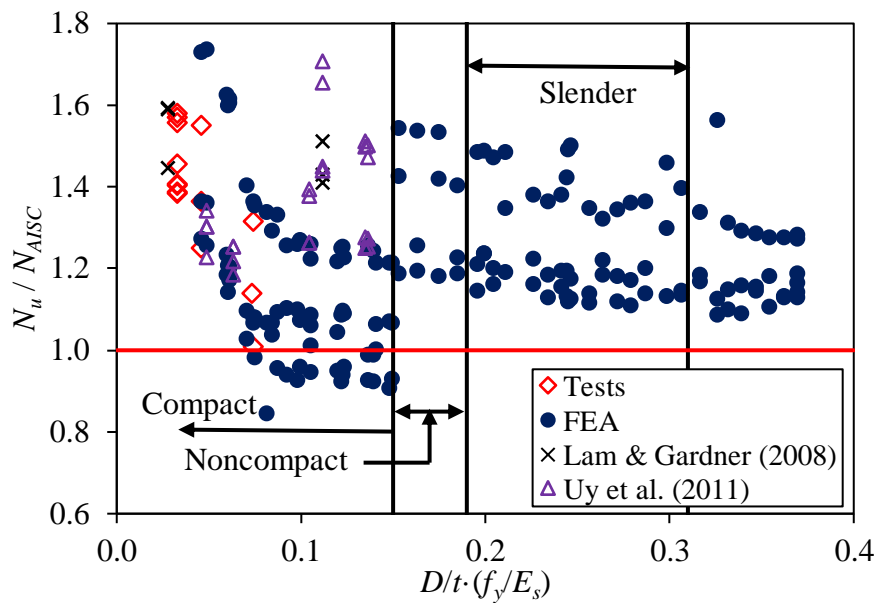


Figure 6.8. Comparison of experimental and numerical strengths with AISC 360 (2016) predicted strengths.

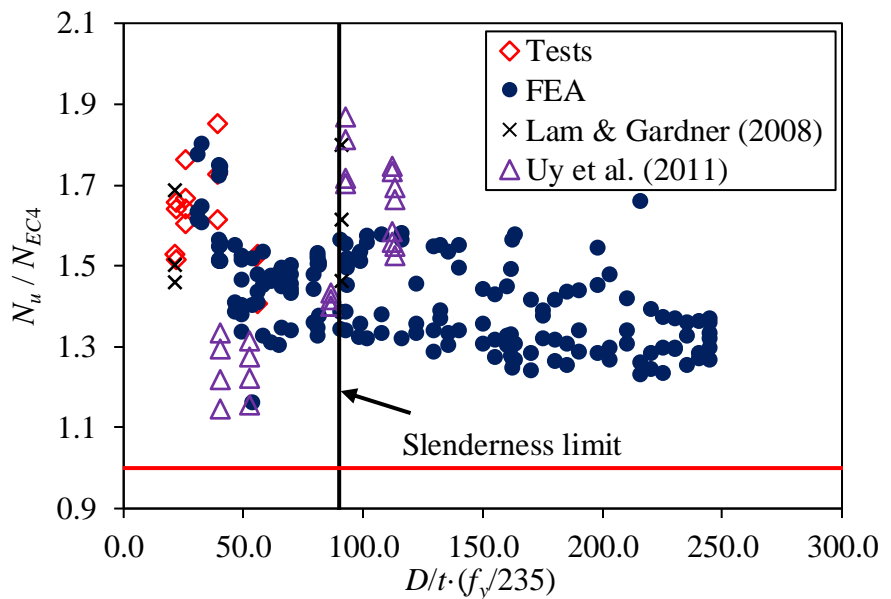


Figure 6.9. Comparison of experimental and numerical strengths with AS 5100.6 (2004) predicted strengths.



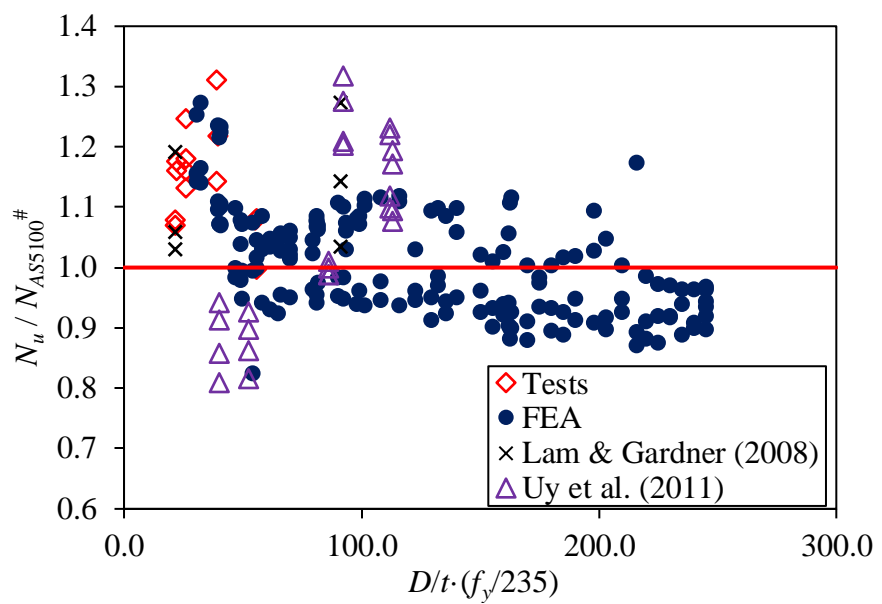


Figure 6.10. Comparison of experimental and numerical strengths with modified AS 5100 predicted strengths.

CHAPTER 7

FLEXURAL BEHAVIOUR OF CONCRETE-FILLED COLD-FORMED FERRITIC STAINLESS STEEL SHS & RHS

7.1 Introduction

Concrete-filled steel tubular (CFST) members are being increasingly used in modern construction by forming a composite between concrete and steel. The CFSTs are primarily used as columns or piers and many studies have proven the enhancement of composite members compared with their bare steel counterpart (Lam and Gardner, 2008; Uy et al., 2011; Young and Ellobody, 2006). The CFSTs are mainly used as the moment frames in Japan and the flexural strength of beams, which is the extreme case of beam-column under no axial load, is more dependent on the shear transfer between the steel and concrete (Probst et al., 2010). Compared with pure steel flexural members, the concrete infill alters the composite members by contributing additional compressive resistance and preventing inward buckling of steel tube.

The flexural performance of CFST members are previously studied by Lu and Kennedy (1994), Elchalakani et al. (2001), Han (2004), Han et al. (2006), Chitawadagi and Narasimhan (2009), Probst et al. (2010) and Wang et al. (2014).



The CFST members behaved in a ductile manner and the flexural strength of the CFST members is about 10%-50% larger than that of pure steel counterpart (Wang et al, 2014). Moreover, the shear-span-to-depth ratio of 1 to 6 had moderate influence on the behaviour of CFST members (Lu and Kennedy, 1994; Han et al., 2006). The aforementioned literatures are focused on conventional carbon steel and limited data on concrete-filled stainless steel flexural members have been reported.

Ferritic stainless steel offers good combination of durability, strength and ductility (Cashell and Baddoo, 2014). It is now becoming an attractive alternative to the more famous austenitic stainless steel. Afshan and Gardner (2013a) studied the flexural behaviour of ferritic stainless steel hollow sections. The axial compressive performance of concrete-filled ferritic stainless steel members is presented in Chapter 5 of this thesis and it was found that the concrete infill can effectively delay the local buckling of stainless steel sections over hollow sections.

The main objective of this chapter is to investigate the flexural performance of concrete-filled cold-formed ferritic stainless steel beams. A total of 23 specimens were tested and a total of 171 numerical results were generated using the verified finite element model. The experimental and numerical results were used to assess the predicted flexural capacities and flexural stiffness obtained from American code AISC 360 (2016), American code ACI 318 (2014), EC4 (2004), AS 5100.6 (2004) and the method proposed by Han (2004). The method proposed by Han (2004) was modified in order to provide a better prediction.

7.2 Experimental Investigation

The concrete-filled cold-formed ferritic stainless steel specimens were tested under four-point bending condition for both the major and minor axes. The stainless steel sections used in this study comprised of one square hollow section (SHS) and three rectangular hollow sections (RHS). A summary of dimensions of the specimens is presented in Table 7.1. The specimens were labelled in such a way that the nominal dimensions including overall depth of the web (D), overall width of the flange (B), material thickness (t) of the cross-section as well as the nominal cylinder compressive strength of the infill concrete can be identified. For example, the label “100×40×2C80” refers to the specimen with nominal cross-sectional dimensions depth (D), width (B) and thickness (t) equals to 100, 40 and 2 mm and the infill concrete nominal cylinder compressive strength of 80 MPa. If the test was a repeated one, a symbol of “R” would be added thereafter. The specimen labelling also reveals on which axis the specimen was tested. For example, the specimen 100×40×2C80 was tested under major axis bending, while specimen 40×100×2C80 was subjected to minor axis bending. The specimens have two different lengths of 1200 and 1400 mm, as shown in Table 4.1. The test specimens used in this experimental study are from the same batch of specimens as those specimens presented in Chapter 3 of the thesis.

Three grades of concrete were designed with nominal cylinder compressive strengths of 40, 80 and 120 MPa. The maximum size of course aggregates used in this study was 10 mm in order to fill in specimens with small cross-sectional area. Standard concrete cylinders of size 150 × 300 mm were cast and six cylinders were cast for each batch of concrete mixed. Two cylinders were tested at 28 days after casting and four cylinders were tested at the time of four-point bending testing. The elastic modulus of concrete (E_c) was determined by suitable



compressometer in accordance to ASTM C469 (2014). The cylinder compressive strengths f_c' were 43.8, 86.3 and 116.2 MPa with elastic moduli of 24.1, 31.3 and 39.0 GPa for the concrete with nominal cylinder strengths of 40, 80 and 120 MPa, respectively.

Four-point bending tests were conducted to assess the flexural performance of concrete-filled cold-formed ferritic stainless steel beams. Half-round and roller supports were designed to simulate the simply-supported condition, as shown in Fig. 7.1. The 1200 mm long specimens had the moment span and shear span of 400 and 330 mm, respectively. For the 1400 mm long specimens, the moment span and shear span were 500 and 380 mm, respectively. Stiffening plates of 90 mm width were employed at the loading points and supports to prevent possible web crippling due to load concentration. Steel bearing plates were also placed between the rollers/half rounds and the specimens in order to spread the concentrated load. A servo-controlled hydraulic testing machine was used to apply compressive force to the specimen by displacement control at a constant loading rate of 1.0 mm/min. Three displacement transducers (LVDTs) were placed at the centerline of the tension surface of each specimen at the loading points and the mid-span of the specimen to record the vertical displacement. Two LVDTs were also placed at the center of each end in the longitudinal direction to record the relative horizontal movement of concrete to stainless steel tube.

7.3 Test Results and Discussion

7.3.1 Moment-curvature curves

The experimental ultimate moment (M_{Exp}) and the corresponding curvature (κ_{Exp}) of each specimen are summarized in Table 7.2. The experimental ultimate



moment was obtained by multiplying half the ultimate applied load to the lever arm, which is the distance from the support to the loading point. The weight of the stiffening plates, bearing plates, half-rounds and rollers were also included in the calculation of experimental moment. The curvature was determined from the displacements recorded by the three LVDTs located at the tension surface by assuming a constant curvature between the transducer locations. The curvature was calculated using the radius (r) of the curved beam such that $\kappa_{Exp} = 1/r$. The moment-curvature curves for each specimen are shown in Figs 7.2 – 7.5.

The experimental ultimate moment (M_{Exp}) and the corresponding curvature (κ_{Exp}) of each specimen was compared with pure stainless steel section of the same size as reported in Chapter 4 of the thesis. The ratio of M_{Exp}/M_{Hollow} indicates the advantage of concrete filling compared with hollow stainless steel section. It is found that the flexural strength of CFSST members obtained about 17% to 51% enhancement compared with their pure stainless steel counterpart. The strength enhancement is better for minor-axis bending specimens than major axis condition. The maximum increase on M_{Exp}/M_{Hollow} is found on the specimen with the largest slenderness limit (d/t). This increase in moment resistance is mainly because the slender sections are more susceptible to local buckling and the infill concrete can help to delay local buckling and hence enhance the moment resistance. The use of high strength concrete seems not much advantage when comparing M_{Exp}/M_{Hollow} filling with different strength of concrete for the same size of tubes. Similar findings on the use of high strength concrete was also reported by Lu and Kennedy (1994), and Chitawadagi and Narasimhan (2009). The infill concrete participates in increasing the moment resistance in a way of taking the compressive loading and the use of high strength concrete that can lead to the shift

of neutral axis and fewer area of concrete is participated in resisting the compressive load.

7.3.2 Relative horizontal movement of concrete to stainless steel tube

The relative horizontal movement of concrete to stainless steel tube at ultimate moment (Δ_u) is reported in Table 7.2. The amount of relative horizontal movement of concrete to stainless steel tube is believed to be proportional to the volume of the crushed concrete inside the specimen (Probst et al., 2010). The maximum relative movement is found to be 1.306 mm for specimen 120×80×3C120. However, the relative movement of stocky sections was found to be small or even zero. The relative movement was larger for major axis bending than that of minor axis bending for the same sections. It is found that the relative movement is more sever as the concrete strength increases, which indicates that the bonding between the concrete and stainless steel becomes poorer as the concrete strength increases. This also attributes to the fact that not much advantage is obtained by using the high strength concrete. A typical relative horizontal movement of concrete to stainless steel tube versus moment curve is plotted for the specimen 80×120×3C80 in Fig. 7.6 and the corresponding curvature-moment relation is also plotted in the same graph for reference. It can be found that the relative movement is small at the initial stage (from 0 to approximately 3.5 kNm), which is because minor concrete crushing takes place at this stage and the initial Poisson's ratio of steel ($\nu_s=0.3$) is larger than that of concrete ($\nu_c=0.2$). After the previous stage, the increase in relative movement indicates that substantial amount of concrete crushing occurs and the increase of slope of $\Delta-M$ curve implies that amount of concrete crushing keeps rising at a faster fashion. Stresses in the interface of steel and concrete starts to develop at



this elastic-plastic stage (Wang et al., 2014) and this interaction stress is generally referred as confinement pressure. The rapid expansion of concrete would push against the steel tube and larger confining pressure can be achieved (Lai, 2015).

7.3.3 Flexural stiffness

Flexural stiffness is an important indicator of resistance for a member against bending deformation and it plays a notable role in serviceability limit design. The flexural stiffness EI_{Exp} was determined as the initial slope from the moment-curvature curve, as shown in Table 7.3. The design specifications define this design parameter as follows:

$$EI_{AISC} = E_s I_s + C_3 E_c I_c \text{ by AISC 360 (2016)} \quad (7.1)$$

$$\text{where } C_3 = 0.6 + 2 \left(\frac{A_s}{A_c + A_s} \right) \leq 0.9$$

$$EI_{ACI} = E_s I_s + \frac{0.2 E_c I_c}{1 + \beta_{dns}} \text{ by ACI 318 (2014)} \quad (7.2)$$

where β_{dns} is a ratio related to axial load and it is set to be zero in this study since flexural member with no axial load is concerned.

$$EI_{EC4} = E_s I_s + 0.6 E_c I_c \text{ by EC4 (2004)} \quad (7.3)$$

$$EI_{AS5100} = E_s I_s + E_c I_c \text{ by AS 5100.6 (2004)} \quad (7.4)$$

The flexural stiffness predicted by different design rules are shown in Table 7.3. It is shown that all the design rules are unconservative in predicting the flexural



stiffness and the ACI provision provides the best prediction with the mean value of 0.94 and coefficient of variation (*COV*) of 0.054. The ACI provision utilizes the smallest concrete stiffness by the reduction factor of 0.2 and this is reasonable since relatively little concrete is under compression when the CFST member is subjected to bending (Roeder et al., 2010).

7.4 Finite Element Model and Verification

7.4.1 Element and mesh

Finite element model was established using the finite element package Abaqus version 6.14 (ABAQUS, 2014) to simulate the beam experiments. Based on the geometric characteristic of concrete and stainless steel, a fine mesh of four-noded S4R shell element was adopted to build up the stainless steel tubes and the eight-noded solid element with reduced integration (C3D8R) were used to model the concrete infill. Similar elements were also used by Lai et al. (2014) to model the concrete-filled structures and it is believed that the C3D8R element is computationally effective for modelling concrete cracking (Lai et al., 2014).

7.4.2 Material modelling of cold-formed ferritic stainless steel tubes

The measured material properties of stainless steel from flat and corner coupon tests as reported in Chapter 3 of this thesis were used in the material constitutive model. The stress-strain curve comprises of an elastic portion up to proportional limit with the measured elastic modulus and a plastic part with the true stress and logarithmic true strain curve converted from the static stress-stain curve. The true plastic stress-strain curves obtained from flat and corner coupon tests were used as



the material properties in modelling the flat and corner portion of the stainless steel tubes, respectively. In order to account for the corner strength enhancement due to cold-rolling process, the corner properties were extended by two times the sectional thickness from the corner portion into the flat portion of the section. Similar consideration for the strength enhancement of corner properties was also adopted by Ma et al. (2015b).

7.4.3 Material modelling of confined concrete

The concrete damaged plasticity model was used to simulate the confined concrete in this numerical study. The elastic modulus of concrete (E_c) was taken as the measured value and the Poisson's ratio (ν_c) was taken as 0.2 as recommended in ACI 318 (2014). The stress-strain relationship proposed by Tao et al. (2013) was used, which consists of a strain hardening/softening function. The fracture energy expression for tensile concrete given in Tao et al. (2013) was original for concrete-filled carbon steel tube, and an enhancement factor α is proposed in this study to account for the enhancement of tensile strength of concrete due to the extra confinement provided by the stainless steel tube. The enhancement factor is related to the strength of infill concrete and the fracture energy equation is presented in Eq. (7.5).

$$G_F = \alpha \cdot \left(0.0469 d_{\max}^2 - 0.5 d_{\max} + 26 \right) \left(\frac{f_c'}{10} \right)^{0.7} \quad (7.5)$$

where $\alpha = -0.005 f_c' + 1.7$, f_c' is concrete cylinder compressive strength in MPa and d_{\max} is the maximum coarse aggregate size (in mm) and it is taken as 10 mm in this study since it is the value of maximum size aggregate used in the experimental study.



7.4.4 Boundary and loading conditions

The two loading points were modelled as two reference points located at the outer surface of the composite specimens. In the four-point bending tests of concrete-filled flexural specimens, the vertical loading was applied to the roller or half-round onto the steel bearing plates then to the specimens. The corresponding regions of the steel bearing plates were partitioned from the specimens and then coupled to the reference points built previously. The reference points were restrained against all degrees of freedom except for the vertical displacement and displacement in the longitudinal direction along the flexural member. Additionally, the rotations about the bending axis were also relaxed for the reference points.

Similarly, the two supports were modelled by coupling the contact surfaces with two reference points located at the bottom flange of the specimen. The simply-supported boundary condition was modelling by solely releasing the rotation about the bending axis for the half-round and roller support, while the longitudinal displacement along the flexural member was released for the roller end support. The vertical load was applied to the two loading reference points by displacement control method with a specified displacement value. The displacement value was carefully selected to ensure the numerical analysis can reach ultimate load. Since it is easier to converge for the nonlinear calculation under displacement loading (Wang et al., 2014), the static RIKS method was adopted for the load step and the maximum allowable arc length was set to be 1 in order to obtain sufficient points before reaching the ultimate load. The nonlinear geometric parameter (*NLGEOM) was used to perform the large displacement analysis.



7.4.5 Interaction of contact surface between concrete infill and stainless steel tube

The contact interaction between the stainless steel tube and concrete was modelled in both the normal and tangential directions. Similar to Lai et al. (2014), the hard contact pressure-overclosure relationship with penalty method was used in the normal direction. The contact in tangential direction followed the Coulomb friction model proposed by Han et al. (2007). The friction model allows stress transmission between the stainless steel tube and concrete up to the limit τ_{crit} . The coulomb friction coefficient between the stainless steel tube and the concrete infill was set to be 0.6. No additional bond between the stainless steel tube and concrete infill such as adhesive bonding was included in the model. The shear stress limit was calculated in accordance with Eq. (7.6) as specified in Han et al. (2007) as follows:

$$\tau_{crit} = 0.75 \left[2.314 - 0.0195 (\max[D, B] / t) \right] > 0 \quad (7.6)$$

7.4.6 Verification of the finite element model

The developed finite element model was used to predict the ultimate moment of the specimens in the experimental study. The moment capacities (M_{FEA}) predicted by the finite element analysis were compared with the test results (M_{Exp}). Good overall agreement is achieved with the average value of M_{Exp} / M_{FEA} equals to 1.04 and the *COV* of 0.029, as shown in Table 7.2. This indicates that the model can predict the ultimate moment response of the flexural members. A maximum difference of 12% is found between the experimental and numerical moment resistances for the specimen 40×100×2C40. The verification of the finite element



model is shown in Appendix E of this thesis by plotting the moment-curvature curves obtained from the test and FEA results.

7.5 Parametric Study

A complementary parametric study was performed to expand the database of ultimate strength of concrete-filled cold-formed ferritic stainless steel flexural members. A total of 171 numerical data was obtained using the verified finite element model. The ferritic stainless steel stress-strain curves adopted in the parametric study were obtained from the flat and corner coupon tests of section 100×40×2 as reported in Chapter 3 of this thesis. A total of six SHS sections and three RHS sections were studied for both the major and minor axes in this parametric study. The thickness of the sections varied in order to cover a wide range of slenderness limits of compact, noncompact and slender sections. A wide range of aspect ratios (D/B) of 0.33-3.00 and flat-depth-to-thickness (d/t) ratios of 7.1-146.0 were examined in the parametric study. The maximum tube section dimension and thickness were 400 mm and 10 mm, which is practical section size for construction. The moment span between the two loading points was 1000 mm and the shear span between the loading points and the supports were 930 mm for all the specimens. The same labelling system used in the experimental study was adopted in the parametric study for the specimens. The ultimate moment capacities predicted by the finite element analysis are summarized in Table 7.4.

7.6 Reliability Analysis

The available specifications on concrete-filled steel tube members are designated for carbon steel sections but not for stainless steel sections. The applicability of these design specifications to stainless steel sections are assessed by reliability



analysis. Reliability analysis is detailed in the specification AISC 360 (2016). A target reliability index (β_0) of 2.50 is used in this study and the larger the value of β_0 means more reliable and safer the design. The resistance factor (ϕ_0) of 0.90 was used for flexural members in the reliability analysis. Load combination of 1.2DL+1.6LL was used for specifications AISC 360 (2016), ACI 318 (2014), method proposed by Han (2004) and the modified Han's method. The combinations of 1.35DL+1.5LL and 1.2DL+1.5LL were used for EC4 (2004) and Australian standard AS 5100.6 (2004), respectively. Live load to dead load ratio of 0.2 was used. Statistical parameters $M_m = 1.10$, $F_m = 1.00$, $V_M = 0.10$ and $V_F = 0.05$ were adopted in the calculation of the reliability index, where M_m is the mean value of material factor, F_m is the mean value of fabrication factor, V_M is the coefficient of variation of material factor, and V_F is the coefficient of variation of fabrication factor. The statistic parameters P_m and V_p are the mean value of tested-to-predicted or FEA-to-predicted load ratios and coefficient of variation of tested-to-predicted or FEA-to-predicted load ratios, respectively. The correction factor C_p was also used in the calculation of reliability index in order to compensate the influence due to limited number of data sample. The values of the reliability indices for all design rules are shown in Table 7.5 .

7.7 Comparison Between Test and Code Predicted Moment Capacities

7.7.1 General

There are several existing design specifications available for the determination of moment capacities of concrete-filled steel tube members. The well-known design specifications include American specification AISC 360 (2016), American code ACI 318 (2014), EC4 (2004) and AS 5100.6 (2004). Han (2004) also proposed a



simplified model to calculate the flexural strength of rectangular CFST members. All the partial safety factors are set to be unity and the material properties are taken as the measured values for the comparison made in this section. The limits on applying the design rules such as restriction on steel tube slenderness ratio and concrete strengths are ignored to check the feasibility of the design rules on concrete-filled cold-formed stainless steel flexural members beyond the prescribed limits.

7.7.2 AISC 360

The American specification AISC 360 (2016) classified the rectangular CFST members into three different classes based on the slenderness ratio of b/t for flange and d/t for web under flexural loading condition. The classification of the steel tube flange in compression under bending condition shared the same slenderness limits of CFST members subjected to axial compression, as shown in Table 7.6. However, a different set of slenderness limits is designated for webs subjected to stress gradient over their depth since only a portion of depth is under compression. The web is less vulnerable to local buckling with the plate buckling coefficient K of value 23.9 as reported in Ziemian (2010) and the compactness limit (λ_p) is conservatively determined as $3.00\sqrt{E_s/f_y}$ (Lai et al., 2014). The noncompactness limit (λ_r) is $5.70\sqrt{E_s/f_y}$ and this value is also the maximum allowable limit for web elements of CFST flexural members. Thus, the flange elements have compact, noncompact and slender classes and only compact or noncompact web elements are available for the CFST flexural members. The section which has slender flange and noncompact web is classified as slender section.



The flexural resistance is provided by the tensile and compressive force contributed by the steel tube and the concrete in compression. The tensile force by concrete is ignored in the design calculation. The compact section could develop their plastic moment (M_p), which assumes the rigid-plastic material behaviour of both the stainless steel and concrete. Yield stresses f_y are developed at both the compressive and tensile portion of the steel tube and the concrete strength in compression equals to $0.85f_c'$ since it is believed that the steel tube can provide sufficient confinement to the core concrete (Lai et al., 2014). The nominal moment for noncompact section (M_r) is determined based on the elastic-plastic behaviour of stainless steel in tension and elastic behaviour up to yield strength f_y in compression. The slenderness of the stainless steel plate cannot sustain the compressive stress and not sufficient confinement can be provided to the core concrete so that the concrete infill can only develop its strength linearly from the neutral axial to extreme compressive fiber of $0.70f_c'$. This is because concrete has significant volumetric dilation after exceeding $0.70f_c'$ under compression (Lai et al., 2014). Further deduction of the stainless steel stress is introduced to slender section due to elastic local buckling. It is assumed the stainless steel in tension could develop the elastic stress up to yield strength f_y and the portion in compression can only reach the local buckling critical stress f_{cr} linearly from the neutral axis to the extreme fiber. The local buckling critical stress f_{cr} was calculated from $f_{cr} = 9E_s / (b/t)^2$. Similar to noncompact section, the concrete infill could only develop its strength linearly from the neutral axial to extreme compressive fiber of $0.70f_c'$.

The AISC 360 (2016) predicts the flexural strength of concrete-filled cold-formed ferritic stainless steel members quite conservatively with the mean value of M_u / M_{AISC} equals to 1.56 and the COV of 0.217. The reliability index of 3.30

indicates that the design rule is very reliable for flexural design. The ratios of M_u / M_{AISC} are plotted against the plate slenderness parameter $\lambda = (b/t)\sqrt{f_y/E_s}$ for flange and web, respectively, as shown in Fig. 7.7 (a) and (b). The predictions become more conservative as the class of the section becomes slender. The mean values of $M_u / M_{Compact}$, $M_u / M_{Noncompact}$, $M_u / M_{Slender}$ and M_u / M_{Limit}^* for compact, noncompact, slender and those beyond the maximum allowable slenderness limits are 1.28, 1.41, 1.84 and 1.95 with the COV of 0.048, 0.101, 0.156 and 0.159, respectively. It is revealed that the AISC 360 (2016) performs the best for compact sections and the conservatism could be due to the use of plastic distribution method which does not consider the material strain hardening. However, the reduction on concrete strength and the use of critical elastic local buckling stress further underestimate the flexural resistance for noncompact and slender sections, as shown in Fig. 7.7 and Table 7.7. As far as concrete strength is concerned, the mean values of M_u / M_{AISC} for specimens with nominal cylinder compressive strengths of 40, 80 and 120 MPa are 1.50, 1.52 and 1.57 with COV of 0.205, 0.233 and 0.204, respectively. The reliability indices of 3.23, 3.26 and 3.37 indicate that the use of concrete with 80 and 120 MPa cylinder compressive strengths are applicable since all the reliability indices pass the target value of 2.50.

7.7.3 ACI 318

The ACI 318 (2014) adopts a bilinear steel material curve up to yield stress. The concrete stress distribution is a rectangular stress block with a $0.85f_c'$ compressive stress acting over a depth of neutral axis multiplied by a deduction factor β_1 . The deduction factor β_1 depends on the strength of concrete. Equilibrium of both axial load and flexural moment shall be satisfied. The ACI



318 (2014) provides conservative predictions with the mean value of M_u / M_{ACI} equals to 1.33 and the COV of 0.133. The reliability index (β_0) is 3.30, which is greater than the target reliability index of 2.50. The maximum allowable slenderness ratio d/t shall be smaller than $\sqrt{3E_s/f_y}$ and the prediction M_u / M_{Limit} for specimens within this limit is 1.24 and the COV is 0.049. For the specimens with slenderness ratio larger than the allowable limit, the ratio of M_u / M_{Limit}^* is 1.34 with COV of 0.139.

7.7.4 Eurocode 4

The EC4 (2004) assumes a full plastic stress distribution in the composite section. The concrete lying in the tension zone is assumed to have no contribution to the flexural strength. The EC4 (2004) predictions are similar to that of the compact sections in AISC 360 (2016) except that the reduction factor of 0.85 for concrete is ignored. It is believed that the development of concrete strength is better in composite sections since peeling off of concrete is impossible (CIDECT, 1998). The mean value of the M_u / M_{EC4} ratio is 1.37 and the COV equals to 0.130. This approach is considered to be reliable with the reliability index (β_0) of 3.29. The EC4 (2004) limits the use of steel tube slenderness ratio (D/t) not larger than $52\sqrt{235/f_y}$. The mean value of M_u / M_{Limit} ratio is 1.25 and the COV equals to 0.044 for specimens within the limit. The mean value of M_u / M_{Limit}^* ratio is 1.39 and the COV equals to 0.133 for specimens beyond the abovementioned limit. The reliability index (β_0) for both cases are 3.32 and 3.31, respectively.



7.7.5 AS 5100

The AS 5100.6 (2004) determines the strength of CFST beams based on rectangular stress blocks. Plastic stress distribution is adopted. The concrete compressive stress is $0.90f_c'$ and the steel stress is $0.90f_y$ for both compressive and tensile regions. The tensile contribution of concrete is ignored. The AS 5100.6 (2004) predictions are quite conservative with the mean value of the M_u / M_{AS5100} ratio of 1.52 and the *COV* equals to 0.130. The AS 5100.6 (2004) limits the use of steel tube slenderness ratio (D/t) of not larger than $40\sqrt{235/f_y}$. The mean value of M_u / M_{Limit} ratio is 1.42 and the *COV* equals to 0.041 with the reliability index (β_0) of 3.77 for specimens within the aforementioned limit. For those specimens exceeding the slenderness ratio, the mean value of M_u / M_{Limit}^* ratio is 1.52 and the *COV* equals to 0.132, which is more conservative than the specimens within the limit. The predictions beyond the limit are also reliable with the reliability index (β_0) equals to 3.61, larger than the target reliability index of 2.50. It should be noted that the slenderness limit for the CFST members are identical to those of the hollow steel sections so that the benefit of delaying local buckling from the infill concrete is neglected (Tao et al., 2008).

7.7.6 Method proposed by Han (2004) and modification of Han's method

Han (2004) proposed a simplified method for the calculation of moment capacity of composite beams. The calculation involves the determination of confinement factor ξ , which is related to the cubic strength (f_{cu}) of concrete. The conversion formula from cylinder strength to cubic strength of concrete follows the equation $f_{cu} = 1.1719 f_c' + 2.0029$. This conversion formula is derived from the table of concrete strength stipulated in EC2 (2004) by fitting a straight line passing all the



tabulated data. Lai (2015) adopted the same method in deriving the conversion formula. The method proposed by Han (2004) provides a good prediction with the mean value of M_u / M_{Han} ratio of 1.31 and the COV equals to 0.134. The proposed method is reliable with the reliability index (β_0) equals to 3.26, as shown in Table 7.5.

The method proposed by Han (2004) is modified to provide a better prediction on the flexural strength of composite beams. The flexural strength index (γ_m) originated expressed as $\gamma_m = 1.04 + 0.48 \cdot \ln(\xi + 0.1)$ is modified as Eq. (7.7).

$$\gamma_m = 1.61 - 1.28 \cdot \text{Exp}(-\xi / 0.67) \quad (7.7)$$

The other parameters such as the nominal yielding strength f_{scy} and section modulus of the composite beam W_{scm} are defined in Han (2004). The modified Han's method provides the best predictions for the composite beams with the mean value of $M_u / M_{Han}^{\#}$ ratio equals to 1.05 and the COV of 0.112, as shown in Table 7.5 and Fig. 7.8. The modified Han's method is considered to be reliable with the reliability index (β_0) equals to 2.55.

7.8 Concluding Remarks

The flexural performance of concrete-filled cold-formed ferritic stainless steel members was assessed by experimental and numerical investigations. A total of 23 four-point bending tests were carried out on both the square and rectangular sections. The adopted stainless steel tube of ferritic grade EN 1.4003 and the concrete infill had nominal cylinder compressive strengths of 40, 80 and 120 MPa were used. A finite element model was developed and verified in order to duplicate the experimental results, and it is shown that the model can accurately



predict the flexural behaviour of concrete-filled cold-form ferritic stainless steel tubes. An extensive parametric study was conducted to cover a wide range of slenderness of specimens. The experimental and numerical results were used to assess the applicability of predicted strength that designated for concrete-filled carbon steel member as specified in the current specifications American code AISC 360 (2016), American code ACI 318 (2014), EC4 (2004) and AS 5100.6 (2004). The method proposed by Han (2004) was also assessed in this study and modification to Han's method provides a better prediction on the flexural strength of composite beams. It is shown that the modified Han's method provides the best prediction and therefore it is recommended to be used in the design concrete-filled cold-formed ferritic stainless steel flexural members of square and rectangular sections.



Specimen	<i>D</i> (mm)	<i>B</i> (mm)	<i>t</i> (mm)	<i>d/t</i>	<i>b/t</i>	<i>r_o</i> (mm)	<i>r_i</i> (mm)	<i>L</i> (mm)
60×40×4C40	59.9	40.10	3.813	12.3	7.1	6.5	3.8	1199.8
60×40×4C40R	59.9	40.10	3.795	12.4	7.1	6.5	3.8	1200.0
60×40×4C80	59.9	40.10	3.828	12.2	7.1	6.5	3.8	1199.0
60×40×4C120	59.9	40.10	3.827	12.2	7.1	6.5	3.8	1198.0
40×60×4C40	40.1	59.90	3.834	7.1	12.2	6.5	3.8	1200.0
40×60×4C80	40.1	59.90	3.825	7.1	12.3	6.5	3.8	1199.8
40×60×4C120	40.1	59.90	3.823	7.1	12.3	6.5	3.8	1199.5
60×60×3C40	60.3	60.10	2.846	17.1	17.0	5.8	3.8	1200.0
60×60×3C80	60.3	60.00	2.843	17.1	17.0	5.8	3.8	1199.3
60×60×3C120	60.2	60.10	2.826	17.2	17.2	5.8	3.8	1200.0
60×60×3C120R	60.3	60.10	2.836	17.2	17.1	5.8	3.8	1199.5
100×40×2C40	99.7	40.20	1.944	45.4	14.8	5.7	4.0	1401.5
100×40×2C80	99.7	40.20	1.943	45.5	14.8	5.7	4.0	1401.0
100×40×2C80R	99.7	40.20	1.944	45.4	14.8	5.7	4.0	1399.5
100×40×2C120	99.7	40.20	1.947	45.4	14.8	5.7	4.0	1400.5
40×100×2C40	40.2	99.70	1.945	14.8	45.4	5.7	4.0	1399.8
40×100×2C80	40.2	99.70	1.945	14.8	45.4	5.7	4.0	1400.1
120×80×3C40	120.0	79.90	2.811	38.2	24.0	6.3	4.1	1401.0
120×80×3C80	120.0	79.90	2.796	38.4	24.1	6.3	4.1	1400.4
120×80×3C120	120.0	79.90	2.810	38.2	24.0	6.3	4.1	1400.1
80×120×3C40	79.9	120.00	2.808	24.0	38.2	6.3	4.1	1400.5
80×120×3C80	79.9	120.00	2.792	24.1	38.5	6.3	4.1	1399.8
80×120×3C120	79.9	120.00	2.811	24.0	38.2	6.3	4.1	1400.5

Note: *d* and *b* are the flat portion of depth and width of the cross-section.

Table 7.1. Measured dimensions of beam specimens.



Specimen	M_{Exp} (kN)	κ_{Exp} ($\times 10^{-4} \text{ mm}^{-1}$)	$\frac{M_{Exp}}{M_{Hollow}}$	$\frac{\kappa_{Exp}}{\kappa_{Hollow}}$	M_{FEA} (kN)	$\frac{M_{Exp}}{M_{FEA}}$	Δ_u (mm)
60×40×4C0#	7.2	6.4	1.00	1.00	--	--	--
60×40×4C40	8.2	8.4	1.14	1.30	7.53	1.09	0.002
60×40×4C40R	8.2	8.5	1.14	1.33	7.53	1.09	0.002
60×40×4C80	8.1	8.1	1.13	1.27	7.80	1.04	0.014
60×40×4C120	8.2	5.8	1.14	0.91	7.82	1.04	0.030
40×60×4C0#	5.0	6.4	1.00	1.00	--	--	--
40×60×4C40	5.7	9.0	1.15	1.41	5.32	1.07	0.010
40×60×4C80	5.8	7.9	1.17	1.24	5.54	1.05	0.028
40×60×4C120	5.9	7.4	1.19	1.16	5.62	1.05	0.012
60×60×3C0#	6.9	5.0	1.00	1.00	--	--	--
60×60×3C40	8.3	10.7	1.21	2.15	7.50	1.11	0.006
60×60×3C80	8.6	10.6	1.25	2.13	7.96	1.08	0.048
60×60×3C120	8.5	3.7	1.23	0.73	7.94	1.07	0.180
60×60×3C120R	8.5	8.5	1.23	1.71	7.94	1.07	0.236
100×40×2C0#	7.3	1.8	1.00	1.00	--	--	--
100×40×2C40	10.2	8.2	1.40	4.50	9.46	1.08	0.000
100×40×2C80	10.7	3.2	1.47	1.77	10.48	1.03	0.040
100×40×2C80R	10.8	3.6	1.48	1.99	10.48	1.03	0.040
100×40×2C120	11.0	3.0	1.51	1.64	10.06	1.10	0.040
40×100×2C0#	3.0	1.6	1.00	1.00	--	--	--
40×100×2C40	5.0	9.5	1.65	6.14	4.42	1.12	0.000
40×100×2C80	5.2	9.1	1.72	5.86	4.80	1.08	0.002
120×80×3C0#	20.6	1.3	1.00	1.00	--	--	--
120×80×3C40	25.7	4.5	1.25	3.42	25.18	1.02	0.114
120×80×3C80	27.6	3.8	1.34	2.84	28.14	0.98	1.022
120×80×3C120	27.9	3.0	1.35	2.29	26.76	1.04	1.306
80×120×3C0#	13.0	1.0	1.00	1.00	--	--	--
80×120×3C40	18.6	7.2	1.43	7.30	18.32	1.01	0.040
80×120×3C80	19.1	4.1	1.47	4.22	20.27	0.94	0.826
80×120×3C120	19.2	3.1	1.47	3.14	19.46	0.99	1.042
						Average	1.04
						COV	0.029

Date obtained from Chapter 4 of this thesis.

Table 7.2. Experimental results.



Specimen	EI_{Exp} (kNm ²)	$\frac{EI_{Exp}}{EI_{AISC}}$	$\frac{EI_{Exp}}{EI_{ACI}}$	$\frac{EI_{Exp}}{EI_{EC4}}$	$\frac{EI_{Exp}}{EI_{AS5100}}$
60×40×4C40	59.23	0.89	0.99	0.93	0.88
60×40×4C40R	56.77	0.83	0.93	0.87	0.82
60×40×4C80	57.10	0.79	0.90	0.83	0.77
60×40×4C120	61.59	0.87	1.03	0.93	0.85
40×60×4C40	30.49	0.83	0.89	0.85	0.82
40×60×4C80	29.54	0.78	0.86	0.81	0.77
40×60×4C120	29.30	0.80	0.90	0.84	0.78
60×60×3C40	68.06	0.82	0.96	0.87	0.80
60×60×3C80	73.18	0.82	1.01	0.89	0.80
60×60×3C120	69.43	0.74	0.95	0.82	0.72
60×60×3C120R	70.45	0.75	0.97	0.83	0.73
100×40×2C40	116.91	0.68	0.90	0.75	0.64
100×40×2C80	123.33	0.64	0.91	0.72	0.60
100×40×2C80R	126.00	0.65	0.93	0.74	0.61
100×40×2C120	140.52	0.68	1.02	0.78	0.63
40×100×2C40	29.64	0.78	0.93	0.83	0.76
40×100×2C80	32.35	0.79	1.00	0.86	0.76
120×80×3C40	421.56	0.72	0.94	0.78	0.67
120×80×3C80	455.47	0.69	0.98	0.77	0.64
120×80×3C120	425.45	0.60	0.89	0.68	0.55
80×120×3C40	214.09	0.71	0.88	0.76	0.67
80×120×3C80	229.92	0.70	0.92	0.76	0.65
80×120×3C120	218.23	0.62	0.86	0.69	0.58
Average		0.75	0.94	0.81	0.72
COV		0.107	0.054	0.085	0.130

Table 7.3. Flexural stiffness results.

Specimen	κ_u ($\times 10^{-4}$ mm $^{-1}$)	M_{FEA} (kNm)	Specimen	κ_u ($\times 10^{-4}$ mm $^{-1}$)	M_{FEA} (kNm)
300×300×10C40	1.36	689.8	100×300×2C120	2.30	51.6
300×300×10C80	0.94	752.7	350×200×6C40	0.77	468.0
300×300×10C120	1.27	791.4	350×200×6C80	0.72	526.6
300×300×8C40	0.80	583.3	350×200×6C120	0.64	535.5
300×300×8C80	0.73	639.8	350×200×5C40	0.62	412.5
300×300×8C120	0.58	659.6	350×200×5C80	0.59	469.4
300×300×5C40	0.66	417.7	350×200×5C120	0.46	470.8
300×300×5C80	0.63	480.5	350×200×4C40	0.40	347.2
300×300×5C120	0.59	482.0	350×200×4C80	0.40	405.6
300×300×4C40	0.45	348.3	350×200×4C120	0.34	397.8
300×300×4C80	0.38	414.0	350×200×3.5C40	0.29	309.5
300×300×4C120	0.28	395.5	350×200×3.5C80	0.28	321.5
300×300×3C40	0.37	295.0	350×200×3.5C120	0.26	358.9
300×300×3C80	0.37	355.9	350×200×3C40	0.32	266.8
300×300×3C120	0.35	340.0	350×200×3C80	0.76	334.1
300×300×2C40	0.37	272.0	350×200×3C120	0.27	312.1
300×300×2C80	0.37	302.5	350×200×2.5C40	0.67	245.7
300×300×2C120	0.35	289.0	350×200×2.5C80	0.77	301.2
250×250×10C40	1.41	457.7	350×200×2.5C120	0.79	283.8
250×250×10C80	1.39	493.5	200×350×6C40	0.90	279.7
250×250×10C120	1.89	524.6	200×350×6C80	1.10	312.9
250×250×8C40	1.10	392.2	200×350×6C120	0.61	313.0
250×250×8C80	1.07	429.9	200×350×5C40	0.82	260.9
250×250×8C120	0.85	447.3	200×350×5C80	1.15	279.7
250×250×5C40	0.60	273.2	200×350×5C120	0.92	276.9
250×250×5C80	0.86	306.9	200×350×4C40	1.10	232.4
250×250×5C120	0.47	305.2	200×350×4C80	1.82	272.3
250×250×4C40	0.99	233.2	200×350×4C120	1.17	275.9
250×250×4C80	0.92	266.2	200×350×3.5C40	0.71	208.8
250×250×4C120	0.94	255.3	200×350×3.5C80	1.58	252.7
250×250×3.5C40	1.08	213.7	200×350×3.5C120	1.07	257.1
250×250×3.5C80	1.36	252.3	200×350×3C40	1.08	173.8
250×250×3.5C120	1.10	239.5	200×350×3C80	1.15	207.0
250×250×3C40	1.14	198.4	200×350×3C120	0.50	225.1
250×250×3C80	1.32	235.3	200×350×2.5C40	1.56	155.1
250×250×3C120	1.10	221.5	200×350×2.5C80	1.15	206.2
250×250×2C40	0.28	143.9	200×350×2.5C120	0.65	180.3
250×250×2C80	0.32	176.5	400×200×8C40	0.72	707.9
250×250×2C120	0.31	165.2	400×200×8C80	0.70	786.0

Table 7.4. Parametric study results (Cont.).



300×100×9C40	1.17	321.2	400×200×8C120	0.69	813.3
300×100×9C80	0.94	340.5	400×200×6C40	0.62	582.3
300×100×9C120	0.93	363.1	400×200×6C80	0.58	657.9
300×100×7C40	1.02	265.1	400×200×6C120	0.46	664.0
300×100×7C80	0.86	284.5	400×200×5C40	0.38	506.6
300×100×7C120	0.98	299.5	400×200×5C80	0.36	583.0
300×100×5C40	0.89	207.2	400×200×5C120	0.31	578.0
300×100×5C80	0.76	227.4	400×200×4.5C40	0.27	464.6
300×100×5C120	0.90	235.8	400×200×4.5C80	0.27	537.7
300×100×4C40	0.90	175.8	400×200×4.5C120	0.27	536.1
300×100×4C80	0.84	197.0	400×200×3.5C40	0.49	377.1
300×100×4C120	0.80	200.1	400×200×3.5C80	0.55	452.8
300×100×3.5C40	0.80	160.5	400×200×3.5C120	0.19	436.2
300×100×3.5C80	0.82	182.2	400×200×3C40	0.38	326.3
300×100×3.5C120	0.61	182.4	400×200×3C80	0.31	402.4
300×100×3C40	0.52	142.5	400×200×3C120	0.45	380.2
300×100×3C80	0.44	162.2	200×400×8C40	1.82	412.6
300×100×3C120	0.41	158.4	200×400×8C80	1.76	453.1
300×100×2.5C40	0.29	119.0	200×400×8C120	2.16	472.5
300×100×2.5C80	0.52	140.8	200×400×6C40	0.74	306.5
300×100×2.5C120	0.62	135.5	200×400×6C80	1.77	384.9
300×100×2C40	0.20	96.1	200×400×6C120	1.49	386.1
300×100×2C80	0.20	115.6	200×400×5C40	0.75	264.1
300×100×2C120	0.15	103.8	200×400×5C80	1.08	299.8
100×300×9C40	5.03	134.5	200×400×5C120	0.70	294.8
100×300×9C80	7.47	141.3	200×400×4.5C40	1.26	250.5
100×300×9C120	8.02	152.5	200×400×4.5C80	0.60	278.2
100×300×7C40	7.42	111.7	200×400×4.5C120	0.73	275.3
100×300×7C80	3.95	120.1	200×400×3.5C40	0.79	238.8
100×300×7C120	5.02	131.2	200×400×3.5C80	1.21	248.4
100×300×5C40	1.62	79.1	200×400×3.5C120	0.43	229.1
100×300×5C80	1.75	85.8	200×400×3C40	0.33	189.1
100×300×5C120	0.90	89.6	200×400×3C80	0.54	225.5
100×300×4C40	8.79	56.5	200×400×3C120	0.36	209.5
100×300×4C80	6.20	60.2	220×220×2C40	0.61	121.6
100×300×4C120	0.55	67.9	220×220×2C80	0.76	134.9
100×300×3.5C40	2.32	58.3	220×220×2C120	0.84	131.4
100×300×3.5C80	2.02	64.6	210×210×2C40	0.62	100.9
100×300×3.5C120	1.09	64.0	210×210×2C80	0.65	121.5
100×300×3C40	2.30	52.4	210×210×2C120	0.63	115.6
100×300×3C80	2.46	61.3	190×190×2C40	1.23	77.9
100×300×3C120	0.78	58.6	190×190×2C80	1.07	94.5
100×300×2.5C40	6.22	53.5	190×190×2C120	1.52	91.1
100×300×2.5C80	2.08	55.7	180×180×2C40	1.10	65.7
100×300×2.5C120	0.60	51.4	180×180×2C80	1.21	79.1
100×300×2C40	1.45	45.5	180×180×2C120	1.77	80.4
100×300×2C80	1.20	50.9			

Table 7.4. Parametric study results (Cont.).



	$\frac{M_u}{M_{AISC}}$	$\frac{M_u}{M_{ACI}}$	$\frac{M_u}{M_{EC4}}$	$\frac{M_u}{M_{AS5100}}$	$\frac{M_u}{M_{Han}}$	$\frac{M_u}{M_{Han}^{\#}}$
Number of data	194	194	194	194	194	194
Mean (P_m)	1.56	1.33	1.37	1.52	1.31	1.05
$COV (V_p)$	0.217	0.133	0.130	0.130	0.134	0.112
Resistance factor (ϕ_0)	0.90	0.90	0.90	0.90	0.90	0.90
Reliability index (β_0)	3.30	3.30	3.29	3.61	3.26	2.55

Table 7.5. Comparison of test and FEA strengths with design strengths for all specimens.

	Description of element	λ_p	λ_r	λ_{limit}
Axial compression	Walls of rectangular HSS	$2.26 \sqrt{\frac{E_s}{f_y}}$	$3.00 \sqrt{\frac{E_s}{f_y}}$	$5.00 \sqrt{\frac{E_s}{f_y}}$
Flexural	Flanges of rectangular HSS	$2.26 \sqrt{\frac{E_s}{f_y}}$	$3.00 \sqrt{\frac{E_s}{f_y}}$	$5.00 \sqrt{\frac{E_s}{f_y}}$
	Webs of rectangular HSS	$3.00 \sqrt{\frac{E_s}{f_y}}$	$5.70 \sqrt{\frac{E_s}{f_y}}$	$5.70 \sqrt{\frac{E_s}{f_y}}$

Table 7.6. Slenderness limits for rectangular CFST members.

	AISC				ACI		EC 4		AS 5100	
	$\frac{M_u}{M_{Compact}}$	$\frac{M_u}{M_{Noncompact}}$	$\frac{M_u}{M_{Slender}}$	$\frac{M_u}{M_{Limit}^*}$	$\frac{M_u}{M_{Limit}}$	$\frac{M_u}{M_{Limit}^*}$	$\frac{M_u}{M_{Limit}}$	$\frac{M_u}{M_{Limit}^*}$	$\frac{M_u}{M_{Limit}}$	$\frac{M_u}{M_{Limit}^*}$
Number of data	65	48	57	24	35	159	29	165	14	180
Mean (P_m)	1.28	1.41	1.84	1.95	1.24	1.34	1.25	1.39	1.42	1.52
$COV (V_p)$	0.048	0.101	0.156	0.159	0.049	0.139	0.044	0.133	0.041	0.132
Resistance factor (ϕ_0)	0.90	0.90	0.90	0.90	0.90	0.90	0.90	0.90	0.90	0.90
Reliability index (β_0)	3.58	3.72	4.28	4.41	3.42	3.32	3.32	3.31	3.77	3.61

Note: M_{Limit}^* is the predicted moment for specimens exceeding the slenderness limit for corresponding design code.

Table 7.7. Comparison of test and numerical results with the design moment capacities.

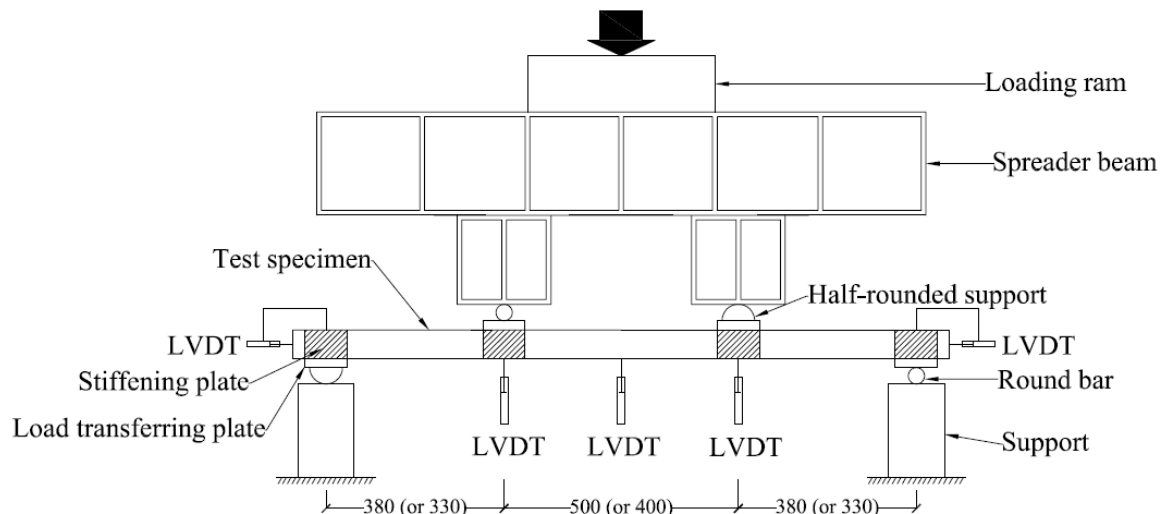


Figure 7.1. Schematic setup of four-point bending test.

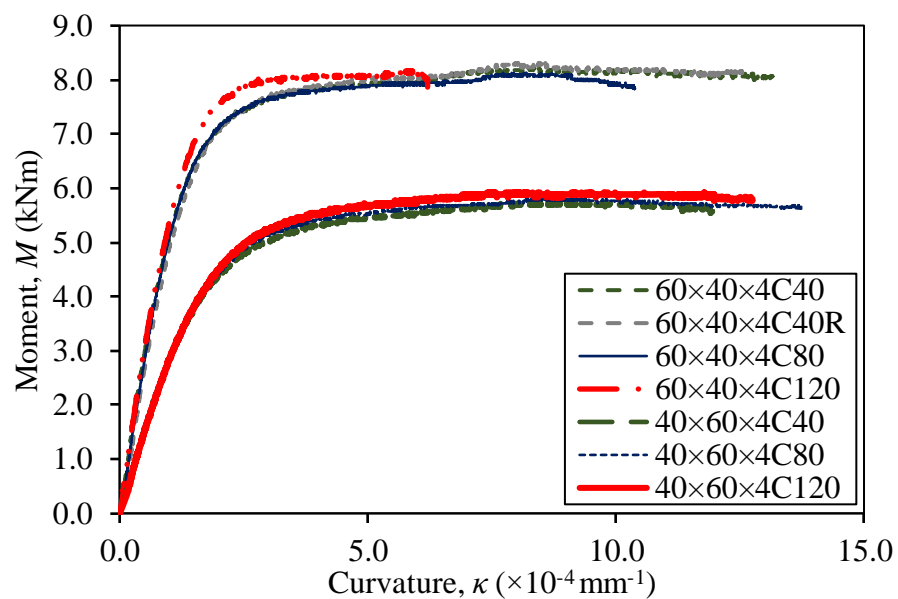


Figure 7.2. Moment-curvature curves of Section 60×40×4.

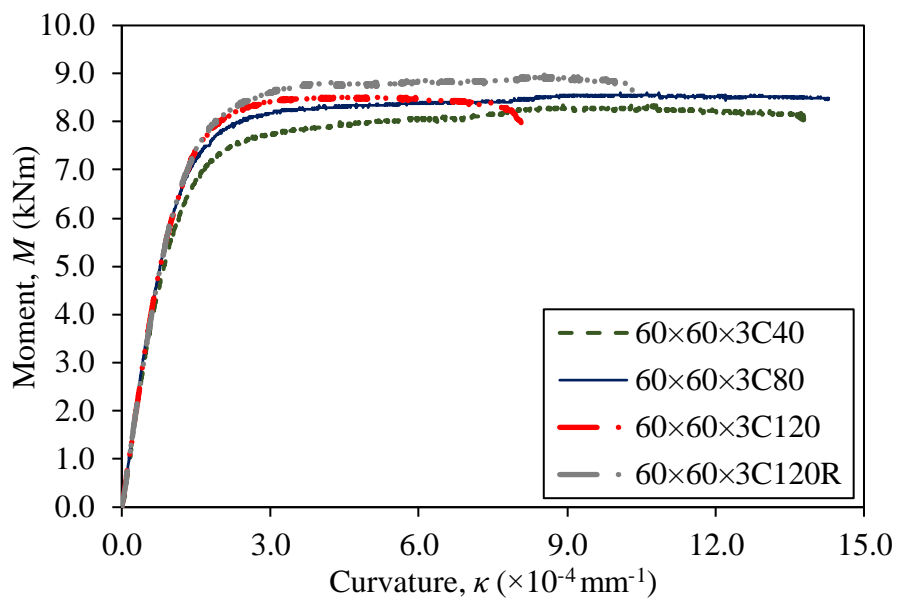


Figure 7.3. Moment-curvature curves of Section 60×60×3.

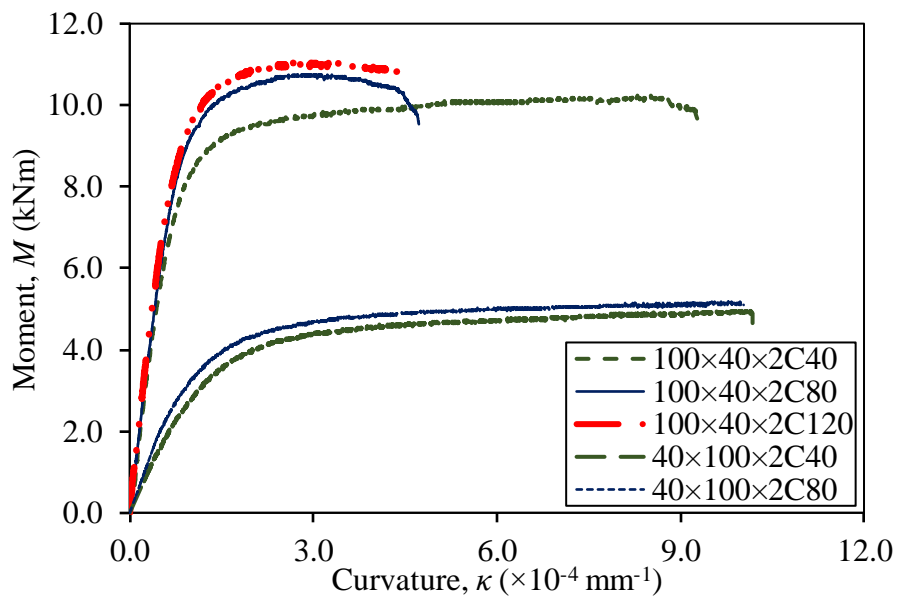


Figure 7.4. Moment-curvature curves of Section 100×40×2.



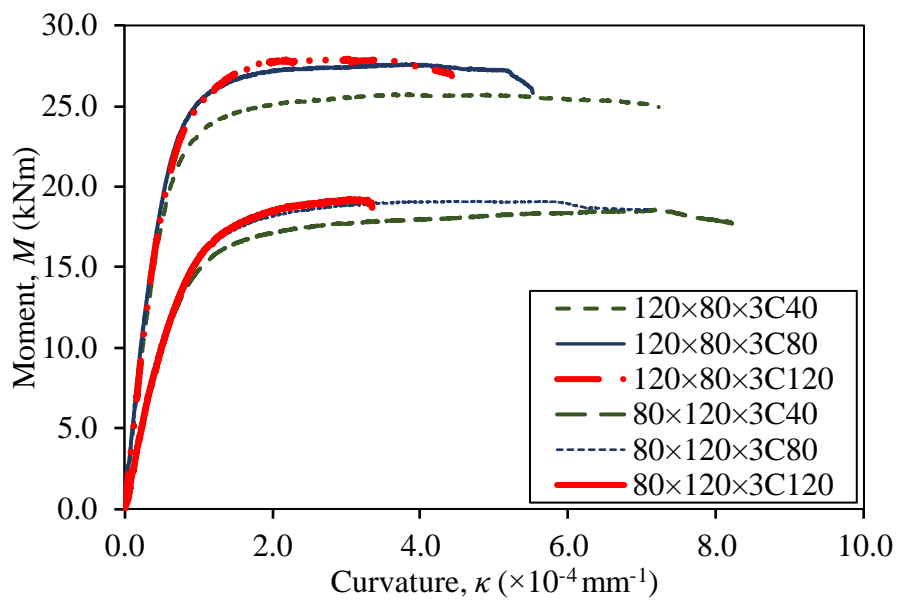


Figure 7.5. Moment-curvature curves of Section 120×80×3.

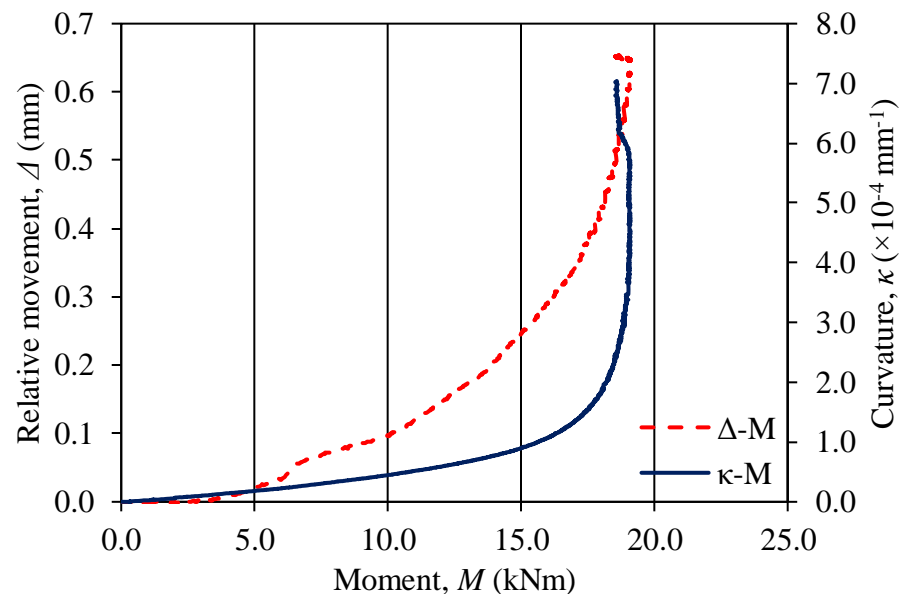
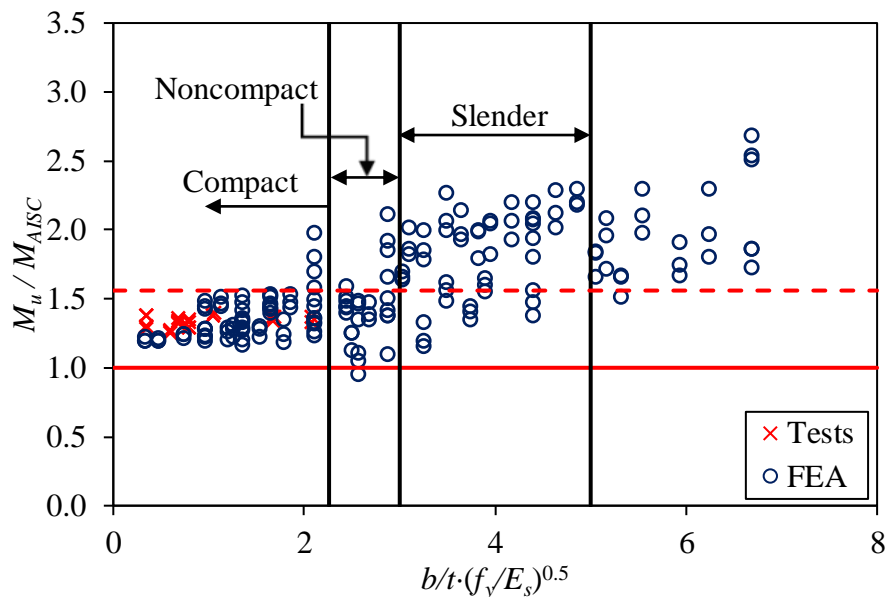
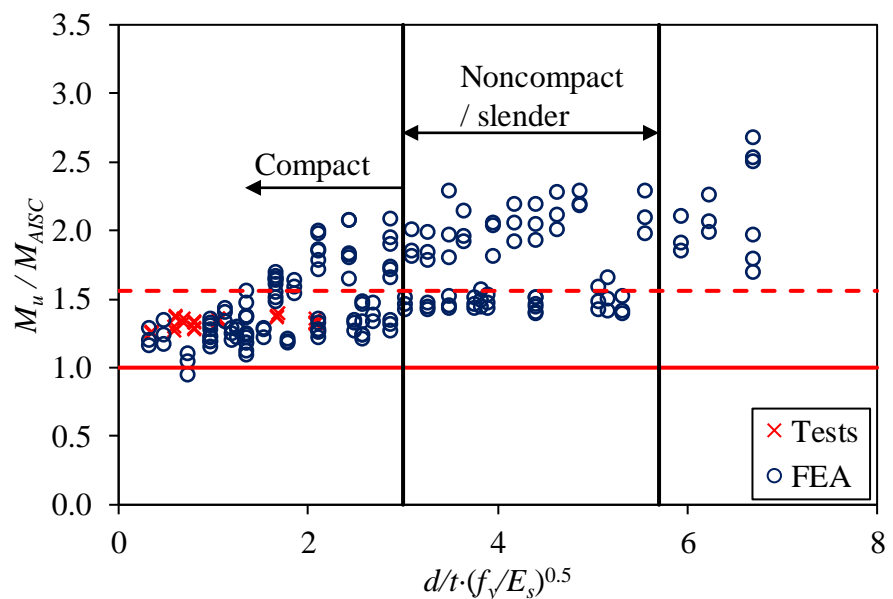


Figure 7.6. Relative movement-moment-curvature curve of specimen 80×120×3C80.





(a) Element subjected to compression



(b) Element subjected to bending

Figure 7.7. Comparison of experimental and AISC predicted strengths.



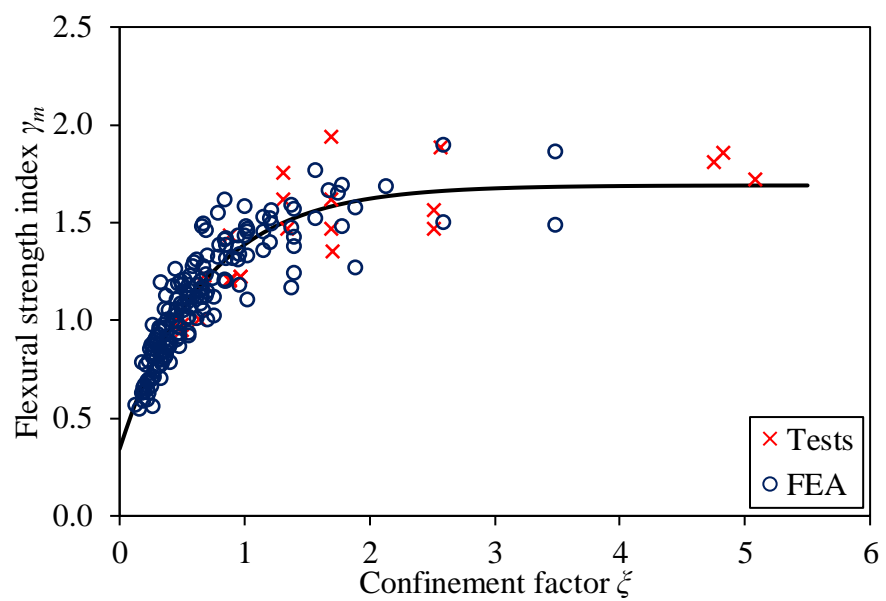


Figure 7.8. γ_m and ξ relationship for the modified Han's method.



CHAPTER 8

FLEXURAL BEHAVIOUR OF CONCRETE-FILLED COLD-FORMED AUSTENITIC STAINLESS STEEL CHS

8.1 Introduction

The main objective of this chapter is to investigate the concrete-filled cold-formed circular austenitic stainless steel tubes subjected to pure bending. A total of 18 specimens were tested and 165 numerical results were generated using the verified finite element model. The experimental and numerical results were used to assess the predicted flexural capacities and flexural stiffness obtained from American specification AISC 360 (2016), American code ACI 318 (2014), EC4 (2004) and AS 5100.6 (2004). Reliability analysis was also conducted to assess the applicability of the current design method on concrete-filled carbon steel members for concrete-filled stainless steel members. The design method proposed by Han (2004) was also assessed and a more accurate and reliable design method was modified based on Han's method for the design of concrete-filled circular stainless steel members under bending condition.



8.2 Experimental Investigation

8.2.1 General

A total of 18 specimens, of which there are 14 concrete-filled specimens and 4 hollow specimens, were prepared for the investigation on the flexural behaviour of concrete-filled circular stainless steel members. The specimens were fabricated using austenitic stainless steel and concrete varied from normal to high strengths. All the specimens were tested until failure under pure bending.

Three mix designs with different water/cement ratios in order to achieve concrete of nominal cylinder compressive strengths 40, 80 and 120 MPa were used in this study. Concrete of the same grade was made in one batch and poured into the specimens. For each batch, six standard cylinders (150 mm diameter \times 300 mm height) were prepared and both ends of the cylinders were capped flat in order to achieve uniform loading. Aggregate of maximum size 10 mm was used in order to fill in specimens with small cross-sectional area. Before the compression test of the cylinders, elastic modulus of concrete (E_c) was determined by suitable compressometer according to ASTM C469 (2014). Two cylinders were crushed at 28 days after casting and four more concrete cylinders were tested at the same time of the four-point bending tests. The measured cylinder compressive strengths f_c' were 38.5, 81.2 and 120.5 MPa with elastic moduli of 23.9, 33.1 and 39.0 GPa for the concrete with nominal cylinder compressive strengths of 40, 80 and 120 MPa, respectively.



8.2.2 Specimens

A total of 18 specimens were tested comprising 14 concrete-filled specimens and 4 hollow specimens for comparison. The specimens were labelled in such a way that the nominal dimensions including the outer diameter (D), material thickness (t) and the nominal infill concrete cylinder compressive strength can be identified. For example, the label $114.3 \times 3.0\text{C}120$ indicates the specimen of outer diameter 114.3 mm and thickness equals to 3.0 mm. The symbol “C120” means that the specimen had nominal infill concrete cylinder compressive strength equals to 120 MPa. A symbol “C0” indicates the specimen without any infill concrete. If the test was repeated, a symbol “R” would be added after the concrete strength. The measured specimen dimensions are shown in Table 8.1.

8.2.3 Four-point bending tests

Four-point bending tests were conducted in order to achieve pure bending condition for each specimen, for which the specimens were simply supported at the two ends and loaded at the two loading points symmetrically between two supports, as shown in Fig. 8.1. Half-round and roller supports were designed to simulate the simply supported condition. The specimens made of sections CHS 60.5×2.8 , CHS 76.0×3.0 and CHS 114.3×3.0 were cut to the length of 1200 mm, while those of section CHS 165.2×3.0 have the length of 1500 mm in order to avoid any possible shear failure in the shear spans. The 1200 mm long specimens had the moment span and shear span of 400 and 350 mm, respectively. For the 1500 mm long specimens, the moment span and shear span were 500 and 450 mm, respectively. A set of special sittings were used to spread the forces onto the circular specimens and plastic rubber sheets were used between the sittings and specimen surfaces to ensure uniform contact if necessary, as shown in Fig. 8.2.



Steel bearing plates were also placed between the rollers/half rounds and the sittings in order to spread the concentrated load. A servo-controlled hydraulic testing machine of 1000 kN capacity was used to apply compressive force to the specimen by displacement control method at a constant loading rate of 1.0 mm/min. Three displacement transducers (LVDTs) were placed at the bottom of the tension surface of each specimen at the loading points and the mid-span of the specimen to record the vertical displacement. Two LVDTs were also placed at the center of each end in the longitudinal direction to record the relative horizontal movement of concrete to stainless steel tube.

8.3 Test Results and Discussion

8.3.1 Moment-curvature curves

The specimens were tested to failure under monotonic bending by displacement controlled method. All the specimens were failed in the moment span and no out-of-plane bending was observed in the tests. The experimental ultimate moment (M_{Exp}) and the corresponding curvature (κ_{Exp}) of each specimen are summarized in Table 3. The experimental ultimate moments (M_{Exp}) were obtained using half of the ultimate applied load multiplied by the lever arm (distance from the end support to the loading point) for the beam specimens. The weight of the stiffening plates, bearing plates, half-rounds and rollers are also included in the calculation of experimental moment. The curvature was determined from the vertical displacements recorded by the three LVDTs located at the tension surface by assuming a constant curvature between the transducer locations. The curvature was calculated using the radius (r) of the curved beam from the relationship $\kappa_{Exp} = 1/r$. The moment-curvature curves for each steel section are shown in Figs 8.3 – 8.6.



The beneficial effect due to the concrete infill can be indicated by the ratio of ultimate bending moment over their corresponding hollow stainless steel section counterpart M_{Exp} / M_{Hollow} . An increase in moment capacity of 22% to 80% was found for the concrete-filled specimens. The enhancement in strength was more significant for the specimens with larger D/t ratio, which is attributed to the fact that the slender section is more vulnerable to local buckling and the concrete infill could help to delay local buckling. This advantage is also reflected on the ratio of curvature for respective ultimate moment to that of hollow section $\kappa_{Exp} / \kappa_{Hollow}$. A dramatic enhancement of 455% was found for the specimen 165.2×3.0C40, which is the specimen with the largest D/t ratio and lowest concrete strength in this study. The increase in ductility for the stockier sections was not as significant as those slender sections, but 14% enhancement can be anticipated. Although the use of high strength concrete could improve the moment resistance, reduced ductility was found due to the brittle nature of high strength concrete. Generally, the ductility was greatly improved for the slender sections with normal strength concrete, while high strength concrete would result in deduction of ductility compared with the normal strength concrete infilled specimens.

8.3.2 Flexural stiffness

The flexural stiffness is the resistance of a member against bending deformation, and it is a function of elastic modulus and second moment of area of the cross-section. The flexural stiffness EI_{Exp} was determined from the initial slope of the moment-curvature curve for each specimen and summarized in Table 8.2. The formulae for the flexural stiffness of the composite section in different design codes are expressed in a form of $EI = E_s I_s + \alpha E_c I_c$ and detailed as follows:

$$EI_{AISC} = E_s I_s + C_3 E_c I_c \text{ by AISC 360 (2016)} \quad (8.1)$$



where $C_3 = 0.6 + 2 \left(\frac{A_s}{A_c + A_s} \right) \leq 0.9$

$$EI_{ACI} = E_s I_s + \frac{0.2E_c I_c}{1 + \beta_{dns}} \text{ by ACI 318 (2014)} \quad (8.2)$$

where β_{dns} is a ratio related to axial load and it is set to be zero in this study since flexural member with no axial load.

$$EI_{EC4} = E_s I_s + 0.6E_c I_c \text{ by EC4 (2004)} \quad (8.3)$$

$$EI_{AS5100} = E_s I_s + E_c I_c \text{ by AS5100.6 (2004)} \quad (8.4)$$

The predictions on flexural stiffness by different design rules are unconservative, as shown in Table 8.2. The AISC 360 (2016), EC4 (2004) and AS 5100.6 (2004) provided very unsafe predictions on flexural stiffness of CFST members and this was also found by Han et al. (2006). The ACI 318 (2014) provided better predictions, though unsafe, with a mean value of 0.82 on the ratio of EI_{Exp} / EI_{ACI} and the coefficient of variation (COV) of 0.091. The ACI provisions utilize the smallest concrete stiffness with the reduction factor of 0.2 and it is the reason for the better prediction since relatively small portion of concrete is under compression when the CFST member is subjected to bending (Roeder et al., 2010).

8.4 Finite Element Model and Verification

8.4.1 Finite element model

The experimental study provided valuable data points on the design of concrete-filled circular stainless steel members under pure bending condition. However, there were some gaps in the experimental database especially for those noncompact and slender sections. The finite element analysis approach was selected to address these gaps and further generate data on design of concrete-



filled circular stainless steel members. A finite element model was developed to simulate the experimental study using nonlinear finite element analysis package ABAQUS version 6.14 (ABAQUS, 2014). The results obtained from the finite element analysis were first verified with the experimental results and good agreement was found. The verified model was then used to conduct an extensive parametric study on specimens with a wide range of D/t ratio and a total of 165 numerical results were generated.

The stainless steel tubes adopted in this study were from the same batch of specimens as reported in Chapter 3 of this thesis so the measured stress-strain curves of each section obtained from tensile coupon tests were used in the finite element model. The stress-strain curves were expressed in the multi-linear form including the elastic part up to the proportional limit as well as the plastic curves of the true stress and logarithmic true plastic strain. The true stress (σ_{true}) and logarithmic plastic strain (ε_{pl}) were converted from the static engineering stress (σ) and strain (ε) obtained from the tensile coupon tests in the experimental study. The concrete-damaged plasticity model in ABAQUS library was used and the modified confined concrete constitutive model described in Chapter 6 of this thesis was also used.

The interface between stainless steel and concrete was simulated by contact interaction in ABAQUS (ABAQUS, 2014). The contact interaction is defined along both the normal and tangential interface direction between the stainless steel and concrete. The “hard contact” relation is selected in the normal direction, which allows separation from each other but penetration was not allowed. The tangential mechanical property of the contact interaction was simulated by Coulomb friction model. The friction model allows stress transmission between



the stainless steel tube and concrete up to the limit τ_{crit} . The coulomb friction coefficient between the stainless steel tube (master surface) and the concrete infill (slave surface) was set to be 0.6. The shear stress limit was calculated by Eq. (8.5) as specified in Han et al. (2007) as follows:

$$\tau_{crit} = 2.314 - 0.0195(D/t) > 0 \quad (8.5)$$

The four-noded S4R shell elements were selected to model the stainless steel section. These quadrangular first-order reduced-integration shell elements had six degrees of freedom per node and they were widely used in modelling hollow stainless steel sections (Huang and Young, 2012; Zhao et al., 2016b) and concrete-filled steel tubes (Lai and Varma, 2015). The concrete core was meshed with the first-order reduced-integration 3D hexahedral solid element (C3D8R). These elements had three degrees of freedom per node and reduced integration, which is computationally effective for modelling concrete cracking (Lai and Varma, 2015).

The purpose of four-point bending tests was to apply uniform bending moment on the moment span until failure of the specimen, thus, only the moment span was modelled and the shear spans were neglected in the finite element model. The boundary conditions were modelled by two reference points which are coupled with the surfaces of the composite section at both ends. The bending moments were applied to the moment span of specimens at both ends, by adding rotations of a preselected value, which was large enough for the specimens to obtain ultimate moment resistances. Static RIKS step in the ABAQUS library was used to apply the loading and the nonlinear geometric parameter (*NLGEOM) was also included to allow large displacement analysis. Besides, the computational time of

the moment span model was about one third of that consumed for modelling the whole full member, thus it is suggested to model moment span only.

8.4.2 Verification of finite element model

The developed finite element model was used to predict the ultimate moment resistance in the experimental study. Comparison of the strengths from the finite element analysis and the corresponding tests are shown in Table 8.2. The mean value of M_{Exp} / M_{FEA} equals to 1.03 with the corresponding coefficient of variation (COV) of 0.050 were obtained. A maximum difference of 15% is found between the experimental and numerical ultimate bending moment for specimens 114.3×3.0C40. A good agreement has been achieved for the concrete-filled circular stainless steel beam specimens in terms of the ultimate moment resistances.

8.5 Parametric Study

In order to expand the database on concrete-filled circular stainless steel tubes under pure bending conditions, an extensive parametric study was conducted upon the verified finite element model. The parametric study aims at addressing specimens with wider slenderness ratio (D/t), covering noncompact and slender sections, and further checking against the existing design methods and proposing new design methods if necessary. The stainless steel material property was taken from the tensile coupon tests of the CHS 76.3×3.0 specimen as reported in Chapter 3 of this thesis. A total of 165 finite element analyses were conducted in this parametric study covering the slenderness ratio (D/t) from 30.0 to 245.0 that include compact, noncompact and slender sections. The diameter of the analyzed specimens ranged from 140.0 to 406.0 mm and the material thickness varied from



1.0 to 10.0 mm. The three different concrete strengths and the corresponding elastic modulus (E_c) in the experimental study were used for each thickness of each profile. The length of moment span for each specimen was taken as 5 times the outer diameter (D). The specimens in the parametric study shared the same labelling system as that of the test specimens and the ultimate bending moments obtained from parametric study are listed in Table 8.3.

8.6 Reliability Analysis

In order to assess the applicability of current design methods on concrete-filled circular stainless steel tubes subjected to pure bending, reliability analysis was conducted on each design method. It is noteworthy that all the design methods were designated for concrete-filled carbon steel members and none of them address the design of concrete-filled stainless steel members. Reliability analysis is detailed in the specification AISC 360 (2016). The target reliability index (β_0) of 2.50 is used in this study and the design rule is considered to be reliable if the reliability index is greater than or equal to 2.50. The resistance factor (ϕ_0) of 0.90 was used for the composite circular stainless steel members. The load combination of 1.2DL+1.6LL was used for specifications AISC 360 (2016) and ACI 318 (2014). The combinations of 1.35DL+1.5LL was used for EC4 (2004), and 1.2DL+1.5LL was used for both the Australian standard AS 5100.6 (2004) and the modified AS 5100 method. The load combination of 1.2DL+1.6LL was also used for design method proposed by Han (2004) and modified Han's method. The live load to dead load ratio of 1/5 was used. Statistical parameters $M_m = 1.10$, $F_m = 1.00$, $V_m = 0.10$ and $V_F = 0.05$ were adopted in the calculation of the reliability index, where M_m is the mean value of material factor, F_m is the mean value of fabrication factor, V_m is the coefficient of variation of material factor and V_F is the coefficient of variation of fabrication factor. The statistic parameters P_m



and V_p are the mean value of tested-to-predicted or FEA-to-predicted load ratios and coefficient of variation of fabrication factor, respectively. The correction factor C_p was also used in the calculation of reliability index in order to compensate the influence due to limited number of data sample. The values of reliability index are shown in Table 8.4 for all design rules.

8.7 Comparison Between Test and Code Predicted Strengths

8.7.1 General

There are several existing design specifications for composite members including American specification AISC 360 (2016), American code ACI 318 (2014), EC4 (2004) and Australian standard AS 5100.6 (2004). However, all the abovementioned design methods are applicable for concrete-filled carbon steel members and none of them address the design of concrete-filled stainless steel flexural members. Based on the experimental and numerical studies presented in this chapter, the design codes are compared with the experimental and numerical results. Besides, the proposed design equations by Han (2004) were also assessed in this section and modified Han's method was also proposed. For the comparison, all the material partial safety factors are set to be unity and the material properties are taken as the measured values. In addition, all the limitations on the concrete strength and steel strength are ignored in order to check the feasibility of the design codes.



8.7.2 AISC 360

The AISC Specification AISC 360 (2016) defines the compactness limit (λ_p) and noncompactness limit (λ_r) for concrete-filled steel tubes subjected to bending to be $\lambda_p = 0.09E_s / f_y$ and $\lambda_r = 0.31E_s / f_y$, respectively. There has been no development of theoretical background for local buckling of composite circular flexural members so that the compactness limit was taken as 25% enhanced over hollow sections, i.e. $\lambda_p = 0.07E_s / f_y$ of hollow flexural members (Lai and Varma, 2015). The noncompactness limit was identical to that for hollow sections in AISC 360. In addition, the maximum permitted limit was also set conservatively as $\lambda_{\text{limit}} = \lambda_r = 0.31E_s / f_y$ due to lack of data and this limit was ignored in this study to check the feasibility of the design method beyond this limit.

The flexural resistance was calculated by taking the compressive force in concrete, and both the tensile and compressive force by the stainless steel section. The concrete contribution in tension is ignored due to cracking. The moment resistance of compact sections can be calculated as the plastic moment (M_p) using the plastic distribution method. Rigid-plastic behaviour of both stainless steel and concrete was assumed, for which the stainless steel tube could fully develop the yield stress under both compression and tension, and the concrete strength equals to $0.95f_c'$ in compression and zero in tension. The calculation of neutral axis is established by force equilibrium between compression and tension of the cross-section, as shown in Fig. 8.7. For the noncompact sections, the nominal moment for noncompact section (M_r) was calculated based on elastic-plastic behaviour for the stainless steel in tension and elastic behaviour up to yield stress in extreme compressive fiber. The concrete in compression could develop compressive stress up to $0.7f_c'$ linearly from the neutral axis to the extreme



compressive fiber. It is believed that concrete has significant volumetric dilation after exceeding $0.70f_c'$ under compression (Lai and Varma, 2015).

The ratios of experimental or numerical strengths over the design strengths (M_u / M_{AISC}) obtained from AISC 360 (2016) are plotted against the slenderness parameter $\lambda = D/t \cdot (f_y/E_s)$, as shown in Fig. 8.8. The AISC 360 (2016) are very safe with the mean value of experimental or numerical strengths to design strengths ratio M_u / M_{AISC} equals to 2.64 and COV of 0.401, as shown in Table 8.4. This conservatism was mainly due to the underestimation of strain-hardening effect of the stainless steel section, for which the ratio of ultimate tensile strength to yield strength f_u / f_y equals to 2.31 to 2.75 in this study, respectively, as given in Chapter 3 of this thesis. The calculation of bending resistance uses the stainless steel strength up to the yield strength only. The predictions for specimens filled with normal strength concrete are better than those with high strength concrete, as illustrated in Fig. 8.8. The reliability index (β_0) for AISC is 3.39, which is considered to be reliable.

8.7.3 ACI 318

The American Concrete Institute design guidance ACI 318 (2014) allows the use of concrete-filled circular composite columns with slenderness ratio (D/t) smaller than or equals to $\sqrt{8E_s/f_y}$. The calculation of flexural strength of composite section is similar to that of reinforced concrete section with compatibility assumptions, as illustrated in Fig. 8.7. A linear strain distribution is assumed with the maximum strain in extreme compressive fiber of concrete within the tube equals to 0.003 mm/mm. The concrete stress distribution is a rectangular stress block with a $0.85f_c'$ compressive stress acting over a depth $\beta_l x$, which is the



depth of neutral axis (x) multiplied by a reduction factor (β_1) depending on the strength of concrete. A bilinear steel material curve is assumed and equilibrium relations should be satisfied on the axial force aspect. The ACI predictions are also very conservative with the mean value of experimental or numerical strengths to design strengths ratio M_u / M_{ACI} equals to 2.71 and COV of 0.458, and it is reliable with the reliability index (β_0) of 3.11, which is larger than the target value of 2.50. These inaccurate predictions were also attributed to the depreciation of stainless steel stain-hardening effect.

8.7.4 Eurocode 4

The EC4 (2004) assumes full plastic stress distribution on the whole cross-section. The concrete strength in tension is neglected due to cracking. The EC4 (2004) predictions are similar to that of the compact sections in AISC 360 (2016) except that the reduction factor of 0.95 for concrete is ignored. It is believed that the development of concrete strength is better in composite sections since peeling off of concrete is impossible (CIDECT, 1998). The EC4 allows the design of circular steel tubes with slenderness ratio (D/t) of not larger than $90 \cdot (235 / f_y)$. The EC4 design strengths also undervalued the experimental and numerical results with the mean value of 2.45 and COV of 0.406, as illustrated in Fig. 8.9 and Table 8.4. The EC4 (2004) is very reliable with the reliability index (β_0) equals to 3.13.

8.7.5 AS 5100.6

The Australian standard AS 5100.6 (2004) assumes that the steel yields before the concrete reaches its ultimate stress state (Tao et al., 2008). The formula used for calculating the flexural strength of composite circular sections is virtually the



same as those suggested in EC4 (2004), except that different values have been used for the capacity factors. The capacity factors ϕ and ϕ_c are 0.9 and 0.9, respectively, as specified in AS 5100 for section capacity of steel and concrete. The AS 5100 underestimated the flexural capacity with the mean value of 2.73 and *COV* of 0.406 due to the applied capacity factors. The reliability index (β_0) for AS 5100 is 3.31, which is very reliable.

8.7.6 Method proposed by Han (2004) and modification of Han's method

Han (2004) proposed a simplified method for the calculation of flexural capacity of composite beam sections. The calculation of moment capacity for a composite beam consists of three parameters and the multiplication of these three values yields the moment resistance, which include flexural strength index γ_m , section modulus of the composite beam W_{scm} and nominal yielding strength f_{scy} . The determination of the three parameters proposed by Han (2004) is shown in Eqs (8.6) – (8.8).

$$\gamma_m = 1.1 + 0.48 \cdot \ln(\xi + 0.1) \quad (8.6)$$

$$W_{scm} = \pi D^3 / 32 \quad (8.7)$$

$$f_{scy} = (1.14 + 1.02\xi) \cdot f_{ck} \quad (8.8)$$

The calculation involves the determination of confinement factor ξ , which is related to the cube strength (f_{cu}) of concrete. The conversion formula from cylinder strength to cube strength of concrete follows the equation $f_{cu} = 1.1719 \cdot f_c + 2.0029$. This conversion formula is derived from the table of concrete strength stipulated in EC2 (2004) by fitting a straight line passing all the



tabulated data. Lai (2015) adopted the same method in deriving the conversion formula. The parameter f_{ck} is the characteristic concrete strength, which equals to $0.67f_{cu}$. The method proposed by Han (2004) provides very safe predictions with the mean value of M_u / M_{Han} ratio of 2.19 and the *COV* equals to 0.320. The proposed method is considered to be reliable with the reliability index (β_0) equals to 3.51, as shown in Fig. 8.10 and Table 8.4.

Modification on the method proposed by Han (2004) is carried out in order to provide better predictions on the flexural strength of composite beams. The flexural strength index (γ_m) is modified in this study as Eq. (8.9).

$$\gamma_m = \ln(1.807 + 4.346\xi) \quad (8.9)$$

The other parameters such as the nominal yielding strength f_{scy} and section modulus of the composite beam W_{scm} remained unchanged as defined in Han (2004). The modified Han's method provides the best predictions of the composite beams with the mean value of $M_u / M_{Han}^{\#}$ ratio of 1.00 and the *COV* equals to 0.062, as shown in Fig. 8.11 and Table 8.4. The modified Han's method is considered to be reliable to with the reliability index (β_0) equals to 2.52.

8.8 Concluding Remarks

An experimental study together with an extensive numerical study on concrete-filled circular stainless steel tubes subjected to pure bending have been presented in this chapter. The experimental program including a total of 18 four-point bending tests were conducted. A finite element model was developed to duplicate the experimental results using a modified confined concrete model proposed in Chapter 6 of this thesis. The finite element model is able to predict the



experimental results very well, hence, an extensive parametric study was carried out using the verified finite element model. A total of 182 experimental and numerical results were used to assess the existing design rules for flexural capacity of conventional concrete-filled carbon steel beams as detailed in American specification AISC 360 (2016), American code ACI 318 (2014), EC4 (2004) and Australian standard AS 5100.6 (2004). The design method proposed by Han (2004) was also examined and modification to Han's method is proposed in this study. The modified design method is found to provide the most accurate predictions on concrete-filled circular stainless steel tubes subjected to pure bending.

Specimen	<i>D</i> (mm)	<i>t</i> (mm)	<i>A_s</i> (mm ²)	<i>A_c</i> (mm ²)	<i>f_{c'}</i> (MPa)	<i>E_c</i> (GPa)
60.5×2.8C0	60.8	2.77	504.6	--	--	--
60.5×2.8C40	60.5	2.76	500.5	2372.3	38.5	23.9
60.5×2.8C40R	60.6	2.77	503.3	2383.1	38.5	23.9
60.5×2.8C80	60.7	2.78	505.7	2389.5	81.2	33.3
60.5×2.8C120	60.7	2.78	505.0	2386.6	120.5	39.0
76.0×3.0C0	76.5	2.99	690.5	--	--	--
76.0×3.0C40	76.3	2.93	675.3	3902.5	38.5	23.9
76.0×3.0C80	76.8	2.94	682.8	3947.3	81.2	33.3
76.0×3.0C80R	76.6	2.95	682.5	3920.4	81.2	33.3
76.0×3.0C120	76.4	2.92	674.8	3910.1	120.5	39.0
114.3×3.0C0	114.5	2.91	1018.6	--	--	--
114.3×3.0C40	114.5	2.92	1023.6	9265.1	38.5	23.9
114.3×3.0C80	114.6	2.92	1023.8	9285.6	81.2	33.3
114.3×3.0C120	114.4	2.90	1016.8	9260.2	120.5	39.0
165.2×3.0C0	165.1	2.95	1503.7	--	--	--
165.2×3.0C40	165.7	2.96	1510.8	20044.8	38.5	23.9
165.2×3.0C80	164.8	2.97	1508.6	19809.1	81.2	33.3
165.2×3.0C120	165.1	2.96	1506.5	19908.4	120.5	39.0

Table 8.1. Measured dimensions of beam specimens.

Specimen	κ_{Exp} (%)	M_{Exp} (kNm)	$\frac{\kappa_{Exp}}{\kappa_{Hollow}}$	$\frac{M_{Exp}}{M_{Hollow}}$	M_{FEA} (kNm)	$\frac{M_{Exp}}{M_{FEA}}$	EI_{Exp} (kNm ²)	$\frac{EI_{Exp}}{EI_{AISC}}$	$\frac{EI_{Exp}}{EI_{ACI}}$	$\frac{EI_{Exp}}{EI_{EC4}}$	$\frac{EI_{Exp}}{EI_{AS5100}}$
60.5×2.8C0	9.2	3.8	1.00	1.00	--	--	31.62	--	--	--	--
60.5×2.8C40	12.5	4.6	1.35	1.22	4.7	0.97	33.44	0.66	0.78	0.71	0.65
60.5×2.8C40R	11.9	4.6	1.29	1.23	4.7	0.98	33.60	0.66	0.78	0.71	0.65
60.5×2.8C80	11.7	4.8	1.27	1.29	4.7	1.03	38.30	0.71	0.88	0.77	0.69
60.5×2.8C120	10.5	4.9	1.14	1.32	4.8	1.02	34.35	0.61	0.78	0.67	0.59
76.0×3.0C0	7.4	6.0	1.00	1.00	--	--	68.49	--	--	--	--
76.0×3.0C40	11.6	7.9	1.57	1.33	7.9	1.01	85.06	0.72	0.87	0.78	0.70
76.0×3.0C80	12.2	8.6	1.65	1.45	8.5	1.02	85.37	0.66	0.85	0.73	0.64
76.0×3.0C80R	11.4	8.3	1.55	1.39	8.5	0.98	88.75	0.69	0.88	0.76	0.67
76.0×3.0C120	12.2	8.7	1.65	1.45	8.4	1.04	79.12	0.59	0.78	0.66	0.57
114.3×3.0C0	3.1	12.9	1.00	1.00	--	--	233.41	--	--	--	--
114.3×3.0C40	10.3	19.3	3.31	1.49	16.8	1.15	254.01	0.57	0.73	0.62	0.53
114.3×3.0C80	12.2	21.3	3.89	1.65	18.8	1.13	315.63	0.64	0.87	0.70	0.58
114.3×3.0C120	9.6	21.2	3.08	1.64	21.0	1.01	370.86	0.70	1.00	0.78	0.64
165.2×3.0C0	1.3	23.1	1.00	1.00	--	--	868.27	--	--	--	--
165.2×3.0C40	7.3	39.1	5.55	1.70	36.7	1.07	874.59	0.56	0.76	0.60	0.50
165.2×3.0C80	7.1	41.0	5.42	1.78	40.3	1.02	900.01	0.51	0.74	0.55	0.44
165.2×3.0C120	7.1	41.6	5.41	1.80	41.1	1.01	1040.97	0.54	0.84	0.60	0.47
Average							1.03		0.63	0.82	0.69
COV							0.050		0.108	0.091	0.141

Table 8.2. Experimental results and comparison.

Specimen	M_{FEA} (kNm)	Specimen	M_{FEA} (kNm)	Specimen	M_{FEA} (kNm)
140×1C40	13.4	245×3.5C80	138.9	406×4.5C120	662.7
140×1C80	19.9	245×3.5C120	165.6	406×5C40	414.2
140×1C120	24.9	245×4C40	118.3	406×5C80	572.5
140×1.5C40	17.3	245×4C80	148.0	406×5C120	684.5
140×1.5C80	22.8	245×4C120	173.8	406×7C40	545.9
140×1.5C120	27.7	245×5C40	141.5	406×7C80	672.3
140×2C40	21.2	245×5C80	166.1	406×7C120	782.4
140×2C80	25.7	245×5C120	190.1	406×10C40	735.0
140×2C120	30.6	245×8C40	202.5	406×10C80	822.8
140×2.5C40	24.9	245×8C80	229.6	406×10C120	919.3
140×2.5C80	28.6	245×8C120	243.8	150×1C40	12.1
140×2.5C120	32.7	324×1.5C40	122.7	150×1C80	23.3
140×3C40	29.0	324×1.5C80	213.7	150×1C120	29.0
140×3C80	31.7	324×1.5C120	270.3	155×1C40	13.3
140×3C120	36.1	324×2C40	140.4	155×1C80	25.6
140×3.5C40	34.3	324×2C80	231.4	155×1C120	32.0
140×3.5C80	34.9	324×2C120	291.5	160×1C40	14.5
140×3.5C120	38.9	324×2.5C40	157.1	160×1C80	27.9
198×1C40	29.6	324×2.5C80	246.9	160×1C120	35.0
198×1C80	50.7	324×2.5C120	306.8	170×1C40	17.1
198×1C120	65.1	324×3C40	174.9	170×1C80	33.1
198×1.5C40	35.9	324×3C80	258.7	170×1C120	41.9
198×1.5C80	57.0	324×3C120	322.0	175×1C40	18.6
198×1.5C120	71.1	324×4C40	211.9	175×1C80	35.9
198×2C40	42.6	324×4C80	294.3	175×1C120	45.5
198×2C80	62.4	324×4C120	352.3	180×1C40	20.1
198×2C120	76.7	324×5C40	253.5	180×1C80	38.9
198×2.5C40	49.8	324×5C80	324.8	180×1C120	49.2
198×2.5C80	68.6	324×5C120	382.5	185×1C40	21.7
198×2.5C120	78.6	324×6C40	295.6	185×1C80	41.9
198×3C40	57.8	324×6C80	356.4	185×1C120	52.5
198×3C80	74.4	324×6C120	410.8	190×1C40	23.3
198×3C120	86.4	324×8C40	374.6	190×1C80	45.3
198×4C40	73.3	324×8C80	421.2	190×1C120	57.6
198×4C80	86.4	324×8C120	470.4	210×1C40	30.9
198×4C120	99.2	324×10C40	442.6	210×1C80	59.8
198×5C40	87.4	324×10C80	494.5	210×1C120	76.5
198×5C80	99.0	324×10C120	530.4	220×1C40	35.2
198×5C120	110.3	406×2C40	248.3	220×1C80	67.8

Table 8.3. Parametric study results (Cont.).



245×1C40	51.8	406×2C80	423.7	220×1C120	87.6
245×1C80	91.6	406×2C120	539.8	225×1C40	37.4
245×1C120	119.8	406×2.5C40	274.9	225×1C80	72.5
245×1.5C40	61.9	406×2.5C80	452.2	225×1C120	92.9
245×1.5C80	102.3	406×2.5C120	567.4	230×1C40	39.8
245×1.5C120	130.2	406×3C40	301.6	230×1C80	77.1
245×2C40	71.5	406×3C80	477.0	230×1C120	99.5
245×2C80	112.1	406×3C120	591.0	235×1C40	41.7
245×2C120	139.5	406×3.5C40	328.7	235×1C80	81.9
245×2.5C40	81.8	406×3.5C80	497.9	235×1C120	105.0
245×2.5C80	121.0	406×3.5C120	616.7	240×1C40	44.6
245×2.5C120	148.1	406×4C40	356.0	240×1C80	87.3
245×3C40	92.8	406×4C80	526.1	240×1C120	112.6
245×3C80	129.8	406×4C120	638.6	245×1C40	47.2
245×3C120	157.1	406×4.5C40	384.7	245×1C80	91.6
245×3.5C40	105.7	406×4.5C80	549.4	245×1C120	119.8

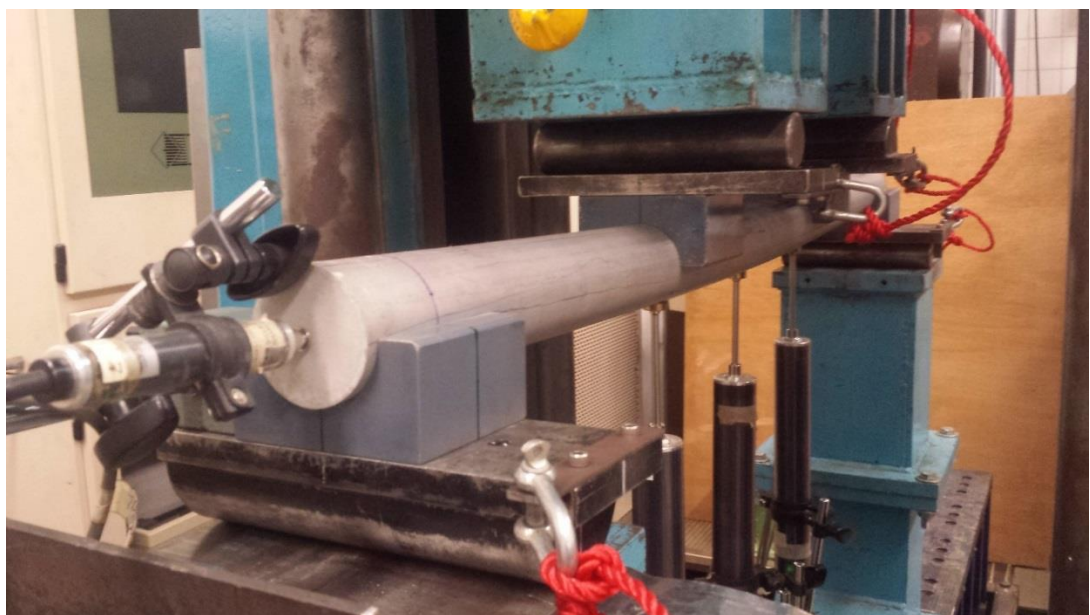
Table 8.3. Parametric study results (Cont.).

	$\frac{M_u}{M_{AISC}}$	$\frac{M_u}{M_{ACI}}$	$\frac{M_u}{M_{EC4}}$	$\frac{M_u}{M_{AS5100}}$	$\frac{M_u}{M_{Han}}$	$\frac{M_u}{M_{Han}^{\#}}$
Number of data	182	182	182	182	182	182
Mean (P_m)	2.64	2.71	2.45	2.73	2.19	1.00
COV (V_p)	0.401	0.458	0.406	0.406	0.320	0.062
Resistance factor (ϕ_0)	0.90	0.90	0.90	0.90	0.90	0.90
Reliability index (β_0)	3.39	3.11	3.13	3.31	3.51	2.52

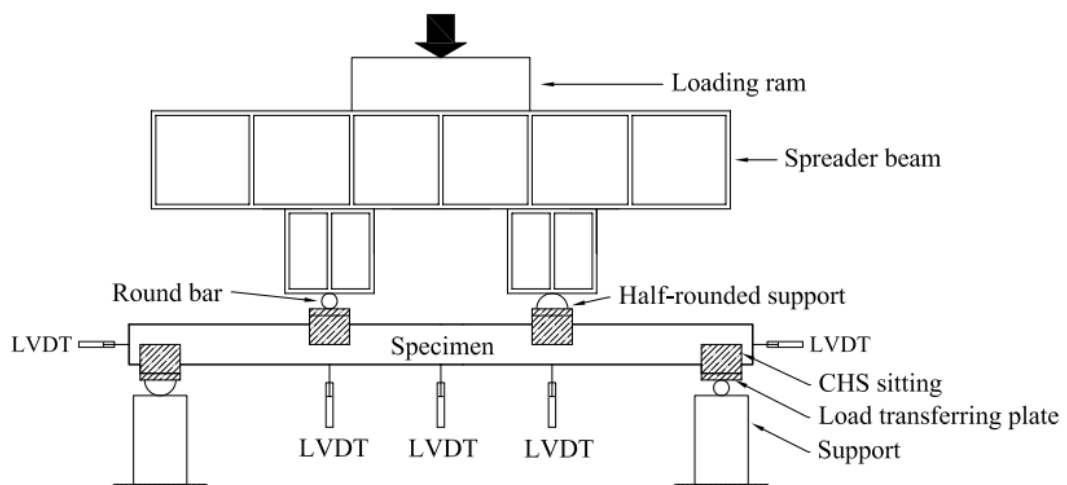
Note: $M_{Han}^{\#}$ modified Han (2004) method.

Table 8.4. Comparison of test and FEA strengths with design strengths.





(a)



(b)

Figure 8.1. Test arrangement for four-point bending tests.

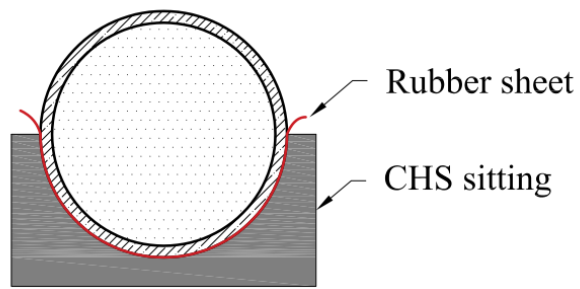


Figure 8.2. Stiffening at support.

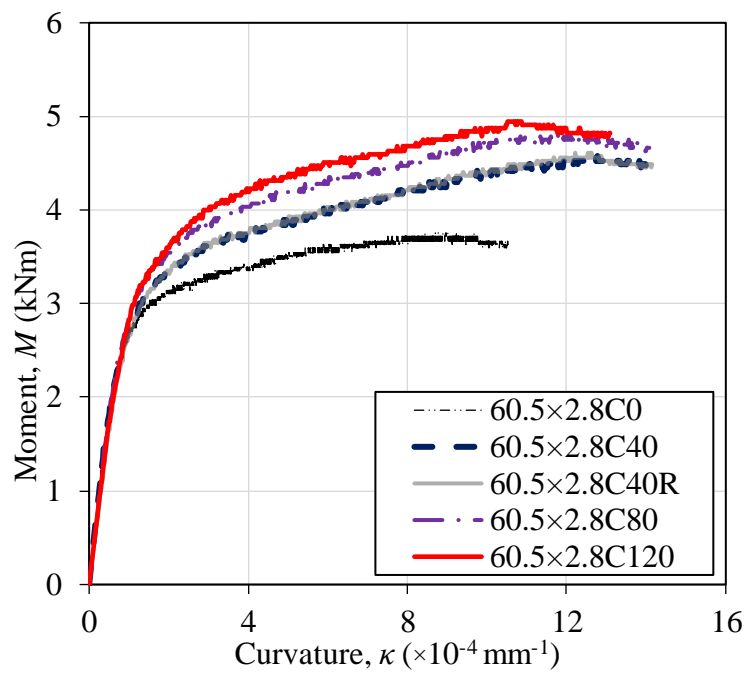


Figure 8.3. Moment-curvature curves of Section 60.5×2.8.



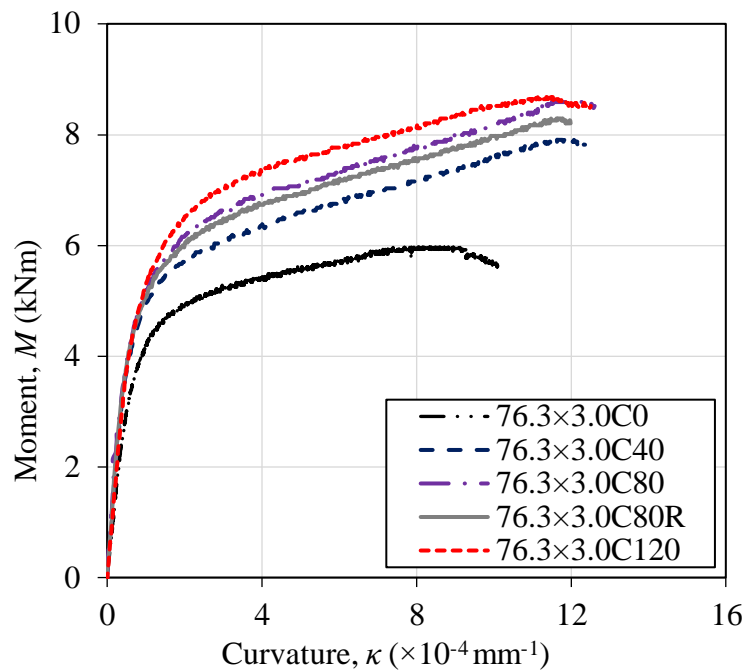


Figure 8.4. Moment-curvature curves of Section 76.3×3.0.

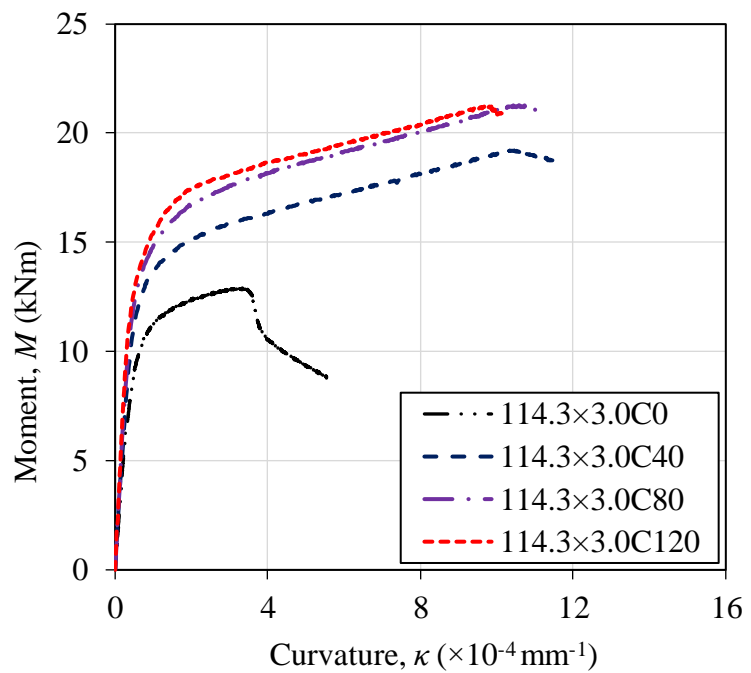


Figure 8.5. Moment-curvature curves of Section 114.3×3.0.



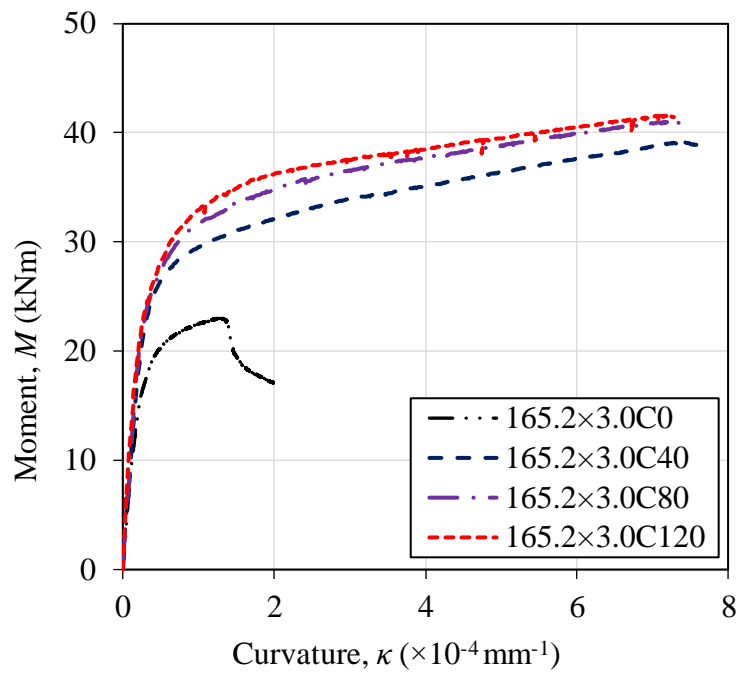


Figure 8.6. Moment-curvature curves of Section 165.2×3.0.

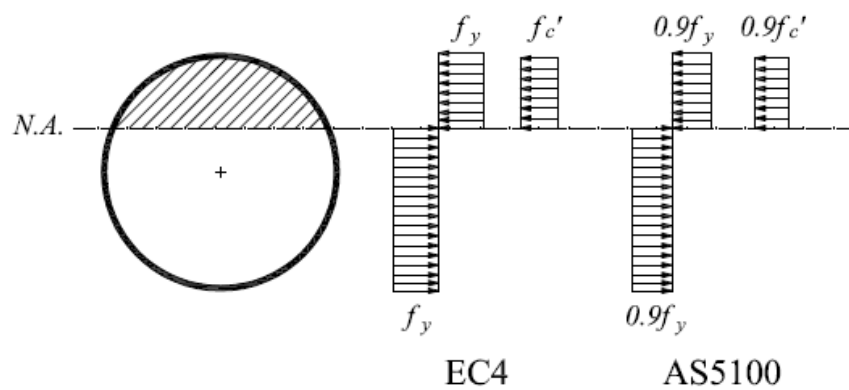
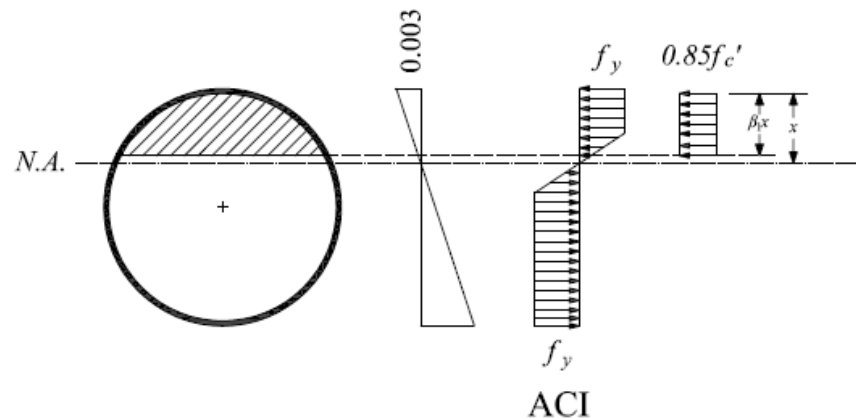
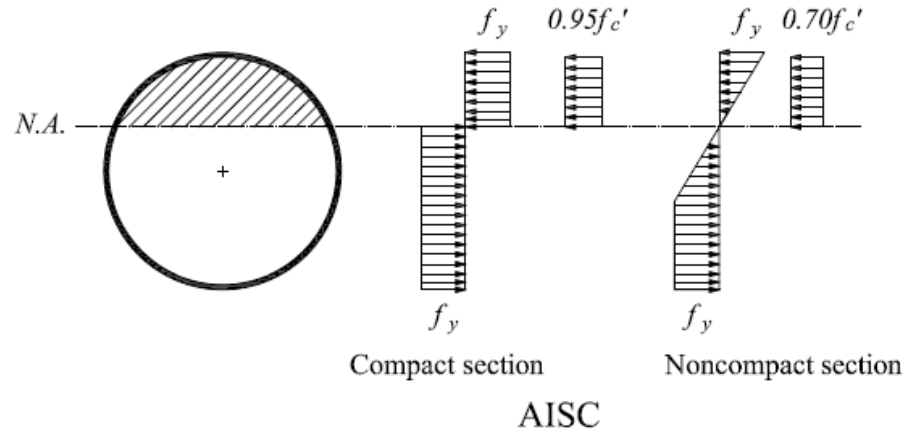


Figure 8.7. Stress blocks used to calculate the flexural strength of circular CFT beams.



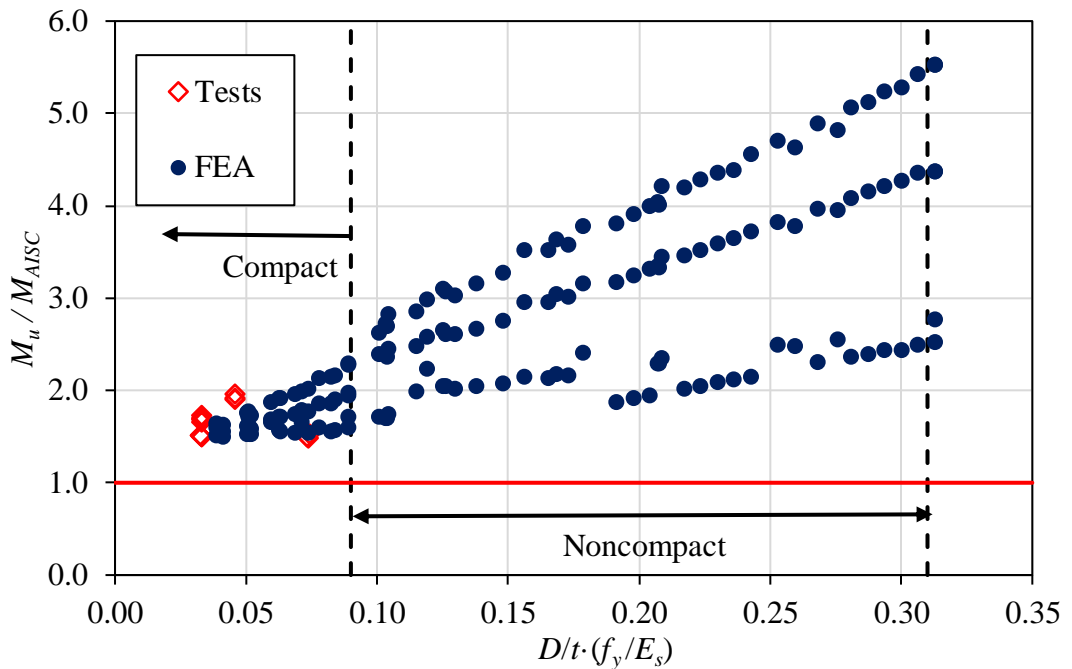


Figure 8.8. Comparison of experimental and numerical strengths with AISC 360 (2016) predicted strengths.

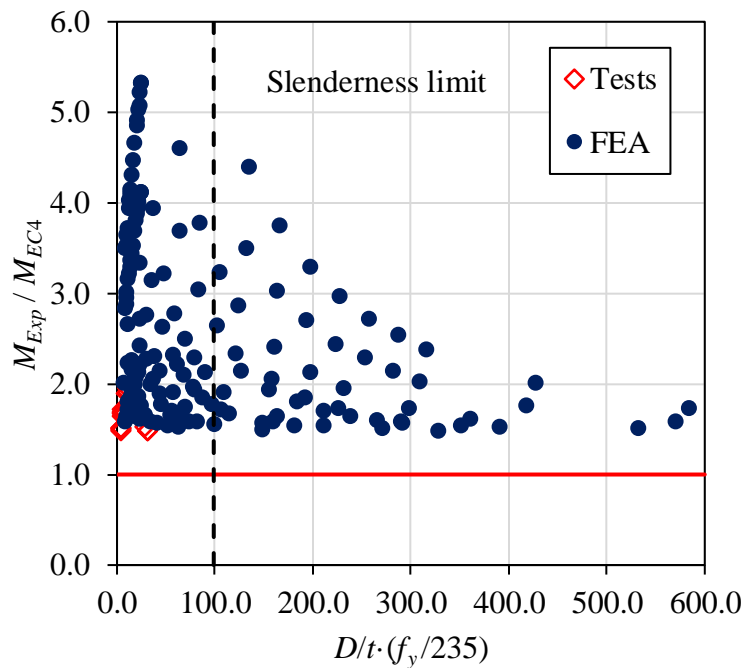


Figure 8.9. Comparison of experimental and numerical strengths with EC4 (2004) predicted strengths.



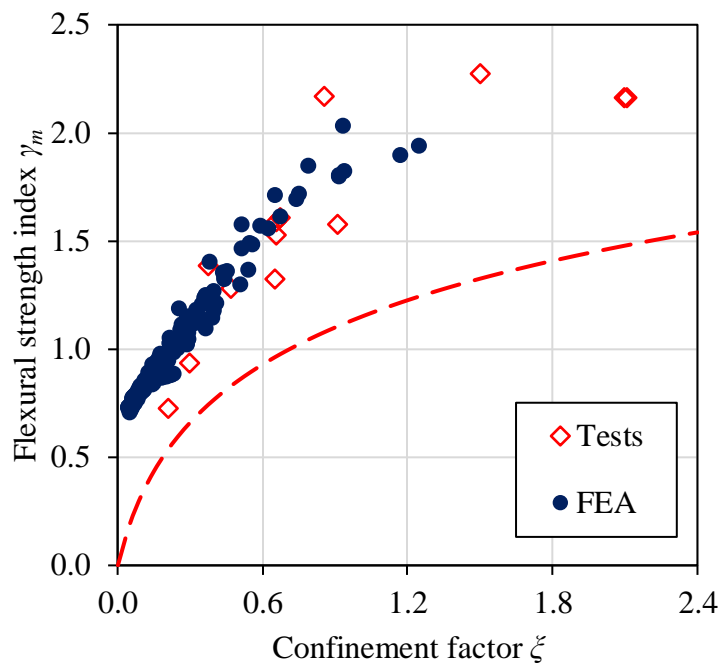


Figure 8.10. Comparison of experimental and numerical strengths with Han's (2004) predicted strengths.

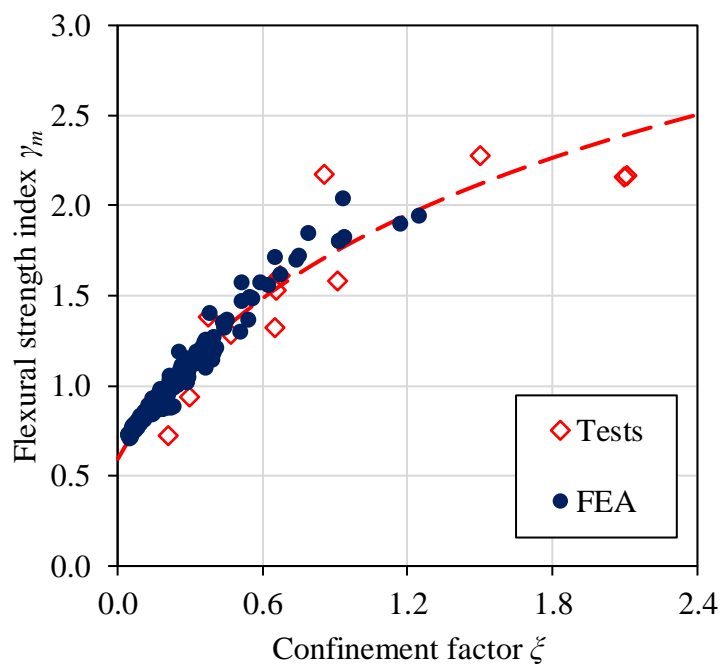


Figure 8.11. Comparison of experimental and numerical strengths with modified Han's method predicted strengths.



CHAPTER 9

BEAM-COLUMN BEHAVIOUR OF CONCRETE-FILLED COLD-FORMED FERRITIC STAINLESS STEEL SHS & RHS

9.1 Introduction

Ferritic stainless steel grade has a lower and stable price compared with the commonly used austenitic stainless steel grade. This is due to the low or even no nickel content. Cashell and Baddoo (2014) provides an overview of ferritic stainless steel, covering the basic physical and mechanical properties as well as the structural performance of ferritic stainless steel grade. Afshan and Gardner (2013a) studied the flexural behaviour of ferritic stainless steel hollow sections. Bock et al. (2015) studied the material and local buckling response of ferritic stainless steel sections. Zhao et al. (2015) studied the behaviour of ferritic stainless steel tubular cross-sections under combined loadings. Arrayago et al. (2015) performed a numerical study on the interaction of bending and axial load of ferritic stainless steel RHS columns. An experimental study on ferritic stainless steel SHS and RHS beam-columns was carried out by Arrayago et al. (2016). Zhao et al. (2016a) conducted a comprehensive experimental and numerical study on the member buckling behaviour of ferritic stainless steel tubes under combined axial load and bending. However, to date, the structural performance of concrete-



filled ferritic stainless steel members under combined axial load and uniform first order moment remains unexplored and it is one of the objectives of this study.

An experimental programme on concrete-filled cold-formed ferritic stainless steel beam-columns was carried out covering 48 combined loading tests. A finite element model was developed by verifying the test results. The verified model was also used to simulate the concrete-filled cold-formed ferritic stainless steel beam-columns and obtain further data in the parametric study that covering a wide range of section sizes and slenderness ratios. The experimental data together with the numerical results were used to assess the applicability of the current beam-column design provision provided in AISC 360 (2016), ACI 318 (2014) and EC4 (2004). The design proposals by other researchers were also carefully evaluated.

9.2 Experimental Investigation

9.2.1 General

A test program on the beam-column response of concrete-filled cold-formed ferritic stainless steel members was conducted. Ferritic stainless steel grade EN 1.4003 was used. Four different cross-sections, including one square hollow section and three rectangular hollow sections, were tested under minor axis bending. These cross-sections include SHS 60×60×3, RHS 40×60×4, RHS 40×100×2 and RHS 80×120×3. The infill concrete with nominal cylinder compressive strengths of 40 and 80 MPa was investigated. The specimens were labelled in such a way that the nominal dimensions including the overall depth of the web (D), overall width of the flange (B), thickness (t) of the cross sections, the nominal cylinder strength of the infill concrete and the nominal eccentricity can be identified. For example, the label “40×100×2C80e40” refers to the specimen



with nominal cross-sectional dimensions of depth (D), width (B), thickness (t) equal to 40, 100 and 2 mm, the infill concrete of nominal cylinder strength of 80 MPa and the nominal eccentricity was 40 mm. If a test was repeated, then a symbol of “R” would be added thereafter.

9.2.2 Material testing

Both the tensile flat and corner coupon tests were conducted to determine the stress-strain response of each cross-section. The test specimens used in this experimental study are from the same batch of specimens as those specimens presented in Chapter 3 of this thesis.

Standard concrete cylinders of size 150×300 mm were cast and tested to determine the compressive strength (f_c') and the elastic modulus (E_c) of infill concrete. Two cylinders were tested at 28 days after casting and four further cylinder tests were performed on the day of respective beam-column tests. To ensure the homogeneity and avoid any possible air trapped inside the specimens, a maximum aggregate size of 10 mm was specified for all concrete mixes. The elastic modulus of concrete was determined by suitable compressometer in according to ASTM C469 (2014). The average measured concrete cylinder compressive strengths for the nominal 40 and 80 MPa concrete were 37.8 and 81.9 MPa, whilst the corresponding elastic moduli were 24.9 and 35.4 GPa, respectively.



9.2.3 Test specimens

Concrete-filled cold-formed ferritic stainless steel members were tested under combined axial compressive load and bending in this study. A total of 48 specimens was tested and bent about the minor axis. The specimens of cross-sections RHS 40×60×4, RHS 40×100×2 and SHS 60×60×3 were cut into the length of 490 mm and the section RHS 80×120×3 was cut into 470 mm due to the limited headroom of the testing machine. All the specimens were milled flat at the two ends before welding to end plate at one end, while the other end was left open for concrete casting. In order to fill the small gap due to shrinkage and achieve uniform compressive load to the stainless steel tube and concrete, a thin layer of plaster was applied to the open end of the specimen before welding of the other end plate. The specimen dimensions are reported in Tables 9.1 – 9.4, where D is the overall depth of cross-section, B is the overall width of cross-section, t is the plate thickness, r_o and r_i are the external and internal corner radii, L_e is the effective member length measured between the pinned ends, A_s and A_c are the cross-sectional area of stainless steel section and concrete portion, respectively, f_c' is the measured cylinder strength of the specimens. The measured eccentricity values ($e + \delta_0$) that include the global imperfections δ_0 are also reported in the last column of the tables.

The specimens were grouped into 8 series according to the sections and the strength of infill concrete. In each series, one specimen was loaded concentrically with the eccentricity smaller than 0.3 mm, which is considered as a column loaded through the centroid and represent the ‘end point’ on the axial load axis of the load-moment interaction curve. The other 5 beam-columns were loaded with different eccentricities to provide a range of axial load-to-moment ratio. Three specimens were chosen to be repeated to check the reliability of the tests.



9.2.4 Imperfection measurements

Prior to the member tests, the initial geometric local imperfections of the specimens were measured for each section. Measurements were not conducted specifically for each test specimen but carried out over a representative length of each section size. The maximum measured local imperfections were 0.249, 0.168, 0.341 and 0.468 mm for sections 40×60×4, 60×60×3, 40×100×2 and 80×120×3, respectively, as mentioned in Chapter 5 of this thesis.

Initial global geometric imperfections δ_0 were measured for each beam-column specimen. After the specimen was positioned in the test rig and prior to applying loading, a Leica TCR405 total-station was used to obtain readings from the mid-height and near both ends of the specimen. The measurements were taken at the flat width near the corner of the section, and the sign convention of the measurements is shown in Fig. 9.2. The measured values of global imperfections are summarized in Table 9.5 and were divided by the corresponding member length. The average absolute values of the global geometric imperfections at mid-height were L/3289, L/1851, L/5926 and L/3167 for specimens of series 40×60×4, 60×60×3, 40×100×2 and 80×120×3, respectively. These numbers are significantly smaller than the prescribed value of L/300 specified in EC4 (2004).

9.2.5 Beam-column tests

Six beam-column tests under uniaxial bending and compression were performed for each cross-section for different concrete strengths. The nominal initial loading eccentricities were carefully chosen to obtain an evenly distributed range of load-moment interaction curve. The beam-column tests of series 40×60×4, 60×60×3 and 40×100×2 were conducted using a 1000 kN hydraulic testing machine, as



shown in Fig. 9.3. While the series 80×120×3 were conducted using an INSTRON 5000 kN hydraulic testing machine due to the loading capacity of the testing machine, as shown in Fig. 9.4. Pin-ended conditions were simulated by two pin-ended bearings, which allowed free rotation about the minor axis only. Each pin-ended bearing was made of a wedge plate containing a knife-edge wedge and compressed between the parallel pit plates with V-shaped grooves. The specimens were welded to 25 mm end plates and bolted to the wedge plates. It should be noted that the wedge plates had slot holes to allow the adjustment of different loading eccentricities measured based on the relative positions of the centerline of the specimens to the knife-edge.

The axial shortening and end-rotation of the specimens were measured by three displacement transducers (LVDTs) located vertically at one end of the members, as shown in Figs 9.3 and 9.4. The two LVDTs placed at the front were positioned 70 mm from the knife-edge wedge and the end-rotation was determined by dividing the absolute difference of the two LVDTs to the horizontal distance. The horizontal deflections of the beam-columns during loading were captured by the LVDT positioned at the mid-height of the specimens. Four strain gauges were attached in the longitudinal direction on either side of the sections near the corners at mid-height of the specimens, as shown in Fig. 9.5. The readings from the strain gauges comprise two components, strains due to axial compression and strains due to bending moment. The strains due to bending moment were used to determine the actual initial loading eccentricities, similar procedures were adopted in Zhao et al., (2016a), Huang and Young, (2014b), Ma et al., (2015a). An additional strain gauge was attached at the center parallel to the other two gauges of the more compressed face in order to detect any local buckling. The beam-column tests were conducted under displacement-control method with a constant



loading rate of 0.3 mm/min throughout the tests. The applied load, readings from LVDTs and strain gauges were recorded at a regular interval.

9.2.6 Determination of loading eccentricities

The loading eccentricities were carefully measured for each specimen and the measured eccentricities were used to determine the nominal strengths. Prior to beam-column testing, the specimens were carefully put onto the wedge plates with the designated eccentricities. Four strain gauges and the horizontal transducer were connected to the data acquisition system to obtain the strain and lateral deflection at mid-height of the specimens. To ensure full contact of the beam-column specimens, a compressive load of less than 3 kN was applied. The pre-loading force was negligible compared to the ultimate loads.

The actual eccentricities were determined by two methods for each specimen. The strain gauge method involves determination of curvature (κ) of the specimen. The loading eccentricity was calculated by $e + \delta_0 = EI\kappa / N - \delta_y$, where δ_0 is the initial global geometric imperfection, EI is the flexural rigidity of the cross-section about the plane of bending, δ_y is the lateral deflection at mid-height of the member for each loading step N . Similar method was adopted by Arrayago et al., (2016), Zhao et al., (2016a), Huang and Young, (2014b) and Ma et al., (2015a). The total station method involves comparing the space coordinates of the center point on the front face of the specimen and the center of the knife edges. The center point on the front face of the specimen was carefully marked prior to testing, which is similar to Ma et al. (2015a). The measured loading eccentricities were taken from the strain gauge method for eccentricities up to 40 mm, while the values from the total station method was used for eccentricities beyond 40 mm.



The results of the measured eccentricities are presented in the last columns of Tables 9.1 – 9.4.

9.3 Experimental Results

9.3.1 Failure mode and ultimate loads

All the tested beam-columns failed by global flexural buckling, and most of them exhibited large second-order effects under axial loads, as shown in Fig. 9.6 for the series 40×60×4C80. The ultimate loads obtained from the experiments $N_{u,\text{exp}}$ are presented in Table 9.6, along with the ultimate end moment $M_{u,\text{end}} = N_{u,\text{exp}} \cdot e$ and the second-order inelastic ultimate moment at mid-height calculated by $M_{u,\text{mid}} = N_{u,\text{exp}} \cdot (e + \delta_0 + \delta_y)$ corresponding to ultimate axial loads. The pure bending moment capacities of all the sections were obtained through four-point bending tests and reported in Chapter 7 of this thesis. Full measured experimental axial load N versus the end moment M_{end} and mid-height moment M_{mid} curves for all the tested specimens are presented in Fig. 9.7 (a)-(h).

9.3.2 Load-deformation behaviour

The load-deformation behaviour of the beam-columns generally refer to axial load against lateral deflection at mid-height (δ_y) and axial load versus axial displacement (Δ), as shown in Fig. 9.8 (a)-(b) for series 80×120×3C40. The lateral deflection at mid-height at ultimate axial load is directly affected by the load eccentricity (e) and as the eccentricity increases, the lateral deflection at mid-height at ultimate axial load increases. The lateral deflection was not obvious before the peak load was reached and developed progressively after the peak load was reached, especially for those specimens with small loading eccentricities. The



loading eccentricity (e) has insignificant influence on the column axial stiffness, as shown in the axial load versus axial displacement curves. Owing to the utilization of stainless steel, all the composite columns exhibited ductile behaviour.

9.3.3 Confinement factor

The confinement factor (ξ), used by Han (2004) and it is commonly known as relative strength ratio by Lai et al. (2015) or constraining factor by Han (2002), is adopted herein to depict the sectional property of the specimen. The relative strength ratio is defined as follows:

$$\xi = \frac{A_s f_y}{A_c f_c} \quad (9.1)$$

This factor combines the effect of the tube cross-sectional area (A_s / A_c) and the material strength ratio (f_y / f_c). Generally, as the relative strength ratio (ξ) increases, the beam-column behaves more like a column. While the behaviour of beam-column and its corresponding P-M interaction becomes more like that of a reinforced concrete member (Lai et al., 2015), as shown in Fig. 9.9 (a). The values of ξ are summarized in Table 9.6. The ultimate axial loads and corresponding moments are normalized by the estimation of axial and flexural strength predicted by AISC 360 (2016) and plotted based on the average relative strength ratio for some of the test specimen series, as shown in Fig. 9.9 (b). The effect of relative strength ratio is graphically presented and agreed with the findings reported by Lai et al. (2015).



9.3.4 Strength index

The strength index (SI) is used by McCann et al. (2015) and Chan et al. (2015) to depict the utilization of the full compressive resistance of a concrete-filled steel tube column. The strength index is defined as $SI = N_{u,\text{exp}} / N_0$, where N_0 is the nominal squash load defined as sum of the strengths contributed by the individual components $N_0 = A_s f_y + A_c f_c'$.

The values of the SI were calculated based on the measured geometric and material properties for individual specimen and summarized in Table 9.6. It is clearly shown that the beam-columns with smaller load eccentricities utilize more of their plastic resistance as expected. In addition, the beam-columns filled with normal strength concrete utilize more of their plastic resistance than those with high strength beam-columns. This suggests that the combination of the ferritic stainless steel and normal strength concrete better utilize both the stainless steel and concrete material strength by developing favor composite action.

9.3.5 Ductility index

The ductility index (DI) is an indicator of the ductility on maintaining the ultimate load adopted by Han (2002) and Chan et al. (2015). The DI is detailed in Section 5.3.5 of this thesis. The values of DI are shown in Table 9.6 and the values of some specimens are not available due to the tests were stopped before the load drop to 85% of the ultimate load. Generally, the values of DI for specimens with normal strength concrete infill are larger than those with high strength concrete infill, which indicates that the specimens with normal strength concrete infill failed in a more ductile manner.



9.4 Finite Element Model and Verification

9.4.1 Development of finite element model

The experiments provided valuable data for assessing the available design rules. However, there are still gaps in the experimental database. Therefore, finite element model was developed to conduct an extensive parametric study and extend the pool of data to cover a wider range of slenderness ratios, especially for the noncompact and slender sections. The development of the finite element models for predicting the behaviour of concrete-filled ferritic stainless steel stub columns and beams are detailed in chapters 5 and 7 of this thesis. The details of the finite element model of concrete-filled ferritic stainless steel beam-columns are similar to those presented earlier and also reported here for the ease of reference. The finite element package ABAQUS version 6.14 (ABAQUS, 2014) was used to perform the numerical study in parallel with the experimental study. The finite element model was verified against the experimental results presented in this chapter.

9.4.2 Element types

The stainless steel tubes of the concrete-filled members were modelled using the 4-noded shell element with reduced integration (S4R), which is a robust quadrilateral element used for modelling steel section. The S4R element has six degrees of freedom per node and reduced integration in the plan of elements, which can reduce the computational time compared with the S4 element. The S4R element can take account for finite membrane strains and arbitrarily large rotation, which is suitable for large strain analysis (Ellobody, 2015). The infill concrete was modelled using the continuum elements having 3D eight nodes with reduced



integration (C3D8R). These elements have three degrees of freedom per node and reduced integration. This kind of elements can be computationally effective in modelling cracking of concrete (Ellobody, 2015).

9.4.3 Material modelling

The stainless steel material behaviour was defined using nonlinear stress-strain curves, comprising an elastic part up to the proportional limit and a plastic portion of true stress and logarithmic true plastic strain. The measured stainless steel stress-strain curves from flat and corner tensile coupon tests were included in the finite element model. In order to account for the significant strength enhancement of the corner region due to the cold-rolling process, the corner properties were extended beyond the curved corner portions into the flat portions by the length of two times the thickness of the section, as shown in Fig. 9.10. Gardner and Nethercot (2004b) and Ma et al. (2015b) also considered the strength enhancement of the corner region that extended into the flat portions. Residual stress was not explicitly included in the steel material model. Previous researchers (Huang and Young, 2012; Ma et al., 2015c) have illustrated that the membrane residual stress was small compared to that of bending residual stress and the membrane residual stress was negligible in the model. Considering the bending residual stress, which is approximately reintroduced during tensile coupon testing when the coupon specimen was returned to straight under the tensile force, is thus considered to be inherently included in the obtained material property from the tensile coupon tests (Zhao et al., 2016b).

The concrete material multiaxial behaviour was modelled using damaged plasticity material model. The elastic modulus of concrete (E_c) was taken as the



measured value in the experimental study and the Poisson's ratio (ν_c) was taken as 0.2 as recommended by ACI 318 (2014). All the key parameters and the stress-strain relationship of confined concrete followed the proposed values in Tao et al. (2013).

9.4.4 Boundary conditions

The beam-columns were compressed under pin-ended condition and bent about the minor axis. The end boundary condition was simulated by coupling all degrees of freedom, except for rotations about minor axis and longitudinal displacement, to an eccentric reference point for the applied load end. Similar configuration was setup for the other end of the members, except that the longitudinal displacement was also restrained. The nodes other than the two ends were free to rotate and translate in any directions. The effective length (L_e) of the column was assumed to be equal to the distance between the two knife-edge wedges, in accordance with the actual experimental setup. The eccentric reference point was offset longitudinally from end of the specimen by 87.4 mm, which is sum of the thickness of end plate (25.4 mm) and thickness of wedge plate (38 mm) as well as the thickness of knife-edge wedge (24 mm). The eccentricity was equal to the corresponding measured value employed in the tests.

9.4.5 Interaction of contact surface between concrete infill and stainless steel tube

The contact interaction between the stainless steel and concrete infill was modelled in both the normal and tangential directions. The interaction in the normal direction was simulated using hard contact with penalty method. The hard contact relationship can minimize the penetration of the slave surface to the



master surface at the constraint locations. The contact in tangential direction follows the Coulomb friction model proposed by Han et al. (2007). The friction model allows stress transmission between the stainless steel tube and concrete up to the limit τ_{crit} . The coulomb friction coefficient between the stainless steel tube (master surface) and the concrete infill (slave surface) was set to be 0.6. No additional bond between the stainless steel tube and concrete infill such as adhesive bonding was included in the model. The shear stress limit was calculated using Eq. (9.3) specified in Han et al. (2007) as follows:

$$\tau_{crit} = 0.75 \left[2.314 - 0.0195 (\max[D, B]/t) \right] > 0 \quad (9.3)$$

9.4.6 Global imperfections and loading conditions

The measured overall global imperfections of the columns were also included in the finite element model. The lowest global buckling mode shapes, which were obtained by conducting eigenvalue buckling analysis and representing the most unfavorable imperfection pattern, were incorporated into the finite element model. The BUCKLE procedure available in the ABAQUS library was used and the values of the lowest buckling mode were normalized to 1.0 and then the buckling mode was factored by the measured imperfection magnitudes (δ_0) of each column. Three more different imperfection amplitudes were also utilized to factor the lowest buckling mode shape in the model, including the two commonly assumed global imperfection values $L/1500$ and $L/1000$ as well as the value $L/300$ specified in EC4 (2004), in order to investigate the sensitivity of the finite element model to various imperfection levels and seek the most suitable amplitude in modelling the global imperfection. Upon the incorporation of global imperfection, axial loads were applied by specifying an axial displacement to the loaded end



using a static RIKS step. Large displacement analysis was allowed by using nonlinear geometric parameter (*NLGEOM).

9.4.7 Validation of finite element model

The finite element model was validated with the pin-ended beam-columns tests conducted in the experimental study. Key parameters, such as ultimate load, moment at ultimate load and load-deformation curves derived from numerical results are presented. Table 9.7 summarizes the ratios of experimental to numerical ultimate loads and corresponding moments, for various imperfection amplitudes. It is observed that the predicted ultimate loads agree well with the experimental ultimate loads for the four imperfection amplitudes. The largest difference (7%) in term of the average experimental-to-numerical ratio ($N_{u,\text{exp}} / N_{\text{FEA}}$) was found on the specimens with imperfection amplitude of $L/300$. This indicates that the ultimate loads are relatively insensitive to the change of global imperfection amplitudes. In contrast to the ultimate load predictions, the moments at ultimate loads were sensitive to the imperfection amplitudes. The model with measured imperfection amplitudes (δ_0) provide the most accurate predictions with $M_{u,\text{exp}} / M_{\text{FEA}}$ equals to 1.06 and *COV* of 0.172, whereas the model with imperfection amplitude of $L/300$ provides the worst predictions with $M_{u,\text{exp}} / M_{\text{FEA}}$ equals to 1.18 and *COV* of 0.942. Overall, the model with the measured imperfection amplitudes (δ_0) achieved the best agreement between the experimental and numerical results for providing safe, accurate and consistent results. It is thus chosen to perform the parametric study of the concrete-filled cold-formed ferritic stainless steel beam-columns.

Comparisons between the experimental and numerical load-deformation curves are shown in Fig. 9.11, where the numerical load-lateral deflection at mid-height curves seems accurately simulated the experimental results. It is observed that the finite element model can accurately predict the loading history including the initial stiffness, ultimate strength and deformation of the columns.

9.5 Parametric Study

In this section, a series of parametric study is presented using the validated finite element model described in Section 9.4 of this thesis, in order to generate more data on concrete-filled stainless steel columns under combined axial load and bending. The adopted ferritic stainless steel stress-strain curve was obtained from the tensile flat and corner coupon tests on material cut from the specimen RHS $80 \times 120 \times 3$ as presented in Chapter 3 of this thesis. The measured concrete cylinder compressive strengths for the nominal 40 and 80 MPa in the experimental tests were used in the parametric study. Residual stresses and the initial local imperfections were not explicitly incorporated in the finite element model. The global imperfection amplitudes were taken as the average value of $L/3000$ measured from the experimental specimens, which were shown to provide the most accurate predictions. All the specimens in the parametric study were bent about the minor axis. The end section boundary conditions were applied by coupling all degrees of freedom of the end section to an eccentric reference point of 87.4 mm from the ends of the specimen, which is identical to that in the experimental study. The end sections were allowed to translate in longitudinal direction and rotated about the axis of buckling only.

The parametric study consists of two parts, targeting in both the cross-sectional and member resistances. The cross-sectional resistances to combined loading were



studied by specifying the length of each specimen equal to 600 mm. The selected length was less than three times the outer cross-sectional width. The sections of SHS 300×300 and RHS 350×200 were adopted and the thicknesses were varied to cover a wide range of section slenderness. The cross-sectional thickness (t) ranged from 2.5 to 10.0 mm and resulting in flat-width-to-thickness ratios (b/t) from 26.0 to 136.0, covering both compact, noncompact and slender sections according to the slenderness limits in AISC 360 (2016). A total of 149 numerical results on the cross-sectional behaviour of concrete-filled cold-formed ferritic stainless steel beam-columns were generated and summarized in Table 9.8.

Specimens with length of 2800 mm were used to investigate the member resistances of concrete-filled cold-formed ferritic stainless steel members subject to combined loading conditions. The sections of SHS 300×300 and RHS 350×200 were adopted and the thicknesses were varied from 3.5 to 10.0, with the flat-width-to-thickness ratio (b/t) ranging from 26.0 to 71.0, which covers mainly compact sections. A total of 90 numerical results were generated and summarized in Table 9.9. The 90 numerical results together with the 48 experimental results were used to assess the available design equations for member resistances of CFTs under combined loading conditions.

The numerical specimens were labelled in the same way as that for the experimental specimens. The nominal dimensions including the overall depth of the web (D), overall width of the flange (B), thickness (t) of the cross-section, the nominal cylinder compressive strength of the infill concrete and the nominal eccentricity can be identified. For example, the label “200×350×5C80e200” refers to the specimen with nominal cross-sectional dimensions depth (D), width (B), thickness (t) equals to 200, 350 and 5 mm, the infill concrete nominal cylinder



strength of 80 MPa and the nominal eccentricity is 200 mm. The initial loading eccentricities ranged between 0 mm and 600 mm to obtain evenly distributed points on the axial load-moment interaction curves.

9.6 Reliability Analysis

Reliability reflects the ability of a structure or a structural member to fulfill the specified requirements and the reliability of design rules and expressions can be assessed by rationalized approaches detailed in different design codes or specifications. The reliability of design rules and expressions should pass the prescribed target reliability index, which is determined on a probabilistic basis. The aim of the reliability analysis is to derive the reliability index and partial safety factors for each design method to assess whether the level of reliability of the resistance function is in accordance with American specification AISC 360 (2016) and European code EC0 (2002).

9.6.1 AISC approach

Reliability analysis by the AISC approach is detailed in the Chapter B in the Commentary of AISC 360 (2016). The generic Load and Resistance Factor Design (LRFD) limit state design format given in AISC 360 is $\sum_{i=1}^j \gamma_i Q_{im} \leq \phi R_n$, where Q_{im} is the mean load effect, γ_i is the load factor corresponding to Q_{im} , R_n is the nominal resistance and ϕ is the resistance factor corresponding to R_n . Since the target reliability index (β_0) is not specified for concrete-filled stainless steel tube members in the specification, the value of 2.50 is used as a lower limit in this study. In addition, the AISI Commentary AISI-S100C (2016) also recommends β_0 to be taken as 2.50 for structural members. The design rules are considered to be reliable and safe if the reliability index is greater than 2.50. The resistance



factor (ϕ_0) of 0.90 is used in this study for the concrete-filled cold-formed ferritic stainless steel tubes under combined axial load and bending. The load combinations of 1.2DL+1.6LL and 1.35DL+1.5LL were used in calculating the reliability index (β_0) for AISC 360 and EC4 respectively, where DL is the dead load and LL is the live load. The load combination of 1.2DL+1.6LL was used for the proposed design equations by Choi et al. (2006), Choi et al. (2008) and Lai et al. (2015).

The Eq. C-B3-2 in AISC 360 (2016) was used in calculating the reliability index.

The reliability expressions for AISC and EC4 are shown in Eqs (9.4) and (9.5):

$$\beta = \frac{1}{\sqrt{V_R^2 + V_Q^2}} \ln \left[\frac{R_m}{0.657\phi R_n} \right] \quad \text{AISC} \quad (9.4)$$

$$\beta = \frac{1}{\sqrt{V_R^2 + V_Q^2}} \ln \left[\frac{R_m}{0.683\phi R_n} \right] \quad \text{EC4} \quad (9.5)$$

where V_Q is the coefficient of variation of the mean load effect and it is taken as 0.21 in this study and,

$$V_R = \sqrt{V_M^2 + V_F^2 + C_p V_P^2} \quad (9.6)$$

$$C_p = \sqrt{\frac{n-1}{n-3}} \quad (9.7)$$

$$\frac{R_m}{R_n} = M_m \times F_m \times P_m \quad (9.8)$$

where C_p is a correction factor considering the number (n) of tests, P_m is the mean values of experimental-to-design or FEA-to-design load ratios, and V_P is the coefficients of variation of experimental-to-design or FEA-to-design load ratios. The statistical parameters $M_m = 1.10$, $F_m = 1.00$, $V_m = 0.10$ and $V_F = 0.05$,



which are the mean values and coefficients of variation for material properties and fabrication factors were adopted. The values of reliability index are shown in Table 9.10 for corresponding design rules.

9.6.2 Eurocode approach

The EC0 (2002) employs first order reliability method (FORM) for calibration of design functions. The design working life for building structures and other common structures is 50 years as specified in EC0 (2002). The minimum reliability index for a 50-years structure is 3.8, which implies that all the designs using Eurocode with the required partial safety factors could bring a structure with β greater than 3.8 and corresponds to a probability of failure of 10^{-6} per year over a 50-year design life. The aim of the reliability analysis is to determine appropriate partial safety factors for the cross-sectional and member resistance. The partial safety factors reflect the level of reliability of the resistance functions are determined conforming to EC0 (2002).

The reliability of the proposed design equations was demonstrated through statistical analysis in accordance with EC0 (2002). Table 9.11 summarizes the key statistical parameters adopted in the Eurocode reliability analysis. These parameters include the design (ultimate limit state) fractile factor $k_{d,n}$, which was determined for the case “ V_x unknown” for n tests and n is the population of the experimental and numerical data under consideration, and b is the average ratio of experimental and numerical data to design model resistance based on a least square fit to all data, V_δ is the *COV* of the tests and numerical simulations relative to the resistance model, V_r is the combined *COV* incorporating both model and basic variable uncertainties, and γ_{M0} and γ_{M1} are the partial safety factors. The



currently adopted values of γ_{M0} and γ_{M1} for cross-sectional and member resistance are 1.10 in EC3 (2015). The ratio of mean to nominal yield strengths (i.e. the material over-strength) is 1.2 and the *COV* of yield strength and geometrical properties are taken as 0.045 and 0.050, as recommended by Afshan et al. (2015). The material over-strength ratio is defined as the ratio of the mean value of the yield strength produced by the manufacturers to the specified value in EN 10088-4 (2009). The results from reliability analysis by Eurocode approach are presented in Table 9.11.

9.7 Comparisons Between Tests and Code Predicted Strengths

9.7.1 General

There are several well-known national standards or recommendations to address the design of concrete-filled carbon steel tubes under combined axial load and bending. However, none of these design codes or specifications is available for concrete-filled stainless steel members. Based on the comprehensive experimental and numerical results obtained in this chapter, the design codes were compared with the test and finite element results to assess their applicability. For all the comparison made in this study, all the material partial safety factors are set to be unity and the material properties are taken as the measured values. In addition, limitations in all the codes on the concrete strength and steel strength are ignored to check the feasibility of the design codes beyond the current limits.

The accuracy of each design code or method is assessed against the experimental and numerical results under combined axial load and bending. The comparison was made by calculating the axial load ratio $N_u / N_{u,pred}$, in which N_u is the



experimental or numerical axial load corresponding to the distance on the axial load-moment (N - M) interaction curve from the origin to the experimental or numerical data point, while $N_{u,prep}$ is the predicted axial load corresponding to the distance from the origin to the interaction point with the design interaction curve, assuming proportional loading. An example showing the determination of $N_{u,prep}$ from the experimental or numerical axial load and the interaction curve for combined axial load and bending is illustrated in Fig. 9.12. The value of $N_u / N_{u,pred}$ larger than unity with the experimental or numerical data lying outside the interaction curve indicates that the design is safe. This comparison method is adopted for all the following design codes or methods, except for EC4 (2004).

There are mainly three forms of methods or approaches adopted by different design codes or specifications. The Form-A method uses a nonlinear function to represent the axial load-moment curve, which is based on numerical integration of resultant sectional strength. The European code EC4 (2004) adopted this method to describe the CFT column response to combined axial load and bending. The Form-B method simplifies the Form-A expression by using a multilinear curve connecting the four critical points. The Form-C is further simplifying Form-B by using the bilinear functions to reflect the predicted behaviour of CFT columns, as shown in Fig. 9.13. This form of expression is simple and convenient to use but conservative results can be anticipated compared with the other two methods.

9.7.2 AISC 360

The concrete-filled steel tubes are categorized as compact, noncompact or slender sections depending on the governing slenderness ratio (b/t) and the respective slenderness limits specified in AISC 360 (2016). The slenderness limit also



depends on the loading conditions including either axial compression or flexure, as shown in Table 9.12. The slenderness limit of member subjected to both axial compression and flexure should be the governing one determined from both the axial compression slenderness and flexure slenderness separately. The member is classified as compact if the governing slenderness ratio is less than the compactness limit (λ_p). If the tube slenderness ratio is larger than the compactness limit (λ_p) while smaller than the noncompactness limit (λ_r), then it is classified as noncompact. Those members with governing slenderness ratio larger than the noncompactness limit (λ_r) are categorized as slender sections. The design of CFTs in AISC 360 (2016) is limited to members within the maximum allowable limit (λ_{limit}).

The AISC 360 (2016) provides two design methods for the design of CFT beam-columns. The Method 1, referred as AISC-1 in the following, uses the Eqs (9.9) and (9.10) for the interaction curve between axial load and moment for columns in all classes including the noncompact and slender ones. The interaction equations for pure steel columns are maintained and applied for CFT columns, for which the expected beneficial effects from the concrete core are ignored.

$$\text{When } \frac{N_u}{N_n} \geq 0.2 \quad \frac{N_u}{N_n} + \frac{8}{9} \frac{M_u}{M_n} \leq 1.0 \quad (9.9)$$

$$\text{When } \frac{N_u}{N_n} < 0.2 \quad \frac{N_u}{2N_n} + \frac{M_u}{M_n} \leq 1.0 \quad (9.10)$$

where N_u is the required axial strength and M_u is the required flexural strength; the nominal axial strength N_n and nominal flexural strength M_n are specified in AISC 360. The nominal axial strength N_n for sectional strength of CFT member is determined from Section I2.2 of the AISC 360 (2016), while the axial strength in member scale is calculated conformed to Section I2.1 of the AISC 360 (2016).



The AISC Method 1 is expected to provide conservative predictions on the beam-column response of CFT members. The mean ratio of experimental and numerical strengths to predicted strengths N_{u-s} / N_{AISC-1} is 1.84 with *COV* of 0.230 in terms of cross sectional strength, as shown in Table 9.10 and Fig. 9.14 (a) and (b). The reliability index (β_0) was found to be 3.69, which is very reliable compared with the target reliability index of 2.50. The reliability analysis by the Eurocode approach obtained partial factor γ_{M0} of 1.14, slightly greater than 1.10 as reported in Table 9.11. For the 138 experimental and numerical specimens on member resistance, the mean value of experimental and numerical strengths to predicted strengths N_{u-m} / N_{AISC-1} equals to 1.55 with a *COV* of 0.155. The reliability index (β_0) of 3.72 reveals the high reliability of this design method for member strengths. The partial factor γ_{M1} is 1.00, smaller than the upper limit of 1.10 and validates that this method is safe in application. The conservatism of this method for concrete-filled members under combined axial load and bending results from (1) the expected beneficial effects of axial compression on flexural strength is ignored, and (2) the use of linear interaction curves, which underscores the favorable effects of concrete infill and spread of plasticity, and (3) the inaccurate predictions of the end points, both the nominal axial strength (N_n) and nominal flexural strength (M_u), of the interaction curves, which only takes account of the yield strength of steel tube and no explicit of confinement effect was included.

The AISC 360 (2016) also provides an alternative design method for the compact sections based on plastic stress distribution. This method referred as AISC-2 and detailed in the commentary of AISC 360-16, Section I5. The AISC-2 is applied to doubly symmetric composite beam-columns and the Form-B method mentioned above is adopted. The four representative points are determined by plastic stress distribution and length effects are considered by slenderness reduction factor



$\rho = N_n / N_{no}$, where N_{no} is the sectional strength of specimen calculated from $N_{no} = 0.85f_y A_s + F_c' A_c$ and N_n is the corresponding member resistance determined as Eqs (9.11) and (9.12).

$$\text{When } \frac{N_{no}}{N_e} \leq 2.25 \quad N_n = N_{no} \left[0.658^{\frac{N_{no}}{N_e}} \right] \quad (9.11)$$

$$\text{When } \frac{N_{no}}{N_e} > 2.25 \quad N_n = 0.877N_e \quad (9.12)$$

where N_e is the elastic critical buckling load and determined as $N_e = \pi^2(EI_{eff})/(KL)^2$. The effective stiffness of the composite section is calculated by $EI_{eff} = E_s I_s + C_3 E_c I_c$ and the coefficient for calculating the effective rigidity of CFT member is $C_3 = 0.6 + 2A_s/(A_c + A_s) \leq 0.9$. All the experimental and numerical results were used to assess the AISC Method 2 including compact, noncompact and slender sections. For the 149 specimens on cross-sectional strength basis, the average value of N_{u-s} / N_{AISC-2} equals to 1.13 with COV of 0.158, as shown in Table 9.10 and Fig. 9.15 (a) and (b). The reliability index (β_0) of the method 2 was found to be 2.58 by the AISC approach, and the partial factor (γ_{M0}) is 1.32, larger than the required value of 1.10, as shown in Table 9.11. In terms of member strength under combined axial load and bending, the average value of N_{u-m} / N_{AISC-2} is 1.21 with COV equals to 0.115. The reliability index (β_0) of 3.06 indicating this design method is very reliable for member strengths. The partial factor γ_{M1} is 1.19, negates the reliability of this method.

9.7.3 EC4

The EC4 (2004) takes into account the better condition of confinement for the concrete core by fully utilizing the compressive strength of concrete. In terms of cross-sectional strength, EC4 (2004) adopts a polygonal diagram, which is



illustrated as Form-B design method in Fig. 9.13, to represent the interaction curve. The EC4 assumes that fully plastic distribution of stresses and the concrete did not act in tension. The unity material strength reduction factor, instead of 0.85 in AISC specification, was applied to concrete strength in determining the axial force and moment. The design resistances predicted from by EC4 (2004) are compared with the experimental results, as shown in Table 9.10 and Fig. 9.16 (a) and (b). The predictions by EC4 (2004) are generally conservative when compared with the experimental results. The specimens on cross-sectional strength basis obtained the mean value of experimental and numerical strengths to predicted strengths ratio N_{u-s} / N_{EC4} equals to 1.07 with COV of 0.138. The reliability index (β_0) was found to be 2.51, succeeded to meet the required target value of 2.50. The partial factor (γ_{M0}) was 1.29, failed to satisfy the codified value of 1.10.

The determination of member resistance under combined compression and bending involves both the load curve and resistance curve. The member resistance, in terms of the axial load, is the interaction point of the load curve and resistance curve. The first order design moment (M_{Ed}) arising from the eccentric application of axial load (N_{Ed}) is uniform through the length of the specimen. By considering the initial global imperfection (δ_0), the first order design moment is calculated by Eq. (9.13).

$$M_{Ed} = N_{Ed}(e + \delta_0) \quad (9.13)$$

The second order effects due to the significant lateral deflection of the column are accounted for by multiplying the greatest first-order design bending moment (M_{Ed}) by a factor k defined as:



$$k = \frac{\beta}{1 - N_{Ed} / N_{cr,eff}}, \geq 1.0 \quad (9.14)$$

where β is an equivalent moment factor and taken as 1.1 in according to Table 6.4 in EC4 (2004) for the equal end moment and $N_{cr,eff}$ is the elastic critical buckling load calculated from the following equation:

$$N_{cr,eff} = \frac{\pi^2(EI)_{eff,\text{II}}}{L^2} \quad (9.15)$$

The effective flexural stiffness $(EI)_{eff,\text{II}}$ is defined as follows:

$$(EI)_{eff,\text{II}} = 0.9(E_s I_s + E_c I_c) \quad (9.16)$$

The load curve related to the axial load (N_{Ed}) and design moment (M_{Ed}) is defined as above and the resistance curve is determined by the plastic stress distribution method by assuming full plasticity of the cross-section and ignoring the concrete contribution in tension. Numerical integration was employed to calculate the bending moment at a given axial load. The EC4 (2004) specified that the following expression for which the interaction curve should be satisfied:

$$\frac{M_{Ed}}{M_{pl,N,Rd}} \leq \alpha_M \quad (9.17)$$

where $M_{pl,N,Rd}$ is the plastic bending resistance taking into account the axial load (N_{Ed}). The EC4 (2004) recommended that for steel grades between S235 and S355 inclusive, the coefficient α_M should be taken as 0.9 and for steel grades S420 and S460 as 0.8. The yield strength of the ferritic stainless steel adopted in this study was around 420MPa and the value of 0.8 was adopted in this study. An example of axial load-moment interaction curves for the specimen 60×60×3C40e8 on the determination of design resistance for members in combined compression and bending is shown in Fig. 9.17.



In terms of the 138 beam-column specimens on member resistance, the average value of experimental and numerical strengths to design strengths P_{u-m} / P_{EC4} equals to 1.10 with the *COV* of 0.202. This design resistance for beam-column members led to the calculated reliability index (β_0) of 2.17 and the partial factor of 1.73, both of which were failed to meet the required values. The predictions of concrete-filled members under combined loading were more accurate for those specimens with small eccentricity-to-depth (e/D) ratios, as shown in Fig. 9.18. The compressive axial load dominates for those specimens with small eccentricity-to-depth (e/D) ratios while the bending moment plays more important roles for those specimens with large e/D ratios. This reflects that the determination of axial compressive strength is very reliable while the bending moment is not accurate attributes to the negligence of beneficial effects on the bending moment due to axial load.

9.7.4 Proposed equations by Lai et al. (2015)

Lai et al. (2015) proposed a set of design equations using the bilinear equations, Form-C method as discussed earlier, to represent the interaction curve of concrete-filled members under combined axial load and bending. By conducting a series of experimental and numerical studies on concrete-filled carbon steel tube columns, it was found that the maximum ratio of moment (M_u / M_n) and the corresponding axial load (N_u / N_n) increase as the confinement factor (ξ) increases. Regression analyses were conducted to develop relationships between c_{sr} , c_p and c_m , where c_p and c_m are the ordinate and abscissa of Point D corresponding to the balance point. For rectangular CFT beam-columns, the Eqs (9.18) – (9.22) were proposed by Lai et al. (2015) presenting the interaction relationship.

$$\text{When } \frac{N_u}{N_n} \geq c_p, \quad \frac{N_u}{N_n} + \frac{1-c_p}{c_m} \frac{M_u}{M_n} \leq 1.0 \quad (9.18)$$

$$\text{When } \frac{N_u}{N_n} < c_p, \quad \frac{1-c_m}{c_p} \frac{N_u}{N_n} + \frac{M_u}{M_n} \leq 1.0 \quad (9.19)$$

where

$$c_p = 0.17\xi^{-0.4} \quad (9.20)$$

$$\text{When } \xi \geq 0.5, \quad c_m = 1.06\xi^{-0.11} \geq 1.0 \quad (9.21)$$

$$\text{When } \xi < 0.5, \quad c_m = 0.90\xi^{-0.36} \leq 1.67 \quad (9.22)$$

These design equations provide conservative predictions. The mean value of 1.54 together with *COV* of 0.118 were obtained for the experimental and numerical strengths to design strengths in terms of cross-sectional resistance of concrete-filled cold-formed ferritic stainless steel tube members under combined axial load and bending, as shown in Table 9.10. The reliability index (β_0) of 3.94 was obtained using AISC 360 reliability analysis method, indicating very safe designs provided by this method. The partial factor (γ_0) derived from Eurocode approach equals to 0.90, which is smaller than the upper limit of 1.10 indicating the high reliability of this method. The 138 beam-column specimens on member resistance provided the average value of experimental and numerical strengths to design strengths N_{u-m} / N_{Lai} of 1.38 with the *COV* of 0.097. This design resistance for beam-column members obtained the calculated reliability index (β_0) of 3.65 and the partial factor of 0.92, both of which are successful in meeting the required values.

9.7.5 Proposed equations by Choi et al. (2006)

Choi et al. (2006) proposed a set of design equations in order to improve the over-conservativism in the AISC 360 for CFT members under combined loading



conditions. The proposed equations are similar in the form of the proposed equations by Lai et al. (2015) but only covers the design of square CFT columns. The proposed equations are expressed in the normalized form with axes normalized against the nominal moment strength and nominal axial strength, respectively. The factors c_p and c_m are formulated as a function of slenderness ratio (b/t) and strength ratio (f_c' / f_y) as follows:

$$c_m = \left(0.5 \sqrt{\frac{B}{t}} - 1.5 \right) \frac{f_c'}{f_y} + 0.95 \quad (c_m \leq 1.5) \quad (9.23)$$

$$c_p = 0.34 \left(\sqrt{\frac{B}{t}} - 2 \right) \frac{f_c'}{f_y} + 0.08 \quad (0.2 \leq c_p \leq 0.4) \quad (9.24)$$

These equations are meant for square CFT members and the comparisons were also made with the rectangular CFT members in order to assess the feasibility on applying these equations. The B is taken as the breath of the specimens for rectangular CFT members bent about the minor axis in this study, which yields larger value of c_m and c_p compared with using the depth of specimens. Conservative predictions were still obtained from this design method. The average values of experimental and numerical strengths to design strengths are 1.45 and 1.29 with the COVs equals to 0.129 and 0.112 for the specimens on cross-section and member basis, respectively. The reliability indices (β_0) calculated by AISC approach provided the values of 3.65 and 3.31 for cross-sectional strength and member strength, respectively, indicating that very safe design is given by this method. The partial factor by Eurocode approach yielded the values of γ_{M0} and γ_{M1} of 0.97 and 1.01 respectively, which are less than the maximum target value of 1.10 for cross-sectional strength and member strength.



9.7.6 Modified design method

It is recommended to adopt the cross-sectional strength predictions in EC4 (2004) for the concrete-filled cold-formed ferritic stainless steel section subjected to combined axial load and bending. However, the predictions for member strength were failed to pass the reliability analysis. Improvements are needed in order to provide a safe and reliable design method for member strength of concrete-filled cold-formed ferritic stainless steel sections under combined axial load and bending.

Similar treatment for the member strength derived from the cross-sectional strength in AISC 360 (2016) Method-2 was adopted in optimizing the EC4 member design strength. After obtaining the cross-sectional interactional polygonal curve, the whole curve was reduced by the slenderness reduction factor ρ , where $\rho = \min(1.35N_n / N_{no}, 1.0)$. The calculation of N_n is identical to the specified procedure in AISC 360 (2016), except that N_{no} is calculated conformed to EC4 with $N_{no} = f_y A_s + f_c' A_c$. This modified design method provides an average value of experimental and numerical strengths to design strengths $N_{u-m} / N_{\text{modified}}$ equals to 1.08 with the COV of 0.132 as illustrated in Fig. 9.19, which is the most accurate among the aforementioned design methods. This design resistance for beam-column members resulted in the calculated reliability index (β_0) of 2.55, which considered to be reliable by passing the target reliability index of 2.50. The partial factor of 1.41, which is better than the original EC4 design method.



9.8 Concluding Remarks

An experimental study was carried out on concrete-filled cold-formed ferritic stainless steel beam-columns to investigate the structural performance of the members under combined axial load and bending moment. A total of 48 combined loading tests were conducted on both square and rectangular sections of ferritic grade EN 1.4003. The nominal concrete cylinder compressive strengths of 40 and 80 MPa were investigated. The beam-column tests were conducted under a wide range of loading eccentricities to study the behaviour of columns under different loading ratios on the axial load-moment interaction curves. A finite element model was developed and agreed well with the experimental results. The finite element model is suitable to perform an extensive parametric study. The parametric study covered specimens on cross-sectional and member strengths. Both the experimental and numerical results were compared with the strength predictions determined from the current American specification AISC 360 (2016), European code EC4 (2004) and proposals by different researchers (Choi et al., 2006; Lai et al., 2015) for the design of concrete-filled carbon steel members. The available design methods are found to be conservative and scatter for concrete-filled cold-formed ferritic stainless steel members under combined loading conditions. EC4 predictions for cross-sectional strengths are recommended. Improved design rules for member strength are proposed and good agreement is shown based on the experimental and numerical results. Reliability analyses by both the AISC approach and EC4 approach were conducted to check the feasibility on applying the design methods described in this chapter.



Specimen	<i>B</i> (mm)	<i>D</i> (mm)	<i>t</i> (mm)	<i>r_o</i> (mm)	<i>r_i</i> (mm)	<i>L_e</i> (mm)	<i>A_s</i> (mm ²)	<i>A_c</i> (mm ²)	<i>f_{c'}</i> (MPa)	<i>e+δ₀</i> (mm)
40×60×4C40e0	59.89	40.14	3.84	6.50	3.80	664.8	656.2	1682.0	37.8	0.27
40×60×4C40e3	59.87	40.13	3.79	6.50	3.80	663.8	648.9	1689.0	37.8	2.75
40×60×4C40e8	59.87	40.10	3.80	6.50	3.80	664.8	649.2	1686.7	37.8	7.86
40×60×4C40e20	59.88	40.13	3.80	6.50	3.80	663.8	650.1	1687.9	37.8	17.28
40×60×4C40e40	59.86	40.11	3.81	6.50	3.80	663.8	651.3	1684.5	37.8	39.77
40×60×4C40e150	59.91	40.11	3.82	6.50	3.80	663.8	653.3	1684.3	37.8	150.29
40×60×4C80e0	59.91	40.13	3.80	6.50	3.80	663.8	649.8	1689.6	81.9	0.39
40×60×4C80e3	59.89	40.14	3.84	6.50	3.80	664.1	656.2	1682.0	81.9	3.47
40×60×4C80e8	59.87	40.14	3.79	6.50	3.80	664.1	648.1	1690.5	81.9	8.21
40×60×4C80e20	59.87	40.10	3.81	6.50	3.80	664.8	650.6	1685.2	81.9	19.06
40×60×4C80e60	59.87	40.12	3.83	6.50	3.80	664.3	654.4	1682.0	81.9	60.21
40×60×4C80e60R	59.87	40.12	3.83	6.50	3.80	664.8	654.4	1682.0	81.9	59.73

Table 9.1. Specimen dimensions and measured eccentricities of series RHS 40×60×4.

Specimen	<i>B</i> (mm)	<i>D</i> (mm)	<i>t</i> (mm)	<i>r_o</i> (mm)	<i>r_i</i> (mm)	<i>L_e</i> (mm)	<i>A_s</i> (mm ²)	<i>A_c</i> (mm ²)	<i>f_{c'}</i> (MPa)	<i>e+δ₀</i> (mm)
60×60×3C40e0	60.07	60.27	2.84	5.80	3.80	664.8	611.1	2957.8	37.8	0.11
60×60×3C40e3	60.09	60.26	2.84	5.80	3.80	663.8	611.9	2957.5	37.8	4.63
60×60×3C40e8	60.03	60.25	2.84	5.80	3.80	664.8	611.5	2953.7	37.8	8.47
60×60×3C40e20	60.06	60.23	2.83	5.80	3.80	664.8	610.0	2956.0	37.8	21.15
60×60×3C40e50	60.08	60.29	2.84	5.80	3.80	664.8	612.6	2958.0	37.8	49.87
60×60×3C40e130	60.08	60.29	2.84	5.80	3.80	664.8	612.6	2958.0	37.8	130.60
60×60×3C80e0	60.07	60.27	2.84	5.80	3.80	664.8	611.1	2957.8	81.9	0.50
60×60×3C80e3	60.04	60.25	2.84	5.80	3.80	664.3	611.2	2954.7	81.9	3.91
60×60×3C80e8	60.09	60.26	2.83	5.80	3.80	664.3	610.8	2958.8	81.9	7.25
60×60×3C80e20	60.04	60.26	2.84	5.80	3.80	664.8	611.1	2955.4	81.9	21.27
60×60×3C80e40	60.06	60.24	2.84	5.80	3.80	662.8	611.7	2954.8	81.9	40.11
60×60×3C80e80	60.03	60.26	2.84	5.80	3.80	664.3	612.0	2953.8	81.9	79.94

Table 9.2. Specimen dimensions and measured eccentricities of series RHS 60×60×3.

Specimen	<i>B</i> (mm)	<i>D</i> (mm)	<i>t</i> (mm)	<i>r_o</i> (mm)	<i>r_i</i> (mm)	<i>L_e</i> (mm)	<i>A_s</i> (mm ²)	<i>A_c</i> (mm ²)	<i>f_{c'}</i> (MPa)	<i>e + δ₀</i> (mm)
40×100×2C40e0	99.73	40.28	1.94	5.70	4.00	664.8	506.8	3474.9	37.8	0.05
40×100×2C40e3	99.72	40.24	1.95	5.70	4.00	664.8	508.0	3469.2	37.8	2.41
40×100×2C40e8	99.70	40.22	1.95	5.70	4.00	664.8	507.6	3466.8	37.8	8.16
40×100×2C40e15	99.71	40.23	1.94	5.70	4.00	664.8	506.8	3469.2	37.8	14.14
40×100×2C40e30	99.69	40.22	1.94	5.70	4.00	664.8	507.1	3466.9	37.8	30.22
40×100×2C40e80	99.72	40.20	1.95	5.70	4.00	664.8	508.1	3465.1	37.8	80.30
40×100×2C80e0	99.72	40.19	1.95	5.70	4.00	664.8	508.5	3463.6	81.9	0.03
40×100×2C80e3	99.69	40.23	1.95	5.70	4.00	664.8	508.8	3466.1	81.9	3.26
40×100×2C80e8	99.71	40.24	1.95	5.70	4.00	664.8	507.5	3469.3	81.9	7.12
40×100×2C80e20	99.74	40.24	1.95	5.70	4.00	664.8	509.5	3468.3	81.9	17.64
40×100×2C80e20R	99.74	40.24	1.95	5.70	4.00	664.8	509.5	3468.3	81.9	18.27
40×100×2C80e50	99.71	40.22	1.94	5.70	4.00	664.8	507.0	3467.9	81.9	50.21

Table 9.3. Specimen dimensions and measured eccentricities of series RHS 40×100×2.



Specimen	<i>B</i> (mm)	<i>D</i> (mm)	<i>t</i> (mm)	<i>r_o</i> (mm)	<i>r_i</i> (mm)	<i>L_e</i> (mm)	<i>A_s</i> (mm ²)	<i>A_c</i> (mm ²)	<i>f_{c'}</i> (MPa)	<i>e + δ₀</i> (mm)
80×120×3C40e0	119.99	79.89	2.80	6.30	4.10	644.8	1050.1	8483.6	37.8	0.01
80×120×3C40e6	119.96	79.90	2.80	6.30	4.10	644.8	1049.6	8482.9	37.8	4.78
80×120×3C40e15	119.94	79.88	2.81	6.30	4.10	644.8	1051.5	8476.9	37.8	16.14
80×120×3C40e30	119.99	79.89	2.81	6.30	4.10	644.8	1053.9	8479.5	37.8	29.64
80×120×3C40e60	119.99	79.90	2.80	6.30	4.10	644.8	1051.5	8483.2	37.8	60.42
80×120×3C40e130	119.97	79.88	2.80	6.30	4.10	644.8	1051.0	8479.8	37.8	131.30
80×120×3C80e0	119.96	79.90	2.80	6.30	4.10	644.8	1049.3	8483.3	81.9	0.26
80×120×3C80e5	119.97	79.90	2.80	6.30	4.10	644.8	1051.4	8481.8	81.9	4.95
80×120×3C80e15	120.02	79.91	2.79	6.30	4.10	644.8	1047.2	8491.5	81.9	15.02
80×120×3C80e15R	119.96	79.90	2.81	6.30	4.10	644.8	1051.7	8480.6	81.9	14.17
80×120×3C80e35	119.97	79.90	2.80	6.30	4.10	644.8	1049.7	8483.6	81.9	36.17
80×120×3C80e80	119.97	79.88	2.81	6.30	4.10	644.8	1052.7	8478.0	81.9	80.88

Table 9.4. Specimen dimensions and measured eccentricities of series RHS 80×120×3.

Specimen	δ_0 (mm)	δ_0 / L	Specimen	δ_0 (mm)	δ_0 / L
40×60×4C40e0	0.00	0	40×100×2C40e0	0.00	0
40×60×4C40e3	-0.20	-1/2464	40×100×2C40e3	0.00	0
40×60×4C40e8	0.00	0	40×100×2C40e8	0.40	1/1235
40×60×4C40e20	-0.20	-1/2464	40×100×2C40e15	-0.20	-1/2469
40×60×4C40e40	0.40	-1/1233	40×100×2C40e30	0.00	0
40×60×4C40e150	0.00	0	40×100×2C40e80	0.00	0
40×60×4C80e0	0.00	0	40×100×2C80e0	-0.40	-1/1235
40×60×4C80e3	0.00	0	40×100×2C80e3	0.00	0
40×60×4C80e8	0.00	0	40×100×2C80e8	0.00	0
40×60×4C80e20	-0.40	-1/1234	40×100×2C80e20	0.00	0
40×60×4C80e60	-0.40	-1/1233	40×100×2C80e20R	0.00	0
40×60×4C80e60R	-0.20	-1/2469	40×100×2C80e50	0.00	0
60×60×3C40e0	-0.40	-1/1234	80×120×3C40e0	-0.76	-1/617
60×60×3C40e3	0.40	1/1232	80×120×3C40e6	-0.25	-1/1850
60×60×3C40e8	0.00	0	80×120×3C40e15	0.00	0
60×60×3C40e20	0.40	1/1234	80×120×3C40e30	0.13	1/3701
60×60×3C40e50	0.20	1/2469	80×120×3C40e60	-0.13	-1/3701
60×60×3C40e130	-0.40	-1/1234	80×120×3C40e130	-0.13	-1/3701
60×60×3C80e0	0.40	1/1235	80×120×3C80e0	0.13	1/3701
60×60×3C80e3	0.20	1/2467	80×120×3C80e5	0.00	0
60×60×3C80e8	-0.20	-1/2467	80×120×3C80e15	-0.13	-1/3701
60×60×3C80e20	0.20	1/2469	80×120×3C80e15R	0.00	0
60×60×3C80e40	-0.20	-1/2459	80×120×3C80e35	0.00	0
60×60×3C80e80	0.20	1/2467	80×120×3C80e80	0.13	1/3615

Table 9.5. Measured global geometric imperfections at mid-length of the test specimens.

Specimen	$N_{u,\text{exp}}$ (kN)	$M_{u,\text{end}}$ (kNm)	$M_{u,\text{mid}}$ (kNm)	ξ	SI	DI
40×60×4C40e0	329.0	0.1	1.0	4.93	0.87	1.77
40×60×4C40e3	265.8	0.7	2.4	4.85	0.71	2.07
40×60×4C40e8	203.6	1.6	3.2	4.86	0.54	2.75
40×60×4C40e20	144.3	2.5	4.1	4.87	0.39	3.15
40×60×4C40e40	91.3	3.6	5.0	4.88	0.24	--
40×60×4C40e150	30.6	4.6	5.0	4.90	0.08	--
40×60×4C80e0	381.7	0.1	1.5	2.24	0.85	1.69
40×60×4C80e3	304.1	1.1	2.8	2.27	0.67	2.10
40×60×4C80e8	235.3	1.9	4.0	2.24	0.53	2.38
40×60×4C80e20	155.7	3.0	4.9	2.25	0.35	2.93
40×60×4C80e60	71.8	4.3	5.5	2.27	0.16	--
40×60×4C80e60R	71.5	4.3	5.5	2.27	0.16	--
60×60×3C40e0	401.6	0.0	0.9	2.46	1.04	1.43
60×60×3C40e3	329.0	1.5	3.2	2.46	0.85	2.86
60×60×3C40e8	285.3	2.4	4.3	2.46	0.74	2.96
60×60×3C40e20	206.9	4.4	6.3	2.45	0.54	--
60×60×3C40e50	120.7	6.0	7.7	2.46	0.31	--
60×60×3C40e130	52.9	6.9	7.7	2.46	0.14	--
60×60×3C80e0	513.4	0.3	1.7	1.13	0.99	1.62
60×60×3C80e3	433.7	1.7	3.5	1.14	0.84	2.12
60×60×3C80e8	363.8	2.6	4.7	1.13	0.70	2.22
60×60×3C80e20	249.7	5.3	7.4	1.13	0.48	2.78
60×60×3C80e40	167.9	6.7	8.4	1.14	0.32	2.85
60×60×3C80e80	95.3	7.6	8.9	1.14	0.18	--
40×100×2C40e0	357.3	0.0	0.1	1.62	1.04	1.32
40×100×2C40e3	253.4	0.6	1.9	1.63	0.74	2.15
40×100×2C40e8	192.8	1.6	3.0	1.63	0.56	2.07
40×100×2C40e15	158.9	2.2	3.7	1.62	0.46	2.02
40×100×2C40e30	102.0	3.1	4.2	1.63	0.30	--
40×100×2C40e80	47.9	3.8	4.6	1.63	0.14	--
40×100×2C80e0	498.5	0.0	0.4	0.75	1.00	1.22
40×100×2C80e3	341.0	1.1	3.1	0.75	0.69	--
40×100×2C80e8	279.0	2.0	4.1	0.75	0.56	1.46
40×100×2C80e20	172.7	3.0	4.8	0.75	0.35	1.57
40×100×2C80e20R	169.9	3.1	4.8	0.75	0.34	1.69
40×100×2C80e50	83.3	4.2	5.4	0.75	0.17	2.24
80×120×3C40e0	803.9	0.0	0.9	1.25	1.11	1.47
80×120×3C40e6	689.9	3.3	5.4	1.25	0.96	1.71
80×120×3C40e15	532.6	8.6	11.2	1.25	0.74	1.90
80×120×3C40e30	394.2	11.7	14.1	1.25	0.55	1.96
80×120×3C40e60	248.9	15.0	17.1	1.25	0.34	2.16
80×120×3C40e130	121.6	16.0	17.2	1.25	0.17	--
80×120×3C80e0	1201.8	0.3	0.9	0.58	1.10	1.15
80×120×3C80e5	961.1	4.8	6.4	0.58	0.88	1.90
80×120×3C80e15	727.2	10.9	12.9	0.57	0.66	1.48
80×120×3C80e15R	767.9	10.9	13.5	0.58	0.70	1.47
80×120×3C80e35	467.6	16.9	18.9	0.58	0.43	1.24
80×120×3C80e80	244.8	19.8	21.6	0.58	0.22	1.47

Table 9.6. Experimental results.

Specimen	δ_0		L/1500		L/1000		L/300	
	$M_{u,\text{exp}} / M_{\text{FEA}}$	$N_{u,\text{exp}} / N_{\text{FEA}}$						
40×60×4C40e0	0.88	1.01	1.16	1.02	1.00	1.00	1.26	0.92
40×60×4C40e3	1.09	1.01	0.79	1.02	0.81	1.02	0.86	0.96
40×60×4C40e8	1.04	1.01	1.04	1.04	1.04	1.03	1.03	0.99
40×60×4C40e20	0.99	0.98	0.99	1.07	1.03	1.07	1.00	1.04
40×60×4C40e40	1.08	1.02	0.98	1.03	0.97	1.03	0.98	1.03
40×60×4C40e150	0.98	1.00	1.03	1.01	1.03	1.01	0.99	0.99
40×60×4C80e0	1.19	1.00	0.85	0.96	0.83	0.94	1.02	0.87
40×60×4C80e3	0.98	1.02	0.89	0.96	0.90	0.95	0.99	0.90
40×60×4C80e8	1.18	1.00	0.97	0.97	0.97	0.97	0.92	0.93
40×60×4C80e20	1.06	0.95	0.92	1.02	0.92	1.02	0.89	0.99
40×60×4C80e60	1.02	0.97	0.95	1.01	0.94	1.01	0.91	0.95
40×60×4C80e60R	1.00	0.98	0.99	1.02	0.98	1.02	0.95	0.97
60×60×3C40e0	1.45	1.06	1.00	0.98	0.94	0.97	1.20	0.92
60×60×3C40e0	1.24	1.06	0.44	0.98	0.32	0.97	0.34	0.94
60×60×3C40e3	1.17	1.08	0.32	0.98	0.32	0.98	0.86	0.95
60×60×3C40e8	1.19	1.08	0.87	0.98	0.86	0.97	0.86	0.95
60×60×3C40e20	1.13	1.09	0.93	0.98	0.92	0.98	0.89	0.94
60×60×3C40e50	1.08	1.06	0.96	0.97	0.96	0.97	0.91	0.94
60×60×3C40e130	1.42	1.03	0.72	0.90	0.72	0.89	1.02	0.84
60×60×3C80e0	1.20	1.05	0.83	0.90	0.85	0.89	0.84	0.86
60×60×3C80e3	1.12	1.03	0.99	0.94	0.88	0.94	0.95	0.91
60×60×3C80e8	1.11	1.07	0.91	0.93	0.91	0.93	0.88	0.90
60×60×3C80e20	1.12	1.08	0.91	0.93	0.91	0.93	0.89	0.91
60×60×3C80e40	1.11	1.10	0.88	0.91	0.88	0.91	0.86	0.89
60×60×3C80e80	0.32	1.03	5.99	0.90	5.10	0.88	8.01	0.80

Table 9.7. Comparison of the test failure loads with FE failure loads for varying imperfection amplitudes (Cont.).

40×100×2C40e0	1.29	1.02	0.96	1.04	0.85	1.04	0.96	0.98
40×100×2C40e3	1.10	1.00	0.90	1.05	1.02	1.03	0.97	1.00
40×100×2C40e8	1.15	1.05	0.92	1.01	0.86	1.00	0.83	0.97
40×100×2C40e15	1.09	1.01	1.02	1.05	0.99	1.05	0.99	1.02
40×100×2C40e30	1.11	1.04	0.93	0.99	0.90	0.97	0.89	0.87
40×100×2C40e80	0.54	1.11	3.14	0.85	3.27	0.83	3.72	0.75
40×100×2C80e0	1.21	1.03	0.83	0.95	0.81	0.94	0.78	0.89
40×100×2C80e3	1.17	1.04	0.79	0.94	0.81	0.94	0.82	0.89
40×100×2C80e8	1.02	0.99	0.93	1.03	0.92	1.02	0.93	0.96
40×100×2C80e20	0.95	0.99	1.04	1.00	1.03	0.99	1.00	0.97
40×100×2C80e20R	1.09	1.03	0.93	0.97	0.93	0.97	0.93	0.96
40×100×2C80e50	0.97	1.03	0.84	0.94	0.88	0.93	1.23	0.90
80×120×3C40e0	1.08	0.99	1.04	0.96	1.03	0.96	1.09	0.93
80×120×3C40e6	1.07	1.03	0.92	0.94	0.96	0.95	0.95	0.93
80×120×3C40e15	1.02	1.02	0.99	1.00	1.00	1.00	0.98	0.99
80×120×3C40e30	1.05	1.01	0.99	1.01	0.98	1.00	0.93	0.97
80×120×3C40e60	1.00	0.98	1.03	1.03	1.02	1.03	0.98	1.00
80×120×3C40e130	0.75	1.02	2.07	0.96	2.08	0.95	2.48	0.89
80×120×3C80e0	0.87	1.03	1.09	0.96	1.11	0.96	1.11	0.93
80×120×3C80e5	0.96	1.01	1.01	0.98	1.03	0.97	1.01	0.94
80×120×3C80e15	1.12	1.11	0.95	0.93	0.95	0.92	0.93	0.90
80×120×3C80e15R	1.03	1.04	0.95	0.95	0.95	0.95	0.93	0.93
80×120×3C80e35	1.07	1.06	0.96	0.95	0.96	0.95	0.93	0.94
Mean	1.06	1.03	1.09	0.98	1.07	0.97	1.18	0.93
COV	0.172	0.036	0.747	0.048	0.673	0.050	0.942	0.060

Table 9.7. Comparison of the test failure loads with FE failure loads for varying imperfection amplitudes (Cont.).

Specimen	N_{FEA} (kN)	M_{FEA} (kN)	Specimen	N_{FEA} (kN)	M_{FEA} (kN)	Specimen	N_{FEA} (kN)	M_{FEA} (kN)
300×300×10C80e0	12425.0	14.4	300×300×4C40e75	3179.9	251.3	200×350×5C80e100	2722.8	287.6
300×300×10C80e18	10882.0	218.8	300×300×4C40e150	2106.8	324.8	200×350×5C80e200	1464.1	305.6
300×300×10C80e37	9431.1	374.5	300×300×4C40e300	1110.6	338.9	200×350×5C80e400	690.8	284.9
300×300×10C80e75	7418.5	572.3	300×300×4C40e600	531.4	322.3	200×350×5C40e0	5180.8	2.1
300×300×10C80e150	5037.9	767.9	300×300×3.5C80e1	8422.0	19.2	200×350×5C40e12	4477.5	58.2
300×300×10C80e300	2828.0	857.8	300×300×3.5C80e18	7196.2	168.4	200×350×5C40e25	3918.2	103.3
300×300×10C80e375	2250.9	853.5	300×300×3.5C80e37	6174.4	259.0	200×350×5C40e50	3146.4	163.1
300×300×10C40e1	8547.1	23.9	300×300×3.5C80e75	4670.0	369.7	200×350×5C40e100	2204.0	226.0
300×300×10C40e18	7494.8	156.7	300×300×3.5C40e1	5115.4	10.5	200×350×4C80e0	6628.9	78.9
300×300×10C40e37	6612.5	268.3	300×300×3.5C40e18	4402.9	99.3	200×350×4C80e12	5693.9	81.7
300×300×10C40e75	5321.7	421.0	300×300×3.5C40e37	3840.6	159.5	200×350×4C80e25	4885.8	136.4
300×300×10C40e150	3745.9	580.7	300×300×3.5C40e75	2986.5	236.6	200×350×4C80e50	3818.6	206.3
300×300×10C40e300	2177.4	667.0	300×300×3.5C40e150	1937.5	298.4	200×350×4C80e100	2436.8	257.3
300×300×10C40e600	1113.7	676.7	300×300×3C80e1	8250.0	19.0	200×350×4C80e400	591.5	244.3
300×300×8C80e0	11393.6	18.1	300×300×3C80e18	7017.8	160.1	200×350×4C40e1	4244.0	9.5
300×300×8C80e18	9983.9	201.7	300×300×3C80e37	6031.1	254.9	200×350×4C40e12	3675.6	52.7
300×300×8C80e37	8628.4	343.0	300×300×3C80e75	4518.7	357.2	200×350×4C40e25	3201.8	88.8
300×300×8C80e75	6812.4	529.3	300×300×3C40e1	4920.8	11.4	200×350×4C40e50	2561.9	137.8
300×300×8C80e150	4558.7	697.0	300×300×3C40e18	4224.7	99.2	200×350×4C40e200	961.2	198.6
300×300×8C80e300	2466.2	748.1	300×300×3C40e37	3664.0	154.1	200×350×3.5C80e1	6457.9	8.7
300×300×8C80e375	1963.1	742.4	300×300×3C40e75	2832.7	224.5	200×350×3.5C80e12	5491.6	79.5
300×300×8C40e0	8302.0	0.5	300×300×3C40e150	1805.9	278.3	200×350×3.5C80e25	4729.7	133.2
300×300×8C40e18	7240.7	151.1	300×300×2.5C80e1	8170.6	11.3	200×350×3.5C80e50	3660.2	196.7
300×300×8C40e37	6345.7	249.1	300×300×2.5C80e18	6906.1	149.0	200×350×3.5C80e100	2307.9	243.9

Table 9.8. Parametric study results for specimens on cross-sectional strength (Cont.).

300×300×8C40e75	5097.9	400.1	300×300×2.5C80e37	5915.2	250.7	200×350×3.5C80e400	539.1	222.9
300×300×8C40e150	3555.0	548.1	300×300×2.5C80e75	4373.4	348.6	200×350×3.5C40e1	3990.1	6.8
300×300×8C40e300	2063.8	626.7	300×300×2.5C80e150	2477.3	382.6	200×350×3.5C40e12	3445.9	48.6
300×300×8C40e375	1664.4	631.7	300×300×2.5C40e1	4844.1	7.1	200×350×3.5C40e25	3002.1	84.1
300×300×5C80e0	9513.2	7.5	300×300×2.5C40e18	4086.5	92.0	200×350×3.5C40e50	2395.9	128.3
300×300×5C80e18	8211.6	177.0	300×300×2.5C40e37	3522.3	149.9	200×350×3.5C40e100	1625.7	170.0
300×300×5C80e37	7152.0	287.1	300×300×2.5C40e75	2683.1	214.3	200×350×3C80e1	6276.3	15.0
300×300×5C80e75	5549.7	430.8	300×300×2.5C40e150	1663.9	256.7	200×350×3C80e12	5332.6	76.0
300×300×5C80e150	3558.9	545.1	200×350×6C80e0	5857.1	3.2	200×350×3C80e25	4604.3	128.9
300×300×5C80e300	1800.8	545.7	200×350×6C80e12	5066.6	70.1	200×350×3C80e50	3512.7	189.1
300×300×5C80e375	1421.1	537.8	200×350×6C80e25	4408.5	122.3	200×350×3C40e1	3808.3	9.2
300×300×5C40e0	6312.2	4.5	200×350×6C80e50	3773.2	201.1	200×350×3C40e12	3261.1	46.4
300×300×5C40e18	5893.4	125.1	200×350×6C80e100	2518.3	259.4	200×350×3C40e25	2825.9	78.1
300×300×5C40e37	4824.4	191.6	200×350×6C80e200	1555.9	315.8	200×350×3C40e50	2235.1	119.4
300×300×5C40e75	3876.2	303.5	200×350×6C80e400	816.2	330.4	200×350×3C40e100	1501.4	158.4
300×300×5C40e150	2588.4	394.6	200×350×6C40e0	5885.9	2.9	200×350×3C40e200	790.4	164.3
300×300×5C40e300	1296.4	390.6	200×350×6C40e12	4890.7	71.8	200×350×2.5C80e12	5265.5	73.5
300×300×4C80e1	8616.3	23.8	200×350×6C40e25	4284.4	118.9	200×350×2.5C80e25	4450.1	124.5
300×300×4C80e18	7397.3	166.2	200×350×6C40e50	3479.7	184.7	200×350×2.5C80e50	3410.9	183.5
300×300×4C80e37	6408.4	265.9	200×350×6C40e100	2509.5	256.7	200×350×2.5C80e100	2009.7	212.7
300×300×4C80e75	4884.6	387.6	200×350×6C40e200	1573.8	321.2	200×350×2.5C40e1	3730.0	9.1
300×300×4C80e150	2984.9	461.3	200×350×6C40e400	798.9	323.9	200×350×2.5C40e12	3121.7	43.9
300×300×4C80e600	649.5	395.0	200×350×5C80e1	7094.7	18.0	200×350×2.5C40e25	2696.9	74.7
300×300×4C40e1	5371.9	12.5	200×350×5C80e12	6070.5	98.6	200×350×2.5C40e50	2118.4	111.7
300×300×4C40e18	4651.5	105.7	200×350×5C80e25	5266.9	157.1	200×350×2.5C40e100	1383.7	144.6
300×300×4C40e37	4059.1	168.6	200×350×5C80e50	4152.2	228.3			

Table 9.8. Parametric study results for specimens on cross-sectional strength (Cont.).

Specimen	N_{FEA}	M_{FEA}	Specimen	N_{FEA}	M_{FEA}	Specimen	N_{FEA}	M_{FEA}
	(kN)	(kN)		(kN)	(kN)		(kN)	(kN)
300×300×10C80e0	14.9	9395.0	300×300×5C80e37	373.5	4834.7	200×350×6C40e25	187.2	3520.2
300×300×10C80e18	259.0	7280.3	300×300×5C80e75	452.4	3620.5	200×350×6C40e50	219.2	2793.1
300×300×10C80e37	381.1	6333.0	300×300×5C80e150	475.4	2277.1	200×350×6C40e100	296.9	1988.0
300×300×10C80e75	520.6	5052.5	300×300×5C80e300	456.8	1222.2	200×350×6C40e200	305.6	1230.2
300×300×10C80e150	661.2	3565.1	300×300×5C40e0	10.8	6222.9	200×350×6C40e400	308.9	673.5
300×300×10C80e300	738.2	2157.0	300×300×5C40e18	147.3	4957.7	200×350×5C80e1	80.4	4178.4
300×300×10C80e600	751.6	1782.7	300×300×5C40e37	221.2	4239.1	200×350×5C80e12	194.8	3394.4
300×300×10C40e0	44.3	8725.6	300×300×5C40e75	331.3	3367.5	200×350×5C80e25	220.2	2872.7
300×300×10C40e18	243.9	7132.3	300×300×5C40e150	431.2	2312.7	200×350×5C80e50	249.9	2224.5
300×300×10C40e37	349.0	6179.1	300×300×5C40e300	447.2	1311.7	200×350×5C80e100	262.7	1515.4
300×300×10C40e75	526.2	4944.9	300×300×5C40e375	446.2	1064.4	200×350×5C80e200	251.6	896.6
300×300×10C40e150	659.0	3506.9	300×300×4C80e1	147.8	6614.7	200×350×5C40e0	25.3	4357.7
300×300×10C40e300	735.3	2123.8	300×300×4C80e19	273.7	5125.4	200×350×5C40e12	105.9	3411.5
300×300×10C40e600	745.5	1138.6	300×300×4C80e38	337.8	4349.5	200×350×5C40e25	169.2	2960.9
300×300×8C80e0	2.4	7492.2	300×300×4C80e75	407.3	3255.5	200×350×5C40e50	199.9	2340.9
300×300×8C80e18	307.9	8471.3	300×300×4C80e150	419.1	2006.2	200×350×5C40e100	254.0	1651.9
300×300×8C80e37	451.7	7251.2	300×300×4C40e1	66.8	4342.6	200×350×5C40e200	264.1	1021.0
300×300×8C80e75	601.3	5650.2	300×300×4C40e18	150.6	3453.8	200×350×5C40e400	266.8	561.7
300×300×8C80e150	707.2	3778.6	300×300×4C40e37	207.4	2982.7	200×350×4C80e1	101.0	3653.8
300×300×8C80e300	727.1	2115.3	300×300×4C40e75	273.9	2291.7	200×350×4C80e100	226.9	1337.7
300×300×8C80e375	726.1	1710.2	300×300×4C40e150	310.0	1514.8	200×350×4C80e200	217.4	778.1

Table 9.9. Parametric study results for specimens on member strength (Cont.).

300×300×8C40e0	11.9	8140.9	200×350×6C80e0	29.2	5332.8	200×350×4C80e400	209.7	421.3
300×300×8C40e18	221.6	6300.6	200×350×6C80e12	131.0	4219.4	200×350×4C40e1	48.3	2654.9
300×300×8C40e37	327.9	5460.2	200×350×6C80e25	180.8	3616.4	200×350×4C40e100	185.6	1100.7
300×300×8C40e75	457.6	4341.6	200×350×6C80e50	231.8	2879.0	200×350×4C40e200	188.6	673.3
300×300×8C40e150	578.5	3034.1	200×350×6C80e100	284.0	2040.5	200×350×4C40e400	185.7	373.1
300×300×8C40e300	628.2	1813.8	200×350×6C80e200	322.6	1262.0	200×350×3.5C80e1	117.4	3454.0
300×300×8C40e375	630.6	1488.7	200×350×6C80e400	320.9	695.6	200×350×3.5C80e100	206.4	1221.9
300×300×5C80e1	125.2	7328.1	200×350×6C40e0	26.3	5297.8	200×350×3.5C80e200	196.6	712.6
300×300×5C80e18	273.6	5709.8	200×350×6C40e12	119.1	4089.0	200×350×3.5C80e400	192.4	384.0

Table 9.9. Parametric study results for specimens on member strength (Cont.).

	$\frac{N_{u-s}}{N_{AISC-1}}$	$\frac{N_{u-m}}{N_{AISC-1}}$	$\frac{N_{u-s}}{N_{AISC-2}}$	$\frac{N_{u-m}}{N_{AISC-2}}$	$\frac{N_{u-s}}{N_{EC4}}$	$\frac{N_{u-m}}{N_{EC4}}$	$\frac{N_{u-s}}{N_{Lai}}$	$\frac{N_{u-m}}{N_{Lai}}$	$\frac{N_{u-s}}{N_{Choi}}$	$\frac{N_{u-m}}{N_{Choi}}$	$\frac{N_{u-m}}{N_{Modified}}$
Number of data	149	138	149	138	149	138	149	138	149	138	138
Mean (P_m)	1.84	1.55	1.13	1.21	1.07	1.10	1.54	1.38	1.45	1.29	1.08
$COV(V_p)$	0.230	0.155	0.158	0.115	0.138	0.202	0.118	0.097	0.129	0.112	0.132
Resistance factor (ϕ)	0.90	0.90	0.90	0.90	0.90	0.90	0.90	0.90	0.90	0.90	0.90
Reliability index (β_0)	3.69	3.72	2.58	3.06	2.51	2.17	3.94	3.65	3.65	3.31	2.55

Table 9.10. Reliability analysis for different design rules by AISC approach.

	$\frac{N_{u-s}}{N_{AISC-1}}$	$\frac{N_{u-m}}{N_{AISC-1}}$	$\frac{N_{u-s}}{N_{AISC-2}}$	$\frac{N_{u-m}}{N_{AISC-2}}$	$\frac{N_{u-s}}{N_{EC4}}$	$\frac{N_{u-m}}{N_{EC4}}$	$\frac{N_{u-s}}{N_{Lai}}$	$\frac{N_{u-m}}{N_{Lai}}$	$\frac{N_{u-s}}{N_{Choi}}$	$\frac{N_{u-m}}{N_{Choi}}$	$\frac{N_{u-m}}{N_{Modified}}$
n	149	138	149	138	149	138	149	138	149	138	138
$k_{d,n}$	3.157	3.162	3.157	3.162	3.157	3.162	3.157	3.162	3.157	3.162	3.162
b	1.553	1.422	1.043	1.069	1.039	0.933	1.449	1.329	1.387	1.259	0.965
V_δ	0.223	0.151	0.142	0.115	0.133	0.193	0.123	0.101	0.133	0.115	0.138
V_r	0.233	0.166	0.157	0.133	0.149	0.204	0.140	0.121	0.149	0.133	0.153
γ_M	1.14	1.00	1.32	1.19	1.29	1.73	0.90	0.92	0.97	1.01	1.41

Table 9.11. Reliability analysis for different design rules by Eurocode approach.

Loading condition	Description of element	Width-to-thickness ratio	λ_p Compact/noncompact	λ_r Noncompact/slender	λ_{limit} Maximum permitted
Axial compression	Walls of rectangular HSS	b/t	$2.26 \sqrt{\frac{E_s}{f_y}}$	$3.00 \sqrt{\frac{E_s}{f_y}}$	$5.00 \sqrt{\frac{E_s}{f_y}}$
Flexural	Flange of rectangular HSS	b/t	$2.26 \sqrt{\frac{E_s}{f_y}}$	$3.00 \sqrt{\frac{E_s}{f_y}}$	$5.00 \sqrt{\frac{E_s}{f_y}}$
	Web of rectangular HSS	d/t	$3.00 \sqrt{\frac{E_s}{f_y}}$	$5.70 \sqrt{\frac{E_s}{f_y}}$	$5.70 \sqrt{\frac{E_s}{f_y}}$

Table 9.12. Slenderness limits in AISC 360 (2016).

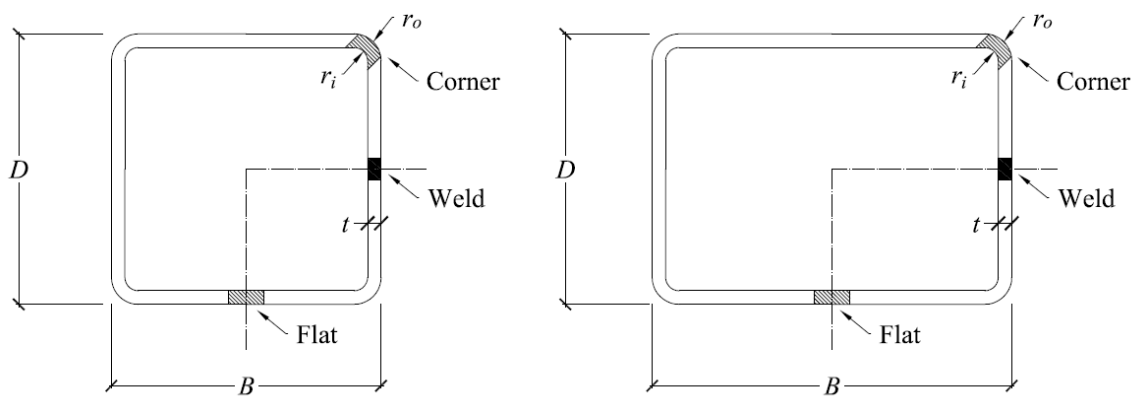


Figure 9.1. Locations of tensile corner and flat coupons in the cross-sections.

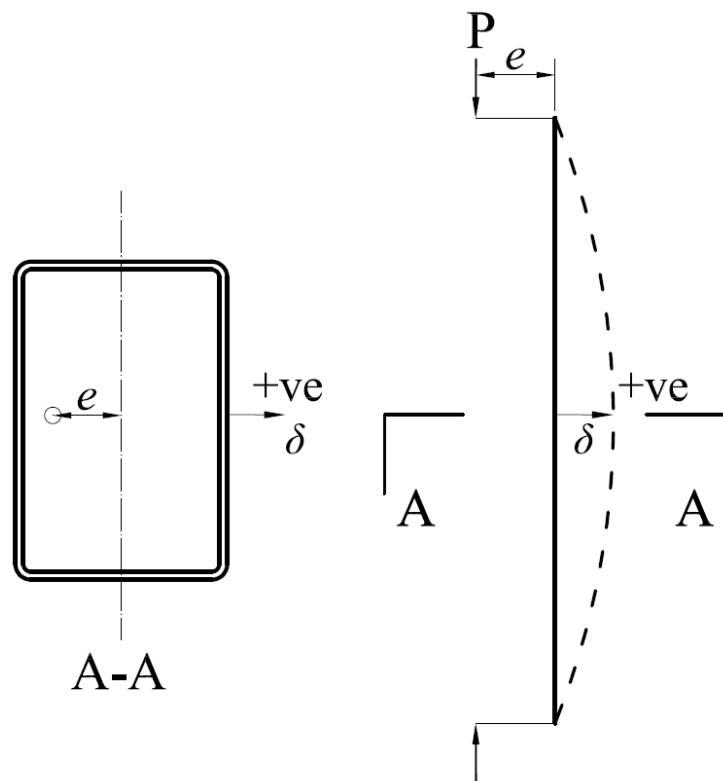


Figure 9.2. Sign convention and location of global geometric imperfection measurements.



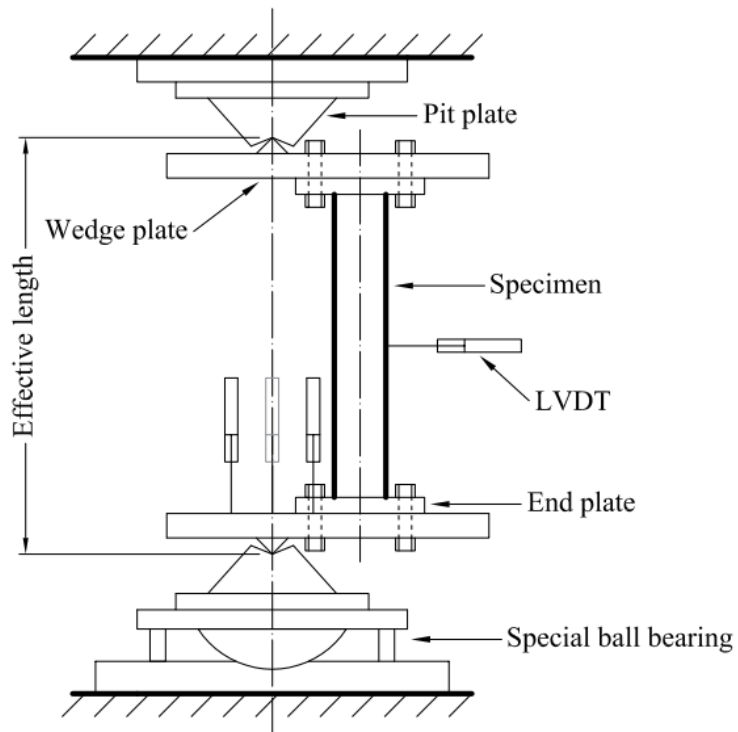
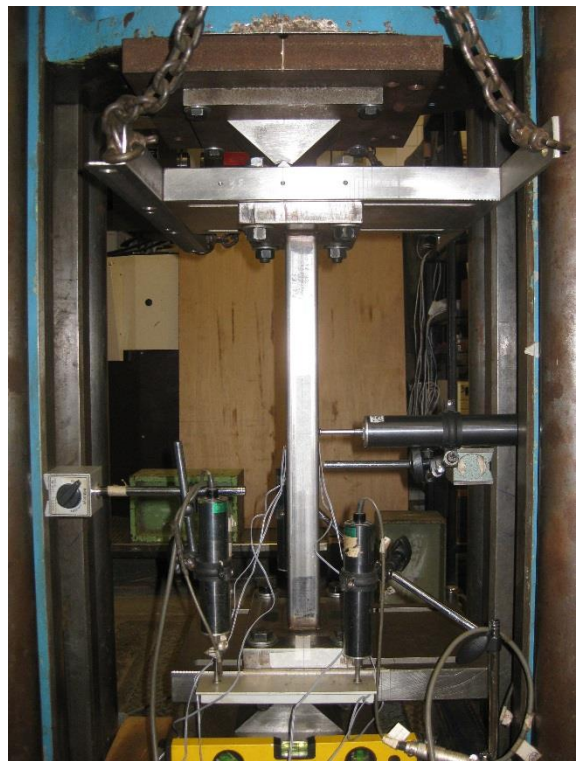


Figure 9.3. Schematic arrangement for beam-column tests for series $40 \times 60 \times 4$, $60 \times 60 \times 3$ and $40 \times 100 \times 2$.

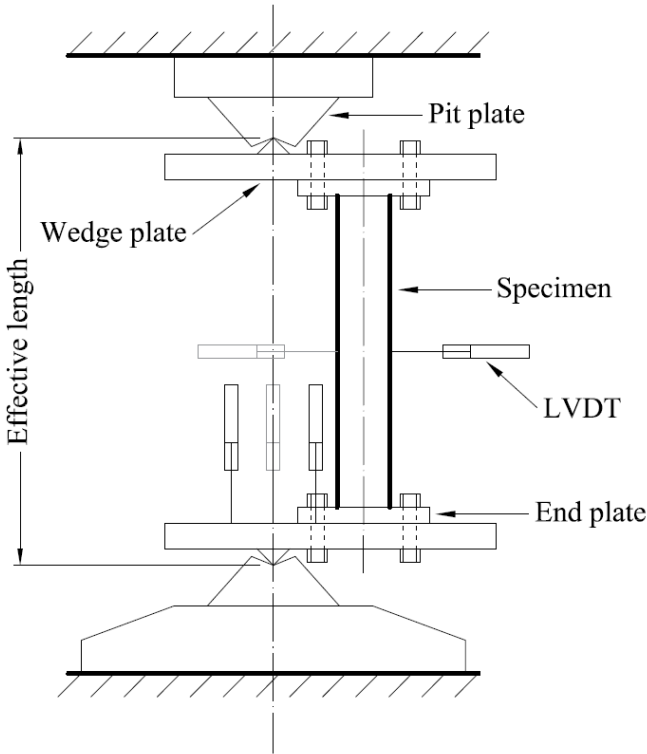


Figure 9.4. Schematic arrangement for beam-column tests for series 80×120×3.

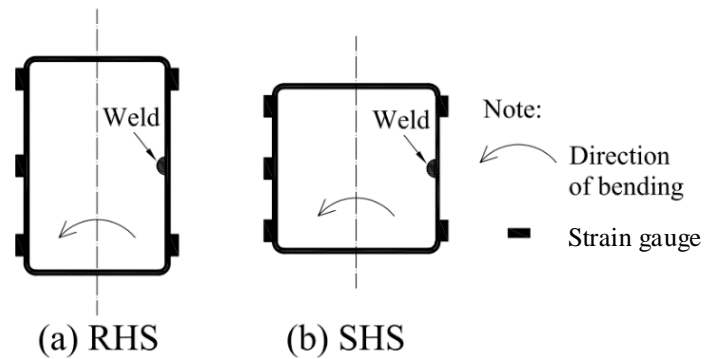
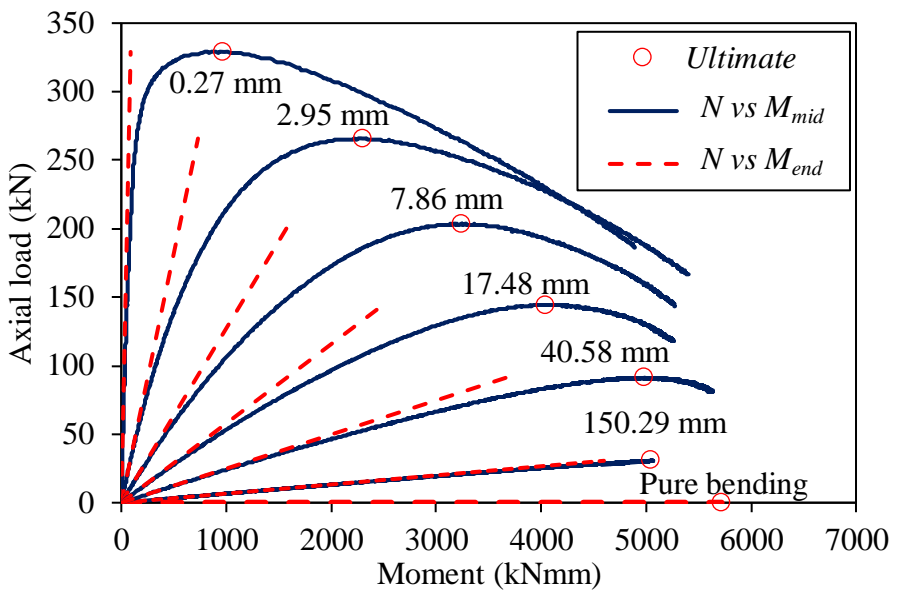


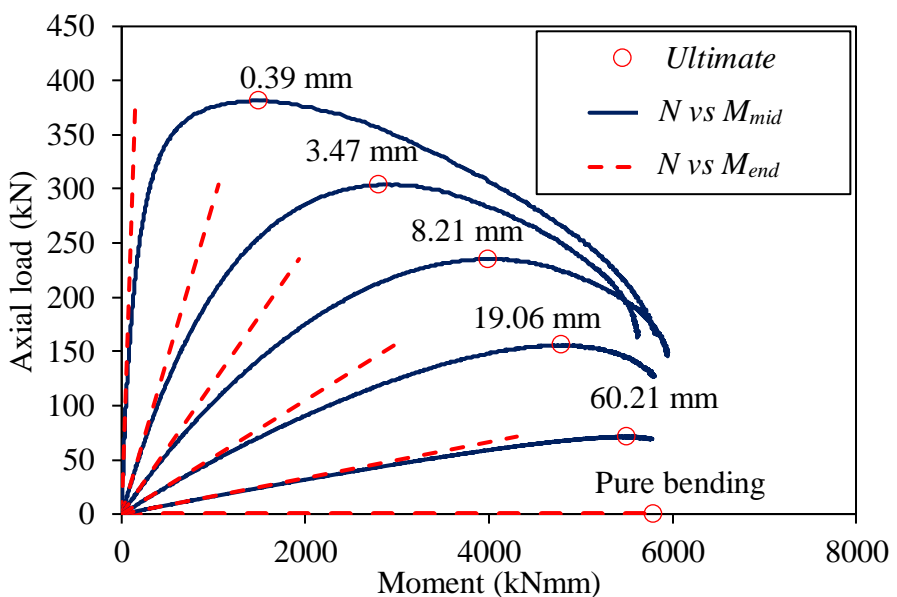
Figure 9.5. Arrangement of strain gauges for beam-column tests.



Figure 9.6. Flexural buckling of series 40×60×4C80.

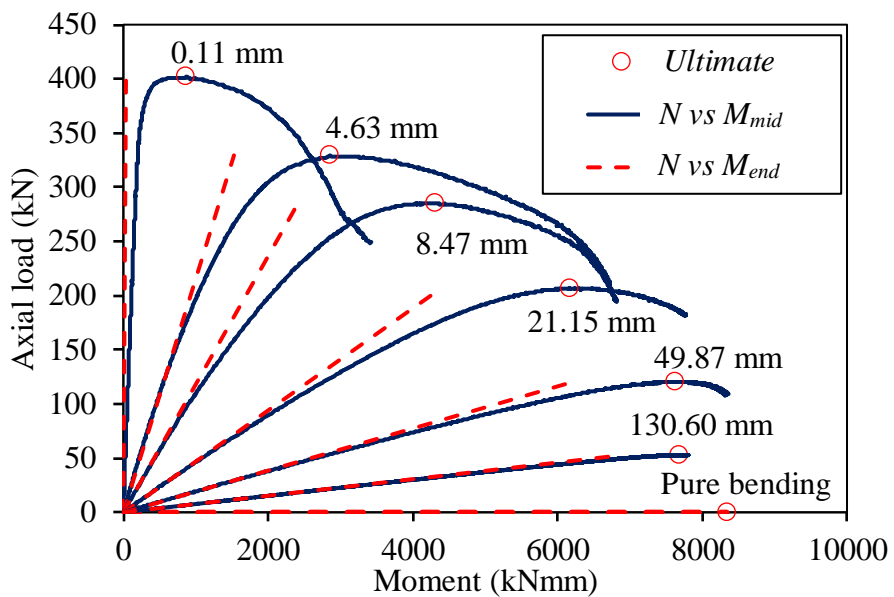


(a) Test curves for series 40×60×4C40

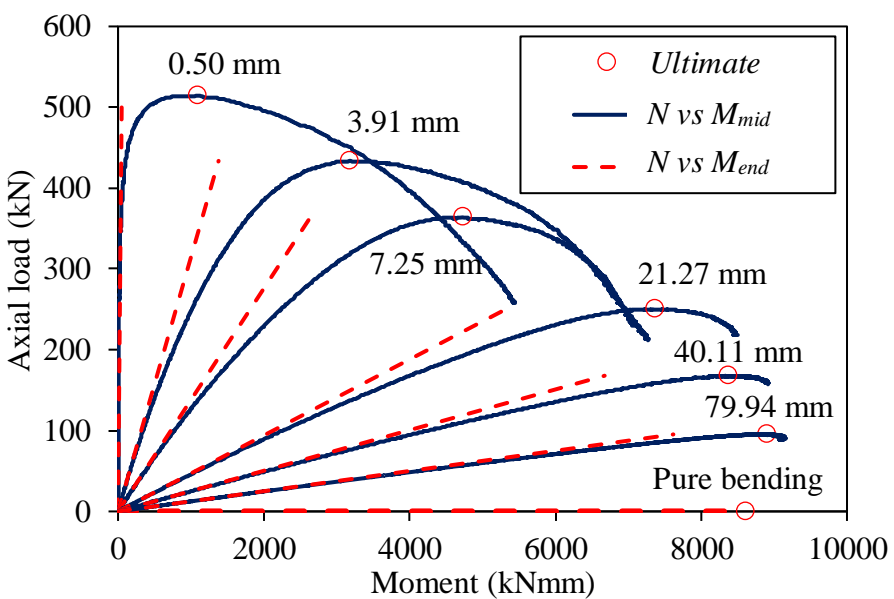


(b) Test curves for series 40×60×4C80

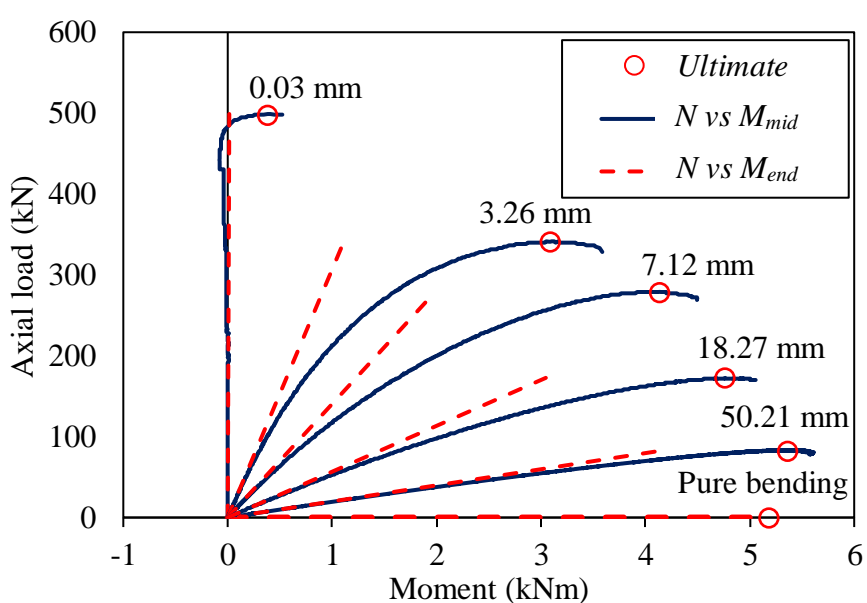
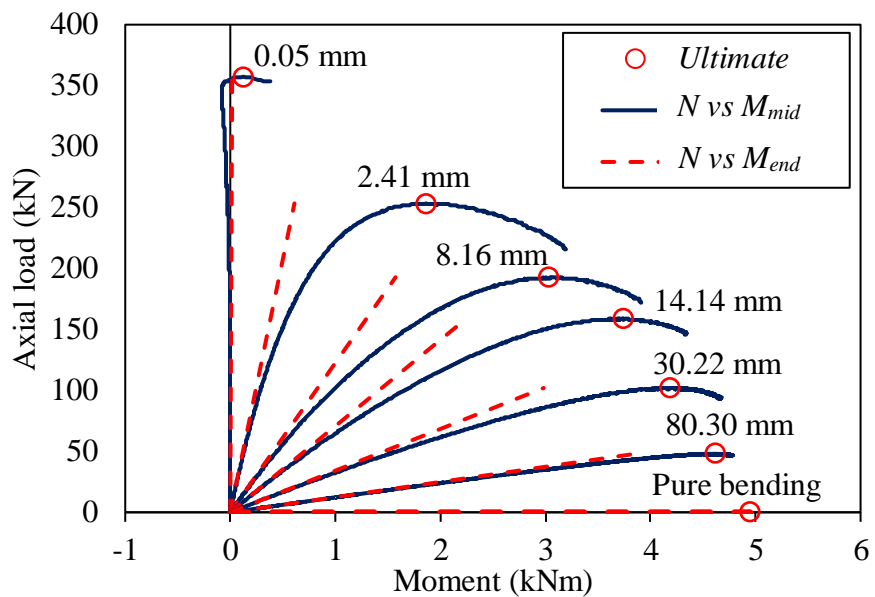




(c) Test curves for series 60×60×3C40



(d) Test curves for series 60×60×3C80



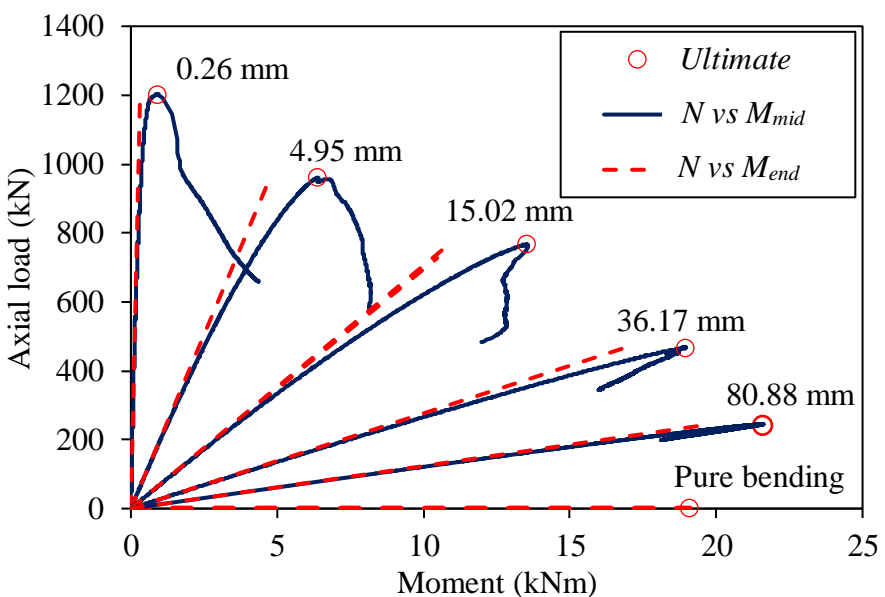
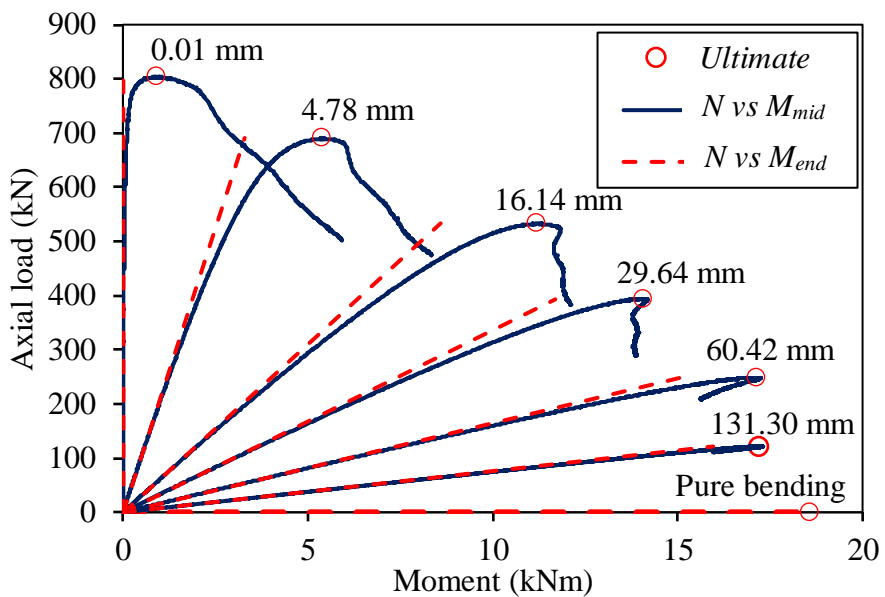
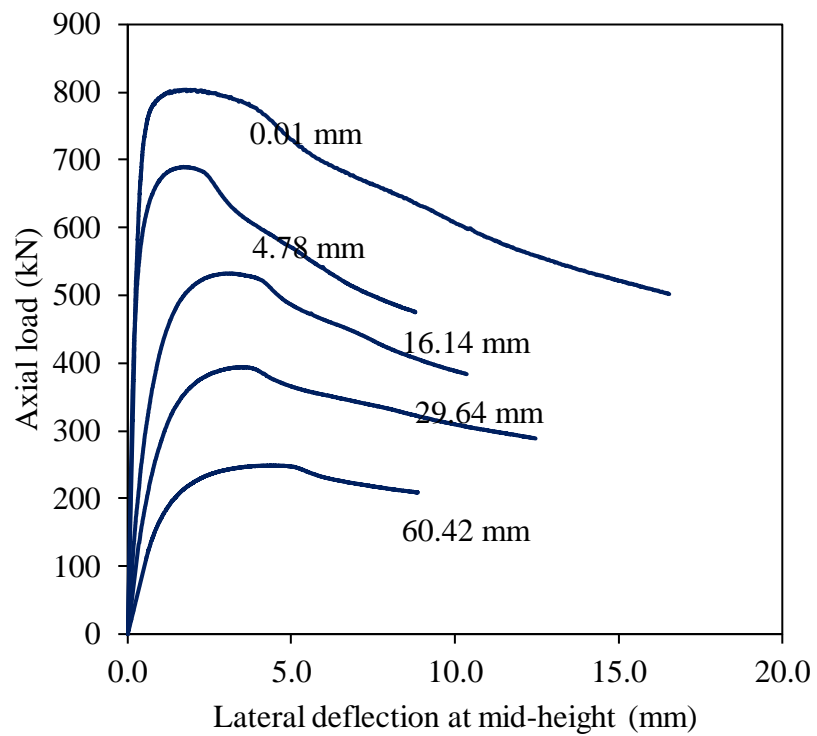
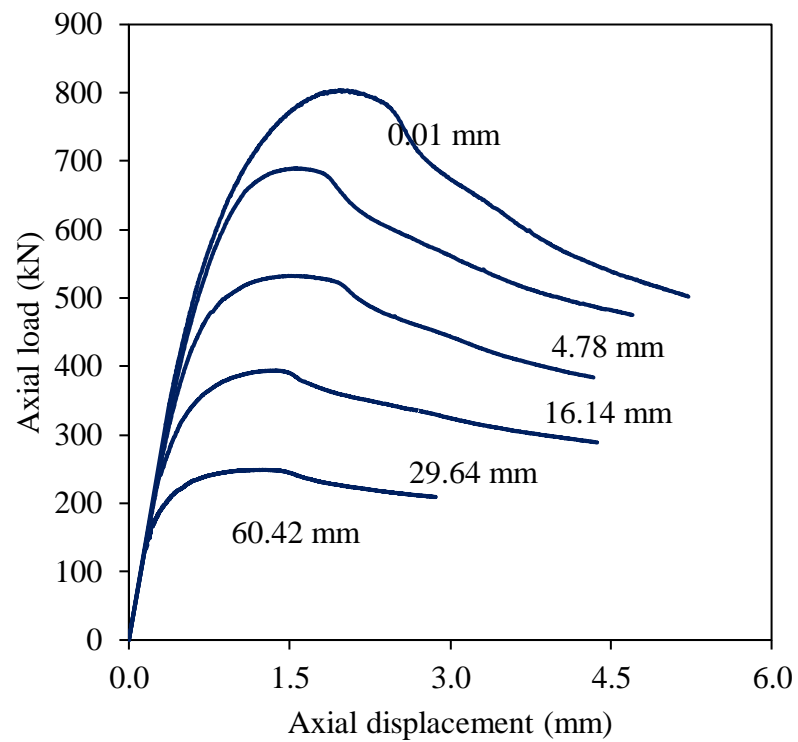


Figure 9.7. Axial load versus moment curves for combined loading tests.



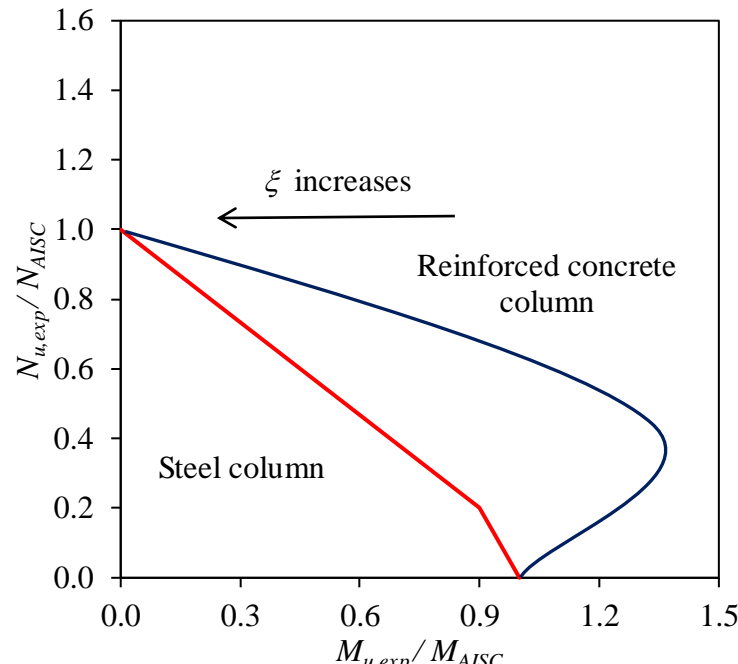


(a) Axial load-lateral deflection at mid-height

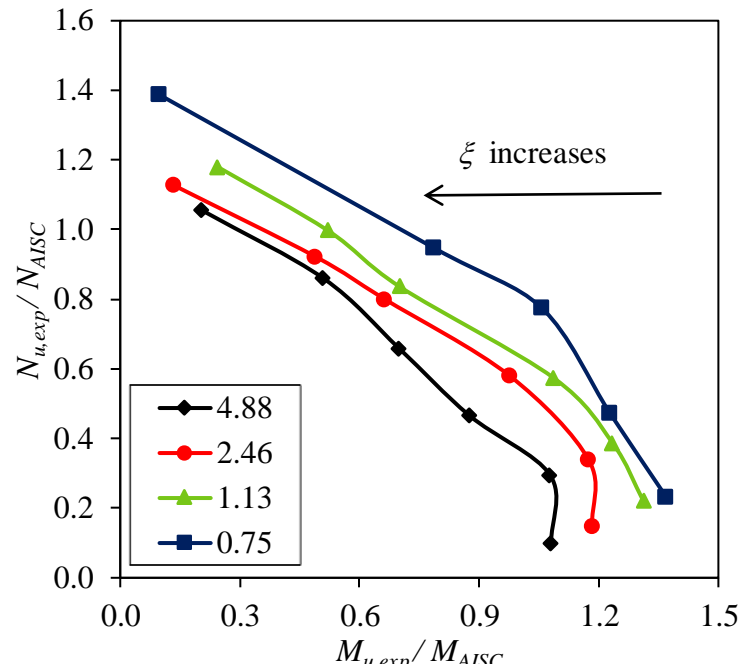


(b) Axial load-axial displacement

Figure 9.8. Load-deflection behaviour of series 80×120×3C40.



(a)



(b)

Figure 9.9. Effect of the relative strength ratio on the shape of the P-M interaction curve.

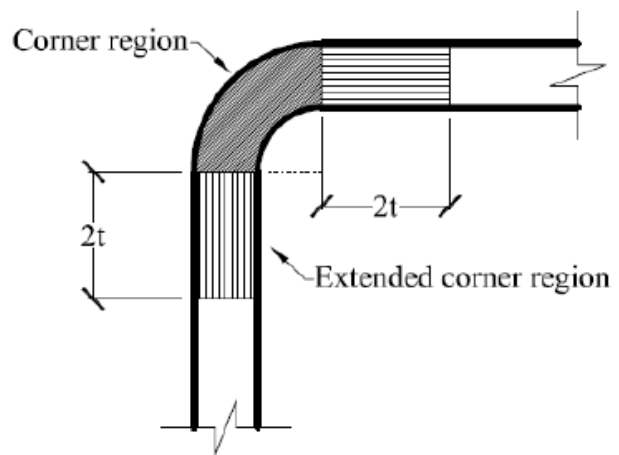


Figure 9.10. Extension of corner material properties to flat portions.



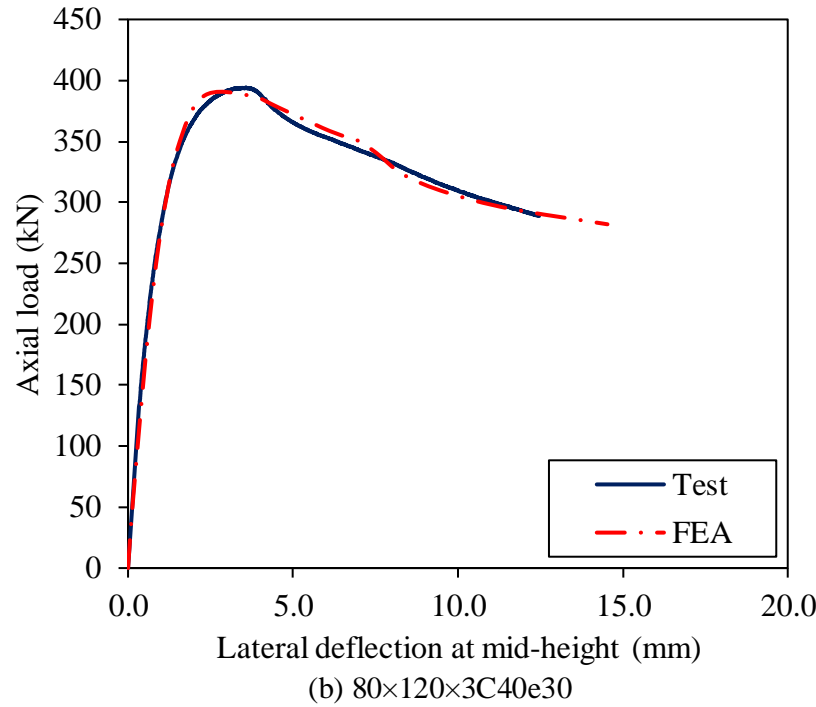
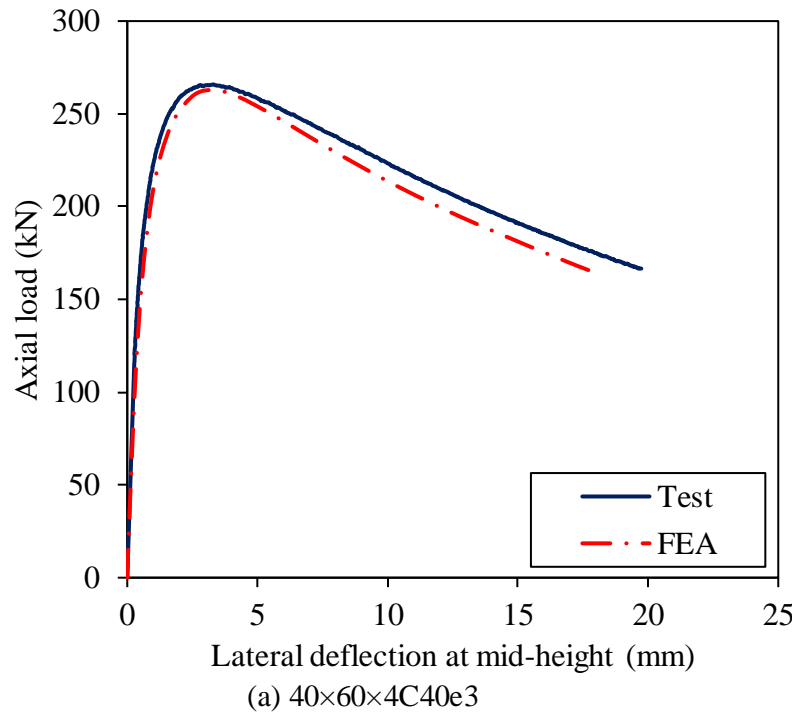


Figure 9.11. Experimental and numerical load-lateral deflection at mid-height curves for typical combined loading specimens.

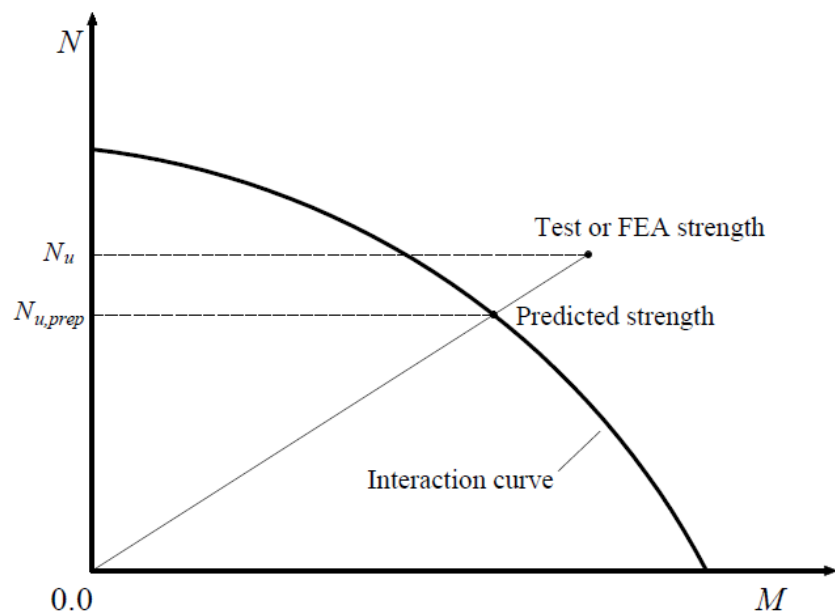


Figure 9.12. Definition of N_u and $N_{u,prep}$ on the beam-column interaction curve.

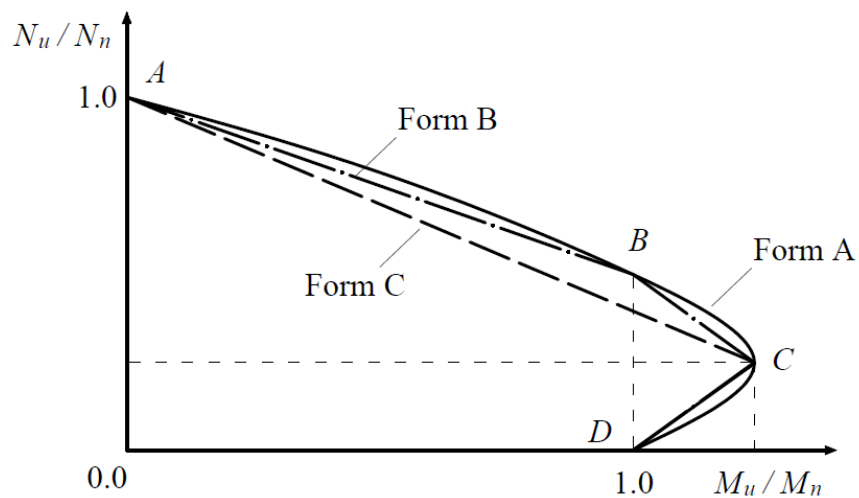
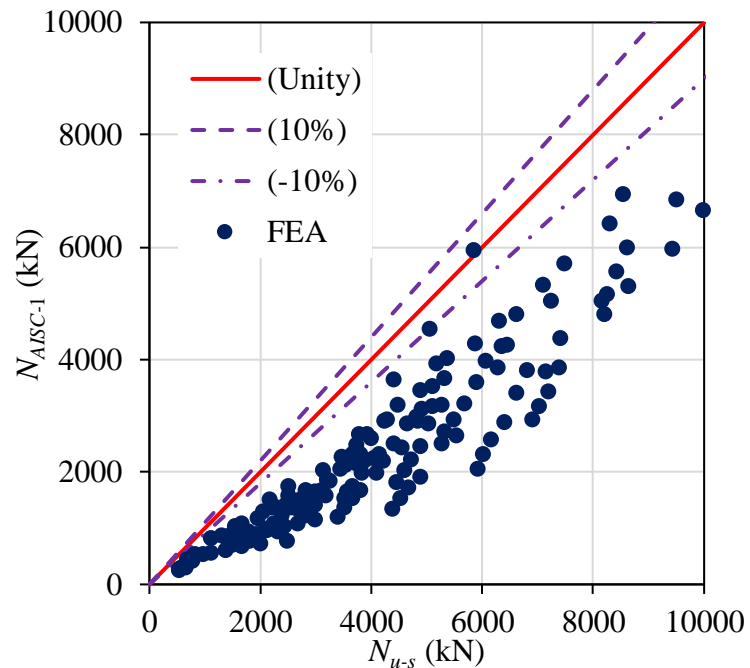
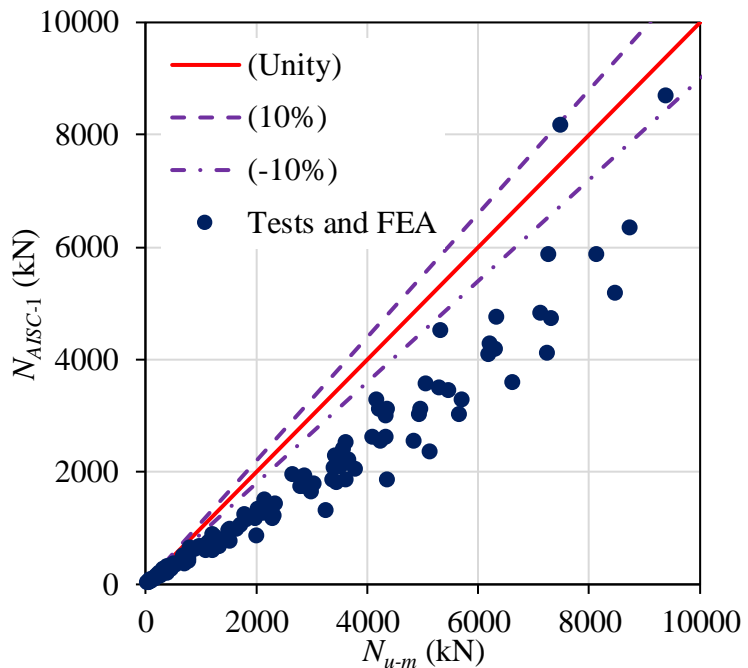


Figure 9.13. Different form of interaction curves for CFT beam-columns.





(a) Predictions for cross-sectional strengths



(b) Predictions for member strengths

Figure 9.14. Comparison with AISC Method-1 predicted strengths.

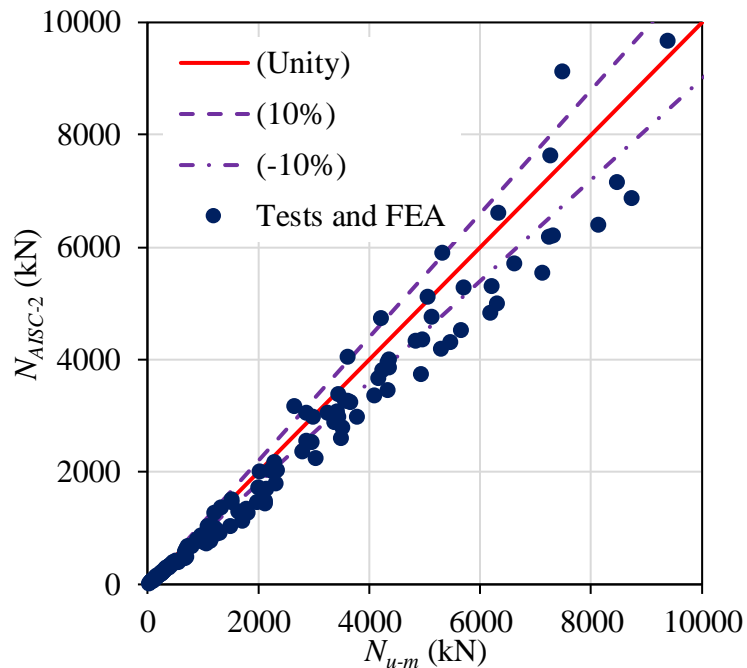
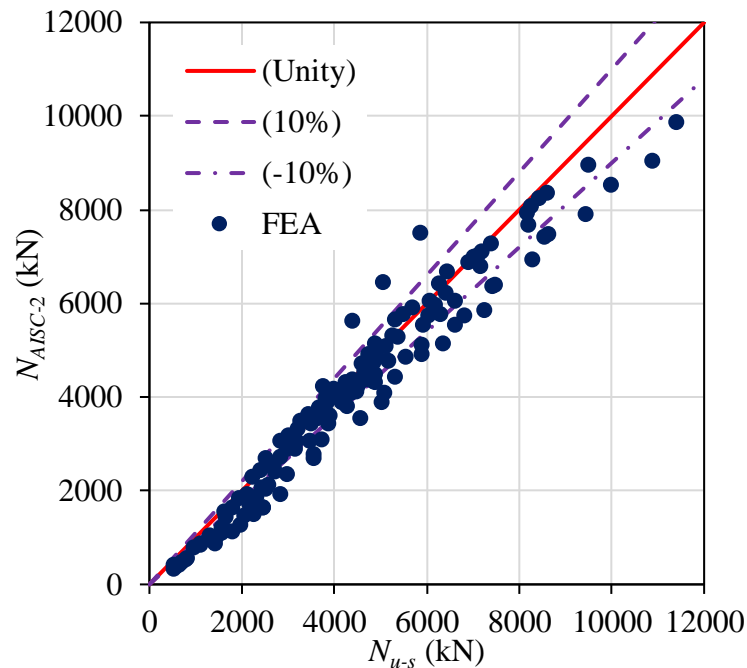
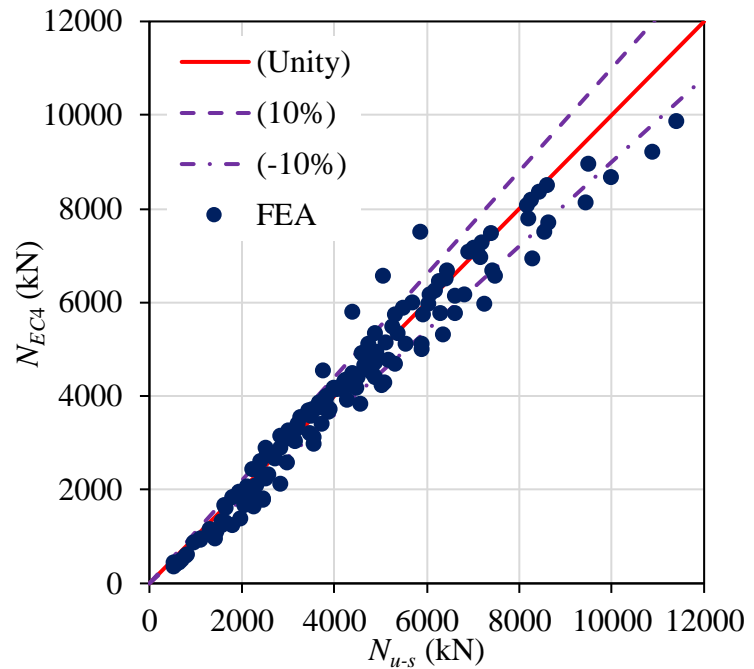
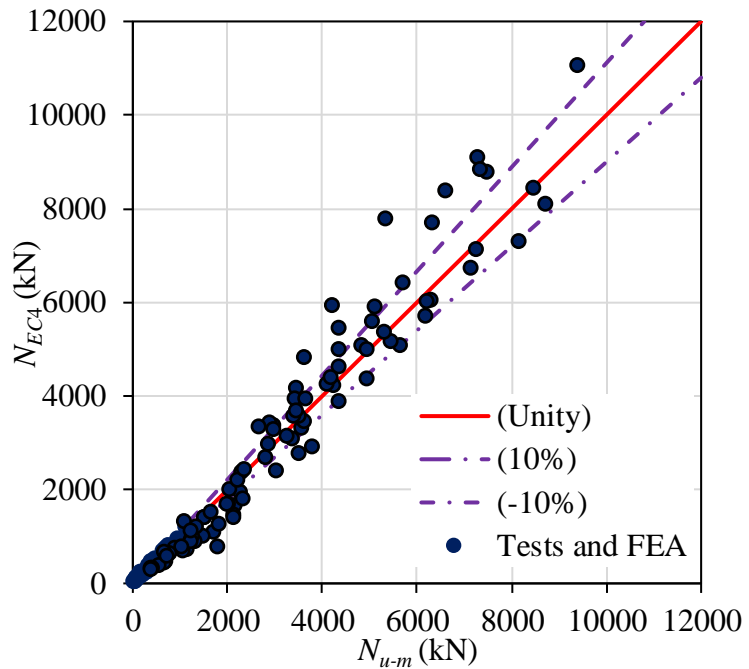


Figure 9.15. Comparison with AISC Method-2 predicted strengths.



(a) Predictions for cross-sectional strengths



(b) Predictions for member strengths

Figure 9.16. Comparison with EC4 predicted strengths.

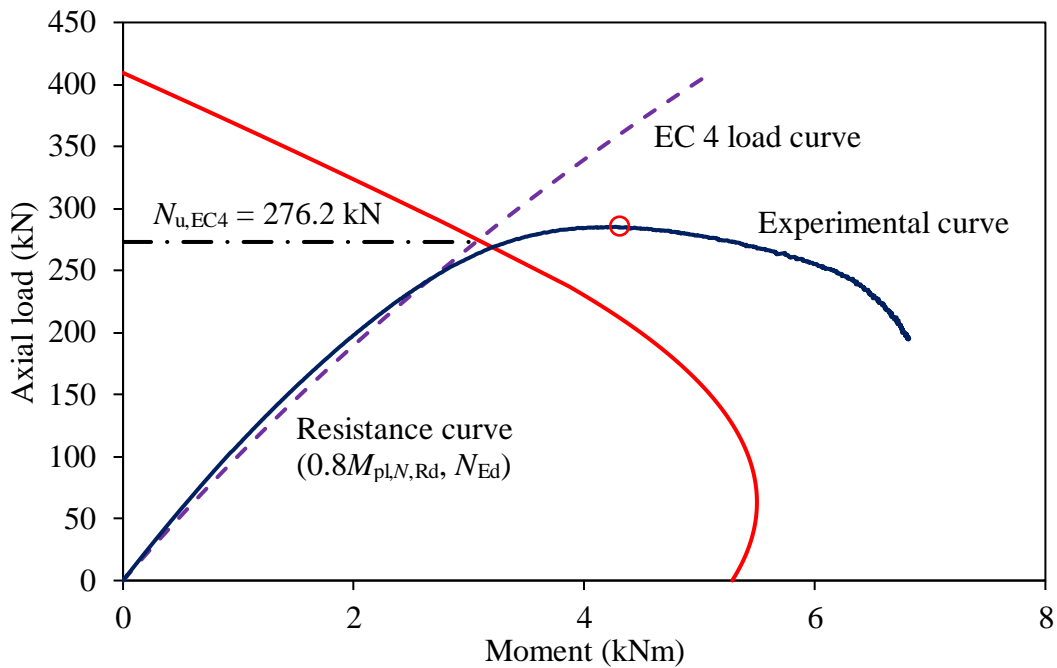


Figure 9.17. Example of determination of design resistance from EC4 for specimen 60×60×3C40e8.

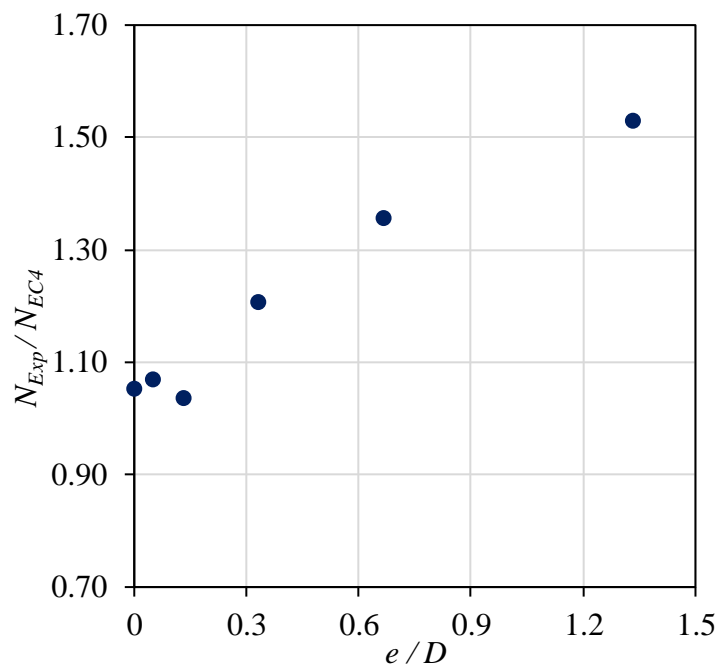


Figure 9.18. The predictions from EC4 versus different e/D ratio.

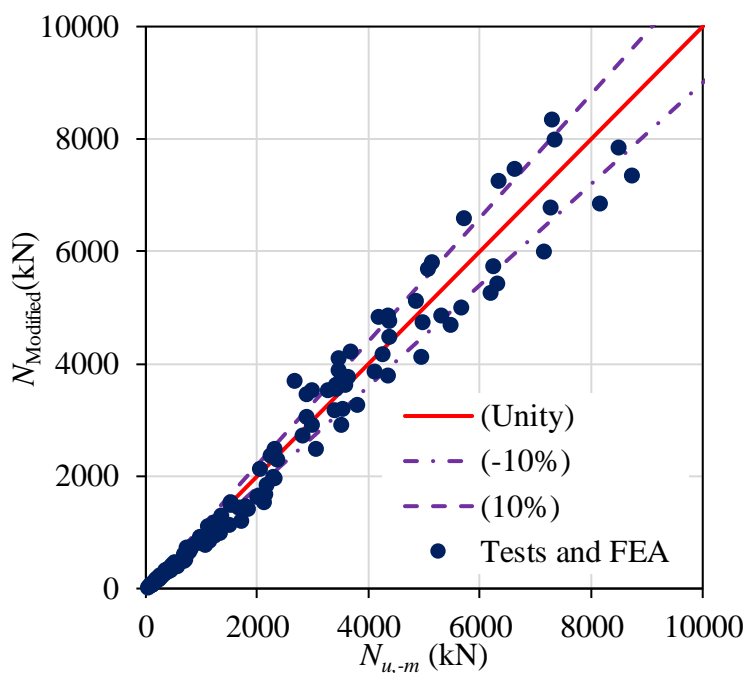


Figure 9.19. Comparison with modified predicted member strengths.



CHAPTER 10

CONCLUSIONS

10.1 Experimental Study

The experimental investigation on the material properties and member strengths of concrete-filled cold-formed stainless steel members was conducted. The test program includes material tests as well as stub column, beam and beam-column tests. The specimens consisted of different cross-sectional shapes. The square and rectangular hollow sections were cold-formed from ferritic stainless steel grade EN 1.4003, while the circular hollow sections were fabricated by cold-formed austenitic stainless steel EN 1.4301.

Tensile coupon tests were conducted to determine the material properties of cold-formed ferritic stainless steel and austenitic stainless steel at room temperatures. Tensile flat and corner coupons were extracted from cold-formed ferritic stainless steel square and rectangular hollow sections. Tensile curved coupons were extracted from cold-formed austenitic stainless steel circular hollow sections. The material properties of cold-formed ferritic stainless steel under elevated temperatures were also determined. A total of 56 tensile coupon tests were conducted using both the steady state and transient state methods.

A total of 22 stub column tests, 23 four-point bending tests and 48 beam-columns were conducted on concrete-filled cold-formed ferritic stainless steel square and



rectangular members. The ultimate axial strengths, flexural capacities and beam-column interaction relationship were obtained in this research study. In addition, a total of 10 four-point bending tests were conducted on cold-formed ferritic stainless steel hollow sections to assess the slenderness limits for classification of ferritic stainless steel sections. A total of 18 stub column tests and 18 four-point bending tests were carried out on concrete-filled cold-formed austenitic stainless steel circular members. The ultimate axial resistances and flexural capacities were also reported in this thesis.

10.2 Numerical Study

Finite element models were developed in order to simulate the experimental results. The finite element models are capable of predicting the ultimate resistance of the experimental tests. The verified finite element models were used to conduct a comprehensive parametric study and complementary data were generated by the finite element analyses using the developed models.

The parametric study on concrete-filled cold-formed ferritic stainless steel members included 165 stub column specimens, 171 beam specimens and 239 beam-column specimens. A wide range of cross-section dimensions and thicknesses were considered for the square and rectangular sections. Different initial eccentricities and lengths were also examined for the beam-column specimens. A total of 149 out of 239 beam-column specimens were short member length in order to investigate the sectional resistance of concrete-filled cold-formed ferritic stainless steel members under combined axial load and bending condition. The rest of 90 specimens were long member length to study the member axial load versus moment interaction behaviour.



A total of 168 stub column specimens and 165 beam specimens were performed on concrete-filled cold-formed austenitic stainless steel members. A wide range of outer diameter-to-thickness ratio was studied in the parametric study.

10.3 Design Recommendations

For the material properties of cold-formed ferritic stainless steel under elevated temperatures, the EC3 (2005b) predicted the elastic modulus quite well from ambient temperature to 450°C, but unconservatively predicted from 450°C onwards. The unified equation proposed by Chen and Young (2006) provided safe predictions for elastic modulus. The reduction factors of yield strength are accurately predicted by EC3 (2005b) from ambient temperature to 400°C, but unconservatively from 400°C onwards. The unified equation proposed by Chen and Young (2006) provided safe predictions from ambient temperature to 550°C but unconservative predictions from 550°C onwards for the yield strength. The reduction factors of ultimate strength predicted by EC3 (2005b) overestimated the performance of ferritic stainless steel at elevated temperatures, whereas the predictions by Chen and Young (2006) agrees well with the test results up to 400°C, but unconservative for temperature of 400°C and above. The thermal expansion predictions by EC3 (2005b) covers the austenitic stainless steel only. It is shown that the EC3 (2005b) overestimated the thermal elongation, and hence could not apply to ferritic stainless steel. A new set of predictive equations was proposed for the reduction factor of elastic modulus, yield strength and ultimate strength based on the test results and the available data (Manninen and Säynäjäkangas, 2012) for ferritic stainless steel.



For the cold-formed ferritic stainless steel hollow sections, the design predictions obtained from SEI/ASCE-8 (2002), AS/NZS-4673 (2001), EC3 (2015), direct strength method (AISI-S100, 2016), modified direct strength method proposed by Huang and Young (2014b) and continuous strength method (Afshan and Gardner, 2013b) were assessed. It is found that the modified DSM equations proposed by Huang and Young (2014b) provided the most accurate predictions for cold-formed ferritic stainless steel beams. Modification to the current European code is proposed and the modified equation provides more accurate and less scatter predictions compared to the current EC3 (2015). It is recommended that the modified direct strength method proposed by Huang and Young (2014b) can be used in the design of cold-formed ferritic stainless steel beams of square and rectangular hollow sections. Furthermore, it is shown that the current slenderness limits in EC3 (2015) for element subject to bending is suitable for ferritic stainless steel, but not for element subject to compression and the limits can be relaxed. Therefore, new slenderness limits are proposed for element subject to compression in cold-formed ferritic stainless steel.

The current design specifications and standards such as the American Specification AISC 360 (2016), American Code ACI 318 (2014), EC4 (2004) and AS 5100.6 (2004) for composite members are used for the design of concrete-filled carbon steel tubular members. The design specifications were assessed to check their applicability to concrete-filled stainless steel tubular members by comparing with the experimental and numerical results obtained from stub columns, beams and beam-columns.

As for the concrete-filled stainless steel stub columns, the American Specification AISC 360 (2016), American Code ACI 318 (2014), EC4 (2004) and Australian Standard AS 5100.6 (2004) were assessed. It is found that the EC4 (2004)



provides the best predictions on the axial compressive strength of concrete-filled cold-formed ferritic stainless steel stub columns. As for the concrete-filled cold-formed austenitic stainless steel stub columns, the American Specification AISC 360 (2016), American Code ACI 318 (2014), EC4 (2004) and Australian Standard AS 5100.6 (2004) are found to be conservative in predicting the axial resistances. Modification to AS 5100.6 was also carried out. It is found that the modified AS 5100.6 provides the most accurate predictions on concrete-filled circular stainless steel stub columns.

For the concrete-filled stainless steel flexural members subjected to bending, the current American Code AISC 360 (2016), American Code ACI 318 (2014), EC4 (2004) and AS 5100.6 (2004) are found to be conservative in predicting the flexural resistances. The method proposed by Han (2004) was also assessed in this study. Modification to the method proposed by Han (2004) provides the best predictions on the flexural strength of composite beams. Therefore, it is recommended that the modified Han's method can be used in the design of concrete-filled cold-formed ferritic stainless steel flexural members of square and rectangular sections. For the concrete-filled cold-formed austenitic stainless steel flexural members, conservative predictions are obtained from the American Specification AISC 360 (2016), American Code ACI 318 (2014), EC4 (2004) and Australian Standard AS 5100.6 (2004). The design method proposed by Han (2004) was also examined and modification to Han's method is also proposed. The modified design method is found to provide the most accurate predictions on concrete-filled austenitic stainless steel circular tubes subjected to pure bending.

The current American Specification AISC 360 (2016), European Code EC4 (2004) and proposal from different researchers (Choi et al., 2006; Lai et al., 2015) for the design of concrete-filled carbon steel members were compared with the

experimental and numerical results of concrete-filled cold-formed ferritic stainless steel beam-columns. The available design methods are found to be conservative and scattered for concrete-filled ferritic stainless steel members under combined axial load and bending. EC4 predictions for cross-section strengths are recommended. Improved design rules for member strengths are proposed and good agreement compared with the experimental and numerical results.

10.4 Future Research

Concrete-filled stainless steel members, due to their aesthetic appearance, favourable ductility and energy absorption capacities, offer a good option for structural applications. Although extensive experimental and numerical investigations have been presented in this thesis, there are still rooms for future works.

The actual compressive behaviour of confined concrete inside the stainless steel tube is remained unknown. The constitutive model of confined concrete is different from that of concrete-filled carbon steel tube due to the different interface bonding conditions and ductile behaviour of stainless steel.



REFERENCES

ABAQUS. (2012) ABAQUS/Standard user's manual volumes I-III and ABAQUS CAE manual. Version 6.12. Hibbit, Karlsson & Sorensen, Inc., Pawtucket, USA.

ABAQUS. (2014), *ABAQUS Standard User's Manual*. Dassault Systemes Simulia Corp., Version 6.14, USA.

ACI 318. (1999), *Building code requirements for structural concrete*, (ACI 318-99). Detroit (MI): American concrete institute (ACI).

ACI 318. (2014), *Building code requirements for structural concrete*, (ACI 318-14). Detroit (MI): American concrete institute (ACI).

Afshan, S., Francis, P., Baddoo, NR. and Gardner, L. (2015), “Reliability analysis of structural stainless steel design provisions”, *Journal of Constructional Steel Research*, 114, 293-304.

Afshan, S. and Gardner, L. (2013a), “Experimental study of cold-formed ferritic stainless steel hollow sections”, *Journal of Structural Engineering*, 139(5), 717-728.

Afshan, S. and Gardner, L. (2013b), “The continuous strength method for structural stainless steel design”, *Thin-Walled Structures*, 68, 42-49.

AISC (1999), *Load and resistance factor design (LRFD) specification for structural steel buildings*, American institute of steel construction (AISC), Chicago, USA.



AISC 360 (2010), *Specification for structural steel buildings* (ANSI/AISC 360-10), fourth printing: American institute of steel construction (AISC), Chicago, USA.

AISC 360 (2016), *Specification for structural steel buildings* (ANSI/AISC 360-16), American institute of steel construction (AISC), Chicago, USA.

AISI-S100 (2016), *North American Specification for the design of cold-formed steel structural members*. American Iron and Steel Institute, Washington, USA.

AISI-S100C (2016), *Commentary on North American Specification for the design of cold-formed steel structural members*. American Iron and Steel Institute, Washington, USA.

Arrayago, I., Picci, F., Mirambell, E. and Real, E. (2015), “Interaction of bending and axial load for ferritic stainless steel RHS columns”, *Thin-Walled Structures*, 91, 96-107.

Arrayago, I., Real, E. and Mirambell, E. (2016), “Experimental study on ferritic stainless steel RHS and SHS beam-columns”, *Thin-Walled Structures*, 100, 93-104.

AS 5100.6 (2004), *Bridge design, Part 6: steel and composite construction*. Standards Australia AS 5100.6, Sydney, Australia.

ASCE. (2002), *Specification for the design of cold-formed stainless steel structural members*, SEI/ASCE 8-02. American Society of Civil Engineers. Reston, Virginia, USA.



Ashraf, M., Gardner, L. and Nethercot, D.A. (2006), “Finite element modelling of structural stainless steel cross-sections”, *Thin-walled Structures*, 44(10), 1048-1062.

ASTM C469/C469M. (2014), *Standard test methods for static modulus of elasticity and Poisson’s ratio of concrete in compression*. C469/C469M-14, American Society for Testing and Materials, West Conshohocken, USA.

ASTM E8. (2015), *Standard test methods for tension testing of metallic materials*, ASTM E8/E8M-15a, American Society of Testing and Materials, West Conshohocken, USA.

ASTM E21. (2009), *Standard test methods for elevated temperature tension tests of metallic materials*, ASTM E21-09, American Society of for Testing and Materials, West Conshohocken, USA.

ASTM E384. (2016), *Standard test method for Knoop and Vickers Hardness of material*, ASTM E384-16, American Society of Civil Engineers, West Conshohocken, USA.

AS/NZS. (2001), *Cold-formed stainless steel structures*. AS/NZS 4673, Australian/New Zealand Standard, Sydney, Australia.

Baddoo, N. R. (2008). “Stainless steel in construction: A review of research, applications, challenges and opportunities”, *Journal of Constructional Steel Research*, 64(11), 1199-1206.

Binici, B. (2005), “An analytical model for stress-strain behavior of confined concrete”, *Engineering Structures*, 27(7), 1040-1051.



Bock, M., Arrayago, I. and Real, E. (2015), “Experiments on cold-formed ferritic stainless steel slender sections”, *Journal of Constructional Steel Research*, 109, 13-23.

Bradford, M.A., Loh, H.Y. and Uy, B. (2002), “Slenderness limits for filled circular steel tubes”, *Journal of Constructional Steel Research*, 58(2), 243-252.

Cashell, K.A. and Baddoo, N.R. (2014), “Ferritic stainless steels in structural applications”, *Thin-Walled Structures*, 83, 169-181.

Chan, T.M., Huai, Y.M. and Wang, W. (2015), “Experimental investigation on lightweight concrete-filled cold-formed elliptical hollow section stub columns”, *Journal of Constructional Steel Research*, 115, 434-444.

Chitawadagi, M.V. and Narasimhan, M.C. (2009), “Strength deformation behaviour of circular concrete filled steel tubes subjected to pure bending”, *Journal of Constructional Steel Research*, 65(8), 1836-1845.

Chen, J. and Young, B. (2006), “Stress-strain curves for stainless steel at elevated temperatures”, *Engineering Structures*, 28(2), 229-239.

Choi, I.R., Chung, K.S., and Kim, D.H. (2014), “Thermal and mechanical properties of high-strength structural steel HSA800 at elevated temperatures”, *Materials & Design*, 63, 544-551.

Choi, Y.H., Foutch, D.A. and LaFave, J.M. (2006), “New approach to AISC P-M interaction curve for square concrete filled tube (CFT) beam-columns”, *Engineering Structures*, 28(11), 1586-98.



Choi, Y.H., Kim, K.S. and Choi, S.M. (2008), “Simplified P–M interaction curve for square steel tube filled with high-strength concrete”, *Thin-Walled Structures*, 46(5), 506-15.

CIDECT. (1998), *CIDECT Design Guide 5: For concrete-filled hollow section columns under static and seismic loading*. International committee for development and study of tubular structures.

EC0. (2002), *Eurocode 0: Basis of structural design*. European committee for standardization, EN 1990, CEN, European committee for standardization, Brussels.

EC2. (2004), *Design of concrete structures: part 1-1: general rules and rules for buildings*. BS EN 1992-1-1, British Standards Institution, London (UK).

EC3. (2005a), *Design of steel structures – Part 1.1: General rules and rules for buildings*. EN 1993-1-1, European committee for standardization, Brussels.

EC3. (2005b), *Eurocode 3: Design of steel structures – Part 1.2: General rules – Structural fire design*, EN 1993-1-2, CEN, European Committee for Standardization, Brussels.

EC3. (2006), *Eurocode 3: Design of steel structures – Part 1.4: General rules – Supplementary rules for stainless steels*, ENV 1993-1-4, CEN, European Committee for Standardization, Brussels.

EC3. (2015), *Eurocode 3: Design of steel structures: Part 1-4: General rules: Supplementary rules for stainless steel*, EN 1993-1-4:2006+A1:2015, CEN, European Committee for Standardization, Brussels.



EC4. (1994), *Eurocode 4: Design of composite steel and concrete structures. Part 1-1: General rules and rules for buildings*, EN-1994-1-1, British Standards Institution.

EC4. (2004), *Eurocode 4: Design of composite steel and concrete structures. Part 1-1: General rules and rules for buildings*, EN-1994-1-1, CEN, European Committee for Standardization, Brussels.

Elchalakani, M., Zhao, X.L. and Grzebieta, R.H. (2001), “Concrete-filled circular steel tubes subjected to pure bending”, *Journal of Constructional Steel Research*, 57(11), 1141-1168.

Ellobody, E. (2015), *Finite Element Analysis and Design of Steel and Steel-Concrete Composite Bridges*, Butterworth-Heinemann.

Ellobody, E., Young, B. and Lam, D. (2006), “Behaviour of normal and high strength concrete-filled compact steel tube circular stub columns”, *Journal of Constructional Steel Research*, 62(7), 706-715.

Ellobody, E. and Young, B. (2006), “Design and behaviour of concrete-filled cold-formed stainless steel tube columns”. *Engineering Structures*, 28(5), 716-728.

Elremaily, A. and Azizinamini, A. (2002), “Behavior and strength of circular concrete-filled tube columns”, *Journal of Constructional Steel Research*, 58(12), 1567-1591.

EN 10088-4. (2009), *Stainless steels – technical delivery conditions for sheet/plate and strip of corrosion resisting steels for construction purposes*, CEN, European committee for standardization, Brussels.



EN ISO 6892-1. (2016), *Metallic materials - Tensile testing Part 1: Method of test at ambient temperature*, CEN, Brussels.

Furlong, R.W. (1967), “Strength of steel-encased concrete beam columns”, *Journal of the Structural Division*, ASCE, 93, 113.

Gardner, L. (2005), “The use of stainless steel in structures”, *Progress in Structural Engineering and Materials*, 7(2), 45-55.

Gardner, L., Insausti, A., Ng, K.T. and Ashraf, M. (2010), “Elevated temperature material properties of stainless steel alloys”, *Journal of Constructional Steel Research*, 66(5), 634-647.

Gardner, L. and Nethercot, D.A. (2004a), “Experiments on stainless steel hollow sections - Part 1: Material and cross-sectional behaviour”, *Journal of Constructional Steel Research*, 60(9), 1291-1318.

Gardner, L. and Nethercot, D.A. (2004b), “Numerical modeling of stainless steel structural components-A consistent approach”, *Journal of Structural Engineering*, 130(10), 1586-1601.

Gardner, L. and Theofanous, M. (2008), “Discrete and continuous treatment of local buckling in stainless steel elements”, *Journal of Constructional Steel Research*, 64(11), 1207-1216.

Gardner, N.J. and Jacobson, E.R. (1967), “Structural behavior of concrete filled steel tubes”, *In Journal Proceedings*, 64(7), 404-413.

Ge, H. and Usami, T. (1992), “Strength of concrete-filled thin-walled steel box columns: experiment”, *Journal of Structural Engineering*, 118(11), 3036-3054.



Gho, W.M. and Liu, D. (2004), “Flexural behaviour of high-strength rectangular concrete-filled steel hollow sections”, *Journal of Constructional Steel Research*, 60(11), 1681-1696.

Giakoumelis, G. and Lam, D. (2004), “Axial capacity of circular concrete-filled tube columns”, *Journal of Constructional Steel Research*, 60(7), 1049-1068.

Han, L.H. (2002), “Tests on stub columns of concrete-filled RHS sections”, *Journal of Constructional Steel Research*, 58(3), 353-372.

Han, L.H. (2004), “Flexural behaviour of concrete-filled steel tubes”, *Journal of Constructional Steel Research*, 60(2), 313-337.

Han, L.H., Li, W. and Bjorhovde, R. (2014), “Developments and advanced applications of concrete-filled steel tubular (CFST) structures: Members”, *Journal of Constructional Steel Research*, 100, 211-228.

Han, L.H., Lu, H., Yao, G.H. and Liao, F.Y. (2006), “Further study on the flexural behaviour of concrete-filled steel tubes”. *Journal of Constructional Steel Research*, 62(6), 554-565.

Han, L.H., Yang, Y.F. and Tao, Z. (2003a), “Concrete-filled thin-walled steel SHS and RHS beam-columns subjected to cyclic loading”, *Thin-Walled Structures*, 41(9), 801-833.

Han, L.H., Yao, G.H. and Zhao, X.L. (2005), “Tests and calculations for hollow structural steel (HSS) stub columns filled with self-consolidating concrete (SCC)”, *Journal of Constructional Steel Research*, 61(9), 1241-1269.



Han, L.H., Yao, G.H. and Tao, Z. (2007), “Performance of concrete-filled thin-walled steel tubes under pure torsion”, *Thin-Walled Structures*, 45(1), 24-36.

Han, L.H., Zhao, X.L., Yang, Y.F. and Feng, J.B. (2003b), “Experimental study and calculation of fire resistance of concrete-filled hollow steel columns”, *Journal of Structural Engineering*, 129(3), 346-356.

Hill, H.N. (1944), “Determination of stress strain relations from the offset yield strength values”, *Technical Note No. 927*, National Advisory Committee for Aeronautics, Washington, D.C.

Hu, H.T., Huang, C.S., Wu, M.H., and Wu, Y.M. (2003), “Nonlinear analysis of axially loaded concrete-filled tube columns with confinement effect”, *Journal of Structural Engineering*, 129(10), 1322-1329.

Huang, Y. and Young, B. (2012), “Material properties of cold-formed lean duplex stainless steel sections”, *Thin-walled Structures*, 54, 72-81.

Huang, Y. and Young, B. (2014a), “Stress-strain relationship of cold-formed lean duplex stainless steel at elevated temperatures”, *Journal of Constructional Steel Research*, 92, 103-113.

Huang, Y. and Young, B. (2014b). “Experimental investigation of cold-formed lean duplex stainless steel beam-columns”, *Thin-Walled Structures*, 76, 105-117.

Huang, Y. and Young, B. (2014c), “The art of coupon tests”, *Journal of Constructional Steel Research*, 96, 159-175.



Inai, E., Mukai, A., Kai, M., Tokinoya, H., Fukumoto, T. and Mori, K. (2004), “Behavior of concrete-filled steel tube beam columns”, *Journal of Structural Engineering*, 130(2), 189-202.

Johansson, M. (2002), “The efficiency of passive confinement in CFT columns”, *Steel and Composite Structures*, 2(5), 379-396.

Kankanamge, N.D. and Mahendran, M. (2011), “Mechanical properties of cold-formed steels at elevated temperatures”, *Thin-Walled Structures*, 49(1), 26-44.

Kodur, V.K.R. (1999), “Performance-based fire resistance design of concrete-filled steel columns”, *Journal of Constructional Steel Research*, 51(1), 21-36.

Lai, M. (2015), *Behaviour of CFST columns with external confinement under uni-axial compression*. The University of Hong Kong, PhD thesis.

Lai, Z. and Varma, A.H. (2015), “Noncompact and slender circular CFT members: Experimental database, analysis, and design”, *Journal of Constructional Steel Research*, 106, 220-233.

Lai, Z., Varma, A.H. and Griffis, L.G. (2015), “Analysis and Design of Noncompact and Slender CFT Beam-Columns”, *Journal of Structural Engineering*, 142(1), 1-14.



Lai, Z., Varma, A.H. and Zhang, K. (2014), “Noncompact and slender rectangular CFT members: Experimental database, analysis, and design”, *Journal of Constructional Steel Research*, 101, 455-468.

Lam, D. and Gardner, L. (2008), “Structural design of stainless steel concrete filled columns”, *Journal of Constructional Steel Research*, 64(11), 1275-1282.

Liang, Q.Q. and Uy, B. (2000), “Theoretical study on the post-local buckling of steel plates in concrete-filled box columns”, *Computers and Structures*, 75(5), 479-490.

Liew, J.Y.R. (2015), “Design of composite columns with high strength steel and concrete”. *Proceedings of the Eighth International Conference on Advances in Steel Structures*, Lisbon.

Liew, J.R. and Xiong, D.X. (2012), “Ultra-high strength concrete filled composite columns for multi-storey building construction”, *Advances in Structural Engineering*, 15(9), 1487-1503.

Lu, H., Han, L.H. and Zhao, X.L. (2009), “Analytical behavior of circular concrete-filled thin-walled steel tubes subjected to bending”. *Thin-Walled Structures*, 47(3), 346-358.

Lu, Y.Q. and Kennedy, D.L. (1994), “The flexural behaviour of concrete-filled hollow structural sections”, *Canadian Journal of Civil Engineering*, 21(1), 111-130.



Ma, J.L., Chan, T.M., Young, B. (2015a), “Behaviour of cold-formed high strength tubular beam-columns of steel grade up to 900 MPa”, *In Eighth International Conference on Advances in Steel Structures*, Lisbon.

Ma, J.L., Chan, T.M. and Young, B. (2015b), “Experimental Investigation on Stub-Column Behavior of Cold-Formed High-Strength Steel Tubular Sections”, *Journal of Structural Engineering*, 142(5), 04015174.

Ma, J.L., Chan, T.M. and Young, B. (2015c), “Material properties and residual stresses of cold-formed high strength steel hollow sections”, *Journal of Constructional Steel Research*, 109, 152-165.

Mäkelänen, P. and Outinen, J. (1998), “Mechanical properties of an austenitic stainless steel at elevated temperatures”, *Journal of Constructional Steel Research*, 46, 455-455.

Mander, J. B., Priestley, M. J., and Park, R. (1988a), “Theoretical stress-strain model for confined concrete”, *Journal of Structural Engineering*, 114(8), 1804-1826.

Mander, J.B., Priestley, M.J.N. and Park, R. (1988b), “Observed stress-strain behavior of confined concrete”, *Journal of Structural Engineering*, 114(8), 1827-1849.

Manninen, T. and Säynäkkangas, J. (2012), “Mechanical Properties of Ferritic Stainless Steels at Elevated Temperature”, *In Proceedings of the Fourth International Experts Seminar on Stainless Steel in Structures*.



McCann, F., Gardner, L. and Qiu, W. (2015), “Experimental study of slender concrete-filled elliptical hollow section beam-columns”, *Journal of Constructional Steel Research*, 113, 185-194.

Mirambell, E., and Real, E. (2000), “On the calculation of deflections in structural stainless steel beams: An experimental and numerical investigation”, *Journal of Constructional Steel Research*, 54(1), 109–133.

Mursi, M. and Uy, B. (2004), “Strength of slender concrete filled high strength steel box columns”, *Journal of Constructional Steel Research*, 60(12), 1825-1848.

O'Shea, M.D. and Bridge, R.Q. (1998), “Tests on circular thin-walled steel tubes filled with medium and high strength concrete”, *Australian Civil Engineering Transactions*, 40, 15.

O'Shea, M.D. and Bridge, R.Q. (2000), “Design of circular thin-walled concrete filled steel tubes”, *Journal of Structural Engineering*, 126(11), 1295-1303.

Probst, A.D., Kang, T.H.K., Ramseyer, C. and Kim, U. (2010), “Composite flexural behavior of full-scale concrete-filled tubes without axial loads”, *Journal of Structural Engineering*, 136(11), 1401-1412.

Quach, W.M., Teng, J.G. and Chung, K.F. (2008), “Three-stage full-range stress-strain model for stainless steels”, *Journal of Structural Engineering*, 134(9), 1518-1527.



Ramberg, W. and Osgood, W. R. (1943), “Description of stress-strain curves by three parameters”, *Technical Note No. 902*, National Advisory Committee for Aeronautics, Washington, D.C.

Rasmussen, K.J. (2003), “Full-range stress–strain curves for stainless steel alloys”, *Journal of Constructional Steel Research*, 59(1), 47-61.

Richart, F.E., Brandtzaeg, A., and Brown, R.L. (1928), “A study of the failure of concrete under combined compressive stresses”. University of Illinois Bulletin; 26(12).

Roeder, C.W., Lehman, D.E. and Bishop, E. (2010), “Strength and stiffness of circular concrete-filled tubes”, *Journal of Structural Engineering*, 136(12), 1545-1553.

Saenz, L.P. (1964), “Discussion of ‘Equation for the stress-strain curve of concrete’ by P. Desayi, and S. Krishnan”, *Journal of the American Concrete Institute*, 61, 1229-1235.

Sakino, K., Nakahara, H., Morino, S. and Nishiyama, I. (2004), “Behavior of centrally loaded concrete-filled steel-tube short columns”, *Journal of Structural Engineering*, 130(2), 180-188.

Samani, A. K., and Attard, M. M. (2012), “A stress–strain model for uniaxial and confined concrete under compression”, *Engineering Structures*, 41, 335-349.

Schafer, B.W. and Ádány, S. (2006), “Buckling analysis of cold-formed steel members using CUFSM: conventional and constrained finite strip methods”, *In Eighteenth international specialty conference on cold-formed steel structures*, 39-54.



Schneider, S.P. (1998), "Axially loaded concrete-filled steel tubes", *Journal of Structural Engineering*, 124(10), 1125-1138.

Tao, Z., Brian, U.Y., Han, L.H. and He, S.H. (2008), "Design of concrete-filled steel tubular members according to the Australian Standard AS 5100 model and calibration", *Australian Journal of Structural Engineering*, 8(3), 197-214.

Tao, Z., Han, L.H. and Zhao, X.L. (2004), "Behaviour of concrete-filled double skin (CHS inner and CHS outer) steel tubular stub columns and beam-columns", *Journal of Constructional Steel Research*, 60(8), 1129-1158.

Tao, Z., Wang, Z. B., and Yu, Q. (2013), "Finite element modelling of concrete-filled steel stub columns under axial compression", *Journal of Constructional Steel Research*, 89, 121-131.

Theofanous, M. and Gardner, L. (2010), "Experimental and numerical studies of lean duplex stainless steel beams", *Journal of Constructional Steel Research*, 66(6), 816-825.

Tomii, M., Yoshimura, K. and Morishita, Y. (1977), "Experimental studies on concrete-filled steel tubular stub columns under concentric loading", *In Stability of Structures Under Static and Dynamic Loads*, National Science Foundation, Washington, D.C., 718-741.

Uy, B. (2001), "Strength of short concrete filled high strength steel box columns", *Journal of Constructional Steel Research*, 57(2), 113-134.

Uy, B. and Bradford, M.A. (1996), "Elastic local buckling of steel plates in composite steel-concrete members", *Engineering Structures*, 18(3), 193-200.



Uy, B., Tao, Z. and Han, L.H. (2011), “Behaviour of short and slender concrete-filled stainless steel tubular columns”, *Journal of Constructional Steel Research*, 67(3), 360-378.

Varma, A.H., Ricles, J.M., Sause, R. and Lu, L.W. (2002), “Experimental behavior of high strength square concrete-filled steel tube beam-columns”, *Journal of Structural Engineering*, 128(3), 309-318.

Varma, A.H., Ricles, J.M., Sause, R. and Lu, L.W. (2004), “Seismic behavior and design of high-strength square concrete-filled steel tube beam columns”, *Journal of Structural Engineering*, 130(2), 169-179.

Venkataramaiah, K.R. and Roorda, J. (1982), “Analysis of local plate buckling experimental data”, *6th International Specialty Conference on Cold-Formed Steel Structures*, University of Missouri, Rolla, MO, 45–74.

Wang, R., Han, L.H., Nie, J.G. and Zhao, X.L. (2014), “Flexural performance of rectangular CFST members”. *Thin-Walled Structures*, 79, 154-165.

Wright, H.D. (1995), “Local stability of filled and encased steel sections”, *Journal of Structural Engineering*, 121(10), 1382-1388.

Young, B. and Ellobody, E. (2006), “Experimental investigation of concrete-filled cold-formed high strength stainless steel tube columns”, *Journal of Constructional Steel Research*, 62(5), 484-492.

Young, B. and Hartono, W. (2002), “Compression tests of stainless steel tubular members”, *Journal of Structural Engineering*, 128(6), 754-761.



Zhou, F., Chen, Y. and Young, B. (2013), “Cold-formed high strength stainless steel cross-sections in compression considering interaction effects of constituent plate elements”, *Journal of Constructional Steel Research*, 80, 32-41.

Zhao, O., Gardner, L. and Young, B. (2016a), “Buckling of ferritic stainless steel members under combined axial compression and bending”, *Journal of Constructional Steel Research*, 117, 35-48.

Zhao, O., Gardner, L. and Young, B. (2016b), “Structural performance of stainless steel circular hollow sections under combined axial load and bending—Part 1: Experiments and numerical modelling”, *Thin-Walled Structures*, 101, 231-239.

Zhao, O., Rossi, B., Gardner, L. and Young, B. (2015), “Experimental and Numerical Studies of Ferritic Stainless Steel Tubular Cross Sections under Combined Compression and Bending”, *Journal of Structural Engineering*, 142(2), 04015110.

Zhao, X.L. and Grzebieta, R. (1999), “Void-filled SHS beams subjected to large deformation cyclic bending”, *Journal of Structural Engineering*, 125(9), 1020-1027.

Ziemian, R.D. (2010), *Guide to stability design criteria for metal structures*, 6th Edition, Wiley, Hoboken, NJ, USA.



APPENDIX A

STRESS-STRAIN CURVES OF COLD-FORMED STAINLESS STEELS IN TENSILE COUPON TESTS

This Appendix presents the stress-strain curves of cold-formed stainless steel specimens obtained from the tensile coupon tests at elevated temperatures. The stress-strain curves for cold-formed ferritic stainless steel grade EN 1.4003 obtained from flat and corner coupon tests are shown in Figures A1 and A2, respectively. The stress-strain curves for cold-formed austenitic stainless steel grade EN 1.4301 (AISI 304) are presented in Figures A3.



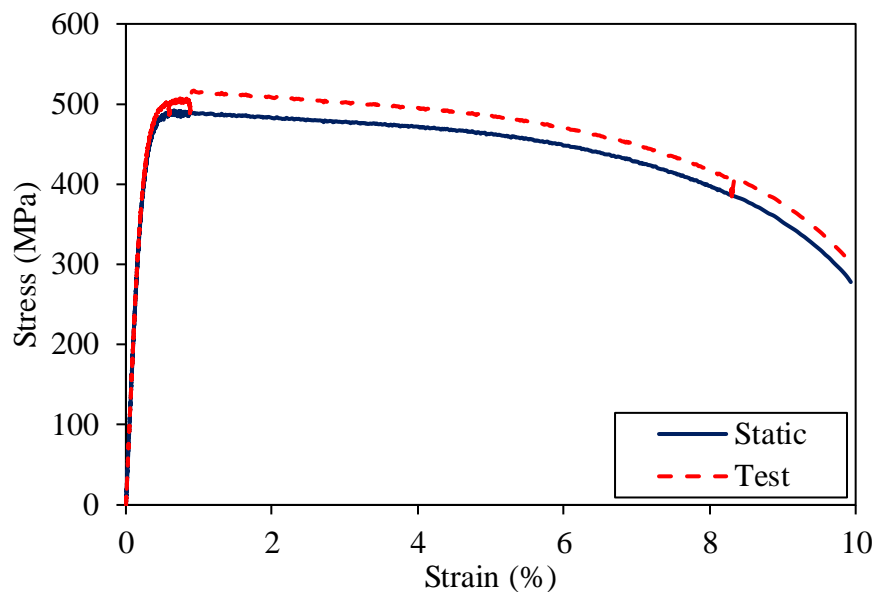


Figure A1-1. Static and test stress-strain curves of flat coupon specimen for section 60×40×4.

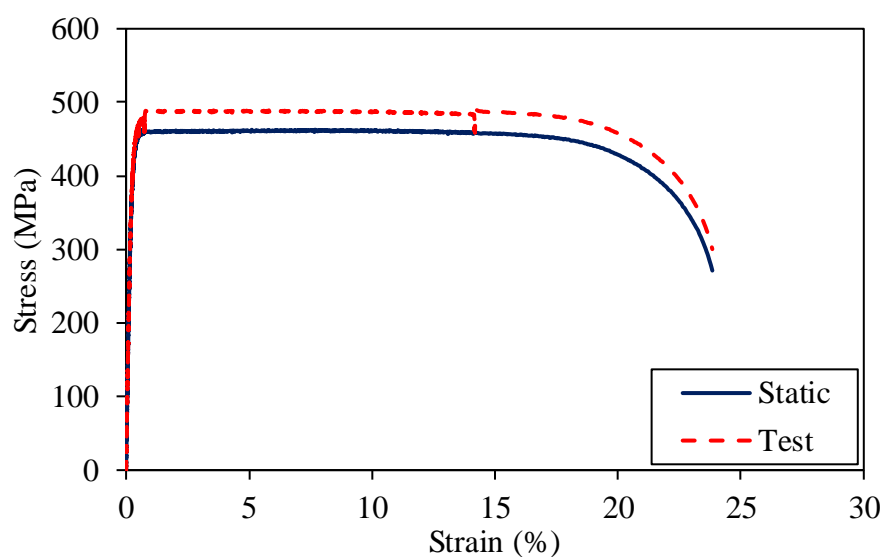


Figure A1-2. Static and test stress-strain curves of flat coupon specimen for section 60×60×3.



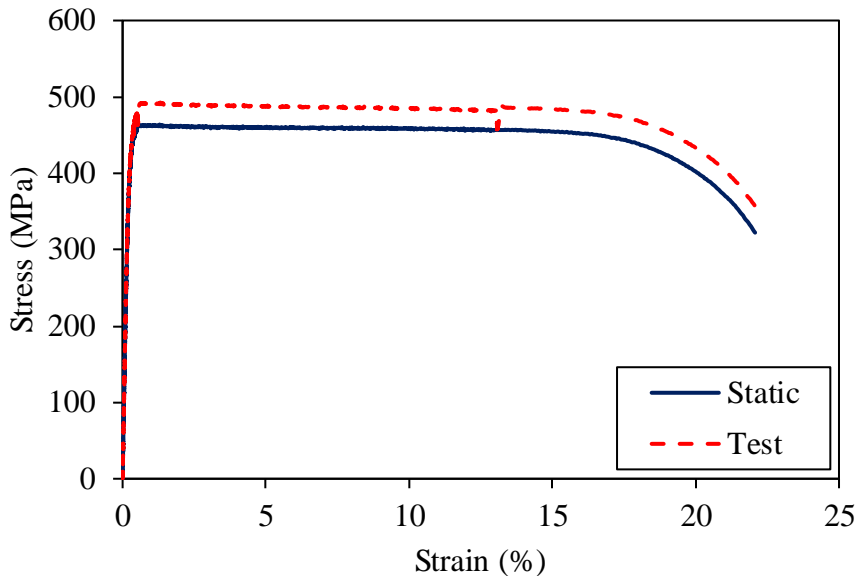


Figure A1-3. Static and test stress-strain curves of flat coupon specimen for section 80×60×4.

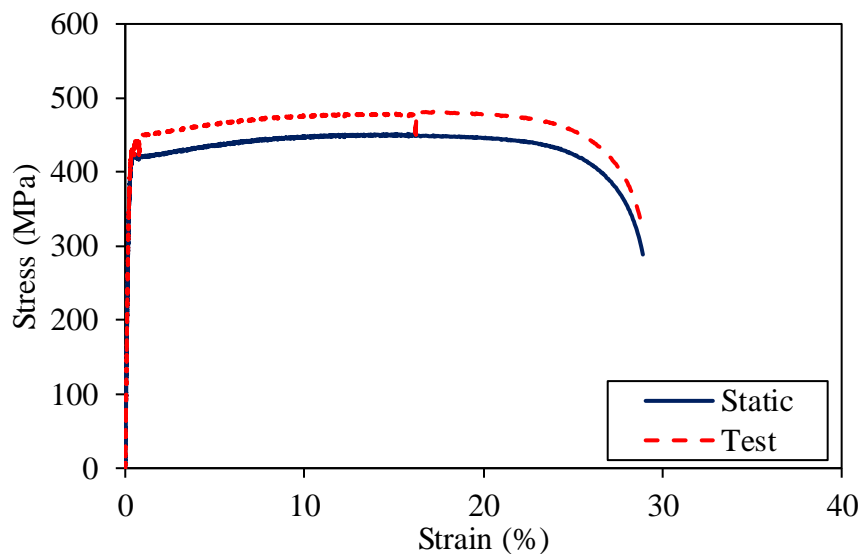


Figure A1-4. Static and test stress-strain curves of flat coupon specimen for section 100×40×2.



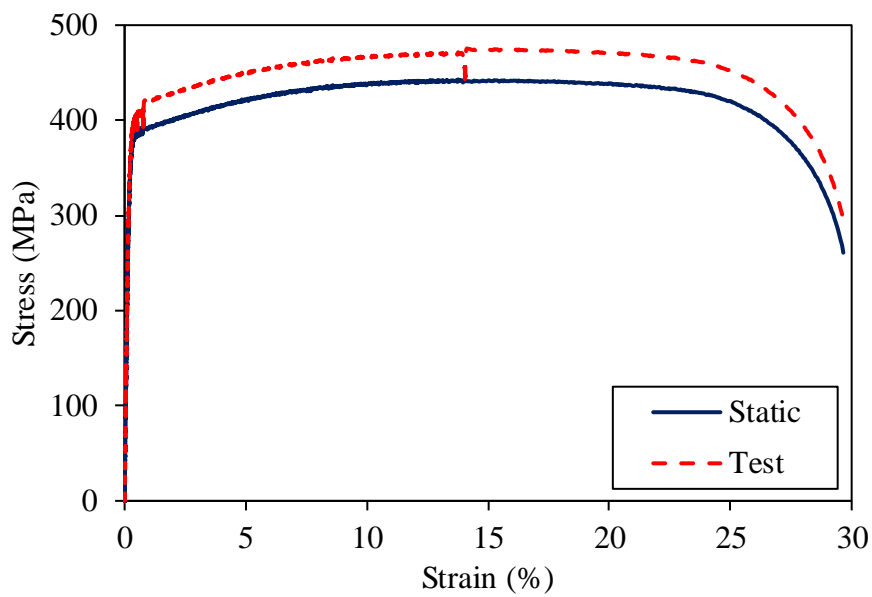


Figure A1-5. Static and test stress-strain curves of flat coupon specimen for section $120 \times 80 \times 3$.

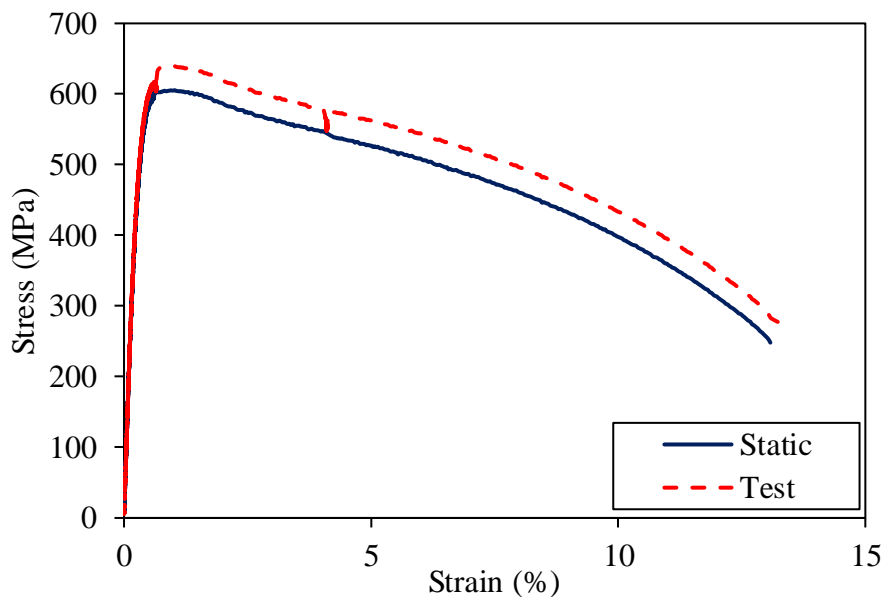


Figure A2-1. Static and test stress-strain curves of corner coupon specimen for section $60 \times 40 \times 4$.



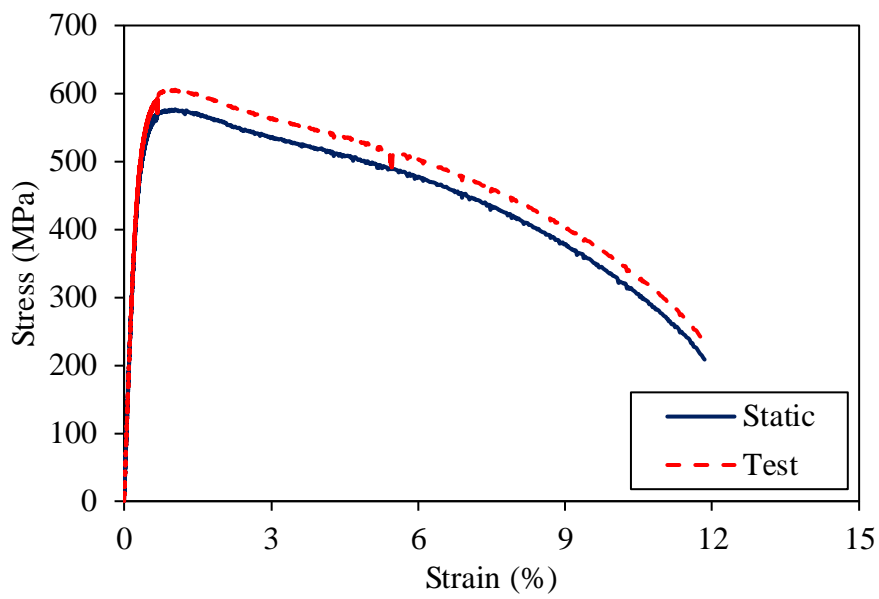


Figure A2-2. Static and test stress-strain curves of corner coupon specimen for section $60 \times 60 \times 3$.

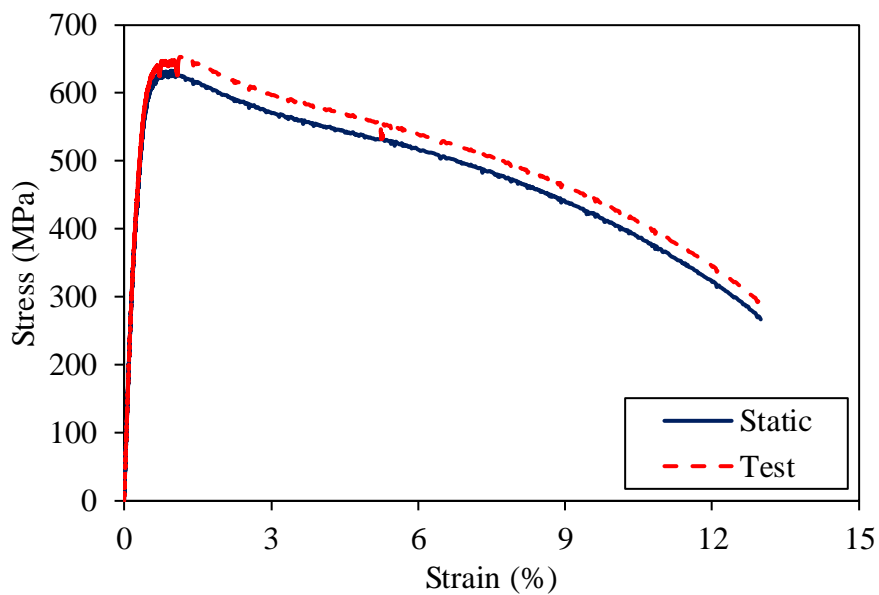


Figure A2-3. Static and test stress-strain curves of corner coupon specimen for section $80 \times 60 \times 4$.



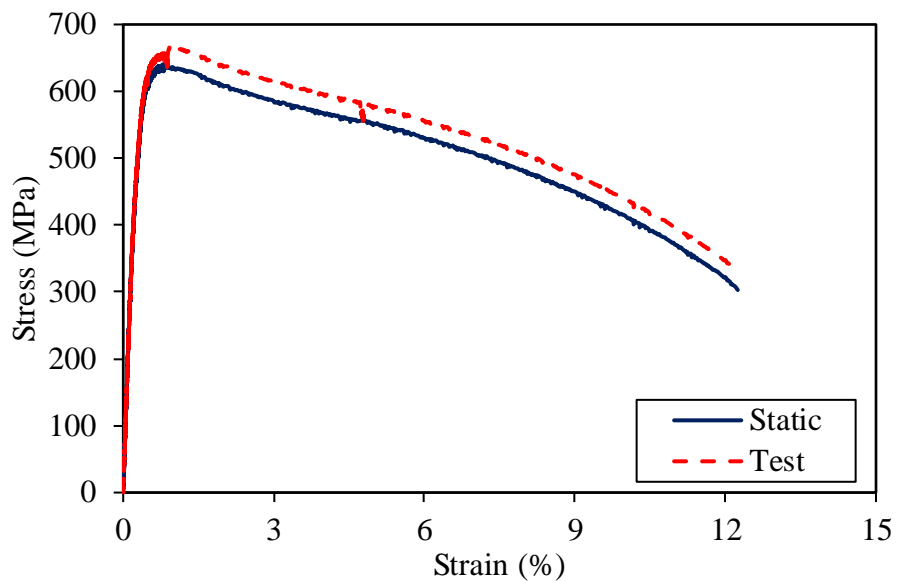


Figure A2-4. Static and test stress-strain curves of corner coupon specimen for section 100×40×2.

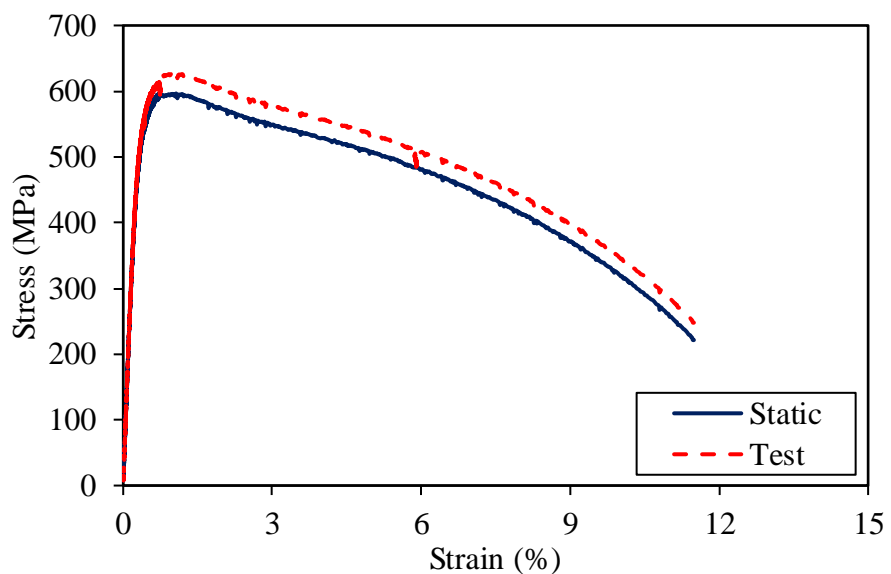


Figure A3-1. Static and test stress-strain curves of corner coupon specimen for section 120×80×3.



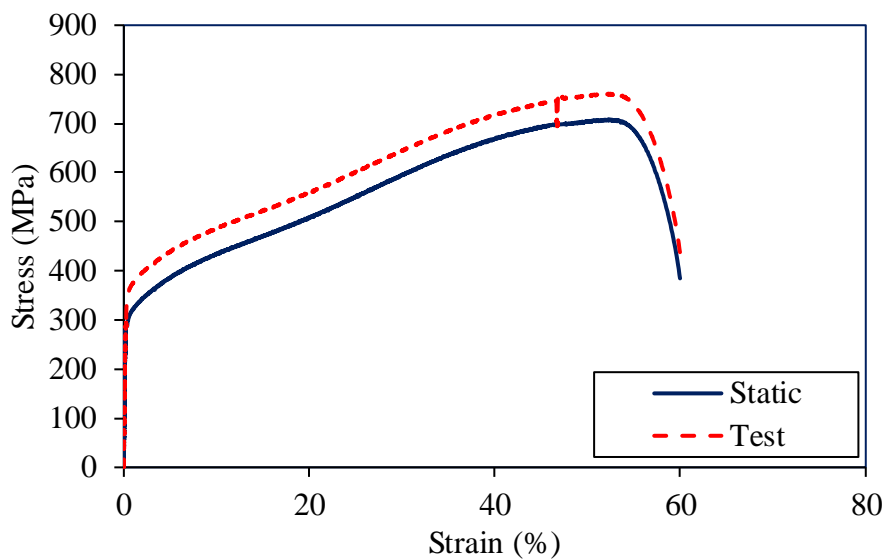


Figure A3-2. Static and test stress-strain curves of curved coupon specimen for section 60.5×2.8.

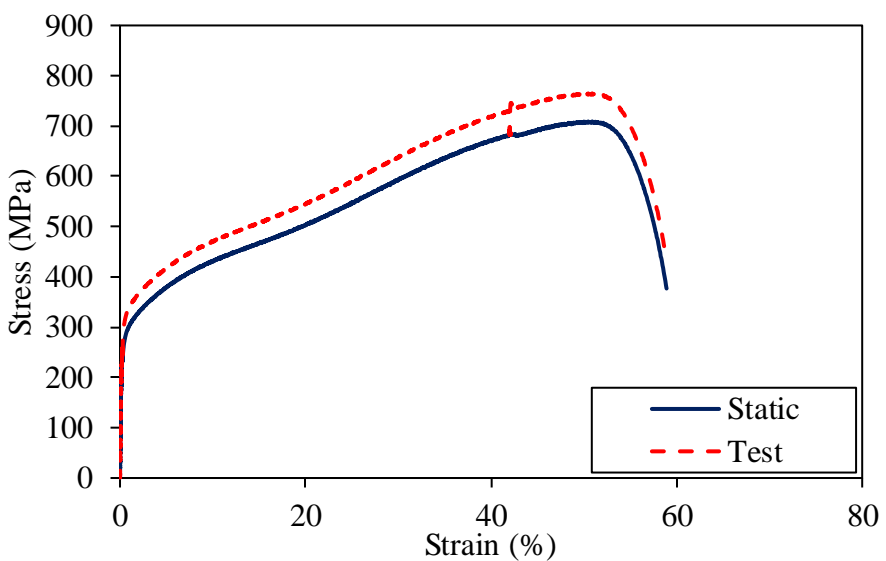


Figure A3-3. Static and test stress-strain curves of curved coupon specimen for section 76.0×3.0.



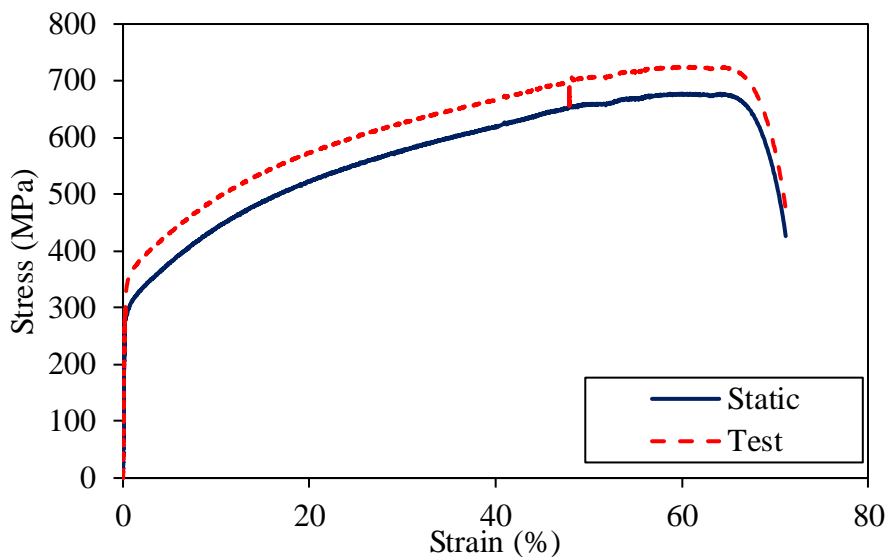


Figure A3-4. Static and test stress-strain curves of curved coupon specimen for section 114.3×3.0.

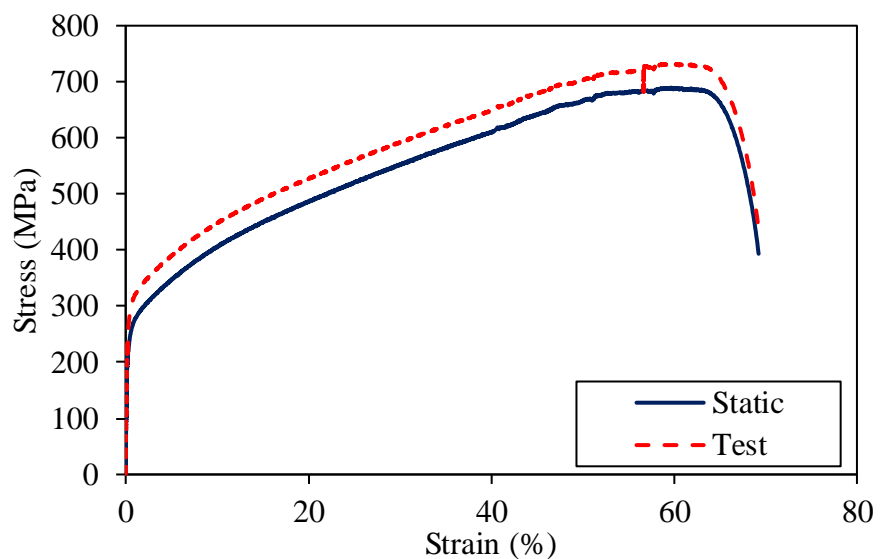


Figure A3-5. Static and test stress-strain curves of curved coupon specimen for section 165.2×3.0.



APPENDIX B

COLD-FORMED FERRITIC STAINLESS STEEL

HOLLOW SECTIONS BEAM TESTS

The bending behaviour of cold-formed ferritic stainless steel hollow sections were investigated through four-point bending tests. The test and static moment-curvature curves obtained from flexural tests are given in Appendix B1. The finite element models were validated against the test results and shown in Appendix B2.



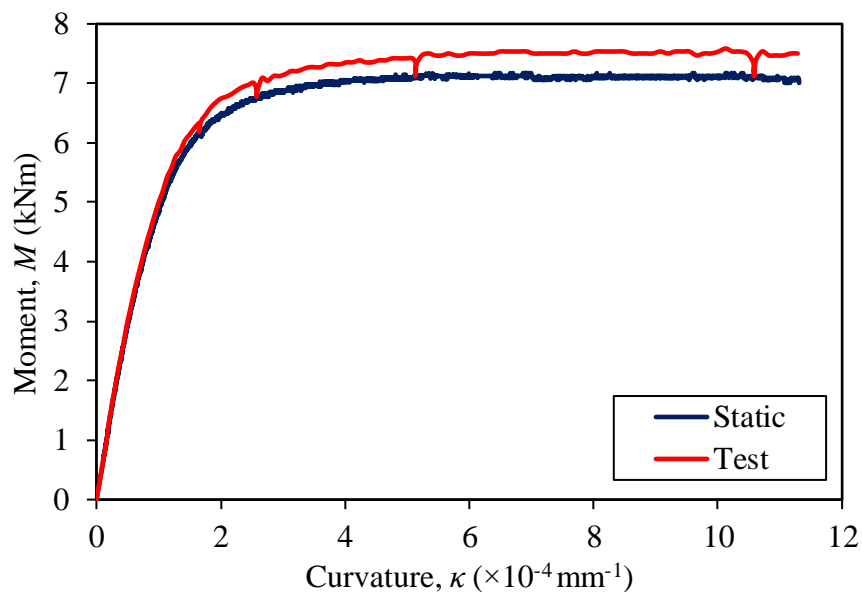


Figure B1-1. Moment-curvature curves for specimen 60×40×4.

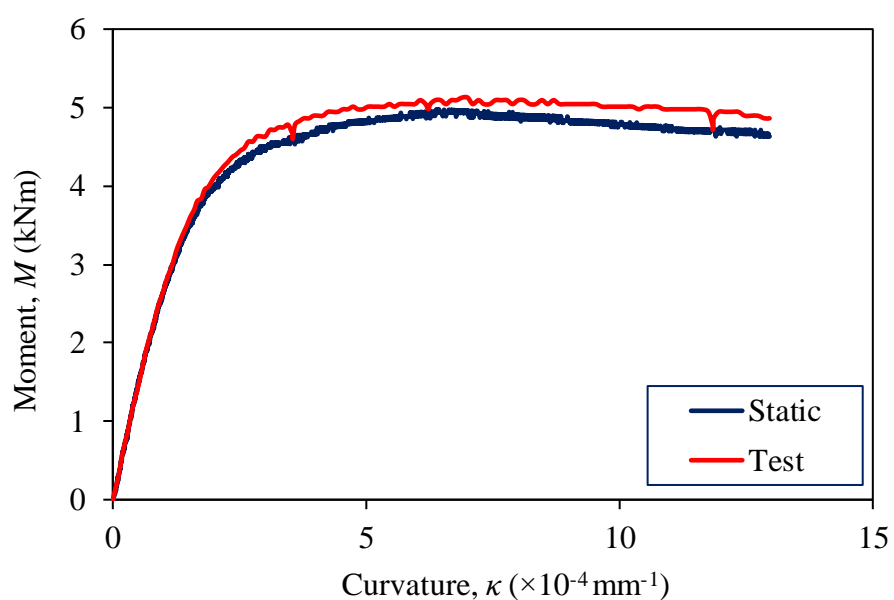


Figure B1-2. Moment-curvature curves for specimen 40×60×4.



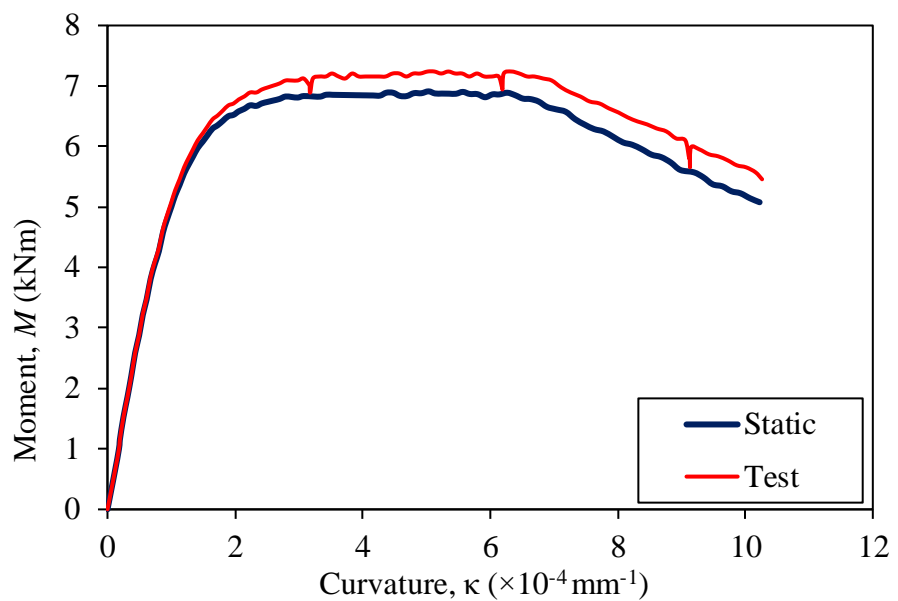


Figure B1-3. Moment-curvature curves for specimen 60×60×3.

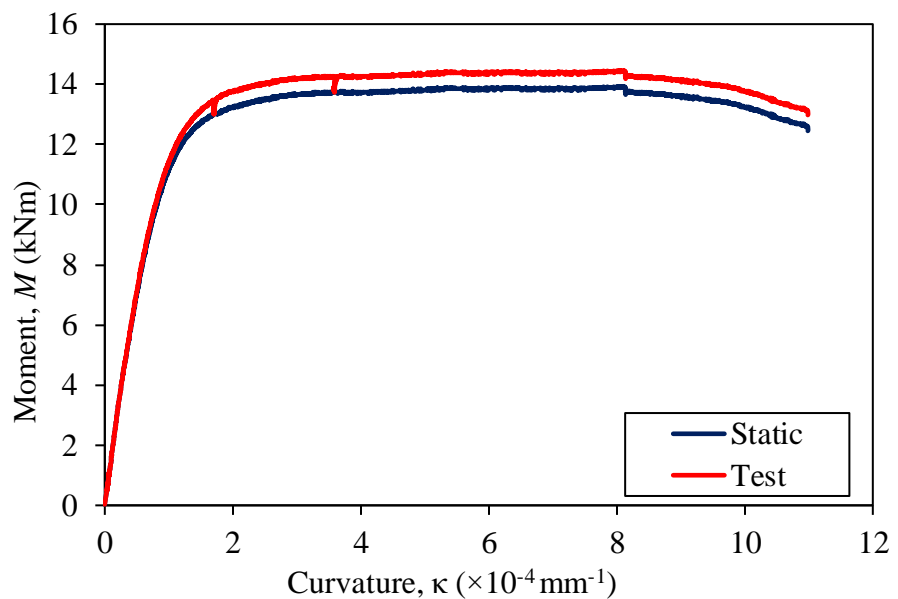


Figure B1-4. Moment-curvature curves for specimen 80×60×4.



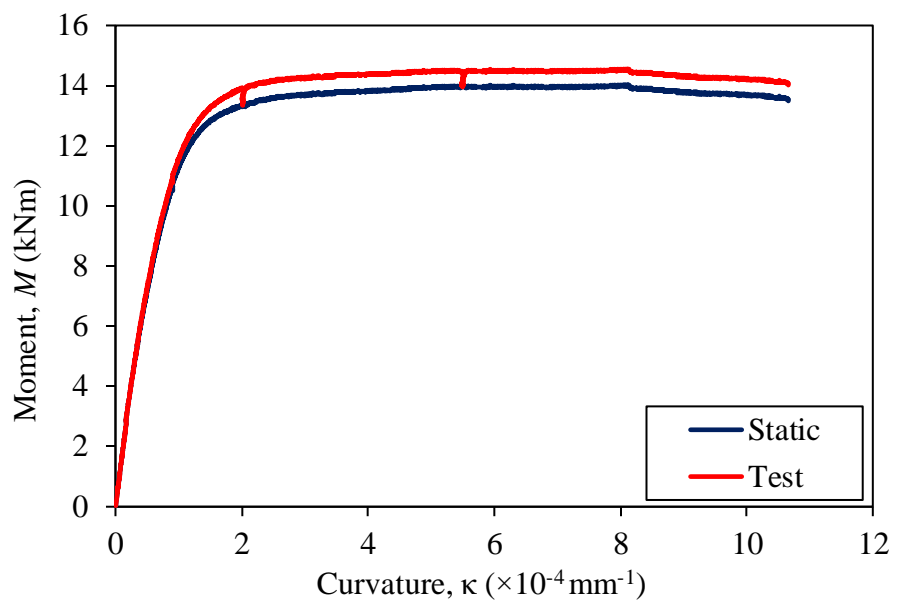


Figure B1-5. Moment-curvature curves for specimen 80×60×4R.

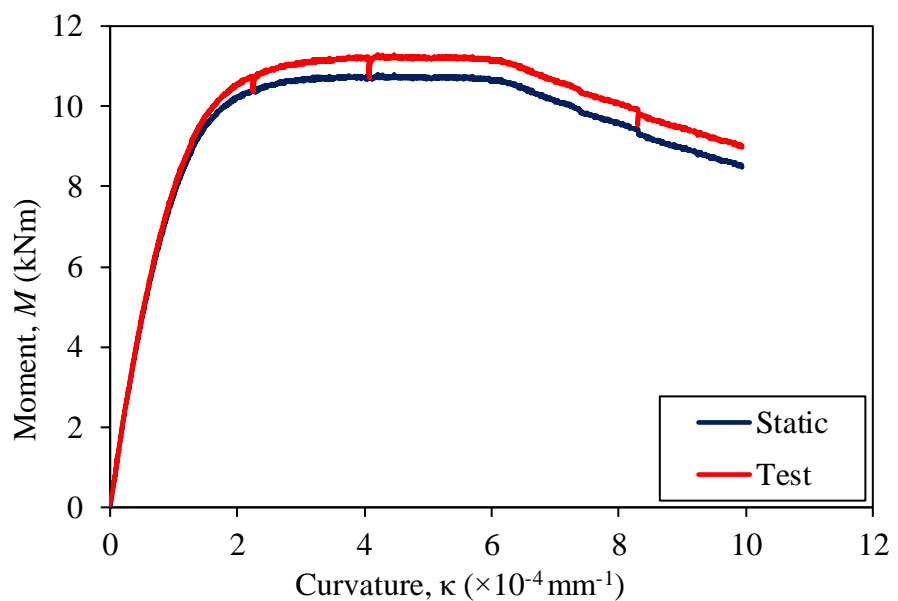


Figure B1-6. Moment-curvature curves for specimen 60×80×4.



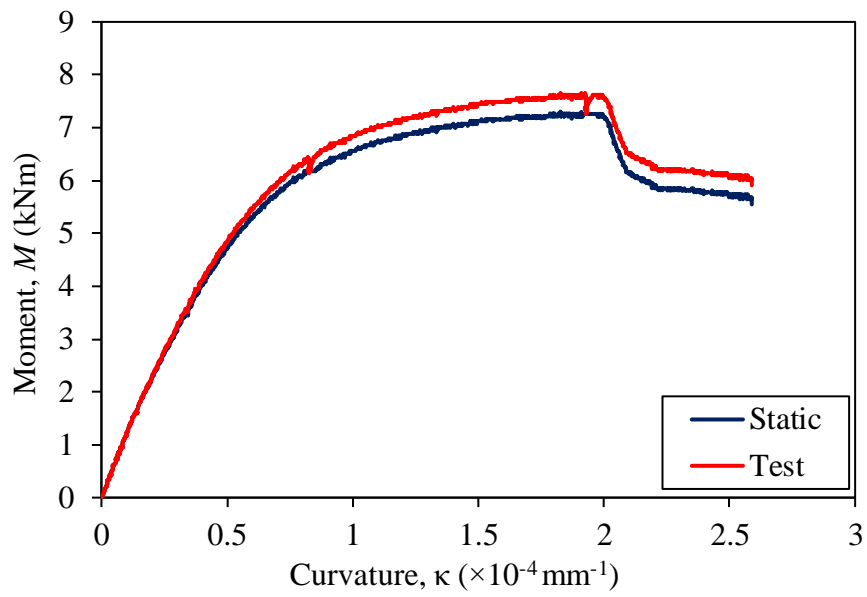


Figure B1-7. Moment-curvature curves for specimen 100×40×2.

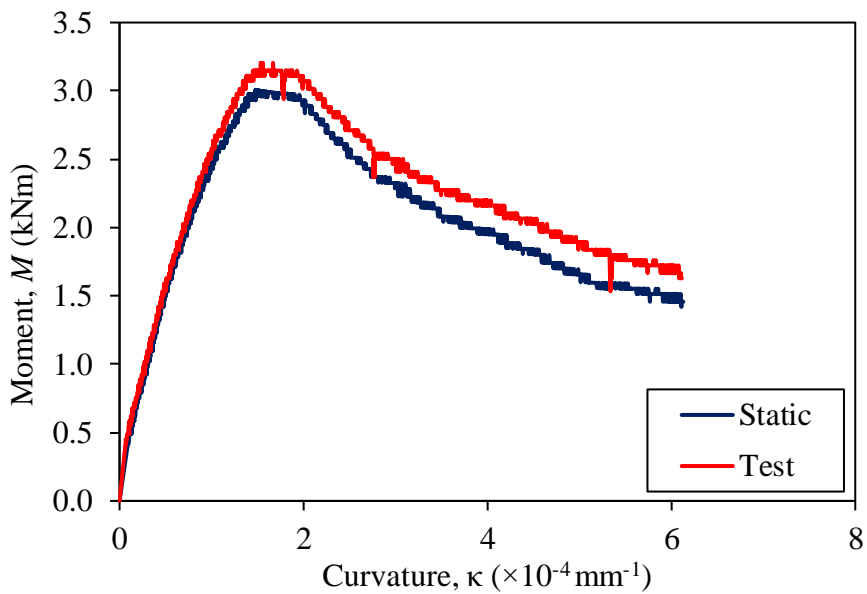


Figure B1-8. Moment-curvature curves for specimen 40×100×2.



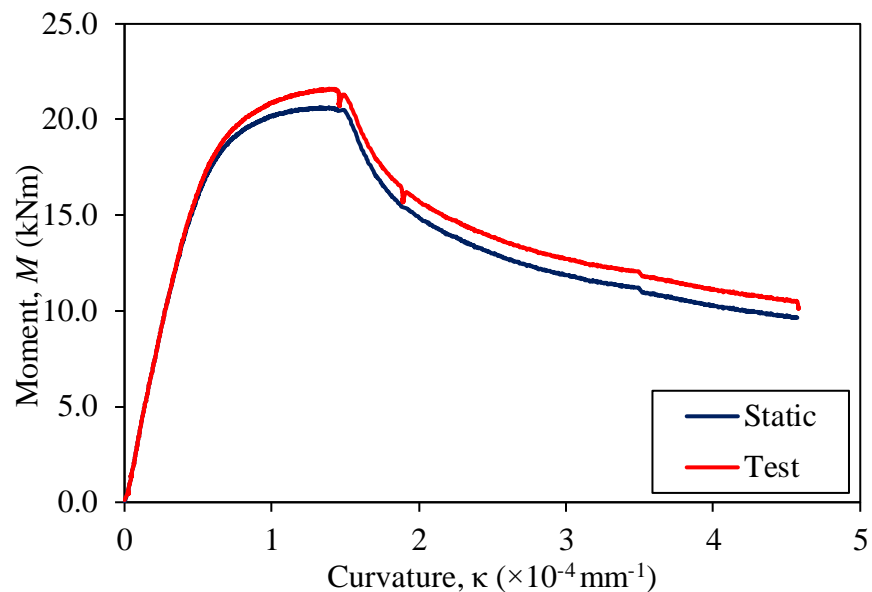


Figure B1-9. Moment-curvature curves for specimen 120×80×3.

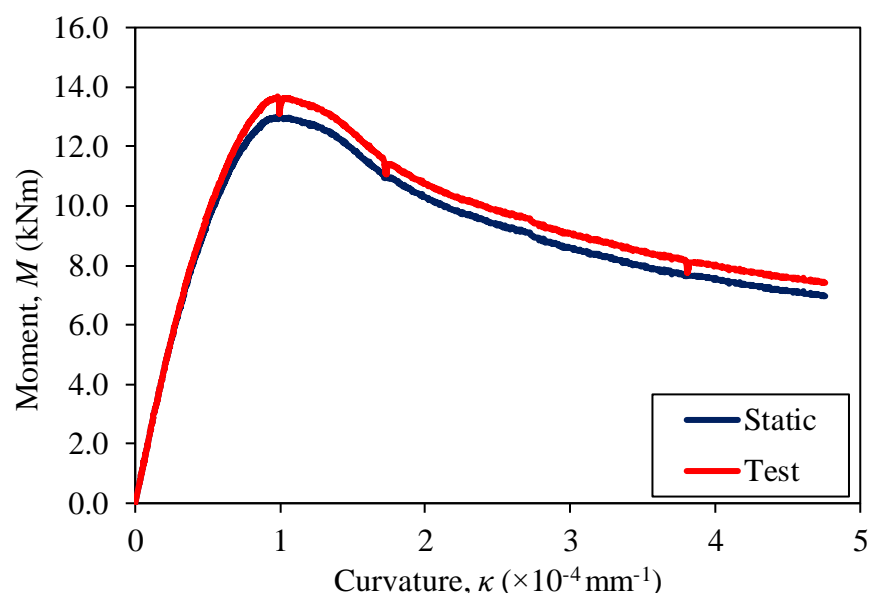


Figure B1-10. Moment-curvature curves for specimen 80×120×3.



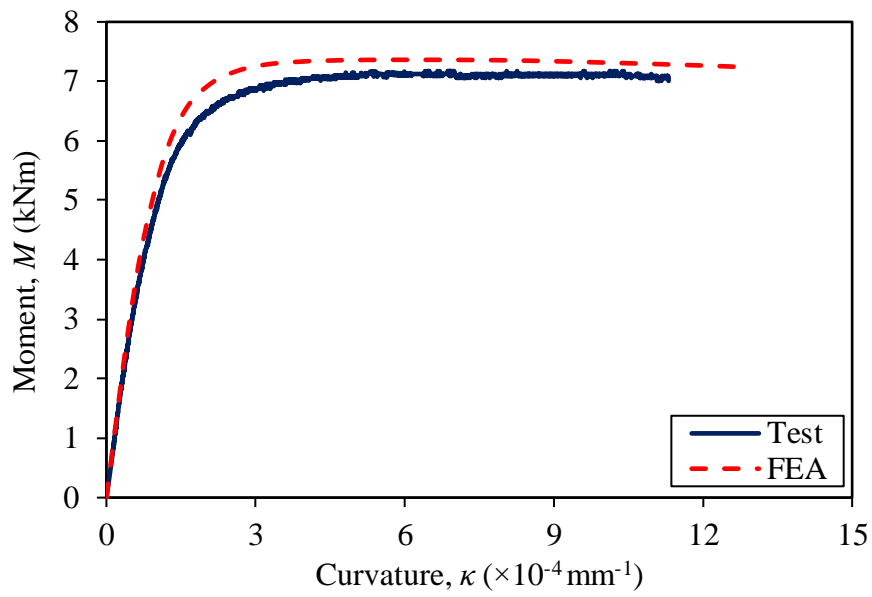


Figure B2-1. Moment-curvature curves obtained from test and FEA for specimen
 $60 \times 40 \times 4$.

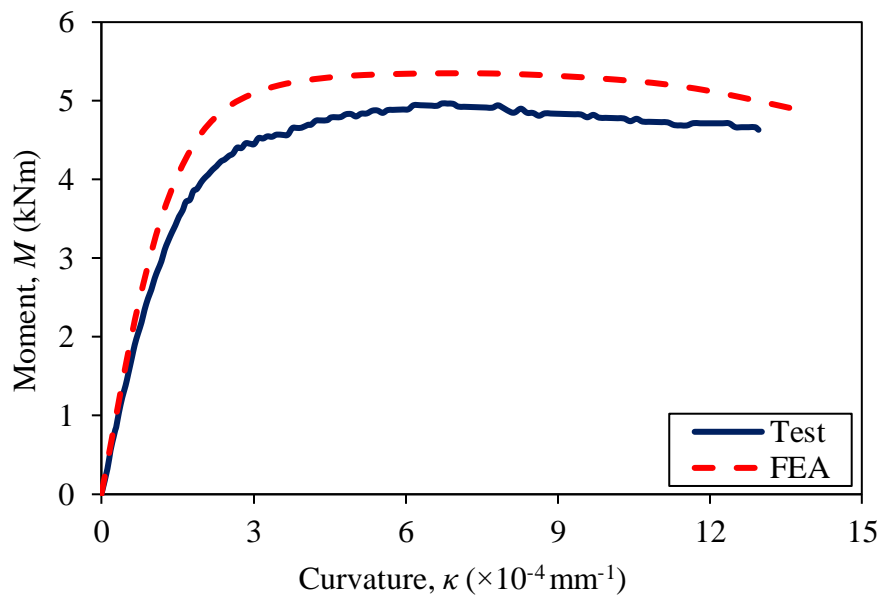


Figure B2-2. Moment-curvature curves obtained from test and FEA for specimen
 $40 \times 60 \times 4$.



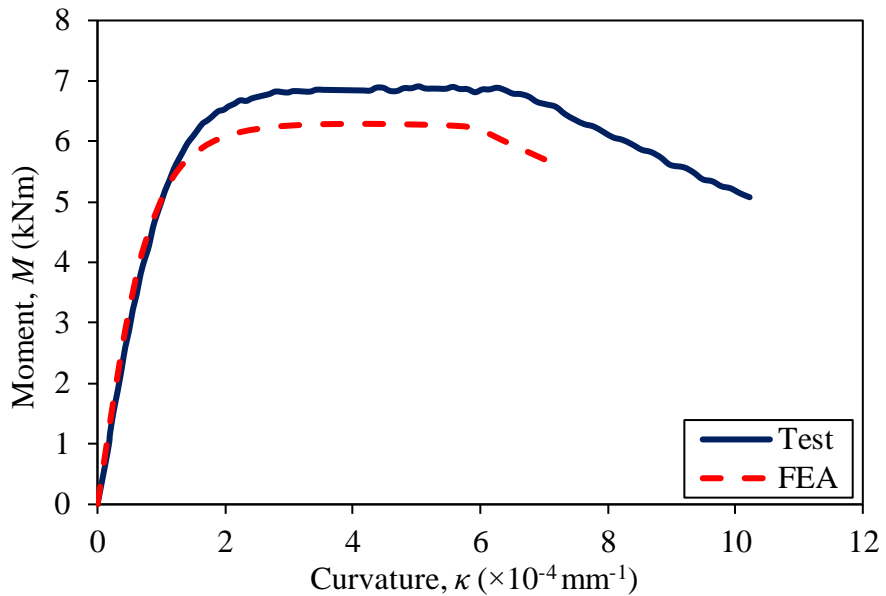


Figure B2-3. Moment-curvature curves obtained from test and FEA for specimen
60×60×3.

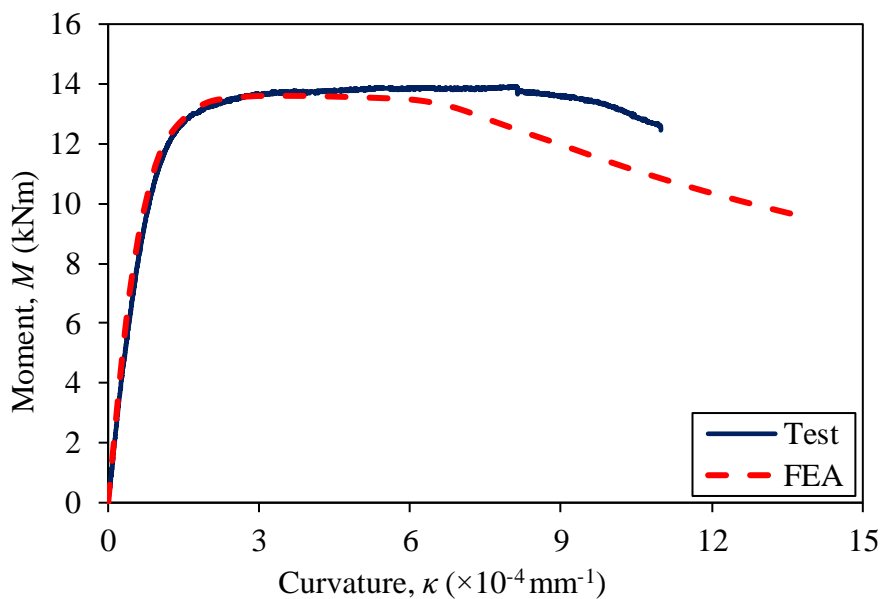


Figure B2-4. Moment-curvature curves obtained from test and FEA for specimen
80×60×4.



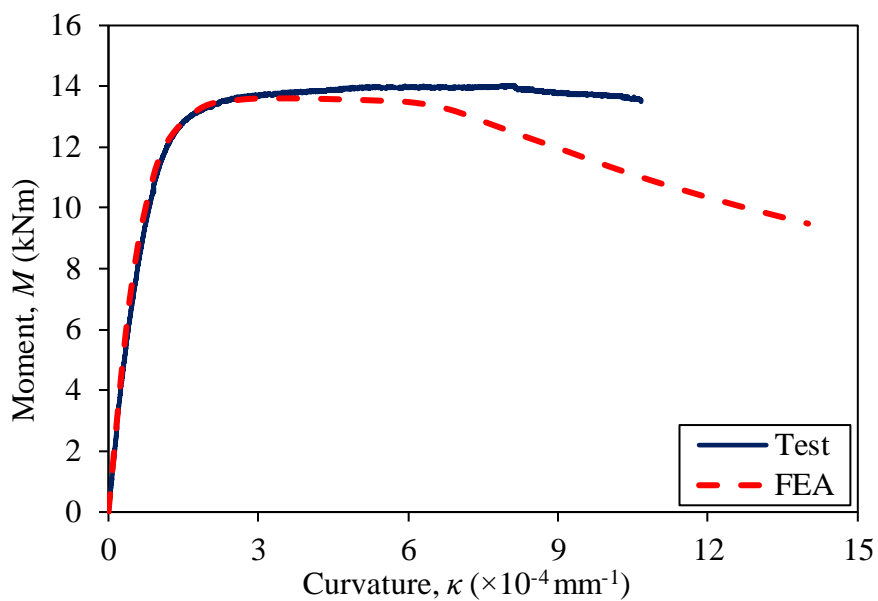


Figure B2-5. Moment-curvature curves obtained from test and FEA for specimen
80×60×4R.

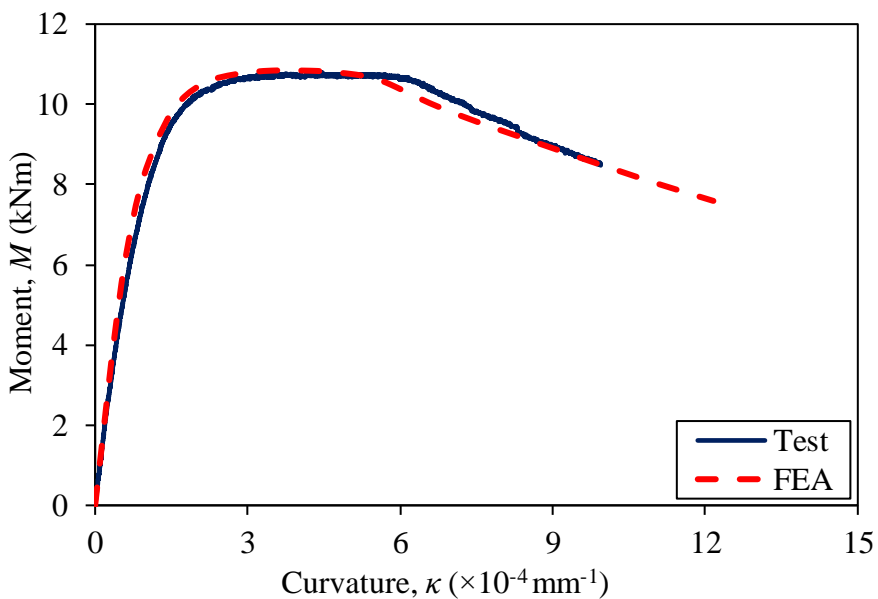


Figure B2-6. Moment-curvature curves obtained from test and FEA for specimen
60×80×4.



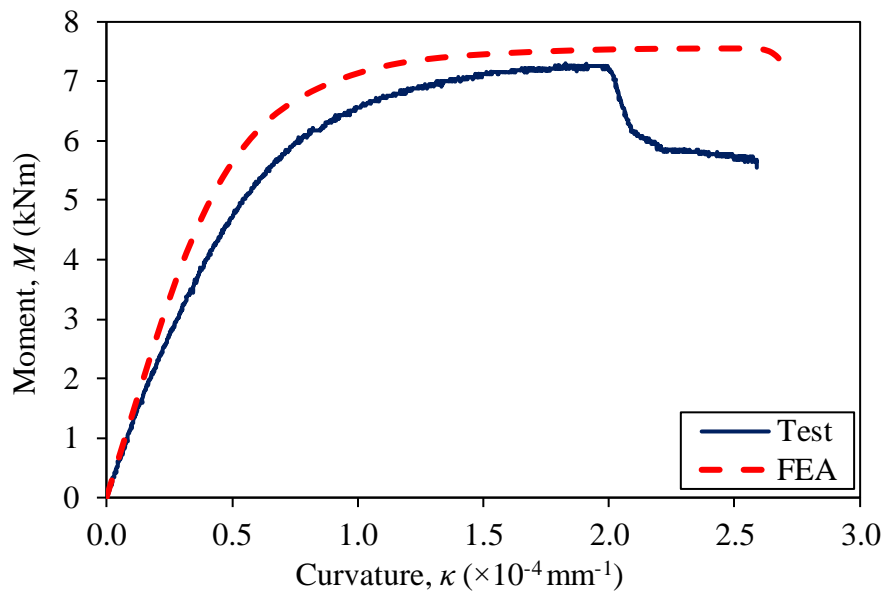


Figure B2-7. Moment-curvature curves obtained from test and FEA for specimen
100×40×2.

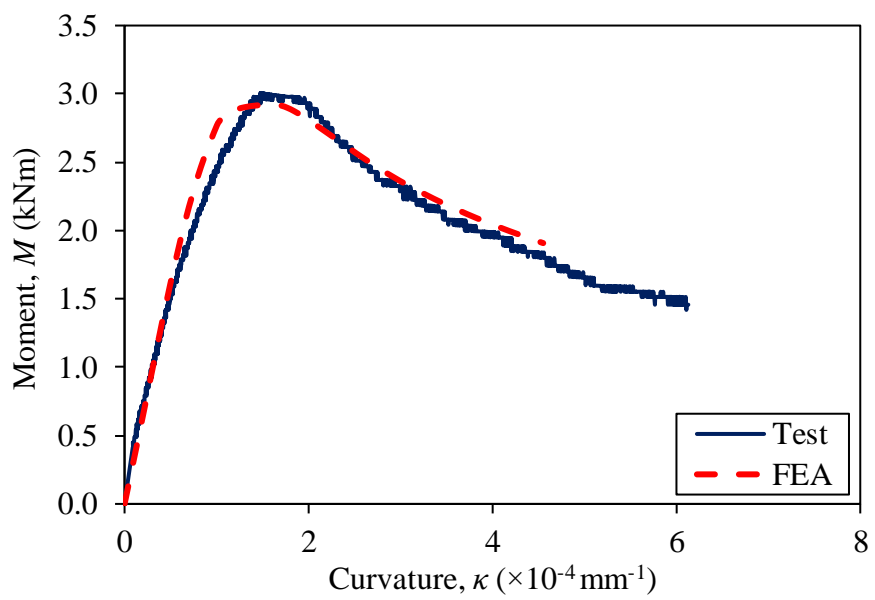


Figure B2-8. Moment-curvature curves obtained from test and FEA for specimen
40×100×2.



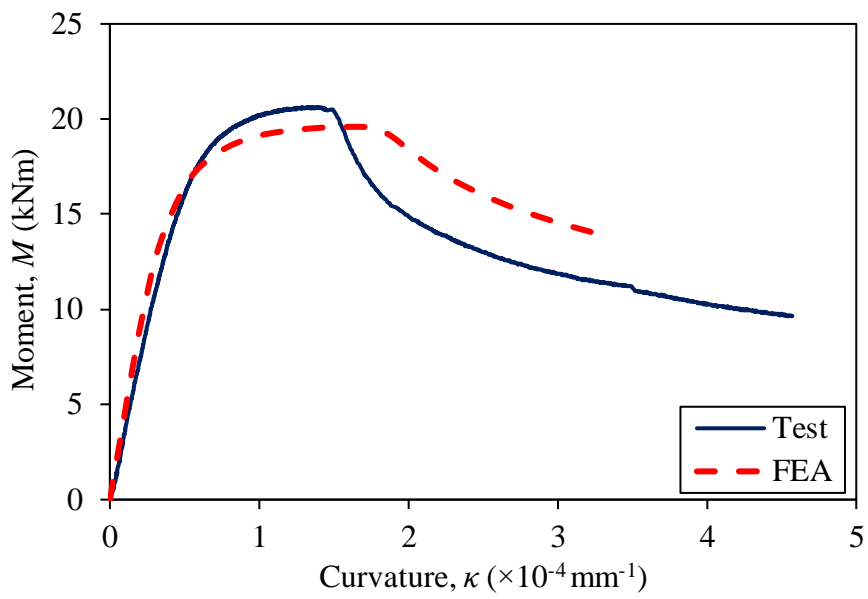


Figure B2-9. Moment-curvature curves obtained from test and FEA for specimen
120×80×3.

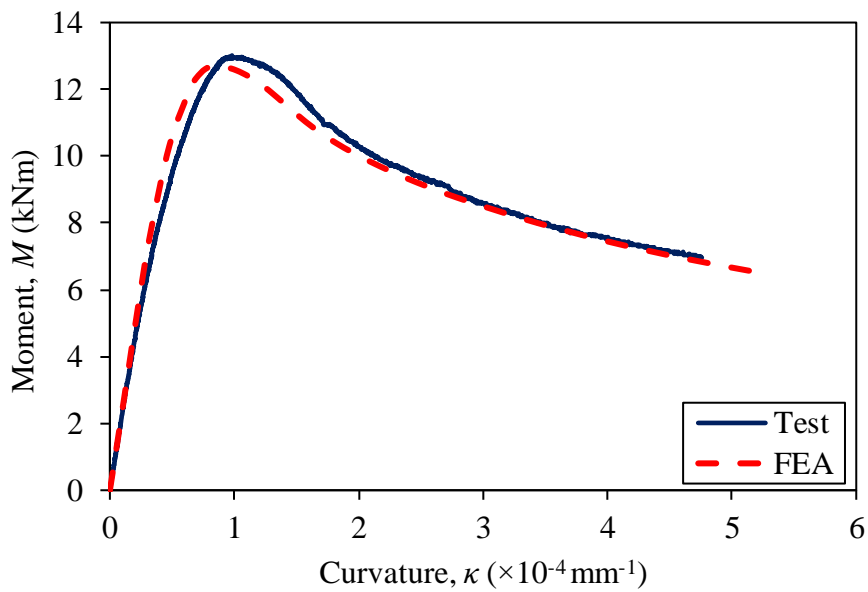


Figure B2-10. Moment-curvature curves obtained from test and FEA for specimen
80×120×3.



APPENDIX C

CONCRETE-FILLED COLD-FORMED FERRITIC STAINLESS STEEL STUB COLUMNS

The stub column behaviour of concrete-filled cold-formed ferritic stainless steel sections were investigated. The measured local plate imperfection profiles along the four sides for all sections are shown in Figures C1. The finite element models were validated against the test results and shown in Appendix C2.



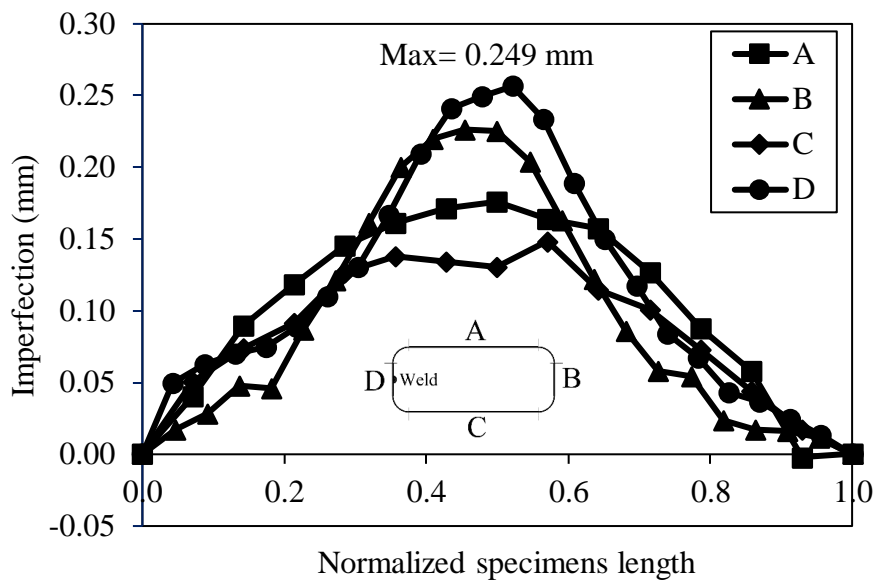


Figure C1-1. Measured local plate imperfection profiles for Section 60×40×4.

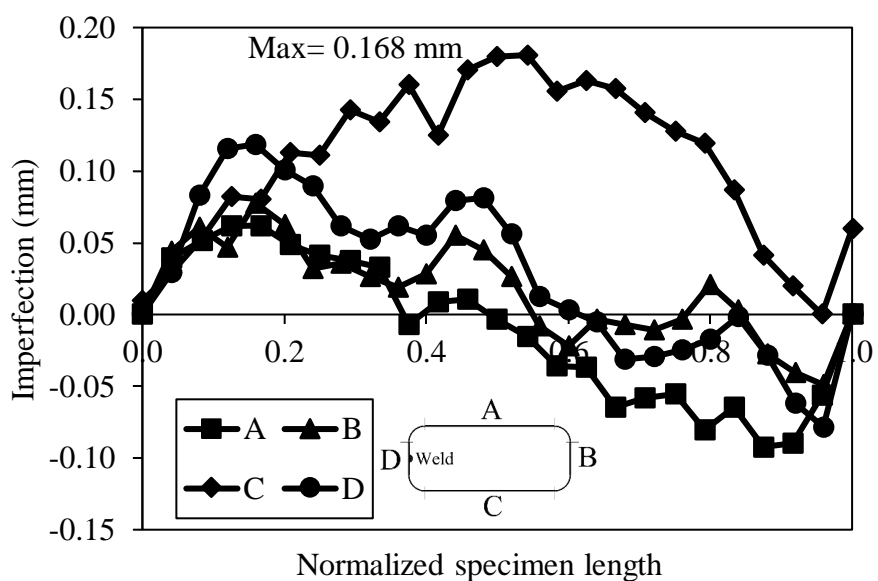


Figure C1-2. Measured local plate imperfection profiles for Section 60×60×3.



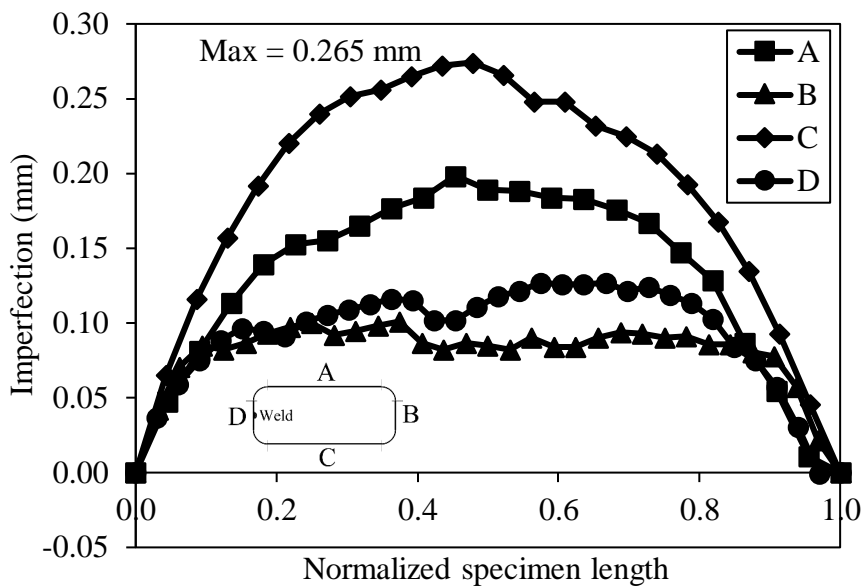


Figure C1-3. Measured local plate imperfection profiles for Section 80×60×4.

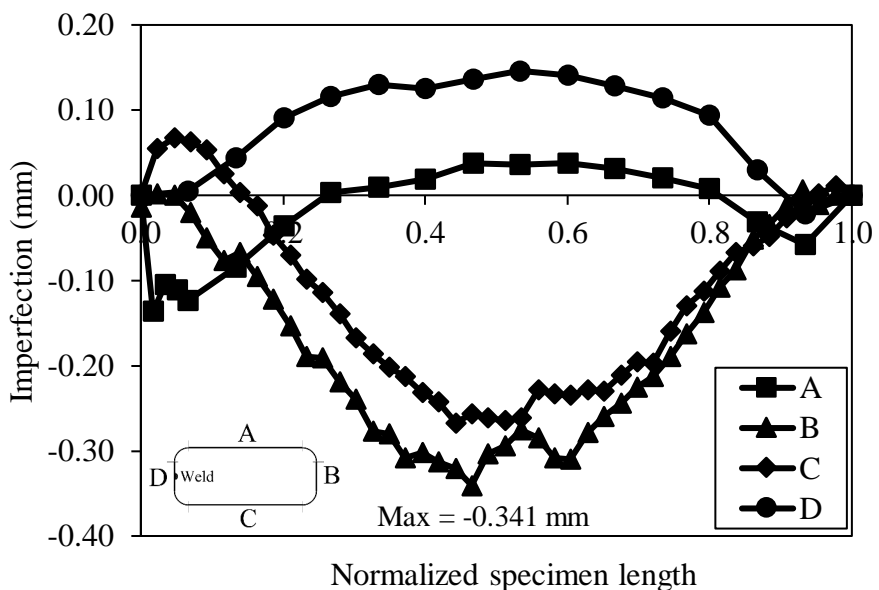


Figure C1-4. Measured local plate imperfection profiles for Section 100×40×2.

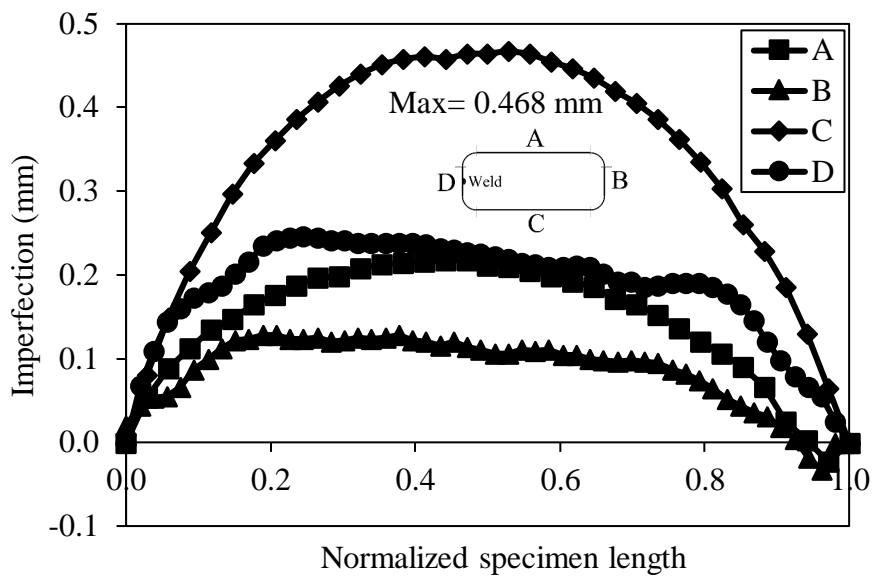


Figure C1-5. Measured local plate imperfection profiles for Section 120×80×3.

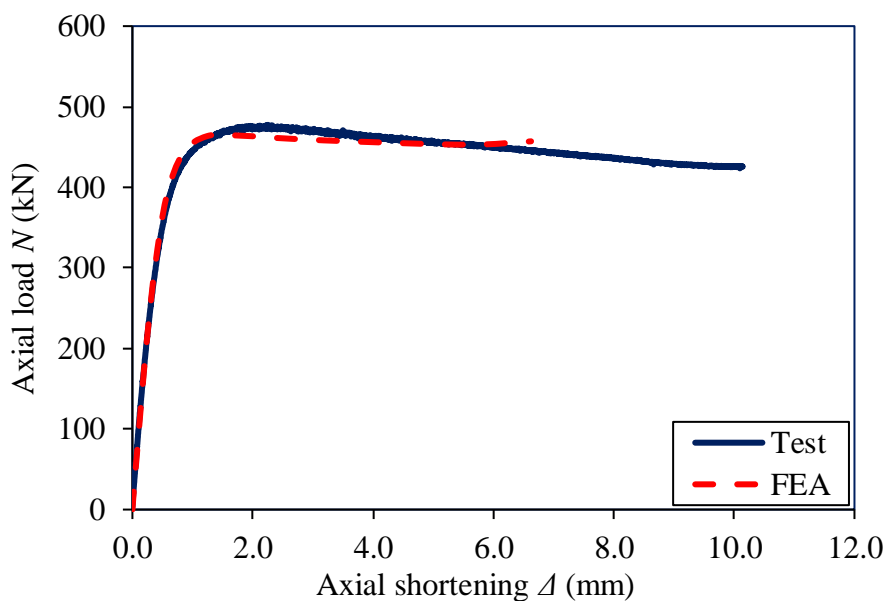


Figure C2-1. Axial load-axial shortening curves obtained from test and FEA for specimen 60×40×4C40.



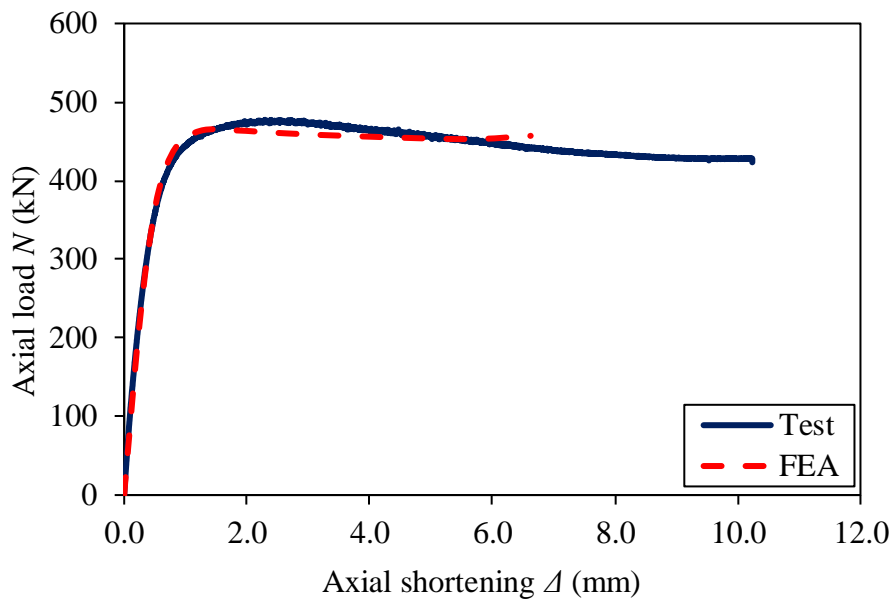


Figure C2-2. Axial load-axial shortening curves obtained from test and FEA for specimen 60×40×4C40R.

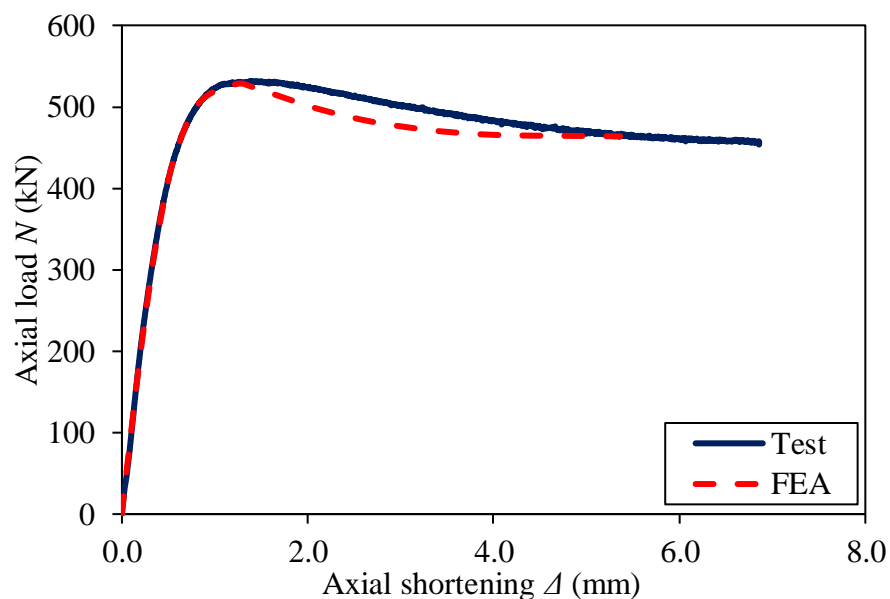


Figure C2-3. Axial load-axial shortening curves obtained from test and FEA for specimen 60×40×4C80.



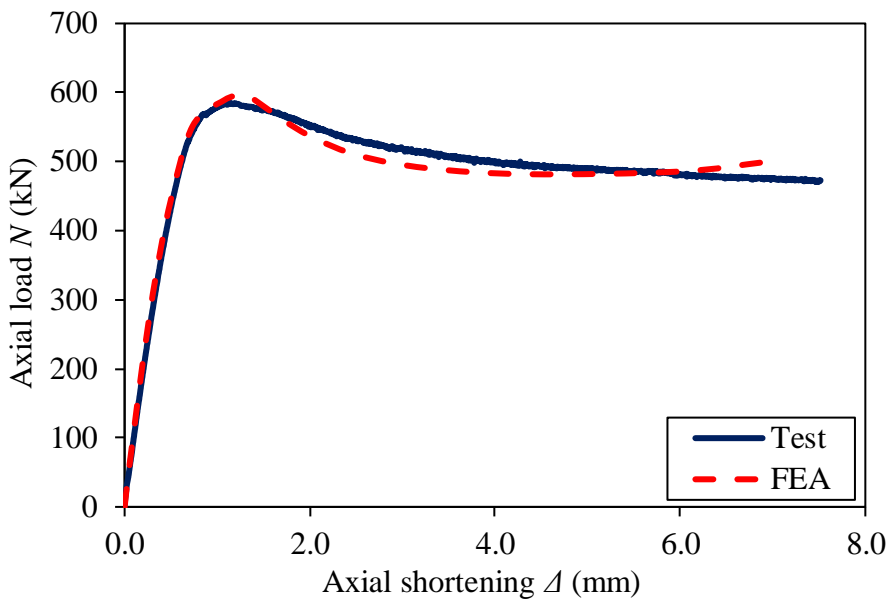


Figure C2-4. Axial load-axial shortening curves obtained from test and FEA for specimen 60×40×4C120.

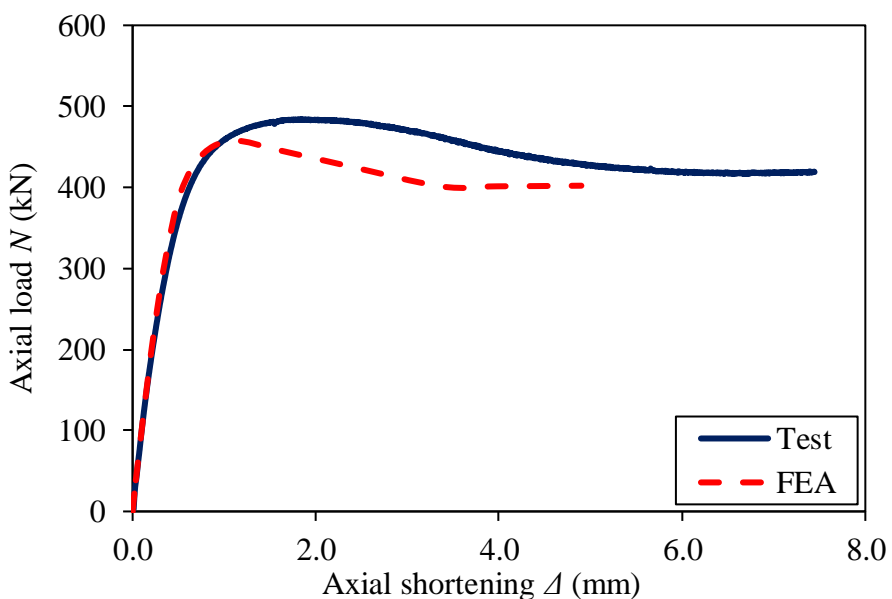


Figure C2-5. Axial load-axial shortening curves obtained from test and FEA for specimen 60×60×3C40.



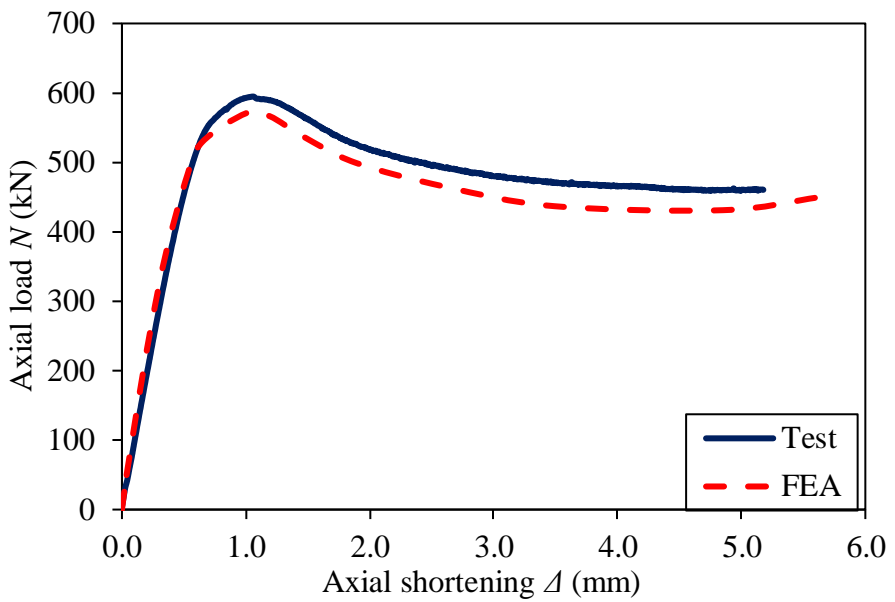


Figure C2-6. Axial load-axial shortening curves obtained from test and FEA for specimen 60×60×3C80.

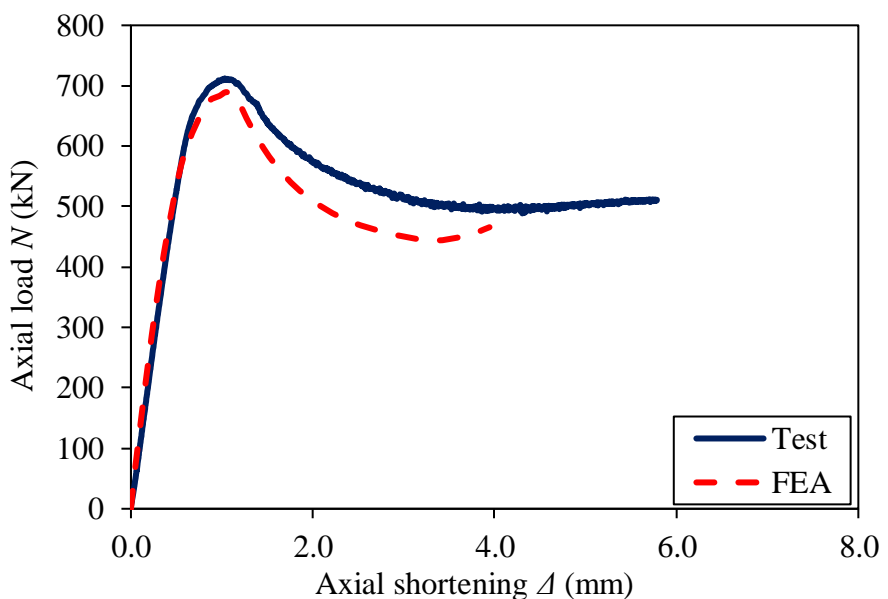


Figure C2-7. Axial load-axial shortening curves obtained from test and FEA for specimen 60×60×3C120.



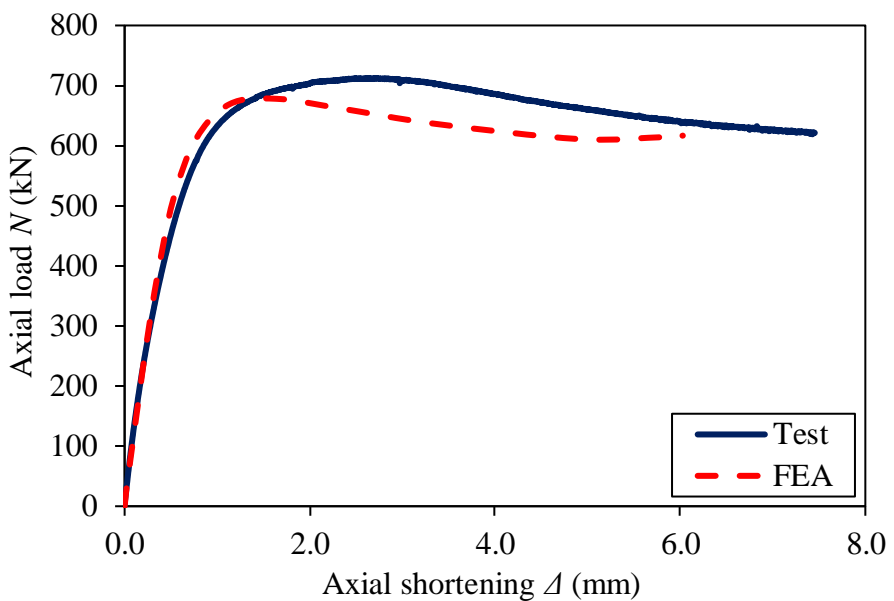


Figure C2-8. Axial load-axial shortening curves obtained from test and FEA for specimen 80×60×4C40.

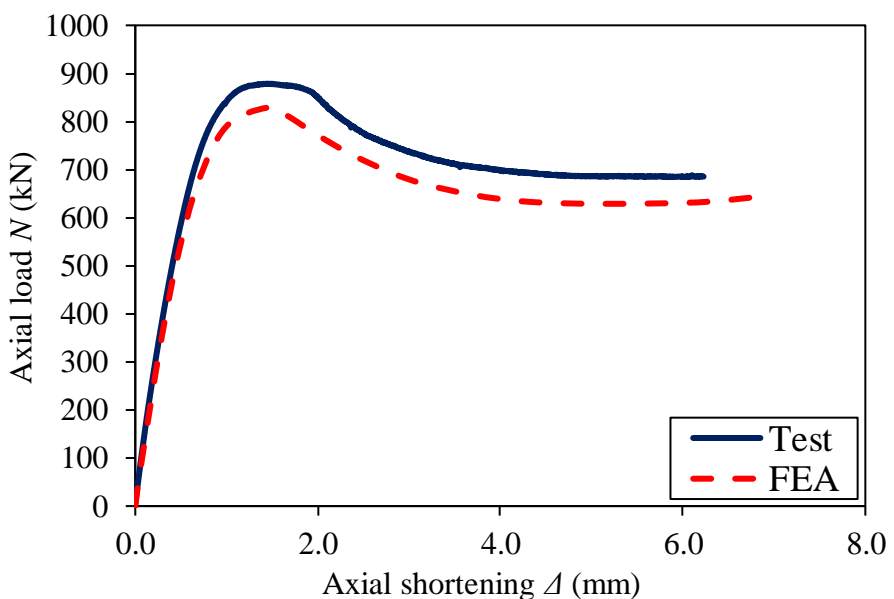


Figure C2-9. Axial load-axial shortening curves obtained from test and FEA for specimen 80×60×4C80.



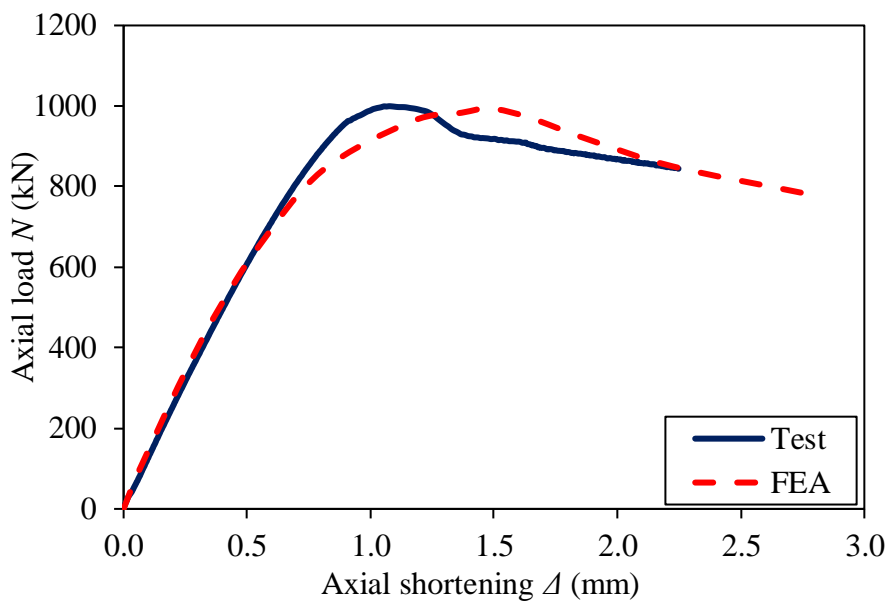


Figure C2-10. Axial load-axial shortening curves obtained from test and FEA for specimen 80×60×4C120.

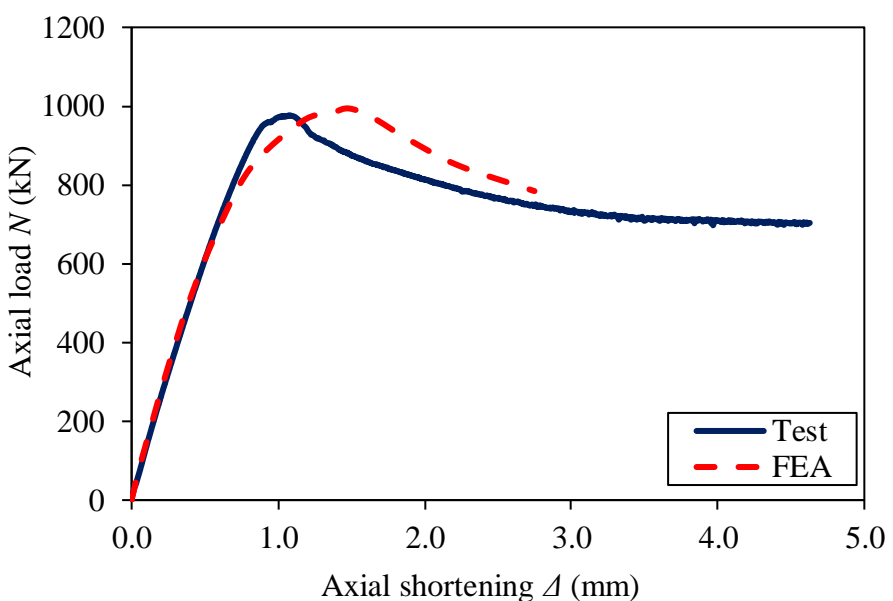


Figure C2-11. Axial load-axial shortening curves obtained from test and FEA for specimen 80×60×4C120R.



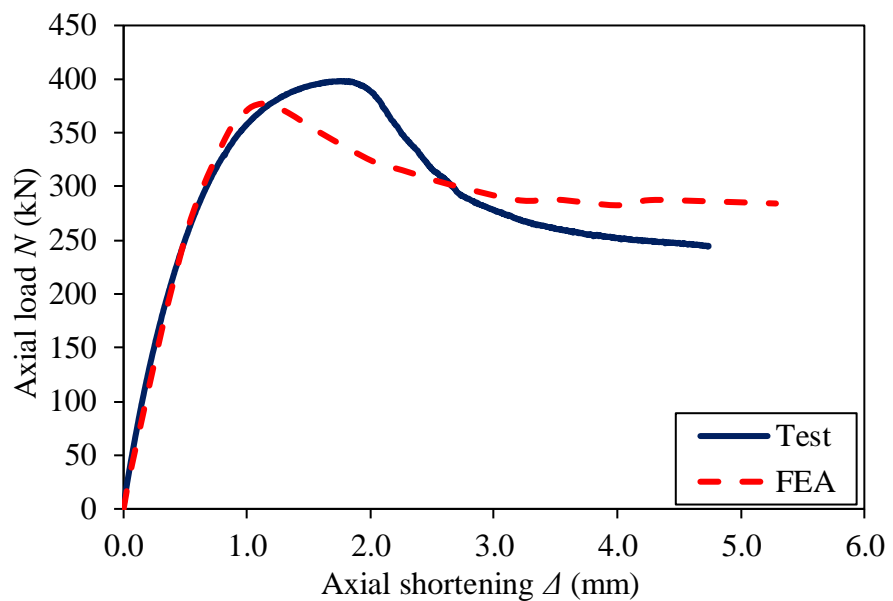


Figure C2-12. Axial load-axial shortening curves obtained from test and FEA for specimen 100×40×2C40.

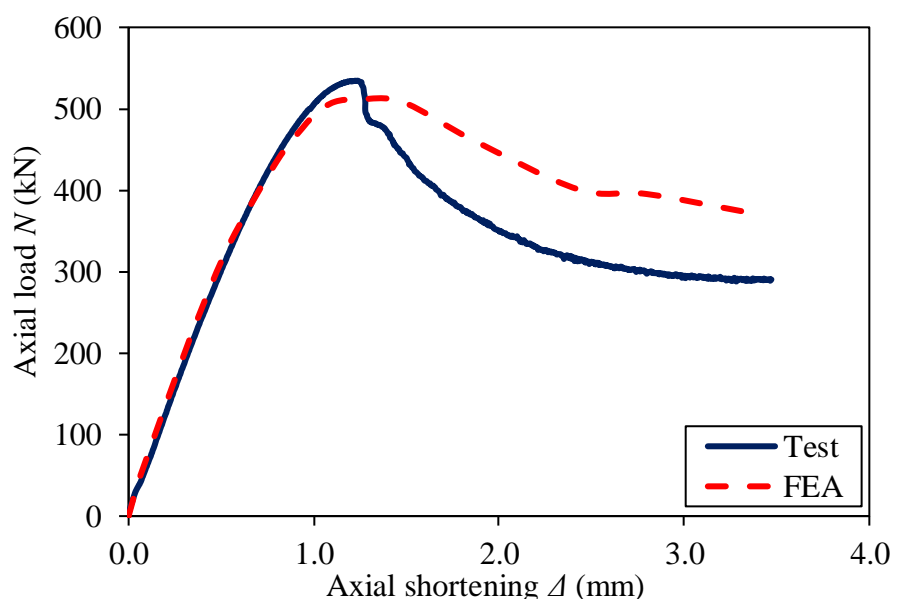


Figure C2-13. Axial load-axial shortening curves obtained from test and FEA for specimen 100×40×2C80.



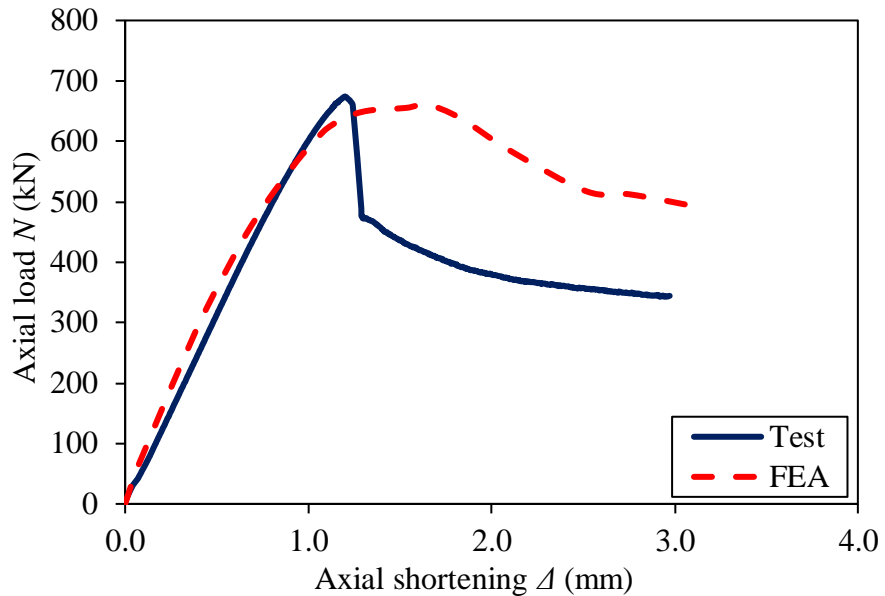


Figure C2-14. Axial load-axial shortening curves obtained from test and FEA for specimen 100×40×2C120.

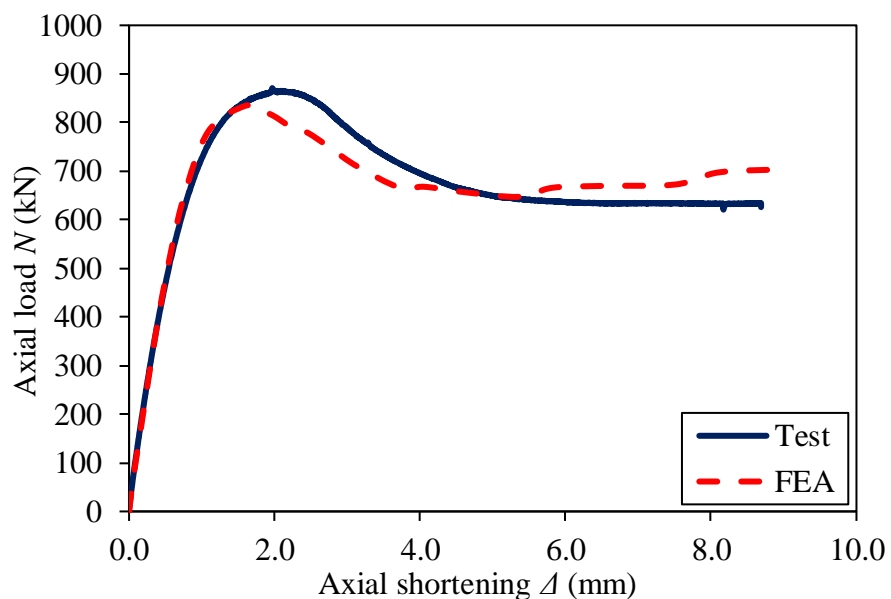


Figure C2-15. Axial load-axial shortening curves obtained from test and FEA for specimen 120×80×3C40.



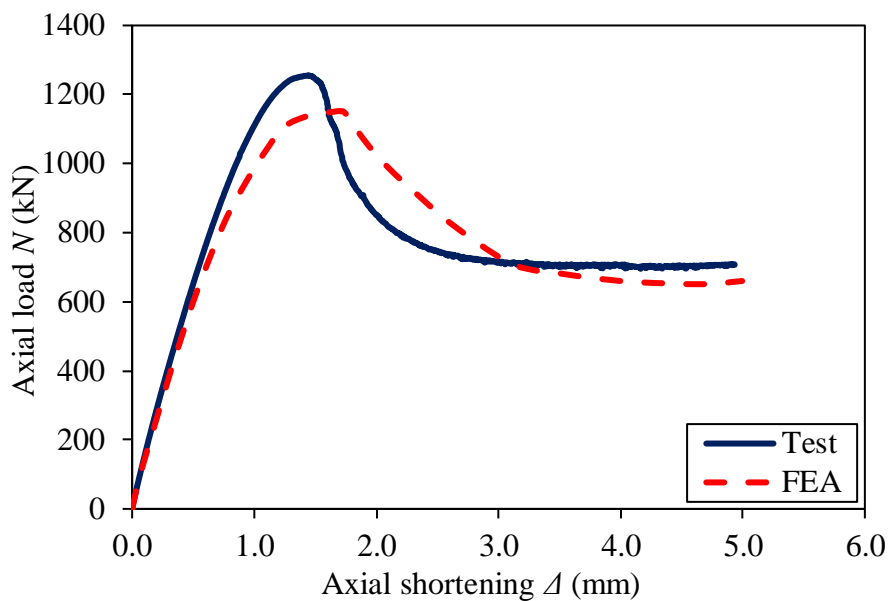


Figure C2-16. Axial load-axial shortening curves obtained from test and FEA for specimen 120×80×3C80.

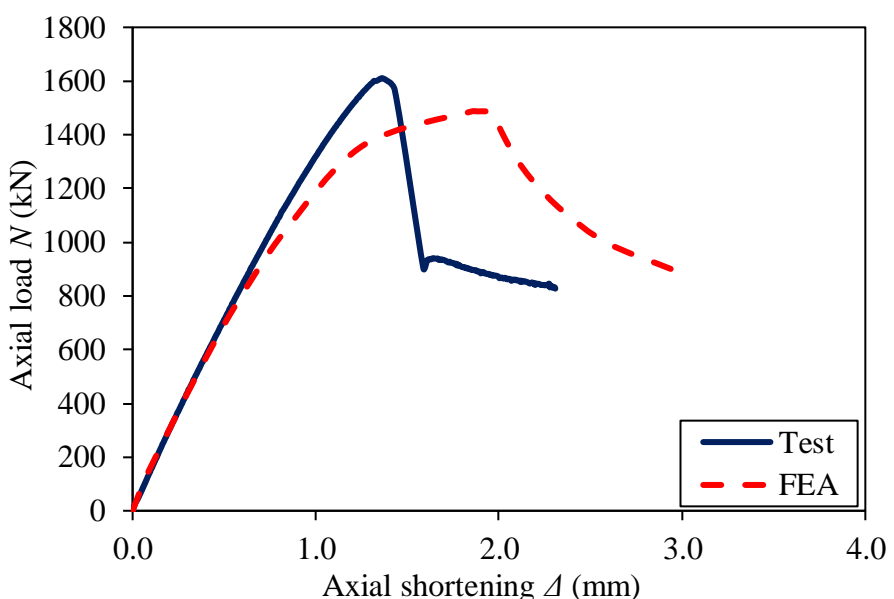


Figure C2-17. Axial load-axial shortening curves obtained from test and FEA for specimen 120×80×3C120.



APPENDIX D

CONCRETE-FILLED COLD-FORMED AUSTENITIC STAINLESS STEEL STUB COLUMNS

The stub column behaviour of concrete-filled cold-formed austenitic stainless steel sections were investigated. The finite element models were validated against the test results and shown in Appendix D.



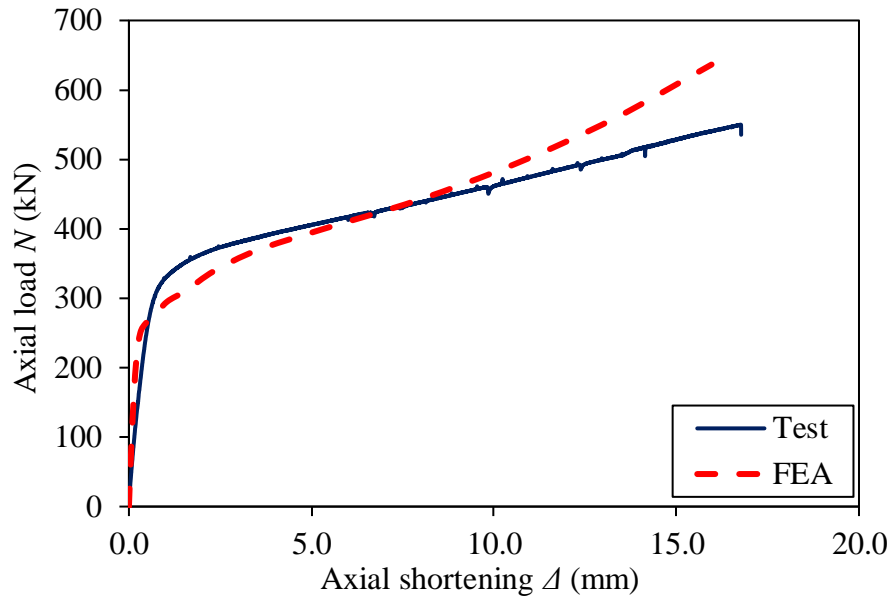


Figure D1. Axial load-axial shortening curves obtained from test and FEA for specimen 60.5×2.8C40.

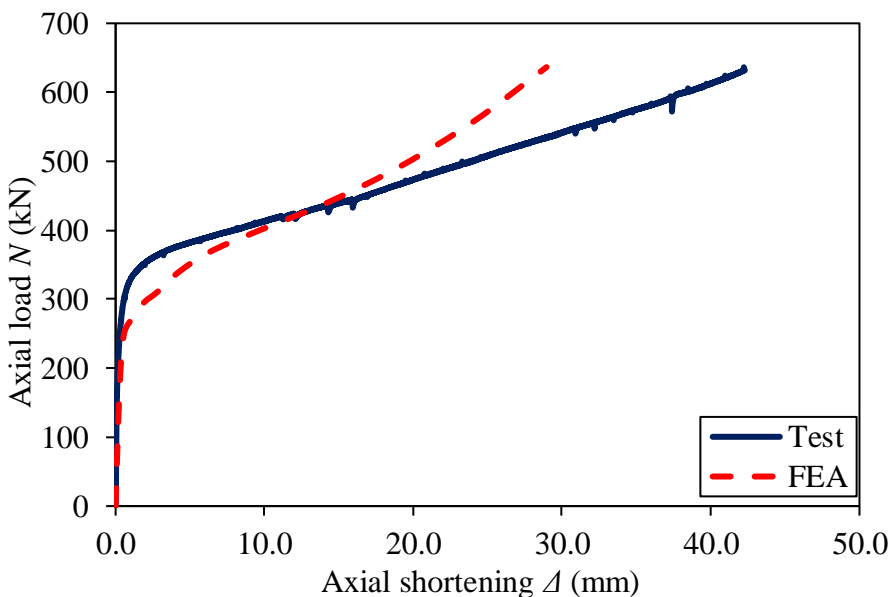


Figure D2. Axial load-axial shortening curves obtained from test and FEA for specimen 60.5×2.8C40R.



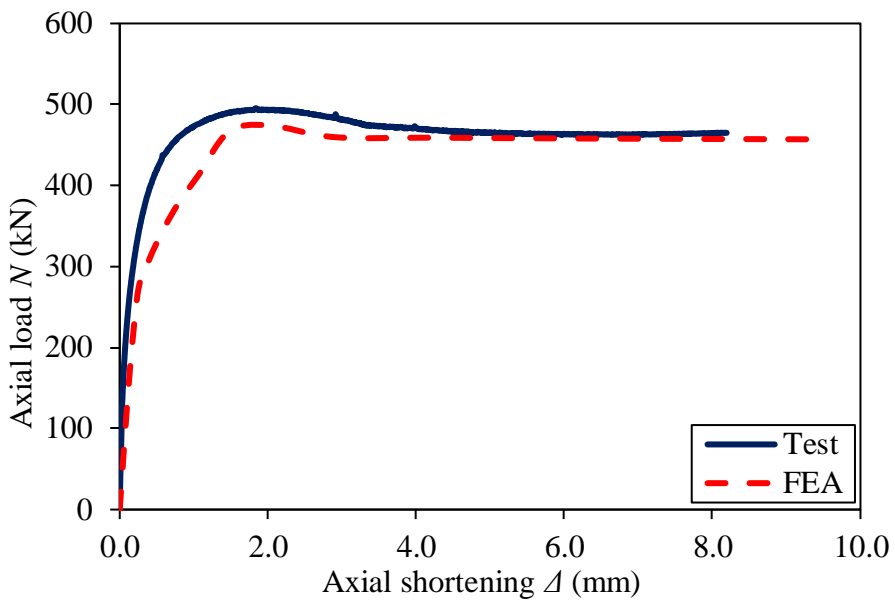


Figure D3. Axial load-axial shortening curves obtained from test and FEA for specimen 60.5×2.8C80.

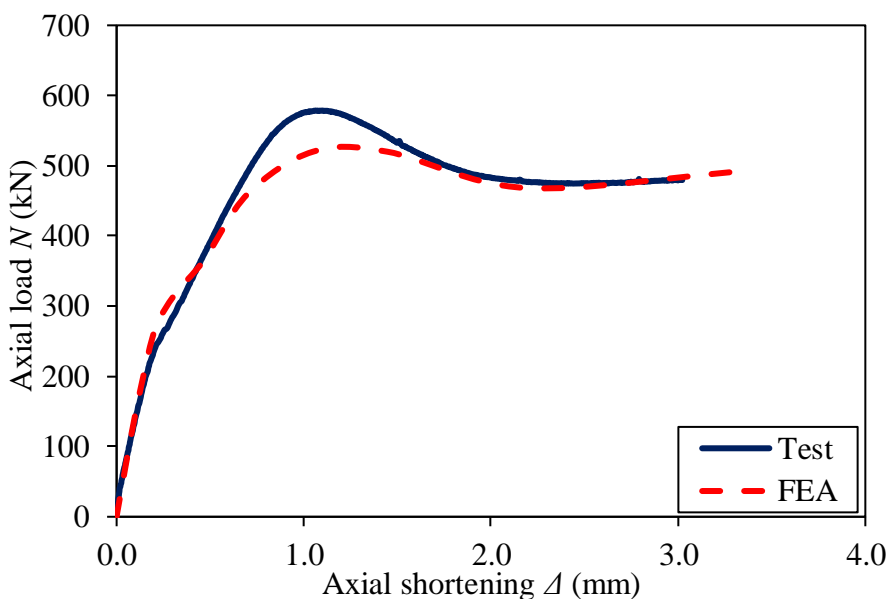


Figure D4. Axial load-axial shortening curves obtained from test and FEA for specimen 60.5×2.8C120.



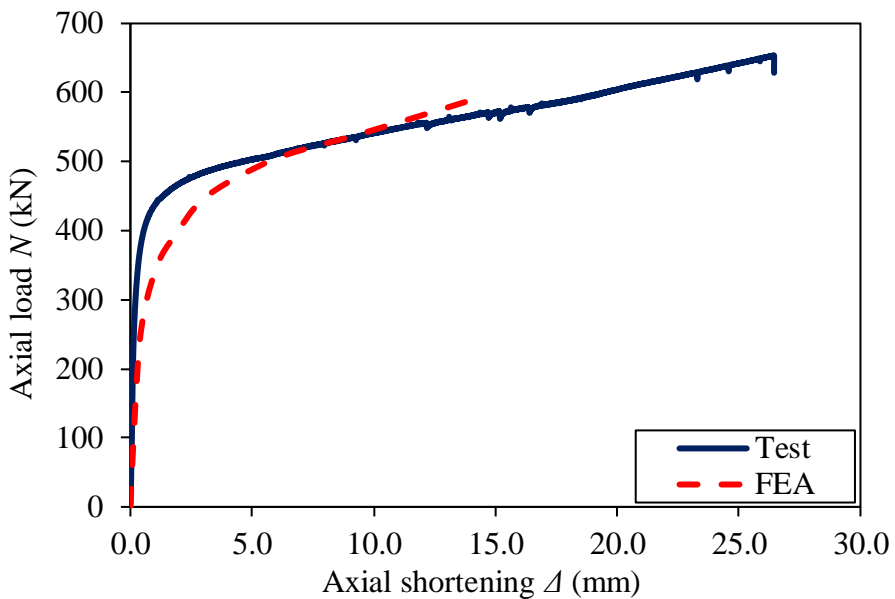


Figure D5. Axial load-axial shortening curves obtained from test and FEA for specimen 76.3×3.0C40.

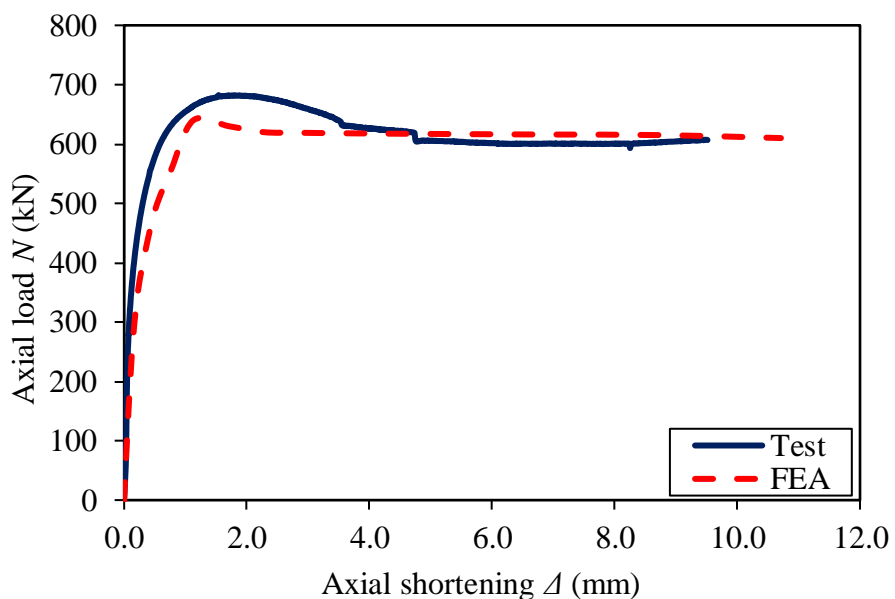


Figure D6. Axial load-axial shortening curves obtained from test and FEA for specimen 76.3×3.0C80.



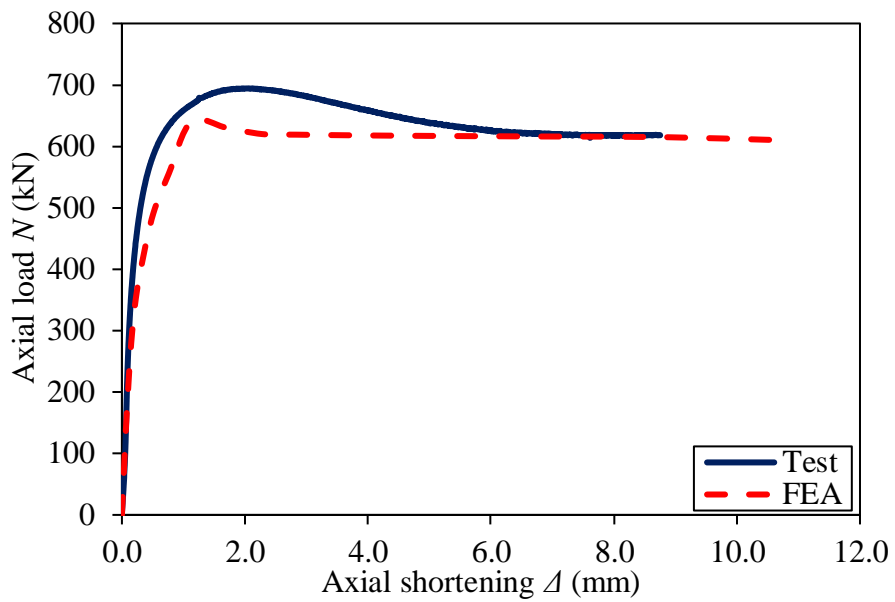


Figure D7. Axial load-axial shortening curves obtained from test and FEA for specimen 76.3×3.0C80R.

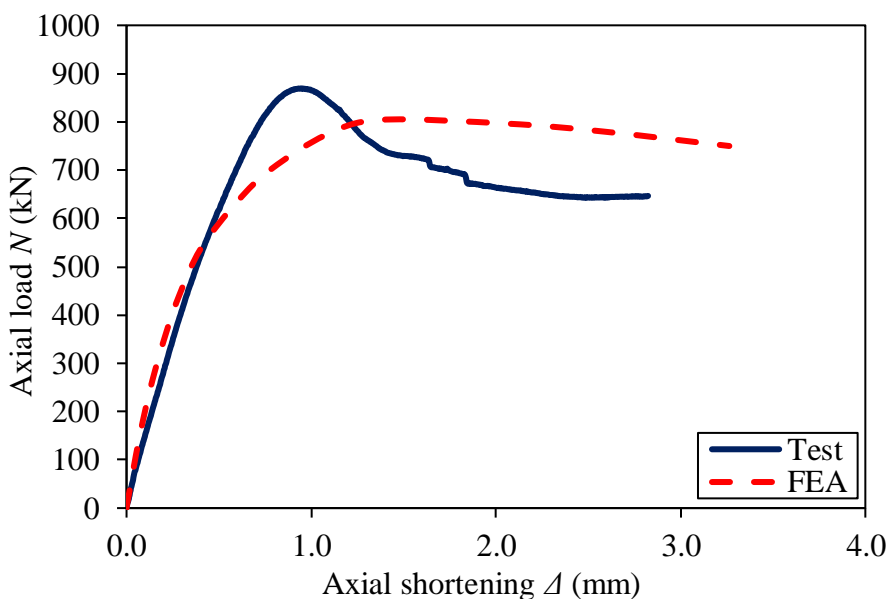


Figure D8. Axial load-axial shortening curves obtained from test and FEA for specimen 76.3×3.0C120.



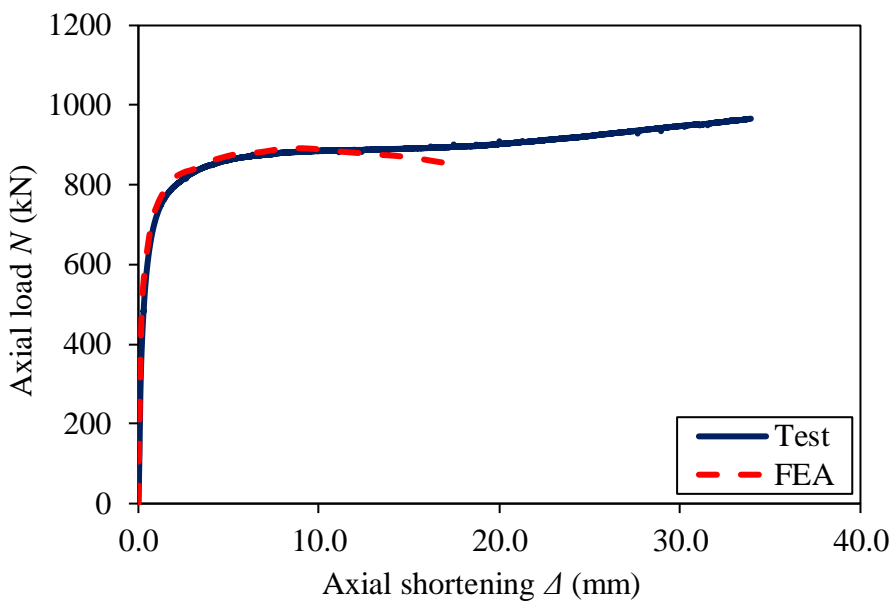


Figure D9. Axial load-axial shortening curves obtained from test and FEA for specimen 114.3×3.0C40.

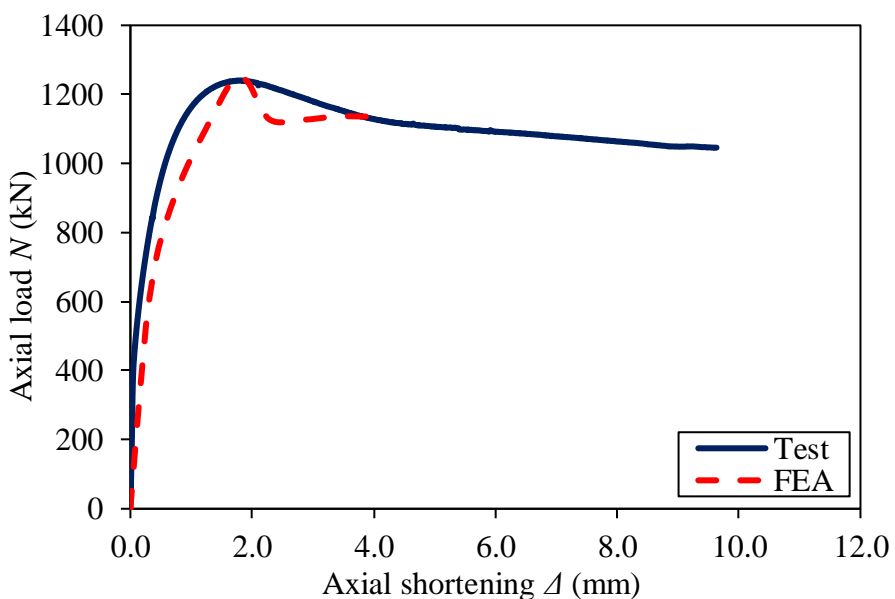


Figure D10. Axial load-axial shortening curves obtained from test and FEA for specimen 114.3×3.0C80.



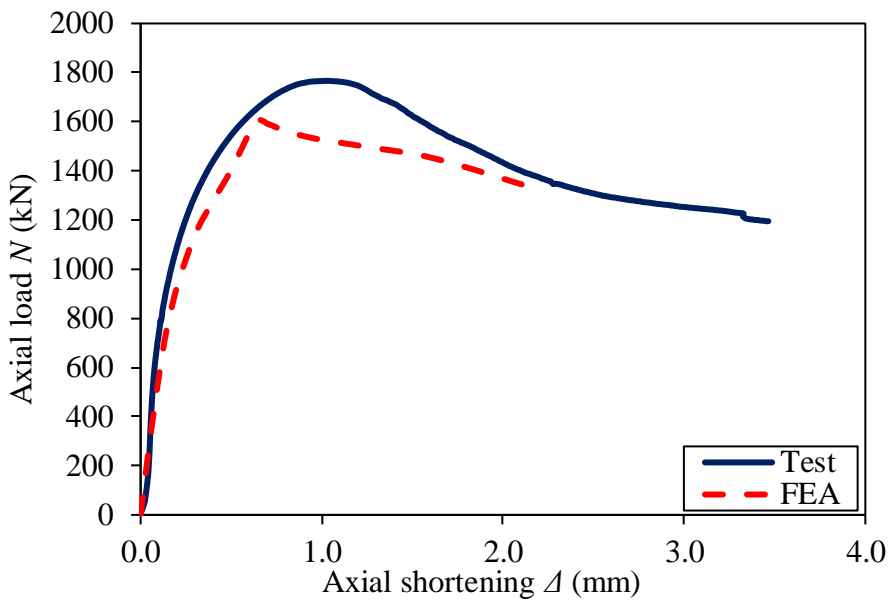


Figure D11. Axial load-axial shortening curves obtained from test and FEA for specimen 114.3×3.0C120.

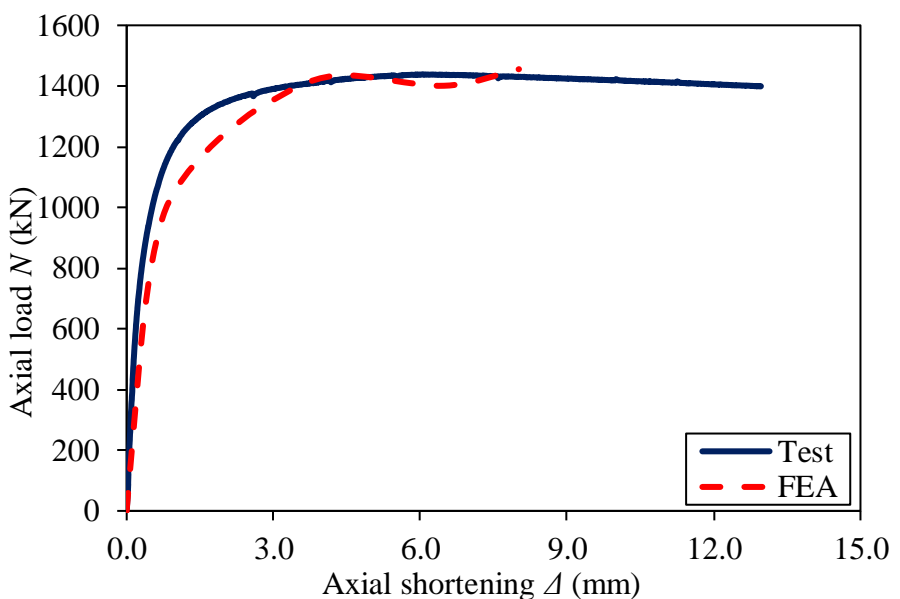


Figure D12. Axial load-axial shortening curves obtained from test and FEA for specimen 165.0×3.0C40.



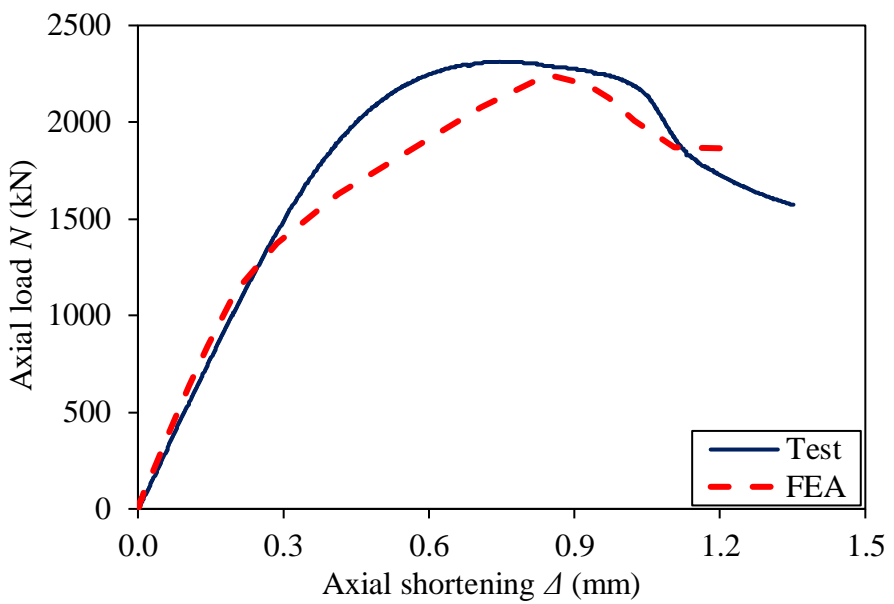


Figure D13. Axial load-axial shortening curves obtained from test and FEA for specimen 165.0×3.0C80.

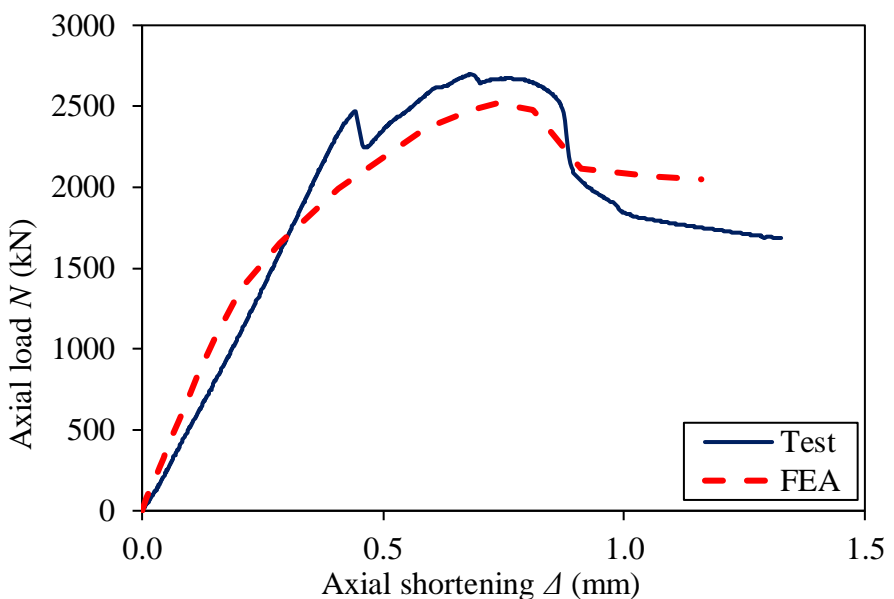


Figure D14. Axial load-axial shortening curves obtained from test and FEA for specimen 165.0×3.0C120.



APPENDIX E

CONCRETE-FILLED COLD-FORMED FERRITIC STAINLESS STEEL FLEXURAL MEMBERS

The flexural behaviour of concrete-filled cold-formed ferritic stainless steel sections were investigated. The finite element models were validated against the test results and shown in Appendix E.



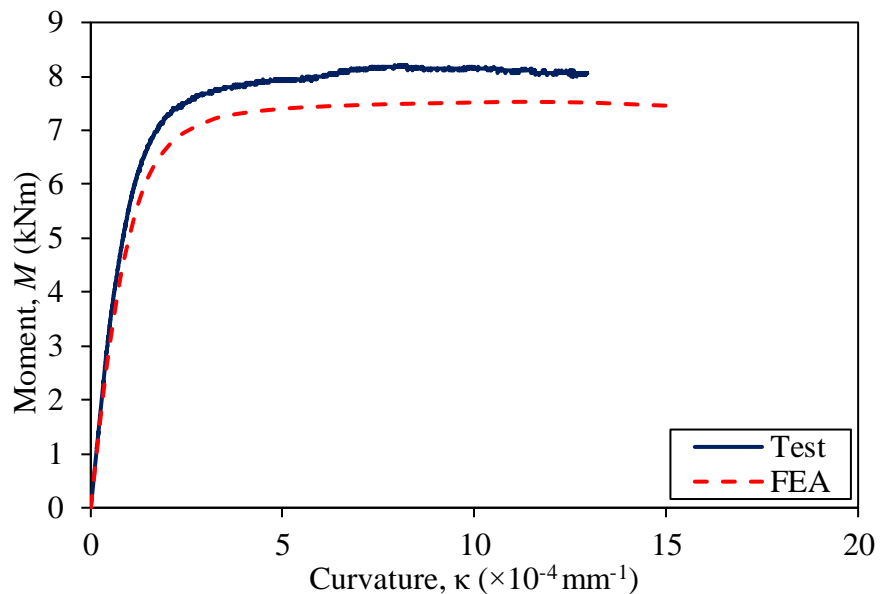


Figure E-1. Moment-curvature curves obtained from test and FEA for specimen
60×40×4C40.

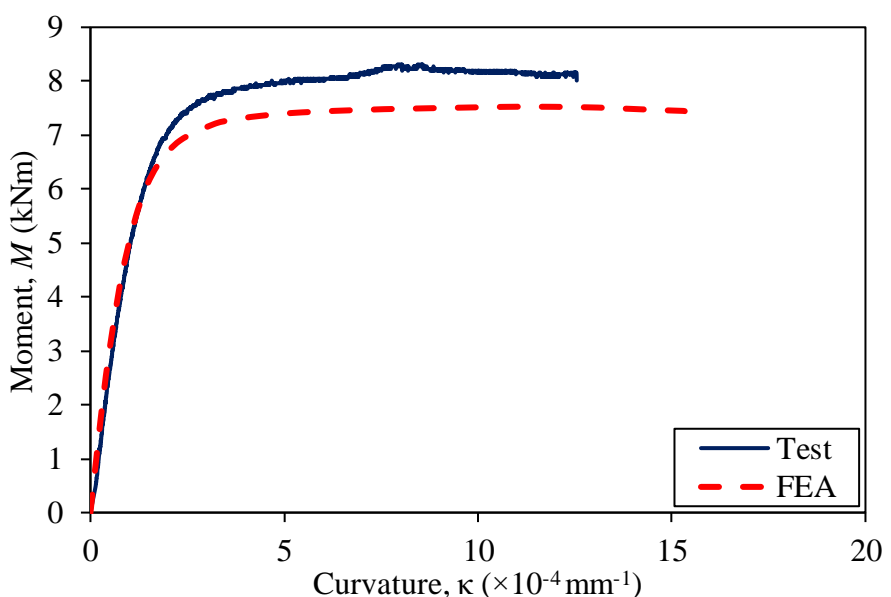


Figure E-2. Moment-curvature curves obtained from test and FEA for specimen
60×40×4C40R.



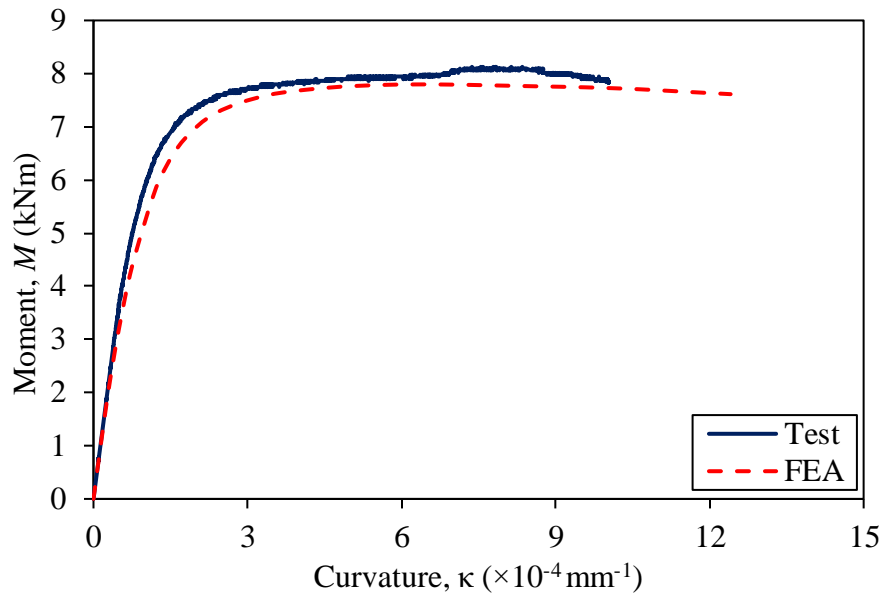


Figure E-3. Moment-curvature curves obtained from test and FEA for specimen
60×40×4C80.

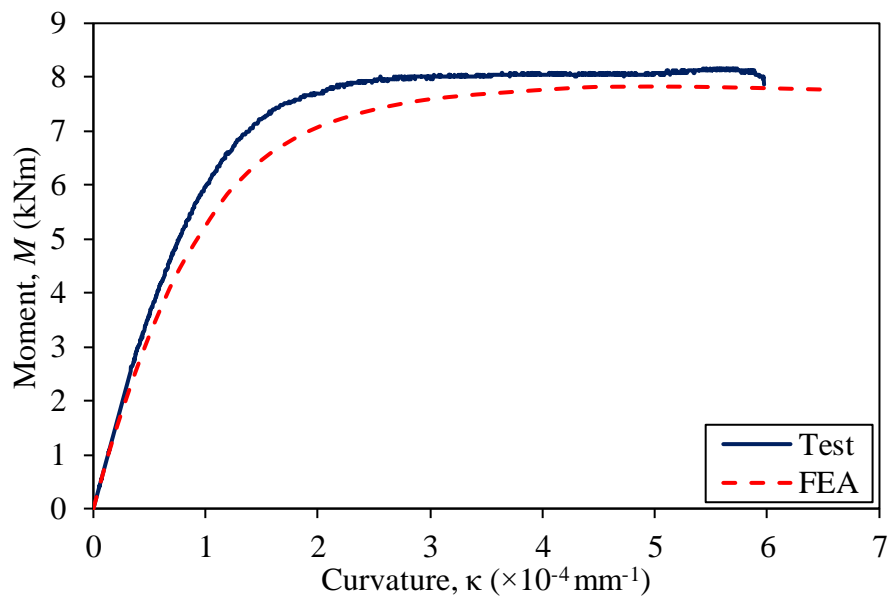


Figure E-4. Moment-curvature curves obtained from test and FEA for specimen
60×40×4C120.



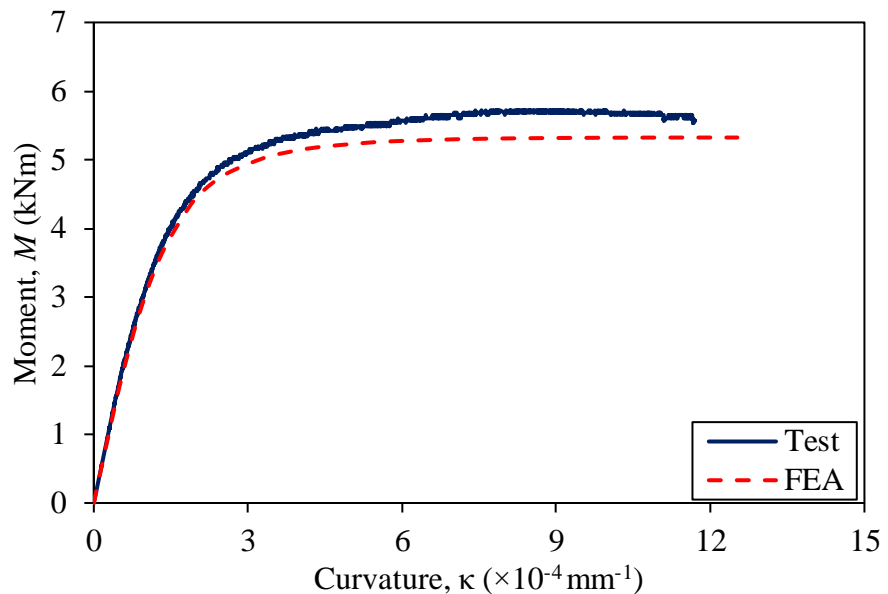


Figure E-5. Moment-curvature curves obtained from test and FEA for specimen
40×60×4C40.

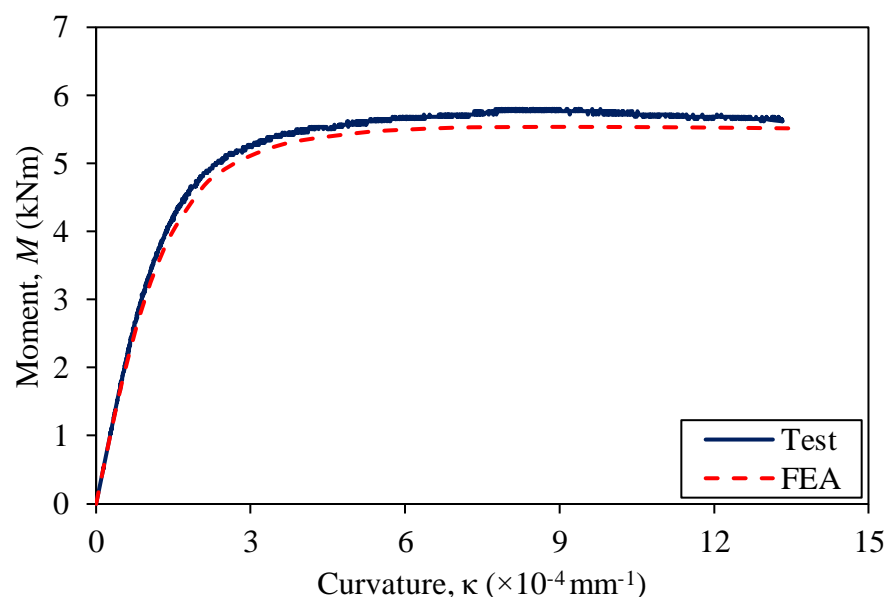


Figure E-6. Moment-curvature curves obtained from test and FEA for specimen
40×60×4C80.



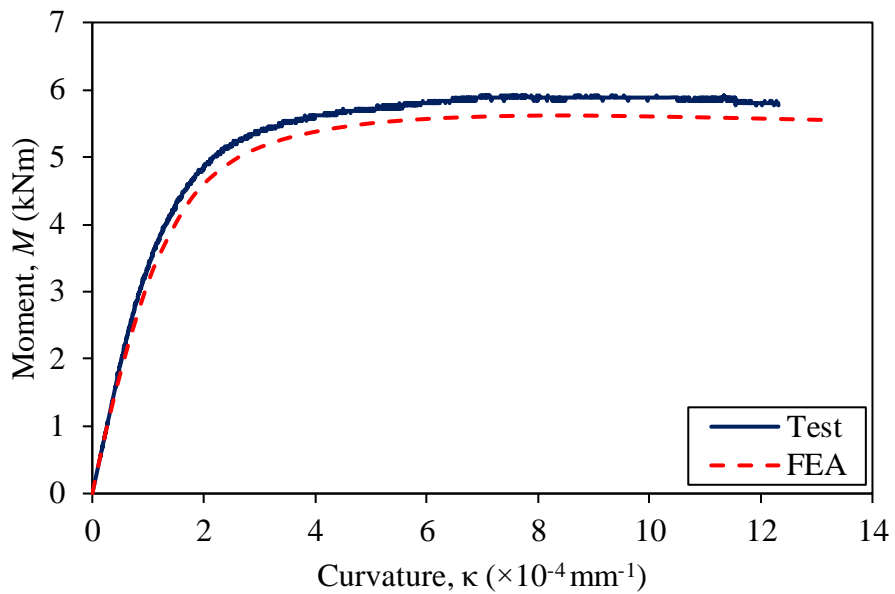


Figure E-7. Moment-curvature curves obtained from test and FEA for specimen
40×60×4C120.

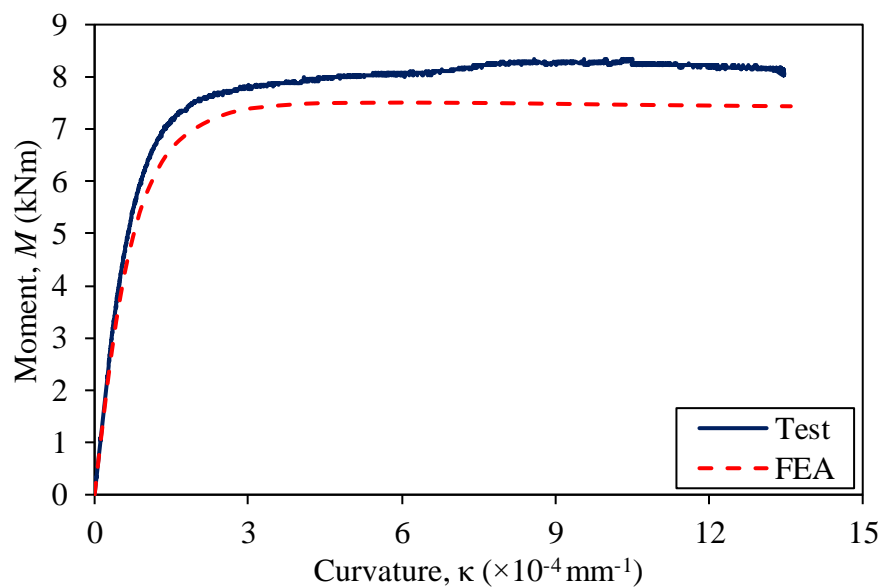


Figure E-8. Moment-curvature curves obtained from test and FEA for specimen
60×60×3C40.



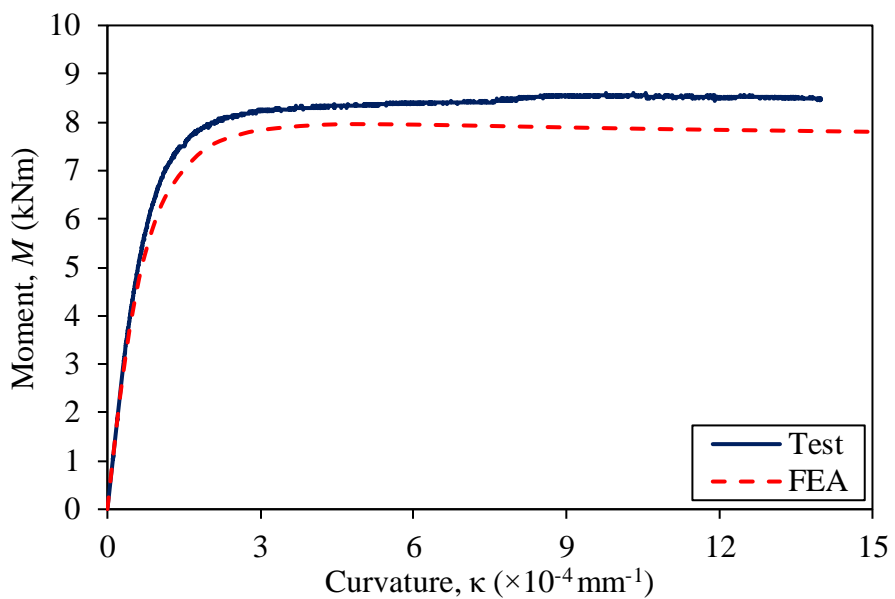


Figure E-9. Moment-curvature curves obtained from test and FEA for specimen
60×60×3C80.

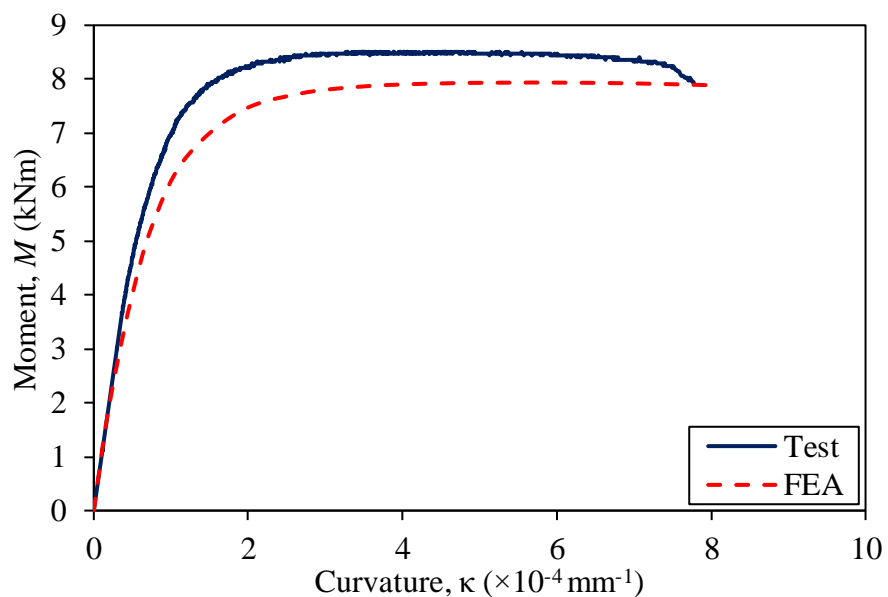


Figure E-10. Moment-curvature curves obtained from test and FEA for specimen
60×60×3C120.



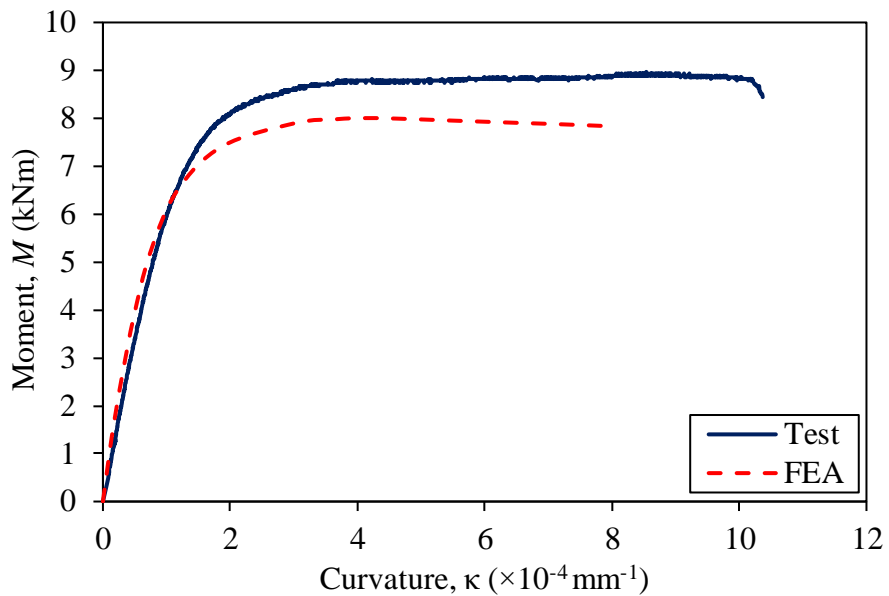


Figure E-11. Moment-curvature curves obtained from test and FEA for specimen
60×60×3C120R.

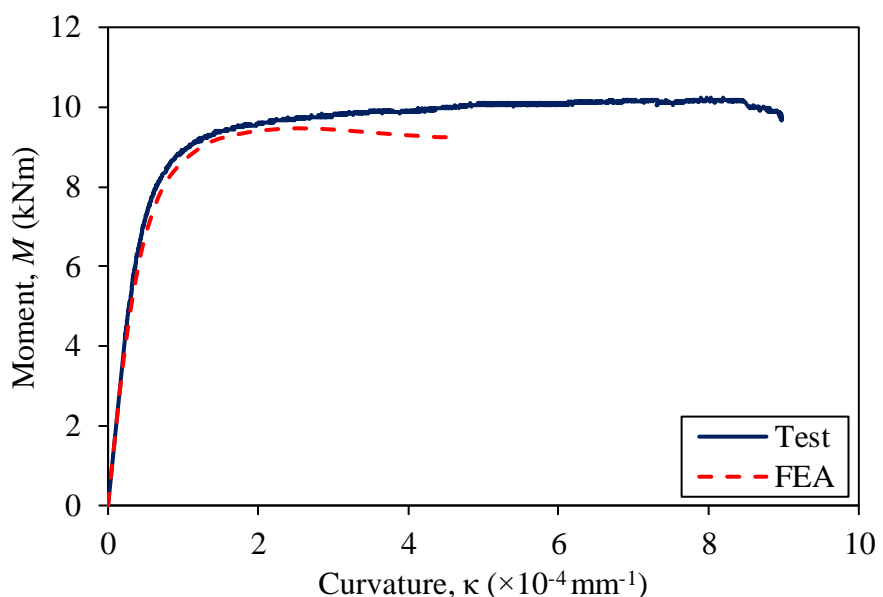


Figure E-12. Moment-curvature curves obtained from test and FEA for specimen
100×40×2C40.



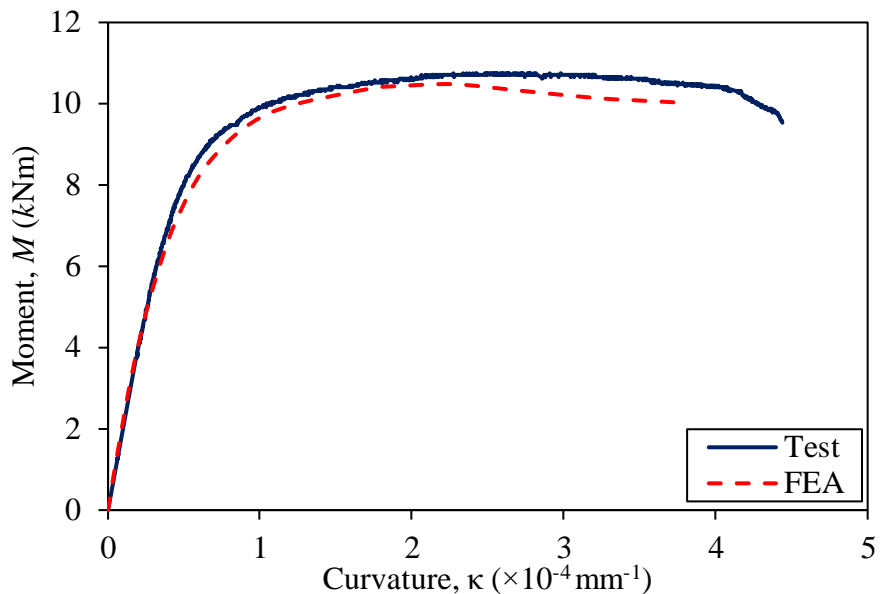


Figure E-13. Moment-curvature curves obtained from test and FEA for specimen
100×40×2C80.

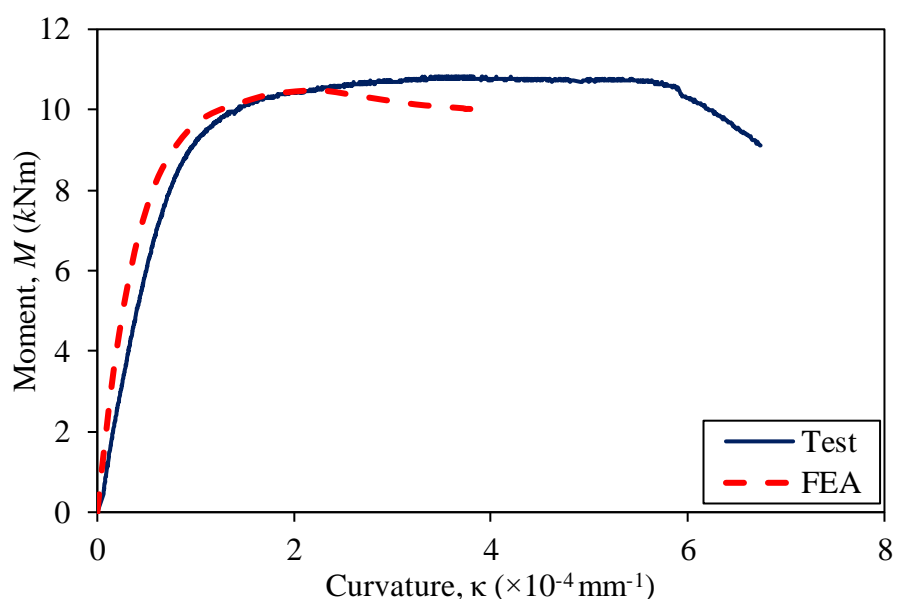


Figure E-14. Moment-curvature curves obtained from test and FEA for specimen
100×40×2C80R.



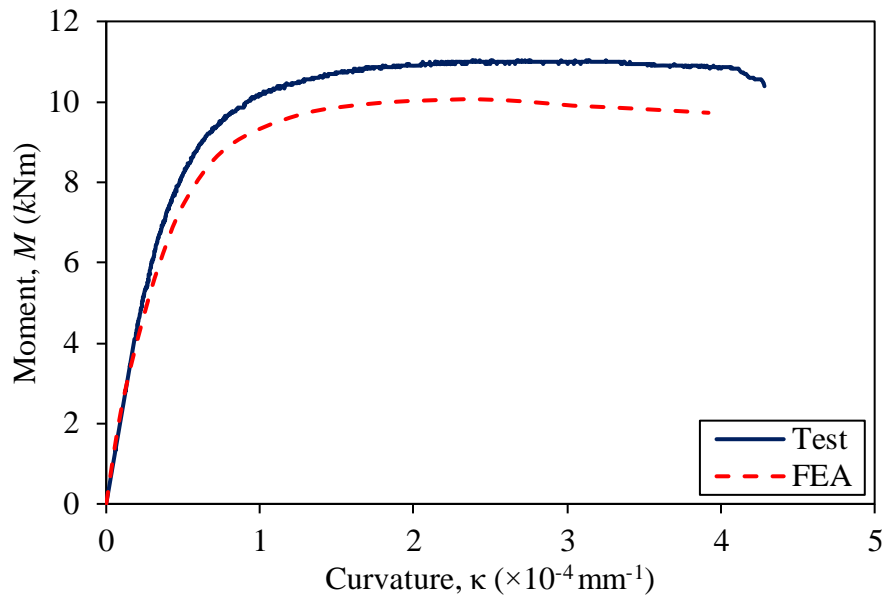


Figure E-15. Moment-curvature curves obtained from test and FEA for specimen
100×40×2C120.

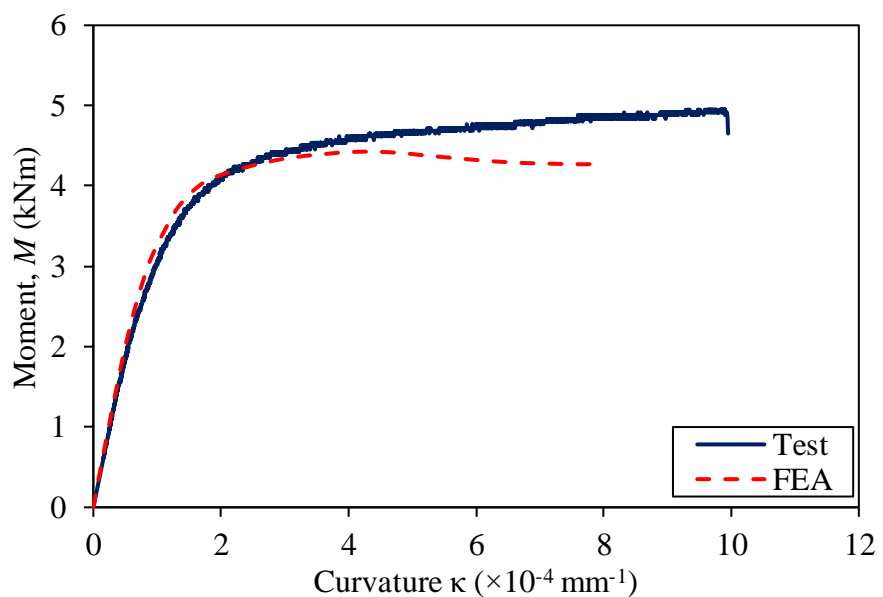


Figure E-16. Moment-curvature curves obtained from test and FEA for specimen
40×100×2C40.



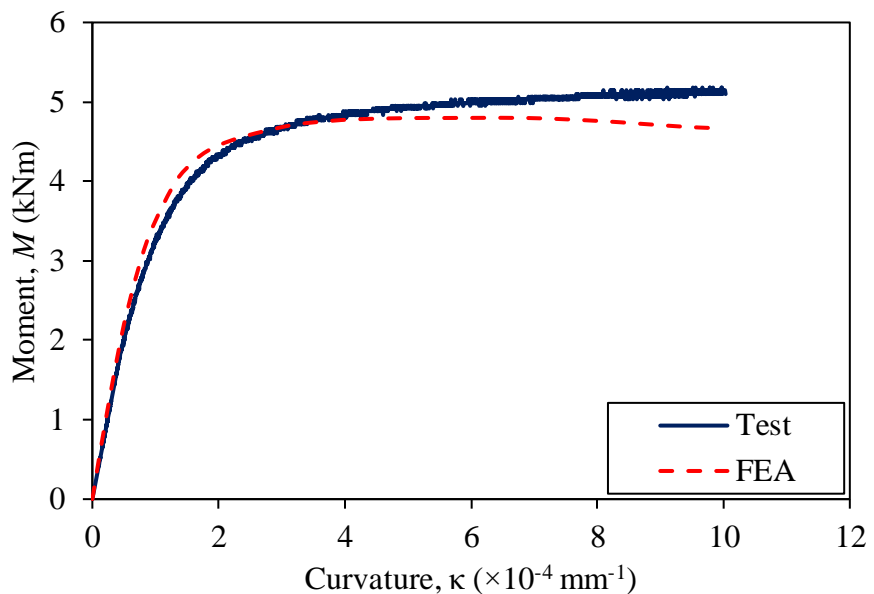


Figure E-17. Moment-curvature curves obtained from test and FEA for specimen
40×100×2C80.

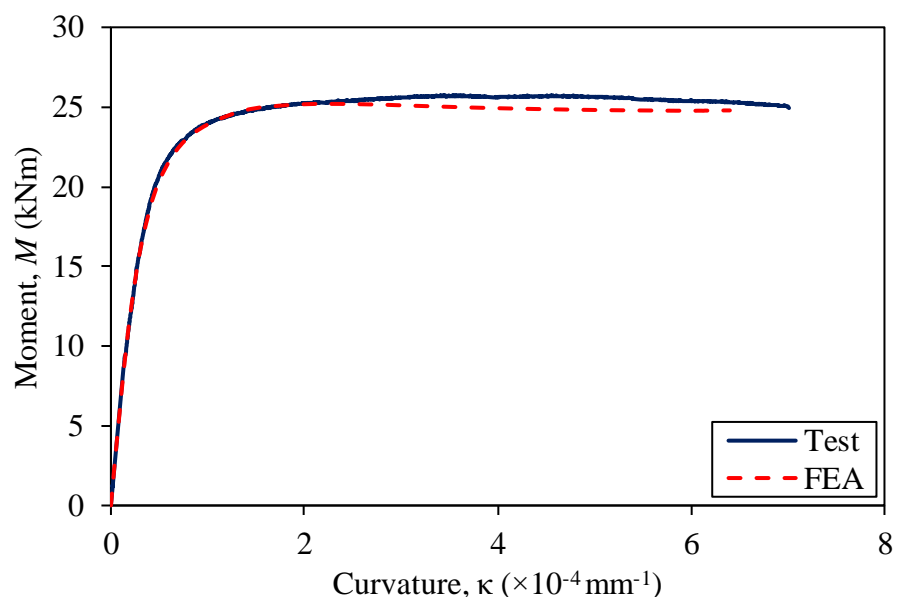


Figure E-18. Moment-curvature curves obtained from test and FEA for specimen
120×80×3C40.



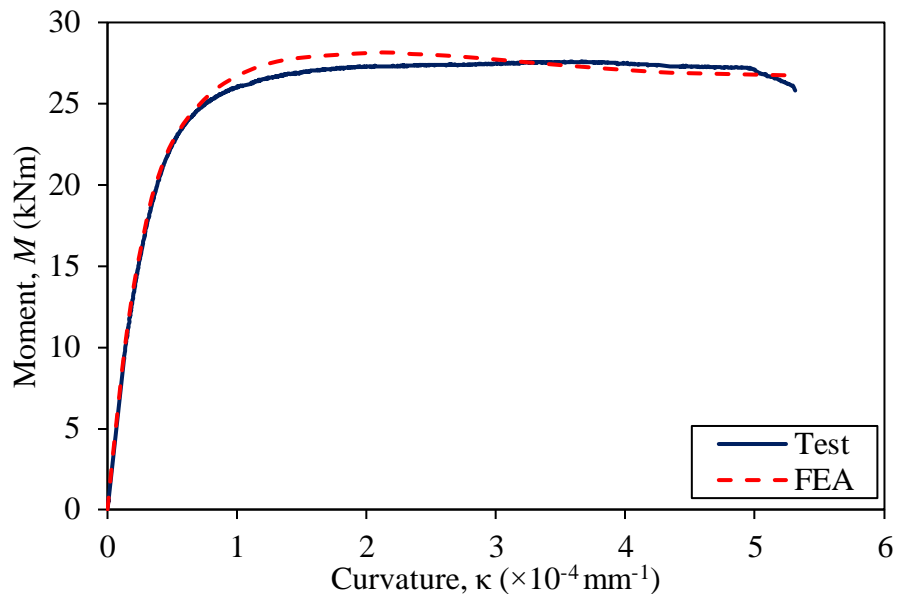


Figure E-19. Moment-curvature curves obtained from test and FEA for specimen
120×80×3C80.

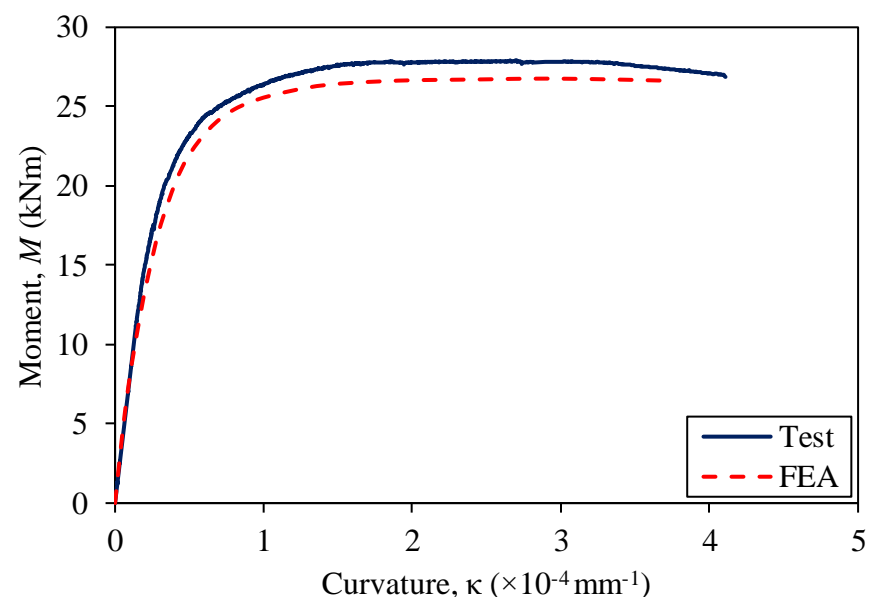


Figure E-20. Moment-curvature curves obtained from test and FEA for specimen
120×80×3C120.



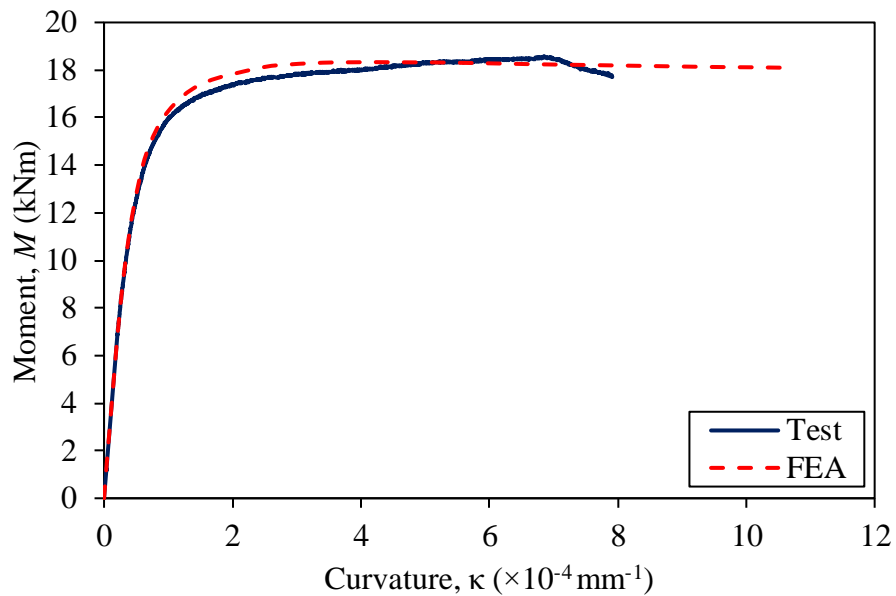


Figure E-21. Moment-curvature curves obtained from test and FEA for specimen
80×120×3C40.

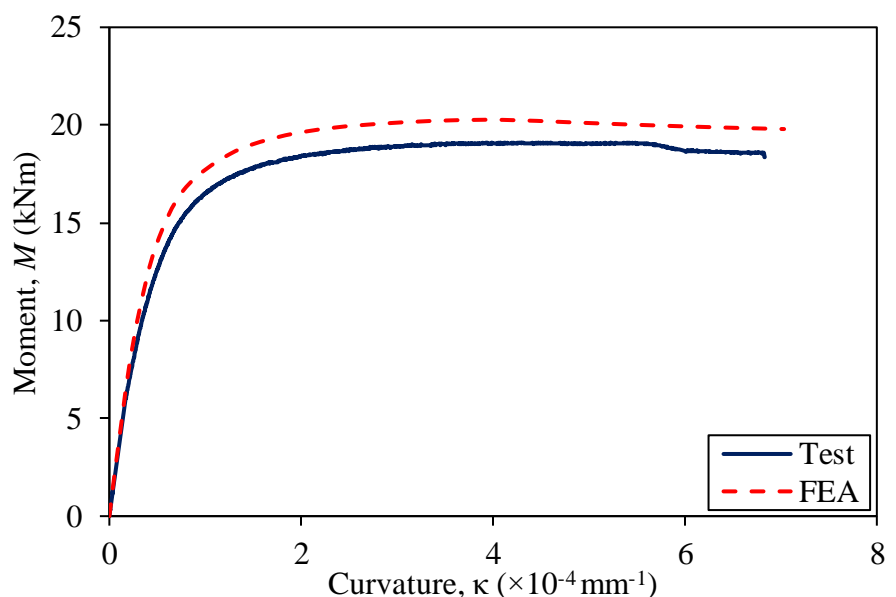


Figure E-22. Moment-curvature curves obtained from test and FEA for specimen
80×120×3C80.



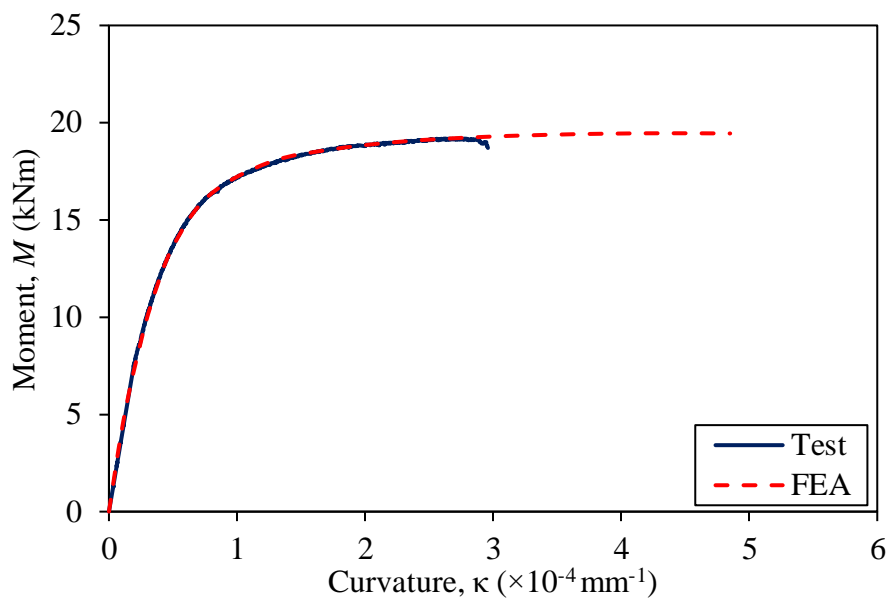


Figure E-23. Moment-curvature curves obtained from test and FEA for specimen
80×120×3C120.



APPENDIX F

CONCRETE-FILLED COLD-FORMED AUSTENITIC STAINLESS STEEL FLEXURAL MEMBERS

The flexural behaviour of concrete-filled cold-formed austenitic stainless steel sections were investigated. The finite element models were validated against the test results and shown in Appendix D.



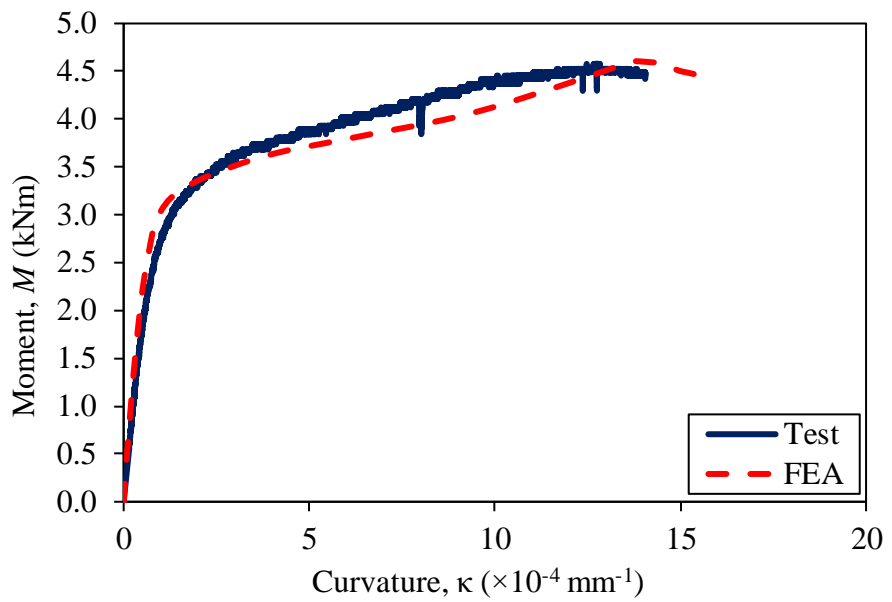


Figure F-1. Moment-curvature curves obtained from test and FEA for specimen
60.5×2.8C40.

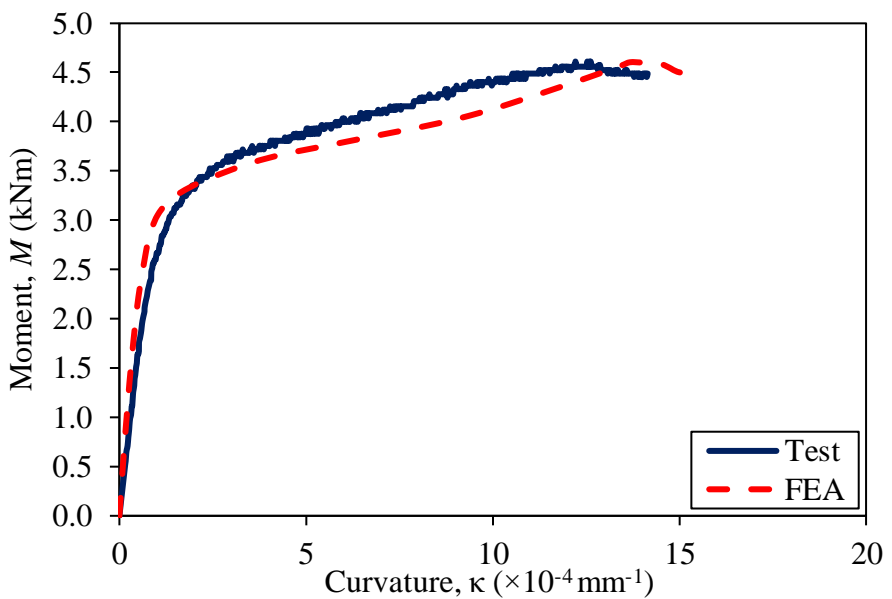


Figure F-2. Moment-curvature curves obtained from test and FEA for specimen
60.5×2.8C40R.



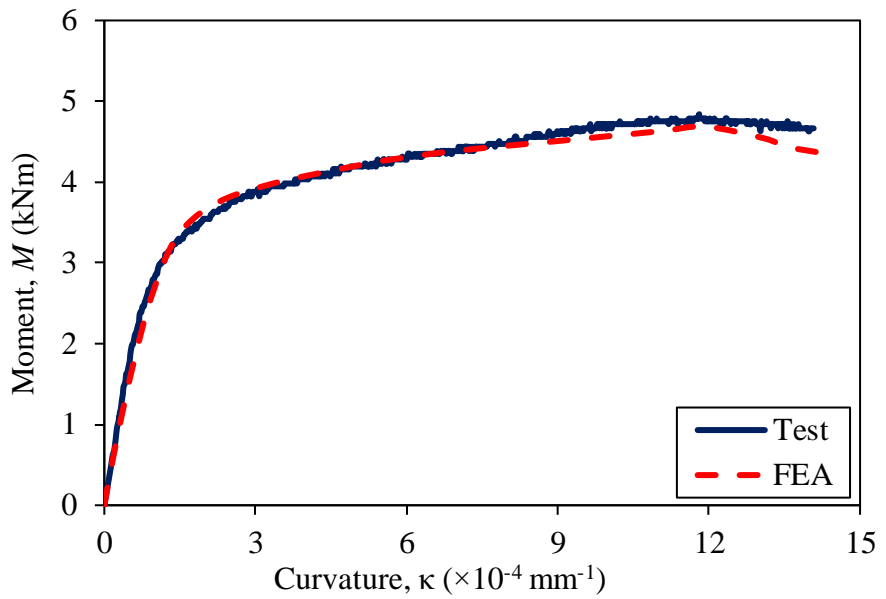


Figure F-3. Moment-curvature curves obtained from test and FEA for specimen
60.5×2.8C80.

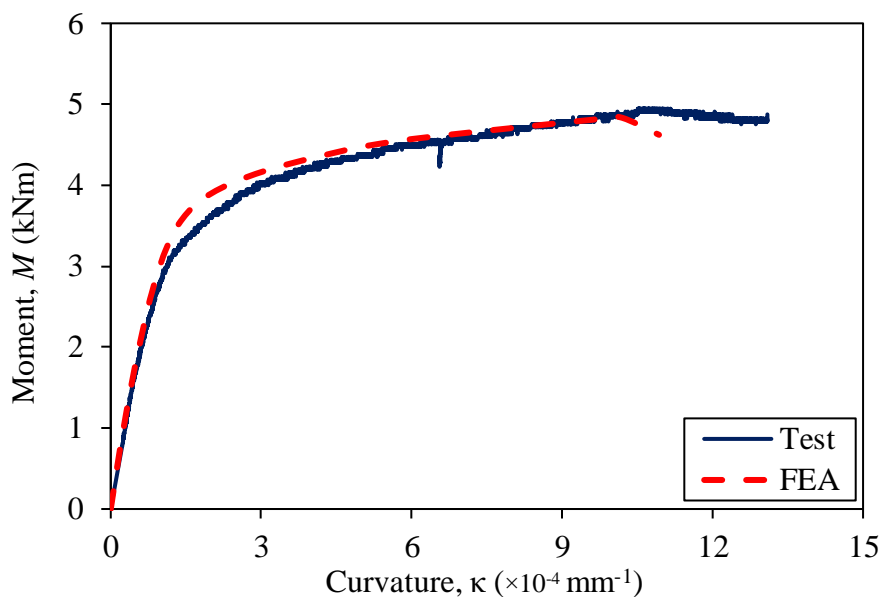


Figure F-4. Moment-curvature curves obtained from test and FEA for specimen
60.5×2.8C120.



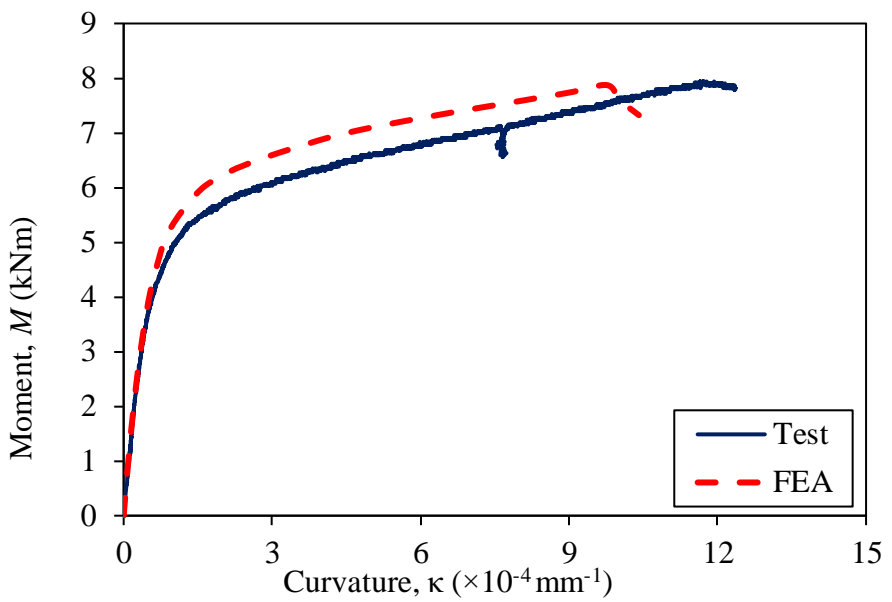


Figure F-5. Moment-curvature curves obtained from test and FEA for specimen
76.3×3.0C40.

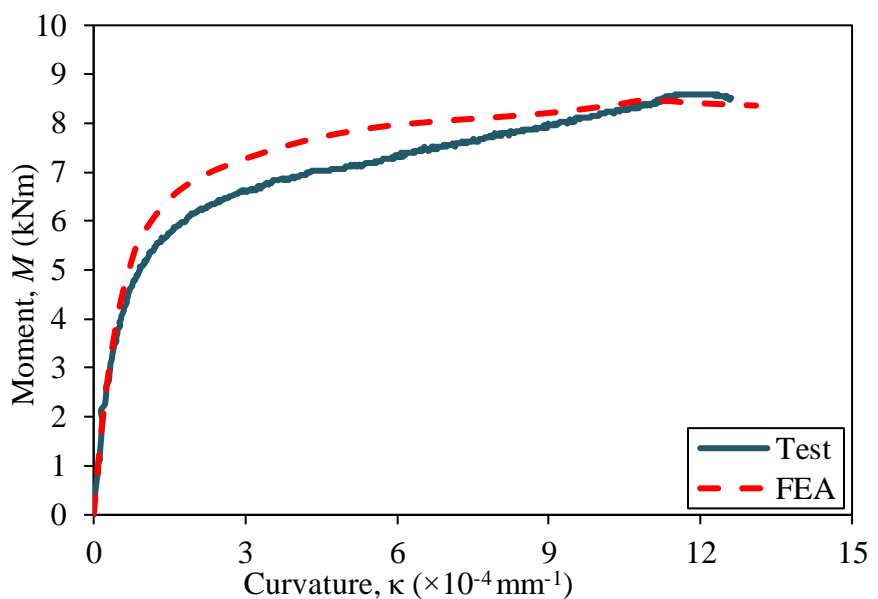


Figure F-6. Moment-curvature curves obtained from test and FEA for specimen
76.3×3.0C80.

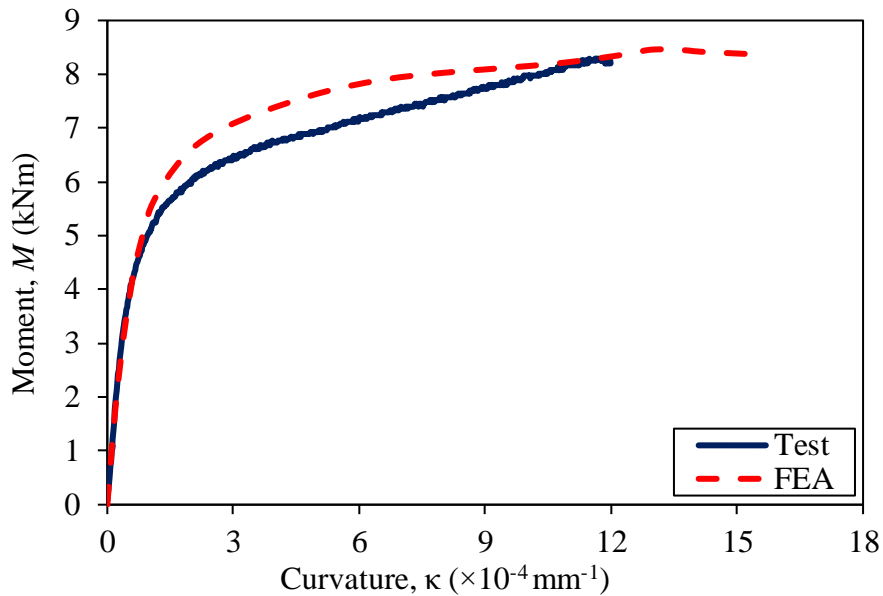


Figure F-7. Moment-curvature curves obtained from test and FEA for specimen
76.3×3.0C80R.

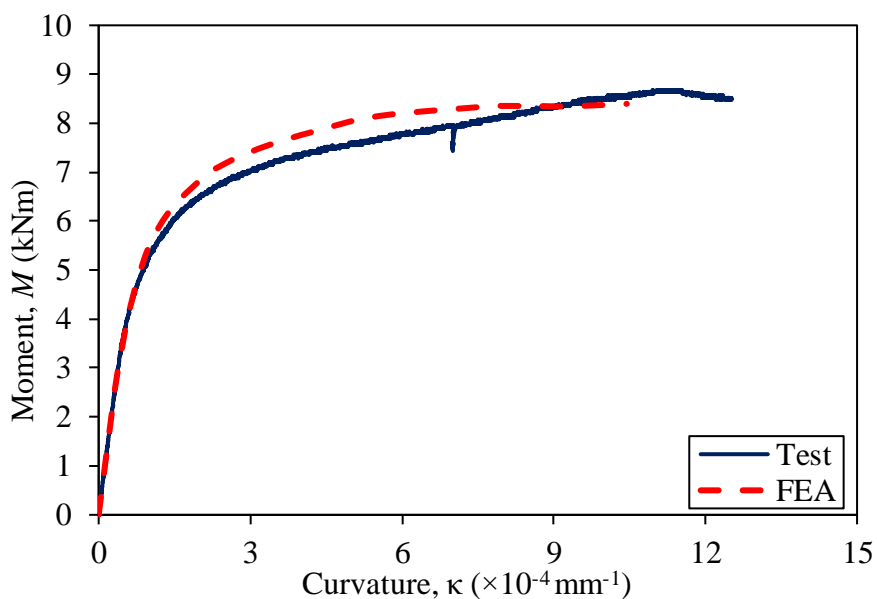


Figure F-8. Moment-curvature curves obtained from test and FEA for specimen
76.3×3.0C120.



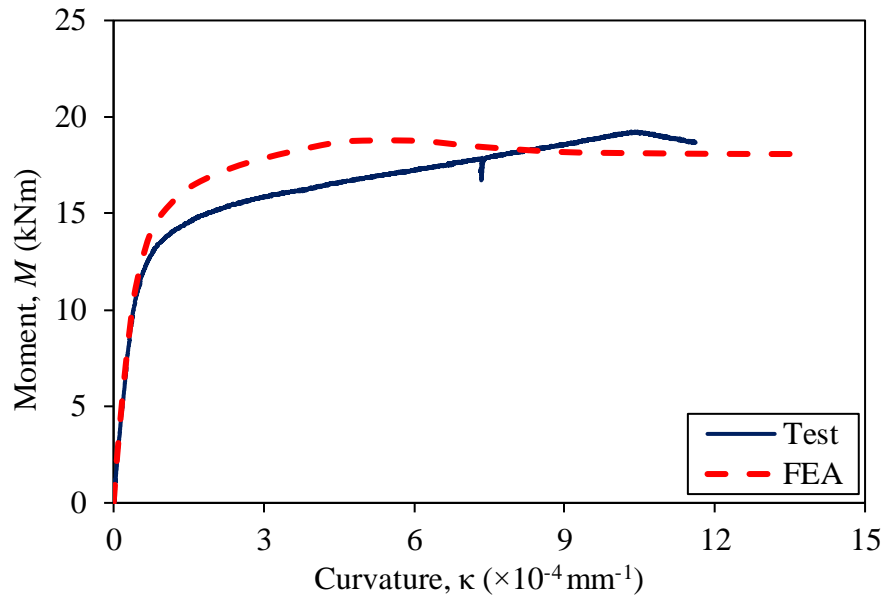


Figure F-9. Moment-curvature curves obtained from test and FEA for specimen
114.3×3.0C40.

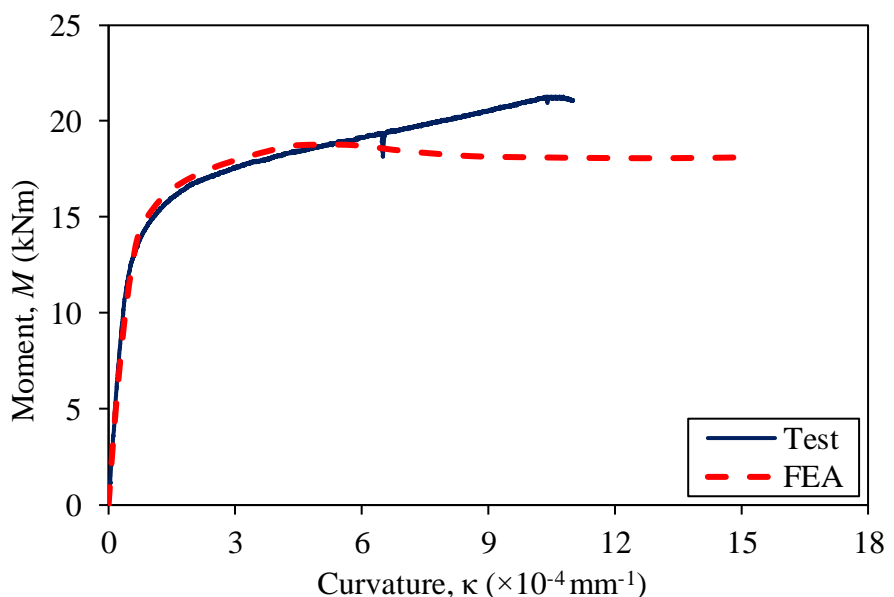


Figure F-10. Moment-curvature curves obtained from test and FEA for specimen
114.3×3.0C80.



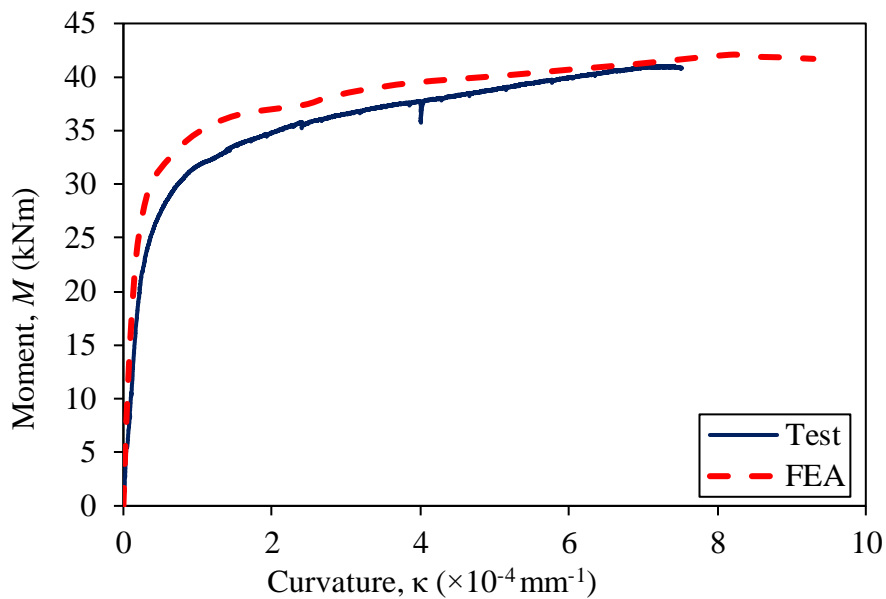


Figure F-11. Moment-curvature curves obtained from test and FEA for specimen
114.3×3.0C120.

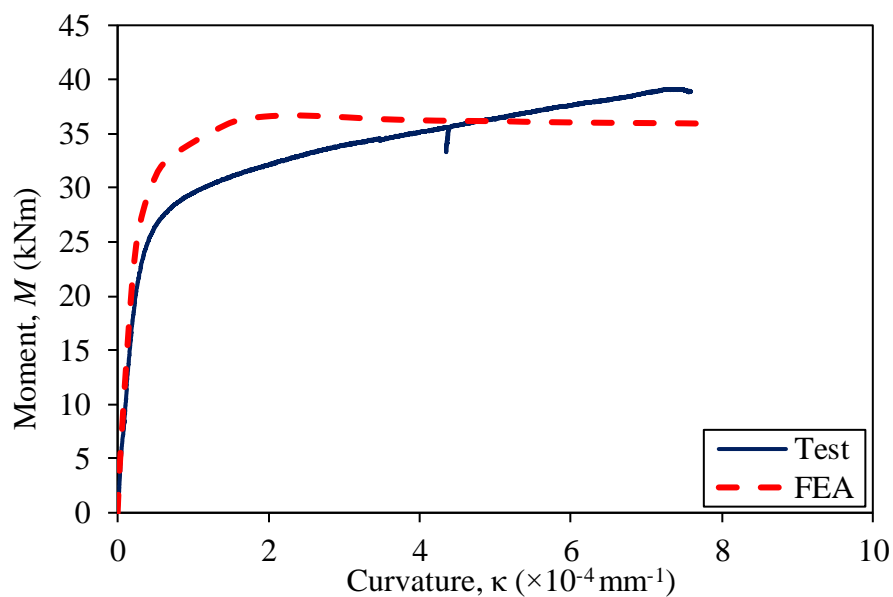


Figure F-12. Moment-curvature curves obtained from test and FEA for specimen
165×3.0C40.



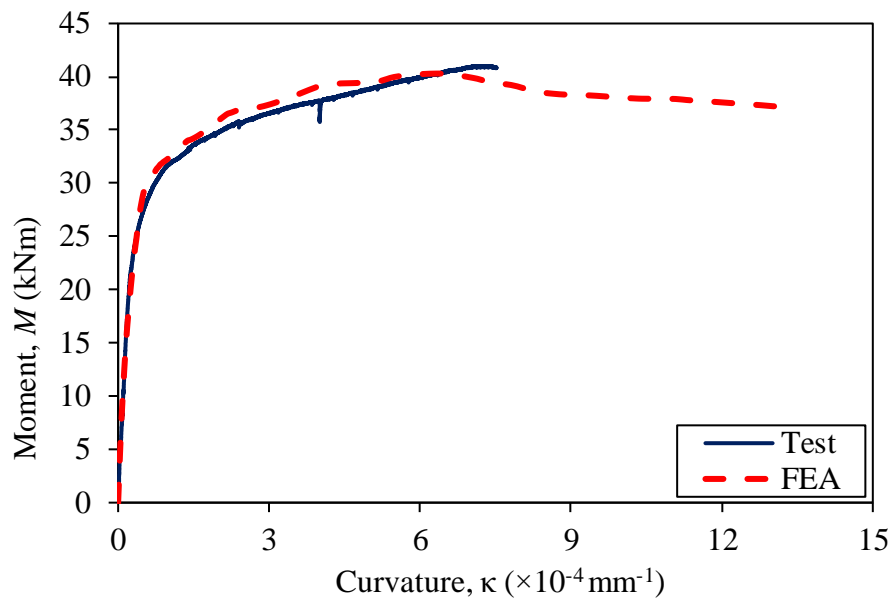


Figure F-13. Moment-curvature curves obtained from test and FEA for specimen
165×3.0C80.

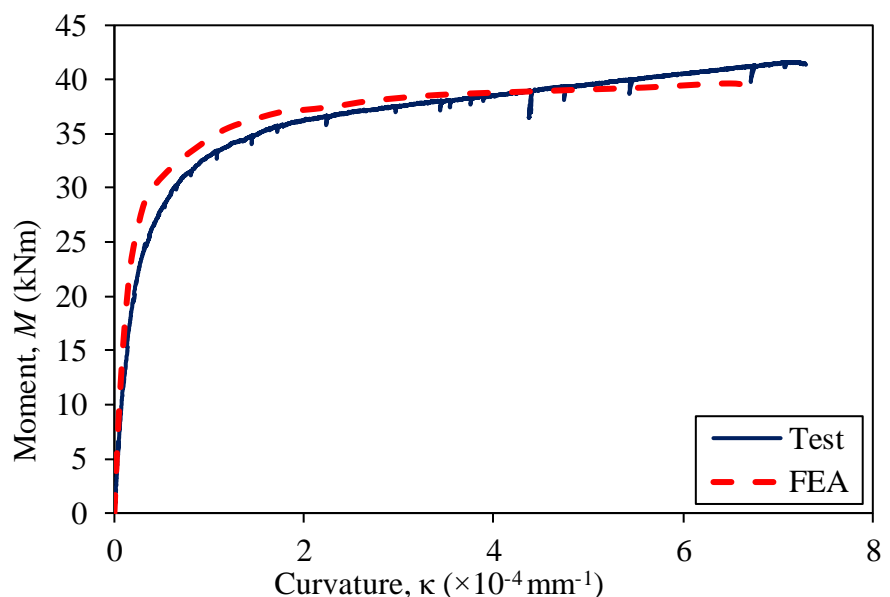


Figure F-14. Moment-curvature curves obtained from test and FEA for specimen
165×3.0C120.



APPENDIX G

CONCRETE-FILLED COLD-FORMED FERRITIC STAINLESS STEEL BEAM-COLUMNS

The beam-column behaviour of concrete-filled cold-formed ferritic stainless steel sections were investigated. The finite element models were validated against the test results and shown in Appendix G.



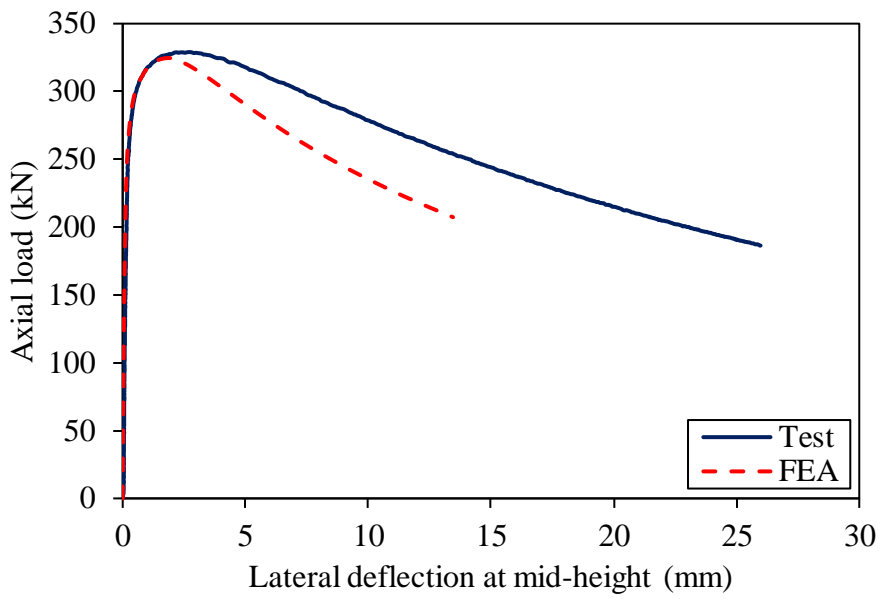


Figure G-1. Test and FEA axial load-lateral deflection at mid-height of specimen
40×60×4C40e0.

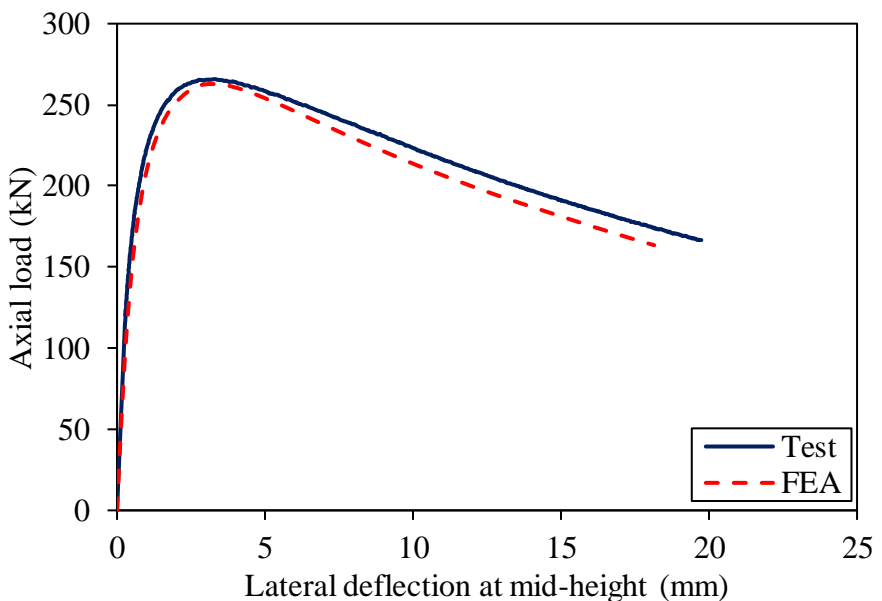


Figure G-2. Test and FEA axial load-lateral deflection at mid-height of specimen
40×60×4C40e3.



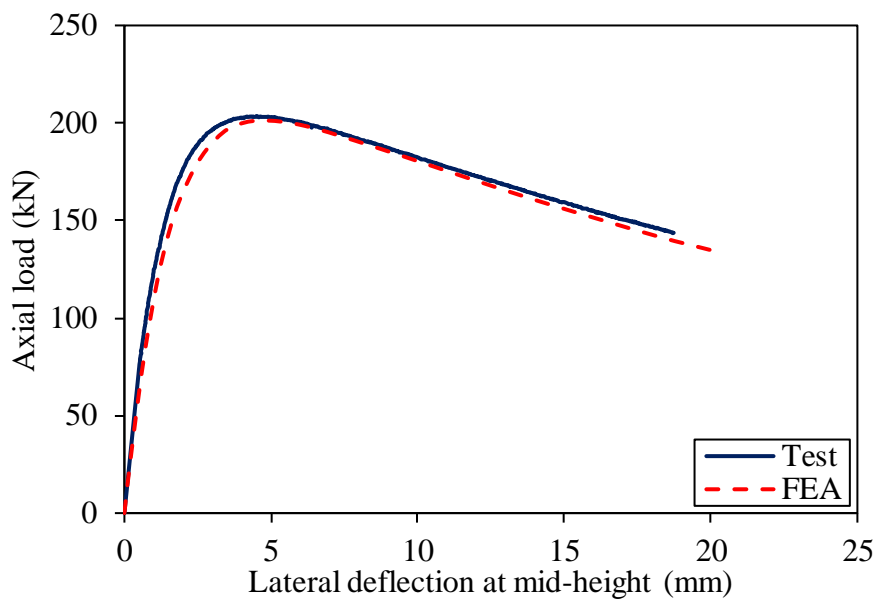


Figure G-3. Test and FEA axial load-lateral deflection at mid-height of specimen
40×60×4C40e8.

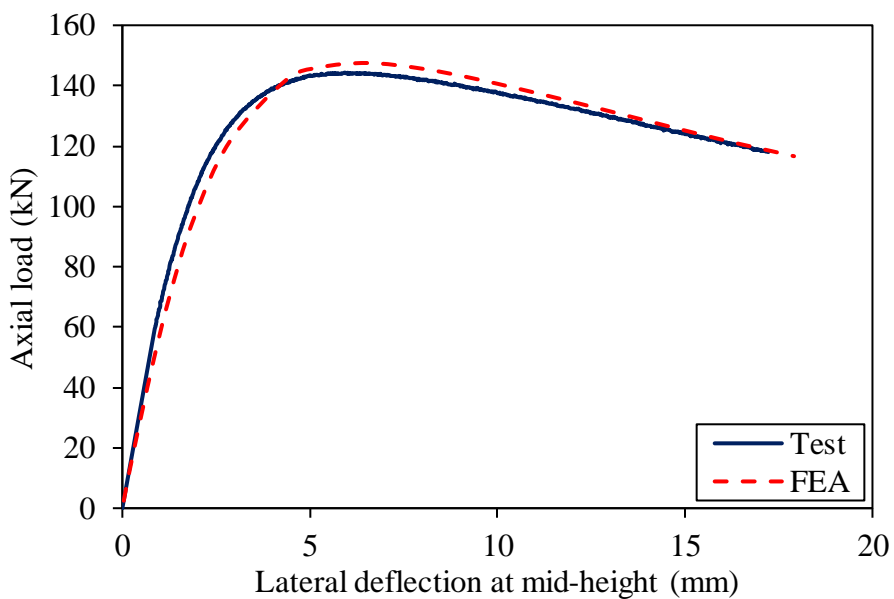


Figure G-4. Test and FEA axial load-lateral deflection at mid-height of specimen
40×60×4C40e20.



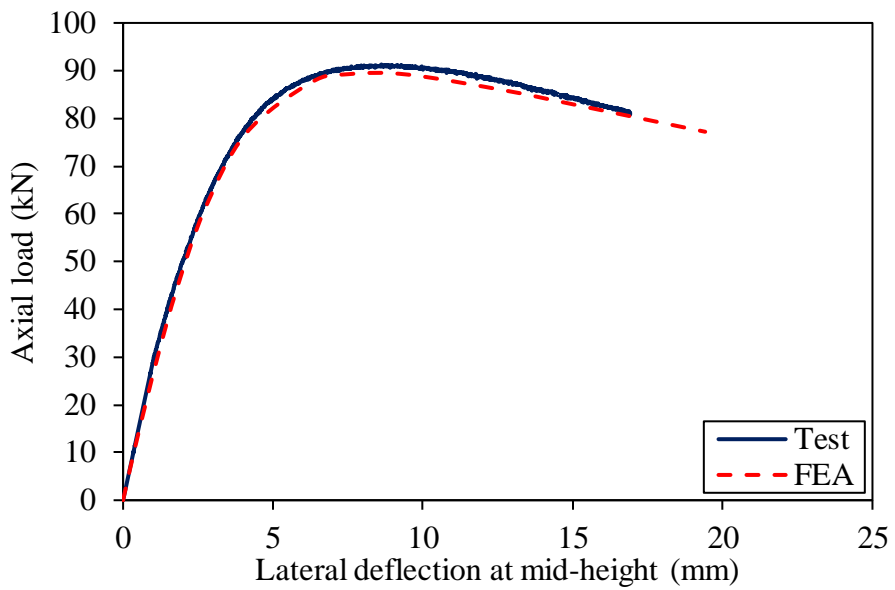


Figure G-5. Test and FEA axial load-lateral deflection at mid-height of specimen
 $40 \times 60 \times 4\text{C}40\text{e}40$.

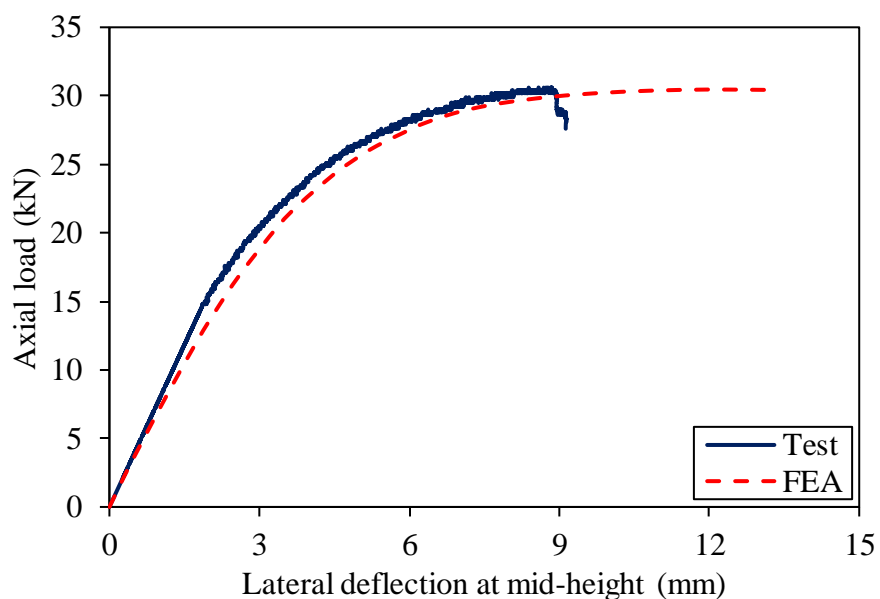


Figure G-6. Test and FEA axial load-lateral deflection at mid-height of specimen
 $40 \times 60 \times 4\text{C}40\text{e}150$.



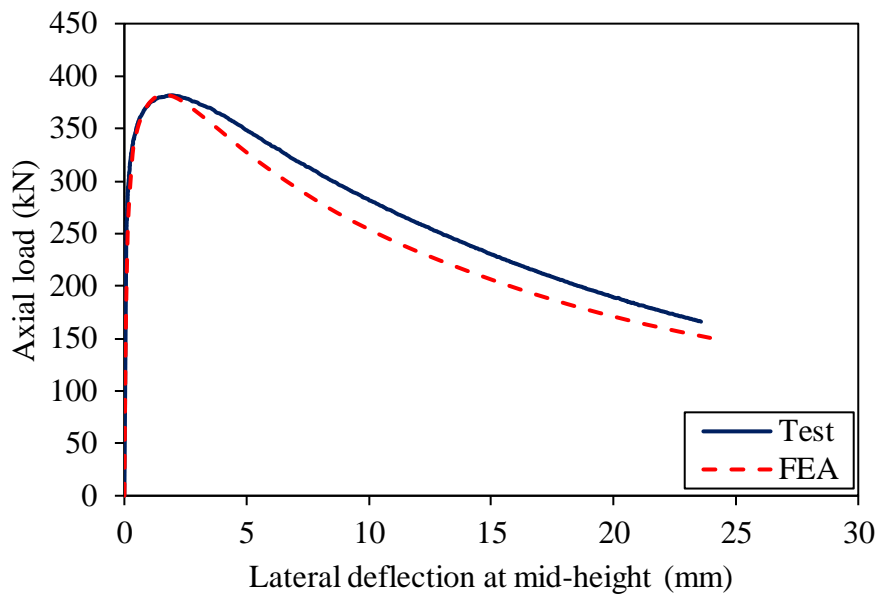


Figure G-7. Test and FEA axial load-lateral deflection at mid-height of specimen
40×60×4C80e0.

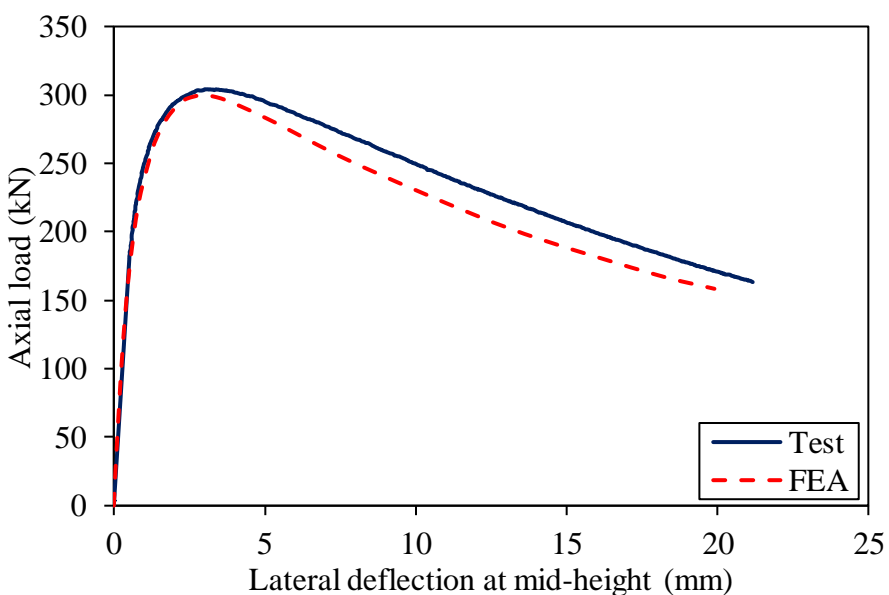


Figure G-8. Test and FEA axial load-lateral deflection at mid-height of specimen
40×60×4C80e3.



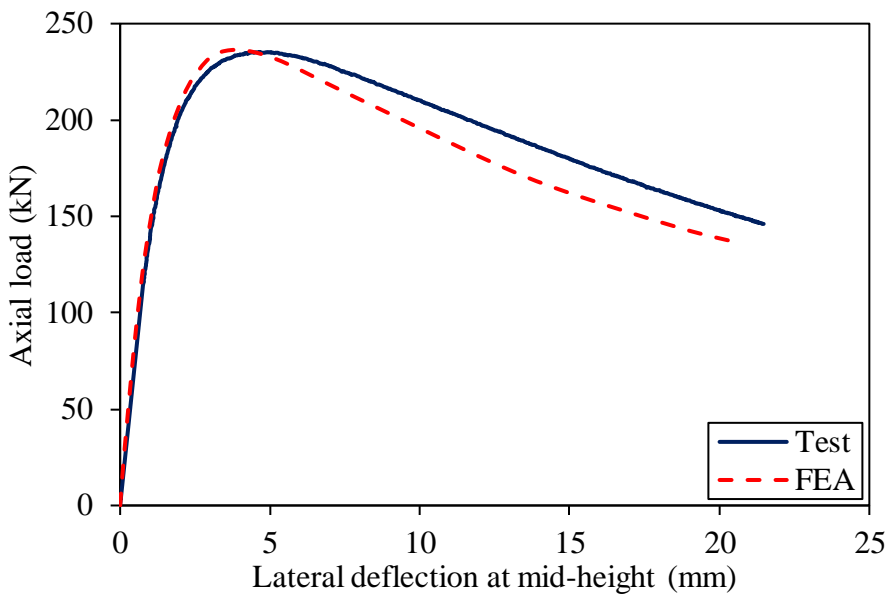


Figure G-9. Test and FEA axial load-lateral deflection at mid-height of specimen
40×60×4C80e8.

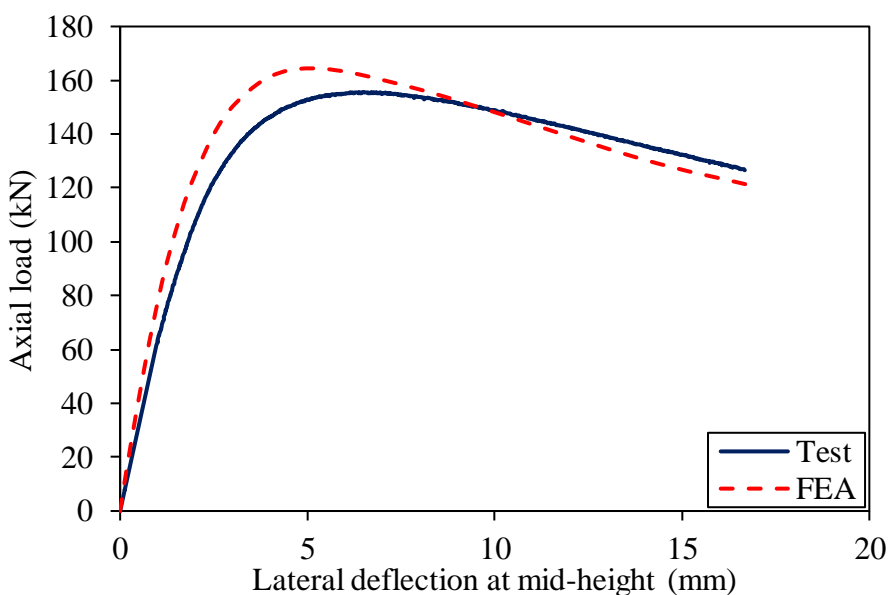


Figure G-10. Test and FEA axial load-lateral deflection at mid-height of specimen
40×60×4C80e20.



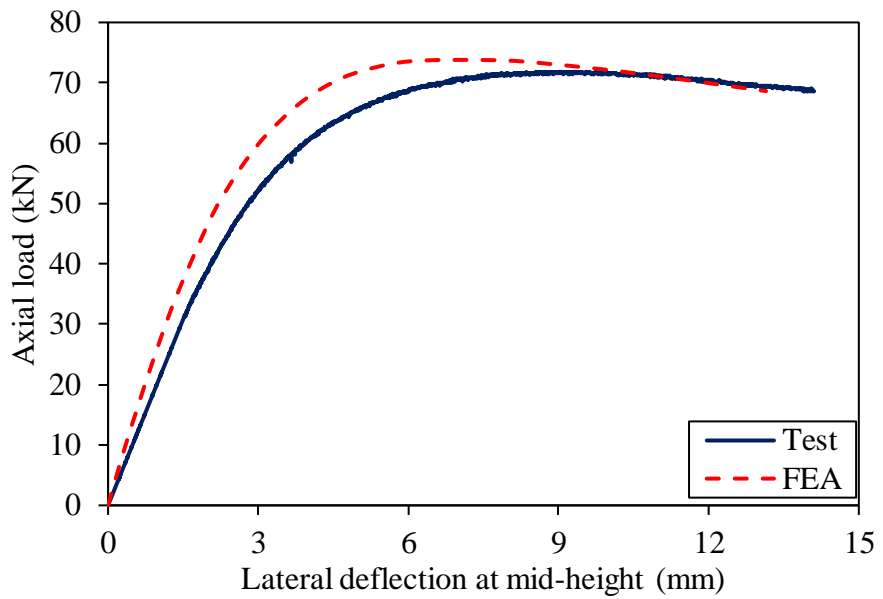


Figure G-11. Test and FEA axial load-lateral deflection at mid-height of specimen
40×60×4C80e60.

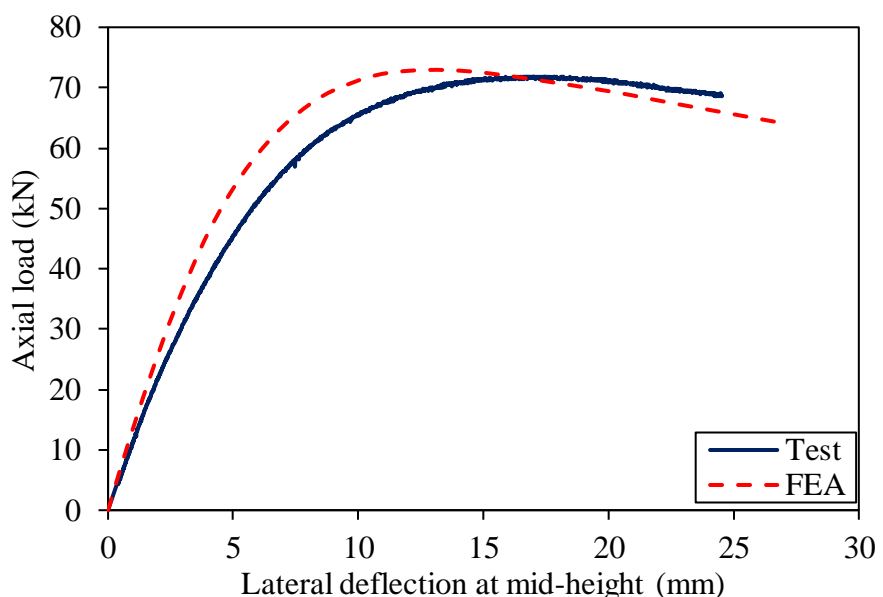


Figure G-12. Test and FEA axial load-lateral deflection at mid-height of specimen
40×60×4C80e60R.



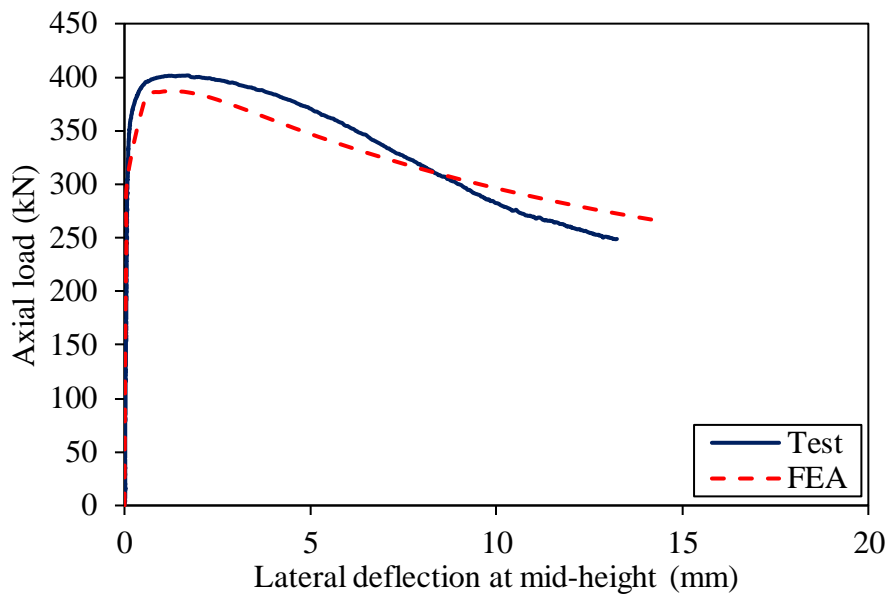


Figure G-13. Test and FEA axial load-lateral deflection at mid-height of specimen
60×60×3C40e0.

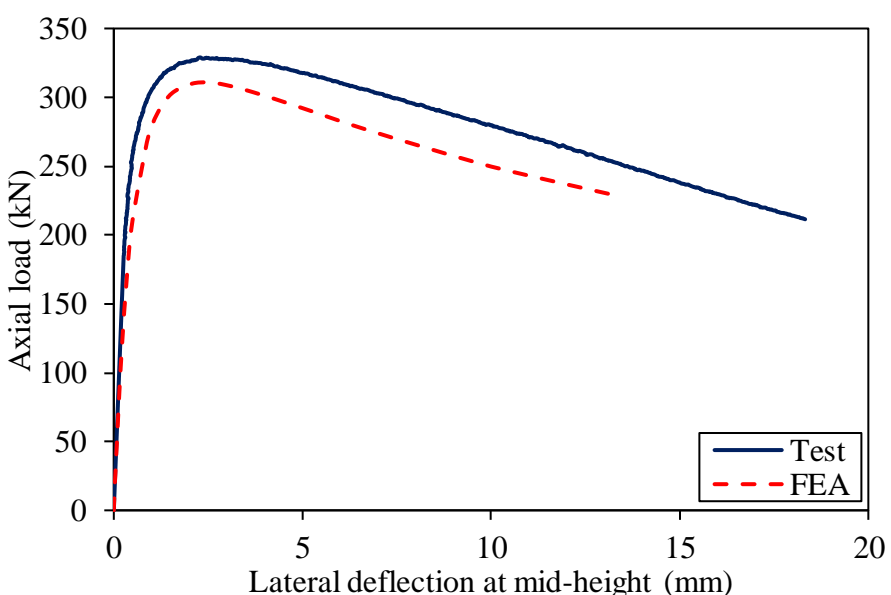


Figure G-14. Test and FEA axial load-lateral deflection at mid-height of specimen
60×60×3C40e3.



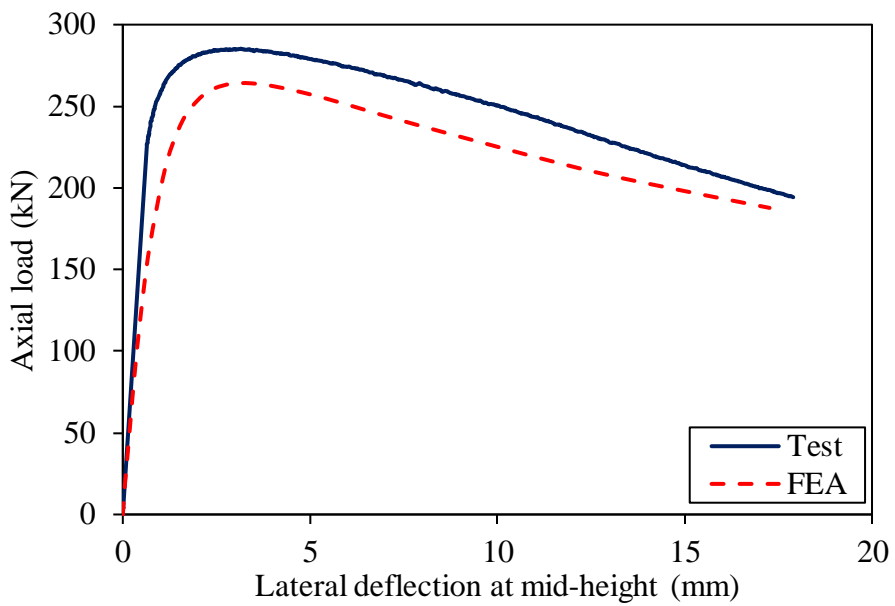


Figure G-15. Test and FEA axial load-lateral deflection at mid-height of specimen
60×60×3C40e8.

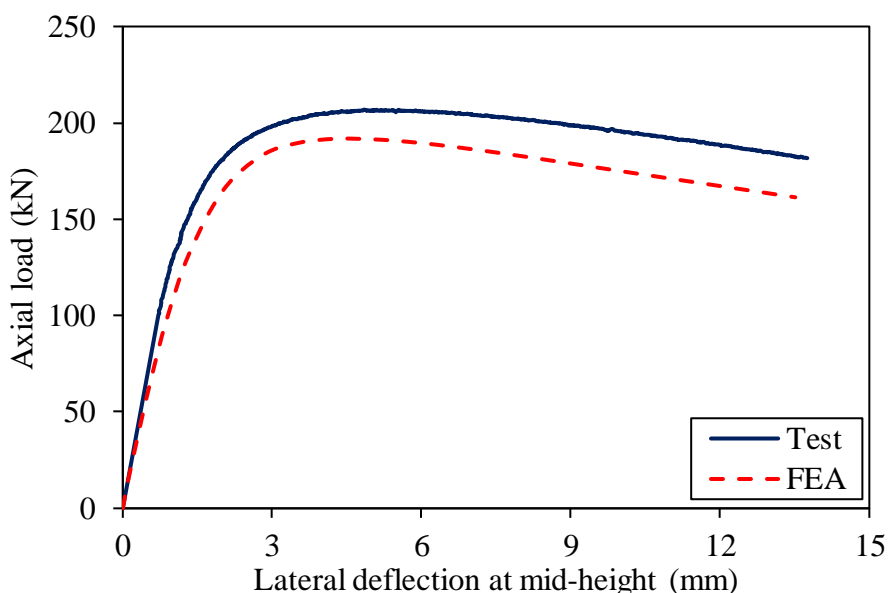


Figure G-16. Test and FEA axial load-lateral deflection at mid-height of specimen
60×60×3C40e20.



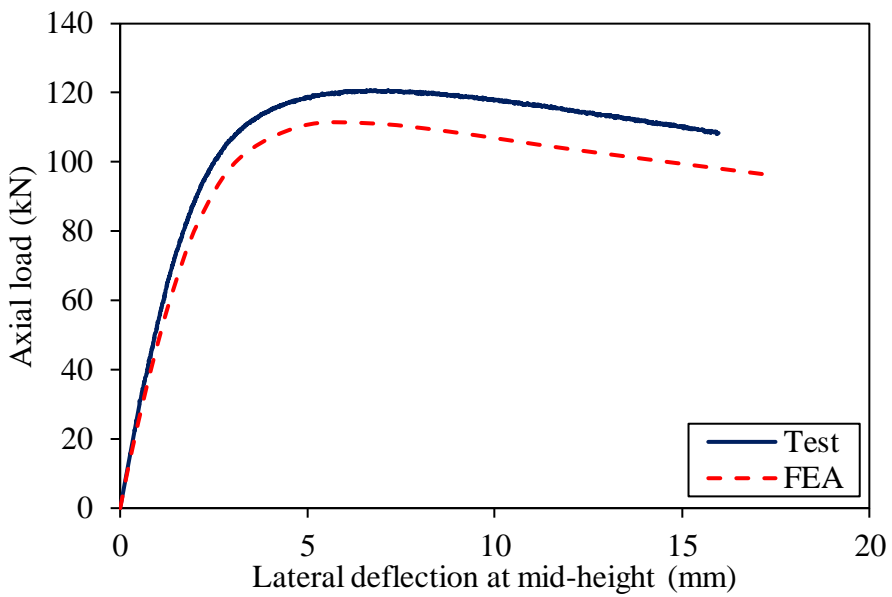


Figure G-17. Test and FEA axial load-lateral deflection at mid-height of specimen
60×60×3C40e50.

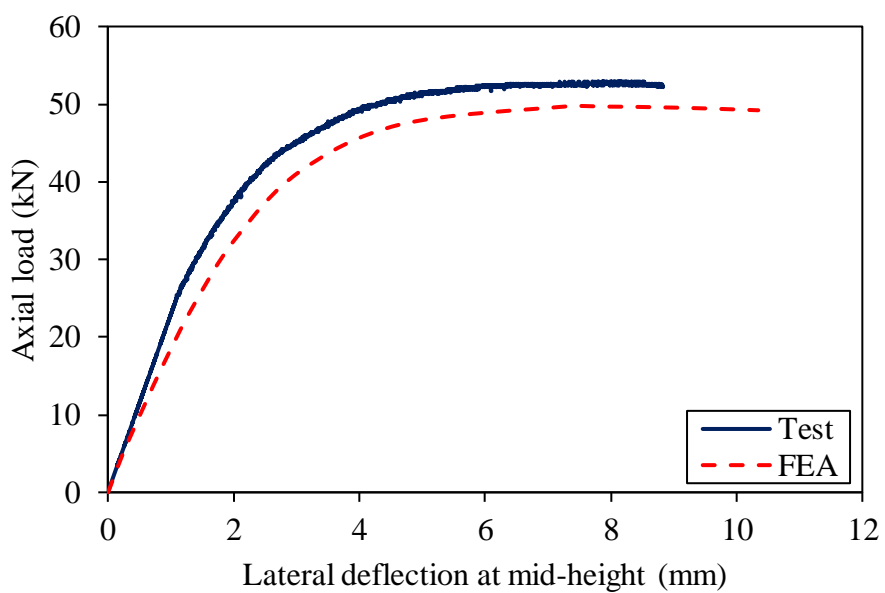


Figure G-18. Test and FEA axial load-lateral deflection at mid-height of specimen
60×60×3C40e130.



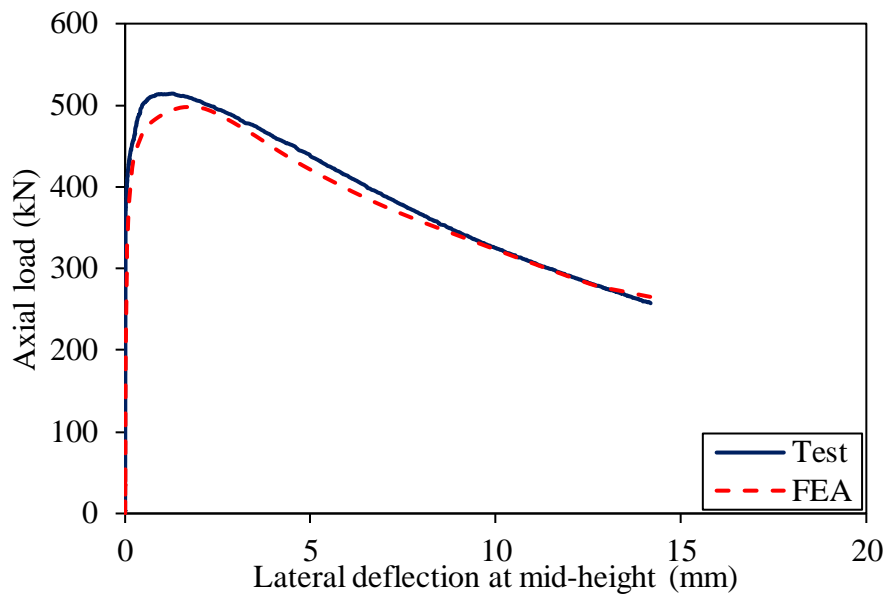


Figure G-19. Test and FEA axial load-lateral deflection at mid-height of specimen
60×60×3C80e0.

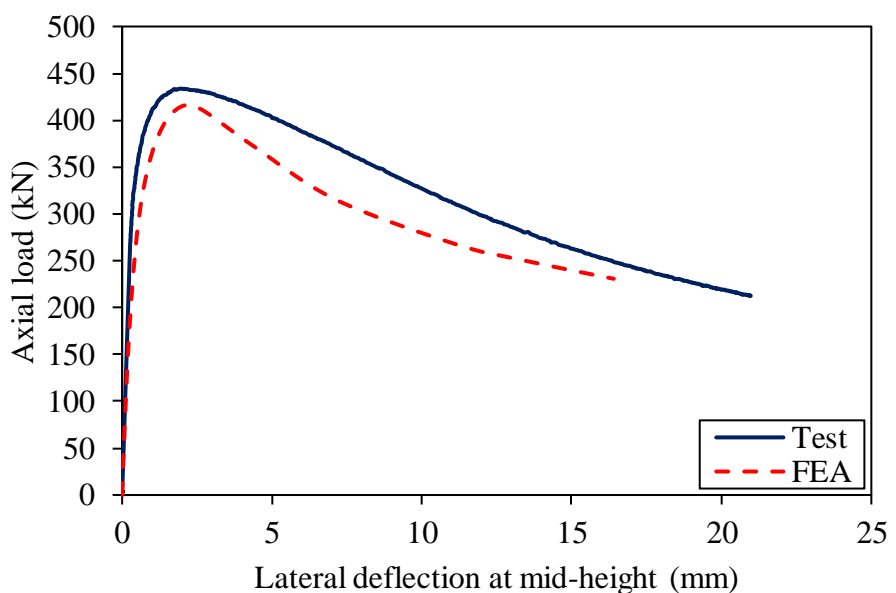


Figure G-20. Test and FEA axial load-lateral deflection at mid-height of specimen
60×60×3C80e3.



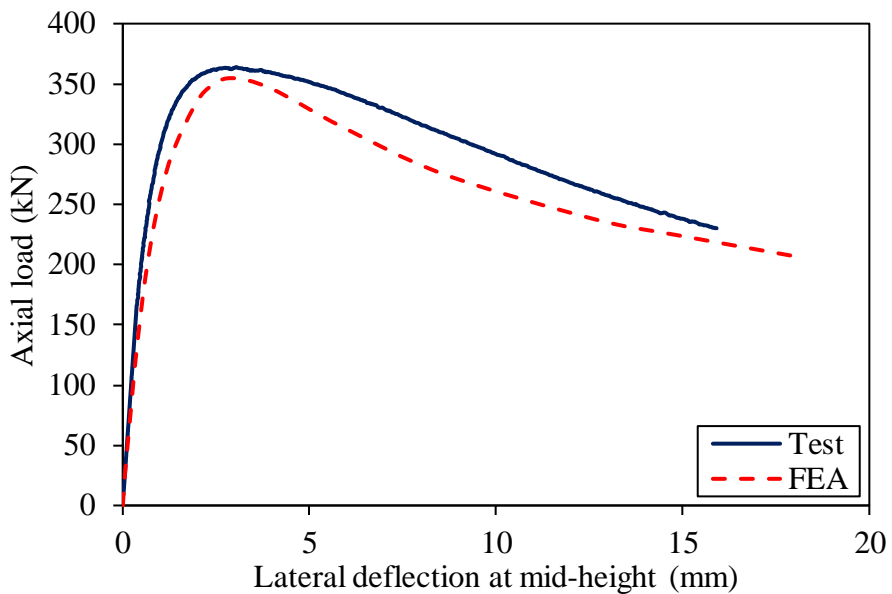


Figure G-21. Test and FEA axial load-lateral deflection at mid-height of specimen
60×60×3C80e8.

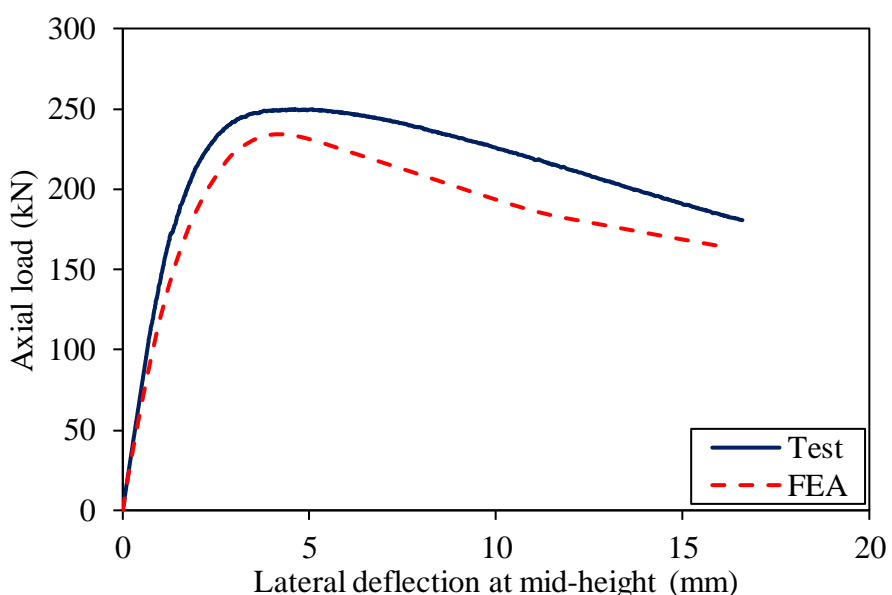


Figure G-22. Test and FEA axial load-lateral deflection at mid-height of specimen
60×60×3C80e20.



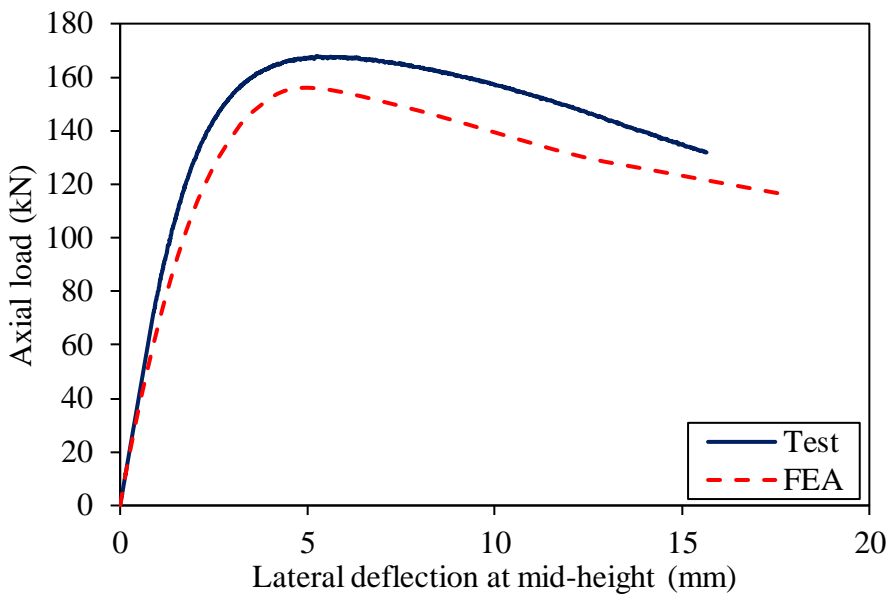


Figure G-23. Test and FEA axial load-lateral deflection at mid-height of specimen
60×60×3C80e40.

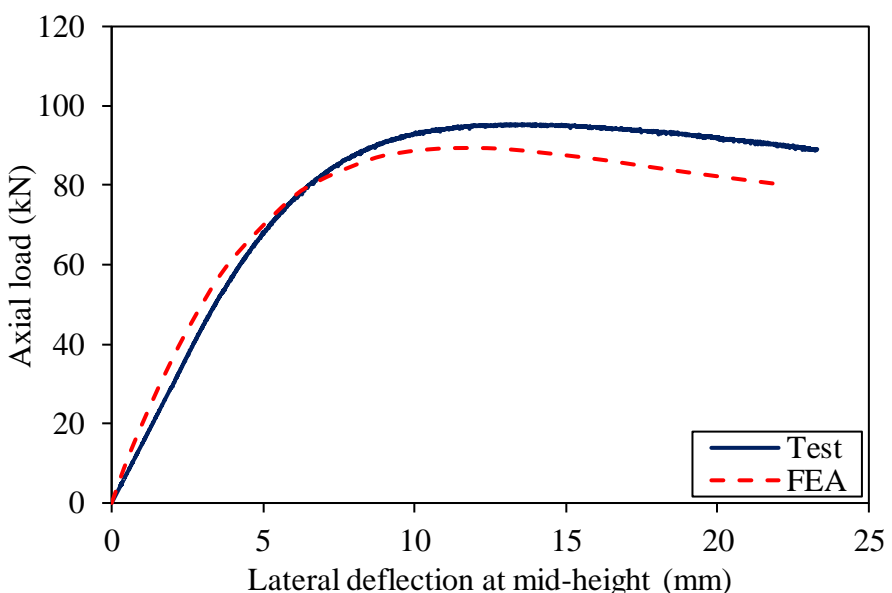


Figure G-24. Test and FEA axial load-lateral deflection at mid-height of specimen
60×60×3C80e80.



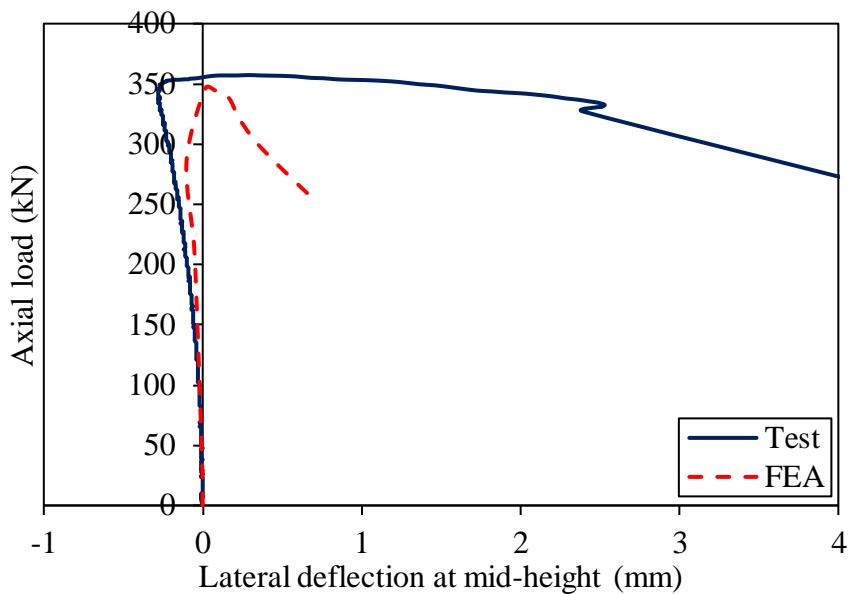


Figure G-25. Test and FEA axial load-lateral deflection at mid-height of specimen
40×100×2C40e0.

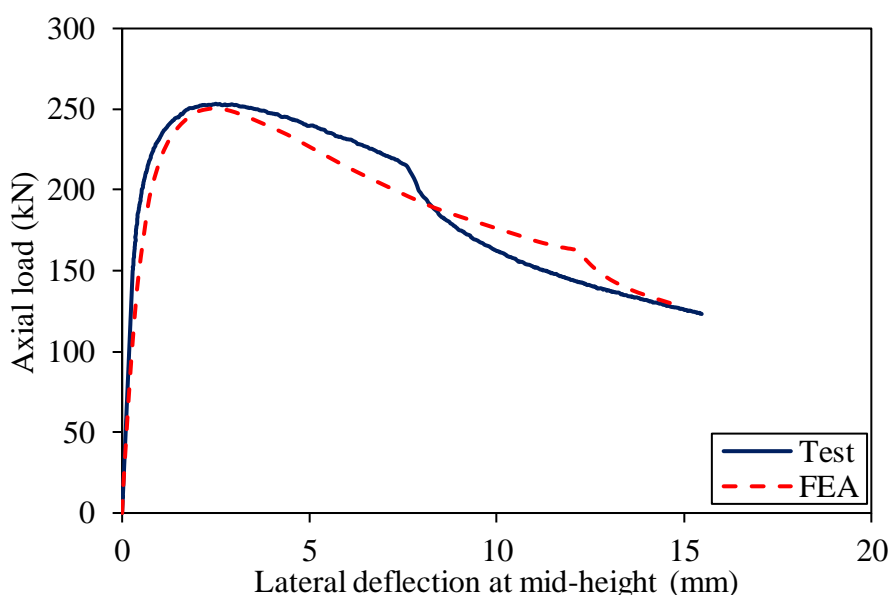


Figure G-26. Test and FEA axial load-lateral deflection at mid-height of specimen
40×100×2C40e3.



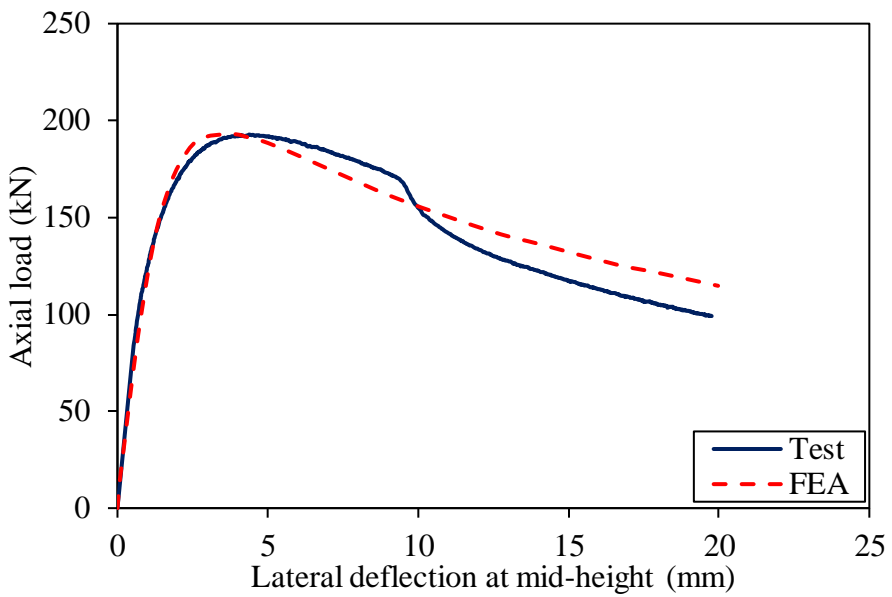


Figure G-27. Test and FEA axial load-lateral deflection at mid-height of specimen
40×100×2C40e8.

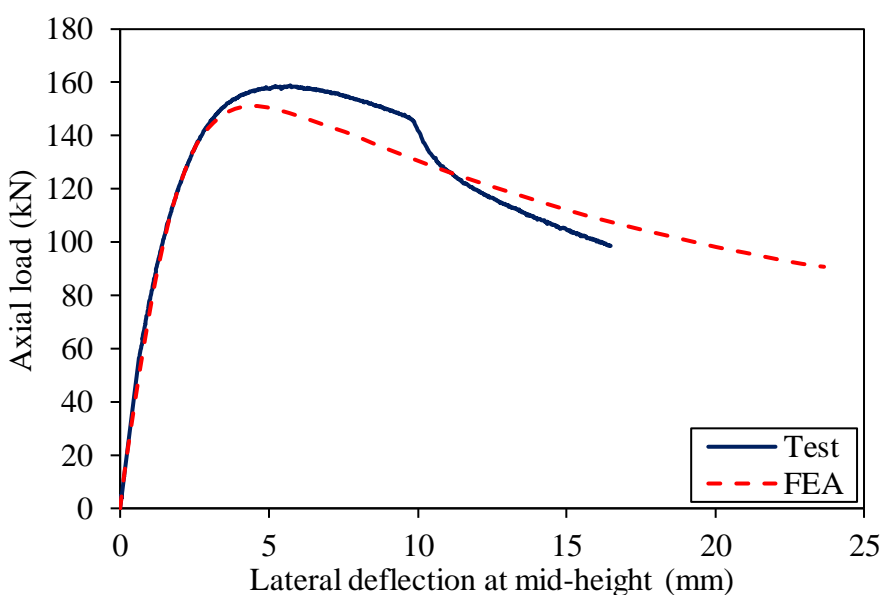


Figure G-28. Test and FEA axial load-lateral deflection at mid-height of specimen
40×100×2C40e15.



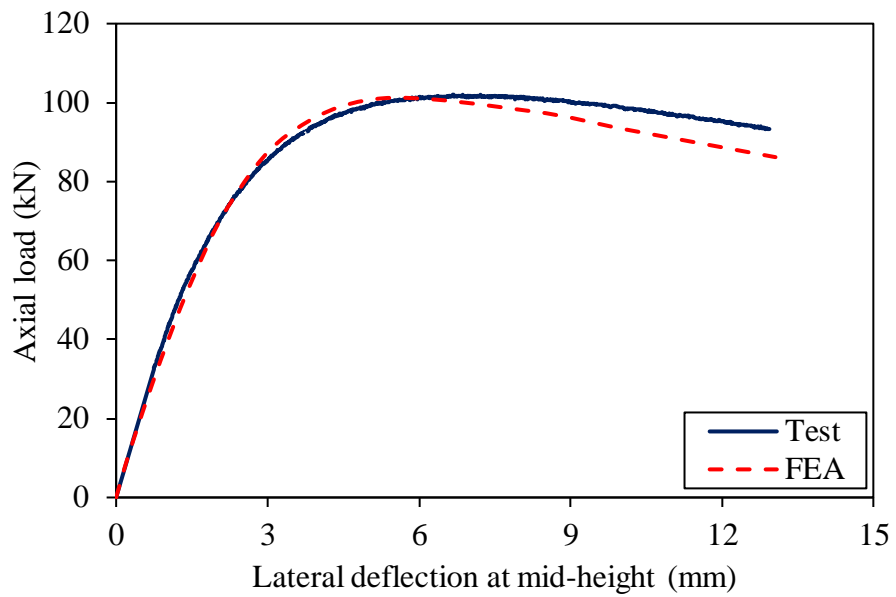


Figure G-29. Test and FEA axial load-lateral deflection at mid-height of specimen
40×100×2C40e30.

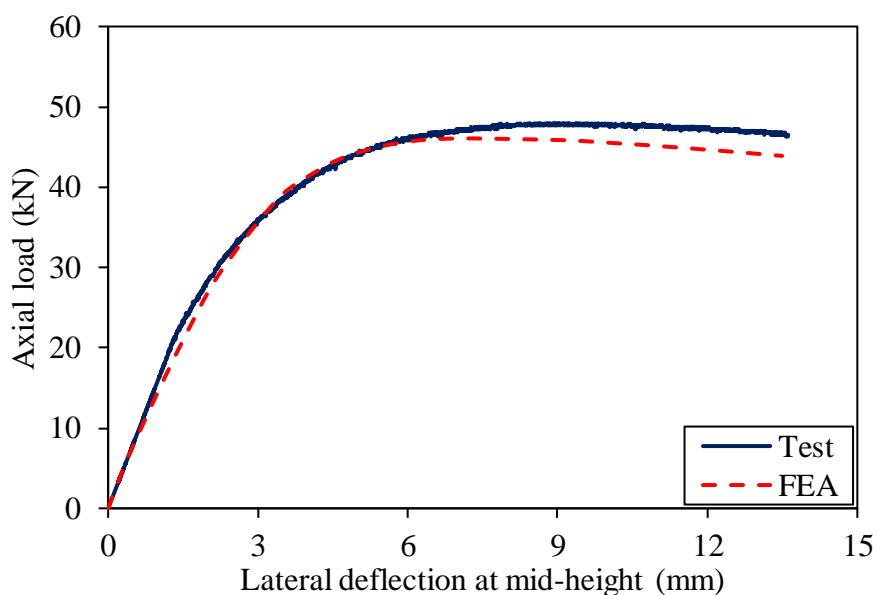


Figure G-30. Test and FEA axial load-lateral deflection at mid-height of specimen
40×100×2C40e80.



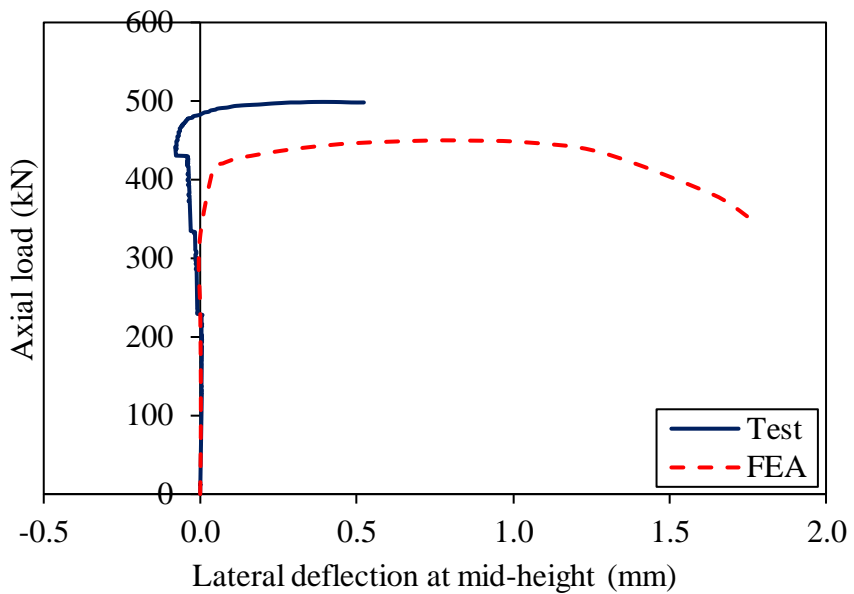


Figure G-31. Test and FEA axial load-lateral deflection at mid-height of specimen
40×100×2C80e0.

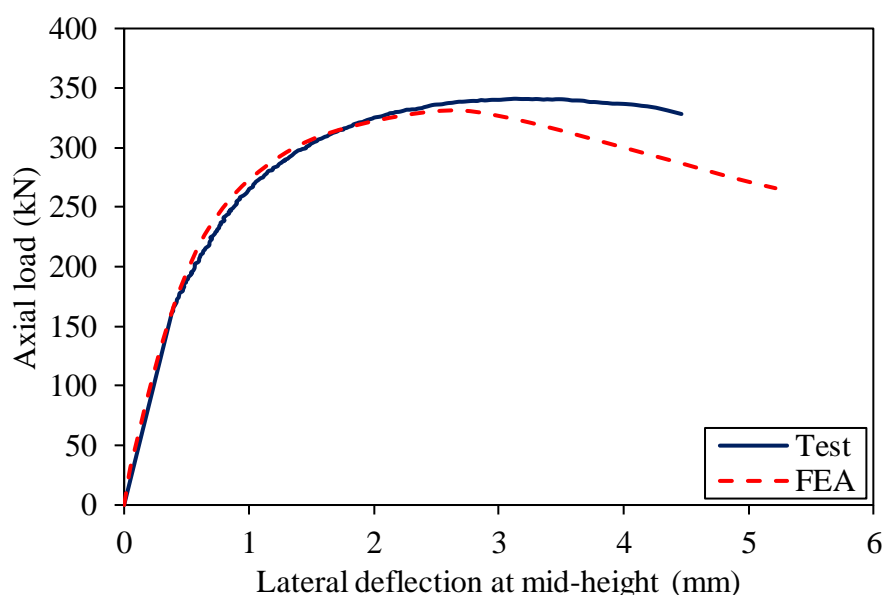


Figure G-32. Test and FEA axial load-lateral deflection at mid-height of specimen
40×100×2C80e3.



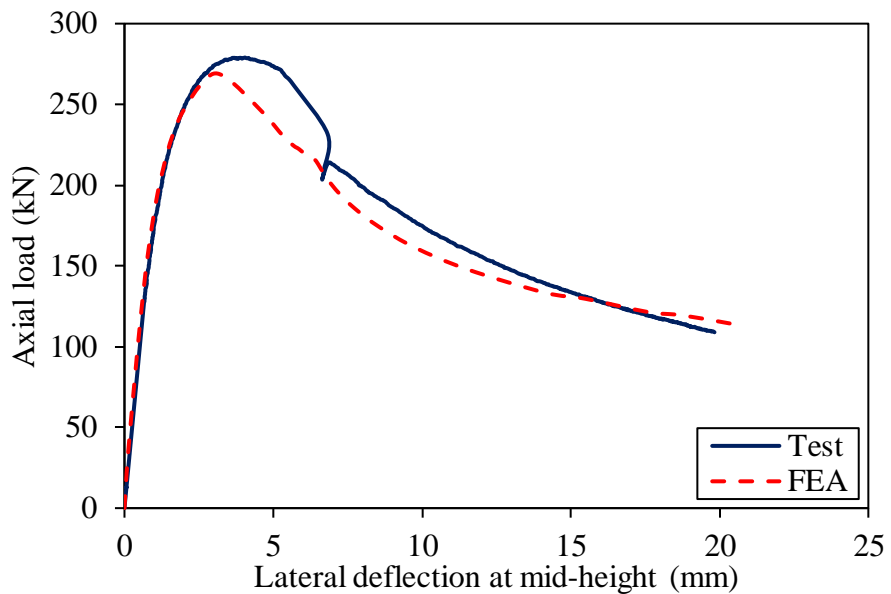


Figure G-33. Test and FEA axial load-lateral deflection at mid-height of specimen
40×100×2C80e8.

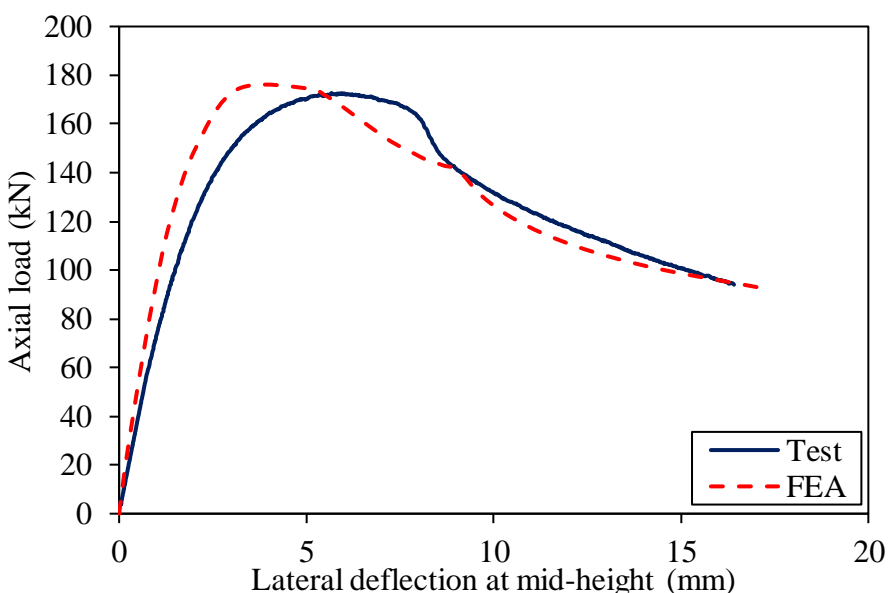


Figure G-34. Test and FEA axial load-lateral deflection at mid-height of specimen
40×100×2C80e20.



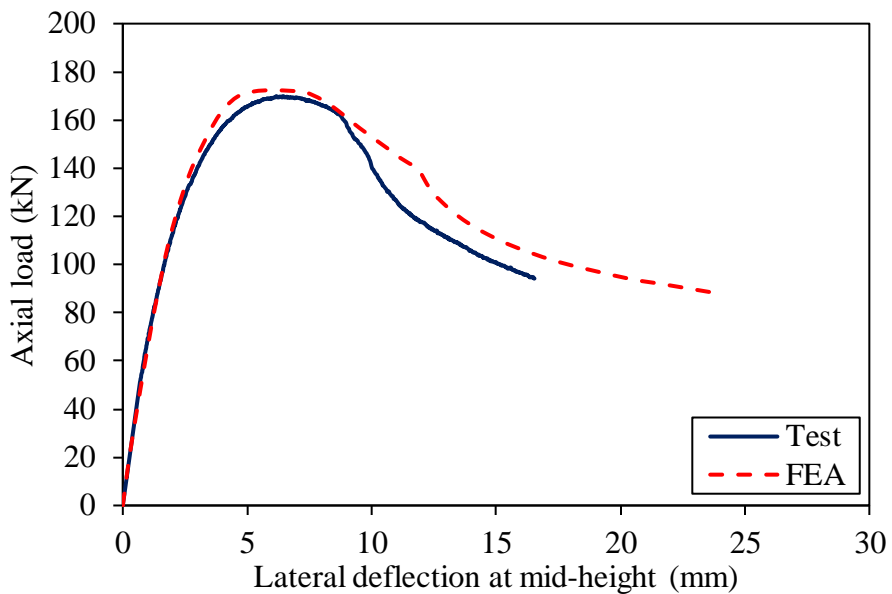


Figure G-35. Test and FEA axial load-lateral deflection at mid-height of specimen
40×100×2C80e20R.

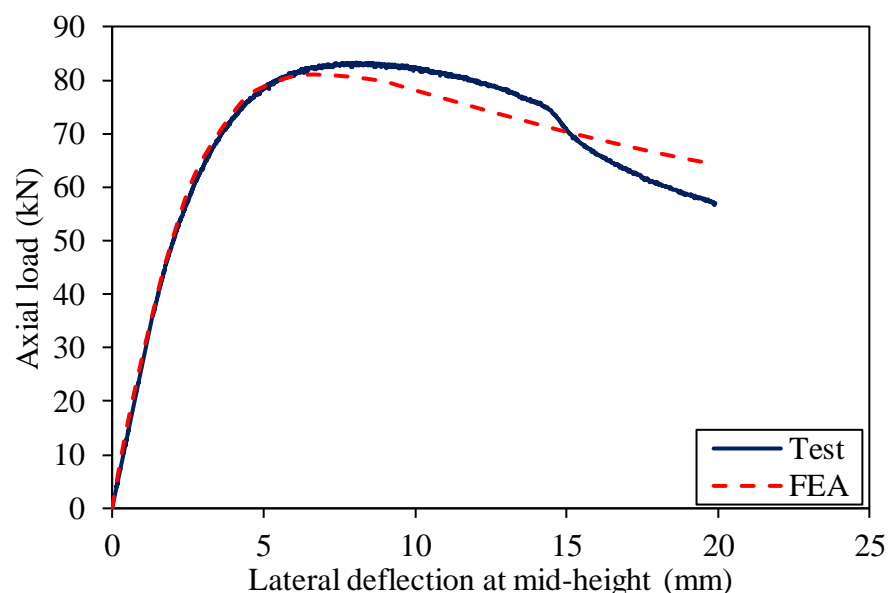


Figure G-36. Test and FEA axial load-lateral deflection at mid-height of specimen
40×100×2C80e50.



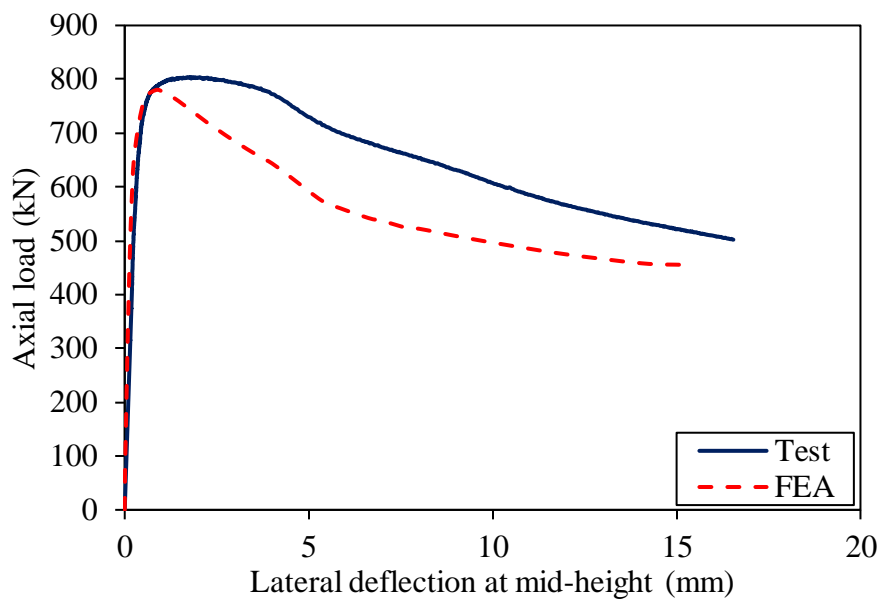


Figure G-37. Test and FEA axial load-lateral deflection at mid-height of specimen
 $40 \times 120 \times 3C40e0$.

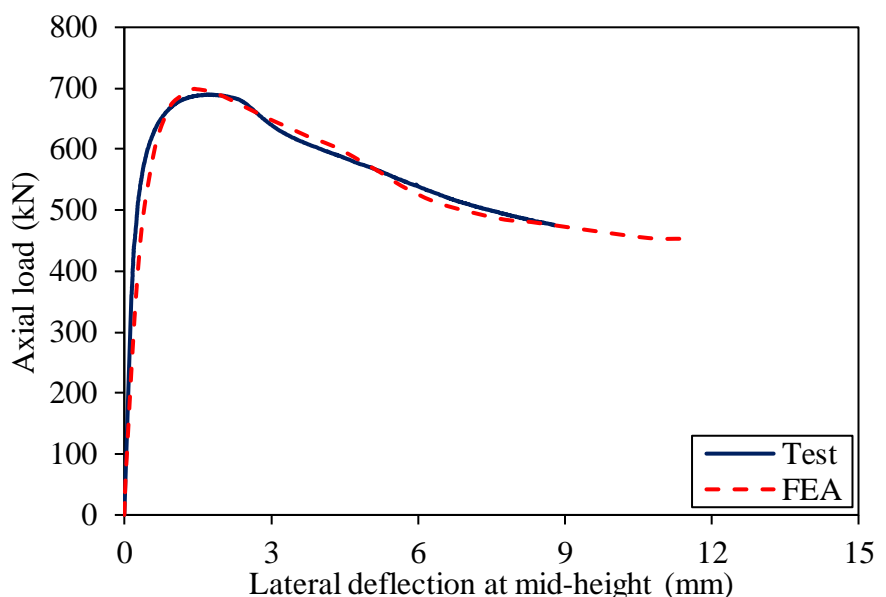


Figure G-38. Test and FEA axial load-lateral deflection at mid-height of specimen
 $40 \times 120 \times 3C40e5$.



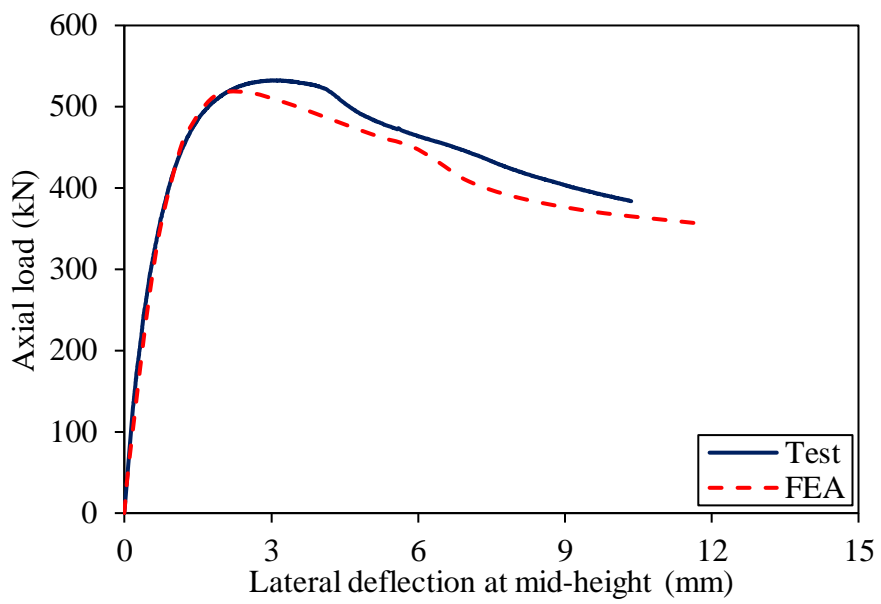


Figure G-39. Test and FEA axial load-lateral deflection at mid-height of specimen
40×120×3C40e15.

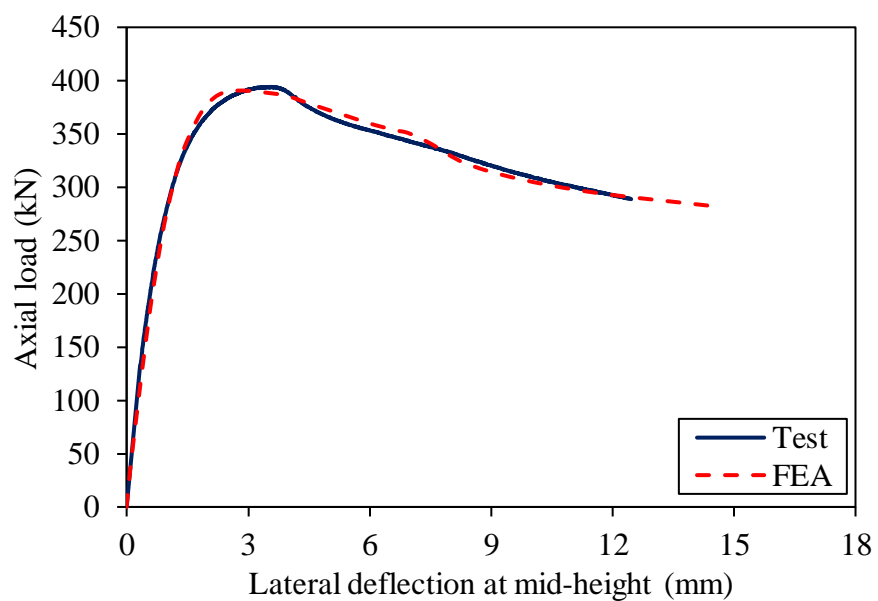


Figure G-40. Test and FEA axial load-lateral deflection at mid-height of specimen
40×120×3C40e30.



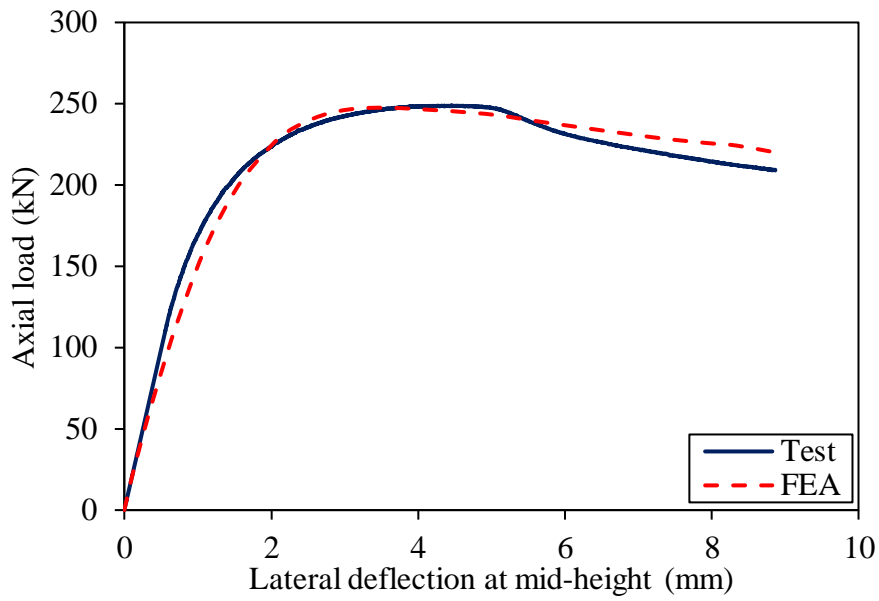


Figure G-41. Test and FEA axial load-lateral deflection at mid-height of specimen
40×120×3C40e60.

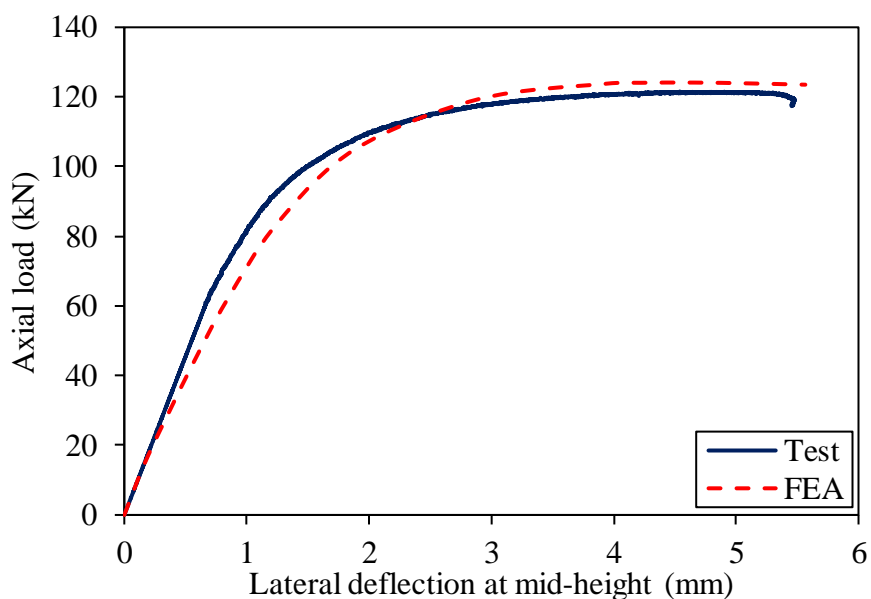


Figure G-42. Test and FEA axial load-lateral deflection at mid-height of specimen
40×120×3C40e130.



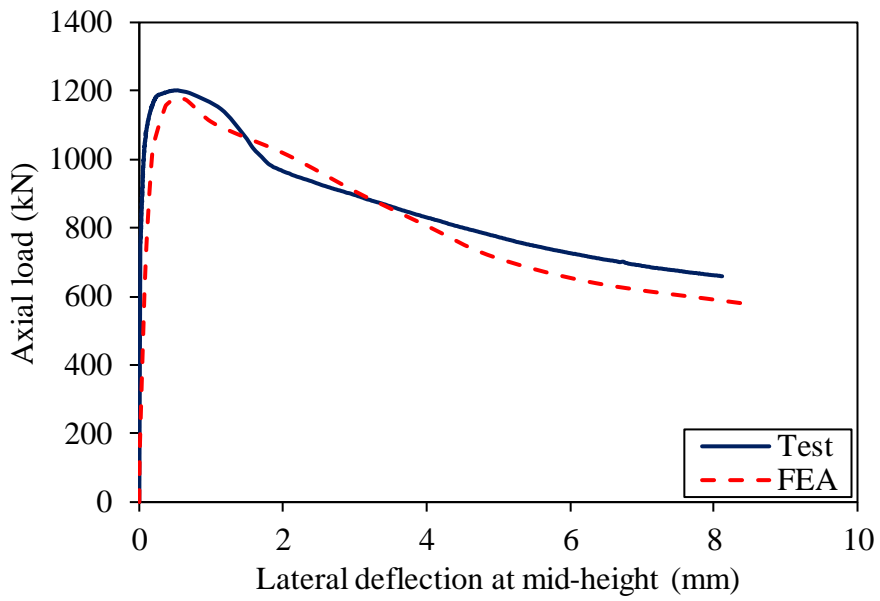


Figure G-43. Test and FEA axial load-lateral deflection at mid-height of specimen
40×120×3C80e0.

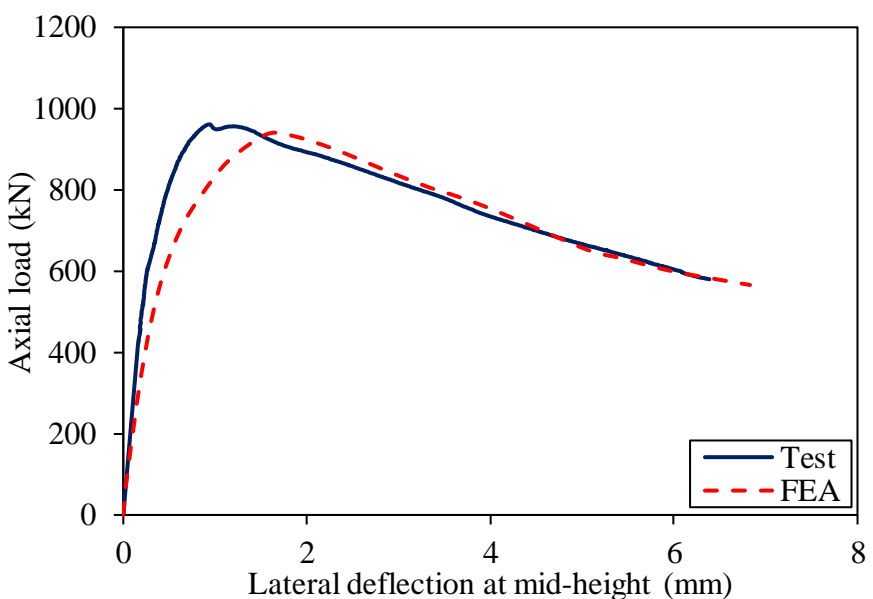


Figure G-44. Test and FEA axial load-lateral deflection at mid-height of specimen
40×120×3C80e5.



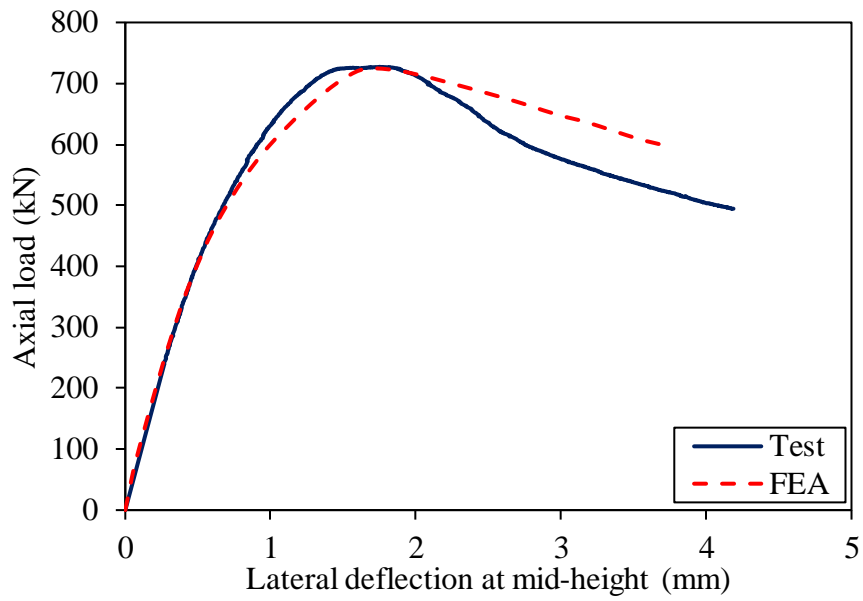


Figure G-45. Test and FEA axial load-lateral deflection at mid-height of specimen
40×120×3C80e15.

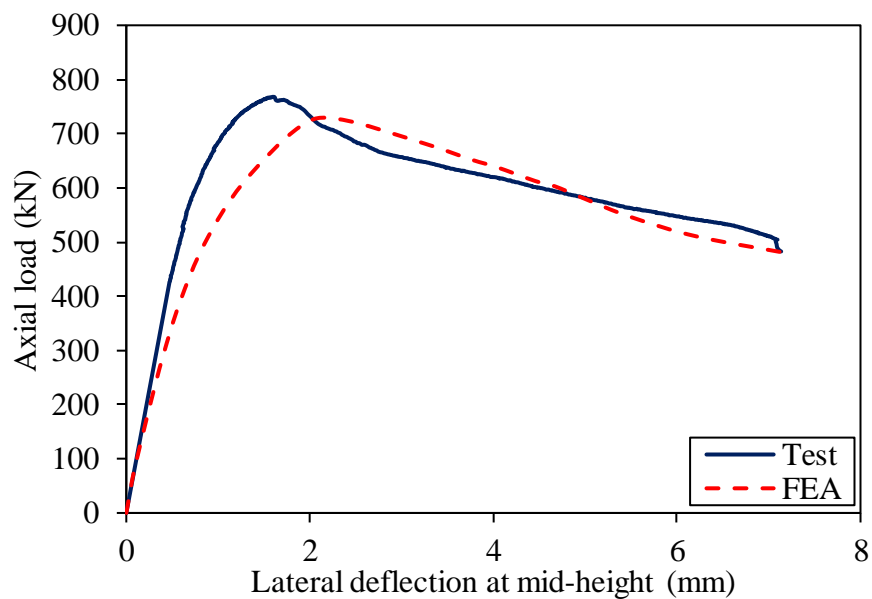


Figure G-46. Test and FEA axial load-lateral deflection at mid-height of specimen
40×120×3C80e15R.



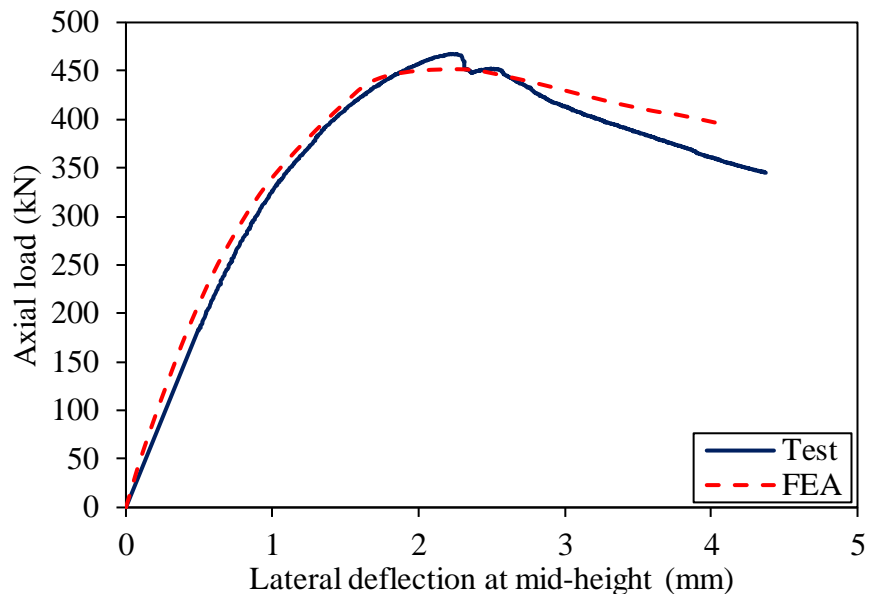


Figure G-47. Test and FEA axial load-lateral deflection at mid-height of specimen
 $40 \times 120 \times 3C80e35$.

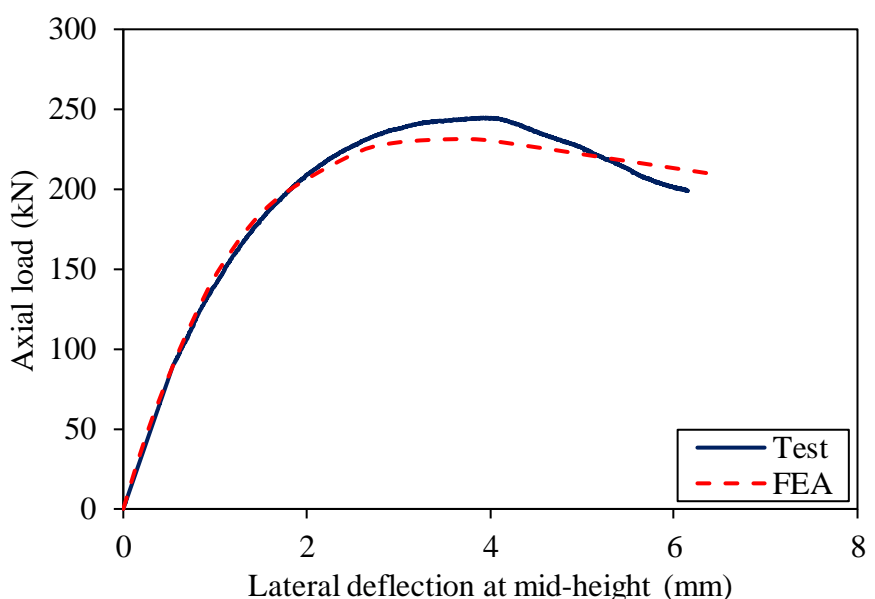


Figure G-48. Test and FEA axial load-lateral deflection at mid-height of specimen
 $40 \times 120 \times 3C80e80$.



PUBLICATIONS

Four supporting international conference papers have been published based on the work presented in this thesis.

- 1) Li, L. and Young, B. (2015), “Material properties of cold-formed ferritic stainless steel at elevated temperatures”, *In Eighth International Conference on Advances in Steel Structures*, Lisbon.
- 2) Li, L. and Young, B. (2016a), “Tests of cold-formed ferritic stainless steel beams”, *In Proceedings of Wei-Wen Yu International Specialty Conference on Cold-Formed Steel Structures 2016*, USA.
- 3) Li, L. and Young, B. (2016b), “Design and behaviour of cold-formed ferritic stainless steel SHS and RHS beams”, *In Proceedings of the 8th International Conference on Steel and Aluminium Structures*, Hong Kong.
- 4) Li, L. and Young, B. (2016c), “Structural performance of concrete-filled ferritic stainless steel members under combined axial load and bending”, *In Proceedings of the 8th International Conference on Steel and Aluminium Structures*, Hong Kong.

